MATERIALS SCIENCE

Guokui Liu
Bernard Jacquier (Eds.)

Spectroscopic Properties of Rare Earths in Optical Materials





Springer Series in
MATERIALS SCIENCE 83

Springer Series in

MATERIALS SCIENCE

Editors: R. Hull R. M. Osgood, Jr. J. Parisi H. Warlimont

The Springer Series in Materials Science covers the complete spectrum of materials physics, including fundamental principles, physical properties, materials theory and design. Recognizing the increasing importance of materials science in future device technologies, the book titles in this series reflect the state-of-the-art in understanding and controlling the structure and properties of all important classes of materials.

62 **Epitaxy**
Physical Principles
and Technical Implementation
By M.A. Herman, W. Richter, and H. Sitter

63 **Fundamentals**
of Ion-Irradiated Polymers
By D. Fink

64 **Morphology Control of Materials**
and Nanoparticles
Advanced Materials Processing
and Characterization
Editors: Y. Waseda and A. Muramatsu

65 **Transport Processes**
in Ion-Irradiated Polymers
By D. Fink

66 **Multiphased Ceramic Materials**
Processing and Potential
Editors: W.-H. Tuan and J.-K. Guo

67 **Nondestructive**
Materials Characterization
With Applications to Aerospace Materials
Editors: N.G.H. Meyendorf, P.B. Nagy,
and S.I. Rokhlin

68 **Diffraction Analysis**
of the Microstructure of Materials
Editors: E.J. Mittemeijer and P. Scardi

69 **Chemical-Mechanical Planarization**
of Semiconductor Materials
Editor: M.R. Oliver

70 **Applications of the Isotopic Effect**
in Solids
By V.G. Plekhanov

71 **Dissipative Phenomena**
in Condensed Matter
Some Applications
By S. Dattagupta and S. Puri

72 **Predictive Simulation**
of Semiconductor Processing
Status and Challenges
Editors: J. Dabrowski and E.R. Weber

73 **SiC Power Materials**
Devices and Applications
Editor: Z.C. Feng

74 **Plastic Deformation**
in Nanocrystalline Materials
By M.Yu. Gutkin and I.A. Ovid'ko

75 **Wafer Bonding**
Applications and Technology
Editors: M. Alexe and U. Gösele

76 **Spirally Anisotropic Composites**
By G.E. Freger, V.N. Kestelman,
and D.G. Freger

77 **Impurities Confined**
in Quantum Structures
By P.O. Holtz and Q.X. Zhao

78 **Macromolecular Nanostructured**
Materials
Editors: N. Ueyama and A. Harada

79 **Magnetism and Structure**
in Functional Materials
Editors: A. Planes, L. Manõsa,
and A. Saxena

80 **Ion Implantation**
and Synthesis of Materials
By M. Nastasi and J.W. Mayer

81 **Metallopolymer Nanocomposites**
By A.D. Pomogailo and V.N. Kestelman

82 **Plastics for Corrosion Inhibition**
By V.A. Goldade, L.S. Pinchuk,
A.V. Makarevich and V.N. Kestelman

83 **Spectroscopic Properties of Rare Earths**
in Optical Materials
Editors: G. Liu and B. Jacquier

Volumes 10–61 are listed at the end of the book.

Guokui Liu Bernard Jacquier (Eds.)

Spectroscopic Properties of Rare Earths in Optical Materials

With 194 Figures and 61 Tables



Springer

Dr. Guokui Liu
Chemistry Division
Argonne National Laboratory
Argonne, IL 60439
USA
E-mail: gkliu@anl.gov

Professor Bernard Jacquier
Université Lyon1, CNRS
10 rue André Marie Ampère
69622 Villeurbanne
France
E-mail: jacquier@pcml.univ-lyon1.fr

Series Editors:

Professor Robert Hull
University of Virginia
Dept. of Materials Science and Engineering
Thornton Hall
Charlottesville, VA 22903-2442, USA

Professor Jürgen Parisi
Universität Oldenburg, Fachbereich Physik
Abt. Energie- und Halbleiterforschung
Carl-von-Ossietzky-Straße 9–11
26129 Oldenburg, Germany

Professor R. M. Osgood, Jr.
Microelectronics Science Laboratory
Department of Electrical Engineering
Columbia University
Seeley W. Mudd Building
New York, NY 10027, USA

Professor Hans Warlimont
Institut für Festkörper-
und Werkstofforschung,
Helmholtzstraße 20
01069 Dresden, Germany

ISSN 0933-033X

ISBN 3-540-23886-7 Springer Berlin Heidelberg New York

ISBN 7-302-07409-7 Tsinghua University Press

Library of Congress Control Number: 2004114853

This work is subject to copyright. All rights are reserved, whether the whole or part of the material is concerned, specifically the rights of translation, reprinting, reuse of illustrations, recitation, broadcasting, reproduction on microfilm or in any other way, and storage in data banks. Duplication of this publication or parts thereof is permitted only under the provisions of the German Copyright Law of September 9, 1965, and the Chinese Copyright Law of September 7, 1999, in their current versions, and permission for use must always be obtained from Springer and Tsinghua University Press. Violations are liable to prosecution under the German and Chinese Copyright Law.

Springer is a part of Springer Science+Business Media.

springeronline.com

© Tsinghua University Press and Springer-Verlag Berlin Heidelberg 2005
Printed in P.R. China

The use of general descriptive names, registered names, trademarks, etc. in this publication does not imply, even in the absence of a specific statement, that such names are exempt from the relevant protective laws and regulations and therefore free for general use.

Cover concept: eStudio Calamar Steinen
Cover production: *design & production* GmbH, Heidelberg

Printed on acid-free paper SPIN: 10926611 57/3141/di 5 4 3 2 1 0

《Spectroscopic Properties of Rare Earths in Optical Materials》

Preface

Decades of scientific research on spectroscopic properties of f-shell electrons has spawned an extensive array of applications for rare-earth activated luminescent and laser materials. From phosphors activated by Eu^{2+}, Eu^{3+} and Tb^{3+} ions for lighting and display to crystals and glasses doped with Er^{3+} and Yb^{3+} for infrared-to-visible up-conversion, rare-earths represent a large share of the lighting materials market. Currently, Nd^{3+} doped crystals such as Nd^{3+}: YAG ($Y_3Al_5O_{12}$) and Nd^{3+}: YVO_4 are the dominant laser media for high power and compact solid-state lasers, while Er^{3+} doped phosphate and silicate glasses prevalent in optical fiber amplifiers and microlasers used in optical telecommunications. Thanks also to materials science development, rare-earths will receive even wider use in the future, entering in the new world of nanotechnologies for instance. In addition to rare-earth activated phosphors and solid-state lasers, optical applications of rare-earths are already an integral part of internet and data communications and are expected to be applied to information storage and processing, and organic and biological devices.

Since the 1960s, several classic books on spectroscopy of rare-earth ions in solids have been published, including those by Wybourne (1965) and Hüfner (1978). More recent advances in spectroscopic theory and laser experiments involving rare-earth ions in solids were also reviewed, for example, in the book edited by Kaplyanskii and Macfarlane (1987). However, in the f-elements research community, we feel the need of a book that updates the information of recent progresses in the field and facilitates understanding and applications of the principles and concepts that are required in rare-earth optical materials characterization and development. The goal of this book is to provide a connection between basic research and materials science through analysis of fundamental spectroscopic properties of rare-earth activated luminescent and laser optical materials. In addition, this book will serve as an updated reference for materials research by covering a number of currently active topics in the field of rare-earth photo-physics and photo-chemistry. Fundamental topics of optical

spectroscopy are addressed with an emphasis on the physical interactions that determine the primary optical properties, including energy level schemes, transitions intensities, line broadening, mechanisms of non-radiative relaxation and energy transfer. Topics of applied research are selected from recent advances in concepts and techniques that created significant opportunities for present and future applications of rare-earth optical materials.

An international collaboration, which includes contributions from authors with both experimental and theoretical expertise, enables us to offer the reader a systematic review of fundamental aspects and to provide a wide coverage on new applications that utilize the electronic transitions of rare-earth ions in solid-state materials. From free-ion and crystal-field energy level structures to transition intensities and line broadening induced by ion-ion and ion-phonon interactions, the first four chapters survey the fundamentals of f-element photo-physics and spectroscopy, and provide a theoretical framework for the subjects that are discussed in the rest of the book. From Chapter 5 onwards, each chapter is devoted to a particular area of importance in new materials characterization or technology development. From up-conversion phenomena, to materials requirements for frequency-domain and time-domain optical memory, to current progress in rare-earth laser materials and phosphors, the concepts and principles discussed in this book were taken directly from the forefront of research in rare-earth optical materials. Moreover, illustration of current progress in fundamental aspects of quantum confinement and quantum electrodynamics is also discussed. To make it easier to read, and also to avoid cluttering up Chapters 1, 2 and 3, the more theoretical derivations of these chapters are given in Appendices A and B. We hope that this book will provide useful information to researchers and students in the field of f-element spectroscopy and materials development.

Although chapters in this book are written independently by individual authors, significant efforts have been made to achieve a coherent connection and systematic balance for the book as a whole. We are grateful to all authors of this book for their excellent contributions.

Guokui Liu
Argonne, Illinois, USA

B. Jacquier
Lyon, France

Contents

1 Electronic Energy Level Structure 1
1.1 Introduction 1
1.2 Electronic States and Coupling Schemes 4
1.2.1 Central Field Approximation 4
1.2.2 *LS* Coupling and Intermediate Coupling 7
1.3 Free-ion Interactions 11
1.3.1 Coulomb Interaction 11
1.3.2 Spin-orbit Interaction 14
1.3.3 Corrections to Free-ion Hamiltonian 15
1.3.4 Reduced Matrices and Free-ion State Representation 17
1.3.5 Parameterization of the Free-ion Interactions 18
1.3.6 Energy Levels of $4f^N$ Configurations and Binding Energies Relative to Host Band 23
1.4 Crystal-field Interaction 26
1.4.1 Crystal-field Hamiltonian and Matrix Element Evaluation 28
1.4.2 Symmetry Rules 32
1.4.3 Empirical Evaluation of Crystal-field Parameters 37
1.4.4 Theoretical Evaluation of Crystal-field Parameters 39
1.4.5 Corrections to the Crystal-field Hamiltonian 46
1.5 Analysis of Crystal-field Spectra 50
1.5.1 Experimental Data 51
1.5.2 Computational Modeling 54
1.6 Modeling of $4f^N - 4f^{N-1}5d$ Spectra 57
1.6.1 Energy Gaps Between the $4f^N$ and Excited Configurations 57
1.6.2 Hamiltonian for $4f^{N-1}5d$ Configurations 59
1.6.3 Determination of Hamiltonian Parameters 60
1.7 Magnetic and Hyperfine Interactions 64
1.7.1 Zeeman Effect 65
1.7.2 Magnetic Hyperfine Interaction 67
1.7.3 Nuclear Electric Quadrupole Interaction 69
1.7.4 Ion-ligand Hyperfine Interaction 72
1.7.5 Pr^{3+} 73
1.7.6 Eu^{3+} 76

1.7.7 Tb^{3+} 85
1.7.8 Other Ions 88
References 89

2 Transition Intensities 95
2.1 Introduction 95
2.2 Basic Equations 96
2.2.1 Electric and Magnetic Dipole Operators 96
2.2.2 Polarization Selection Rules 98
2.2.3 Vibronic Transitions 100
2.3 One Photon Transitions Within the $4f^N$ Configuration 102
2.3.1 General Theory 103
2.3.2 Transitions Between Crystal-field Levels 104
2.3.3 Transitions Between J Multiplets 108
2.3.4 Selection Rules 109
2.3.5 Vibronic Transitions 109
2.3.6 Circular Dichroism 110
2.3.7 Parameter Fits 111
2.3.8 Comparison with First-principles Calculations 117
2.3.9 Extensions to the Models 121
2.4 Higher-energy Transitions 122
2.4.1 $4f^N \leftrightarrow 4f^{N-1}$ 5d Transitions 122
2.4.2 Charge Transfer 123
2.5 Two-photon Processes 124
2.5.1 $f^N \leftrightarrow f^N$ Transitions 124
2.5.2 $4f^N \leftrightarrow 4f^{N-1}$ 5d Transitions 126
2.6 Conclusions 126
References 126

3 Ion-phonon Interactions 130
3.1 Introduction 130
3.2 Basic Concepts: Hamiltonian of the Ion-phonon Interaction, Adiabatic and Nonadiabatic Terms 131
3.3 Coupling Constants 139
3.4 Density Matrix Formalism in the Quantum Theory of Relaxation 145
3.5 Thermal Shifts of Zero-phonon Line Positions 151
3.6 Non-radiative Transitions Between Crystal Field Energy Levels 153
3.6.1 One- and Two-phonon Transition Rates 153
3.6.2 Phonon Contributions to Linewidths 155
3.6.3 Multiphonon Relaxation 158

3.7 Vibrational Structure of the Optical Spectra ····· 166
3.8 Simulations of the Ion-phonon Interaction Effects ····· 170
3.8.1 Impurity Rare Earth Single Ion Centers in the $LiYF_4$ Crystal ····· 171
3.8.2 Relaxation Broadening of Optical Transitions in Pr^{3+} Dimer Centers in $CsCdBr_3$ ····· 182
3.9 Conclusions ····· 185
References ····· 186

4 Line Broadening Mechanisms and Their Measurement ····· 191
4.1 Introduction ····· 191
4.2 Inhomogeneous Broadening ····· 194
4.2.1 Zero-phonon Linewidths of 4f→4f and 4f→5d Transitions ····· 194
4.2.2 Line Broadening from Defects and Disorder ····· 195
4.2.3 Site-selective Spectroscopy ····· 197
4.2.4 Ultranarrow Inhomogeneous Linewidths ····· 201
4.3 Non-inhomogeneous Sources of Line Structure ····· 202
4.3.1 Hyperfine Structure and Isotope Shifts ····· 202
4.3.2 Vibronic Sidebands ····· 203
4.4 Homogeneous Broadening ····· 204
4.4.1 Ion-phonon Interactions ····· 205
4.4.2 Ion-ion Interactions ····· 208
4.4.3 Ion-nuclear Spin-spin Interactions ····· 213
4.5 Measurement of Line Broadening and Examples ····· 214
4.5.1 Fluorescence Line-narrowing ····· 215
4.5.2 Spectral Hole Burning ····· 218
4.5.3 Coherent Transient Spectroscopy ····· 227
4.6 Disordered, Low-dimensional and Nanostructure Crystalline Materials ····· 238
4.6.1 Disordered Materials ····· 239
4.6.2 Low Dimensional Systems ····· 246
4.6.3 Nanocrystalline Materials ····· 251
4.7 Conclusions ····· 257
References ····· 257

5 Up-conversion in RE-doped Solids ····· 266
5.1 Introduction and Historical Background ····· 267
5.2 Energy Transfers Between RE Ions; Role of Energy Diffusion in Up- and Down-conversion ····· 268
5.2.1 Recall of Basics of Energy Transfer with

Activator in Its Ground State ····· 268
5.2.2 Up-conversion Processes by Sequential Energy Transfers; Comparison with ESA and Typical Examples ····· 276
5.3 Up-conversion in Single-ion and Pair-level Level Description; Theoretical and Experimental Discrimination ····· 279
5.3.1 Application of Cooperative Luminescence; Theory and Examples ····· 284
5.3.2 Some Experimental Results for APTE Effect and Their Implications in Various Field ····· 286
5.4 Cross-relaxation and the Photon Avalanche Effect ····· 296
5.4.1 The Avalanche Process as a Positive Feedback System ····· 298
5.4.2 Conditions for Observing an Avalanche Threshold ····· 300
5.4.3 Er^{3+}:$LiYF_4$ as an Avalanche Model Experiment ····· 302
5.4.4 Photon Avalanche in Er^{3+}-doped Fluoride Glasses in Fibre and Bulk Shape ····· 306
5.4.5 Avalanche in Co-doped Systems ····· 309
5.4.6 Up-conversion Laser with Multiphonon-assisted Pumping Scheme and Photon Avalanche ····· 310
5.5 Perspectives and Future Advances ····· 311
5.5.1 Up-conversion UV Tunable Lasers ····· 311
5.5.2 New Materials for Low-intensity IR Imaging ····· 312
5.5.3 Up-conversion Material Intrinsic Bistability ····· 312
5.6 Conclusions ····· 314
References ····· 315

6 Current Topics in Rare-earth Lasers ····· 320
6.1 Introduction ····· 320
6.2 Spectroscopic and Laser Parameters ····· 321
6.2.1 Basic Laser Parameters ····· 322
6.2.2 Determination of Absorption Cross Sections ····· 328
6.2.3 Determination of Emission Cross Sections ····· 329
6.2.4 Determination of Radiative Lifetimes and Branching Ratios ····· 336
6.3 UV-visible Laser Sources ····· 340
6.3.1 Compact and Tunable UV Lasers Based on Ce^{3+} Doped Crystals; Prospects with Other Ions ····· 340
6.3.2 Lasers Based on Nd^{3+} and Yb^{3+} Doped Nonlinear Crystals ····· 345
6.4 Near- and Mid-infrared Laser Sources ····· 349
6.4.1 High-power and Ultrafast Lasers Based on Yb^{3+} Doped Materials ····· 349

6.4.2 Rare-earth Doped Crystals for Telecommunications and Eyesafe Laser Applications ····· 355
6.4.3 Low-frequency Phonon Materials for Mid-infrared Lasers ····· 364
6.5 Conclusions ····· 369
Appendix ····· 370
6.A Laser Threshold Condition ····· 370
6.B Minimum Fraction of Excited Population β_{min} ····· 371
6.C Energy Transfer Rates ····· 371
6.D Einstein Coefficients ····· 372
6.E List of Acronyms ····· 372
References ····· 373

7 Rare Earth Materials in Optical Storage and Data Processing Applications ····· 379
7.1 Introduction ····· 379
7.1.1 Equivalence of Holeburning and Photon Echoes in Storage and Signal Processing Applications ····· 381
7.1.2 Material Parameters for Optical Data Storage ····· 382
7.1.3 Dephasing and Spectral Diffusion ····· 382
7.2 Eu^{3+} Materials ····· 384
7.2.1 Properties of Y_2SiO_5 ····· 385
7.2.2 $Eu^{3+}:Y_2SiO_5$ ····· 386
7.2.3 Other Experiments in $Eu^{3+}:Y_2SiO_5$ ····· 391
7.2.4 $Eu^{3+}:Y_2O_3$ ····· 391
7.2.5 $Eu^{3+}:YAlO_3$ ····· 393
7.3 Pr^{3+} Materials ····· 394
7.3.1 $Pr^{3+}:Y_2SiO_5$ ····· 394
7.3.2 $Pr^{3+}:YAlO_3$ ····· 397
7.3.3 $Pr^{3+}:Y_3Al_5O_{12}$ ····· 398
7.3.4 $Pr^{3+}:LaF_3$ ····· 399
7.4 Tm^{3+} Materials ····· 399
7.4.1 $Tm^{3+}:Y_3Al_5O_{12}$ ····· 401
7.4.2 $Tm^{3+}:Lu_3Al_5O_{12}$ ····· 404
7.4.3 $Tm^{3+}:Y_{1.5}Lu_{1.5}Al_5O_{12}$ ····· 405
7.4.4 $Tm^{3+}:Y_3Ga_5O_{12}$ ····· 406
7.4.5 $Tm^{3+}:LaF_3$ ····· 407
7.4.6 $Tm^{3+}:Y_2SiO_5$ ····· 407
7.4.7 $Tm^{3+}:Y_2Si_2O_7$ ····· 408
7.4.8 $Tm^{3+}:Y_2O_3$ ····· 409
7.4.9 $Tm^{3+}:YAlO_3$ ····· 409
7.4.10 Tm^{3+} Materials Summary ····· 410

7.5 Er^{3+} Materials 411
7.5.1 Properties of $Er^{3+}:Y_2SiO_5$ 412
7.5.2 Properties of $Er^{3+}:Y_2O_3$ 416
7.5.3 Properties of $Er^{3+}:LiNbO_3$ 416
7.5.4 Properties of $Er^{3+}:YAlO_3$ 417
7.5.5 Properties of $Er^{3+}:Y_3Al_5O_{12}$ 419
7.5.6 Properties of Er^{3+} Doped Tungstates 420
7.5.7 Er^{3+} Materials Summary 420
7.6 Other Materials 421
7.6.1 Eu^{2+} Materials 422
7.6.2 Deuterated Fluorides 423
7.6.3 Eu^{3+} Persistence 424
7.6.4 Nd^{3+} Systems 424
7.7 Conclusions 426
References 426

8 Rare Earth Doped Confined Structures for Lasers and Amplifiers 430
8.1 Introduction 430
8.2 Propagation and Amplification: the Key Parameters 432
8.2.1 Opto-geometrical Parameters 432
8.2.2 Spectroscopic Parameters 433
8.2.3 Amplification into a Waveguide 438
8.2.4 Material Requirements for Fabrication of Waveguide 441
8.2.5 Other Specific Properties: Photosensitivity and Photorefractivity 442
8.3 Waveguide Amplifiers and Lasers 443
8.3.1 Erbium-doped Fiber Amplifier 444
8.3.2 Praseodymium-doped Fiber Amplifier 449
8.3.3 Thulium-doped Fiber Amplifier 450
8.3.4 Fiber Lasers 452
8.3.5 Optical Integrated Amplifiers and Lasers 453
8.4 Optical Microcavities and Nanoconfinement 454
8.4.1 Optical Confinement 455
8.4.2 Experimental Evidences 456
8.4.3 Various Devices 457
8.5 Conclusions 458
References 458

9 Rare Earth Luminescent Centers in Organic and Biochemical Compounds 462
9.1 Introduction 462

9.2 Sensitizing the Luminescence of Trivalent Lanthanide Ions 464
9.2.1 Establishing the Importance of the Triplet State 464
9.2.2 Mechanisms of Energy Transfer 467
9.3 Preventing Nonradiative Deactivation of the Metal Ion Luminescent States 469
9.3.1 Vibrational Deactivation Processes 469
9.3.2 Electronic Deactivation Processes 472
9.4 Designing a Luminescent Probe 476
9.4.1 Qualitative Rules 476
9.4.2 Quantitative Estimates 477
9.5 Luminescent Lanthanide Complexes with Organic Ligands 481
9.6 Applications in Biomedical Analyses 486
9.6.1 Fluoroimmunoassays 486
9.6.2 Responsive Systems 489
9.7 Conclusions 491
Appendix 491
9.A Chemical Formulae of Compounds Cited in the Text 491
9.B Glossary and Chemical Formulae 496
References 497

10 Rare Earth Ions in Advanced X-ray Imaging Materials 500
10.1 X-ray Phosphors 500
10.2 X-ray Phosphors Used for Intensifying Screens 502
10.2.1 Calcium Tungstate 503
10.2.2 Rare Earth Tantalate Based Phosphors 504
10.2.3 Europium Activated Barium Fluoro-chloride Phosphors 509
10.2.4 Tb- and Tm-activated Lanthanum Oxybromides 511
10.2.5 Tb^{3+}-activated Gadolinium Oxysulfide 513
10.3 X-ray Storage Phosphors and Their Applications 514
10.3.1 Physical Mechanism of Photostimulated Luminescence 515
10.4 X-ray Phosphors for Computed Tomography 518
10.4.1 Scintillators for X-ray Computed Tomography 521
10.5 Scintillators for Electromagnetic Calorimetric Detection 524
10.5.1 Cerium Fluoride 525

10.5.2 Ce^{3+}-activated Gd_2SiO_5 and Lu_2SiO_5 ····· 526
10.6 Conclusions ····· 527
References ····· 527
Appendix A Effective Operator Calculations ····· 530
A.1 Effective Hamiltonians and Effective Operators ····· 530
A.2 Perturbation Expansions ····· 531
A.3 Symmetries and Selection Rules ····· 534
A.4 Implications ····· 535
References ····· 536

Appendix B Matrix Elements of Tensor Operators ····· 537
B.1 Angular Momentum States and Operators ····· 537
B.2 Clebsh-Gordan Coefficients and 3-j Symbols ····· 537
B.3 Tensor Operators and the Wigner-Eckart Theorem ····· 538
B.4 More Complex Situations ····· 539
References ····· 540

Keywords Index ····· 541

Materials Index ····· 545

List of Contributors

Editors:

Guokui Liu — Chemistry Division, Argonne National Laboratory, Argonne, Illinois 60439, USA
Tel. 630 262 4630, Fax 630 252 4225
E-mail: gkliu@anl.gov

B. Jacquier — Universite Claude Bernard Lyon 1, 43 bd du 11 Novembre 1918, Villeurbanne F-69622, France
Tel. 33-(0)4 72 44 83 36, Fax 33-(0)4 72 43 11 30
E-mail: Jacquier@pcml.univ-lyon1.fr

Chapter Authors:

Guokui Liu (Chapter 1)

M. F. Reid (Chapter 2) — Department of Physics & Astronomy, University of Cantebury, Christchurch 8020, New Zealand
Tel. 64 3 364 2548, Fax 64 3 364 2469
E-mail: m.reid@phys.canterbury.ac.nz

B. Z. Malkin (Chapter 3) — Physics Department, Kazan State University, 420008 Kazan, Russia Federation
E-mail: boris.malkin@ksu.ru

R. S. Meltzer (Chapter 4) — Department of Physics and Astronomy, University of Georgia, Athens, GA 30602, USA
Tel. 706 542 5515, Fax 706 542 2492
E-mail: rmeltzer@hal.physast.uga.edu

F. Auzel
(Chapter 5)
Centre National de la Recherche Scientifique, GOTR, UMR 7574, France
E-mail: francois. auzel@wanadoo. fr

R. Moncorgé
(Chapter 6)
CIRIL, UMR 6637 CNRS-CEA-ISMRA, Université de Caen, 6 Boulevard Maréchal Juin, 14050 Caen, France
E-mail: moncorge@spalp255. ismra. fr

Y. C. Sun
(Chapter 7)
Physics Department, Montana State University, Bozeman, Montana 59717, USA
Tel. 406 994 6163, Fax 406 994 4452
E-mail: sun@physics. montana. edu

B. Jacquier
(Chapter 8)
B. Jacquier, L. Bigot, S. Guy, A. M. Jurdyc
University Claude Bernard Lyon 1
Villeurbanne F-69622, France

J. -C. G. Bünzli
(Chapter 9)
Chemistry Department, University of Lausanne, BCH 1402, Lausanne, CH-1015, Switzerland
Tel. 41 21 692 3821, Fax 41 21 692 3825
E-mail: Jean-claude. bunzli@icma. unil. ch

M. Z. Su
(Chapter 10)
College of Chemistry and Molecular Engineering, Peking University, Beijing, 100871, China
Tel. 86 10 6275 1715, Fax 86 10 6275 1708
E-mail: sumz@pku. edu. cn

W. Zhao
(Chapter 10)
Department of Chemistry, University of Arkansas, 2801 South University Ave. Little Rock, AR 72204, USA
E-mail: wxzhao@ualr. edu

1 Electronic Energy Level Structure

Guokui Liu

1.1 Introduction

From fluorescent lamps, solid-state lasers, to optical amplifiers in fiber optics, rare earth (RE) elements, or lanthanides, have been widely used to activate luminescent and photonic materials. A majority of applications involve electronic transitions between states within a $4f^N$ configuration of trivalent (or divalent) RE ions doped into transparent host materials. The popular solid-state laser of Nd^{3+}: YAG, for example, utilizes the 1.05-μm electronic transition from the $^4F_{3/2}$ to $^4I_{11/2}$ multiplets within the $4f^3$ configuration of the Nd^{3+} ion (see Chapter 6). Similarly, the Er^{3+} fluorescence at 1.5-μm, emitted from the first excited multiplet $^4I_{13/2}$ of the $4f^{11}$ configuration, is important because of its high quantum efficiency and optimal wavelength for optical amplification in telecommunications. Green fluorescence of Er^{3+} from the $^4S_{3/2}$ state can be induced through up-conversion excitation from several states at lower energies (see Chapter 5). These applications utilize the unique properties of the 4f electrons that have localized states and exhibit weak coupling to ligand electrons and lattice vibrations. The 4f spectroscopic properties, including the energy level structure and the dynamics of the electronic transitions of RE ions in solids, thus primarily define the optical properties of an RE activated device.

With energy levels at more than 30,000 cm^{-1} above the ground states of the $4f^N$ configurations, there are 5d, 6s, 6p orbitals in the RE ion electronic structure. The 5d states exhibit less localized nature and stronger coupling to lattice vibrations, and since the inter-configuration $4f^N$ to $4f^{N-1}5d$ transitions of the RE ions are parity-allowed, they have intensities up to 10,000 times stronger than the strongest $4f^N$ to $4f^N$ transitions (see Chapter 2). Due to these electronic properties, $4f^N$ to $4f^{N-1}5d$ transitions have become increasingly important in recent years for applications in fast scintillators and ultraviolet laser sources. A fundamental understanding of the electronic energy levels of RE ions in the $4f^N$ and $4f^{N-1}5d$ configurations is essential not only in spectroscopy but also in materials characterization.

What appears to be unique in solid-state RE spectroscopy is that the electronic energy level structure is established primarily using the quantum theory of atomic spectroscopy, and all collective solid-state effects can be treated as a perturbation known as the crystal-field interaction (Stevens, 1952; Wybourne, 1965; Newman and Ng, 2000). Such a simple approximation works very well

for RE ions in a $4f^N$ configuration in which the electrons in the partially occupied 4f shell are shielded by the electrons in the 5s and 5p shells from interacting with the ligands and, therefore, have little participation in chemical bond formation (Reisfeld and Jφrgensen, 1977). Figure 1.1 shows, with Nd^{3+} as an example, the radial distribution of electrons in different shells. It is clear that most of the 4f orbitals are much less extended than the 5s and 5p orbitals. As a result, the electronic transitions between the 4f states are very sharp and have atomic-like spectral characteristics. It is based on the localized nature of the electronic properties that a general theoretical framework of solidstate RE spectroscopy was developed (Stevens, 1952; Judd, 1963a; Wybourne, 1965; Dieke, 1968).

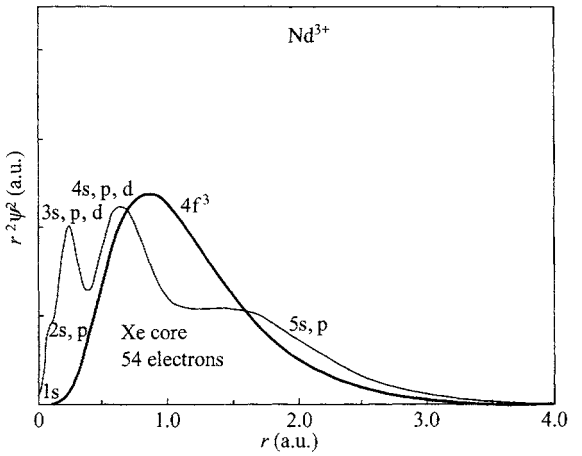


Figure 1.1 Radial wave function $r^2\psi^2$ as a function of r in atomic radius for $4f^3$ electrons of Nd^{3+} in comparison with the charge distribution of its core (Xe) configurations

When a 4f electron is excited into a 5d orbital that extends beyond the 5s and 5p orbitals, the spectroscopic properties of RE ions in an electronic configuration such as $4f^{N-1}$ 5d are influenced more strongly by the lattice. Therefore, the electronic transitions between the $4f^N$ and $4f^{N-1}5d$ states, through absorption or emission of photons, are expected to be characteristically very different from transitions within the $4f^N$ configuration. A modification of the crystal-field theory is necessary for modeling stronger ion-lattice interactions in analysis of the energy level splitting and the excited state dynamics.

With restrictions on localized electronic interactions in a well-defined crystalline environment, the overall spectroscopic properties of an RE ion may be determined by evaluating interactions in various forms of mechanisms. Table 1.1 lists the scales of electronic energy levels in terms of different mechanisms of electronic interactions. Accordingly, theoretical analyses of the electronic interactions and their contribution to energy level splitting will be discussed in the

order of energy level scales. Historically, the development of a complete Hamiltonian for $4f^N$ configurations was approached in two stages. The first dealt with the fundamental electronic interactions, including electrostatic Coulomb interactions and spin-orbit coupling. The second dealt with the crystal field interaction that arises when the ion is in a condensed phase. Subsequently, additional effective operators dealing with higher order free-ion interactions and corrective crystal-filed interactions were introduced to reproduce more accurately the energy level structures observed in experiments. The theoretical framework, thus utilizes well-established theories in two conventional fields: (1) the quantum theory of atomic spectroscopy that is the foundation for establishing free-ion energy level structures; (2) the point group theory that facilitates the determination of crystal-field splittings according to the symmetry properties of a crystalline lattice.

As listed in Table 1.1, the scale of crystal-field splitting is smaller than that of the free-ion splitting, while the hyperfine energy level structures are even smaller, thus ensuring the legitimate application of perturbation theory to calculations of crystal-field splitting and hyperfine structures. In the framework of crystal-field modeling, electronic energy levels are calculated by diagonalizing an effective-operator Hamiltonian with the basis free-ion wave functions, and the parameters of the effective operators are determined by fitting the experimentally observed energy levels to the calculated ones. As an empirical approach to modeling the energy level structure of RE ions in solids, crystal-field theory was very successful not only in predicting the exact number of crystal-field levels for an RE ion in a given host material, but also in accurately determining their energies.

Table 1.1 Energy level scales of rare earth ions in crystals

Interaction Mechanism	Energy (cm^{-1})	Optical Probe
Configuration splitting ($4f^N - 4f^{N-1}\,5d$)	10^5	UV and VUV spectroscopy
Splitting within a $4f^N$ configuration		
Non-central electrostatic field	10^4	Absorption, fluorescence or laser excitation spectroscopy
Spin-orbit interaction	10^3	
Crystal field interaction	10^2	
Ion-ion interaction induced band structure (in stoichiometric compounds)	$10^{-2} - 10$	
Hyperfine splitting	$10^{-3} - 10^{-1}$	Selective and nonlinear laser spectroscopy
Superhyperfine splitting (ion-ligand hyperfine interaction)	$10^{-4} - 10^{-2}$	

In this chapter, we discuss the electronic energy level structure of RE ions in crystalline solids. Given that the theoretical foundation has already be established and discussed comprehensively in several books (Judd, 1963a; Wybourne, 1965; Dieke 1968; Abragam and Bleaney, 1986; Hüfner, 1978; Weissbluth, 1978; Cowan, 1981; Newman and Ng, 2000), we will not enter into details of

the spectroscopic theory. Instead, an overview of modeling the electronic energy level structure of RE ions in dielectric crystals is provided. An effective operator Hamiltonian is introduced with tensor operators defined according to the nature of electronic interactions. The terms of Hamiltonian include free-ion interactions such as electrostatic Coulomb interactions and spin-orbit coupling, the ion-ligand interactions described in the framework of crystal-field theory, and the hyperfine interactions treated as a perturbation on electronic energy levels. Solutions to the Hamiltonian are obtained primarily through empirical approaches in which the phenomenological parameters of the effective operators of the Hamiltonian are determined. The calculations of the electronic energy level structures of RE ions require complicated tensor operation and the theory of angular momentum coupling (Judd, 1963a; Weissbluth, 1978; Cowan, 1981). In Appendices A and B of this book, properties of tensor operators, particularly the effective-operator Hamiltonian, and angular momentum coupling are briefly discussed.

Spectroscopic studies of magnetic and hyperfine interactions of RE ions in solids are an important part of solid-state RE spectroscopy and have gained significant applications in both fundamental understanding of physical interactions and materials characterization (see Chapters 4, 5 and 7). The advances in high resolution and nonlinear laser spectroscopic techniques have facilitated the measurements of RE hyperfine energy levels in great detail (Levenson, 1982; Macfarlane and Shelby, 1987). In Section 1.6, we discuss various mechanisms of hyperfine interactions and Zeeman effect. Their contributions to energy level splittings from the GHz to the kHz spectral range are evaluated on the same basis of crystal-field interaction.

It is the author's intention to outline the practical procedures of analyzing experimental spectra and, at the same time, to provide the reader a clear theoretical understanding of the electronic interactions, including crystal-field and hyperfine interactions of RE ions in crystals. In this regard, this chapter may stand alone as a useful guide to chemists and materials scientists in analysis of RE spectra. However, more importantly, this chapter serves as an introduction to other chapters, which assume the reader's understanding of the concepts of electronic interactions and the RE energy level structures.

1.2 Electronic States and Coupling Schemes

1.2.1 Central Field Approximation

A conventional approach to solving Schrödinger equation for an N-electron atomic system is to use the central field approximation and Hartree-Fock method (Hartree, 1957; Slater, 1960; Weissbluth, 1978). In the central field approximation, each electron is assumed to move independently in the field of the nucleus and a central field that is made up of the spherically averaged

potential fields of each of the other electrons. The quantum mechanical solution for such a central field system is the same as that for a single electron hydrogen atom. With the concept of central field approximation, the non-spherical part of the electronic interactions is treated as a perturbation to a spherically symmetric potential, so that the basis of the hydrogen atom wave functions can be used to construct wave functions for an N-electron atom (ion). This method has been used to classify electronic states and evaluate energy levels of lanthanide and actinide ions (Judd, 1963a; Wybourne, 1965).

The primary terms of the Hamiltonian for an N-electron ion in the absence of external fields is commonly expressed as

$$\mathscr{H} = \mathscr{H}_0 + \mathscr{H}_C + \mathscr{H}_{SO} \tag{1.1}$$

where

$$\mathscr{H}_0 = -\sum_{i=1}^{N} \frac{\hbar^2}{2m} \nabla_i^2 - \sum_{i=1}^{N} \frac{Ze^2}{r_i}, \tag{1.2}$$

$$\mathscr{H}_C = \sum_{i<j}^{N} \frac{e^2}{r_{ij}}, \tag{1.3}$$

$$\mathscr{H}_{SO} = \sum_{i}^{N} \xi(r_i) \boldsymbol{l}_i \cdot \boldsymbol{S}_i. \tag{1.4}$$

In Eq. (1.2), the first term is the kinetic energy, and the second term is the potential energy of the electrons in the field of the nucleus, which is purely radial and contributes energy shifts that are the same for all the levels belonging to a configuration without affecting the energy level structure of the configuration. In Eq. (1.3), the term $\mathscr{H}_C$ represents the inter-electron Coulomb repulsion between a pair of electrons at a distance of r_{ij}, which varies for different states of the same configuration. In Eq. (1.4), the term $\mathscr{H}_{SO}$ describes the spin-orbit interactions, which can be understood as magnetic dipole-dipole interactions between the spin and angular moment of the electrons. The spin-orbit coupling constant $\xi(r_i)$ is defined as a sole function of r_i.

Exact solutions of Schrödinger equation are not possible for systems with more than one electron. In the framework of the central field approximation, one assumes that it is possible to construct a potential energy function $U(r_i)$ which is a spherically symmetric, one-electron operator and is a good approximation to the actual potential energy of the electron i in the field of the nucleus and the other $N-1$ electrons. Therefore, $\mathscr{H}_0$ can be replaced by (Weissbluth, 1978)

$$\mathscr{H}_0' = \sum_{i=1}^{N} \left[-\frac{\hbar^2}{2m} \nabla_i^2 + U(r_i) \right], \tag{1.5}$$

with

$$\sum_{i=1}^{N} U(r_i) = -\sum_{i=1}^{N} \frac{Ze^2}{r_i} + \left\langle \sum_{i<j}^{N} \frac{e^2}{r_{ij}} \right\rangle. \tag{1.6}$$

The second term in Eq. (1.6) is the average over a sphere of the electron repulsion. This term is therefore independent of the angular coordinates. $\mathscr{H}'_0$ contains the kinetic energy, the potential energy of N electrons, and most of the inter-electron repulsion, and it is called the Hamiltonian of the central field. Since most of the inter-electron repulsion is included in the central field Hamiltonian of Eq. (1.5), the second term in Eq. (1.1) can be rewritten as

$$\mathscr{H}'_C = \sum_{i<j}^{N} \frac{e^2}{r_{ij}} - \left\langle \sum_{i<j}^{N} \frac{e^2}{r_{ij}} \right\rangle, \tag{1.7}$$

which is small enough to be treated along with the spin-orbit Hamiltonian (1.4) as a perturbation to the central field potential.

The eigenfunctions of $\mathscr{H}'_0$ for an N-electron ion are obtained as a linear combination of one-electron Vave functions that satisfy the Pauli exclusion principle and are subject to the orthonormalty condition. This method, known as Hartree-Fock approach, is generally used for seeking an approximate solution to the N-electron Schrödinger equation (Hartree, 1957; Weissbluth, 1978). The effects of non-central field interactions including spin-orbit coupling and many-body electronic interactions are considered by introducing additional effective operators and diagonalizing the Hamiltonian with parameters determined in comparison with experiments.

In the Hartree-Fock method, the wave function of each electron is expressed as a product of radial and angular functions of the spherical harmonics multiplied by a spin function

$$\Psi_{nlm_lm_s}(\boldsymbol{r}, m_s) = \frac{1}{r} R_{nl}(r) Y_{lm_l}(\theta, \varphi) \sigma(m_s), \tag{1.8}$$

where the radial function $R_{nl}(r)$ depends on the central field potential, which determines the radial charge distribution functions such as those plotted in Fig. 1.1 for Nd^{3+}. The spherical harmonic function $Y_{lm_l}(\theta, \varphi)$ in Eq. (1.8) is characterized by the four quantum numbers n, l, m_l and m_s, which define a unique state of an electron in an atom. For electrons in a $4f^N$ cnfiguration, we have

$$\begin{aligned} &n = 4, \\ &l = 3, \ m_l = -l, -l+1, \cdots, l, \\ &m_s = \pm 1/2. \end{aligned} \tag{1.9}$$

The central field wave function for N-electrons thus may be written in a

determinantal form as

$$\Psi(\lambda_1, \lambda_2, \cdots, \lambda_N) = \frac{1}{\sqrt{N!}} \begin{vmatrix} \psi_1(\lambda_1) & \psi_2(\lambda_1) & \cdots & \psi_N(\lambda_1) \\ \psi_1(\lambda_2) & \psi_2(\lambda_2) & \cdots & \psi_N(\lambda_2) \\ \vdots & & & \\ \psi_1(\lambda_N) & \psi_2(\lambda_N) & \cdots & \psi_N(\lambda_N) \end{vmatrix}, \quad (1.10)$$

in which $\psi_i(\lambda_j)$ are spin orbitals. The subscript i identifies a particular choice of the four quantum numbers n, l, m_l, and m_s, where λ_j represents the space and spin coordinates of the j-th electron. The primary purpose of the central field approximation is to use the N-electron wave functions defined by Eq. (1.10) as the basis functions for the perturbation terms such as the inter-electron Coulomb interactions [see Eq. (1.7)] and spin-orbit interaction [see Eq. (1.4)] of the Hamiltonian.

1.2.2 *LS* Coupling and Intermediate Coupling

To construct wave functions for a multi-electron atom on the basis of the central field approximation, one needs to choose a coupling scheme of momentum summation to determine the wave functions of the N-independent electrons. There are two coupling schemes that are commonly used for two extreme cases in atomic spectroscopy (Judd, 1963a; Cowan, 1981). In lighter atoms, where spin orbit interactions [see Eq. (1.4)] tend to be small compared with the electrostatic interactions between electrons [see Eq. (1.3)], the so-called Russell-Saunders, or *LS* coupling scheme is a good choice, since L and S are, approximately, good quantum numbers. With increasing Z, electrostatic interactions decrease and spin-orbit interactions become more important. In the heavier atoms, spin-orbit interactions become much stronger than the Coulomb interactions. Thus, one should consider the *j-j* coupling scheme. In rare earth ions, the Coulomb electrostatic interactions and spin-orbit interactions have the same order of magnitudes. Therefore, neither coupling scheme is appropriate, and calculations of energy levels of RE ions are mathematically more involved in a scheme called intermediate coupling, which can be developed from the *LS* scheme.

In the *LS* coupling scheme, orbital momentum and spin momentum of individual electrons are summed separately (Weissbluth, 1978). Thus

$$\boldsymbol{L} = \sum_{i=1}^{N} \boldsymbol{l}_i, \quad \boldsymbol{S} = \sum_{i=1}^{N} \boldsymbol{s}_i, \quad (1.11)$$

are the total orbit and total spin momentum operators, respectively, and

$$\boldsymbol{J} = \boldsymbol{L} + \boldsymbol{S}, \quad (1.12)$$

is the total angular momentum operator which has $2J + 1$ eigenstates represented

by the magnetic quantum number $M = -J, -J+1, \cdots, J$.

In the *LS* coupling scheme, the electronic states of an RE ion may be specified completely by writing the basis states as

$$\Psi = |nl\tau LSJM\rangle, \tag{1.13}$$

where *nl*, which is 4f, or 5d for RE ions, represents the radial part of the basis states. Usually, the symbol $^{2S+1}L_J$ is used for naming a free ion state or multiplet. Whereas *S* and *J* are specified with numbers (0, 1/2, 1, ···), *L* is traditionally specified with letters *S, P, D, F, G, H,* ···, respectively, for *L* = 0, 1, 2, 3, 4, 5, ··· Table 1.2 lists the electronic configurations and ground states identified by $^{2S+1}L_J$ for divalent and trivalent ions in the RE series.

Table 1.2 Electronic configurations and ground states of divalent (R^{2+}) and trivalent (R^{3+}) RE ions

Atomic number	Element		R^{2+}	R^{3+}
57	La	Lanthanum	$4f^1$, $^2F_{5/2}$	$4f^0$, $^1S_0$
58	Ce[a]	Cerium	$4f^2$, $^3H_4$	$4f^1$, $^2F_{5/2}$
59	Pr[a]	Praseodymium	$4f^3$, $^4I_{9/2}$	$4f^2$, $^3H_4$
60	Nd	Neodymium	$4f^4$, $^5I_4$	$4f^4$, $^4I_{9/2}$
61	Pm	Promethium	$4f^5$, $^6H_{5/2}$	$4f^4$, $^5I_4$
62	Sm	Samarium	$4f^6$, $^7F_0$	$4f^5$, $^6H_{5/2}$
63	Eu	Europium	$4f^7$, $^8S_{7/2}$	$4f^6$, $^7F_0$
64	Gd	Gadolinium	$4f^8$, $^7F_6$	$4f^7$, $^8S_{7/2}$
65	Tb[a]	Terbium	$4f^9$, $^6H_{15/2}$	$4f^8$, $^7F_6$
66	Dy	Dysprosium	$4f^{10}$, $^5I_8$	$4f^9$, $^6H_{15/2}$
67	Ho	Holmium	$4f^{11}$, $^4I_{15/2}$	$4f^{11}$, $^5I_8$
68	Er	Erbium	$4f^{12}$, $^3H_6$	$4f^{11}$, $^4I_{15/2}$
69	Tm	Thulium	$4f^{13}$, $^2F_{7/2}$	$4f^{12}$, $^3H_6$
70	Yb	Ytterbium	$4f^{14}$, $^1S_0$	$4f^{13}$, $^2F_{7/2}$
71	Lu	Lutecium	$4f^{14}6s$, $^2S_{1/2}$	$4f^{14}$, $^1S_0$

(a) Ce, Pr and Tb may also be stabilized in tetravalent oxidation states. The electronic configuration and ground state of RE in tetravalent oxidation state can be determined from this table. For example, Pr^{4+} is in $4f^1$ ($^2F_{5/2}$) configuration (state).

An additional quantum number τ, called the seniority number, is needed for distinguishing the states that have the same *L* and *S* quantum numbers. In fact, two or more quantum numbers are needed in order completely to define the states in an f^N configuration. One such classification number is $W = (w_1 w_2 w_3)$, with three integers for characterizing the irreducible representations of the seven-dimenisional rotational group R_7. The other classification number is $U = (u_1 u_2)$, for characterizing the irreducible representations of the group G_2. Details in classification of the f^N states are given in the books by Judd (1963a) and Wybourne (1965). Table 1.3 lists the classification of the states for the f^N

Table 1.3 Classification of the free ion states of the f^N configurations (Wybourne, 1965)

N	τ	W	U	^{2S+1}L	N_J	N	τ	W	U	^{2S+1}L	N_J
1	1	(100)	(10)	^{2}F	2	5	(221)		(10)	^{2}F	2
2	2	(110)	(10)	^{3}F	3				(11)	^{2}PH	4
			(11)	^{3}PH	6				(20)	^{2}DGI	6
	2	(200)	(20)	^{1}DGI	3				(21)	^{2}DFGHKL	12
	0	(000)	(00)	^{1}S	1				(30)	^{2}PFGHIKM	14
3	3	(111)	(00)	^{4}S	1				(31)	^{2}PDFFGHHIIKK-LMNO	30
			(10)	^{4}F	4						
			(20)	^{4}DGI	12		3	(210)	(11)	^{2}PH	4
	3	(210)	(11)	^{2}PH	4				(20)	^{2}DGI	6
			(20)	^{2}DGI	6				(21)	^{2}DFGHKL	12
			(21)	^{2}DFGHKL	12		1	(100)	(10)	^{2}F	2
	1	(100)	(10)	^{2}F	2	6	6	(100)	(10)	^{7}F	7
4	4	(111)	(00)	^{5}S	1		6	(210)	(11)	^{5}PH	8
			(10)	^{5}F	5				(20)	^{5}DGI	15
			(20)	^{5}DGI	15				(21)	^{5}DFGHKL	30
	4	(211)	(10)	^{3}F	3		4	(111)	(00)	^{5}S	1
			(11)	^{3}PH	6				(10)	^{5}F	5
			(20)	^{3}DGI	9				(20)	^{5}DGI	15
			(21)	^{3}DFGHKL	18		6	(221)	(10)	^{3}F	3
			(30)	^{3}PFGHIKM	21				(11)	^{3}PH	6
	2	(110)	(10)	^{3}F	3				(20)	^{3}DGI	9
			(11)	^{3}PH	6				(21)	^{3}DFGHKL	18
	4	(220)	(20)	^{1}DGI	3				(30)	^{3}PFGHIKM	21
			(21)	^{1}DFGHKL	6				(31)	^{3}PDFFGHHIIKKLMNO	45
			(22)	^{1}SDGHILN	7		4	(211)	(10)	^{3}F	3
	2	(200)	(20)	^{1}DGI	3				(11)	^{3}PH	6
	0	(000)	(00)	^{1}S	1				(20)	^{3}DGI	9
5	5	(110)	(10)	^{6}F	6				(21)	^{3}DFGHKL	18
			(11)	^{6}PH	9				(30)	^{3}PFGHIKM	21
	5	(211)	(10)	^{4}F	4		2	(110)	(10)	^{3}F	3
			(11)	^{4}PH	7				(11)	^{3}PH	6
			(20)	^{4}DGI	12		6	(222)	(00)	^{1}S	1
			(21)	^{4}DFGHKL	24				(20)	^{1}DGL	3
			(30)	^{4}PFGHIKM	27				(30)	^{1}PFGHIKM	7
	3	(111)	(00)	^{4}S	1				(40)	^{1}SDFGGHIIKLLMNQ	14
			(10)	^{4}F	4		4	(220)	(20)	^{1}DGI	3
			(20)	^{4}DGI	12				(21)	^{1}DFGHKL	6

continue

N τ	W	U	^{2S+1}L	N_J	N τ	W	U	^{2S+1}L	N_J
		(22)	^{1}SDGHILN	7	7	(222)	(00)	^{2}S	1
2	(200)	(20)	^{1}DGI	3			(10)	^{2}F	2
0	(000)	(00)	^{1}S	1			(20)	^{2}DGI	6
7 7	(000)	(00)	^{8}S	1			(30)	^{2}PFGHIKM	14
7	(200)	(20)	^{6}DGI	17			(40)	^{2}SDFGGHIIKL-	27
5	(110)	(10)	^{6}F	6				LMNQ	
		(11)	^{6}PH	9	5	(221)	(10)	^{2}F	2
7	(220)	(20)	^{4}DGI	12			(11)	^{2}PH	4
		(21)	^{4}DFGHKL	24			(20)	^{2}DGI	6
		(22)	^{4}SDGHILN	25			(21)	^{2}DFGHKL	12
5	(211)	(10)	^{4}F	4			(30)	^{2}PFGHIKM	14
		(11)	^{4}PH	7			(31)	^{2}PDFFGHHIIKK-	30
		(20)	^{4}DGI	12				LMNO	
		(21)	^{4}DFGHKI	24	3	(210)	(11)	^{2}PH	4
		(30)	^{4}PFGHIKM	27			(20)	^{2}DGI	6
3	(111)	(00)	^{4}S	1			(21)	^{2}DFGHKL	12
		(10)	^{4}F	4	1	(100)	(10)	^{2}F	2
		(20)	^{4}DGI	12					

configurations with $N \leqslant 7$. Column 5 lists the LS terms with the same S, and Column 6 lists the number of $^{2S+1}L_J$ multiplets in the classification. The LS terms of the $4f^{14-N}$ configuration are identical for those of the $5f^N$ configuration with $N>7$, although the seniority of the states is different.

In the LS coupling scheme, the spin-orbit interaction Hamiltonian commutes with $\boldsymbol{J}^2$ and J_z, but not with $\boldsymbol{L}$ and $\boldsymbol{S}$:

$$\begin{aligned} &[\mathscr{H}_{SO}, \boldsymbol{L}] \neq 0, [\mathscr{H}_{SO}, \boldsymbol{S}] \neq 0, \\ &[\mathscr{H}_{SO}, \boldsymbol{J}^2] = [\mathscr{H}_{SO}, J_z] = 0, \end{aligned} \tag{1.14}$$

which means that inclusion of spin-orbit coupling breaks the symmetry of the LS coupling scheme. In this case, L and S are no longer good quantum numbers, but J and M are still good. The wave functions $|nl\tau LSJM\rangle$ are not eigenfunctions of the Hamiltonian of Eq. (1.1). Based on perturbation theory and the concept of the central field approximation, one may obtain a new set of eigenfunctions by diagonalizing the primary terms of the Hamiltonian defined by Eqs. (1.4) and (1.7) with the basis of $|nl\tau LSJM\rangle$. As a result, the new eigenfunctions are linear combinations of the LS basis sets, and are known as the free-ion wave

functions in the intermediate coupling scheme. If we do not include inter-configurational coupling, the eigenfunctions in the intermediate coupling scheme are expressed as

$$\Psi(nlJ) = \sum_{\tau LS} a_{\tau LSJ} |nl\tau LSJ\rangle, \tag{1.15}$$

where the coefficients $a_{\tau LSJ}$ are determined by the matrix elements,

$$a_{\tau LSJ} = \sum_{\tau' L' S'} \langle nl\tau LSJ | \mathscr{H}_{\mathrm{C}} + \mathscr{H}_{\mathrm{SO}} | nl\tau' L' S' J' \rangle \delta_{JJ'}. \tag{1.16}$$

The energy levels of the free-ion states are independent of M, so they are $(2J+1)$-fold degenerate. The new basis Eq. (1.15) in the intermediate coupling scheme describes the energy states of the Hamiltonian including Coulomb and spin-orbit interactions and is obtained from mixing all LS terms with the same J in a given $4f^N$ configuration. The transformation coefficients of $a_{\tau SLJ}$ are the components of the eigenvector pertaining to the basis state in the LS coupling (Judd, 1963).

1.3 Free-ion Interactions

In spectroscopy, a powerful method for evaluating atomic energy level structure (or RE ion energy level structure in our case) is to define and diagonalize an effective-operator Hamiltonian with the wave functions of the central field Hamiltonian. Racah (1949) used this method for calculating the energy matrix elements of the tensor operators of the electronic angular momentum. Since then, many developments have been made, particularly for applications of the effective operator method to rare earth spectroscopy (Judd, 1963a; Wybourne, 1965). In this section, we will review the primary results of the theory that are important for understanding the free-ion properties of RE ions in solids. The effective operator Hamiltonian and its reduced matrix elements for the Coulomb electrostatic interaction and spin-orbit coupling are discussed, while the effective operators for higher order free-ion interactions are presented without derivations. An essential part of the effective operator method is to determine the irreducible matrix elements of tensor operators using the Wigner-Eckart theorem (see B.9 in Appendix B). For more comprehensive theories of tensor operators and atomic spectroscopy, one may read textbooks by Judd (1963a) and Weissbluth (1978).

1.3.1 Coulomb Interaction

In the central field approximation, orbital electronic wave functions of an RE ion

are represented by products of radial and angular parts as shown in Eq. (1.8). The effective operator for Coulomb electrostatic intra-ion interaction may be expressed by expanding $1/r_{ij}$ into scalar products of the tensor operators of spherical harmonics as follows:

$$\frac{1}{r_{ij}} = \sum_{k=0}^{\infty} \frac{4\pi}{2k+1} \frac{r_<^k}{r_>^{k+1}} \mathrm{Y}_i^{(k)} \cdot \mathrm{Y}_j^{(k)}, \tag{1.17}$$

where $r_<$ indicates the distance from the nucleus to a near electron, and $r_>$ the distance from the nucleus to a further electron, and

$$\mathrm{Y}^{(k)}(i) \cdot \mathrm{Y}^{(k)}(j) = \sum_{-k \leqslant q \leqslant k} (-1)^q \mathrm{Y}_q^{(k)}(\theta_i, \varphi_i) \mathrm{Y}_{-q}^{(k)}(\theta_j, \varphi_j). \tag{1.18}$$

It is convenient to define a tensor $\boldsymbol{C}^{(k)}$ as (Weissbluth, 1978)

$$\boldsymbol{C}^{(k)} = \sqrt{\frac{4\pi}{2k+1}} \mathrm{Y}^{(k)} \tag{1.19}$$

with components given in Appendix B Eq. (B.12). The reduced matrix elements of $\boldsymbol{C}^{(k)}$ may be expressed as

$$\left\langle l \| \boldsymbol{C}^{(k)} \| l' \right\rangle = (-1)^l [(2l+1)(2l'+1)]^{1/2} \begin{pmatrix} l & k & l' \\ 0 & 0 & 0 \end{pmatrix}. \tag{1.20}$$

The 3-j symbol in Eq. (1.20) is defined in Eq. (B.6) in Appendix B. Therefore, for N equivalent electrons in orbital nl, the matrix of the effective operator Hamiltonian for Coulomb electrostatic interaction may be expressed as

$$\left\langle l^N \tau LS \left| \sum_{i>j}^{N} \frac{e^2}{r_{ij}} \right| l^N \tau LS \right\rangle = \sum_k f_k(l, l) F^k(nl, nl), \tag{1.21}$$

where $F^k(nl, nl)$, with $k = 0, 2, 4, 6$, are the Slater radial integrals for the radial part of the electrostatic interaction, which is defined as

$$F^k(nl, nl) = e^2 \int_0^\infty \int_0^\infty \frac{r_<^k}{r_>^{k+1}} [R_{nl}(r_i)]^2 [R_{nl}(r_j)]^2 \mathrm{d}r_i \mathrm{d}r_j. \tag{1.22}$$

The value of F^k may be calculated using the Hartree-Fock method, but in actual cases of spectrum analysis, F^k is considered an experimentally determined parameter. The angular part of matrix (1.21) is defined as

$$f_k(l,l) = \left\langle l^N\tau LS \middle| \sum_{i>j} \boldsymbol{C}^{(k)}(i)\cdot\boldsymbol{C}^{(k)}(j) \middle| l^N\tau LS \right\rangle. \quad (1.23)$$

The matrix elements (1.23) are best handled by introducing the unit tensor operator $\boldsymbol{U}^{(k)}$ (Weissbluth, 1978) with reduced matrix elements expressed in Appendix B Eqs. (B.10) and (B.11). In combination with symmetry properties of angular momentum, $f_k(l,l)$ may be expressed in terms of the reduced matrix elements of $\boldsymbol{U}^{(k)}$ as

$$f_k(l,l) = \frac{1}{2}(2l+1)^2\begin{pmatrix} l & k & l \\ 0 & 0 & 0 \end{pmatrix}^2 \times\left\{\frac{1}{2L+1}\sum_{\tau L'}\left|\left\langle l^N\tau LS \| \boldsymbol{U}^{(k)} \| l^N\tau' L'S'\right\rangle\right|^2 - \frac{N}{2l+1}\right\}. \quad (1.24)$$

In the particular case of $k=0$, it is easy to find that

$$f_0(l,l) = N(N-1)/2. \quad (1.25)$$

For the p^N, d^N, and f^N configurations, the values for the reduced matrix elements of the tensor operator $\boldsymbol{U}^{(k)}$ were tabulated by Nielson and Koster (1963), and may also be displayed in SPECTRA program. Because of the symmetry properties of the 3-j symbol, the matrix in Eq. (1.24) has nonzero elements only if $l+l\geqslant k\geqslant|l-l|$, and k must be even. For the 4f electrons, $l=3$, thus the f_k matrix vanishes except for $k=0,2,4,6$.

To illustrate the use of the reduced matrix elements for energy level calculation in the simple case of f^3 configuration (Nd^{3+}), Table 1.4 lists the values of electrostatic matrix elements in terms of F^k along with other free-ion interaction parameters to be introduced in the Section 1.3.2 and 1.3.3.

Table 1.4 Elements of the $J=1/2$ submatrix of the free-ion Hamiltonian for f^3 configurations (in the first and second columns, 1 stands for ^4D and 2 for ^2P)

Ψ	Ψ'	Coefficient	Parameter
1	1	1.00000000	E_0
2	2	1.00000000	E_0
1	1	0.17264957	F^2
2	2	−0.04957265	F^2
1	1	0.01165501	F^4
2	2	0.00155400	F^4
1	1	−0.19873289	F^6
2	2	0.07321738	F^6
1	1	−0.02446153	0.01α
2	2	−0.02846153	0.01α
1	1	−0.10256410	β

continue

Ψ	Ψ'	Coefficient	Parameter
2	2	-0.26923077	β
1	1	-0.32307690	γ
2	2	0.27692306	γ
1	1	1.11116780	T^2
2	2	-0.25253800	T^2
1	1	0.09759000	T^3
2	2	-0.58554000	T^3
1	1	-1.16700680	T^4
2	2	-1.52362350	T^6
1	1	-1.50000000	ζ
1	1	11.89999944	M^0
1	1	-18.09999640	M^2
1	1	-19.40908767	M^4
1	1	-0.12777776	P^2
1	1	-0.04292929	P^4
1	1	0.03399380	P^6
1	2	-1.58113883	ζ
1	2	-2.42441266	M^0
1	2	2.31900337	M^2
1	2	-0.81452561	M^4
1	2	0.06441676	P^2
1	2	0.01597110	P^4
1	2	-0.03583260	P^6
2	2	4.66666625	M^0
2	2	3.00000097	M^2
2	2	-6.36363739	M^4
2	2	-0.09629627	P^2
2	2	0.07575757	P^4
2	2	-0.04532506	P^6

1.3.2 Spin-orbit Interaction

As defined in Eq. (1.4), the Hamiltonian the for spin-orbit coupling of N electrons in a rare earth ion is a linear summation of independent spin-orbit interactions for a single electron. In LS coupling, the N equivalent electron matrix elements of the spin-orbit interaction are expressible in terms of tensor operator $\boldsymbol{V}^{(11)}$, so that the matrix element of spin-orbit interaction for N equivalent electrons can be expressed as (Sobelman, 1972; Weissbluth, 1978)

$$\left\langle nl^N \tau LSJM \left| \sum_{i=1}^{N} \xi(r_i) \boldsymbol{l}_i \cdot \boldsymbol{S}_i \right| nl^N \tau' L'S'J'M' \right\rangle = \zeta_{nl} A_{SO}(nl), \quad (1.26)$$

where ζ_{nl} is the spin-orbit interaction parameter which is a radial integral defined by

$$\zeta_{nl} = \int_0^\infty [R_{nl}(r)]^2 \xi(r)\, \mathrm{d}r. \quad (1.27)$$

The spin-orbit parameter can be evaluated numerically using the Hartree-Fock central field potential, but it is usually adjusted to the experimentally observed energies. The matrix element in Eq. (1.26) can be expressed as

$$A_{SO}(nl) = (-1)^{L+S'+J} \sqrt{(2l+1)(l+1)l}\,\delta_{JJ'}\delta_{MM'} \times \begin{Bmatrix} L & S & J \\ S' & L' & 1 \end{Bmatrix} \langle \tau LS \| \boldsymbol{V}^{(11)} \| \tau' L'S' \rangle, \quad (1.28)$$

where $\{\ldots\}$ is a 6-j symbol. The values for the reduced matrix elements of the tensor operator $\boldsymbol{V}^{(11)}$ are tabulated in the books by Sobelman (1972) and Nielson and Koster (1963). They may be output from the SPECTRA program.

1.3.3 Corrections to Free-ion Hamiltonian

The electrostatic and spin-orbit interactions give the right order for the energy level splitting of the f^N configurations. However, these primary terms of the free ion Hamiltonian do not accurately reproduce the experimentally measured energy level structures. This is because the parameters F^k and ζ_{nf}, which are associated with interactions within a f^N configuration, cannot absorb all the effects of additional mechanisms such as relativistic effects and configuration interactions. Introduction of new terms to the effective operator Hamiltonian is required to better interpret the experimental data. Judd and Crosswhite (1984) demonstrated that, in fitting the experimental free-ion energy levels of Pr^{3+} (f^2 configuration), the standard deviation could be reduced from 733 cm^{-1} to 24 cm^{-1} by adding nine more parameterized corrective effective operators into the Hamiltonian.

Among several corrective terms included in the effective operator Hamiltonian, a significant contribution to the f^N energy level structure is from configuration interactions between the configurations of the same parity, which can be taken into account by a set of three two-electron operators recommended by Wybourne (1965),

$$\mathscr{H}_{\mathrm{cl}} = \alpha L(L+1) + \beta G(G_2) + \gamma G(R_7), \quad (1.29)$$

where α, β and γ are the parameters associated with $G(G_2)$ and $G(R_7)$ (Rajnak and Wybourne, 1963), the latter being eigenvalues of Casimir operators for the groups G_2 and R_7 (Judd, 1963)

For f^N configurations of $N \geqslant 3$, a three-body interaction term was introduced by Judd (1966) and Crosswhite et al. (1968) as

$$\mathscr{H}_{c2} = \sum_{i=2,3,4,6,7,8} T^i t_i, \tag{1.30}$$

where T^i are parameters associated with three-particle operators t_i. This set of effective operators scaled with respect to the total spin $\boldsymbol{S}$ and total orbital angular momentum $\boldsymbol{L}$ are needed in the Hamiltonian in order to represent the coupling of the f^N states to those in the higher energy configurations (5d, 5p, 5s) via inter-electron Coulomb interactions. It is common to include six three-electron operators $t_i (i = 2, 3, 4, 6, 7, 8)$. When perturbation is carried beyond the second order, an additional eight three-electron operators $t_i (11 \leqslant i \leqslant 19$, with $i = 13$ excluded) are required (Judd and Lo, 1996). A complete table of matrix elements of the 14 three-electron operators for the f-shell were published by Hansen et al. (1996).

In addition to the magnetic spin-orbit interaction parameterized by ζ_{nf}, relativistic effects including spin-spin and spin-other-orbit, both being parameterized by the Marvin integrals M^0, M^2, and M^4 (Marvin, 1947), are included as the third corrective term of the effective operator Hamiltonian (Judd et al., 1968).

$$\mathscr{H}_{c3} = \sum_{i=0,2,4} M^i m_i, \tag{1.31}$$

where m_i is effective operator and M^i is the radial parameter associated with m_i.

As demonstrated by Judd et al. (1968) and Carnall et al. (1983), for improving the parametric fitting of the f-element spectra, two-body effective operators can be introduced to account for configuration interaction through electrostatically correlated magnetic interactions. This effect can be characterized by introducing three more effective operators as

$$\mathscr{H}_{c4} = \sum_{i=2,4,6} P^i p_i, \tag{1.32}$$

where p_i is the operator and P^i is the parameter.

In summary, we have introduced 20 effective operators including those for two- and three-electron interactions. The total effective-operator Hamiltonian of free-ion interactions is

$$\mathscr{H}_{FI} = \sum_{k=0,2,4,6} F^k f_k + \zeta_{nl} A_{SO}(nl) + \alpha L(L+1) + \beta G(G_2) + \gamma G(R_7)$$

$$+ \sum_{i=2,3,4,6,7,8} T^i t_i + \sum_{i=0,2,4} M^i m_i + \sum_{i=2,4,6} P^i p_i. \qquad (1.33)$$

This effective-operator Hamiltonian has been used as the most comprehensive free-ion Hamiltonian in previous spectroscopic analyses of f-element ions in solids (Crosswhite, 1977; Crosswhite and Crosswhite, 1984; Carnall et al., 1984, 1989). The 20 parameters associated with the free-ion operators are adjustable in fitting of experimental data.

1.3.4 Reduced Matrices and Free-ion State Representation

In (1.33), all effective operators for the free-ion interactions have well-defined group-theoretical properties (Judd, 1963a; Wybourne, 1965). Within the intermediate coupling scheme, all matrix elements can be reduced, using the Wigner-Eckart theorem, to new forms that are independent of J, viz.

$$\langle \tau SLJ \mid \mathscr{H}_i \mid \tau' S' L' J' \rangle = P_i \delta_{JJ'} c(SLS'L'J) \langle \tau SL \parallel O_i \parallel \tau' S' L' \rangle, \qquad (1.34)$$

where P_i is the parameter, $c(SLS'L'J)$ is a numerical coefficient, and $\langle \tau SL \parallel O_i \parallel \tau' S' L' \rangle$ is the reduced matrix element of the effective operator O_i. Once the reduced matrix elements are established, it is then not difficult to diagonalize the entire free-ion Hamiltonian with the wave function basis in the *LS*-coupling scheme. All matrix elements of the effective operator Hamiltonian are evaluated in terms of the parameters of the effective operators.

The property of matrix reduction thus allows the matrix of the free-ion Hamiltonian to be reduced into a maximum of 13 independent submatrices for $J = 0, 1, 2, \cdots, 12$ for even N and $J = 1/2, 3/2, 5/2, \cdots, 25/2$ for odd N in an f^N configuration. The numbers of submatrices and their size can be determined from the values of N_J given in Table 1.3. Evaluation of matrix elements is actually a tremendous effort, particularly with inclusion of the effective two- and three-electron operators in the Hamiltonian. For an f^N configuration with $3 < N < 11$, there are more than 10^4 free-ion matrix elements and each of them may have as many as 20 terms to be evaluated on the basis of angular-momentum operations. Fortunately, several groups have made the calculated matrix elements available. For example, one may download from the web site http://chemistry.anl.gov the tables prepared by Crosswhite and co-workers for the free-ion matrix elements, or SPECTRA, to calculate the eigenvalues and eigenfunctions of the free-ion Hamiltonian.

In the Crosswhite files for configurations of f^N with $N = 2$ through 12, the free-ion matrix elements are given in terms of the 20 parameters for all the f^N configurations. As an example, the elements of the free-ion matrix for the $J = 1/2$ submatrix of the f^3 configuration are listed in Table 1.4. Column 3 of Table 1.4 lists the values of the product of $c(SLS'L'J)$ and the values of matrix

elements, Column 4 lists the corresponding parameters. This is one of the simplest cases in which there are only two multiplets: $^4D_{1/2}$ and $^2P_{1/2}$. Except for T^7 and T^8, all 18 other parameters appear in this 2×2 submatrix. Among the interaction terms that contribute to the energy level of these two multiplets, only ζ, $M^{0,2,4}$ and $P^{2,4,6}$ mix the two *LS*-multiplets. In addition, the T^i terms induce a mixture of different multiplets with identical S and L but different τ.

Due to the *SL-S'L'* mixing in the intermediate coupling scheme, labeling a multiplet as $^{2S+1}L_J$ is incomplete. In most cases, the nominal labeling of a free ion state as $^{2S+1}L_J$ only indicates that this multiplet has a leading component from the pure *LS* basis $|LSJ\rangle$. Diagonalization of each of the sub-matrices produces free-ion eigenfunctions in the form (1.15). As an example, for Nd^{3+}, $4f^3$ configuration, we give the leading *LS* terms in the free-ion wavefunctions of the ground states and the excited state at 21,000 cm^{-1}, which were obtained using the values of the parameters listed in Table 1.5:

$$\Psi(4f^3,\ ^4I_{9/2},\ 0\ cm^{-1}) = 0.984\ ^4I - 0.174\ ^2H^1,$$
$$\Psi(4f^3,\ ^2G_{9/2},\ 21,000\ cm^{-1}) = 0.616\ ^2G^1 - 0.494\ ^2G^2 + 0.487\ ^4G + 0.273\ ^4F - 0.208\ ^2H^1,$$

where $^2G^1$ and $^2G^2$ are the first and second $^2G_{9/2}$ terms with $U = (20)$ and (21), respectively, for the *LS* states of f^3 configuration listed in Table 1.3. Other terms with magnitudes less than 0.1 are neglected. These two Nd^{3+} multiplets are commonly labeled as nominal $^4I_{9/2}$ and $^2G_{9/2}$, respectively. In general, *SL-S'L'* mixing becomes more significant in the excited multiplets.

1.3.5 Parameterization of the Free-ion Interactions

One of the characteristics of attempts to parameterize f-configuration spectra is that, because of the heavy mixing of *SL*-basis states brought about by the spin-orbit interactions for each J value, the least-squares fitting method can result in convergence to a false solution. A false solution can be recognized if there is sufficient characterization of the states from supplementary data, such as Zeeman splitting factors or polarized spectra. However, this in itself does not produce the true solution. The true solution can only be found if sufficiently accurate initial parameters are available for the least-squares fitting process to be effective. On the other hand, existing theories of f-element spectroscopy do not accurately reproduce the experimentally observed energy level structure of an f-element ion in solids, and the calculated parameters may be physically different from the phenomenological ones that result from a fitting of the experimental data. Therefore, establishing accurate parameters for the model Hamiltonian essentially relies on systematic analyses that encompass theoretical calculations for incorporating trends of parameter variation across the f-element series. The

Table 1.5 Energy-level parameters for trivalent RE ions in LaF_3 (in cm^{-1}) (Carnall et al., 1989)[a]

	Ce^{3+}	Pr^{3+}	Nd^{3+}	Pm^{3+}	Sm^{3+}	Eu^{3+}	Gd^{3+}	Tb^{3+}	Dy^{3+}	Ho^{3+}	Er^{3+}	Tm^{3+}	Yb^{3+}
F^2		68,878(23)	73,018(19)	76,400	79,805(16)	83,125(31)	85,669(17)	88,995(58)	91,903(69)	94,564(38)	97,483(32)	100,134(23)	
F^4		50,347(69)	52,789(94)	54,900	57,175(45)	[59,268 R]	[60.825 R]	[62,919 R]	64,372(147)	66,397(64)	67,904(67)	69,613(62)	
F^6		32,901(37)	35,757(42)	37,700	40,250(26)	[42,560 R]	44,776(24)	47,252(72)	49,386(139)	52,022(63)	54,010(60)	55,975(104)	
ζ	647(11)	751.7(2)	885.3(1)	1025	1176(1)	1338(3)	1508(2)	1707(2)	1913(2)	2145(1)	2376(2)	2636(1)	2928(10)
α		16.23(0.23)	21.34(0.14)	20.50	20.16(0.89)	[20.16]	18.92(0.83)	18.40(0.19)	18.02(0.23)	17.15(0.11)	17.79(0.20)	17.26(0.30)	
β		−566.6(15)	−593.0(8)	−560	−566.9(8)	[−566.9]	[−600]	−590.9(29)	−633.4(10)	−607.9(6)	−582.1(10)	−624.5(15)	
γ		1371(13)	1445(16)	1475	[1500]	[1500]	[1575]	[1650]	1790(47)	[1800]	[1800]	[1820]	
T^2			298(6)	300	[300]	[300]	[300]	[320]	329(9)	[400]	[400]	[400]	
T^3			35(3)	35	[36]	[40]	[42]	[40]	36(5)	37(2)	43(5)		
T^4			59(4)	58	[56]	[60]	[62]	[50]	127(22)	107(5)	73(5)		
T^6			−285(6)	−310	−347(7)	[−300]	[−295]	−395(28)	−314(16)	−264(16)	−271(11)		
T^7			332(8)	350	373(7)	[370]	[350]	303(17)	404(8)	316(20)	308(18)		
T^8			305(10)	320	348(5)	[320]	[310]	317(13)	315(7)	336(8)	299(17)		
$M^{0(b)}$		2.08(0.3)	2.11(0.1)	2.4	2.60(0.1)	[2.1]	3.22(0.2)	2.39(0.1)	3.39(0.1)	2.54(0.1)	3.86(0.2)	3.81(0.3)	
$P^{2(c)}$		−88.6(47)	192(31)	275	357(28)	[360]	676(75)	373(53)	719(30)	605(24)	594(63)	695(46)	
B_0^2	[−218]	−218(16)	−256(16)	−245	−224(19)	−217(56)	[−231]	−231(24)	−244(18)	[−240]	−238(17)	−249(14)	[−249]
B_0^4	[738]	738(40)	496(73)	470	452(47)	413(86)	[604]	604(49)	506(43)	560(27)	453(90)	457(29)	[457]
B_0^6	[679]	679(48)	641(54)	640	649(47)	558(92)	[280]	280(38)	367(40)	376(28)	373(83)	282(42)	[282]
B_2^2	[−50]	−120(13)	−48(12)	−50	[−50]	[−50]	[−90]	−99(16)	−65(12)	−107(10)	−91(14)	−105(9)	[−105]

continue

	Ce^{3+}	Pr^{3+}	Nd^{3+}	Pm^{3+}	Sm^{3+}	Eu^{3+}	Gd^{3+}	Tb^{3+}	Dy^{3+}	Ho^{3+}	Er^{3+}	Tm^{3+}	Yb^{3+}
B_2^4	[431]	431(27)	521(39)	525	597(29)	[597]	[340]	340(34)	305(33)	250(19)	308(60)	320(21)	[320]
B_4^4	[616]	616(27)	563(41)	490	408(28)	[408]	[452]	452(31)	523(25)	466(19)	417(56)	428(22)	[428]
B_2^6	[-921]	-921(32)	-839(39)	-750	-706(33)	[-706]	[-721]	-721(29)	-590(24)	-576(18)	-489(51)	-482(33)	[-482]
B_4^6	[-348]	-348(41)	-408(35)	-450	-508(34)	[-508]	[-204]	-204(29)	-236(27)	-227(20)	-240(51)	-234(36)	[-234]
B_6^6	[-788]	-788(38)	-831(41)	-760	-692(38)	[-692]	[-509]	-509(33)	-556(25)	-546(22)	-536(49)	-492(36)	[-492]
$\sigma^{(d)}$	7	75	146		232	29	70	146	198	204	127	56	5
$\eta^{(d)}$	51	16	14		13	16	10	12	12	10	19	10	38

(a) Values in parentheses are errors in the indicated parameters. Values in brackets were either not allowed to vary in the parameter fitting, or if followed by an R, were constrained: For Eu^{3+}, $F^4/F^2 = 0.713$, $F^6/F^2 = 0.512$; for Gd^{3+}, $F^4/F^2 = -0.710$; for Tb^{3+}, $F^4/F^2 = 0.707$. All parameters from Pm^{3+} are interpolated values.

(b) M^0 was varied freely, M^2 and M^4 were constrained by the ratios $M^2 = 0.56M^0$, $M^4 = 0.31M^0$.

(c) P^2 was varied freely, P^4 and P^6 were constrained by ratios $P^4 = 0.5P^2$, $P^6 = 0.1P^2$.

(d) Deviation $\sigma = \sum \left[\frac{(\Delta i)^2}{n-p}\right]^{1/2}$, where Δi is the difference between observed and calculated energies, n is the number of levels fit, and p is the number of parameters freely varied.

results of analyses of simpler spectra are carried over to more complex ones through consideration of their symmetry properties (Carnall et al., 1989; Carnall, 1992).

Because lanthanide crystal fields appear as small perturbations on the free-ion levels, efforts to gain a theoretical understanding of free-ion interactions are essential in the development of parametric modeling of crystal field spectra. An important procedure that was taken in establishing the parametric model for f-configurations was to conduct a series of Hartree-Fock (HF) calculations, which, although they require corrections that must be calibrated by comparison with experimental data, predict free-ion parameter trends across the lanthanide series. Detailed results of HF calculations on f-electrons were previously discussed by Crosswhite and Crosswhite (1984) and Carnall et al. (1983).

The most important trends are those of the electrostatic-interaction parameters F^k and spin-orbit parameter ζ_{nf} which increase with the number of f-electrons, N. The experimentally determined values of F^k and ζ_{4f} for trivalent RE ions R^{3+} in LaF_3 and $LaCl_3$ are shown in Fig. 1.2 as a function of N. These values were obtained from systematic analyses of data from a series of experiments (Crosswhite, 1977; Carnall et al., 1989). Figure 1.2 indicates that for trivalent RE ions in crystals, not only the systematic trends are independent of

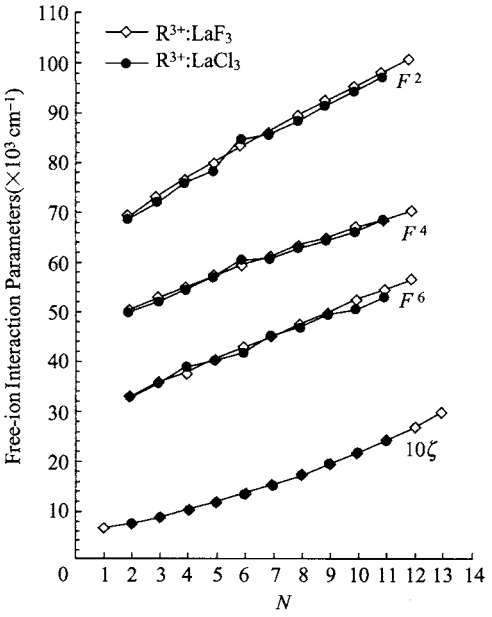


Figure 1. 2 Systematic variation of experimentally determined free-ion interaction parameters F^k and ζ as a function of number of f-electrons (N) for trivalent RE ions R^{3+} in crystal lattice of LaF_3 and $LaCl_3$

hosts, but the values of F^k and ζ_{4f} do not vary significantly in different host crystals. Calculated HF values predict the same trends cross the series, but the HF values of the F^k and ζ_{nf} are always larger than those obtained by allowing them to vary as parameters in fitting experimental data. A comparison is given in Fig. 1.3 between the Hartree-Fock relativistic (HFR) values and experimental values of F^2, F^4, F^6, and ζ_{4f} for trivalent RE ions (Crosswhite, 1977; Carnall et al., 1983). The HFR values of ζ_{4f} agree remarkably with empirical values, while the F^k values remain considerably larger than the empirical values. This is presumably because, in addition to relativistic effects, f-electron coupling with orbitals of higher-lying energies reduces the radial integrals assumed in the HFR approximation. Moreover, the experimental results are frequently obtained for an ion in a condensed phase, not in a gaseous phase, which leads on average to 5% change (Crosswhite, 1977). Because of the absence of mechanisms that absorb these effects in the HFR model, HFR values of F^k cannot be directly used as initial parameters for the least squares fitting process. As shown in Fig. 1.3, although the HFR values of F^k are much larger than the experimental ones, the

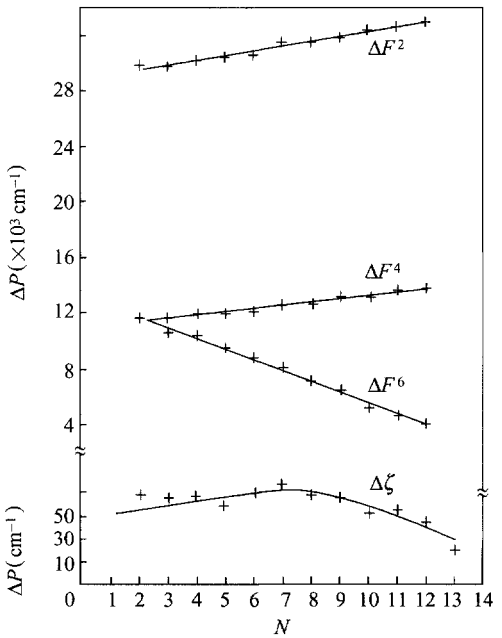


Figure 1.3 Variation of the parameter difference, $\Delta P = P(\text{HFR}) - P(\text{Exp.})$, between the HFR computed values and that determined from experimental data as a function of number of f-electrons

differences between the HFR and the experimental values of F^k have been shown to be nearly a linear function cross the RE series. With this characteristic, linear extrapolations of model parameters from one ion to another lead to values

consistent with those obtained in the actual fitting process.

In addition to HFR calculations of F^k and ζ_{nf}, estimated values for M^k, $k = 0, 2, 4$, can also be computed using the HFR method (Judd et al., 1967). These parameters do not vary dramatically across the f-series. In practice, experience has shown that they can be taken as given or varied as a single parameter by maintaining the HFR ratios $M^2/M^0 = 0.56$ and $M^4/M^0 = 0.31$ (Carnall et al., 1989) (see Table 1.5).

For the rest of the free-ion effective operators introduced above, no direct HF-values can be derived. Only a term-by-term HFR calculation is possible to give additional guidance for parameter estimates. For example, the HFR values of P^ks for Pr^{2+} and Pr^{3+} have been determined by Copland et al. (1971). In establishing systematic trends of parameters for Ln^{3+}: LaF_3, Carnall et al. (1989) constrained the P^k parameters by the ratios $P^4 = 0.5P^2$ and $P^6 = 0.1P^2$ while P^2 was varied freely along with other parameters. These ratios are consistent with the HFR estimation. The variation of these parameters across the series is not significant, and no obvious systematic trends have been established.

Once the systematic trends of free-ion parameters are established, constraints can be imposed on other parameters that are relatively insensitive to the available experimental data. Some parameters such as T^k, M^k and P^k do not vary significantly across the series and to a good approximation have the same values for neighboring ions in the same series. In fact, most of the free-ion parameters are not host sensitive. Typically, there are approximately 1% changes in the values of the free-ion parameters between different lattice environments. Table 1.5 lists parameters for trivalent rare earth ions in LaF_3. The free-ion parameters given in the table can be used as initial inputs for least-squares fitting of energy level structure of a trivalent f-element ion in any crystalline lattice. If there is a limited number of experimental data, one may only allow F^k and ζ_{nf} to vary freely along with the crystal-field parameters and keep other parameters fixed. For further improvement, α, β and γ can be released. For final refinement, M^0 and P^2 may be varied freely with $M^{2,4}$ and $P^{4,6}$ varied following M^0 and P^2 respectively at fixed ratios.

1.3.6 Energy Levels of $4f^N$ Configurations and Binding Energies Relative to Host Band

The free-ion Hamiltonain of Eq. (1.33) and the values of free-ion interaction parameters listed in Table 1.5 are essential in RE spectroscopy and provide a framework useful for analyzing spectra of trivalent RE ions (R^{3+}) in solutions and solids. While the values of free-ion interaction parameters vary within 1% for different hosts, the calculated energy levels of the $4f^N$ multiplets are also expected to vary approximately within 1% for different matrices. The widely-

circulated Dieke chart of energy level structure in the RE series was first created for trivalent ions in $LaCl_3$ based on the analyses of limited spectra (Dieke, 1968) and extended to R^{3+}: LaF_3 by Carnall et al. (1989) with more systematic analyses. The Dieke chart for R^{3+}: LaF_3, Fig. 1.4, is based entirely on the computed energy levels up to 50,000 cm^{-1}, including crystal-field splittings. The computations were conducted with the values of the free-ion and crystal-field parameters listed in Table 1.5. This chart should provide a useful basis for comparison with spectra of trivalent RE ions in other matrices.

While the energy levels of R^{3+} in $4f^N$ configurations extend to higher than 50,000 cm^{-1} for $4 \leqslant N \leqslant 10$, and even extend to higher than 150,000 cm^{-1} for $N=6,7,8$, energy levels accessible by optical excitation are often below 30,000 cm^{-1}. Using excitation with UV sources or two-visible photons, spectra containing energies above 30,000 have been analyzed (Schwiesow and Crosswhite, 1969; Carnall et al., 1989, Liu et al., 1994a) for parameterization of the effective-operator Hamiltonian of Eq. (1.33). Using the values of interaction parameters determined with experimental data for the low-lying states, we anticipate that calculated energy levels below 50,000 cm^{-1} are more accurate than those at higher energies, in which configuration interactions are significant. As a result, the corrections Eqs. (1.35) – (1.38) to the free-ion (and crystal-field, to be discussed in next section) Hamiltonian are either inadequate, or the values of the parameters are expected to be different from these for the low energy states.

So far, we have only discussed the $4f^N$ electronic energy levels of the RE ions. However, interactions between the localized $4f^N$ electronic states of RE ions and the delocalized band states of the crystal lattice can strongly affect the optical properties of technologically important RE-doped materials. Relative energies of $4f^N$ electronic states and crystal band states are important for a fundamental understanding of RE-doped optical materials and a practical understanding of each material's potential performance in specific applications. In contrast to the well-developed understanding of the $4f^N$ states, relatively little is known about the relationships between these states and the electronic states of the crystal. The $4f^N$ ground state binding energies of rare earth ions were recently studied in the gallium garnets by Thiel et al. (2001) using resonant photoemission spectroscopy and compared with the aluminum and iron garnet hosts. The 4d – 4f photoemission resonance was used to separate and identify the $4f^N$ and valence band components of the spectra, and theoretical 4f photoemission spectra were fit to experimental results to accurately determine electron binding energies. A two-parameter empirical model was used to describe the relative energies of the $4f^N$ ground states in these materials. This model can be expressed as

$$E_{4f} = I_{4f} - E_L + \alpha_R(R - R_0) - E_{VBM}, \qquad (1.35)$$

where I_{4f} is the free-ion ionization potential, E_L is the uniform shift experienced

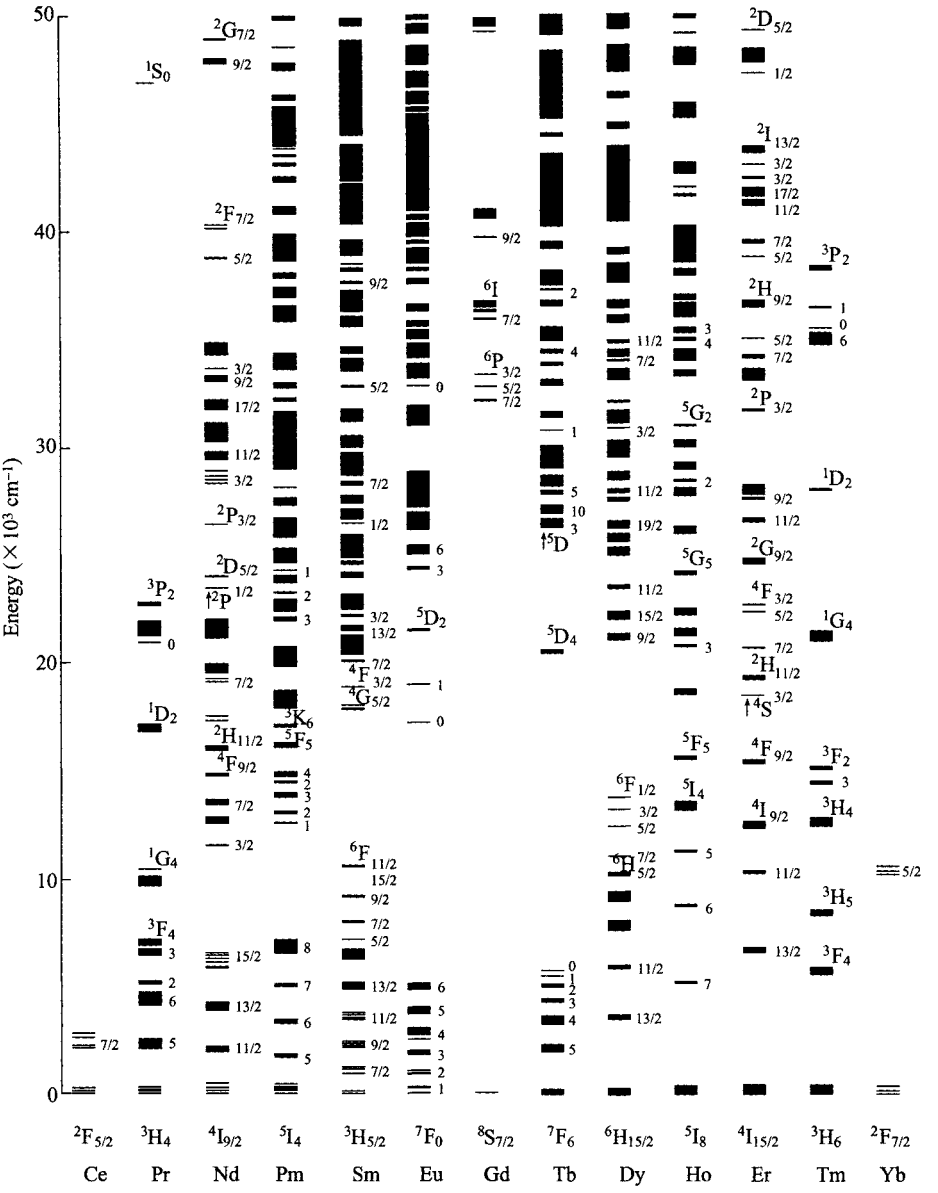


Figure 1.4 Energy level structure of R^{3+}: LaF_3 based on calculated free-ion and crystal-field splittings (Carnall et al., 1989)

by the RE ions, α_R is the binding energy shift per unit change in ionic radius, R and R_0 are the effective ionic radii of the trivalent RE ion and the ionic radius reference. $E_{VBM} = 8.3$ eV is the binding energy of the valence band maximum

(VBM). The value of two parameters in Eq. (1.35), $E_L = 31.6$ eV and $\alpha_R = 9.2$ eV/Å when $R_0 = R(Yb^{3+})$, were obtained by Thiel et al. (2001) in fitting the model to the observed binding energies in gallium garnets. Figure 1.5 shows the calculated and experimental values of binding energies of $4f^N$ electrons in the RE ions relative to VBM in gallium garnets. The experimental data are 7.8, 10.9 and 11.6 eV for TbGG, ErGG, and YbGG, respectively (Thiel et al., 2001), the ionization potentials, I_{4f}, are calculated by Martin et al. (1974), and the effective ionic radii are from Shannon (1976).

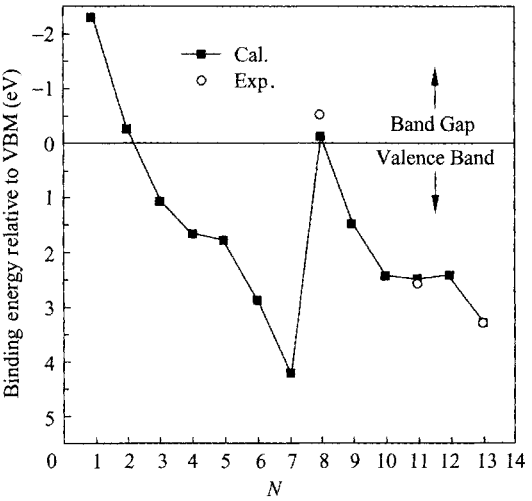


Figure 1.5 Systematic variation of $4f^N$ binding energies relative to the valence band maximum (8.7 eV) in gallium garnets. Circles represent measured binding energies for TbGG (7.8 eV), ErGG (10.9 eV), and TbGG(11.6 eV) (Thiel et al., 2001). The squares connected by solid lines are calculated

The success of this empirical model indicates that measurements on as few as two different RE ions in a host are sufficient to predict the energies of all RE ions in that host. It is shown that systematic shifts in the relative energies of $4f^N$ states and crystal band states between different garnets arise entirely from shifts of the band states, while each RE ion maintains the same absolute binding energy for all garnets studied. These results suggest that further studies of additional host compounds using both photoemission and optical spectroscopy will rapidly lead to a broader picture of the host crystal's effect on 4f electron binding energies.

1.4 Crystal-field Interaction

On placing a rare earth ion in a dielectric crystal, the spherical symmetry of its electronic structure is destroyed, and ionic energy levels split under the influence

of the electric field produced by the crystalline environment. The f-electrons, which participate primarily in ionic bonding with the ligands, have very localized states that are conventionally described in the framework of crystal-field theory (Stevens, 1952; Wybourne, 1965). Using effective operator techniques and the parameterization method, crystal-field theory was developed on the same basis eigenfunctions of the effective operator Hamiltonian for the free-ion interactions as we discussed in the previous section. Applications of group theory along with operator techniques (Tinkham, 1964; Judd, 1963a) have made the crystal-field theory a great success in characterization of the RE ion energy level structure (Görller-Walrand and Binnemans, 1996; Newman and Ng, 2000).

We pointed out in the introduction that, because of the weak ion-ligand interaction, the crystal-field intraconfigurational $4f-4f$ spectra of RE ions contain very sharp spectral lines and are much like the gas phase atomic spectra. The degree to which the $2J+1$ fold degeneracy of a free-ion state is removed depends only on the point symmetry about the ion. The magnitude of crystal-field splittings is determined primarily by the crystal-field strength expressed in terms of the crystal-field parameters of the effective operator Hamiltonian. Because of the complicated electronic interactions in solids, various interaction mechanisms that influence the electronic states of the RE ion in a solid environment may not be accurately calculated in the framework of current crystal-field theory. Evaluation of the crystal-field parameters, however, is theoretically much more difficult than predicting the number of energy levels for each free-ion state. An empirical approach is so far the most effective method for evaluation of the crystal-field parameters (Crosswhite, 1977; Carnall et al., 1984; 1989), while phenomenological modeling and *ab initio* calculations of ion-ligand interactions are able to provide theoretical guidance to the analysis.

From theoretical approaches, analytical expressions of crystal field parameters using phenomenological models are available for calculating the crystal-field parameters of RE ions in specific crystalline lattice. The exchange charge model (ECM) (Malkin et al., 1970, 1987) and the superposition model (SP) (Newman, 1971; Newman and Ng, 1989) are two crystal-field models that have achieved significant success and are very useful for guiding spectrum analysis. From the theoretical point of view, *ab initio* calculations of solid-state electronic energy level structure have advanced significantly along with the rapid development of computer technology and have potential for future applications. However, *ab initio* calculations of f^N crystal field splittings have not reached the accuracy of the observed crystal-field splittings ($< 10\ cm^{-1}$). This accuracy is essential in many cases for determining physical properties of rare earth activated materials (see Chapters 2 – 6).

In this section, we discuss the concepts and methods of crystal field modeling. Applications of empirical methods and model calculations are reviewed with examples of RE activated crystalline materials that have been extensively studied or commonly used as laser media. To gain a more comprehensive understanding of crystal-field theory, the reader may refer to

more detailed reviews (Wybourne, 1965; Hüfner, 1978; Görller-Walrand and Binnemans, 1996; Newman and Ng, 2000).

1.4.1 Crystal-field Hamiltonian and Matrix Element Evaluation

Based on the concept that the crystal-field interaction can be treated approximately as a point charge perturbation on the free-ion energy states, which have their eigenfunctions constructed with the basis of harmonic functions, the effective operators of crystal-field interaction may be defined with the tensor operators of spherical harmonics $\boldsymbol{C}^{(k)}$. Following Wybourne's formalism (Wybourne, 1965), the crystal-field potential may be defined by

$$\mathscr{H}_{\mathrm{CF}} = \sum_{k,q,i} B_q^k C_q^{(k)}(i), \tag{1.36}$$

where the summation involving i is over all the electrons of the ion of interest; B_q^k are crystal-field parameters and, as defined by Eqs. (1.19) and (B.12) in Appendix B, $C_q^{(k)}$ are components of tensor operators $\boldsymbol{C}^{(k)}$ that transform like spherical harmonics.

In addition to Wybourne's formalism for crystal field parameters B_q^k, the older Stevens' notations $A_k^q\langle r^k\rangle$ is often found in the literature. Table 1.6 gives the relationship between B_q^k and $A_k^q\langle r^k\rangle$.

Table 1.6 Relationship between parameters B_q^k and $A_k^q\langle r^k\rangle$

$B_0^2 = 2A_2^0\langle r^2\rangle$	$B_0^6 = 16\,A_6^0\langle r^6\rangle$
$B_2^2 = \frac{\sqrt{6}}{3} A_2^2\langle r^2\rangle$	$B_2^6 = \frac{16\sqrt{105}}{105} A_6^2\langle r^6\rangle$
$B_0^4 = 8A_4^0\langle r^4\rangle$	$B_3^6 = -\frac{8\sqrt{105}}{105} A_6^3\langle r^6\rangle$
$B_2^4 = \frac{2\sqrt{10}}{5} A_4^2\langle r^4\rangle$	$B_4^6 = \frac{8\sqrt{14}}{21} A_6^4\langle r^6\rangle$
$B_3^4 = -\frac{2\sqrt{35}}{35} A_4^3\langle r^4\rangle$	$B_6^6 = \frac{16\sqrt{231}}{231} A_6^6\langle r^6\rangle$
$B_4^4 = \frac{4\sqrt{70}}{35} A_4^4\langle r^4\rangle$	

With the harmonic tensor operators, evaluation of the crystal field matrix elements can be performed with the same methods used for the free-ion matrix elements. With applications of the Wigner-Eckart theorem (Appendix B), the matrix elements of the crystal-field interaction can be expressed with the reduced matrix elements of a unit tensor $\boldsymbol{U}^{(k)}$ (Wybourne, 1965; Weissbluth, 1978):

$$\left\langle l\tau SLJM \left| \sum_i C_q^k(i) \right| l\tau' S'L'J'M' \right\rangle = (-1)^{J-M} \begin{pmatrix} J & k & J' \\ -M & q & M' \end{pmatrix} \times \langle l\tau SLJ \parallel \boldsymbol{U}^{(k)} \parallel l'\tau' S'L'J' \rangle \times \langle l \parallel \boldsymbol{C}^{(k)} \parallel l \rangle. \quad (1.37)$$

In *LS* coupling, the matrix elements of the unit tensor can be further reduced to

$$\langle l\tau LSJ \parallel \boldsymbol{U}^{(k)} \parallel l\tau' L'S'J' \rangle = (-1)^{S+L'+J+k} [(2J+1)(2J'+1)]^{1/2} \times \begin{Bmatrix} J & J' & k \\ L' & L & S \end{Bmatrix} \langle l\tau SL \parallel \boldsymbol{U}^{(k)} \parallel l\tau' L'S' \rangle. \quad (1.38)$$

With Eqs. (1.20), (1.37) and (1.38), we may write the reduced matrix elements of the crystal-field Hamiltonian as

$$\langle l\tau SLJM \mid \mathscr{H}_{\mathrm{CF}} \mid l\tau' S'L'J'M' \rangle = \sum_{k,q} B_q^k (-1)^{J-M} \begin{pmatrix} J & k & J' \\ -M & q & M' \end{pmatrix} D_J^k, \quad (1.39)$$

where

$$D_J^k = (-1)^{S+L'+J+k} [(2J+1)(2J'+1)]^{1/2} \begin{Bmatrix} J & J' & k \\ L' & L & S \end{Bmatrix} \times \langle l\tau SL \parallel \boldsymbol{U}^{(k)} \parallel l\tau' S'L' \rangle (-1)^l (2l+1) \begin{pmatrix} l & k & l \\ 0 & 0 & 0 \end{pmatrix} \quad (1.40)$$

with $l=3$ for f^N configurations. Since all the coefficients, including the values of the 3-j ( ) and 6-j { } symbols, and the doubly reduced matrix elements of the unit tensor, are known for a given free-ion multiplet, it is obvious that evaluation of crystal-field splitting only needs input values of the crystal field parameters B_q^k.

The doubly reduced matrix elements of $\boldsymbol{U}^{(k)}$ may be obtained directly from the tables of Nielson and Koster (1963) or from the SPECTRA program. For configurations of $N > 7$ in the second half of the f-series, the $\boldsymbol{U}^{(k)}$ matrix elements are identical to those of 14-N in the first half of the f-series. The values of the 3-j and 6-j symbols can be obtained from the book of Rotenberg et al. (1959). The values of k and q for which the matrix elements are non-zero are determined by the symmetry of the crystal field and the f-electron angular momentum. For f^N configurations ($l=3$), the 3-j symbols in Eq. (1.40) require that $k=0$, 2, 4, 6, and $|q| \leqslant k$. The values of q are also restricted by the point group of the RE ion site, since the crystal field Hamiltonian has to be invariant under all symmetric operations of the point group. Restrictions due to point group symmetry properties on the non-zero matrix elements of crystal field Hamiltonian

are illustrated in the second part of this section.

For the matrix element of $k = q = 0$, the zero-order of crystal-field interaction is spherically symmetric and does not split the free-ion energy levels, but induces a shift to all energy levels in the same f^N configuration. In general, B_0^0 is not included in evaluation of the crystal-field splitting. Therefore, its contribution to energy level shift is combined with the spherically symmetric component of the free-ion electrostatic interaction. One parameter, namely F^0, absorbs contributions from spherically symmetric components of free-ion and crystal-field interactions.

Once the matrix elements [see Eq. (1.40)] are evaluated, the Hamiltonian of the crystal-field interaction may be diagonalized together with the free-ion Hamiltonian to obtain the crystal-field splitting as a function of the crystal-field parameters. In general, the free-ion parameters may also be considered as variables for fitting an experimental spectrum. As a result, each of the $^{2S+1}L_J$ multiplets splits into crystal-field levels. Because the off-diagonal matrix elements between different J-multiplets may not be zero, as shown in Eqs. (1.39) and (1.40), crystal-field operators can induce J-mixing. Therefore, for RE ions in crystals, both J and M are no longer good quantum numbers.

As a result of J-mixing, as shown in Eq. (B.4) in Appendix B, the eigenfunction of a crystal-field level is of the form,

$$|\mu\rangle = \sum_{J,M} a_{JM} |JM\rangle, \tag{1.41}$$

where, in principle, the summation is over all JM terms of a given f^N configuration. However, inclusion of all J multiplets results in extremely large matrices, particularly, for the configurations with $4 \leqslant N \leqslant 10$. Diagonalization of the effective operator Hamiltonian on the entire $LSJM$ basis could be very time consuming and not actually necessary in an analysis of an experimental spectrum, which usually covers energy levels less than 40,000 cm^{-1}. Off-diagonal matrix elements between free-ion states separated in such a large energy gap are negligibly small. As an approximation, crystal field calculation without including J mixing is appropriate for the isolated multiplets, such as $^1D_2$ of Pr^{3+}, $^8S_{7/2}$ of Gd^{3+}, and $^5D_4$ of Tb^{3+}. In practice, the crystal-field energy level structure of an f^N configuration is usually calculated in a limited energy region in which experimental data are available. Free-ion multiplets with energy levels far from this region may not be included in the calculation. Namely, the eigenfunction basis may be truncated before diagonalizing the matrix of crystal-field Hamiltonian. Theoretically, this truncation of free ion states is legitimate because crystal-field coupling diminishes between two free-ion multiplets as their energy gap increases. From the perturbation point of view, the leading contribution of J mixing to the energy level splitting of the J multiplets is proportional to $1/\Delta E_{JJ'}$. Given that the crystal-field splitting of a free-ion multiplet is on the order of $100 - 1000$ cm^{-1}, the multiplets that are separated by 10^4 cm^{-1} should have no

significant influence on each other.

In computational analyses of experimental spectra, one may truncate the free-ion states whose energy levels are far from the region of interest. This can be readily accomplished after diagonalization of the free-ion matrix to produce the free-ion energy level structure. The later may be considered approximate centers of gravity for the crystal field splitting (Carnall et al., 1984). One chooses the numbers of J multiplets to be included in the crystal-field matrices for each J value. Therefore, the remaining J multiplets are still complete sets of free-ion eigenfunctions that contain all SL components of the given J. This way of free-ion state truncation ensures that no contribution from the free-ion interactions is lost from constructing the free-ion wavefunctions for each J multiplet.

One example is the $^8\mathbf{S}_{7/2}$ ground state of ions in a $4f^7$ configuration for Eu^{2+} and Gd^{3+}, in which both diagonal and off-diagonal matrix elements of crystal field operators vanish. The observed crystal field splittings must be attributed to the contributions of the mixture of other LS terms into the ground state free-ion wavefunction and non-zero off-diagonal matrix elements between different J. Because of large energy gaps from the ground state to the excited multiplets, J mixing is negligible in this case. It has been shown (Liu et al., 1993) that for the $^8\mathbf{S}_{7/2}$ ground state splitting, the leading contributions are from the fourth and higher orders of the coupled matrix elements between the spin-orbit ($\boldsymbol{V}^{(11)}$) and crystal field ($\boldsymbol{U}^{(k)}$) operators. Without inclusion of J mixing, the leading contributions to the crystal-field splitting of the $^8S_{7/2}$ multiplet of an f^7 configuration are from the mixed matrix elements such as

$$\langle {}^8S \| \boldsymbol{V}^{(11)} \| {}^6P \rangle \langle {}^6P \| \boldsymbol{U}^{(2)} \| {}^6D \rangle \langle {}^6D \| \boldsymbol{U}^{(2)} \| {}^6P \rangle \langle {}^6P \| \boldsymbol{V}^{(11)} \| {}^8S \rangle$$

and

$$\langle {}^8S \| \boldsymbol{V}^{(11)} \| {}^6P \rangle \langle {}^6P \| \boldsymbol{U}^{(6)} \| {}^6I \rangle \langle {}^6I \| \boldsymbol{U}^{(6)} \| {}^6P \rangle \langle {}^6P \| \boldsymbol{V}^{(11)} \| {}^8S \rangle.$$

It is obvious that truncation of LS terms in the $J = 7/2$ multiplets should affect the scale of the coupled matrix elements, and thus affect the crystal-field splitting. The same effect is expected for the off-diagonal matrix elements between different J, but this is less important because of the large energy gap between the ground state and the first excited state.

In the literature, the crystal-field interaction is often characterized by quantitative comparison of the crystal-field strength defined as (Auzel, 1983)

$$N_v = \left[\frac{1}{4\pi} \sum_{q,k} \frac{(B_q^k)^2}{2k+1} \right]^{1/2}, \tag{1.42}$$

or as (Chang et al., 1982)

$$S = \left\{ \frac{1}{3} \sum_{k=2,4,6} (2k+1)^{-1} \left[(B_0^k)^2 + 2 \sum_{q>0} | B_q^k |^2 \right] \right\}^{1/2}. \qquad (1.43)$$

1.4.2 Symmetry Rules

We now discuss the geometric properties of the crystal-field operators and parameters in more detail. In addition to the angular momentum of the RE ions that restricts k and q for a set of non-vanishing crystal-field operators, the site symmetry of RE ion in a crystalline lattice also imposes limits on crystal field operators, because the tensor operators for the crystal-field interaction must be invariant under the point group symmetry operations. Here our interest is to identify the non-vanishing components of crystal-field operators and their matrix elements. First, if we restrict our attention to the states of the same parity, namely $l = l'$, k must have even values. It is also required that B_q^k must be real in any symmetry group that contains a rotation operation about the Y-axis by π or a reflection through the X-Z plane; otherwise $B_q^k (q \neq 0)$ is complex. In the later case, one of the B_q^k can be made real by a rotation of system of coordinates about the Z-axis. The B_q^k for $q < 0$ are related to the imaginary ones for $q > 0$ by

$$B_{-q}^k = (-1)^q B_q^{k*}. \qquad (1.44)$$

Also under the invariant conditions of the point group theory, the crystallographic axis of lowest symmetry determines the values of q for the non-vanishing crystal-field operators. For example, at a site with C_{3v} symmetry, there is a threefold axis of rotational symmetry with a reflection plane that contains the C_3 axis (Tinkham, 1964; Hüfner, 1978). The ligand electric field must exhibit this symmetry and hence if a $2\pi/3$ rotation is made on the crystal field potential, followed by a reflection with regard to the plane, the potential is invariant only if $q = 0, \pm 3$, and ± 6. Thus, within an f^N configuration, the crystal field Hamiltonian may be written as

$$\begin{aligned} \mathcal{H}(C_{3v}) = \sum_i \{ & B_0^2 C_0^{(2)}(i) + B_0^4 C_0^{(4)}(i) + B_3^4 [C_{-3}^{(4)}(i) - C_3^{(4)}(i)] \\ & + B_0^6 C_0^{(6)}(i) + B_3^6 [C_{-3}^{(6)}(i) - C_3^{(6)}(i)] \\ & + B_6^6 [C_{-6}^{(6)}(i) + C_6^{(6)}(i)] \}. \end{aligned} \qquad (1.45)$$

If the reflection plane is perpendicular to the C_3 axis, the site symmetry becomes C_{3h}, which occurs for RE ions in all the lanthanide ethylsulfates and trichlorides such as $LaCl_3$ and bromides such as $LaBr_3$ (Morosin, 1968). The potential invariant property requires $q = 0, \pm 6$ only, but since there is no rotation symmetry about the y-axis by π or a reflection through the X-Z plane for the C_{3h}

site, there is an imaginary non-cylindrical term in the Hamiltonian:

$$\mathscr{H}(C_{3h}) = \sum_j \{B_0^2 C_0^{(2)}(j) + B_0^4 C_0^{(4)}(j) + B_0^6 C_0^{(6)}(j) + B_6^6[C_{-6}^{(6)}(j) + C_6^{(6)}(j)] + iB'^6_6[C_6^{(6)}(j) - C_{-6}^{(6)}(j)]\}. \tag{1.46}$$

D_{3h} is a symmetry group that includes all rotation and reflection operations of C_{3v} and C_{3h}(Tinkham, 1964; Hüfner, 1978). The crystal field operators for RE ions at a D_{3h} site are the real terms for C_{3h} without the imaginary term $iB'^6_6(C_6^{(6)} - C_{-6}^{(6)})$. The non-vanishing terms of crystal field operators for various lattice sites of RE ions in crystals are listed in Table 1.7.

Table 1.7 Non-vanishing terms of crystal-field (CF) parameters B_q^k, numbers of reduced matrices and crystal-field quantum number μ for f^N configurations in crystals of various symmetries[a, b]

Crystal structure	Site symmetry	Example	B_q^k	μ (S, D, T, Q)[c] for even N	μ (S, D, T, Q)[c] for odd N
Monoclinic	C_s, C_2, C_{2h}	LaF_3	B_0^2, B_0^4, B_0^6, Re(B_2^2) $B_2^4, B_2^6, B_4^4, B_4^6, B_6^6$	S: ±0, ±1	D: 1/2
Rhombic	C_{2v}, D_2, D_{2h}	$Y_3Al_5O_{12}$	B_0^2, B_0^4, B_0^6, Re(B_2^2, $B_2^4, B_2^6, B_4^4, B_4^6, B_6^6$)		
Trigonal	C_3, $S_6(C_{3i})$	$LiNbO_3$	B_0^2, B_0^4, B_0^6, Re(B_3^4), B_3^6, B_6^6	S: ±0 D: 1	D: 1/2, 3/2
	C_{3v}, D_3, D_{3d}	Y_2O_2S	B_0^2, B_0^4, B_0^6, Re(B_3^4, B_3^6, B_6^6)		
Tetragonal	C_4, S_4, C_{4h}	$LiYF_4$	B_0^2, B_0^4, B_0^6, Re(B_4^4), B_4^6	S: ±0, ±2, D: 1	D: 1/2, 3/2
	D_4, C_{4v}, D_{2d}, D_{4h}	YPO_4	B_0^2, B_0^4, B_0^6, Re(B_4^4, B_4^6)		
Hexagonal	C_6, C_{3h}, C_{6h}, D_6, C_{6v}, D_{3h}, D_{6h}	$LaCl_3$	B_0^2, B_0^4, B_0^6, Re(B_6^6)	S: ±0, ±3 D: 1, 2	D: 1/2, 3/2, 5/2
Cubic	T, T_d, T_h, O, O_h	CeO_2	B_0^4, B_0^6, Re(B_4^4, B_4^6)[d]	S: ±0, ±4 D: 2, 6 T: 1	D: μ = 1/2, 7/2 Q: μ = 3/2

(a) Morrison et al., 1982;
(b) Hüfner, 1978;
(c) S: singlet, D: doublet, T: triplet, Q: quadruplet;
(d) $B_4^4 = \frac{5}{\sqrt{70}} B_0^4$, $B_4^6 = -\sqrt{\frac{7}{2}} B_0^6$.

Because of the 3-j symbols in Eq. (1.39), the degeneracy in M may be completely or partially removed by crystal-field coupling between states of different JM. In the crystal-field matrix, the terms for which $M - M' = q$ are mixed by $C_q^{(k)}$. Otherwise the crystal-field matrix elements are zero. Based on this property, the crystal-field matrix may be reduced into a number of independent submatrices each of which is characterized by a crystal quantum number μ (or Γ). Each μ represents a group of M, such that $M - M' = q$ (0, 2, 3, 4, 6) belongs to the same submatrix (Hüfner, 1978). All matrix elements between the submatrices are zero. The crystal-field quantum number may be used to classify the crystal-field energy levels even when J and M are not good quantum numbers. To consider C_{3h} (and D_{3h}) as an example, the JM and $J'M'$ with $M - M' = 6$ belong to the same crystal-field submatrix. For even number of f electrons, there are four independent submatrices, and for odd number of f electrons, there are three independent submatrices. The parameters of non-vanishing crystal-field terms for symmetries of common crystal hosts of f-element ions are given in Table 1.7 along with the numbers of reduced crystal-field matrices.

Without a magnetic field, the electrostatic crystal field alone does not completely remove the free-ion degeneracy for the odd-numbered electronic configurations. Known as Kramers' degeneracy (Kramers, 1930), all crystal field levels are at least doubly degenerate. The crystal quantum number and JM classification are given for C_{3h} and D_{3h} in Table 1.8. In calculation of energy level structure for degenerate doublets, one may cut off a half of the submatrix elements.

In many cases, calculations of crystal-field energy levels have been successful by using higher site symmetry than the real one so that a smaller number of parameters are required. First of all, this is because RE ions in many solids occupy a low site symmetry and the limited number of observed energy levels could not accurately determine a large number of crystal-field parameters. Secondly, many crystal lattices do not have mirror symmetries in their coordinates so that the crystal-field parameters with $q \neq 0$ are complex (see Table 1.7). If one makes an approximation by using only the real part of the crystal-field operators, the energy level calculation becomes much easier. Since the high symmetry approximation is equivalent to up-grading a lower symmetry site to a higher one within the same symmetry group, this is called the descent-of-symmetry method (Görller-Walrand and Binnemans, 1996). This method may be applied to the groups of monoclinic, trigonal, and tetragonal structures listed in Table 1.7. For example, the S_4 site symmetry of trivalent lanthanide ions in $LiYF_4$ is often treated as D_{2d} (Esterowitz, 1979; Görller-Walrand, 1985, Liu et al., 1994a). Similarly, the actual C_2 symmetry of LaF_3 is replaced by C_{2v} (Carnall et al., 1989) and the C_{3h} symmetry of $LaCl_3$ by D_{3h} (Morrison and Leavitt, 1982).

Table 1.8 Classification of crystal field energy levels for C_{3h} and D_{3h} symmetry

(a) Even number of electrons

J	$M(\mu=0$ $^1\Gamma_{12})$	$M(\mu=\pm1$ $^2\Gamma_5)$	$M(\mu=\pm2$ $^2\Gamma_6)$	$M(\mu=3$ $^1\Gamma_{34})$	No. (Levels)
0	0				1
1	0	±1			2
2	0	±1	±2		3
3	0	±1	±2	3, −3	5
4	0	±1	±2, ∓4	3, −3	6
5	0	±1, ∓5	±2, ∓4	3, −3	7
6	−6, 0, 6	±1, ∓5	±2, ∓4	3, −3	9
7	−6, 0, 6	±7, ±1, ∓5	±2, ∓4	3, −3	10
8	−6, 0, 6	±7, ±1, ∓5	±8, ±2, ∓4	3, −3	11

(b) Odd number of electrons

J	$M(\mu=\pm12$ $^2\Gamma_7)$	$M(\mu=\pm3/2$ $^2\Gamma_8)$	$M(\mu=\pm5/2$ $^2\Gamma_9)$	No. (Levels)
1/2	±1/2			1
3/2	±1/2	±3/2		2
5/2	±1/2	±3/2	±5/2	3
7/2	±1/2	±3/2	±5/2, ∓7/2	5
9/2	±1/2	±3/2, ∓9/2	±5/2, ∓7/2	6
11/2	±1/2, ∓11/2	±3/2, ∓9/2	±5/2, ∓7/2	7
13/2	±13/2, ±1/2, ∓11/2	±3/2, ∓9/2	±5/2, ∓7/2	8
15/2	±13/2, ±1/2, ∓11/2	±15/2, ±3/2, ∓9/2	±5/2, ∓7/2	9

In practical cases, the crystal field of C_{3h} symmetry has been found to exhibit an effective potential appropriate to D_{3h} symmetry because the imaginary term of $\mathrm{Im}B_6^6$ in the C_{3h} potential is negligibly small. This is known because the nearest ligands have D_{3h} symmetry. When the second shell of coordination is considered, the site symmetry reduces to C_{3h} because the second nearest ligands add a smaller contribution to the crystal field at the lanthanide site. As illustrated in Fig. 1.6 on the X-Y plane, a rotation ($\Delta\phi$) of the next nearest ligand (NNL) coordinates about the Z-axis converts the structure of $LaCl_3$ from C_{3h} to D_{3h} symmetry. For the actual structure of the lanthanide ethylsulfates and trichlorides, $\Delta\phi$ may be less than 1°. Similarly for lanthanide ions in $LiYF_4$, the value of $\mathrm{Im}B_4^6$ in the S_4 potential is less determined. With zero $\mathrm{Im}B_4^6$, an effective site symmetry of D_{2d} has been used in practical cases (Morrison and Leavitt, 1982).

Conversion of the $LiYF_4$ structure from S_4 symmetry to D_{2d} symmetry only involves the NNL fluorine ions connected in a tetrahedron. The actual crystallographic site symmetry is a slight distortion of D_{2d}. This implies a distortion of the ϕ-coordinates from the dodecahedron D_{2d} values (Blanchfield, 1983; Urland, 1981). In addition to a rotation of $\Delta\phi$ about the Z-axis, a small change in the radial distance from the Y^{3+} center to the NNL is required in order to construct a perfect D_{2d} symmetry for the two tetrahedrons of the fluorine ions.

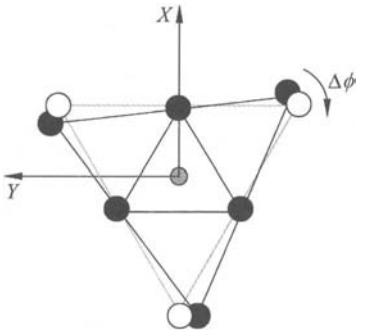


Figure 1. 6 Illustration of descent-of-symmetry operations for $LaCl_3$ type of hexagonal crystals. A rotation of the next nearest lignds on the larger trigonal prism by a small angle $\Delta\phi$ about the Z-axis converts C_{3h} to D_{3h}. The next nearest ligands move from their actual positions to the D_{3h} sites shown by the circles

In general, use of the descent-of-symmetry method may have more complicated consequences than that of the above two examples. For a specific symmetry modification, one may estimate the changes in crystal-field parameters based on the rotation symmetry of point charges in polar coordinates (θ, ϕ) and assume that ligand ions in each shell of coordination are at the same distance from the f-element ion. For an arbitrary rotation, the B_0^k parameters should only depend on the θ-coordinates, whereas the B_q^k parameters ($q \neq 0$) depend on both θ- and ϕ-coordinates. Changes in the ϕ-coordinates have no influence on B_0^k and $|B_q^k| = [(\mathrm{Re}B_q^k)^2 + (\mathrm{Im}B_q^k)^2]^{1/2}$. Descent-of-symmetry operations that have this property are $C_{nh} \rightarrow D_{nh}$, $S_4 \rightarrow D_{2d}$, and $C_n \rightarrow C_{nv}$. The symmetry changes that incorporate a change in θ-coordinates will change all parameters, such as $D_{nh} \rightarrow C_{nv}$ and $D_{nh} \rightarrow C_n$. If the symmetry of the f-element site is lowered, not only are additional parameters required, but there are also changes in the crystal-field parameters present in the higher symmetry. Therefore, there is far less rational for using D_{nh} as an approximation for C_n and C_{nv}.

As mentioned above, site distortion is a common phenomenon when doping f-element ions into crystals. A dopant ion likely has a lower symmetry site than that of the host ion. Accordingly, both the sign and magnitude of crystal-field parameters are subjected to change. The descent-of-symmetry, although not

realized, is actually enacted in analyses of the crystal-field spectra of doped systems in which lowering the site symmetry does not necessarily further reduce the degeneracy of the energy states. As we discussed above, different crystal structures may undergo different types of distortion that reflect the properties of the specific coordination polyhedra in a given crystal. Görller-Walrand and Binnemans (1996) gave a detailed description of the effects of structure distortion in terms of changes in the θ- and ϕ-coordinates. However, changes in radial distances may occur as well. For ions at a distorted site that further reduces the degeneracy of electronic states, analyses of crystal-field spectra must be conducted using a lower symmetry, although in many cases determination of actual site symmetry is difficult. An extensively studied system is trivalent rare earth ions in CaF_2 which has an intrinsic site of cubic symmetry. Due to charge imbalance between a trivalent dopant and a Ca^{2+} ion, more than 20 distinct defect sites have been identified (Seelbinder and Wright, 1979; Tissue and Wright, 1987). In addition to cubic site symmetry, defect sites of C_{4v}, C_{3v} were also found, and many of these defect sites have symmetries lower than C_{nv}.

1.4.3 Empirical Evaluation of Crystal-field Parameters

In modeling crystal-field splittings, we have the same problems as we pointed out in Section 1.3.5 for parameterization of the free-ion Hamiltonian. Theoretical calculations do not accurately reproduce the observed spectra, while the least-squares method for empirical evaluation of crystal-field parameters can result in convergence to a false solution. However, from the experimental point of view, theoretical calculations using the point charge approximation provide a necessary guidance to establishing the parameters for the effective operator Hamiltonian. For RE ions in crystals of well-defined site symmetry, crystal-field theory is widely used along with group theory for predicting the number of energy levels and determining selection rules for electronic transitions between crystal-field levels (see Chapter 2). Whereas the number of non-vanishing crystal-field parameters can be determined by the symmetry arguments, their values are usually determined by analyzing the experimentally observed crystal-field splittings. In general, abundant experimental data that carry supplementary spectroscopic information, such as polarized transitions allowed by electric or magnetic dipolar coupling, ensure the accuracy of the experimentally fitted crystal-field parameters (Liu et al., 1994a). In addition, temperature dependence of crystal-field splitting may be analyzed to distinguish pure electronic lines from vibronic features (see Chapter 3). If multiple sites exist, site-resolved spectra are required to distinguish energy levels of ions at different sites (Tissue and Wright, 1987; Liu et al., 1994a, b). Accordingly, as a procedure of parametric modeling, correct assignment of observed energy levels to the calculated ones is crucial to avoid a false solution. For spectra that lack sufficient experimental information for exclusive assignment, this procedure may

involve several iterations of trial calculations and analyses that again require understanding the basics of crystal-field splitting of free-ion states (Carnall et al., 1989; Carnall, 1992). Based upon the symmetry properties expressed as 3-j symbols in Eqs. (1.39) and (1.40), several criteria may be applied with the assumption that J mixing is small, which is true for isolated multiplets:

(1) Splitting of $J=1$ (or 3/2) states depends only on B_q^2; that of $J=2$ (or 5/2) depends on B_q^2 and also on B_q^4;

(2) The B_0^k parameters dominate splittings between the crystal-field levels that have the same leading M components;

(3) The sign of crystal-field parameters determines the ordering of crystal-field levels in terms of $\mu(JM)$.

For setting initial parameters of the crystal-field Hamiltonian to be fitted by observed energy levels, one may simply use the previously established parameters for different f-element ions in the same or similar host materials. For the entire series of trivalent rare earth ions in one of the most extensively studied crystals LaF_3, the parameters of free-ion and crystal-field interactions are listed in Table 1.5. Comprehensive summaries of previously studied systems were given by Morrison and Leavitt (1982) and also by Görller-Walrand and Binnemans (1996). Alternatively, the signs and magnitudes of crystal-field parameters can be predicted according to the coordination of the f-element ion and using the point charge model of electrostatic crystal-field potential. For this purpose, only the nearest ligand (NL) atoms need to be considered. As a function of the radial and angular coordinates, the expressions for the B_q^k parameters are given in next section. The signs of the crystal-field parameters are merely determined by the angular part of the electrostatic potential and may be obtained by symmetry analysis. The predicted signs are of great importance for checking the signs of the parameters obtained by the fitting procedure. Some sign combinations may correspond to a coordination that is physically impossible. Generally, determination of the magnitudes requires more quantitative calculations of the overlap integrals between the f-electrons and the electrons of the ligands. The electrostatic interactions beyond the nearest ligands may bring about significant contributions to the parameters with $k = 2$. For those parameters, the total contribution from the long range interactions may exceed that of the NL so that a change in the sign of B_q^2 determined by the NL atoms is possible (Zhorin and Liu, 1998). Moreover, the electrostatic point charge model is not realistic in describing the short-range interactions between the f-element ion and its nearest ligands. Charge exchange interactions including covalent effect may dominate the crystal-field parameters with $k=4, 6$. For these reasons, the empirical approach with theoretical guidance is necessary to ensure that the parameterization is within the limitations of physical interactions.

In a nonlinear least-squares fitting process, the magnitudes and signs of crystal-field parameters are varied to best reproduce the observed energy level structure. This is actually a process of optimizing crystalline structure within a

given restriction through variation of the crystal-field parameters. The parameters that have higher weight are better determined than the parameters that have less influence on the observed energy levels. Adding an imaginary parameter may only change the real part of the term that has the same q and k but does not have much influence on other parameters. If the values of the crystal-field parameters for a system of higher symmetry are used as initial values of the parameters for a different system of lower symmetry, the fitting may either fall into a false solution or leave the added parameters less determined. In this case, one should assign the unambiguously observed energy levels, most likely the isolated multiplets, and only allow the most weighted crystal-field parameters to vary freely. Once these weighted parameters settled down, further fitting should be performed on the entire set of crystal-field parameters along with the variation of the free-ion parameters.

1.4.4 Theoretical Evaluation of Crystal-field Parameters

Quantum mechanical calculations of crystal-field energies and corresponding crystal-field parameters for RE ions in compounds with different chemical characteristics were carried out by several groups of authors in the framework of the cluster approximation. For a RE ion and its nearest ligands (chlorine, fluorine or oxygen ions), the fully antisymmetric and orthonormalized wave functions of zero-order are constructed as linear combinations of products of individual ion wave functions, and the energy matrix is built with the complete Hamiltonian that contains one- and two-electron operators including the interaction with the electrostatic field created by the rest of the crystal. The effective crystal-field Hamiltonian is introduced satisfying the requirements that its matrix elements in the basis of 4f-functions of the RE ion coincide with the corresponding matrix elements of the complete Hamiltonian (see Appendix A). The first order contributions to the energy matrix include integrals over one-electron wave-functions of the occupied states of the cluster. Higher order contributions correspond to configuration mixing. The procedure and details of calculations have been described in original and review papers by Newman (1971), Eremin (1989), Garcia and Faucher (1995), Shen and Bray (1998), and Newman and Ng (2000). Here we present only a brief description of the results of *ab initio* simulations that are important for modeling of the main physical mechanisms responsible for crystal-field splittings in the spectra of RE ions.

The first order terms in the energy matrix include Coulombic, exchange and overlap integrals over 4f orbitals of the RE ion and outer orbitals of ligand ions. From these terms, the 4f-electron energy in the electrostatic field of the ligand point multipole moments and the charge penetration contribution may be singled out. The second order terms may be classified according to the intermediate (virtual) excited state of the cluster. In this regard, the following electronic

excitations are considered:

(1) Intra-ion excitations from the filled electronic shell of the RE ion to the empty excited shell (in particular, $5p^6 \rightarrow 5p^5 5d^1$). These processes shield the inner valence $4f^N$-shell and may be accounted for, at least partly, by introducing shielding (or antishielding) factors into the multipole moments of the valence electron ($\langle 4f|r^k|4f\rangle \rightarrow (1-\sigma_k)\langle 4f|r^k|4f\rangle$) (Rajnak and Wybourne, 1964). The shielding factors for RE ions were computed by Gupta and Sen (1973) using the variational method.

(2) Intra-ion excitations from the valence shell into empty shells and from the filled shells into the valence shell (in particular, $4f^N \rightarrow 4f^{N-1}5d^1$ or $5p^6 \rightarrow 5p^5 4f^{N+1}$). These processes contribute to the linear shielding and cause additional corrections to parameters of the effective Hamiltonian bilinear in parameters of the electrostatic field.

(3) Inter ion excitations, mainly into the charge transfer states of the RE ion with the extra electron in the valence shell excited from the ligand outer filled shell. Actually, mixing of the ground configuration with the charge transfer states corresponds to the partial covalent character of chemical bonding between an RE ion and its ligands.

It should be noted that the effective Hamiltonian (see Eq. (1.36)) with a single set of crystal-field parameters, operating within the total space of wave functions of the $4f^N$ configuration, can be introduced if all excited configurations of the cluster under consideration are separated from the ground configuration by an energy gap that is much larger than the width of the energy spectrum of the ground configuration. Otherwise the crystal-field parameters become term (*LSJ*) dependent. In particular, the crystal-field analysis fulfilled on an extended basis containing the ground $4f^2$ and excited 4f5d, 4f6p configurations of Pr^{3+} in YPO_4 (Moune et al., 2002) greatly improved the agreement between the experimental data and the calculated energy levels. An example of the quasiresonant mixing of the ground $4f^{13}$ configuration with the charge transfer states of the $Yb^{3+}Br_6^-$ cluster in $CsCdBr_3$ and its effect on the splitting of the excited $^2F_{5/2}$ multiplet of the Yb^{3+} ion was described by Malkin et al. (2000).

A general conclusion concerning the dominant role of overlap and covalent contributions to the crystal-field parameters B_q^4 and B_q^6 follows from all *ab initio* calculations carried out up to the present time. When the Hartree-Fock one-electron wave functions of free ions are used in simulations, relative differences between the theoretical and experimental values of these parameters do not exceed 50%. However, for the parameters B_q^2 of the quadrupole component of the crystal field, contributions from the long-range interactions of valence electrons with point charges, dipole and quadrupole moments of ions in the crystal lattice are comparable to contributions from the interactions with the nearest ligand ions, and the theoretical estimations differ substantially from the experimental data.

Whereas the free-ion parameters vary smoothly across the 4f series, series

trends in crystal-field parameters, particularly B_q^4 and B_q^6, usually break at the f^7 configuration. Experimental evidence was obvious from systematic analysis of the spectra of the trivalent lanthanides doped into single crystal LaF_3 (Carnall et al., 1989) and trivalent actinides in $LaCl_3$ (Carnall, 1992). An abrupt change in the magnitude of parameters with $k = 4$ and 6 occurs at the center of the series. Judd has interpreted this effect as a problem of the one-electron operators of the crystal-field Hamiltonian (Judd, 1979). One-electron operators, U^k, change sign at the center of the series. Inclusion of two-electron operators in the crystal-field Hamiltonian would likely remove this discontinuity.

1.4.4.1 Superposition Model

Although extensive Hartree-Fock calculations have been utilized for establishing systematic trends of free-ion interactions that lead to the determination of the parameters of the effective-operator Hamiltonian, most analyses of crystal-field interactions are carried out with the crystal-field parameters determined in fitting of experimental data. Attempts to calculate the crystal-field parameters from first principles may not be realistic. Given the complexity of electronic interactions in solids, *ab initio* calculations of electronic structure of heavy element ions in solids are currently not capable of achieving resolution that is comparable to experimental results. Therefore, theoretical models, more or less phenomenological on the basis of the point charge approximation, are essential in providing a clear theoretical understanding of electronic interactions of rare earth ions in solids. Model calculations do not only generate the phenomenological crystal-field parameters that provide guidance to parametric modeling of the crystal-field spectra of f-element ions in solids, but also reveal more fundamental aspects of the ion-ligand interactions that are poorly characterized by the point-charge approximation itself. Among the crystal-field models introduced in the literature, the Angular Overlap Model (Jørgensen et al., 1963), Exchange Charge Model (Malkin et al., 1970; Malkin, 1987), and Superposition Model (Bradbury and Newman, 1967; Newman, 1971) have been used for calculation of crystal-field parameters for both 4f elements and 5f elements in various crystals.

Detailed discussions of the superposition model of the crystal field and its application to analysis of experimental spectra were provided by Newman and Ng (1989, 2000). The superposition model neglects the ligand-ligand overlap effects and treats the total crystal-field interaction as a linear "superposition" of local RE-ligand pair-wise electrostatic interactions. The crystal-field parameters are expressed as a sum of individual contributions from ions in the host crystal lattice,

$$B_q^k = \sum_L \overline{B}_k(R_L)\, g_{k,q}(\theta_L, \varphi_L), \qquad (1.47)$$

where $g_{k,q}$ are normalized spherical harmonic functions, and R_L, θ_L, φ_L locate

the position of ligand L in the lattice coordination environment. The distance dependent parameters $\bar{B}_k(R_L)$ are referred to as intrinsic crystal-field parameters, which by definition are dependent only on the radial distance between the RE ion and the ligand L. Based on the assumption of the point charge model that the RE-L electrostatic interaction has specific power dependence, the intrinsic parameters can be defined as

$$\bar{B}_k(R_L) = \bar{B}_k(R_0)(R_0/R_L)^{\tau_k}, \tag{1.48}$$

where R_0 is the distance between the RE ion and a reference ligand located on the Z-axis of the crystalline lattice, and τ_k are power law exponents that reflect the distance dependence of the RE-L interaction (Newman and Ng, 2000). As phenomenalogical parameters, $\bar{B}_k(R_0)$ and τ_k can be empirically determined. It should be noticed that τ_k are not generally in agreement with the electrostatic power law components $\tau_2 = 3$, $\tau_4 = 5$, $\tau_6 = 7$. For chloride ligands, in particular, $\tau_4 = 12-16$, $\tau_6 = 5-7$ for different RE ions (Reid and Richardson, 1985). Values of the rank 4 and 6 parameters quickly decrease with R, and the corresponding sums (see Eq. (1.47)) are limited to the nearest neighbors of the RE ion. Because of the long-range effect, values of the rank 2 parameters are often difficult to determine. Levin et al. (1983) broke the rank 2 operator into two terms, labeled as p and s:

$$\bar{B}_2(R_L) = \bar{B}_2^p(R_0)(R_0/R_L)^3 + \bar{B}_2^s(R_0)(R_0/R_L)^{10} \tag{1.49}$$

to represent, respectively, the ligand point charge contribution and the short range contribution.

Apparently, model calculations of crystal-field parameters result in less discrepancy for some systems than for others. This is mainly due to uncertainties in structure information to which crystal-field calculations, particularly of the rank 4 and 6 parameters, are extremely sensitive. Crystal lattice constants determined from X-ray diffraction or neutron scattering may be of very high resolution only for intrinsic sites. For RE ions doped into host materials, an unknown structural distortion is induced in most cases. The doping induced site distortion depends on the ionic radius difference between the host ion and the doped f-element ion. If a model calculation is conducted based on the structurial information for the host, the calculated crystal-field parameters are expected to be more or less different from that determined by experiments.

1.4.4.2 Exchange Charge Model

The exchange charge model (ECM) (Malkin et al., 1970; Larionov and Malkin, 1975; Malkin, 1987) is an extension of the angular overlap model (Jørgensen, 1962). It considers both long-range and short-range interactions between a lanthanide ion and lattice ions. The effective crystal-field Hamiltonian

is assumed to be a sum $\mathscr{H}_{CF} = \mathscr{H}^{pm} + \mathscr{H}^{ec}$, where the first term corresponds to the electrostatic interaction of valence electrons localized on the lanthanide ion with point multipole moments of lattice ions, The second term approximates all contributions due to the spatial distribution of electron density. Both terms have the form Eq. (1.47) with parameters $B_q^{(pm)k}$ and $B_q^{(ec)k}$. Matrix elements of the effective-operator Hamiltonian $\mathscr{H}^{ec}$ in the basis of one-electron wave functions of the lanthanide ion interacting with spherical ligand ions labeled by the index L are written as

$$\langle nlmm_s \mid \mathscr{H}^{ec} \mid n'l'm'm'_s \rangle = 2e^2 \sum_L \sum_{\alpha(L)} \frac{G^{nl,\,n'l'}_{\alpha(L)}}{R_L} \times \langle nlmm_s \mid \alpha(L) \rangle \langle \alpha(L) \mid n'l'm'm'_s \rangle, \tag{1.50}$$

where $G^{nl,\,n'l'}_{\alpha(L)}$ are the dimensionless parameters of the model, $\alpha(L)$ is the spin-orbital $\mid n''l''m''m''_s \rangle_L$ of the ligand L in the local system of coordinates S_L, centered at this ligand ion, with the quantization axis along the ligand radius-vector $\boldsymbol{R}_L$. To calculate the overlap integrals in Eq. (1.50), we have to rotate the coordinate system S in such a way that the axes of the transformed coordinate system S'_L are parallel to the corresponding axes of S_L. Substituting the transformed orbital wave functions $\mid nlm \rangle$ and $\mid n'l'm' \rangle$ of the RE ion, expressed through matrix elements of the irreducible representations $D^{(l)}$ and $D^{(l')}$ of the rotation group and making use of the decomposition of the direct product $D^{(l)} \times D^{(l')}$, into a linear combination of $D^{(L)}$ ($L = \mid l - l' \mid, \cdots, l + l'$), it is possible to single out in Eq. (1.50) matrix elements of spherical operators $\langle nlm \mid C_q^{(k)} \mid n'l'm' \rangle \delta_{m_s m'_s}$ with coefficients,

$$B_q^{(ec)k}(nl, n'l') = \sum_L \frac{2(2k+1)}{[(2l+1)(2l'+1)]^{1/2}} \frac{e^2}{R_L} \times S_k^{(nl,\,n'l')}(R_L)(-1)^q C^{(k)}_{-q}(\theta_L, \varphi_L), \tag{1.51}$$

where

$$S_k^{(nl,\,n'l')}(R_L) = \sum_{n''l''m'' \subset L} G^{nl,\,n'l'}_{n''l''m''}(-1)^{m''} \langle nlm'' \mid n''l''m'' \rangle \times \langle n''l''m'' \mid n'l'm'' \rangle \frac{\begin{pmatrix} l & l' & k \\ -m'' & m'' & 0 \end{pmatrix}}{\begin{pmatrix} l & l' & k \\ 0 & 0 & 0 \end{pmatrix}}. \tag{1.52}$$

Usually, only outer filled $n''s^2$ and $n''p^6$ electron shells of ligand ions (in particular, of oxygen or halogen ions) are considered, and the bilinear forms (see Eq. (1.52)) constructed from the overlap integrals are

$$S_k^{(nl,\,n'l')}(R_L) = G_s^{nl,\,n'l'} S_s^{nl} S_s^{n'l'} + G_\sigma^{nl,\,n'l'} S_\sigma^{nl} S_\sigma^{n'l'} + \gamma_k^{(ll')} G_\pi^{nl,\,n'l'} S_\pi^{nl} S_\pi^{n'l'}, \quad (1.53)$$

where

$$\gamma_k^{(ll')} = -2\frac{\begin{pmatrix} l & l' & k \\ -1 & 1 & 0 \end{pmatrix}}{\begin{pmatrix} l & l' & k \\ 0 & 0 & 0 \end{pmatrix}} = \frac{l(l+1) + l'(l'+1) - (k+1)}{[\,l(l+1)\,l'(l'+1)\,]^{1/2}}, \quad (1.54)$$

and

$$S_s^{nl}(R_L) = \langle nl0 \mid n''00\rangle, \quad S_\sigma^{nl}(R_L) = \langle nl0 \mid n''10\rangle,$$
$$S_\pi^{nl}(R_L) = \langle nl1 \mid n''11\rangle. \quad (1.55)$$

In the definitions of the overlap integrals (see Eq. (1.55)), wave functions of the lanthanide and ligand ions are considered in the reference systems S'_L and S_L with the common quantization axis.

Parameters of the electrostatic interaction of the valence electron with charge distributions localized at the crystal lattice sites are usually presented by a sum of contributions from the electric fields of point charges ($B_q^{(\mathrm{pc})k}$), point dipole and quadrupole moments ($B_q^{(\mathrm{pd})k}$, $B_q^{(\mathrm{pq})k}$). In particular, parameters of the effective crystal-field Hamiltonian are related to the electrostatic field of point charges and averaged over radial wave functions of the lanthanide ion are

$$B_q^{(\mathrm{pc})k}(nl, n'l') = -\sum_L e^2 q_L (1 - \sigma_k^{nl,\,n'l'}) \langle nl \mid r^k \mid n'l'\rangle \times (-1)^q C_{-q}^{(k)}(\theta_L, \varphi_L)/R_L^{k+1}, \quad (1.56)$$

where eq_L is the net charge of the ligand ion L, and $\sigma_k^{nl,\,n'l'}$ are the shielding factors (Sternheimer et al., 1968; Erdos and Kang, 1972). With known lattice structure constants, numerical values of the parameters (see Eq. (1.56)), as well as of the dipole and quadrupole field parameters, for which explicit expressions have been presented by Faucher and Garcia (1982) and Eremin (1989), may be obtained using the Hartree-Fock radial integrals (Freeman and Watson, 1962) and the Ewald method of calculating the lattice sums. However, uncertainties in the estimations of the electrostatic field parameters remain rather large because determination of multipole moments of lattice ions is far from being clear even in crystals with dominant ionic binding (Malkin, 1987).

To gain a greater insight into the approximation (see Eq. (1.50)) of the energy matrix, it is instructive to compare contributions to the crystal-field parameters of Eqs. (1.51) and (1.56). Both expressions contain the same functions of ligand angular coordinates. Therefore, by taking into account the

overlap and covalency effects, ECM introduces the renormalization of the parameters of the electrostatic crystal field only and does not change the structure of the Hamiltonian $\mathscr{H}^{\mathrm{pm}}$. This renormalization may be considered a result of the "nonlocal" interaction of the valence electron with the exchange charges localized at the bonds connecting the lanthanide ion with its nearest neighbor ions. The concept of exchange charge, with which the crystal-field model under consideration was named, was introduced first by Dick and Overhauser (1958) in the theory of dielectric properties of solids. Values of exchange charges are proportional to the bilinear combinations of the overlap integrals of Eq. (1.53) and depend on the rank k of the corresponding tensor $\boldsymbol{B}^{(k)}$ of crystal-field parameters. It is important that ECM allows for consideration of both even and odd components of the crystal field. In particular, integral intensities of spectral lines in the intraconfigurational $4f^N - 4f^N$ spectra and their frequencies may be fitted in the framework of a single model.

Formally, neglecting the electrostatic field contributions $B_q^{(\mathrm{pm})k}$, it is possible to relate the fitting parameters of ECM $G_\alpha^{4f,4f} = G_\alpha (\alpha = s, \sigma, \pi)$, which determine the crystal field affecting states of the $4f^N$-configuration, directly to the parameters of the angular overlap model (orbital 4f-electron energies $\langle 4f, m=0 | \mathscr{H}_{\mathrm{CF}} | 4f, m=0 \rangle = e_s + e_\sigma$, $\langle 4f, m=1 | \mathscr{H}_{\mathrm{CF}} | 4f, m=1 \rangle = e_\pi$ in the field of a ligand placed on the quantization axis). It is also possible to relate the ECM parameters to the intrinsic parameters of the superposition model (see Eq. (1.48)):

$$\bar{B}_k(R_L) = \frac{2k+1}{7} a_k (e_s + e_\sigma + \gamma_k e_\pi) \tag{1.57}$$

$$e_\alpha(R_L) = 2\frac{e^2}{R_L} G_\alpha [S_\alpha^{4f}(R_L)]^2, \tag{1.58}$$

where $a_2 = 1/2$, $a_4 = 1/8$, $a_6 = 1/16$, and $\gamma_k = \gamma_k^{(3,3)}$, $\gamma_2 = 3/2$, $\gamma_4 = 1/3$, $\gamma_6 = -3/2$. Thus, instead of six independent parameters in the superposition model (see Eq. (1.48)), it is possible to fit only three parameters in ECM because the dependence of the exchange charges on the distance between RE and ligand ions is determined by overlap integrals. If all ligand ions are at equivalent sites relative to the RE ion, there are only two parameters to be fit, $e_s + e_\sigma$ and e_π. An order of magnitude of the dimensionless parameters G_α can be estimated from calculations of the Madelung energies at the ligand and RE sites, and, in a general case, we can expect that $G_\sigma > G_\pi > G_s$ due to the covalency effects (Eremin, 1989). However, more often than not it was possible to obtain a satisfactory description of the crystal field in RE-doped dielectric crystals even in the framework of the one-parameter ECM with $G_s = G_\sigma = G_\pi$ (Malkin, 1987). The generalization of the exchange charge model in a case of nonspherical ligands was presented by Avanesov et al. (1992). Specific features of the electron density distribution outside the cluster containing the nearest neighbors of the RE ion, in particular, mixing of σ-, π- and s-orbitals of ligand ions, cause renormalization of

dipole and quadrupole electrostatic field parameters.

As an example of the ECM calculation, Table 1.9 lists the values of crystal-field parameters calculated by using the ECM in comparison with the experimentally determined ones. It is evident that the dominant contributions to B_q^2 are from electrostatic interactions, whereas those to B_q^4 and B_q^6 are from short-range interactions. It is generally realized that the second-order parameters B_q^k with $k = 2$ are less accurately determined by model calculation than by the experimental approach, particularly for disordered lattice. This is because the second-order parameters that characterize the long-range electrostatic interactions are difficult to calculate accurately. It should be noted that contradiction between the calculated and experimental values of the B_0^2 parameter in Nd^{3+}: $LaCl_3$ (in particular, different signs) may be removed when taking into account large contributions due to point dipole and quadrupole moments of chlorine ions (Eremin, 1989). More applications of ECM to modeling crystal-field energies and ion-phonon interaction in $LiYF_4$ crystals activated by lanthanide ions are given in Chapter 3.

Table 1.9 Crystal-field parameters from ECM calculation and experimental fit (cm^{-1})[a]

	Nd^{3+}: $LaCl_3$ Calculated[b]	(C_{3h} symmetry) Experimental[b] (fit to D_{3h})	Cm^{3+}: $LuPO_4$ Calculated[c]	(D_{2d} symmetry) Experimental[c]
B_0^2	−78(39)	81	450(180)	399
B_0^4	−78(−57)	−42	370(230)	363
B_0^6	−44(−41)	−44	−2500(−2050)	−2470
ReB_4^4	–	–	2400(1200)	2261
ReB_4^6	–	–	200(185)	167
ReB_6^6	299(279)	439	–	–
ImB_6^6	−239(−226)	–	–	–

(a) The values in parentheses are contribution from exchange charge interactions;
(b) Zhorin and Liu, 1998;
(c) Liu et al., 1998.

1.4.5 Corrections to the Crystal-field Hamiltonian

1.4.5.1 Electron Correlation in Crystal-field Interaction

As described above in the proceeding sections, the one-electron crystal-field parameterization is able to reproduce the crystal-field energy level structures of RE ions in good agreement with high resolution absorption and fluorescence spectra. The standard deviation in a nonlinear least-squares fit to experimental spectra in the low-lying energy levels ($< 40,000\ cm^{-1}$) can be less than $10\ cm^{-1}$ (Liu et al., 1994a). However, crystal-field modeling of energy levels for some particular states in the 4f configurations is invariably poor as, for

instance, in the cases of the $^2H_{11/2}$ multiplet of Nd^{3+} and $^3K_8$ of Ho^{3+}. Adjustment in the free-ion Hamiltonian does not result in much improvement. This problem is primarily due to the exclusion of the electron correlation effect in the one-electron crystal-field model. The effects of electron-electron interaction cannot be completely absorbed into the effective operator Hamiltonian of the one-electron crystal-field model. Reid and Newman (2000) have reviewed progress in the modification of the one-electron crystal-field theory with inclusion of correlation crystal-field operators in the Hamiltonian.

There are various physical mechanisms that contribute to multiplet-dependent crystal-field splittings and can be described generally as correlation effects. The two obvious mechanisms, namely, the spin-correlated crystal-field potential (Newman, 1971; Judd, 1977a) and the anisotropic ligand polarization effect, also known as nephelauxetic effect (Jørgensen, 1962; Gerloch and Slade, 1973), have been identified as large contributors, although, it is not clear what physical mechanisms produce the dominant contribution to shift the RE electronic energy levels. To correct the discrepancy that appears in analysis of optical spectra with the one-electron crystal-field model, it becomes necessary to introduce a full parameterization of the anisotropic two-electron interaction. To facilitate calculations of the matrix elements with the same basis for the one-electron operator Hamiltonian, Judd's $g_{iq}^{(k)}$ operators (Judd, 1977b), which are orthogonal over the complete f^N basis sets, are used to define the correlation crystal-field (CCF) Hamiltonian (Reid, 1987):

$$\mathscr{H}_{\mathrm{CCF}} = \sum_{ikq} G_{iq}^{k} g_{iq}^{(k)}, \tag{1.59}$$

where G_{iq}^{k} are parameters of the correlation crystal field, The index k runs through the even integers from 0 to 12 (4 for f^N configurations), The parameter q is restricted by symmetry, and the number of operators varies with k. The operators $g_i^{(k)}$ with $k=0$ correspond to Coulomb interactions and those with $i=1$ to one-electron operators, in fact $\boldsymbol{g}_1^{(k)} \equiv \boldsymbol{U}^{(k)}$.

The main problem in the application of the correlation crystal-field Hamiltonian is the very large number of parameters that is necessary to take account of the electron-electron correlation. However, as we pointed out in Section 1.4.3, the success of parameterization of RE crystal-field energy level structure is largely dependent on the accuracy and the number of input observed energy levels. In general, the nonlinear least square fitting requires that the number of assigned energy levels should be much larger than the total number of freely varied parameters. Expanding the effective operator Hamiltonian by including the operators for correlation crystal field interaction is effective only if there are sufficient experimental data and correctly determined parameters for the free-ion and one-electron crystal-field Hamiltonian for initial input. Otherwise,

fits may fall into false minima and produce inconsistent parameters. In fact, many previous parameterization analyses that concentrated on trying to improve fits to certain multiplets in spectra of Pr^{3+}, Nd^{3+}, Ho^{3+}, and Er^{3+} created uncertainties as to which operators are important. To correct the one-electron crystal-field discrepancy by adding more terms to the crystal-field interaction, one should always consider restrictions on operators and introduce constraints based on physical relationships for reducing the number of freely varied parameters.

To reduce the number of independent CCF parameters, Li and Reid (1990) fixed the ratios of CCF parameters with different values of q to have the same ratios as the one-electron crystal-field operators,

$$\mathscr{H}_{\mathrm{CCF}} = \sum_{ik} G_i^k \left(g_{i0}^{(k)} + \sum_{q \neq 0} g_{iq}^{(k)} \frac{B_q^k}{B_0^k} \right), \tag{1.60}$$

with the ratio B_q^k/B_0^k taken from the fits with the one-electron crystal-field model.

Li and Reid (1990) pointed out that for Nd^{3+}, only the $\boldsymbol{g}_{10A}^{(4)}$ and $\boldsymbol{g}_{10B}^{(4)}$ operators have large matrix elements for the $^2H_{11/2}$ multiplet, whereas $\boldsymbol{g}_2^{(4)}$ is effective in improving the fits to other multiplets. Using those three operators in addition with the one-electron parameters, Burdick et al. (1994) performed fits to the spectrum of Nd^{3+}: YAG. With the extra correlation crystal-field parameters G_2^4, G_{10A}^4, and G_{10B}^4 the standard deviation for the $^2H_{11/2}$ multiplet was reduced from 75 cm^{-1} to 10 cm^{-1}, whereas the standard deviation for the 144 assigned levels was reduced from 31 cm^{-1} to 15 cm^{-1}. Table 1.10 compares the values of the parameters for the fits with and without the CCF operators.

1.4.5.2 Effects of Configuration Interaction

As we discussed in Section 1.3.3, the effective-operator Hamiltonian for free-ion interaction includes three corrective terms (1.29) due to configuration interaction. In crystal-field theory, the effect of configuration interaction was also considered (Rajnak and Wybourne, 1964). For a configuration of equivalent electrons l^N, most mechanisms of configuration interaction lead to a simple scaling of the crystal-field parameters B_q^k. However, one-electron excitation, either from the l^N shell to unfilled orbitals or from closed shells into the l^N shell, results also in overt effects that cannot be accommodated by scaling of the B_q^k parameters alone. As a result, the crystal-field parameters are expected to vary from one multiplet to another.

Table 1.10 Parameters obtained from one-electron crystal field (CF) and correlation crystal-field (CCF) analyses of Nd^{3+}: YAG energy levels (cm^{-1}) (Burdick et al., 1994)

Parameter[a]	CF	CF + CCF
B_0^2	−405 ±29	−387 ±15
B_2^2	179 ±25	172 ±12
B_0^4	−2823 ±84	−2766 ±45
B_2^4	540 ±93	529 ±45
B_4^4	1239 ±67	1275 ±36
B_0^6	955 ±101	972 ±51
B_2^6	−390 ±87	−333 ±45
B_4^6	1610 ±56	1611 ±27
B_6^6	−281 ±78	−229 ±39
G_2^4	-	−804 ±135
G_{10A}^4	-	1290 ±80
G_{10B}^4	-	609 ±108
P[b]	25	28
σ[c]	31.1	15.3

(a) Free ion interaction parameters vary less significantly from the values listed in Table 1.5;
(b) Total number of freely varied parameters;
(c) Standard deviations calculated for least-squares energy level fits.

For the weak crystal-field interaction of RE ions in crystals, the usual method of a second-order perturbation theory can be used for characterizing the configuration interaction (Rajnak and Wybourne, 1963, 1964; Judd, 1963b). The single particle operator $C_q^{(k)}$ in Eq. (1.36) can only couple configurations that differ by the excitation of a single electron. Thus, for an nl^N-type configuration, only three types of configurations are coupled:

(1) $nl^N n'l'^{4l'+2}$ with $nl^N n'l'^{4l'+1}n''l''$;
(2) nl^N with $nl^{N-1}n'l'$;
(3) $nl^N n'l'^{4l'+2}$ with $nl^{N+1}n'l'^{4l'+1}$.

As a result of interaction between these configurations, each matrix element of Eq. (1.39) must be replaced by

$$(1+\Delta)\langle l^N \tau SLJM \mid B_q^k C_q^{(k)} \mid l^N \tau' S'L'J, M'\rangle, \tag{1.61}$$

where Δ is known as the configuration interaction correction factor. This factor is the sum of two terms Δ_1 and Δ_2, where

$$\Delta_1 = \frac{-1}{E}\sum_m \frac{\langle nl^N\psi \mid \mathscr{H}_{CF} \mid m\rangle\langle m \mid \mathscr{H}_{CF} \mid nl^N\psi'\rangle}{\langle nl^N\psi \mid \mathscr{H}_{CF} nl^N\psi'\rangle}, \tag{1.62}$$

and

$$\Delta_2 = \frac{-2}{E} \sum_m \frac{\langle nl^N\psi \mid \mathscr{H}_{CF} \mid m\rangle\langle m \mid \mathscr{H}_C \mid nl^N\psi'\rangle}{\langle nl^N\psi \mid \mathscr{H}_{CF} \mid nl^N\psi'\rangle}, \qquad (1.63)$$

where E is the mean excitation energy of the excited electron, m is a state of the perturbing configuration, $\mathscr{H}_{CF}$ is the crystal-field Hamiltonian and $\mathscr{H}_C$ is the Coulomb interaction in the free-ion Hamiltonian.

The first correction factor Δ_1 in Eq. (1.62) corresponds to configuration mixing purely by the crystal field, while the second factor Δ_2 in Eq. (1.63) represents an electrostatically correlated crystal-field interaction between the configurations. Methods for evaluating the matrix elements have been discussed in detail in previous work (Rajnak and Wybourne, 1964; Judd, 1963b). It has been shown that the primary effect of configuration interaction is simply to scale the crystal-field parameters B_q^k. The individual parameters are shielded (or antishielded) by different amounts depending on the perturbing configuration. This overall scaling effect is absorbed into the crystal-field parameters determined from the experimental data. However, it has been shown that the second factor Δ_2 may be different for different SL states. This means that the crystal-field parameters are no longer independent of free-ion states. If this mechanism is at all important, the crystal-field parameters determined in fitting observed states in a narrow energy region of the ground multiplet give inadequate description of the crystal-field splittings of the multiplets at higher energies.

1.5 Analysis of Crystal-field Spectra

Following our discussion of the effective-operator Hamiltonian for free-ion and crystal-field interactions of RE ions in crystals, we now summarize how to practically analyze experimental spectra and parameterize the Hamiltonian with computer programs such as SPECTRA. We use Tb^{3+}: $LiYF_4$ as an example and review the work by Liu et al. (1994a). In that work, the spectrum analysis and parameterization of the Hamiltonian were based on a total of 165 observed crystal-field energy levels of Tb^{3+}. Obtained using polarized one- and two-photon spectroscopic methods, these energy levels cover a relatively broad spectral range from the $^7F_6$ ground state up to the $^5K_7$ multiplet at 42,000 cm^{-1}. Such a large volume of data is essential for reliable parameterization of the effective-operator Hamiltonian for an f^8 configuration, which has hundreds of crystal-field states with energies extending into the deep UV region. In crystal-field analysis, it is also a common problem that transitions due to ions at an intrinsic site cannot be easily distinguished from that at disturbed or defect sites. Moreover, in addition to zero phonon electronic transitions, vibronic side bands may also appear in the experimental spectra and make spectrum assignment difficult. Any incorrect assignment of the observed energy levels thus can result

in discrepancies between the calculated energy levels and the observed ones. When a number of assignments are incorrect, fitting of the calculated energy level structure would produce inconsistent and non-meaningful parameters.

Prior to the comprehensive crystal-field analysis by Liu et al. (1994a), Morrison and Leavitt (1982) reported some of the energy levels of Tb^{3+}: $LiYF_4$ in a review article. Christensen (1978) reported a spectroscopic analysis of the similar compound $LiTbF_4$, based on the observed energy levels of $^7F_J(J=0,\ 1,\ 2,\ 3)$ and $^5D_4$ groups. Liu et al. (1988) analyzed the crystal-field splitting of the $^5D_4$ multiplet and studied the electronic Zeeman effect and hyperfine spectral hole-burning for Tb^{3+}: $LiYF_4$. Huang et al. (1989) investigated the $^5G_6$ multiplet near $40,000\ cm^{-1}$ using direct two-photon absorption. Later two-photon excitation experiments (Huang et al., 1989; Jones, 1990) were conducted to resolve the complicated Tb^{3+} crystal-field levels in the energy range from $39,000\ cm^{-1}$ to $42,000\ cm^{-1}$. Energy levels of Tb^{3+} below this region were obtained with polarized one-photon absorption and fluorescence experiments, and frequency-doubled one-photon absorption experiments. The selections rules (see Chapter 2) for one- and two-photon transitions are given in Table 1.11.

Table 1.11 Selection rules of electric dipole transitions of RE ions in S_4 site symmetry

(a) one-photon absorption (OPA)

	Γ_1	Γ_2	$\Gamma_{3,4}$
Γ_1		π	σ
Γ_2	π		σ
$\Gamma_{3,4}$	σ	σ	π

(b) two-photon absorption (TPA)

	Γ_1	Γ_2	$\Gamma_{3,4}$
Γ_1	$\sigma\sigma,\ \pi\pi$	$\sigma\sigma$	$\sigma\pi$
Γ_2	$\sigma\sigma$	$\sigma\sigma,\ \pi\pi$	$\sigma\pi$
$\Gamma_{3,4}$	$\sigma\pi$	$\sigma\pi$	$\sigma\sigma,\ \pi\pi$

1.5.1 Experimental Data

The Septet ^7F_J Multiplets

The crystal-field energy levels of the septet $^7F_J(J=0,1,2,\cdots,6)$ multiplets have been observed in emission spectra from $^5D_4$ and $^5D_3$ states. The crystal-field levels of the lowest multiplet $^7F_6$ were found to spread over a range of $360\ cm^{-1}$.

The ground state consists of two Γ_2 singlets separated by 0.9 cm^{-1}. These two levels were well resolved in the absorption and excitation spectra. The $^7F_5$ multiplet consists of a total of 8 distinct levels separated into two groups. There are 5 levels between 2110 cm^{-1} and 2196 cm^{-1}. The second group has 3 states near 2400 cm^{-1}.

The Zeeman effect provided an independent identification of the $\Gamma_{3,4}$ and Γ_1, Γ_2 states in the ^7F_J multiplets. In a magnetic field, a $\Gamma_{3,4}$ doublet splits linearly into two components, while Γ_1 and Γ_2 singlets have no linear Zeeman effect; instead, the energy levels of Γ_1 and Γ_2 vary nonlinearly due to coupling to adjacent Γ_1 and Γ_2 singlets.

The $^5D_4$ Multiplet

There are two long-lived emitting states, $^5D_4$ and $^5D_3$, with lifetimes of 5 ms and 2.8 ms, respectively, at 4.2 K. The crystal-field levels of the isolated $^5D_4$ multiplet were probed in absorption and excitation. The selection rules for electric dipole transitions allow one to observe the Γ_1 and $\Gamma_{3,4}$ states in π and σ polarization, respectively. The observed energy levels of the $^5D_4$ multiplet split only 90 cm^{-1} reaching from 20,554 cm^{-1} to 20,645 cm^{-1} (Liu et al., 1988). The lowest two levels of the $^5D_4$ multiplet are Γ_1 and $\Gamma_{3,4}$ separated only by 5 cm^{-1}. After laser excitation at 4.2 K, about 20% of the excited state population stays in the higher $\Gamma_{3,4}$ level, thus emission from both levels could be present in fluorescence spectra. Emission from the higher level of the $^5D_4$ multiplet was eliminated when the sample temperature was reduced to 1.3 K.

Energy Level Structure from 26,300 to 38,500 cm^{-1}

Above a large energy gap of 5750 cm^{-1} between the $^5D_4$ and $^5D_3$ states, there are a total of 227 crystal-field levels of the $4f^8$ configuration that are densely-packed between 26,300 cm^{-1} ($^5D_3$) and 38,100 cm^{-1}. As a result, the wave functions of Tb^{3+} are significantly mixed by both spin-orbit coupling and crystal-field interactions. From 28,000 cm^{-1} to 38,500 cm^{-1}, σ and π polarized excitation spectra were recorded using a frequency-doubled tunable dye laser. The polarized excitation spectra from 34,900 cm^{-1} to 35,400 cm^{-1} that include the multiplets $^5H_3$, $^5H_5$, and $^5I_8$ are plotted in Fig. 1.7a in comparison with the calculated energy levels. Energy levels in the regions from 29,000 cm^{-1} to 31,600 cm^{-1} and from 33,100 cm^{-1} to 34,500 cm^{-1} were not probed. The energy levels of Tb^{3+}: $LiYF_4$ between 26,300 cm^{-1} and 28,000 cm^{-1} were probed in conventional absorption experiments. The crystal-field components in the ultraviolet absorption spectra were not completely resolved because of the low resolution of the spectrophotometer.

Energy Levels from 39,000 to 42,000 cm^{-1}

From $^5K_9$ through $^5K_7$, 48 crystal-field levels out of a total 70 in this energy region were observed in two-photon absorption (TPA) experiments and two-step excitation (TSE) experiments. The crystal-field spectra of the $^5G_6$ and $^5D_2$ multiplets near 40,000 cm^{-1} were probed in the TPA experiments (Huang et al., 1989; Jones, 1990). A portion of the TPA spectra for the $^5G_6$ and $^5D_2$ multiplets is shown in shown in Fig. 1.7b. One laser was scanned while another was fixed at a wavelength below the transition to the intermediate state $^5D_4$. The

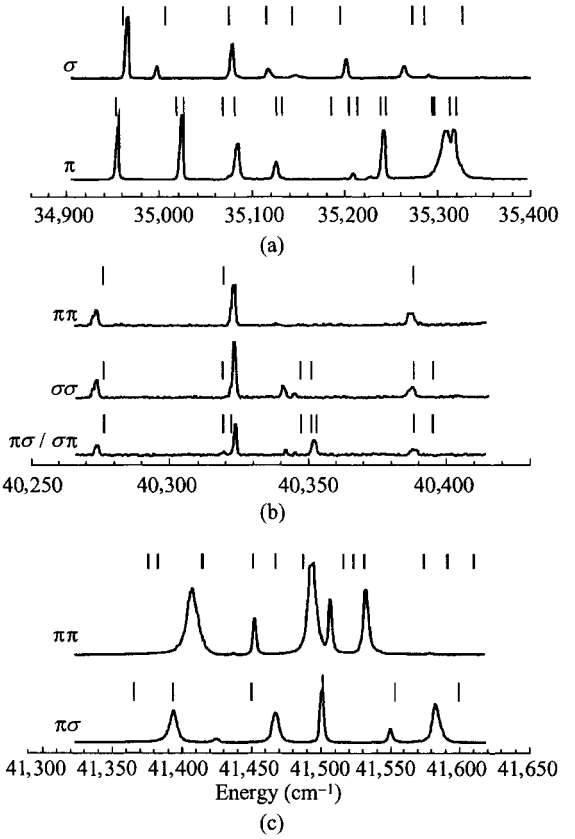


Figure 1.7 Polarized excitation and two-photon absorption spectra of Tb^{3+}: $LiYF_4$ in comparison with calculated crystal-field energy levels (vertical bars). (a) one-photon excitation spectra at 4 K; (b) two-photon absorption spectra at 1.3 K; (c) two-photon two-step excitation spectra at 1.3 K. The values of the free-ion and crystal-field interaction parameters for the calculation are obtained in east-squares fitting of the observed energy levels (Table 1.12)

energy summation of the two lasers was thus tuned to reach the energy levels from 39,500 cm^{-1} to 40,500 cm^{-1}. Combinations of different polarization of the laser beams from the two independent lasers resolved 12 out of a total 14 components of the $^5G_6$ and $^5D_2$ groups. The electric dipole selection rules for two-photon transition were confirmed and the assignment of the observed energy level was unique.

Most energy levels of Tb^{3+} from 40,000 cm^{-1} to 42,000 cm^{-1} were obtained by a TSE technique using the long lived $^5D_4$ as an intermediate state. All upper energy levels probed by TSE are Γ_2 and $\Gamma_{3,4}$ states since the lowest $^5D_4$ Γ_1 level was used as the intermediate state, and Γ_1 to Γ_1 transitions are forbidden for the electric dipole transitions occurring in the second step of the TSE process. A section of the TSE for the $^5K_5$ and $^5G_6$ multiplets is shown in Fig. 1.7c. With the time delay between the two laser pulses of a few nanoseconds, energy transfer to the defect sites did not occur in the intermediate state and most lines observed in the TSE spectra were "intrinsic-site" lines. When the time delay was longer than a few nanoseconds, extra lines were observed in the TSE spectra due to excitation trapping in the $^5D_4$ intermediate state at perturbed crystal sites (Jones, 1990). This excitation transfer to perturbed sites explains why the fluorescence from the $^5D_4$ state does not have the polarization properties expected from S_4 site symmetry.

1.5.2 Computational Modeling

The crystal-field spectrum of the Tb^{3+} ion in $LiYF_4$ was analyzed using a Hamiltonian including effective operators for free-ion interactions (see Eq. (1.33)) and crystal-field interactions (see Eq. (1.36)). The crystal-field calculation was conducted using D_{2d} site symmetry instead of the actual S_4 symmetry (a real B_4^6 was assumed, see Table 1.7). In calculation, a truncation was made to keep the matrix sizes manageable and to cover energy levels from the ground state up to 50,000 cm^{-1}. The observed energy levels are below 42,000 cm^{-1}, and contributions of the states above 50,000 cm^{-1} to the crystal-field states below 42,000 cm^{-1} are generally negligible.

In the first step of the calculation, the initial values for the free-ion interaction parameters were for Tb^{3+}: LaF_3 as listed in Table 1.5. The initial values of the five crystal-field parameters (B_0^2, B_0^4, B_0^6, B_4^4, and B_4^6) were set to those obtained by Christensen (1978) for $LiTbF_4$. The crystal-field parameters were not allowed to vary freely until new values of the primary free-ion parameters F^k and ζ were reasonably established. In subsequent calculations, a least-squares fitting was carried out to diagonalize the complete Hamiltonian and optimize the values of chosen parameters. It was not surprising that fitting the

isolated ^7F_J and $^5D_4$ groups in the low energy region alone did not yield a clear correlation between the calculation and the experimental data in the high energy region. This was understandable because the crystal-field states in the high energy region have very different characteristics in the intermediate coupling wave functions determined by the free-ion parameters than that of the pure ^7F_J and $^5D_4$ states in the low energy region. When only the ^7F_J and $^5D_4$ multiplets were fitted, most of the free-ion parameters could not be allowed to vary freely; any inappropriate constraint or fixed values for certain parameters would force the varied parameters to compensate and to produce improper energy levels in the region where no experimental data were assigned.

Assignment of the $^5G_6$ and $^5D_2$ multiplets with experimental data obtained by two-photon absorption is critical in modeling Tb^{3+} crystal-field energy level structure. Assignment in that region is required in order to properly determine the free-ion parameters. After calculation was locked to the observed energy levels for these two multiplets and the ^7F_J and $^5D_4$ groups with the primary free-ion parameters (F^k, ζ, α, β and γ) varied freely in the least-squares fitting, a clear correlation between the calculated and the observed energy levels were obtained for the levels below the $^5D_2$ multiplet and above the $^5G_6$ multiplet. According to the selections rules in Table 1.11, there was no difficulty in assigning the observed energy levels from the TSE spectra and the frequency doubled excitation spectra, even in the regions where energy levels of different multiplets are mixed. Subsequently, the crystal-field parameters were allowed to vary freely, and the energy levels in the ultraviolet absorption spectrum were assigned. The final fit was based on the assignment of a total of 165 observed energy levels from the ground state $^7F_6$ up to the $^5K_7$ group near 42,000 cm^{-1}. The values of the free-ion and crystal-field parameters that best fit the observed energy levels are listed in Table 1.12.

Whereas the primary free-ion parameters F^k, ζ, α, β and γ were well established in fitting the energy level structure, the three-particle parameters T^i were fixed throughout the analysis, and traditional constraints on M^h and P^f ($M^2 = 0.56M^0$, $M^4 = 0.31M^0$, $P^4 = 0.5P^2$, and $P^6 = 0.1P^2$) were maintained (Carnall et al., 1989; Crosswhite, 1977). These three-particle parameters and the relativistic correction parameters would not be independently determined unless a larger number of experimental data that characterize the entire configuration were provided. Even the 165 observed energy levels covering the energy range of 42,000 cm^{-1} still represent a small portion of the entire $4f^8$ configuration whose energy levels spread up to 190,000 cm^{-1}. Comparing the free-ion parameters of Tb^{3+}: $LiYF_4$ with those of Tb^{3+}: LaF_3 shows that, except for M^0 and P^2, there are only minor differences; thus, we conclude that the free-ion parameters are weakly dependent on crystal field of the host materials.

Table 1.12 Free ion and crystal-field parameters for $Tb^{3+}:LiYF_4$ (cm^{-1})[a]

F^2	88,831 (59)	T^8	[317]
F^4	62,813 (142)	$M^{0\,(b)}$	2.8 (0.1)
F^6	47,147 (132)	$P^{2(c)}$	505 (37)
ζ	1694 (1.6)	B_0^2	412 (14)
α	18,800 (300)	B_0^4	−767 (28)
β	−594 (9.8)	B_0^6	−25 (30)
γ	1593 (47)	B_4^4	996 (18)
T^2	312 (8.2)	B_4^6	735 (19)
T^3	[40]	$N_{v}^{(d)}$	635
T^4	[50]	$\sigma^{(e)}$	9.7
T^6	[−395]	$n^{(e)}$	147
T^7	[303]		

(a) Values in parentheses are uncertainties from a nonlinear least square fit for the indicated parameters; values in the brackets were not allowed to vary in the parameter fitting;

(b) M^0 was varied freely, M^2 and M^4 were constrained by ratios $M^2 = 0.56M^0$, $M^4 = 0.31M^0$;

(c) P^2 was varied freely, P^4 and P^6 were constrained by ratios $P^4 = 0.5P^2$, $P^6 = 0.1P^2$;

(d) N_v is the crystal-field strength defined in Eq. (1.42);

(e) σ is fit deviation and n is the number of levels fit.

The characteristics of the crystal-field eigenfunctions computed in the modeling are very different between the low energy states and the high energy states. Whereas the admixtures of different J-multiplets are less than 0.5% in the nominal ^7F_J and $^5D_4$ states, the states above 26,300 cm^{-1} are significantly mixed. In addition to intermediate coupling induced by free-ion interactions, crystal-field mixing of different J-multiplets is generally higher than 15%, and in some states, J-mixing is as high as 50%.

Except for a modest uncertainty in B_0^6, the crystal-field parameters are well determined and consistent with those for other RE ions in the same host (Görller-Walrand and Binnemans, 1996). The variation of the crystal-field parameters from the initial values likely reflects in part the local structure difference between the Tb^{3+} ion in $LiYF_4$ and in $LiTbF_4$. It was found that different magnitudes of the crystal-field parameters could be obtained by separately fitting the experimental data in the low energy region and in the high energy region. If nonlinear shielding of the crystal field is not important in this system, inadequate experimental data could result in a false solution for the parameterization of crystal-field energy structure. As previously obtained in $LaCl_3$ (Crosswhite et al., 1977, 1984) and LaF_3 (Carnall et al., 1989) because of the one-electron operators for the crystal-field Hamiltonian, the rank 4 and 6 parameters B_0^4, B_4^4, and B_6^6 are likely to exhibit a marked change from Eu^{3+} to Tb^{3+} across the center of the series. It seems that the magnitudes of these parameters are compatible with the systematic trends in the second half of the series. Since less work has been reported on the first half of the series, variation of the rank 4 and 6

parameters in systematic trends across the entire series is not evident for RE ions in $LiYF_4$.

In summary, the effective-operator Hamiltonian (see Eqs. (1.39), (1.41)) can be parameterized to accurately reproduce the crystal-field energy level structure even for an f^8 configuration with a large number of energy states in the UV region. The key procedure is to fit the calculations with a set of reliable experimental data assigned to the representative states in both low and high energy regions of the configuration. Modeling of the energy level structure of Tb^{3+} in $LiYF_4$ is successful based on the analysis of results from a variety of experimental techniques. No constraints on the primary (F^k, ζ) and two-body (α, β, γ) free-ion parameters were necessary, while excellent correlation can be obtained between the experimental data and the computed energy level structure.

1.6 Modeling of $4f^N-4f^{N-1}5d$ Spectra

1.6.1 Energy Gaps Between the $4f^N$ and Excited Configurations

Before extending our discussion to the parameterization of the effective-operator Hamiltonian for calculation of the energy level structure of RE ions in $4f^{N-1}5d$ configurations, we first give a systematic comparison of the energy gaps between the ground states of $4f^N$ configurations and the lowest levels of the excited configurations that can be probed in optical spectroscopy using UV and X-ray sources. The energy required to promote an electron from a 4f to 5d orbital varies rapidly in an irregular manner as nuclear charge is increased, but a large portion of the variation and most of the irregularity can be attributed to the pairing energy within the $4f^N$ configuration (Jørgensen, 1975). A method using thermodynamic and spectroscopic data for calculating energies of various electronic configurations of RE ions was developed by Brewer (1971). Table 1.13 lists the calculated lowest energy levels of $4f^{N-1}5d$, $4f^{N-1}5s$, and $4f^{N-1}5p$ configurations relative to the ground state of $4f^N$ for divalent (R^{2+}) and trivalent (R^{3+}) free ions in the first half of RE series.

Ion-lattice coupling for 5d, 6p, and 6s orbitals, is much stronger than for 4f orbitals. As a result, the energy levels of $4f^{N-1}5d$, $4f^{N-1}6s$, and $4f^{N-1}6p$ configurations exhibit much stronger host dependence than that of the $4f^N$ configurations. Systematic variation of the $4f^{N-1}5d$ energy level structure was measured for trivalent RE ions in CaF_2 in ultraviolet absorption spectra (Loh, 1966). More experimental measurements and theoretical modeling of the inter-configuration $4f^N$ to $4f^{N-1}5d$ transitions of RE ions in $LiYF_4$ and YPO_4 were recently conducted by van Pieterson et al. (2002a, b). Figure 1.8 shows the calculated lowest energy levels of trivalent RE ions in different configurations

(Brewer, 1971, 1983) in comparison with the observed energies of $4f^N$ to $4f^{N-1}$ 5d transitions for trivalent RE ions in CaF_2 (Loh, 1966). Note that in the second-half of the series transitions to the lowest $4f^{N-1}$ 5d states are spin-forbidden. When these states are taken into account, the trends of the experimental points match theory much better (Wegh and Meijerink, 1999).

Dorenbos (2000a, 2000b) has carried out a systematic study of the energies of the lowest $4f^{N-1}$ 5d states of trivalent RE ions in crystals. A simple phenomenological model has been developed to predict the energy gap. Some RE ions are stable in the divalent state in solids. These have a much smaller energy gap between the $4f^N$ and excited configurations than that of the trivalent ions (Rubbio, 1991).

Table 1.13 Calculated lowest energy levels of $4f^{N-1}$ 5d, $4f^{N-1}$6s, and $4f^{N-1}$6p configurations relative to the ground state of $4f^N$ for divalent (R^{2+}) and trivalent (R^{3+}) free ions (Brewer, 1971)

R^{2+}	Config.	Lowest multiplet	10^3 cm^{-1}	R^{3+}	Config.	Lowest multiplet	10^3 cm^{-1}
Ce^{2+}	4f5d	$^1G_4$	3.277	Ce^{3+}	5d	$^2D_{3/2}$	49.737
	4f5s	$^3F_2$	19.236		5s	$^1S_{1/2}$	86.602
Pr^{2+}	$4f^2$5d	$^2H_{9/2}$	12.847	Pr^{3+}	4f5d	$^1G_4$	61.171
	$4f^2$5s	$^4H_{7/2}$	28.399		4f5s	$^3F_2$	100.259
	$4f^2$5p	$^4H_{7/2}$	58.158		4f5p	$^3F_3$	136.851
Nd^{2+}	$4f^3$5d	$^5L_6$	16.0	Nd^{3+}	$4f^2$5d	$^4I_{9/2}$	71.5
	$4f^3$5s	$^5I_4$	30.5		$4f^2$5s	$^4H_{7/2}$	110.0
	$4f^3$5p	$^5K_5$	61.2		$4f^2$5p	$^4I_{9/2}$	147.0
Sm^{2+}	$4f^5$5d	$^7K_4$	24.5	Sm^{3+}	$4f^4$5d	$^6L_{11/2}$	76.0
	$4f^5$5s	$^7H_2$	36.0		$4f^4$5s	$^6I_{7/2}$	113.0
	$4f^5$5p	$^7I_3$	67.5		$4f^4$5p	$^6K_{9/2}$	152.5
Eu^{2+}	$4f^6$5d	$^8H_{3/2}$	34.5	Eu^{3+}	$4f^5$5d	$^7K_4$	85.5
	$4f^6$5s	$^8F_{1/2}$	45.0		$4f^6$5s	$^7H_2$	120.0
	$4f^6$5p	$^8G_{1/2}$	78.0		$4f^6$5p	$^7I_3$	160.0

In addition to excitations from $4f^N$ to excited configurations, an electron may be excited from a ligand to a 4f orbital, giving a charge transfer state, with a configuration consisting of $4f^{N+1}$ plus a ligand "hole". The energies of these states are highly ligand-dependent and, especially in organic systems, they can be at lower energy than the $4f^{N-1}$5d states. Emission from charge-transfer states is relatively rare, but van Pieterson et al. (2002a, b) have made a detailed study of rare-earth charge-transfer emission.

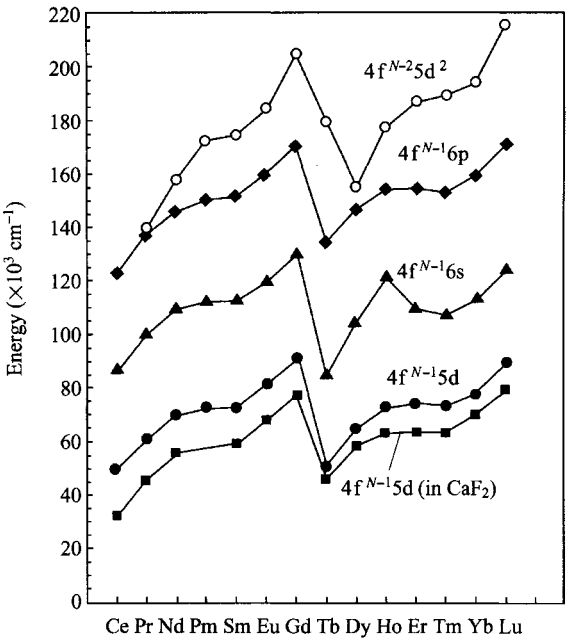


Figure 1.8 Systematic variation of calculated lowest energy levels of trivalent RE ions in low-lying excited configurations relative the ground state of the $4f^N$ configuration (Brewer, 1971) with comparison to the observed lowest $4f^{N-1}$ 5d levels of R^{3+}: CaF_2 (Loh, 1966)

1.6.2 Hamiltonian for $4f^{N-1}5d$ Configurations

It was recently demonstrated by Reid and co-workers (Reid et al., 2000, 2002; van Pieterson et al., 2002a, b) that crystal-field energy levels of $4f^{N-1}$ 5d configurations for the entire series of RE ions in crystals may be modeled using straightforward extensions to the standard calculations for $4f^N$ to include the $4f^{N-1}5d$ states. In such an approach, the effective-operator Hamiltonian expressed in Eq. (1.39) also applies to calculations of energy levels of RE ions in high-lying configurations such as $4f^{N-1}5d$, with minor modifications of the 20 free-ion interaction parameters. Moreover, since one of the 4f electrons has been excited to a 5d orbital, there are several additional contributions to the Hamiltonian. The free-ion Hamiltonian is supplemented by the spin-orbit interaction for the 5d electron and the Coulomb interaction between the 5d electron and the 4f electrons in the cases where $N > 1$. Therefore, the additions to the free-ion Hamiltonian may be defined as (Reid et al., 2000)

$$\mathscr{H}_{\text{fi}}(\text{fd}) = \sum_k F^k(\text{fd}) f_k(\text{fd}) + \sum_j G^j(\text{fd}) g_j(\text{fd}) + \zeta(\text{dd}) A_{\text{so}}(\text{dd}), \tag{1.64}$$

with $k=2$, 4, and $j=1$, 3, 5. The $F^k(\mathrm{fd})$ and $G^j(\mathrm{fd})$ are direct and exchange Slater parameters for the Coulomb interactions between the 4f and 5d electrons (Cowan, 1981). The $\zeta(\mathrm{dd})$ parameter is associated with the spin-orbit interaction of the 5d electron. The 5d electron is also affected by the crystal-field interaction

$$\mathscr{H}_{\mathrm{CF}}(\mathrm{dd}) = \sum_{kq} B_q^k(\mathrm{dd})\, C_q^{(k)}(\mathrm{dd}), \tag{1.65}$$

with $k=2$ and 4, and the same restrictions applied to q as for the 4f electron crystal-field Hamiltonian $H_{\mathrm{CF}}(\mathrm{ff})$ expressed in Eq. (1.36).

The $4f^{N-1}5d$ configuration has a higher average energy than the $4f^N$ configuration. This energy difference contains contributions from several sources (Cowan, 1981), including kinetic energy, Coulomb, and (isotropic) crystal-field effects. These effects cannot be distinguished experimentally and can be considered to contribute to a single term $\Delta_E(\mathrm{fd})\,\delta_E(\mathrm{fd})$ in the Hamiltonian, where the operator $\delta_E(\mathrm{fd})$ is diagonal, with unit matrix elements for $4f^{N-1}5d$ and zero matrix elements for $4f^N$.

Since the $4f^{N-1}5d$ and $4f^N$ configurations have opposite parity, there is no Coulomb configuration interaction between them. However, the odd-parity crystal-field interaction can couple the $4f^{N-1}5d$ and $4f^N$ configurations. The contribution to the Hamiltonian is

$$\mathscr{H}_{\mathrm{CF}}(\mathrm{fd}) = \sum_{kq} B_q^k(\mathrm{fd})\, C_q^{(k)}(\mathrm{fd}), \tag{1.66}$$

with $k=1$, 3, 5. This mixing of configurations is one of the major contributions to electric dipole transitions within the $4f^N$ configuration (see Chapter 2). However, it has only a small effect on energy level splitting in the states of a $4f^{N-1}5d$ configuration (Reid et al., 2000).

1.6.3 Determination of Hamiltonian Parameters

Though, spectra of $4f^N$ to $4f^{N-1}5d$ transitions have long been experimentally investigated, it is only recently that excitation spectra of most ions of the RE series doped into $LiYF_4$, YPO_4, and CaF_2 have been systematically analyzed using extensions to the standard crystal-field model for the $4f^N$ configuration (van Pieterson et al., 2002a, b). Some previous studies on the $4f^{N-1}5d$ configuration have tried to analyze the spectra by considering only the 5d crystal field and the free-ion splitting of the $4f^{N-1}$ core. However, this is not a very good approximation since the Coulomb interaction between the 4f and 5d electrons has a significant effect. As an example, this effect on the $4f^7 5d$ states of Tb^{3+} is illustrated in Fig. 1.9, which shows the splitting of the 5d crystal-field states as

the f-d interaction parameters (F^k(fd), G^j(fd)) are increased from zero to the values predicted for the free ion according to Cowan's program (Cowan, 1981). The parameter A used as the horizontal axis of the graph is a scaling factor for the f-d interaction parameters. The energy difference between the first spin-forbidden and spin-allowed $4f^N \leftrightarrow 4f^{N-1}\,5d$ transitions for Tb^{3+} is dominated by the exchange operators G^k(fd) (van Pieterson et al., 2002b; Reid et al., 2002).

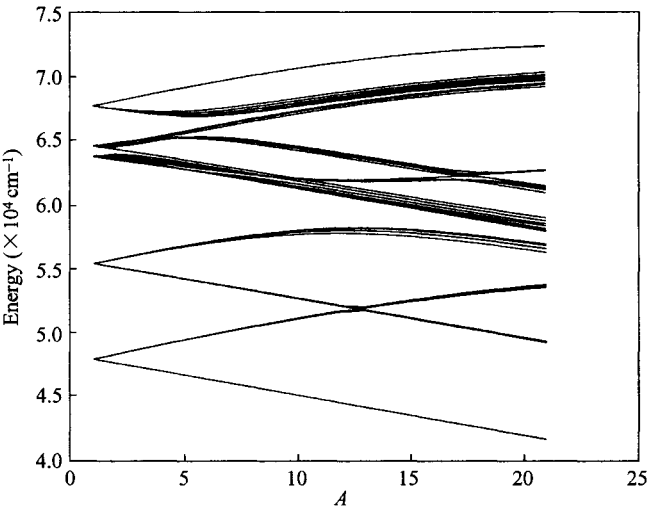


Figure 1.9 Splitting of the five $4f^7$ 5d crystal-field states of Tb^{3+} in $LiYF_4$. The parameter a represents the f-d interactions as explained in the text. On the left ($A = 0$) the parameters for these interactions are set to zero and on the right ($A = 1$) they have the values calculated for the free ion (van Pieterson et al., 2002b)

In contrast to sharp zero-phonon lines of electronic transitions within a $4f^N$ configuration, inter-configuration transitions to the $4f^{N-1}\,5d$ configuration are dominated by broad vibronic bands, with a limited number of observable zero-phonon lines. Fitting all of the free-ion and crystal-field parameters for $4f^{N-1}5d$ is therefore not currently possible. It is crucial to begin with good estimates of the parameters and then use spectroscopic information from as many ions as possible to refine the calculation, since the effect of some parameters is more apparent in particular ions. For example, the $4f^{N-1}5d$ configuration for Ce^{3+} is simply 5d, for which the only parameters are ζ(dd), and the B_q^k(dd), making this ion particularly suitable for determining the 5d crystal-field parameters.

As a general approach, the Hamiltonian parameters may be determined from scaling of initial estimates. The initial estimates may be from:

(1) Parameters for the $4f^{N-1}$ core from parameters for the $4f^N$ configuration of the same ion;

(2) 5d crystal-field parameters B_q^k(dd) from the Ce^{3+} spectrum;

(3) Free-ion parameters involving the 5d electron from *ab initio* calculations.

The atomic calculation methods are described by Cowan (1981). The calculations are Hartree-Fock, with relativistic corrections. In Table 1.14, we give a summary of Hamiltonian parameters for the supplementary terms of the Hamiltonian expressed in Eqs. (1.62) – (1.66). For comparison with the ff parameters listed in Table 1.5, the F^k(ff) parameters increase dramatically across the series, as the 4f orbitals contract. The calculated F^k(fd) and G^k(fd) parameters decrease gradually, since the 5d orbitals do not contract as much as the 4f orbitals. Similarly, the ζ(ff) increase dramatically, and the ζ(dd) somewhat less.

It was found that the calculated F^k(fd) and G^k(fd) parameters are too large, particularly from examining the splitting between the high-spin and low-spin states of the $4f^{N-1}5d$ configuration of the heavy lanthanides (van Pieterson et al., 2002a, b). Better agreement is obtained when the fd parameters are reduced to about 67% of their calculated value (Reid et al., 2002). This reduction is not purely induced by the crystalline environment. The free-ion data indicate that the overestimation is mainly for the F^2(fd) and G^1(fd) parameters. In fact, such a reduction between the Hartree-Fock values and the experimental values for free-ion parameters is similar to that for the free-ion parameters of the $4f^N$ configurations we discussed in Section 1.3. Though the 5d orbitals are perturbed much more by the host lattice than for the 4f orbitals, the F^k(fd) and G^k(fd) parameters are largely determined by the part of the 5d orbitals close to the nucleus where they interact with the 4f orbitals, and the ζ(dd) parameters also have their largest contribution from close to the nucleus. Therefore, the same mechanisms whose effects are not absorbed into the Hartree-Fock values of F^k(fd) and F^k(ff) may be considered.

The crystal-field parameters associated with the 5d electron of the $4f^{N-1}5d$ configuration are large, typically 10 to 20 times the parameters for the 4f electrons. For the host $LiYF_4$, the crystal-field splitting of the 5d orbitals is approximately $20,000\ cm^{-1}$ (van Pieterson et al., 2002a, b). Crystal-field parameters for trivalent RE series in this host are shown in Table 1.14. Whereas the 4f parameters decrease dramatically across the lanthanide series, the 5d parameters decrease by a relatively small amount. Since the 4f orbitals contract somewhat in the $4f^{N-1}$ 5d configuration, their values may also decrease somewhat.

For ions near the beginning or end of the lanthanide series the 5d crystal-field splitting dominates the spectra, with the splitting caused by atomic interactions giving a fine-structure built on top of the crystal-field splitting. Towards the center of the series the atomic splitting of the $4f^{N-1}$ core is quite large and the 5d crystal-field splitting is more difficult to definitively identify. A notable exception is Tb^{3+}, where the large splitting between the lowest states of the $4f^7$ core makes the identification of the 5d crystal-field splitting straightforward (van Pieterson et al., 2002b).

Table 1.14 Energy-level parameters for $4f^{N-1}5d$ configurations of trivalent RE ions in $LiYF_4$ (in cm^{-1}) (van Pieterson et al., 2002a, b)

	Ce^{3+}	Pr^{3+}	Nd^{3+}	Sm^{3+}	Eu^{3+}	Tb^{3+}	Dy^{3+}	Ho^{3+}	Er^{3+}	Tm^{3+}
Δ_E(fd)	43,754	51,690	57,849	68,238	73,057	81,899	85,739	89,516	92,216	95,091
F^2(fd)		30,271	30,300	30,300	30,300	19,665	19,886	19,807	19,724	19,639
F^4(fd)		15,094	15,038	15,038	15,038	9469	9527	9442	9358	9275
G^1(fd)		12,903	12,914	12,914	12,914	8083	8145	8089	8038	7991
G^3(fd)		11,160	11,135	11,135	11,135	6935	6973	6910	6848	6789
G^5(fd)		8691	8659	8659	8659	5376	5400	5345	5292	5240
ζ(dd)	1082	1149	1216	1351	1419	1557	1627	1697	1868	1839
B_0^2	4673	4673	4673	4673	4673	4416	4365	4332	4290	4206
B_0^4	−18,649	−18,649	−18,649	−18,649	−18,649	−17,623	−17,418	−17,288	−17,120	−16,784
B_4^4	−23,871	−23,871	−23,871	−23,871	−23,871	−22,558	−22,296	−22,128	−21,914	−21,484

In summary, an extension to the standard crystal-field model for $4f^N$ provides a good basis for interpreting the spectroscopy of the $4f^{N-1}$ 5d configurations of lanthanide ions in crystals. However, the exact values for many of the Hamiltonian parameters are not yet known. More detailed data (including polarization measurements) are required to give definitive identification of the electronic origins and allow the accurate determination of more of the parameters and hence better calculations of various spectroscopic properties.

1.7 Magnetic and Hyperfine Interactions

The hyperfine energy levels of RE ions in solids range from MHz to GHz on the spectral scale. Because of localized electronic states, the homogeneous line width of transitions between $4f^N$ crystal-field levels in many cases is less than 1 MHz at liquid helium temperatures. Therefore, not only can the electronic Zeeman effect be observed, but hyperfine splitting and even superhyperfine (ligand hyperfine) structures also can be measured when elimination of inhomogeneous line broadening is possible. Laser spectroscopic methods with a resolution of 10^{-9} or higher have proven to be effective in eliminating inhomogeneous line broadening; therefore, they enable energy level splittings on the MHz order to be measured in electronic transitions in the infrared and visible spectral regions (Macfarlane and Shelby, 1987). Spectroscopy in the MHz – GHz range reveals very rich physical information concerning electron nuclear interactions that impact the properties of RE ions as optical activators. In this section, we introduce the primary Hamiltonian of Zeeman and hyperfine interactions. Apart from elucidation of the physical origins for the various terms of the Hamiltonian, emphasis is given to the understanding of experimental spectra. A brief review of recent work on Pr^{3+}, Eu^{3+}, and Tb^{3+} is presented. The importance of studying the Zeeman effect and hyperfine interactions extends far beyond energy level structure. Many fundamental properties and applications of RE ions in solids involving hyperfine interactions are also discussed in other chapters of this book. In particular, since the homogeneous line width of optical transitions between hyperfine energy levels in the ground and excited crystal-field states are much narrower at low temperatures than the inhomogeneous broadening induced by disturbed sites and local field stress, measurements of the line shapes in a hyperfine spectrum are used to characterize line broadening mechanisms. Line broadening mechanisms and line width measurements are discussed in detail in Chapters 3, 4 and 7 of this book.

For RE ions in ground states, extensive studies of Zeeman and hyperfine energy level structures along with spin dynamics have been conducted using electron paramagnetic resonance (EPR) and electron-nuclear double resonance (ENDR) methods (Abragam and Bleaney, 1986). In this chapter, we restrict our attention to optical spectroscopy.

To evaluate the Zeeman effect and hyperfine interactions of RE ions in

crystals, an effective Hamiltonian, in addition to that of the free ion and crystal field interactions as described in proceeding sections, may include terms such as

$$\mathscr{H} = \mathscr{H}_Z + \mathscr{H}_z + \mathscr{H}_{HF} + \mathscr{H}_Q, \tag{1.67}$$

where the first two terms, existing only when an external magnetic field is applied, represent electronic Zeeman effect and nuclear Zeeman effect, respectively. The third term represents the hyperfine interactions between the 4f electrons and the spin of the RE nucleus, and the fourth term is for the nuclear electric quardrupole interaction. In most cases, one can use a perturbation method in analysis of Zeeman and hyperfine spectra. It is always assumed that the wave functions of electronic states and the nuclear spin states are independent from each other. For the electronic states, the crystal-field eigenfunctions with J-mixing in the form of Eq. (1.41) are used as the zero-order wave functions for obtaining the eigenvalues of the Hamiltonian expressed in Eq. (1.67).

1.7.1 Zeeman Effect

In the presence of an external magnetic field, $\boldsymbol{H}$, the degenerate crystal-field states split further, so that the degeneracy of the crystal-field states, including the Kramers' doublets for odd-N configurations, is removed completely. In each J multiplet, there are a total of $2J+1$ energy levels. For the electronic Zeeman effect of RE ions in an isotropic crystal, the interaction Hamiltonian has the simple form,

$$\mathscr{H}_Z = g_J \mu_B \boldsymbol{J} \cdot \boldsymbol{H}, \tag{1.68}$$

and the effective magnetic moment is defined as

$$\boldsymbol{\mu}_J = -\mu_B g_J \boldsymbol{J}, \tag{1.69}$$

where in the LS coupling scheme

$$g_J = 1 + \frac{J(J+1) + S(S+1) - L(L+1)}{2J(J+1)} \tag{1.70}$$

is the effective Landè g factor, and μ_B is the Bohr magneton. In the simple case of an isolated crystal-field doublet where the magnetic field is in parallel to the crystal c-axis, the splitting energy,

$$E_Z = \mu_B g_J H \langle J\Gamma \mid J_Z \mid J\Gamma \rangle = \mu_B g_J H \sum_M a_M^2 M, \tag{1.71}$$

is linear in H and symmetric about the energy level at zero field. Usually, in comparison with a free electron Zeeman split, an effective g factor is defined as

$$g_{\text{eff}} = 2g_J \sum_M a_M^2 M, \tag{1.72}$$

A crystal-field singlet does not split but its energy level may shift due to coupling to other crystal-field levels in the same J multiplet. In the case of weak crystal-field splitting and a relatively strong magnetic field, the Zeeman effect should be evaluated by diagonalizing a matrix that includes the entire group of the crystal-field levels in the multiplet. Apart from the diagonal matrix elements (see Eq. (1.71)), the off-diagonal matrix elements are

$$\langle J\Gamma \mid \mathscr{H}_Z \mid J\Gamma' \rangle = \mu_B g_J H \sum_{M, M'} a_{\Gamma M} a_{\Gamma' M'} M' \delta_{MM'}. \tag{1.73}$$

Depending on the crystal-field energy gaps at zero-field, one may reduce the size of the matrix by considering only those crystal-field levels that are not far separated from each other. As it was demonstrated in the case of $^5D_4$ in Tb^{3+} in $LiYF_4$ (Liu et al., 1988) the calculation of the Zeeman effect for Tb^{3+} at an S_4 site symmetry agrees very well with experimental observation. In other cases, where the density of RE electronic states is high, the Zeeman coupling between multiplets is strong and inclusion of states in different J multiplets is necessary.

In general, when the external magnetic field is not parallel with the c-axis, the Zeeman interaction is anisotropic, but the (X, Y, Z) axes can still be chosen as the principal axes for the tensor operators of Hamiltonian, and Eq. (1.68) should be replaced by (Abragam and Bleaney, 1986)

$$\mathscr{H}_Z = \mu_B [g_{XX} H_X J_X + g_{YY} H_Y J_Y + g_{ZZ} H_Z J_Z]. \tag{1.74}$$

In axial symmetry, $g_{XX} = g_{YY} = g_\perp$; $g_{ZZ} = g_{//}$. It is easy to show that, for non-Kramers' doublets, the diagonal matrix elements of the X and Y components vanish, and only the Z component needs be considered.

Because the electrons shield the nucleus from interaction with an external field, calculations of nuclear Zeeman effect require consideration of the electronic shielding effect. Phenomenologically, an anisotropic tenser $\alpha(\alpha_{XX}, \alpha_{YY}, \alpha_{ZZ})$ is usually introduced based on the consideration of strong shielding of the nuclear magnetic moment by the magnetic field. The Hamiltonian is of the following form:

$$\mathscr{H}_Z = -\gamma_n \hbar H \cdot (\mathbf{1} - \boldsymbol{\alpha}) \cdot I, \tag{1.75}$$

where γ_n is the nuclear gyromagnetic ratio. The shielding parameters (α_{XX}, α_{YY}, α_{ZZ}) may absorb contributions from several mechanisms including coupling to

electronic angular momentum.

1.7.2 Magnetic Hyperfine Interaction

One of the leading electron-nucleus coupling mechanisms is commonly expressed in the form of magnetic interaction. This is based on the understanding of the interaction between the nuclear spin momentum I and the effective magnetic field induced by the electronic angular momentum J. For rare earth ions in crystals of axial symmetry, magnetic hyperfine interaction can be described by the following effective spin Hamiltonian.

$$\mathscr{H}_{\mathrm{HF}} = A_{/\!/} J_Z I_Z + A_{\perp} (J_X I_X + J_Y I_Y), \tag{1.76}$$

where $J_{X,Y,Z}$ and $I_{X,Y,Z}$ are electronic angular and nuclear spin operators, repectively and $A_{/\!/}$ and $A_{\perp}$ are the components of the hyperfine interaction constant parallel and perpendicular to the crystal c-axis, respectively. A theoretical calculation of $A_{/\!/}$ and $A_{\perp}$ is possible based on the assumption of isotropic electron nuclear interactions, so that

$$A_{/\!/} = A_{\perp} = A_J = 2\mu_B \gamma_n \hbar \langle r^{-3} \rangle \langle J \| N \| J \rangle, \tag{1.77}$$

where $\langle r^{-3} \rangle$ is the mean inverse third power of the distance of the electron from the nucleus, and $2\mu_B \langle r^{-3} \rangle N$ is the effective magnetic field induced by the f-electrons at the nucleus. For the ground states of trivalent RE ions, the values of the reduced matrix element $\langle J \| N \| J \rangle$ and the values of A_J are tabulated by Abragam and Bleaney (1986). Using the reduced matrix elements of the tensor $\boldsymbol{V}^{(12)}$, one may calculate A_J for any multiplet from (Wybourne, 1965):

$$A_J = 2\mu_B \gamma_n \hbar \langle r^{-3} \rangle \left[2 - g + 2 \times \left[\frac{14(2J+1)}{J(J+1)} \right]^{1/2} \right.$$
$$\left. \times \langle \mathrm{f}^N \tau S L \| \boldsymbol{V}^{(12)} \| \mathrm{f}^N \tau' S' L' \rangle \begin{Bmatrix} S & S' & 1 \\ L & L' & 2 \\ J & J & 1 \end{Bmatrix} \right]. \tag{1.78}$$

After the value of A_J is determined, the matrix elements of the hyperfine Hamiltonian of Eq. (1.76) can be calculated using the crystal-field eigenfunction, $| J\Gamma \rangle = \sum_M \alpha_M | JM \rangle$, and the independent nuclear wave function, $| I, m \rangle$. The same procedure as that in calculation of Zeeman effect is required for evaluating the hyperfine energy level splittings. Given that hyperfine

splittings are much smaller than spin-orbit coupling and the crystal-field splitting, it is sufficient in most cases to consider the coupling only to the nearest crystal-field levels in the evaluation of the contributions from the off-diagonal matrix elements. As a parameter, the value of A_J may be obtained from analyzing experimental spectra. Knowing A_J from experiments enables one to determine the nuclear magnetic moment if the value of $\langle r^{-3} \rangle$ can be calculated.

For electronic singlets, including all crystal-field levels of non-Kramers' ions at low symmetry sites such as C_2 in LaF_3 or C_s in $YAlO_3$, the diagonal matrix elements of the magnetic hyperfine interaction are quenched. Therefore, there is no first order hyperfine splitting in these electronic states. The contributions to hyperfine splitting are from the off-diagonal matrices between different crystal-field levels and nuclear electric quadrupole interactions.

In a static magnetic field, $\boldsymbol{H}$, the effects of hyperfine and electronic magnetic interactions on a singlet crystal-field level are evaluated using a second order perturbation theory. The effective Hamiltonian, including the nuclear Zeeman effect, can be expressed as (Abragam and Bleaney, 1983; Macfarlane and Shelby, 1987):

$$\mathscr{H}_{\mathrm{HF}} = -g_J^2\mu_B^2 \boldsymbol{H} \cdot \boldsymbol{\Lambda} \cdot \boldsymbol{H} + \mathscr{H}'_Z. \tag{1.79}$$

The first term in Eq. (1.79) is the quadratic electric Zeeman shift, where the tensor $\boldsymbol{\Lambda}$ is given by

$$\Lambda_{\alpha\beta} = \sum_{\Gamma'}^{2J+1} \frac{\langle \Gamma \mid J_\alpha \mid \Gamma' \rangle \langle \Gamma' \mid J_\beta \mid \Gamma \rangle}{\Delta E_{\Gamma,\Gamma'}}, \tag{1.80}$$

with $|\Gamma\rangle$being the levels to which Eq. (1.79) applies, $\alpha(\beta) = X, Y, Z$ being the principle axes of the $\boldsymbol{\Lambda}$ tensor, and $\Delta E_{\Gamma,\Gamma'}$ being the energy difference between level Γ and Γ'. The second term is the enhanced nuclear Zeeman Hamiltonian that can be expressed as

$$\mathscr{H}'_Z = -\hbar[\gamma_X H_X I_X + \gamma_Y H_Y I_Y + \gamma_Z H_Z I_Z], \tag{1.81}$$

where the effective nuclear gyromagnetic ratios are given by

$$\gamma_\alpha = \gamma_N + 2g_J\mu_B A_J \Lambda_{\alpha\alpha}/\hbar. \tag{1.82}$$

Due to the second term, which arises from coupling to the second order hyperfine interaction, the nuclear Zeeman effect is enhanced. In comparison with Eq. (1.75), this is also known as an anti-shielding effect arising from the 4f electrons.

1.7.3 Nuclear Electric Quadrupole Interaction

Because the expectation value of the nuclear electric dipole moment vanishes, the nuclear electric contribution to the electronic energy levels is primarily from quadrupole interactions (Weissbluth, 1978). The nuclear electric quadrupole moment, Q, is defined by

$$Q = \langle I, m = I \left| \sum_p (3Z_p^2 - r_p^2) \right| I, m = I \rangle, \tag{1.83}$$

where the sum is taken over all Z protons. Using tensor operation, the quadrupole interaction Hamiltonian can be written as

$$H_Q = \frac{eQ}{4I(2I-1)} \{ \langle V_{ZZ} \rangle [3I_Z^2 - I(I+1)] + \langle V_{XX} - V_{YY} \rangle (I_{+1}^2 + I_{-1}^2) \}, \tag{1.84}$$

where

$$V_{r_i r_i} = \frac{\partial^2}{\partial r_i \partial r_i} \left(\frac{-e}{r} \right) = -e \frac{3r_i^2 - r^2}{r^5}, \quad r_i = X, Y, Z. \tag{1.85}$$

The expectation values of V_{rr} in Eq. (1.84) are directly related to the components of the electric field gradient in terms of crystal-field parameters that we discussed in the previous section, $V_{ZZ} \propto B_0^2$ and $V_{XX} - V_{YY} \propto B_2^2$. With this convention, the off-diagonal components are eliminated by a suitable choice of quadrupolar tensor axes, while the diagonal components are ordered such as that $|V_{ZZ}| \geqslant |V_{YY}| \geqslant |V_{XX}|$.

Since V is subjected to the Laplace equation ($V_{XX} + V_{YY} + V_{ZZ} = 0$), it is conventional to define an asymmetry parameter of the quadrupole Hamiltonian η by

$$\eta = \frac{\langle V_{XX} - V_{YY} \rangle}{\langle V_{ZZ} \rangle}, \quad (0 \leqslant \eta \leqslant 1), \tag{1.86}$$

and a nuclear electric quadrupole interaction constant P by

$$P = \frac{3eQ\langle V_{ZZ} \rangle}{4I(2I-1)}, \tag{1.87}$$

so that a simplified nuclear electric quadrupole Hamiltonian can be written as

$$\mathscr{H}_Q = P\left[I_Z^2 - \frac{1}{3}I(I+1) + \frac{\eta}{3}(I_{+1}^2 + I_{-1}^2)\right]. \tag{1.88}$$

The value of P depends linearly on $\langle V_{ZZ}\rangle$, the total local electric field gradient along the Z-axis. The nuclear electric quadrupole interaction constant may absorb contributions from more than one origin. For example, in the $^7F_0$ ground state of a $4f^6$ configuration, such as that of Eu^{3+} in which the first order magnetic hyperfine interaction is absent, three mechanisms must be considered in evaluation of nuclear electric quatrupole splittings. Separate contributions to P arise from the 4f-electrons (P_{4f}), from ligand ions in the surrounding lattice (P_{latt}), and from the second order effects of the magnetic hyperfine interaction known as psedoquadrupole effects (P_{pq}). This special case will be discussed in detail in Section 1.6.6.

When we use the connection between the operator V_{ZZ} and Stevens operator equivalent $C_0^{(2)}$, we may write

$$V_{ZZ} = -4er^{-3}\sqrt{\frac{\pi}{5}}Y_{20} = -2er^{-3}C_0^{(2)}. \tag{1.89}$$

Therefore, the first order contribution from the 4f electron states can be evaluated using

$$P_{4f}^{(1)}(J,I) = -\frac{3e^2Q}{2I(2I-1)}(1-R_Q)\langle r^{-3}\rangle\langle f^N\tau SLJ \mid C_0^{(2)} \mid f^N\tau' S'L'J\rangle, \tag{1.90}$$

where $\langle r^{-3}\rangle$ is the expectation value of the inverse cube electron-nuclear distance and R_Q is the electronic shielding factor associated with $\langle r^{-3}\rangle$.

Using equivalent operators for V_{ZZ}, the first order of the 4f electron contribution can be evaluated from:

$$P_{4f}^{(1)}(J,I) = -\frac{3e^2Q}{4I(2I-1)}(1-R_Q)\langle r^{-3}\rangle \times \langle JJ_Z \mid 3J_Z^2 - J(J+1) \mid JJ_Z\rangle\langle J \parallel \alpha \parallel J\rangle. \tag{1.91}$$

The matrix elements of the equivalent operator $\langle J \parallel \alpha \parallel J\rangle$ for the ground states of RE ions were tabulated by Abragam and Bleaney (1986).

The first order 4f electron contribution vanishes in any $J = 0$ electronic states. For these states, one needs to consider the second order contribution that arises from cross-term crystal-field coupling between states of different J (Blok and Shirley, 1966):

$$P_{4f}^{(2)}(J,I) = \frac{3Qe^2B_0^2}{I(2I-1)}\langle r^{-3}\rangle(1-R_Q)\sum_{J'}\frac{|\langle J_0 \mid C_0^{(2)} \mid J_0'\rangle|^2}{|E_J - E_{J'}|}, \tag{1.92}$$

where B_0^2 is the parameter for the rank 2 crystal-field interaction, and $E_J - E_{J'}$ is the energy separation between the two states. Using Eqs. (1.37) and (1.38), the matrix element, $\langle C_0^{(2)}\rangle$, in Eqs. (1.90) and (1.92), can be expressed in terms of the reduced matrix element of unit operator $U^{(2)}$ as

$$\langle J \| C_0^{(2)} \| J'\rangle = (-1)^{2J+L'+S-1}\sqrt{\frac{28}{15}}[(2J+1)(2J'+1)]^{1/2} \times \begin{pmatrix} J' & J & 2 \\ M' & -M & 0 \end{pmatrix}\begin{Bmatrix} J & J' & 2 \\ L' & L & S \end{Bmatrix}\langle \tau LS \| U^{(2)} \| \tau' L'S'\rangle, \tag{1.93}$$

which can be evaluated for any state within a $4f^N$ configuration. The reduced matrix elements in Eq. (1.93) must be transformed from the *LS* coupling to intermediate coupling before being squared in Eq. (1.92). The values of the reduced matrix element in the *LS* basis can be obtained from the tables by Nielson and Koster (1963). Pure *LS* eigenfunctions may be used only for very isolated states.

For the special case of $J=0$ states, such as the $^7F_0$ ground state of Eu^{3+}, the only non-zero matrix element restricted by the 3-j symbol in Eq. (1.93) is from the $J'=2$, $M'=0$ crystal-field levels. Thus,

$$\left|\langle 00 \mid C_0^{(2)} \mid 20\rangle\right|^2 = \frac{28}{15}\left|\begin{Bmatrix} J=0 & J'=2 & 2 \\ L' & L & S \end{Bmatrix}\langle \tau LS \| U^{(2)} \| \tau' L'S'\rangle\right|^2. \tag{1.94}$$

The lattice contribution to the total quadrupole interaction constant is only from the second rank of crystal-field interaction, which can be evaluated from (Blok and Shirley, 1966):

$$P_{\text{latt}} = -\frac{3Q(1-\gamma_\infty)B_0^2}{2I(2I-1)(1-\sigma_2)\langle r^2\rangle_{4f}}, \tag{1.95}$$

where σ_2 is the associated shielding parameter for $\langle r^2\rangle_{4f}$, and γ_∞ is the Sternheimer anti-shielding factor which defines the strength of nuclear coupling to the closed shells whose charge distribution is distorted by the electric field of the lattice (Sternheimer, 1966). For trivalent RE ions, $\gamma_\infty \approx -80$ (Erickson, 1986).

Contributions from higher order coupling should also include the

pseudoquadrupole interaction that arises from the second order magnetic hyperfine coupling between two multipletes J and J'. The interaction constant from this part of contribution is

$$P_{pq} = A_J^2\left[\frac{1}{2}(\Lambda_{XX} + \Lambda_{YY}) - \Lambda_{ZZ}\right], \tag{1.96}$$

where A_J is the hyperfine interaction constant

$$\Lambda_{\alpha\alpha} = \frac{|\langle J | J_\alpha | J' \rangle|^2}{|E_J - E_{J'}|}, \tag{1.97}$$

where α represents the coordinate X, Y and Z. Since A_J is generally on the order of 10^{-2} cm^{-1} and $E_J - E_{J'}$ is larger than 100 cm^{-1} for rare earth ions, the magnitude of P_{pq} is in the kHz range and thus can be neglected in most cases.

In summary, the total effective nuclear electric quadrupole interaction constant includes contributions from four mechanisms, namely,

$$P = P_{4f}^{(1)} + P_{4f}^{(2)} + P_{latt} + P_{pq}. \tag{1.98}$$

1.7.4 Ion-ligand Hyperfine Interaction

Because the 4f electrons are not completely localized on the rare earth ion and their wave functions are perturbed by the ligand ions, an additional splitting of hyperfine structure will occur if the ligand nuclei possess nuclear spin, $I^{(L)} \neq 0$. This type of ion-ligand hyperfine interaction, also known as superhyperfine or transferred hyperfine interaction with energy splittings from kHz to MHz, enables nuclear magnetic resonance to be studied in optical spectroscopy. Energy level structures and spin dynamics of ion-ligand hyperfine interactions have been studied in the 4f – 4f electronic transitions using both frequency domain and time domain laser spectroscopic methods (Macfarlane and Shelby, 1987). The ion-ligand hyperfine interactions are added as perturbation terms to the 4f ion hyperfine Hamiltonian as

$$\begin{aligned}\mathcal{H}_{LHP} =& A_{//}^{(L)} J_Z I_Z^{(L)} + A_{\perp}^{(L)} (J_X I_X^{(L)} + J_Y I_Y^{(L)}) \\ &+ P^{(L)}\left[(I_Z^{(L)})^2 - \frac{1}{3} I^{(L)}(I^{(L)} + 1)\right] - g_I^{(L)} \mu_B \boldsymbol{H} \cdot \boldsymbol{I}^{(L)},\end{aligned} \tag{1.99}$$

where J_X, J_Y and J_Z are angular momentum operators for the 4f electrons, and $I^{(L)}$ is the nuclear spin operator of the ligands.

1.7.5 Pr^{3+}

The element Pr has only one isotope in natural abundance ($A = 141$). ^{141}Pr has nuclear spin $I = 5/2$, and electric quadrupole moment $Q = -8 \times 10^{-26}$ cm^2. In the absence of an external magnetic field, the second order hyperfine and nuclear electric quadrupole interactions in a crystal-field singlet split the $I = 5/2$ nuclear spin state into three levels with $m = \pm 5/2$, $\pm 3/2$, and $\pm 1/2$, respectively. For degenerate crystal-field doublets, the magnetic hyperfine interaction of Eq. (1.76) becomes dominant and the total number of hyperfine levels is six. Figure 1.10 shows a partial energy level diagram for comparing the crystal-field and hyperfine energy level structures of Pr^{3+} in two systems, Pr^{3+}: $LaCl_3$ and Pr^{3+}: LaF_3. The former has a crystal-field doublet ground state, whereas the later has a singlet ground state.

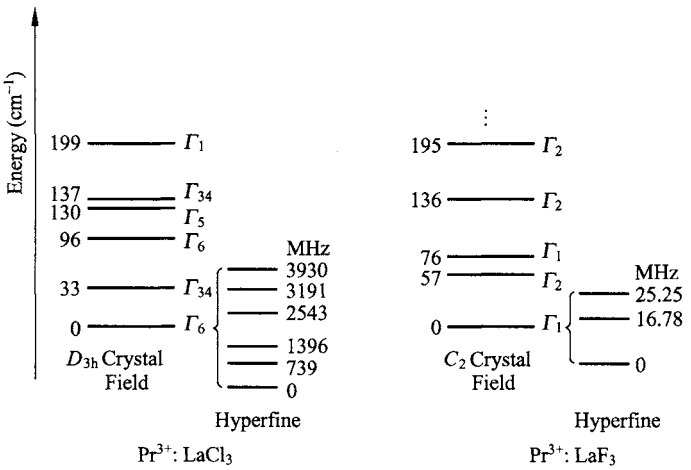


Figure 1.10 Partial crystal field and hyperfine energy levels of Pr^{3+}: $LaCl_3$ in which the ground state of Pr^{3+} is a doublet, and Pr^{3+}: LaF_3 in which the ground state of Pr^{3+} is a singlet

In an external magnetic field, the nuclear Zeeman effect further splits each of the quadrupole levels. For non-Kramers' doublets, the total hyperfine Hamiltonian is

$$\mathscr{H} = g_J \mu_B J_Z H_Z + A J_Z I_Z + P\left[I_Z^2 - \frac{1}{3} I(I+1) + \frac{\eta}{3}(I_{+1}^2 + I_{-1}^2) \right] + \mathscr{H}'_Z. \tag{1.100}$$

As a consequence of time reversal symmetry in an even number f-electron system such as Pr^{3+} (f^2 configuration), the angular momentum perpendicular to the symmetry axis is zero to the first order (Judd and Runciman, 1976; Abragam and Bleaney, 1986). Only the Z component that is parallel to the symmetry axis needs to be considered. As we discussed in the previous section, all second order magnetic hyperfine effects are absorbed into the third term as contributions from quadrupole interactions. The last term is the nuclear Zeeman interaction defined in Eq. (1.81). For crystal field singlets of Pr^{3+}, the first two terms are absent.

Investigation of hyperfine structure of Pr^{3+} in crystals has been centered on the lowest crystal field level of the $^3H_4$ ground state and the $^1D_2$ and $^3P_0$ excited multiplets. Laser spectroscopic measurements of the hyperfine and superhyperfine energy level structures for Pr^{3+} in various crystalline hosts were reviewed by Macfarlane and Shelby (1987). The hyperfine energy level structure of Pr^{3+}, including nuclear electric quadrupole splitting and ligand hyperfine coupling in various insulating crystals, has been extensively studied since the 1970 as a model case for demonstrating high resolution laser spectroscopic techniques such as spectral hole burning (Erickson, 1975; Genack et al., 1976), photon echoes (Grischkowsky and Hartmann, 1970; Chen et al., 1980), and optically detected nuclear magnetic resonance (ODNMR) (Macfarlane and Shelby, 1981a; Reddy and Erickson, 1983). Recently, Wells et al. (1999) studied the Zeeman and hyperfine energy levels in the infrared optical spectra of Pr^{3+} in alkaline earth fluoride crystals, $Pr^{3+}:CaF_2$ and $Pr^{3+}:SrF_2$ where the Pr^{3+} has C_{4v} symmetry. Similar patterns of hyperfine spectra were observed in both systems, and the value of A_J for all multiplets were calculated using Eq. (1.78). In high quality crystals, Pr^{3+} hyperfine energy levels can be observed directly in absorption spectra (Popova et al., 2001).

Many early high resolution and nonlinear laser spectroscopic studies of Pr^{3+} were conducted with the electronic transition from the $^3H_4$ ground state to the $^1D_2$ excited state near $16,600\ cm^{-1}$ (or 600 nm), which is easily accessible by a tunable dye laser. If the lowest crystal-field level is a doublet, such as E_2 for $Pr^{3+}:LaCl_3$, as shown in Fig. 1.10, the first order magnetic hyperfine splitting dominates and the six hyperfine levels spread up to several GHz. For crystal-field singlets, such as the $^3H_4$ ground state of Pr^{3+} in LaF_3, the first order magnetic hyperfine splitting vanishes. Therefore, the nuclear electric quadrupole contribution becomes dominant and the total splitting of the three quadrupole levels is expected to be 10 to 20 MHz. In Table 1.15 the values of the parameters for the electric quadrupole interactions are listed for Pr^{3+} in fluoride, and oxide crystals. The effective enhanced nuclear gyromagnetic ratios determined from the experiments are not very consistent with those calculated using Eqs. (1.80) and (1.82). Table 1.16 lists the values of γ_α for the $^3H_4$ and $^1D_2$ states of Pr^{3+} in several crystalline hosts.

Table 1.15 Parameters of nuclear electric quadrupole interactions for Pr^{3+} in various hosts (absolute value in MHz)

Host (site symmetry)	$P(^3H_4)$	$\eta(^3H_4)$	$P(^1D_2)$	$\eta(^1D_2)$
$LaF_3(C_2)$ [a]	4.19	0.11	1.10	1.31
$LiYF_4(S_4)$ [b]	4.75	0	2.56	0.02
$CaF_2(C_{4v})$ [c]	1.39		0.44	
$YAG(D_2)$ [d]	11.3	0.74	2.24	0.715
$YPO_4(D_{2d})$ [e]	3.08	<0.01	2.27	<0.01
$YAlO_3(C_s)$ [f]	3.53	0.03	0.40	0.37
$Y_2SiO_5(C_1)$ [g], site 1	4.44	0.04	1.36	0.94
$Y_2SiO_5(C_1)$ [g], site 2	1.32	0.69	0.65	1.0

(a) Reddy and Erickson, 1983;
(b) Erickson, 1981;
(c) Macfarlane and Shelby, 1987;
(d) Shelby et al., 1983;
(e) Shelby and Macfarlane, 1984;
(f) Mitsunaga et al., 1985;
(g) Equall et al., 1995.

Table 1.16 Hyperfine and nuclear Zeeman parameters of $^{141}Pr^{3+}$ in different hoste

Host/State	A_J(MHz)	$\gamma_X/2\pi$(kHz/G)	$\gamma_Y/2\pi$(kHz/G)	$\gamma_Z/2\pi$(kHz/G)
$YAlO_3$				
$^3H_4$ [a]		3.881	2.50	11.648
$^1D_2$ [b]		–	1.48	1.570
$LiYF_4$				
$^3H_4$ [c]		8	8	2
$^1D_2$ [c]	616 ±51	1.480 ±0.002	1.480 ±0.002	1.653 ±0.002
YPO_4				
$^3H_4$ [d]		5.41	5.41	2.038
$^1D_2$ [d]		1.72	1.72	1.42
LaF_3				
$^3H_4$ [e]		4.98	2.53	10.16
$^1D_2$ [f]		2.2	1.9	3.6

(a) Erickson, 1979;
(b) Mitsunaga et al., 1985;
(c) Erickson, 1980, 1985;
(d) Shelby et al., 1984;
(e) Reddy and Erickson, 1983;
(f) Macfarlane and Shelby, 1981a.

1.7.6 Eu^{3+}

Natural europium has two isotopes, it is 44.77% ^{151}Eu and 52.23% ^{153}Eu. Like ^{141}Pr, both isotopes have a nuclear spin of 5/2. The nuclear electric quadrupole moments are $(0.95 \pm 0.1) \times 10^{-24}$ cm^2 and 2.42×10^{-24} cm^2 for ^{151}Eu and ^{153}Eu, respectively (Kerbs and Winkler, 1960). The ratio of the bare quadrupole moments, $^{153}Q/^{151}Q$, is approximately 2.55, which is an index for comparison with experiments on Eu^{3+} ions in solids. In crystals, magnetic hyperfine splitting of Eu^{3+} is absent in the $^7F_0$ ground state and the metastable $^5D_0$ excited state. Nuclear electric quadruple interactions split the $J = 0$ crystal field singlets into three hyperfine levels ($m = \pm 1/2, \pm 3/2, \pm 5/2$) separated by 10 – 100 MHz. Figure 1.11 schematically shows partial crystal field and hyperfine energy level structure of Eu^{3+} in LaF_3.

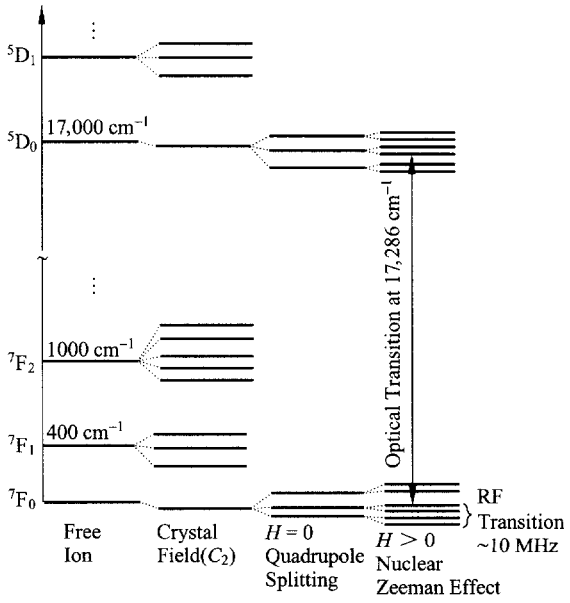


Figure 1.11 Illustration of energy level splitting of Eu^{3+}: LaF_3

In the presence of an external magnetic field, the total effective Hamiltonian for Eu^{3+} in the $^7F_0$ ground state and the $^5D_0$ excited state can be written as

$$\mathscr{H} = P\left[I_Z^2 - \frac{1}{3}I(I+1) + \frac{\eta}{3}(I_{+1}^2 + I_{-1}^2) \right] + \mathscr{H}'_Z. \qquad (1.101)$$

This Hamiltonian has a form identical to that for Pr^{3+} in singlet crystal-field levels. However, in the rare earth series, hyperfine splitting in the $^7F_0$ ground state and the $^5D_0$ excited state of Eu^{3+} in crystals has been a special case subjected to extensive spectroscopic studies for decades. Elliott (1957) first pointed out that the main contribution to the ground state nuclear quadrupole interaction should come from the second order polarization of the 4f electrons due to the coupling of the $J=0$ ground state to the $^7F_2$ excited state, and that the contributions from the lattice were small. Judd et al. (1962) modified this conclusion by realizing that the closed electron shell actually amplifies the field gradient of the lattice. The nuclear quadrupole interaction is strongly affected by the host lattice field gradient through the Sternheimer anti-shielding effect. Later work by Edmonds (1963), and Blok and Shirley (1966) discussed the quadrupole interaction and shielding effects of Eu^{3+} in a theoretical framework for RE ions in general.

It is now known that the effective nuclear quadrupole moment of Eu^{3+} in the $^7F_0$ ground state can be unusually small in comparison with that in the $^5D_0$ excited state. This is because: (1) there is no first order quadrupole interaction, $P_{4f}^{(1)}$ $(^7F_0) = P_{4f}^{(1)}$ $(^5D_0) = 0$, for the $J=0$ state; (2) the contribution from the pseudoquadrupole coupling (1.94) to the $^7F_1$ state, which is more than 300 cm^{-1} above the ground state, is in the kHz range. Therefore, the total quadrupole splitting in both states is due to the second order magnetic hyperfine interaction and the lattice contribution, namely $P = P_{4f}^{(2)} + P_{latt}$, as defined in Eqs. (1.90) and (1.93). Furthermore, in $^7F_0$, $P_{4f}^{(2)}$ and P_{latt} have opposite signs and comparable magnitudes. Therefore the lattice contribution partially cancels the 4f-electron contribution. This cancellation is a general phenomenon with some modification depending on the crystalline environment. For this reason, conventional nuclear magnetic resonance (NMR) and nuclear quadrupole resonance (NQR) of Eu^{3+} in solids have not been successful.

The first successful experimental observation of NMR and NQR of Eu^{3+} in solids was reported by Shelby and Macfarlane (1981) with their measurement of the nuclear quadrupole splitting of Eu^{3+} in $YAlO_3$ using optical spectral hole burning (SHB) and optically detected nuclear quadrupole resonance (ODNQR) techniques. They confirmed that the lattice indeed has an important contribution but the 4f electron coupling is also substantial in the $^7F_0$ ground state. Because the lattice contribution and the electronic contribution have opposite sign, the total nuclear quadrupole splitting is partially canceled. Subsequent work on Eu^{3+} in other hosts has reached the same conclusion. The systems studied include EuP_5O_{14} (Macfarlane et al., 1980), Eu^{3+}: $YAlO_3$ (Erickson and Sharma, 1981; Shelby and Macfarlane, 1981), Eu^{3+}: $LiYF_4$ (Sharma and Erickson, 1985), Eu^{3+}: CaF_2 (Silversmith et al., 1986), Eu^{3+}: LaF_3 (Liu et al., 1995, 1996), and $EuVO_4$ (Cone et al., 1984; Sun, 1993; Hansen et al., 1997). Hyperfine interaction parameters of Eu^{3+} in various hosts are listed in Table 1.17.

Table 1.17 Parameters of nuclear electric quadrupole interactions for $^{151}Eu^{3+}$ and $^{153}Eu^{3+}$ in various hosts (absolute value in MHz)

Host (site symmetry)	$^{153}P/^{151}P$ ($^7F_0$)	$^{153}\eta/^{151}\eta$ ($^7F_0$)	$^{153}P/^{151}P$ ($^5D_0$)	$^{153}\eta/^{151}\eta$ ($^5D_0$)
LaF_3 (C_2) [a]	6.80/2.67	0.49/0.58		
$LiYF_4$ (S_4) [b]	16.95/6.54	0.05/0.05		
CaF_2 (C_{4v}) [c]	19.93/8.26	0/0	56.85/22.23	0/0
$YAlO_3$ (C_s) [d]	29.9/11.5	0.03/0.04	59.6/23.4	0.57/0.55
Y_2SiO_5 (C_1) [e], site-1	32.0/12.4	0.67/0.66	69.7/27.3	0.66/0.66
Y_2SiO_5 (C_1) [e], site-2	37.2/14.4	0.16/0.15	70.4/27.7	0.37/0.37
$EuVO_4$ (defect site D) [f]	17.07/6.78 (Average: 2.55 ± 0.006)	0.41/0.41	25.8/10.2	0.81/0.81
YPO_4 (D_{2d}) [g]	18.40/7.08	0.69/0.65		
EuP_5O_{14} [h]	16.65/6.38	0.59/0.59	21/8.0	0.59/0.59

(a) Liu et al., 1995;
(b) Sharma and Erickson, 1985;
(c) Silversmith et al., 1986;
(d) Shelby and Macfarlane, 1981;
(e) Yano et al., 1991, 1992;
(f) Hansen et al., 1997;
(g) Sun, 1993;
(h) Macfarlane et al., 1980.

Because nuclear quadrupole interactions are sensitive to local crystalline structure, measurements of hyperfine energy level structure yield structural information that may not be obtained with other conventional methods. This is true particularly for RE ions at defect sites. It was observed that in $EuVO_4$ grown from fluxes, Eu^{3+} ions occupy a large number of defect sites (>50) (Cone, et al., 1984). Using spectral hole burning and ODNMR techniques, Sun (1993) and Hansen et al. (1997) observed that Eu^{3+} nuclear electric quadrupole splitting varies significantly from site to site. The measurements of nuclear quadrupole energy levels of Eu^{3+} at various defect sites give the values of P varying from 4.4 to 8 MHz for ^{151}Eu, and from 11 to 19 MHz for ^{153}Eu. However, as a reflection of the intrinsic properties of the nuclear quadrupole moment, the ratio of $P(^{153}Eu)/P(^{151}Eu)$ is almost independent of the defect local structure. The average value is 2.551 ± 0.006, which is in agreement with the bare moment ratio of 2.55 for the two Eu isotopes.

To calculate the value of $P_{4f}^{(2)}$ from Eqs. (1.92) – (1.94), one needs to know the intermediate coupling eigenfunctions of Eu^{3+}. Using the energy parameters for Eu^{3+} in LaF_3 (Table 1.5), we have calculated the eigenfunctions in the intermediate coupling scheme. For the crystal-field levels of the $^7F_0$ and

$^7F_2$ multiplets that contain $M = 0$ components, the eigenfunctions can be expressed in the leading LS terms of $|\tau SLJM\rangle$ (terms with magnitude less than 0.1 are neglected):

$^7F_0(0\ cm^{-1})$: $0.960|13,300\rangle - 1.187|12,200\rangle + 0.167|22,200\rangle$

$^7F_2(1185\ cm^{-1})$: $0.978|13,320\rangle - 0.141|12,220\rangle + 0.117|22,220\rangle$

Using Eq. (1.94), we obtain

$$|\langle {}^7F_0 | C_0^{(2)} | {}^7F_2 \rangle|^2 = 0.0512$$

For $^{151}Eu^{3+}$, the accepted values are $Q = 0.95 \times 10^{-24}\ cm^2$ and $\langle r^{-3} \rangle_{4f} = 50\ Å^{-3}$ (Blok and Shirley, 1966). Placing these values into Eq. (1.92), we obtain

$$P_{4f}^{(2)}({}^7F_0) = 2.14 \times 10^{-2}(1 - R_Q) B_0^2(\text{MHz}), \tag{1.102}$$

where B_0^2 is in cm^{-1}. For the $^5D_0$ excited state, the eigenfunctions are obtained ($M = 0$ terms only) as

$^5D_0(17,284\ cm^{-1})$: $-0.244|13,300\rangle - 0.546|12,200\rangle + 0.678|22,200\rangle$
$-0.178|32,200\rangle - 0.174|11,100\rangle$
$+0.217|31,100\rangle + 0.250|62,200\rangle$

$^5D_2(24,645\ cm^{-1})$: $-0.121|13,320\rangle - 0.427|12,220\rangle$
$+0.535|22,220\rangle - 0.140|32,220\rangle$
$-0.445|12,810-10\rangle + 0.446|1,281,010\rangle$

The eigenfunction of $^5D_2$ is significantly mixed with $^5K_{10}$, and there are no crystal field levels of $^5D_2$ with components of $J = 2$, $M = 0$ at an energy level below $24,645\ cm^{-1}$. These eigenfunctions result in

$$|\langle {}^5D_0 | C_0^{(2)} | {}^5D_2 \rangle|^2 = 0.0115,$$

and

$$P_{4f}^{(2)}({}^5D_0) = 7.7 \times 10^{-4}(1 - R_Q) B_0^2(\text{MHz}). \tag{1.103}$$

For $^{151}Eu^{3+}$ in $LiYF_4$, similar calculations result in

$$P_{4f}^{(2)}({}^7F_0) = 2.45 \times 10^{-2}(1 - R_Q) B_0^2(\text{MHz}), \tag{1.104}$$

and

$$P_{4f}^{(2)}({}^5D_0) = 3.27 \times 10^{-3}(1 - R_Q) B_0^2(\text{MHz}), \tag{1.105}$$

In comparison of the 4f electronic contribution to the quadrupole interactions of Eu^{3+} in $LiYF_4$ and LaF_3, we notice that the values of $P_{4f}^{(2)}$ ($^7F_0$) are

approximately the same, but that of $P_{4f}^{(2)}(^5D_0)$ differ by a factor of 4.8. This is due to the much larger variation in the eigenfunctions and energy levels of the $^5D_0$ and $^5D_2$ multiplets in the two systems. In general, $P_{4f}^{(2)}(^5D_0)$ has a stronger dependence on hosts.

Using Eq. (1.95) and accepted values (Erickson, 1986), $(1-\gamma_\infty)=81$, and $\langle r^2\rangle_{4f}=2.5\times10^{-17}$ cm^2 for $^{151}Eu^{3+}$, the lattice contribution to the quadrupole interaction constant is approximately

$$P_{\text{latt}}=-\frac{1.39\times10^{-2}B_0^2}{(1-\sigma_2)}\,(\text{MHz}), \tag{1.106}$$

with B_0^2 in cm^{-1}. The coefficient of 1.39×10^{-2} in Eq. (1.106) should be the same for Eu^{3+} in both the $^7F_0$ and $^5D_0$ states, and insensitive to crystalline environments.

Comparing Eq. (1.106) with Eqs. (1.103) and (1.105), we conclude that in the $^5D_0$ state, the nuclear quadrupole splitting is dominated by the lattice contribution. The ratio of $P_{4f}^{(2)}(^5D_0)/P_{\text{latt}}$ is expected to be on the order of 10% or less. For all practical purposes, $P(^5D_0)=P_{\text{latt}}$ is a good approximation.

Although the nuclear electric quadrupole splittings in the $^7F_0$ and $^5D_0$ states were measured using spectral hole burning and ODNMR methods and the absolute values of $P(^7F_0)$ and $P(^5D_0)$ were extracted from analysis of the experimental data for Eu^{3+} in a variety of crystalline hosts, the shielding factors, $(1-R_Q)$ and $(1-\sigma_2)$ have not been consistently determined. Using Eqs. (1.102) and (1.106), we can express the ground state quadrupole interaction constant for $^{151}Eu^{3+}$ in $LiYF_4$ as

$$P(^7F_0)=\left[2.14(1-R_Q)-\frac{1.39}{(1-\sigma_2)}\right]\times10^{-2}B_0^2(\text{MHz}), \tag{1.107}$$

with B_0^2 in cm^{-1}, and the ratio of lattice contribution to electronic contribution as

$$\frac{P_{\text{latt}}}{P^{(2)}(^7F_0)}=-\frac{0.65}{(1-\sigma_2)(1-R_Q)}. \tag{1.108}$$

Practically, through experimental measurements of the quadrupole splitting in $^7F_0$ and $^5D_0$, and using the value of B_0^2 determined from crystal field analysis, $(1-R_Q)$ and $(1-\sigma_2)$ can be determined from

$$(1-\sigma_2)=-\frac{1.39}{SR}, \tag{1.109}$$

$$(1-R_Q)=-0.47S(R-1), \tag{1.110}$$

where

$$S = 10^2 \times \frac{P(^7F_0)}{B_0^2}, \tag{1.111}$$

and

$$R = \frac{P(^5D_0)}{P(^7F_0)} \approx \frac{P_{latt}}{P^{(2)}(^7F_0) + P_{latt}}. \tag{1.112}$$

By definition, the value of $(1-R_Q)$ and $(1-\sigma_2)$ must be between 0 and 1. It is known that $P(^5D_0) \approx P_{latt}$ is always negative and $P_{4f}^{(2)}(^7F_0)$ is positive, but $P(^7F_0)$ and B_0^2 can be positive or negative. For a specific system, if $B_0^2 > 0$ and $P(^7F_0) < 0$, then, $S < 0$ and $R > 0$. Hansen et al. (1997) indicated that $R < 0$ leads to a consistent ratio of $P_{latt}/P_{4f}^{(2)}$ for a series of systems, but results in negative $(1-R_Q)$ and $(1-\sigma_2)$ that have no physical basis, but likely indicate differences in the principal axes for the lattice and for the electronic tensor operators in the Hamiltonian.

It is interesting to realize that, based on previous crystal-field analyses of Eu^{3+} energy levels and the measured values of $P(^7F_0)$ in various hosts, the parameter S defined in Eq. (1.111) can be considered a constant independent of hosts. As shown in Fig. 1.12 in which only absolute values of B_0^2 and $P(^7F_0)$ are used, the slopes of the two solid lines give the average values of S, which are approximately 1.83 for $^{151}Eu^{3+}$ and 4.65 for $^{153}Eu^{3+}$. Assuming that these

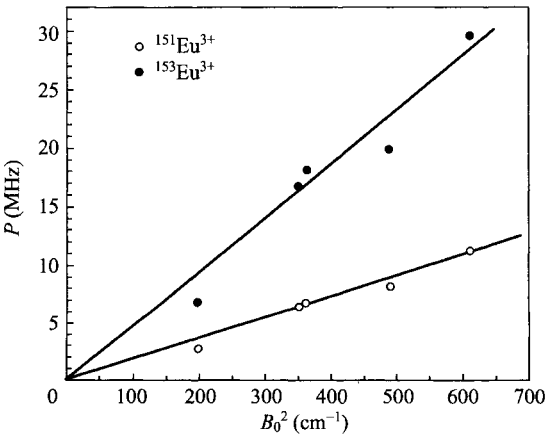


Figure 1.12 Linear dependence of hyperfine interaction constant P on crystal-field parameter B_0^2 for the ground $^7F_0$ state of Eu^{3+} in various hosts

values of S are independent of hosts, one may thus calculate the values of $(1 - R_Q)$ and $(1 - \sigma_2)$ from R, the ratio of the quadrupole interaction constant for the excited and ground states.

For nuclear Zeeman effect expressed in Eq. (1.75), there is no enhancement contribution from what is described in Eq. (1.82). The electronic shielding effect described in Eq. (1.75) is primarily from the second order magnetic hyperfine coupling to the $^7F_1$ state, which can be calculated based on the energy gaps and eigenfunctions. In fact, the anisotropic effective nuclear moment can be defined as $\mu_{\text{eff}} = \gamma \hbar I(1 - \alpha_i)$, where the quenching factor along the i-axis is given by (Shelby and Macfarlane, 1981)

$$\alpha_i = \frac{-4\mu_B^2 \langle r^{-3} \rangle \langle {}^7F_0 \mid L_i + 2S_i \mid {}^7F_1(\Gamma) \rangle \langle {}^7F_1(\Gamma) \mid N_i \mid {}^7F_0 \rangle}{\Delta_\Gamma}, \tag{1.113}$$

where Δ_Γ is the energy of the Γ symmetry component of $^7F_1$ that has the correct symmetry to couple to the ground state when the external magnetic field is along the i-axis. In the absence of J-mixing induced by the crystal field, Eq. (1.113) reduces to

$$\alpha_i = \frac{40\mu_B^2 \langle r^{-3} \rangle}{3\Delta_\Gamma}. \tag{1.114}$$

For Eu^{3+}, $\langle r^{-3} \rangle = 49.6$ Å^{-3} (Shelby and Macfarlane, 1981). Thus we have $\alpha_i = 290/\Delta_\Gamma$. The anisotropy of the quenching comes mainly from the energy denominator Δ_Γ. Since the symmetry of the component of $^7F_1$ may not be uniquely determined for a low symmetry system like LaF_3, the sum $\sum (1/\alpha_i)$ should provide a reasonable estimation. For example, the three crystal field energy levels of the $^7F_1$ state of Eu^{3+} in LaF_3 are at 313, 375, and 415 cm^{-1} (Carnall et al., 1989), which result in $\sum (1/\alpha_i) = 3.8$.

Using an optical-radio frequency double resonance method, Liu et al. (1995, 1996) studied nuclear quadrupole interactions and ODNQR of Eu^{3+}: LaF_3. The ground state nuclear Zeeman splitting and angular dependence of radio frequency (RF) resonance on the applied magnetic field have been measured. As is shown in Fig. 1.13, the Eu^{3+} ODNQR spectrum obtained in the absence of an applied external static magnetic field is a direct measurement of the ground state nuclear quadrupole splitting of $^{151}Eu^{3+}$ and $^{153}Eu^{3+}$. Analysis of the spectrum resulted in the quadrupole interaction constant, P, and the electric field gradient asymmetry parameter, η. In the presence of an external magnetic field, each doubly degenerate nuclear spin level, $\pm \mid m \rangle$, splits into two nuclear Zeeman levels. A single RF transition observed without external static magnetic field is

expected to be split into four lines because all transitions between the nondegenerate nuclear Zeeman levels are allowed in this low symmetry crystal. It was observed that a single line in the zero field spectrum splits into four lines when an external static magnetic field is applied parallel to the crystallographic c-axis. These four lines correspond to the four possible transitions between the Zeeman levels. Mixing of the nuclear spin eigenstates resulting from the asymmetric electric field gradient enables all transitions. The ODNMR spectra became more complicated when the static magnetic field was oriented in an arbitrary direction. It was shown that when the direction of the c-axis was tilted 10° away from the direction of the external magnetic field, a total of eight RF transitions could be identified. As is shown in Fig. 1.14, when the sample was rotated in the applied external static magnetic field, the shifts of the RF transitions reached a maximum not at 0° (c-axis parallel to the applied external static field), but between 70° and 110°. This additional splitting (eight transitions instead of four) in the observed ODNMR spectrum is attributed to magnetically inequivalent sites of Eu^{3+} in LaF_3.

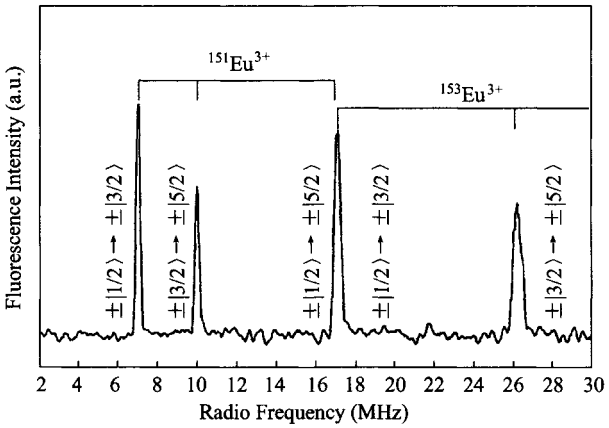


Figure 1.13 ODNQR spectrum of $^{151}Eu^{3+}$ and $^{153}Eu^{3+}$ in LaF_3 at 4K. The $^7F_0 \rightarrow {}^5D_0$ optical excitation was at the center of the inhomogeneous line at 17,286.5 cm^{-1}. The $^5D_0 \rightarrow {}^7F_1$ fluorescence of 16,239 cm^{-1} was monitored while an RF field of 1.4 Gauss was swept at 50 kHz/s and 10 kHz per step. The laser polarization was perpendicular to the crystal c-axis (Liu et al., 1995)

The angular dependent ODNMR observed in Pr^{3+}: LaF_3 (Erickson, 1977) and $EuVO_4$ (Sun, 1993) is understood as a result of anisotropic magnetic interaction between the RE ion and the local field. The result is that the effective operator tensor for the nuclear magnetic interaction has a different orientation for ions at different lattice positions. The crystallographically intrinsic Eu^{3+} sites are magnetically inequivalent. In LaF_3, as many as six inequivalent Eu^{3+} sites are expected (Anderson et al., 1968) when an external static magnetic field is applied

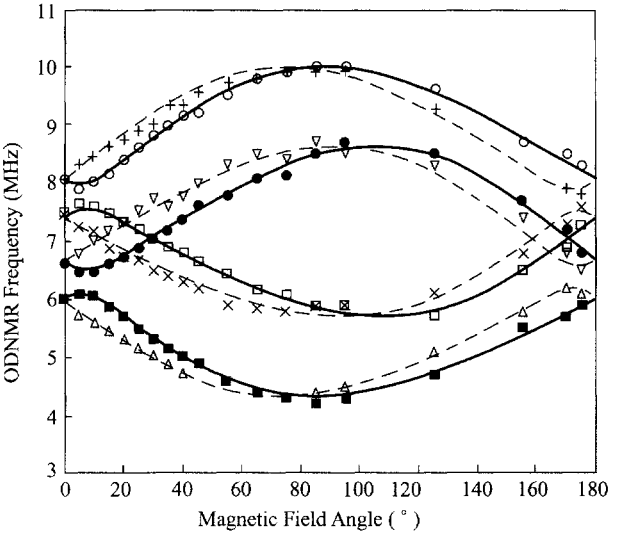


Figure 1. 14 Angular dependence of the observed (symbols) and calculated (curves) ODNMR frequencies of $I_Z = 1/2 \leftrightarrow 3/2$ transitions for $^{151}Eu^{3+}$ in LaF_3 crystal at two magnetically inequivalent sites. Four lines for each site are represented by the solid and dashed curves. The external magnetic field of 0. 26 T was always in a plane containing the c-axis and perpendicular to an a-axis (Liu et al., 1996)

in an arbitrary direction.

Assuming that Eu^{3+} ions substitute for La^{3+} ions in LaF_3 and produce no structural changes, there are six C_2 sites in a unit cell for Eu^{3+} ions. These sites are related by a rotation of $2\pi/3$ around the major crystal axis c_3 and a reflection in a plane perpendicular to the c_3-axis. To analyze the angular dependence of the ODNMR spectra, we define an arbitrary coordinate system $X'Y'Z'$, which is related to the laboratory XYZ coordinate system by three Euler angles (ϕ, β, θ) in the Edmonds convention (Edmonds, 1957). The crystal axes are defined in the XYZ coordinate with c-axis in the Z direction and a-axis in the Y direction. For our calculations, all the matrix elements of Eq. (1. 100) were converted into the new coordinate system using ϕ, β and θ. The resulting 6×6 matrix containing both real and imaginary elements of the spin Hamiltonian was diagonalized. Nuclear magnetic resonance frequencies as a function of field angle were calculated and model parameters were adjusted using a nonlinear least-squares fitting procedure. When the observed ODNMR spectra were assigned to two groups of transitions and all the interaction parameters were allowed to vary freely in the least-squires fitting, the fitting resulted in two sets of parameters that best fit the experimental data. The observed and calculated results are plotted in Fig. 1. 14 and the best-fit parameters are listed in Table 1. 18.

Table 1.18 Least squares best fit parameters for nuclear quadrupole and magnetic interactions of $^{151}Eu^{3+}:LaF_3$ in the $^7F_0$ ground state at 3 K

$\phi^{(a)}$	$-10°(-170°)\pm0.4°$
$\beta^{(a)}$	$82°(98°)\pm0.1°$
θ	$17°\pm0.5°$
$\lvert 1-\alpha_x\rvert$	0.03 ± 0.02
$\lvert 1-\alpha_y\rvert$	0.37 ± 0.2
$\lvert 1-\alpha_z\rvert$	0.65 ± 0.05

(a) The value for ϕ and β in parentheses represents a different Eu^{3+} site (see text).

As listed in Table 1.18, the parameters for the two Eu^{3+} sites are identical except for the values of the Euler angles β and ϕ. This symmetry property suggests that the orientation of interaction tensors for the magnetically inequivalent Eu^{3+} sites are related to each other by a rotation symmetry expected for the metal ion sites, although they are not coincident with any of the crystallographic axes. These results provide evidence that (1) the Z' axis for each of the inequivalent sites is not coincident with the crystal c-axis or a-axis; (2) the Z' axes of two Eu^{3+} ion sites are related to each other by reflection symmetry ($\beta_B=\pi-\beta_A$) with the symmetry plane perpendicular to the c-axis in the Z direction; (3) an a-axis lying in the Y direction is also a c_2-axis of the magnetic interaction tensors for the four Eu^{3+} sites revealed in our ODNMR spectra; (4) given that all six metal ion sites in the unit cell are related by $2\pi/3$ rotations around the Z direction and a reflection about the XY plane, rotation of the sample with an external magnetic field in the ZX plane would presumably allow us to observe transitions from only four of the expected six crystallographic sites for Eu^{3+}.

1.7.7 Tb^{3+}

The element ^{159}Tb has a nuclear spin $I=3/2$, and a nuclear electric quadrupole moment 1.43×10^{-24} cm^2. In crystals, the hyperfine energy level structure of Tb^{3+} is also an interesting case in high resolution spectroscopy. The Tb^{3+} ground state hyperfine interaction was investigated early using paramagnetic resonance methods (Lausen and Holmes, 1974), $Tb^{3+}:LiYF_4$ is one of the systems in which Tb^{3+} hyperfine energy level structure has been extensively investigated using spectral hole burning and photon echo techniques in the $^7F_6$ to $^5D_4$ transition near 20,550 cm^{-1} (Liu et al., 1988).

At an S_4 site, Tb^{3+} in $LiYF_4$ has a Γ_2 singlet ground state and a Γ_1 singlet for the lowest crystal-field level in the $^5D_4$ metastable excited state. Although there is no first order electronic Zeeman effect, the off-diagonal Zeeman coupling is very strong in the ground state, because the next crystal field level is only 0.9 cm^{-1} above the ground level as shown in Fig. 1.15. The next crystal-filed level is at

98 cm^{-1}, thus has little influence to the ground state Zeeman effect. In calculation of Zeeman and hyperfine splittings, the two levels are usually treated as a degenerate doublet with a spin $-1/2$ effective Hamiltonian (Liu et al., 1988):

$$\mathscr{H}_{\text{eff}} = g_{/\!/}\mu_B H_z S_z + \Delta S_\perp + A S_z I_z, \tag{1.115}$$

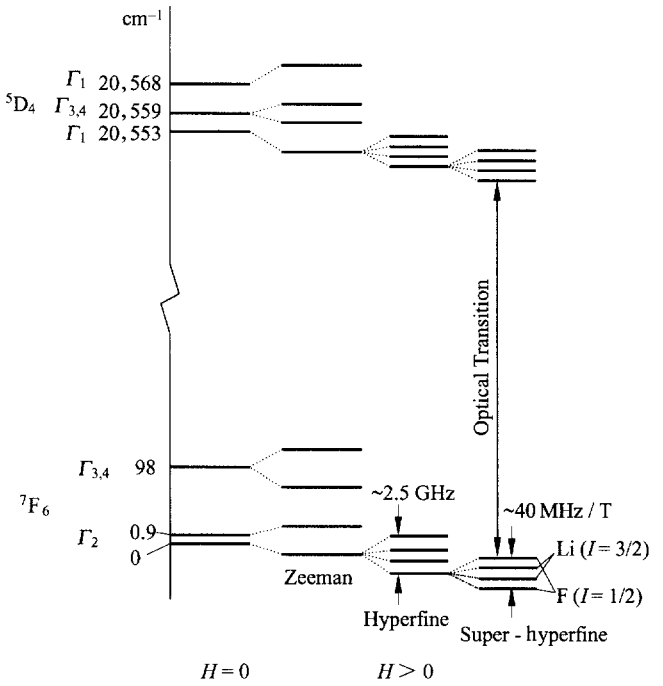


Figure 1. 15 Partial energy levels of Tb^{3+}: $LiYF_4$ for illustration of crystal filed, Zeeman, hyperfine, and superhyperfine splittings in different orders of energy scales

where $g_{/\!/} = 17.8$ is the effective g-factor for the ground state and $g_{/\!/} S_z$ with $S = 1/2$ is equivalent to $g_J J_z$ with $J = 6$; $\Delta = 27.98$ GHz is the gap between the two Γ_2 levels at zero field, and $A = 6.26$ GHz is the magnetic hyperfine interaction constant. The energy levels evaluated from this Hamiltonian are given by

$$E(M = \pm 1/2, m) = M[(g_{/\!/}\mu_B H_z + Am)^2 + \Delta^2]^{1/2}. \tag{1.116}$$

The Zeeman splitting is nonlinear at low fields and becomes linear after H_z is higher than 3 kG so that $g_{/\!/}\mu_B H_z > \Delta$. Because of the large value of A, each of the hyperfine levels quickly split in a field less than 3 kG, and saturate at higher fields. The total ground state hyperfine splitting is approximately 2.5 GHz, as observed in the spectral hole burning spectrum of the $^7F_6(\Gamma_2) \rightarrow {}^5D_4(\Gamma_1)$

transition shown by the anti-holes (Sun et al., 2002). Side holes are due to the excited state hyperfine splitting. Splittings of the hyperfine holes are attributed to superhyperfine interactions induced by coupling of the Tb^{3+} electronic moment to the nuclear spin of F^- ($I=1/2$) and Li^+ ($I=3/2$). An approximate 40 MHz/10 kG splitting due to coupling of F^- nuclear spin in the Tb^{3+} hyperfine energy levels was observed in spectral hole burning and ODNMR. It was also observed that the superhyperfine coupling between Tb^{3+} and Li^+ is about 40% of the splitting induced by F^-. Considering that the magnetic dipole interaction is dominant in contributing to the observed ion-lattice superhyperfine interactions, the effective-operator Hamiltonian can be written as

$$\mathscr{H}_{\mathrm{Tb},L} = \sum_L \langle J_z \rangle \left[(A^{(\mathrm{L})} + B_z^{(\mathrm{L})}) I_z^{(\mathrm{L})} + \frac{B_t^{(\mathrm{L})}}{\sqrt{2}} (I_{-1}^{(\mathrm{L})} e^{+i\varphi} - I_{+1}^{(\mathrm{L})} e^{-i\varphi}) \right] - \sum_L g_I^{(\mathrm{L})} \mu_B H_z I_z^{(\mathrm{L})}, \tag{1.117}$$

where L sums over the nearest neighboring ligands F^- and Li^+. B_z and B_t are two components of the point-dipole coupling constant, which are defined using the coordinate with Tb^{3+} at the origin and a ligand ion at $\boldsymbol{r}$:

$$\begin{aligned} B_z &= B \frac{3z^2 - r^2}{r^5}, \\ B_t &= 3Bz \frac{(x^2 + y^2)^{1/2}}{r^5}, \end{aligned} \tag{1.118}$$

where $B = g_J \mu_B \hbar \gamma^{(\mathrm{L})}$. For a Tb^{3+}-F^- pair, $B = 55.66$ MHz · Å^3 in both the $^7F_6$ and $^5D_4$ states. In Eq. (1.117), an independent parameter $A^{(\mathrm{L})}$ is added to account for the exchange (Fermi contact) interaction, which measures the density of the Tb^{3+} electron clouds at the nuclear sites transferred through the ligand electron clouds.

Instead of calculating the off-diagonal matrix element of J_z, the expectation value of $\langle J_z \rangle$ is used directly as a parameter in the Hamiltonian of Eq. (1.117) so that the matrix diagonalization involves only the nuclear spin states. It should be realized that, in addition to crystal-field parameters, the expectation value of $\langle J_z \rangle$ is also a function of the applied magnetic field if the second order Zeeman coupling is not negligible. Since the two narrowly separated Γ_2 levels in the Tb^{3+} ground state can be treated as a quasi-degenerate doublet that exhibits linear Zeeman splitting in the field above 2 kG, for the ground state, $\langle J_z \rangle_g$ approaches to a constant value of -5.93, which is slightly smaller than $M = -6$ due to a small admixture of the $M = \pm 2$ in the crystal-field wave function. For the lowest level in the $^5D_4$ excited state, there is no first order Zeeman effect for the Γ_1 singlet, and a nonlinear energy level shift occurs due to weaker second order

Zeeman coupling with another Γ_1 singlet at 15 cm^{-1} higher in crystal-field energy. As a result, $\langle J_z \rangle_e$ varies as a function of the external magnetic field and increases to a constant value of -4 when the field is higher than 6 T. Therefore, both Zeeman and hyperfine splittings in the excited state are nonlinear.

With a set of parameters including $\langle J_z \rangle$, the ligand hyperfine splitting can be evaluated by diagonalizing the Hamiltonian in the ligand nuclear spin space. Because no correlation effect is considered between the ligand hyperfine interactions, each ion-ligand pair can be calculated separately. The contribution should be the same for the ligands at equivalent lattice positions. For Tb^{3+} in $LiYF_4$, the largest contribution is from the four nearest F^- ions, and the energy splittings due to such a pair can be calculated from

$$E(I^{(L)} = 1/2) = \pm \frac{(a^2 + b^2)^{1/2}}{2}, \tag{1.119}$$

where

$$\begin{aligned} a &= \hbar \gamma^{(F)} H_z - \langle J_z \rangle (A^{(F)} + B_z^{(F)}) \\ b &= \langle J_z \rangle B_t^{(F)} \end{aligned} \tag{1.120}$$

Superhyperfine energy level splittings on the order of 10 MHz can be easily observed in spectral hole-burning, ODNMR, or photon echo experiments (Liu, 1988; Sun et al., 2002).

1.7.8 Other Ions

As long as the homogeneous line width of an electronic transition is narrower than the hyperfine splittings in the ground and excited states, hyperfine energy levels of any RE ion, in principle, can be probed using an appropriate laser spectroscopic method such as spectral hole burning, ODNMR, or photon echoes. Studies have been limited technically by laser access to certain states. Most of the high resolution laser spectroscopy of RE ions has so far been carried out on Pr^{3+}, Eu^{3+}, and Tb^{3+}. For the non-Kramers' ions, particularly in the crystal-field singlets, the electronic magnetic interactions are generally weaker than in the doublets. This results in longer coherent times and slower spin-relaxation rates for RE ions in the excited and ground states. When phonon-assisted relaxation is reduced at low temperatures, hyperfine spectral hole burning is able to induce a long-lived population redistribution so that hyperfine and superhyperfine energy level structures can be probed. Similarly, slower spin-relaxation enables applications of phonon echoes and ODNMR in measurements of hyperfine and superhyperfine energy levels. From this perspective, other non-Kramers' ions, such as Ho^{3+} ($I = 7/2$), Tm^{3+} ($I = 1/2$), and selected isotopes of Sm^{2+} in the $4f^6$

configuration should exhibit spectroscopic properties similar to those of the Pr^{3+}, Eu^{3+}, and Tb^{3+} systems. Agladze et al. (1991) reported that, in $Ho^{3+}:LiYF_4$, ^6Li and ^7Li superhyperfine splittings were well resolved in the $^5I_8 - {}^5I_7$ absorption spectrum. The isotope shifts between the energy levels of the $Ho^{3+} - {}^6Li$ and $Ho^{3+} - {}^7Li$ superhyperfine interactions were measured from 0.014 to 0.030 cm^{-1} in optical transitions between different crystal-field levels. Using ODNMR and SHB methods, Boonyarith et al. (1993) studied the hyperfine structure of the $^5I_8 - {}^5F_5$ optical transitions within the trigonal center (C_{3v}) of Ho^{3+} in CaF_2. The magnetic hyperfine interaction constant and the nuclear quadrupole interaction constant are $A_{//} = (-3.855 \pm 0.003)$ GHz, and $P = (6.8 \pm 0.5)$ MHz for the ground state doublet, respectively. Hyperfine splittings in the lowest crystal field singlet of the $^5F_5$ excited state were not resolved in that work. However, the splittings in the upper doublets were approximately four times smaller than in the ground states. Much of the previous studies of Ho^{3+}, Tm^{3+}, and Sm^{2+} ions doped into crystalline materials were focused on homogenous line width and coherent relaxation (Macfarlane and Shelby, 1987). This subject is discussed in detail in Chapter 4 by Meltzer and Chapter 7 by Sun.

For Kramers' ions that have an odd number of 4f electrons, relatively strong magnetic ion-ligand interactions, including the interactions between the ions and ligand nuclear spin moments and the ligand nuclear spin flips, result in fast coherent relaxation, and prevent population spectral hole burning in the ground state. Therefore, spectral hole burning or photon echo decay probe of hyperfine energy level structures of Kramers' ions is difficult. Transient laser spectroscopic methods such as ODNMR may still be effective in probing the superhyperfine splittings in the MHz to GHz spectral range. However, the magnetic dipole coupling of the RE ions to ligands at various lattice distances results in very complicated spectrum in which contributions from specific ion-ligand pairs may not easily be resolved. Most of the nonlinear laser spectroscopic studies of Kramers' ions have been conducted on Er^{3+} with interests in coherent relaxation and homogeneous line width. Wang et al. (1992) conducted μs-scale burning-probing hole burning experiments on $Er^{3+}:LiYF_4$. Although no hyperfine energy levels could be resolved because of fast nuclear spin flips, they demonstrated that the measured width of the primary hole was dependent on the time delay between the burning and probing processes. This time-resolved spectral diffusion phenomenon is discussed in detail in Chapter 4.

References

Abragam, A., B. Bleaney. *Electron Paramagnetic Resonance of Transition Ions* (Dover Publication, Inc., New York, 1986).

Abragam, A., B. Bleaney. Proc. R. Soc. London Ser. A **387**, 221(1983).

Agladze, N. I., M. N. Popova, G. N. Zhizhin, V. J. Egorov, and M. A. Petrova. Phys. Rev. Lett. **66**, 477(1991).

Andersson, L. O., W. G. Protor. Z. Kristallogr **127**, 366(1968). Andersson, L. O., G.

Johnsson. *ibid.* **127**, 386(1968).
Auzel, F., O. L. Malta. J. Phys. **44**, 201(1983).
Avanesov, A. G., V. V. Zhorin, B. Z. Malkin, V. F. Pisarenko. Sov. Phys. Solid State **34**, 1552 (1992).
Blanchfield, P., T. Hailing, A. J. Miller, G. A. Saunders, and B. Chapman. J. Phys. C **20**, 3851(1983).
Blok, J. K., D. A. Shirley. Phys. Rev. **143**, 278(1966).
Boonyarith, T., J. P. D. Martin, and N. B. Manson. Phys. Rev. B **47**, 14696(1993).
Bradbury, M. I., D. J. Newman. Chem. Phys. Lett. **1**, 44(1967).
Brewer, L. *NATO ASI Series* (Reidel Publishing Company, Boston, 1983), p. 17.
Brewer, L. J. Opt. Soc. Am. **61**, 1666(1971).
Burdick, G. W., C. K. Jayasankar, F. S. Richardson, and M. F. Reid. Phys. Rev. B **50**, 16, 309(1994).
Carnall, W. T. J. Chem. Phys. **96**, 8713(1992).
Carnall, W. T., G. K. Liu, C. W. Williams, and M. F. Reid. J. Chem. Phys. **95**, 7194 (1991).
Carnall, W. T., G. L. Goodman, K. Rajnak, and R. S. Rana. J. Chem. Phys. **90**, 3443 (1989).
Carnall, W. T., H. M. Crosswhite. *ANL-84-90* (Argonne National Laboratory, Argonne, Illinois, 1984).
Carnall, W. T., J. V. Beitz, H. Crosswhite, K. Rajnak, and J. B. Mann. In: *Systematics and the Properties of the Lanthanides*, ed. S. P. Sinha (D. Reidel Publishing Com., 1983), ch. 9, pp. 389 – 450.
Chang, N. C., J. B. Gruber, R. P. Leavitt, and C. A. Morrison. J. Chem. Phys. **76**, 387 (1982).
Chen, Y. C., K. P. Chiang and S. R. Hartmann. Phys. Rev. B **21**: 40(1980).
Christensen, H. P. Phys. Rev. B **17**, 4060(1978).
Cone, R. L., R. T. Harley, and M. J. M. Leask. J. Phys. C: Solid State Phys. **17**, 3101 (1984).
Copland, G. M., D. J. Newman, and C. D. Taylor. J. Phys. B: Atom. Molec. Phys. **4**, 1388(1971).
Cowan, R. D. *The Theory of Atomic Structure and Spectra* (University of California Press, Berkeley, 1981).
Crosswhite, H. M., and H. Crosswhite. J. Opt. Soc. Am. B **1**, 246(1984).
Crosswhite, H. M. Colloques Internationaux du Centre National de la recherche Scientifique 255, 65(1977).
Crosswhite, H., B. R. Judd. Atomic Data **1**, 329(1970).
Crosswhite, H., H. M. Crosswhite, and B. R. Judd. Phys. Rev. **174**, 89(1968).
Davidova, M. P., S. B. Zdanovitch, B. N. Kazakov, S. L. Koraleva, and A. L. Stolov. Opt. & Spectrosc. **42**, 327(1977).
Dick, B. G., A. Overhauser. Phys. Rev. **112**, 90(1958).
Dieke, G. H. *Spectra and Energy Levels of Rare Earth Ions in Crystals* (Wiley, New York, 1968).
Dorenbos, P. J. Lumin. **91**, 91(2000a) and J. Lumin. **91**, 155(2000b).
Faucher, M., D. Garcia. Phys. Rev. B **26**, 5451(1982).
Freeman, A. J., R. E. Watson. Phys. Rev. **127**, 2058(1962).
Edmonds, A. R. *Angular Momnentum in Quantum Mechanics* (Princeton University Press, Princeton, N. J., 1957).
Eremin, M. V. In: *Spectroscopy of crystals*, ed. A. A. Kaplyanskii (Nauka, Leningrad, 1989), p. 30.

Edmonds, D. T. Phys. Rev. Lett., **10**, 129(1963).
Elliott, R. J. Proc. Phys. Soc. London Sect. B **70**, 119(1957).
Equall, R. W., R. L. Cone, and R. M. Macfarlane. Phys. Rev. B **52**, 3963(1995).
Erdos, P., and J. H. Kang. Phys. Rev. B **6**, 3393(1972).
Erickson, L. E. Phys. Rev. B **34**, 36(1986).
Erickson, L. E., K. K. Sharma. Phys. Rev. B **24**, 3697(1981).
Erickson, L. E. Phys. Rev. B **24**, 5388(1981).
Erickson, L. E. Phys. Rev. B **19**, 4412(1979).
Erickson, L. E. Opt. Commun. **21**, 147(1977).
Erickson, L. E. Phys. Rev. B **11**, 77(1975).
Esterowitz, L., F. J. Bartoli, R. E. Allen, D. E. Wortman, C. A. Morrison, and R. P. Leavitt. Phys. Rev. B **19**, 6442(1979).
Garcia, D., and M. Faucher. In: *Handbook on the Physics and Chemistry of Rare Earths, Vol. 21*, eds. K. A. Gschneidner, Jr. and L. Eyring (Elsevier Science, Amsterdam, 1995), p. 263.
Genack, A. Z., R. M. Macfarlane, R. M. Shelby, and R. G. Brewer. Phys. Rev. Lett. **37**, 1078(1976).
Gerloch, M., and R. C. Slade. *Ligand-Field Parameters* (Cambridge University Press, Cambridge, 1973).
Grischkowsky, D., S. R. Hartmann. Phys. Rev. B **2**, 60(1970).
Görller-Walrand, C., K. Binnemans, In: *Handbook on the Physics and Chemistry of Rare Earths*, eds. K. A. Gschneidner, Jr. and L. Eyring (North-Holland, Amsterdam, 1996), Vol. **23**, Ch. 155, pp. 121 – 283.
Görller-Walrand, C., M. Behets, P. Porcher, O. K. Moune-Minn, and I. Laursen. Inorgaica Chimica Acta **109**, 83(1985).
Gupta, R. P., S. K. Sen. Phys. Rev. A **7**, 850(1973).
Hansen, P. C., M. J. Leask, B. M. Wanklyn, Y. Sun, R. L. Cone, and M. M. Abraham. Phys. Rev. B 56, 7918(1997).
Hansen, J. E., B. R. Judd, and H. Crosswhite. Atomic Data and Nuclear Data Tables **62**, 1 (1996).
Hartree, D. R. *The Calculation of Atomic Structures* (John Wiley & Sons, New York, 1957).
Hüfner, S. *Optical Spectra of Transparent Rare Earth Compounds* (Academic Press, New York, 1978).
Huang, J., G. K. Liu, and R. L. Cone. Phys. Rev. B **39**, 6348(1989).
Jones, R. P. Thesis: Two-step excitation and direct two-photon absorption in Tb^{3+}: $LiYF_4$ (Montana State University, 1990).
Jørgensen, C. K. In: *Strucure and Bonding*, 22, *Rare Earths* (Springer, New York, 1975), p. 49.
Jørgensen, C. K. J. Phys. (Paris) **26**, 825(1965).
Jørgensen, C. K., R. Pappalardo, H. H. Schmidtke. J. Chem. Phys. **39**, 1422(1963).
Jørgensen, C. K. *Orbits in atoms and molecules* (Academic Press, London, 1962).
Judd, B. R., E. Lo. Atomic Data and Nuclear Data Tables **62**, 51(1996).
Judd, B. R. In: *Handbook on the Physics and Chemistry of Rare Earths*, eds. K. A. Gschneidner, Jr., and L. Eyring (North-Holland, Amsterdam, 1988), Ch. 74, pp. 81 – 195.
Judd, B. R., H. Crosswhite. J. Opt. Soc. Amer. B **1**, 255(1984).
Judd, B. R. J. Luminesc. **18/19**, 604(1979).
Judd, B. R. Phys. Rev. Lett. **39**, 242(1977a).
Judd, B. R. J. Chem. Phys. 66, 3163(1977b).

Judd, B. R., W. A. Runciman. Proc. R. Soc. London Ser. A **352**, 91(1976).
Judd, B. R., H. M. Crosswhite, and H. Crosswhite. Phys. Rev. **169**, 130(1968).
Judd, B. R., H. M. Crosswhite, and H. Crosswhite. Phys. Rev. **169**, 130(1967).
Judd, B. R. Phys. Rev. **141**, 4(1966).
Judd, B. R. *Operator Techniques in Atomic Spectroscopy* (McGraw-Hill, New York, 1963a).
Judd, B. R. Proc. Phys. Soc. (London) **82**, 874(1963b).
Judd, B. D., C. A. Lovejoy, and D. A. Shirley. Phys. Rev. **128**, 1733(1962).
Kassman, A. J. J. Chem. Phys. **53**, 4118(1970).
Kerbs, K., R. Winkler, Naturwissenschaften **47**, 490(1960).
Kramers, H. A. Proc. Amsterdam Acad. **33**, 959(1930).
Krupa, J. C. Inorg. Chi. Acta **139**, 223(1987).
Larionov, A. L., B. Z. Malkin. Sov. Phys. Optica and Spectroscopia **39**, 637(1975).
Laursen, I., L. M. Holmes. J. Phys. C **7**, 3765(1974).
Levenson, M. D. *Introduction to Nonlinear Laser Spectroscopy* (Academic Press, New York, 1982).
Levin, L. I., V. I. Cherpanov. Soviet Phys.: Solid State **25**, 394(1983).
Li, C. L., M. F. Reid. Phys. Rev. B **42**, 1903(1990).
Liu, G. K., S. T. Li, V. V. Zhorin, C. – K. Loong, M. M. Abraham, and L. A. Boatner. J. Chem. Phys. **109**, 6800(1998).
Liu, G. K., R. Cao, J. V. Beitz, and J. Huang. Phys. Rev. B **54**, 483(1996).
Liu, G. K., R. Cao, and J. V. Beitz. J. Alloys Compounds **225**, 45(1995).
Liu, G. K., W. T. Carnall, R. P. Jones, R. L. Cone, and J. Huang. J. Alloys and Comp. **207/208**, 69(1994a).
Liu, G. K., W. T. Carnall, G. Jursich, and C. W. Williams. J. Chem. Phys. **101**, 8277 (1994b).
Liu, G. K., J. Huang, R. L. Cone, and B. Jacquier. Phys. Rev. B **38**, 11,061(1988).
Liu, G. K. Ph. D. Thesis (Montana State University, 1988).
Loh, E. Phys. Rev. **147**, 332(1966).
Macfarlane, R. M., and R. M. Shellby. In: *Spectroscopy of Solids Containing Rare Earth Ions*, eds. A. A. Kaplyanskii, and R. M. Macfarlane (North-Holland, Amsterdam, 1987).
Macfarlane, R. M., and R, M. Shelby. Opt. Lett. **6**, 96(1981a).
Macfarlane, R. M., and R, M. Shelby. Opt. Commun. **39**, 169(1981b).
Macfarlane, R. M., R. M. Shelby, A. Z. Genack, and D. A. Weitz. Opt. Lett. **5**, 462 (1980).
Malkin, B. Z., A. M. Leushin, A. I. Iskhakova, J. Heber, M. Altwein, C. Moller, I. I. Fazlizhanov, and V. A. Ulanov. Phys. Rev. B **62**, 7067(2000).
Malkin, B. Z. In: *Spectroscopy of Solids Containing Rare Earth Ions*, eds. A. A. Kaplyanskii, R. M. Macfarlane (North-Holland, Amsterdam, 1987), Ch. 2, pp. 13 – 50.
Malkin, B. Z., Z. I. Ivanenko, and I. B. Aizenberg. Sov. Phys. -Solid State **12**, 1491 (1970).
Martin, W. C., L. Hagan, J. Reader, and J. Sugar. J. Phys. and Chem. Ref. Data **3**, 771 (1974).
Marvin, H. H. Phys. Rev. **71**, 102(1947).
Mitsunaga, M., E. S. Kintzer, and R. G. Brewer. Phys. Rev. B **31**, 6947(1985).
Morosin. B. J. Chem. Phys. **49**, 3007(1968).
Morrison, C. A., R. P. Leavitt. In: *Handbook on the Physics and Chemistry of Rare Earths*, eds. K. A. Gschneidner, Jr., and L. Eyring (North-Holland, Amsterdam, 1982), pp.

461 – 692.
Moune, O. K., M. D. Faucher, N. Edelstein. J. Lumin. **96**, 51(2002).
Newman, D. J., B. Ng. *Crystal Field Handbook* (Cambridge University Press, Cambridge, 2000).
Newman, D. J., B. Ng. Rep. Prog. Phys. **52**, 699(1989).
Newman, D. J. Adv. Phys. **20**, 197(1971).
Nielson, C. W., G. F. Koster. *Spectroscopic Coefficeints for the p^n, d^n, and f^n Configurations* (The MIT Press, Cambridge, 1963).
Popova, M. N., E. P. Chukalina, B. Z. Malkin, A. I. Iskhakova, E. Antic-Fidancev, and P. Porcher. Phys. Rev. B **63**, 075, 103(2001).
Racah, G. Phys. Rev. **76**, 1352(1949).
Rajnak, K., B. G. Wybourne. J. Chem. Phys. **41**, 565(1964).
Rajnak, K., B. G. Wybourne. Phys. Rev. **132**, 280(1963).
Reid, M. F., L. van Pieterson, A. Meijerink. J. Alloys and Compounds **344**, 240(2002).
Reid, M. F., L. van Pieterson, R. T. Wegh, and A. Merijerink. Phys. Rev. B **62**, 14, 744 (2000).
Reid, M. F., D. J. Newman, In: *Crystal Field Handbook*, eds. D. J. Newman, B. Ng (Cambridge University Press, Cambridge, 2000).
Reid, M. F. J. Chem. Phys. **87**, 2875(1987).
Reid, M. F., F. S. Richardson. J. Chem. Phys. **63**, 95(1985).
Reddy, B. R., L. E. Erickson. Phys. Rev B **27**, 5217(1983).
Reisfeld, R. and C. K. Jφrgensen. *Lasers and Excited States of Rare Earths* (Springer-Verlag, Berlin, 1977).
Rotenberg, M., R. Bivins, N. Metropolis, and J. K. Wooten. Jr., *the* 3 – j *and* 6 – j *symbols* (MIT Press, Cambridge, 1959).
Rubbio, O. J. Phys. Chem. Solids, **52**, 101(1991).
Schwiesow, R. L., H. M. Crosswhite. J. Opt. Soc. Am. **59**, 592(1969).
Seelbinder, M. B., J. C. Wright. Phys. Rev. B **20**, 4308(1979).
Shannon, R. D. Acta Crystallogr. Sect. A **32**, 751(1976).
Sharma, K. K., L. E. Erickson. J. Phys. C **18**, 2935(1985).
Shelby R. M., R. M. Macfarlane. J. Lumin. **31/32**, 839(1984).
Shelby, R. M., A. C. Tropper, R. T. Harley, and R. M. Macfarlane. Opt. Lett. **8**, 304 (1983).
Shelby, R. M., R. M. Macfarlane. Phys. Rev. Lett. **47**, 1172(1981).
Shen, Y., and K. L. Bray. Phys. Rev. B **58**, 5305(1998).
Silversmith, A. J., A. P. Radlinski, and N. B. Manson. Phys. Rev. B **34**, 7554(1986).
Slater, J. C. *Quantum Theory of Atomic Structure* (McGraw-Hill, New York, 1960).
Sobelman, I. I. *Theory of atomic spectra* (Pergamon, Oxford, 1972).
Sternheimer, R. M., M. Blume, R. F. Peierls. Phys. Rev. **173**, 376(1968).
Sternheimer, R. M. Phys. Rev. **146**, 140(1966).
Stevens, K. W. H. Proc. Phys. Soc. (London) A **65**, 209(1952).
Sun, Y. Ph. D. Thesis (Montana State University, 1993).
Sun, Y., C. W. Thiel, R. L. Come, Unpublished (2002).
Thiel, C. W., H. Cruguel, H. Wu, Y. Sun, G. J. Lapeyre, R. L. Cone, R. W. Equqll, R. M. Macfarlane. Phys. Rev. B **64**, 085, 107(2001).
Tinkham, M. *Group Theory and Quantum Mechanics* (McGraw-Hill, New York, 1964).
Tissue, B. M., J. C. Wright. Phys. Rev. B **36**, 9781(1987).
Urland, W. Chem. Phys. Lett. **77**, 58(1981).
van Pieterson, L., M. F. Reid, R. T. Wegh, S. Soverna, and A. Meijerink. Phys. Rev. B **65**, 045, 133(2002a), and 65, 045, 134(2002b).

Yano, R., M. Mitsunaga, and N. Usugi. J. Opt. Soc. Am. B **9**, 992(1992).
Yano, R., M. Mitsunaga, and N. Usugi. Opt. Lett. **16**, 1884(1991).
Wang, Y. P., D. P. Landau, R. S. Meltzer, and R. M. Macfarlane. J. Opt. Soc. Am. B **9**, 946(1992).
Weissbluth, M. *Atom and Molecules* (Academic Press, New York, 1978).
Wegh, R. T., A. Meijerink. Phys. Rev. B **60**, 10,820(1999).
Wells, Jon-Paul R., G. D. Jones, and R. Reeves. Phys. Rev. B **60**, 851(1999).
Wybourne, B. G. *Spectroscopy Properties of Rare Earths* (Wiley & Sons, New York, 1965).
Zhorin, V. V., G. K. Liu. J. Alloys Compounds 275 – 277, 137(1998).

Acknowledgements
I wish to express appreciations to my colleagues and post doctoral associates who played an essential part in my research efforts. I especially want to acknowledge the critical comments and contributions from Michael F. Reid, Boris Z. Malkin, and William T. Carnall to the present work. Work at Argonne National Laboratory was performed under the auspices of the Office of Basic Energy Sciences, Division of Chemical Sciences, U. S. Department of Energy under Contract (No. W-31-109-ENG-38).

2 Transition Intensities

M. F. Reid

2.1 Introduction

For many applications not only the energies but also the intensities of the optical transitions is of crucial importance. A range of optical processes are relevant to rare-earth spectroscopy, the most obvious being one-photon transitions within the $4f^N$ configuration. However, other processes are also of interest. These include two-photon transitions (two-photon absorption, Raman scattering and second-harmonic generation), circular dichroism, and transitions outside of the $4f^N$ configuration. In the latter case there is the possibility of exciting a 4f electron into a 5d orbital, or exciting a ligand electron into a 4f orbital, a charge-transfer transition.

Detailed modeling of transition probabilities within the $4f^N$ configuration dates back to Judd (1962) and Ofelt (1962). Early work concentrated on total intensities between J multiplets. However, transitions between crystal-field levels were examined soon after by Axe (1963), who also carried out the first calculations for two-photon processes (Axe, 1964). Electric-dipole transitions within the $4f^N$ configuration are forbidden in the absence of an odd-parity interaction with the crystal. The original papers considered only the mixing of atomic configurations by the crystal field but subsequent work, summarized by Peacock (1975), demonstrated that excitations involving ligand states (dynamic polarization and charge transfer) were also important. Significant progress in both understanding the underlying mechanisms and phenomenological modeling of the transitions has been made over the last two decades, for both one-photon (Görller-Walrand and Binnemans, 1998; Smentek, 1998; Reid, 2000) and two-photon transitions (Downer, 1989; Nguyen, 1997).

In this Chapter we provide an overview of available methods for modeling one-photon transition intensities within the $4f^N$ configuration, with particular emphasis on one-photon transitions between individual crystal-field levels. Both zero-phonon and vibronic transitions are treated. We also discuss two-photon processes and the calculation of transition intensities between the $4f^N$ and $4f^{N-1}5d$ configurations.

2.2 Basic Equations

Spectroscopic experiments measure observables such as absorption cross sections, branching ratios, and radiative lifetimes. These observables may, in principle, be calculated from squares of matrix elements of electric-dipole, magnetic-dipole, and higher-order operators. It is the purpose of this section to show how the matrix elements are related to the observable quantities. Following sections will consider the matrix elements in more detail. A more detailed discussion of the basic principles may be found in, for example, Weissbluth (1978), Piepho and Schatz(1983), Henderson and Imbusch (1989), Henderson and Bartram (2000).

2.2.1 Electric and Magnetic Dipole Operators

The electric dipole operator is

$$-e\boldsymbol{D}_q^{(1)} = -er\boldsymbol{C}_q^{(1)}, \tag{2.1}$$

and the magnetic dipole operator

$$M_q^{(1)} = \frac{-e\hbar}{2mc}(L_q^{(1)} + 2S_q^{(1)}). \tag{2.2}$$

In these equations $\boldsymbol{C}_q^{(1)}$ is a spherical tensor operator. The other operators and physical constants have their usual meanings. We consider only electric dipole and magnetic dipole transitions in what follows. Electric quadrupole contributions to the transition intensities are also possible (Tanner and Siu, 1992) but are usually too small to be significant.

The starting point for our calculations is the line strength (or dipole strength). The electric dipole line strength for a transition between initial and final states I and F with polarization q ($q=0, \pm 1$) is defined as

$$S_{FI,q}^{\mathrm{ED}} = \sum_i \sum_f e^2 \mid \langle Ff \mid D_q^{(1)} \mid Ii \rangle \mid^2, \tag{2.3}$$

and the magnetic dipole line strength is defined as

$$S_{FI,q}^{\mathrm{MD}} = \sum_i \sum_f \mid \langle Ff \mid M_q^{(1)} \mid Ii \rangle \mid^2, \tag{2.4}$$

In these equations the sums are over the components of the initial and final

states.

For linearly polarized light there is no interference between electric dipole and magnetic dipole moments, so the observables may be evaluated by adding the contributions from electric and magnetic dipole strengths. However, for circularly polarized light interference is possible, leading to circular dichroism (Section 2.3.6).

To obtain observables such as oscillator strengths, Einstein coefficients or lifetimes, it is necessary to multiply the line strengths by appropriate constants and average over the possible initial state components by dividing by the degeneracy of the initial state, g_I. If initial states of different energy could be occupied then the appropriate Boltzman factors must also be included. Most of the expressions we give here are for polarized light. However, the quantity of interest is often an average over all possible polarizations, and in those cases the expressions must be summed over the q components and divided by 3, as discussed in the following section.

The observables measured in absorption are directly related to oscillator strengths. The electric dipole and magnetic dipole oscillator strengths are defined as

$$f_{FI,q}^{\mathrm{ED}} = \frac{2m\omega}{\hbar e^2} \frac{\chi_{\mathrm{L}}}{n} \frac{1}{g_I} S_{FI,q}^{\mathrm{ED}} \tag{2.5}$$

and

$$f_{FI,q}^{\mathrm{MD}} = \frac{2m\omega}{\hbar e^2} n \frac{1}{g_I} S_{FI,q}^{\mathrm{MD}}. \tag{2.6}$$

The absorption cross section is related to the oscillator strength by

$$\sigma_{FI,q}^{\mathrm{ED/MD}} = \frac{\pi e^2}{2\varepsilon_0 mc} f_{FI,q}^{\mathrm{ED/MD}}. \tag{2.7}$$

The refractive index n appears in Eqs. (2.5) and (2.6) because the electric and magnetic fields have values in the medium different from their values in free space. The bulk correction factors are supplemented by a local correction to the electric field, χ_{L}, to account for the fact that the ion is less polarizable than the bulk medium. This local electric field correction is usually taken to be

$$\chi_{\mathrm{L}} = \left(\frac{n^2+2}{3}\right)^2. \tag{2.8}$$

This equation is only strictly correct for high-symmetry sites (Henderson and Imbusch, 1989). It is common to define a χ that is a product of our χ_{L} of Eq.

(2.8) and the bulk refractive index correction $1/n$ (e. g., May et al., 1987b). Since the exact form of the local correction has a much more tenuous justification than the bulk correction it seems appropriate to keep them separate.

For spontaneous emission the observable quantities are related to the spontaneous emission rates, i. e., the Einstein A coefficients. The electric dipole and magnetic dipole contributions to the A coefficients for a single polarization are given by

$$A_{Fl,q}^{\mathrm{ED}} = \frac{1}{3}\frac{1}{4\pi\varepsilon_0}\frac{4\omega^3}{\hbar c^3} n\chi_{\mathrm{L}} \frac{1}{g_l} S_{Fl,q}^{\mathrm{ED}} \tag{2.9}$$

and

$$A_{Fl,q}^{\mathrm{MD}} = \frac{1}{3}\frac{1}{4\pi\varepsilon_0}\frac{4\omega^3}{\hbar c^3} n^3 \frac{1}{g_l} S_{Fl,q}^{\mathrm{MD}}. \tag{2.10}$$

Note the 1/3 factor built into these definitions, which is essentially the polarization-averaging factor of Eq. (2.12) but must be included here to obtain the correct transition rates for polarized transitions. The sum of the A coefficients over all polarizations is the inverse of the radiative lifetime, i. e.,

$$\frac{1}{\tau_{\mathrm{radiative}}} = \sum_q (A_{Fl,q}^{\mathrm{ED}} + A_{Fl,q}^{\mathrm{MD}}) \tag{2.11}$$

2.2.2 Polarization Selection Rules

Polarized light is often used to obtain detailed information about optical transitions. Equations (2.3) –(2.4), which are in a spherical basis (q =0, ±1), may be used to calculate dipole strengths for the polarizations of interest.

In cases where the rare-earth ion sites are randomly oriented (as in a powder or solution) or embedded in a cubic crystal (for example, CaF_2, Cs_2NaYCl_6, and many garnets) and the light is unpolarized or linearly polarized, the physical observables are proportional to an average over the polarization components. An isotropic dipole strength may be defined as

$$\bar{S}_{Fl}^{\mathrm{ED}} = \frac{1}{3}\sum_q S_{Fl,q}^{\mathrm{ED}}. \tag{2.12}$$

For polarized light and oriented crystals the situation is more complex. General expressions may be derived by transforming from a spherical (0, ±1) basis to a Cartesian (x, y, z) basis. The electric dipole moment has odd parity, so the transformation involves the odd parity irreducible representation (irrep) 1^-

of the group O_3, which contains rotation, reflection, and inversion operators. The spherical tensor operators in Eq. (2.1) transforming as 1^- may be written as combinations of x, y and z as follows:

$$C_0^{(1)} = z, \quad C_{\pm 1}^{(1)} = \mp \frac{1}{\sqrt{2}}(x \pm iy). \tag{2.13}$$

The magnetic dipole operator has even parity and therefore transforms as the irrep 1^+ of O_3. The decomposition in terms of Cartesian coordinates is

$$\begin{aligned} M_0^{(1)} &= \frac{-e\hbar}{2mc}(L_z + 2S_z), \\ M_{\pm 1}^{(1)} &= \frac{-e\hbar}{2mc}[\mp(L_x \pm iL_y) \mp 2(S_x \pm iS_y)], \end{aligned} \tag{2.14}$$

In the following discussion we generally restrict ourselves to the case of unpolarized radiation or uniaxial crystal systems (i. e. crystals containing sites with parallel axes of at least three-fold symmetry). The traditional experimental arrangements are orthoaxial (propagation vector perpendicular to the high symmetry axis) and axial (propagation vector parallel to the axis). For very low symmetry sites (such as C_1, C_2 or C_s) the polarization properties are not completely characterized by measurements with polarization vectors along the x, y, and z axes, and measurements at intermediate angles would be necessary to extract maximum information (Stedman, 1985, 1990). However, crystals that have such low symmetries generally have sites of several different orientations with respect to the bulk crystal axes and so detailed polarization measurements would not be straightforward.

We begin with the case of an orthoaxial measurement using linearly polarized light with the electric field along the z axis (π polarization). Eq. (2.13) indicates that the expression for the electric dipole line strength is given by the spherical expression of Eq. (2.3) with $q=0$, i. e.,

$$S_{FI,\pi}^{ED} = S_{FI,0}^{ED}, \tag{2.15}$$

The magnetic field of the radiation is perpendicular to the electric field, so for π polarization it is in the x-y plane. Without loss of generality we may choose the magnetic field to be along the x axis. Then, from Eq. (2.14), an expression containing the square moduli of the matrix elements of the operator $(-M_1^{(1)} + M_{-1}^{(1)})/\sqrt{2}$ may be derived. The cross terms cancel to give

$$S_{FI,\pi}^{MD} = \frac{1}{2}(S_{FI,1}^{MD} + S_{FI,-1}^{MD}). \tag{2.16}$$

For linearly polarized light with the electric field perpendicular to the z axis (σ *polarization) the electric dipole strength is*

$$S^{\mathrm{ED}}_{FI,\sigma} = \frac{1}{2}\left(S^{\mathrm{ED}}_{FI,1} + S^{\mathrm{ED}}_{FI,-1}\right), \tag{2.17}$$

$$S^{\mathrm{MD}}_{FI,\sigma} = S^{\mathrm{MD}}_{FI,0}. \tag{2.18}$$

For axial spectra the polarization is irrelevant (as long as it is linear) and the dipole strengths are

$$S^{\mathrm{ED}}_{FI,\mathrm{axial}} = S^{\mathrm{ED}}_{FI,\sigma}, \tag{2.19}$$

$$S^{\mathrm{MD}}_{FI,\mathrm{axial}} = S^{\mathrm{MD}}_{FI,\pi}. \tag{2.20}$$

Circularly polarized measurements are generally performed on isotropic samples or in an axial configuration so that the dichroism of the bulk medium does not obscure the circular dichroism (CD) of the rare earth sites. In the convention used by most chemists (where the incoming radiation is presumed to be viewed from the sample) the $q = \pm 1$ components of the dipole moment operators correspond to the absorption of left and right circular polarization (Piepho and Schatz, 1983). Most physicists use the opposite convention (Henderson and Imbusch, 1989).

Derivations of the selection rules for optical transitions may be found in many references (Wybourne, 1965; Hüfner, 1978; Piepho and Schatz, 1983; Henderson and Imbusch, 1989; Stedman, 1990; Görller-Walrand and Binnemans, 1998; Henderson and Bartram, 2000). For uniaxial crystals the operators corresponding to π and σ polarization transform as different irreps of the point group of the site. The transformation properties may be determined from appropriate tables (Koster et al., 1963; Butler, 1981; Altmann and Herzig, 1994). For example, the transition will be electric dipole allowed if the product of the irrep of the initial state with the irrep of the dipole-moment operator, $\Gamma_{\mathrm{I}} \times \Gamma^{\mathrm{ED}}_{T}$, contains the complex conjugate of the final-state irrep Γ^{*}_{F}. The polarization T may be σ or π in the examples considered here. Recall that the odd parity irrep 1^{-} of O_3 is required for the case of the electric-dipole operator and the even parity irrep 1^{+} of O_3 for the case of the magnetic-dipole operator (Eqs. (2.13) and (2.14)). In addition, it is necessary to take into account that the electric and magnetic fields of the radiation are perpendicular. An example will be discussed in Section 2.3.7.2.

2.2.3 Vibronic Transitions

The initial and final states that appear in the matrix elements discussed above

need not be pure electronic states, but may be combinations of electronic and vibrational (vibronic) states. If the vibrational part of the wavefunction does not change during the transition then it may be ignored. However, if it does change then it is necessary to use wavefunctions that include both electronic and vibrational parts. In the following discussion we consider, for clarity, a single vibrational mode, labeled by frequency ν. The initial and final states, with vibrational quantum numbers n_i and n_f, are now written as

$$| Ii,\ \nu n_I\rangle, \quad | Ff, \nu n_F\rangle. \tag{2.21}$$

There are two extreme cases of interest. The first case applies to transitions within the $4f^N$ configuration. In this case the coupling to the lattice is small and, most importantly, the coupling is almost identical for the initial and final states. Moreover, vibronic transitions are weak, and generally only become important for centrosymmetric systems, where purely electronic electric-dipole transitions are forbidden. Transitions where there is a change of more than one vibrational quantum number are rare. Another case applies to transitions between the $4f^N$ configuration and the $4f^{N-1}$ 5d configuration or charge-transfer states. In this case the coupling to the lattice is very different for the initial and final states and transitions may involve a change of several quanta of vibration. We now discuss these two cases in more detail.

2.2.3.1 Weak Coupling: $4f^N \leftrightarrow 4f^N$ Transitions

Since the coupling of 4f electrons to the lattice is small, vibronic $4f^N \leftrightarrow 4f^N$ transitions generally involve a change of only one quantum of vibration. Vibronic transitions have been studied most thoroughly for cubic systems, especially elpasolite systems (Faulker and Richardson, 1977; Reid and Richardson, 1984c; Crooks et al., 1997), where zero-phonon electric-dipole transitions are forbidden and the only possible electric-dipole transitions are those associated with odd-parity vibrations.

Our approach (Reid and Richardson, 1984c; Crooks et al., 1997) is to use a linear Herzberg-Teller vibronic coupling model (Piepho and Schatz, 1983). In addition to the potential V the effective Hamiltonian is now supplemented by first-order and higher-order corrections in the normal coordinate Q_ν, to become

$$V + \left(\frac{\partial V}{\partial Q_\nu}\right)_{Q_\nu=0} Q_\nu + \frac{1}{2}\left(\frac{\partial^2 V}{\partial Q_\nu^2}\right)_{Q_\nu=0} Q_\nu^2 + \cdots \tag{2.22}$$

In the $4f^N$ configuration the vibronic coupling is weak and only the term firstorder in Q_ν is of interest. The $\partial V/\partial Q_\nu$ provides an additional part to the electronic Hamiltonian transforming as the complex conjugate of the irrep of the vibration,

Γ_ν^*. The Q_ν can connect vibrational states differing by one quantum number, *via* matrix elements $\langle n_I \pm 1 \mid Q_\nu \mid n_I \rangle$. In centrosymmetric systems, this term can allow electric-dipole transitions that would otherwise be parity forbidden, as we will discuss in Section 2.3.5.

2.2.3.2 Strong Coupling: $4f^N \leftrightarrow 4f^{N-1}d$ and Charge-transfer Transitions

For some transitions, such as $4f^N \leftrightarrow 4f^{N-1}5d$ and charge-transfer transitions, the excited states have a strong coupling to the lattice. Consequently, the equilibrium rare earth ligand distance, $Q_\nu^{(0)}$, is very different for the excited electronic state from for the ground electronic state, i. e., the potential-energy parabola for the vibrational mode are displaced in the excited state. If we restrict ourselves to considering only one vibrational mode, usually the totally symmetric one, and label the ground vibrational state as $|\nu_I n_I\rangle$ and the excited vibrational state as $|\nu_F n_F\rangle$. I and F labels have been attached to the ν to emphasize that even if the frequencies are approximately equal for the two electronic states, the equilibrium coordinate $Q_\nu^{(0)}$ is different. In the Franck-Condon approximation (Piepho and Schatz, 1983; Henderson and Imbusch, 1989; Henderson and Bartram, 2000) the transition probability is the product of the electronic transition probability and the square of the overlap of the vibrational wave functions for the ground and excited states

$$|\langle \nu_F n_F \mid \nu_I n_I \rangle|^2. \tag{2.23}$$

Within this approximation it is possible to derive band shapes (Henderson and Imbusch, 1989; Henderson and Bartram, 2000), which consist of a sharp zero-phonon line and series of broad vibronic lines, each corresponding to a different change in the number of vibrational quanta, $n_F - n_I$. However, in many crystals, more than one vibrational mode is active, and only a zero-phonon line and a broad vibronic band is observed (Section 2.4.1).

2.3 One Photon Transitions Within the $4f^N$ Configuration

Now that we have discussed the general principles, we can consider some specific cases. We begin with one-photon transitions within the $4f^N$ configuration. As in the case of crystal-field splittings, fully reliable *ab initio* calculations are at present not possible for ED transitions so we rely on parametrization schemes. This makes use of the concept of effective operators, as explained in Appendix A.

2.3.1 General Theory

Appendix A gives background on the concept of effective Hamiltonians and effective transition operators. Since the electric-dipole moment vanishes between pure $4f^N$ states, instead of the dipole moment operator $D_q^{(1)}$ an effective dipole moment operator is required. This may be derived from the expression for a general effective operator (Appendix A, Eq. (A. 17))

$$\boldsymbol{D}_{\mathrm{eff},q} = \boldsymbol{D}_q^{(1)} + \boldsymbol{D}_q^{(1)} \sum_{\beta \notin M} \frac{|\beta\rangle\langle\beta| V}{E_0 - E_\beta^{(0)}} + \sum_{\beta \notin M} \frac{V|\beta\rangle\langle\beta|}{E_0 - E_\beta^{(0)}} \boldsymbol{D}_q^{(1)} + \cdots \quad (2.24)$$

In this equation the $|\beta\rangle$ are excited states on the rare earth or ligand. This operator is evaluated within the $4f^N$ space. Hence the first term, $D_q^{(1)}$, vanishes because this odd-parity operator cannot connect states of the same parity.

As discussed in Appendix A the denominators in the two summations in Eq. (2.24) are equal term by term and the effective operator is Hermitian. The time-reversal plus Hermiticity symmetry argument that restricts the one-electron phenomenological crystal field to even rank operators (see Chapter 1) may be applied to our effective dipole-moment operator, and only even-rank operators are required to parametrize the one-electron, spin-independent, part of the effective dipole-moment operator. Since they are one-electron operators for the $4f^N$ configuration, which has $l=3$ the rank of the effective operators is restricted to be less than or equal to 6 (see Appendix B).

The denominators in Eq. (2.24) are eigenvalues of H_0 and do not vary for different states within the $4f^N$ configuration or within each excited configuration. This is often referred to as the "closure approximation" (though this terminology sometimes refers to closure only over the excited configuration). Our development emphasizes that this approximation arises naturally when the Rayleigh-Schrödinger expansion is restricted to first order in V. At higher orders there will be additional terms. In a Rayleigh-Schrödinger expansion the denominators will still only contain eigenvalues of H_0. If, instead, exact energies are used (sometimes referred to as relaxing the closure approximation), then we would have a Brillouin-Wigner, rather than Rayleigh-Schrödinger, expansion. However, it is always possible to expand the exact energies to recover a Rayleigh-Schrödinger expansion (Brandow, 1967).

The perturbation V is a sum of one- and two-electron operators (crystal field, coulomb interaction, spin-orbit interaction, etc). At first order in V only one-electron spin-independent operators can occur in $D_{\mathrm{eff},q}$. This is because the only part of V that can contribute is the odd parity part of the crystal-field potential V_{CF}, which is a one-electron operator. This operator can connect the $4f^N$ configuration to rare earth or ligand states of opposite parity. The two-

electron operator V_{Coulomb} or the spin-orbit operator $V_{\text{spin-orbit}}$ (acting within the RE ion) cannot, by themselves, generate non-zero contributions to $D_{\text{eff},q}$, since they cannot connect the $4f^N$ configuration to states of opposite parity. At higher orders two-body and spin-dependent operators can arise because V appears more than once in the perturbation expansion and so the perturbation can involve V_{Coulomb} or $V_{\text{spin-orbit}}$, in addition to V_{CF} (see Section 2.3.9).

2.3.2 Transitions Between Crystal-field Levels

We can now make use of the theory of effective transition operators to derive a parametrization analogous to the crystal-field Hamiltonian. The effective operator for the crystal-field Hamiltonian must transform as the identity irrep of the site symmetry (i.e. as a scalar). This is because, like the crystal-field Hamiltonian discussed in Chapter 1, it must be invariant under symmetry operations of the group.

The effective dipole moment operator (Eq. (2.24)) involves the dipole moment operator $D_q^{(1)}$ and the perturbation operator V. Since each part of V is an invariant of the site symmetry group, the effective operator must transform as the irreps of the dipole moment operator, $D_q^{(1)}$ (e.g. Γ_π^{ED} or $\Gamma_\sigma^{\text{ED}}$ for uniaxial crystals). As discussed above, the effective operator for a one-electron spin-independent parametrization must be a combination of tensor operators of rank less than or equal to 6 and even. A completely scalar operator (rank 0 in spin and orbital spaces) cannot contribute to transitions between different states, so we may write an expression for the effective dipole moment operator as

$$\boldsymbol{D}_{\text{eff},q} = \sum_{\lambda,l} B_{lq}^{\lambda} \boldsymbol{U}_l^{(\lambda)}, \tag{2.25}$$

with $\lambda = 2, 4, 6$. In this equation the notation of Burdick et al. (1999) is used. However, the ideas date back to Newman and Balasubramanian (1975), who referred to Eq. (2.25) as the vector crystal field.

The non-zero B_{lq}^{λ} will yield all linear combinations of $U_l^{(\lambda)}$ with $\lambda = 2, 4, 6$ that transform as Γ_π^{ED} or $\Gamma_\sigma^{\text{ED}}$. Parameters B_{lq}^{λ} and $B_{l\pi}^{\lambda}$ may be defined, and Eqs. (2.13) and (2.25) used to derive expressions for the effective dipole moment operators transforming as Γ_π^{ED} or $\Gamma_\sigma^{\text{ED}}$:

$$\boldsymbol{D}_{\text{eff},\pi} \equiv \boldsymbol{D}_{\text{eff},0} = \sum_{\lambda,l} B_{l\pi}^{\lambda} \boldsymbol{U}_l^{(\lambda)}, \tag{2.26}$$

$$\boldsymbol{D}_{\text{eff},\sigma} \equiv \boldsymbol{D}_{\text{eff},x} = (-\boldsymbol{D}_{\text{eff},1} + \boldsymbol{D}_{\text{eff},-1})/\sqrt{2} = \sum_{\lambda,l} B_{l\sigma}^{\lambda} \boldsymbol{U}_l^{(\lambda)}. \tag{2.27}$$

Until recently Eq. (2.25) had not been used in any data analyses (Burdick et al., 2000; Crooks et al., 2000; Burdick et al., 2002, 2003b). Newman and

Balasubramanian (1975) emphasized a different parametrization, based on the concept of vector spherical harmonics, that is more closely related to the original papers Judd (1962) and Ofelt (1962), and the perturbation theory expansion of Eq. (2.24). An adaption of this parametrization by Reid and Richardson (1983, 1984b) is now in common use. In the notation of Reid and Richardson the effective electric dipole moment operator is written as

$$D_{\mathrm{eff},q} = \sum_{\lambda,t,p} A^{\lambda}_{tp} U^{(\lambda)}_{p+q}(-1)^{q}\langle\lambda(p+q), 1-q \mid tp\rangle, \qquad (2.28)$$

with $\lambda = 2, 4, 6$, $t = \lambda - 1$, λ, $\lambda + 1$ and p restricted by the site symmetry. From Eq. (2.24) it is clear that the effective dipole moment arises from coupling the dipole moment operator $\boldsymbol{D}^{(1)}_{q}$ with the perturbation operator V. Since the perturbation is a scalar of the site symmetry, the A^{λ}_{tp} are non-zero only if tp (or linear combinations of tp) transform as the identity irrep of the site symmetry group. Equation (2.28) emphasizes the coupling between the perturbation (transforming as tp), and the dipole moment operator (transforming as $1q$) to give an effective operator (transforming as $\lambda(p+q)$).

The two parametrizations, Eqs. (2.25) and (2.28), must give identical results and have the same number of independent parameters. The relationship

$$B^{\lambda}_{(p+q)q} = \sum_{t} A^{\lambda}_{tp}(-1)^{q}\langle\lambda(p+q), 1-q \mid tp\rangle, \qquad (2.29)$$

with the spherical-Cartesian transformation of Eq. (2.13), may be used to derive relationships between the A^{λ}_{tp} and the $B^{\lambda}_{l\sigma}$, $B^{\lambda}_{l\pi}$ parameter sets.

Parametrization Eq. (2.28) has been preferred because it is not only more closely related to the earlier work of Judd (1962) but is also amenable to analysis by the superposition model (Section 2.3.2.1). As discussed below, this parametrization is quite suitable for inorganic crystals with simple ligands. However, Burdick et al. (1999) have pointed out that there are inherent ambiguities with the parametrization.

These ambiguities have their origin in the nature of intensities. Because they involve squares of dipole moments intensities are invariant under a sign change of the dipole moments and it is clear from Eq. (2.28) that there are always at least two parameter sets that give identical calculated intensities, related by a change in the sign of all of the A^{λ}_{tp} parameters. However, with parametrization Eq. (2.25), it is clear that there is often more freedom, since the signs of the parameters associated with each distinct polarization may be changed independently. Thus, in the uniaxial case, the $B^{\lambda}_{l\sigma}$ and $B^{\lambda}_{l\pi}$ parameter sets may be changed independently, giving not just two but four different sets of parameters. If we then transform to the A^{λ}_{tp} parameter set using Eqs. (2.29) and (2.13), we will, in general, obtain A^{λ}_{tp} parameter sets that differ not only in sign, but also in magnitude. This multiplicity has obvious implications for attempts to rationalize

fitted parameters in terms of fundamental calculations. Further discussion may be found in (Burdick et al., 1999, 2000; Crooks et al., 2000; Reid, 2000; Burdick et al., 2002, 2003b).

As well as the restrictions on the A^{λ}_{tp} parameters that arise from the necessity to have combinations of tp that are scalar under the site symmetry group there are restrictions that arise from the requirement that the effective operator is Hermitian. This leads to a complex-conjugation symmetry similar to that for crystal field parameters

$$(A^{\lambda}_{tp})^{*} = (-1)^{t+1+p} A^{\lambda}_{t-p}. \tag{2.30}$$

This symmetry restricts parameters with $p = 0$ to be either pure real or pure imaginary for t odd or even respectively.

For the restricted case $t = \lambda \pm 1$, the A^{λ}_{tp} parameters are related to the product $A_{tp}\Xi(t, \lambda)$ from Judd (1962) by

$$A^{\lambda}_{tp} = -A_{tp}\Xi(t, \lambda)\frac{2\lambda + 1}{(2t + 1)^{1/2}}. \tag{2.31}$$

The products $A_{tp}\Xi(t, \lambda)$ have been used as phenomenological parameters by various authors, starting with Axe (1963), and are sometimes referred to as $B_{\lambda tp}$ (Porcher and Caro, 1978a).

To complete the calculation of dipole moments matrix elements of the effective dipole operators discussed above must be evaluated between crystal-field eigenstates. If the eigenstates of the crystal-field Hamiltonian discussed in Chapter 1 are given in terms of JM states as

$$\begin{aligned} |i_0\rangle &= \sum_{\alpha, S, L, J, M} |4f^N \alpha SLJM\rangle C_{i\alpha SLJM}, \\ |f_0\rangle &= \sum_{\alpha', S', L', J', M'} |4f^N \alpha' S'L'J'M'\rangle C_{f\alpha' S'L'J'M'}, \end{aligned} \tag{2.32}$$

where the C are eigenvector coefficients, then the matrix elements of the effective dipole operator Eq. (2.28) are given by

$$\begin{aligned} \langle f_0 | \boldsymbol{D}_{\mathrm{eff}, q} | i_0\rangle = &\sum_{\lambda, t, p} A^{\lambda}_{tp}(-1)^{q}\langle \lambda(p + q), 1 - q | tp\rangle \\ &\times \sum_{\alpha' S'L'J'M'} \sum_{\alpha SLJM} C^{*}_{f\alpha' S'L'J'M'} C_{i\alpha SLJM} \\ &\times \langle 4f^N \alpha' S'L'J'M' | U^{(\lambda)}_{(p+q)} | 4f^N \alpha SLJM\rangle. \end{aligned} \tag{2.33}$$

This expression will be squared, summed over degenerate states, and multiplied by e^2 to give the electric dipole line strength (see Eq. (2.3)).

The calculations in this section have used the JM basis. Many aspects of the

derivation are clearer if point group coupling coefficients and point group basis functions are used instead. This has been discussed by various authors (Reid and Richardson, 1984b; Kibler and Gâcon, 1989; Duan and Reid, 2001).

The Superposition Model

The superposition model was developed by Newman and coworkers (Newman, 1971; Newman and Ng, 1989b, 2000) as a way of comparing crystal-field parameters between crystals with different site symmetries. The same principles may be applied to the A_{tp}^{λ} intensity parameters.

We begin by considering the hypothetical case of a single ligand at R_0 on the z axis. In this case the only nonzero parameters will be those with $p=0$. intrinsic intensity parameters are defined to be the intensity parameters for this situation, i. e.

$$\bar{A}_t^{\lambda} \equiv A_{t0}^{\lambda}. \tag{2.34}$$

The intrinsic parameters are restricted to odd t, since the identity irrep of $C_{\infty v}$ does not occur in the O_3 irrep t^- unless t is odd. Therefore, if the superposition model is applicable then the A_{tp}^{λ} parameters are restricted to $t=\lambda \pm 1$ and the superposition model gives an important prediction about the allowed parameters.

For a set of (identical) ligands the intensity parameters may be written in terms of intrinsic parameters and geometrical factors as follows:

$$A_{tp}^{\lambda} = \bar{A}_t^{\lambda} \sum_L (-1)^p C^t_{-p}(\theta_L, \phi_L) \left(\frac{R_0}{R_L}\right)^{\tau_t^{\lambda}}. \tag{2.35}$$

As in the crystal field case (Newman, 1971; Newman and Ng, 1989b, 2000), the geometric factors $(-1)^p C^t_{-p}(\theta_L, \phi_L)$ are often called coordination factors. They allow for the effect of rotating the ligand from the z axis to angular coordinates (θ_L, ϕ_L). The power-law exponents τ_t^{λ} allow for the effect of changing the radial coordinate from R_0 to R_L.

Equation (2.35) may be used to calculate the intrinsic $\bar{A}_t^{\lambda}$ parameters from the phenomenological A_{tp}^{λ}. We will discuss the $\bar{A}_t^{\lambda}$ parameters derived from various experimental analyses in Section 2.3.7.3.

Most model calculations assume that the ligands may be represented by point charges and isotropic dipole moments. These calculations therefore implicitly contain the superposition model assumptions, restricting t to be odd. Before the work of Newman and Balasubramanian (1975), it was assumed that the equivalent of the A_{tp}^{λ} parametrization with $\lambda=2,4,6$ (i. e. λ even) and $t=\lambda \pm 1$ (i. e. t odd) formed the most general one-electron parametrization. For inorganic systems the A_{tp}^{λ} parametrization with $t=\lambda \pm 1$ appears to be adequate. However, in some circumstances, especially when the ligands are complex organic

molecules, the $t = \lambda$ parameters are essential to the phenomenological fits (May et al., 1987b; Reid, 2000; Burdick et al., 2003b).

2.3.3 Transitions Between *J* Multiplets

Judd (1962) showed that the intensities for total *J*-multiplet to *J*-multiplet transitions may be fitted to a three parameter linear model. The standard parameters are now labeled Ω_λ, with $\lambda = 2, 4, 6$ (Peacock, 1975; Görller-Walrand and Binnemans, 1998). Consider transitions from an initial multiplet $|\alpha_I J_I\rangle$ to a final multiplet $|\alpha_F J_F\rangle$. If all components of the initial multiplet are assumed to be equally populated then it is possible to average over all polarizations and sum the dipole strength over the *M* components of the multiplets, and use the orthogonality of the 3-j symbols to derive an expression for the isotropic dipole strength,

$$\overline{S}^{\,\mathrm{ED}}_{\alpha_F J_F, \alpha_I J_I} = \frac{1}{3} e^2 \sum_\lambda \Omega_\lambda \langle \alpha_F J_F \| \boldsymbol{U}^{(\lambda)} \| \alpha_I J_I \rangle^2, \tag{2.36}$$

with

$$\Omega_\lambda = \sum_{t,p} \frac{1}{2\lambda + 1} | A^\lambda_{tp} |^2. \tag{2.37}$$

Note that the reduced matrix elements in Eq. (2.36) are intermediate-coupled, i. e., take into account mixing of states by the free-ion Hamiltonian (see Chapter 1).

A similar expression applies to the magnetic dipole transitions:

$$\overline{S}^{\,\mathrm{MD}}_{\alpha_F J_F, \alpha_I J_I} = \frac{1}{3} \sum_\lambda \langle \alpha_F J_F \| \boldsymbol{M}^{(1)} \| \alpha_I J_I \rangle^2. \tag{2.38}$$

The parametrization of Eq. (2.36) has the virtue of being linear in the Ω_λ parameters which makes fitting to experimental data quite straightforward. Unfortunately, in forming the sum and reducing the parametrization to just three parameters a considerable amount of information is lost, since each Ω_λ parameter is a combination of A^λ_{tp} parameters with $t = \lambda - 1$, λ, $\lambda + 1$ and vibronic intensity is absorbed into the Ω_λ parametrization. Thus tests of models, such as the superposition model (Section 2.3.2.1), or detailed comparisons with *ab initio* calculations are not possible, since the Ω_λ parameters contain many contributions and furthermore are merely magnitudes, with no sign information. Also, the assumption that the states of the initial multiplet are evenly populated may not be accurate in some cases. Nevertheless, the relative simplicity of the measurements and calculations have permitted extremely useful analyses of large amounts of

experimental data.

2.3.4 Selection Rules

Since the potential V that make electric-dipole $4f^N \leftrightarrow 4f^N$ transitions allowed (see Eq. (2.24)) is invariant under the site symmetry the selection rules at the point-group level discussed in Section 2.2.2 are still valid. In particular, this means that an electric-dipole transition may be distinguished from a magnetic-dipole transition by comparing axial and orthoaxial spectra. For example, according to Eqs. (2.15) – (2.20) an electric dipole transition allowed in π polarization and forbidden in σ polarization will be forbidden in axial polarization, whereas a magnetic dipole transition allowed in π polarization and forbidden in σ polarization will be allowed in axial polarization.

$D_{\text{eff},q}$ contains one-electron spin-independent operators so the selection rule $\Delta S = 0$ should apply. For $M_q^{(1)}$ the selection rule is $\Delta S = 0$ and $\Delta L = 0$. These selection rules are violated because the large spin-orbit coupling in the $4f^N$ configuration mixes states of different S and L (see Chapter 1). For example, $\Delta S = \pm 1$, $\Delta L = \pm 1$ transitions such as $^7F_J \leftrightarrow {}^5D_{J'}$ in Eu^{3+} are routinely observed (see Section 2.3.7.2).

The parametrization also yields various selection rules on J. In the absence of crystal field mixing of the multiplets magnetic dipole transitions are restricted to $\Delta J \leqslant 1$ and not $0 \leftrightarrow 0$, and electric dipole to $\Delta J \leqslant 6$ and $0 \leftrightarrow 2$, 4, 6 only. This selection rule is commonly violated. For Eu^{3+} in some crystals $0 \leftrightarrow 0$ and $0 \leftrightarrow 3$ transitions are routinely observed. In most cases these can be explained by crystal field mixing of the $J = 0$ or $J = 3$ states with other states. The Ω_λ parametrization is unable to take this into account.

To quantitatively explain some transitions spin-dependent or two-electron operators are required. This will be discussed in Section 2.3.9.

2.3.5 Vibronic Transitions

The transitions considered so far do not involve a change in the vibrational state of the crystal. If a lattice phonon (or local mode quantum) is absorbed or emitted at the same time as the photon then a line offset from the zero-phonon line by the energy of the vibration is observed. Various approaches to this problem may be found in Satten et al. (1983), Acevedo et al. (1990), Görller-Walrand and Binnemans (1998). In our approach, the extension of parametrization of Eq. (2.28) to include vibronic processes is relatively straightforward. In Eq. (2.22) we saw that if there is a change of one vibrational quantum number then the perturbation V is supplemented by the term $\partial V / \partial Q_\nu$. While the former is a scalar of the site symmetry, the latter transforms as the complex conjugate of the vibration Γ_ν^*. Therefore in the context of the A_{tp}^λ parametrization we require

tp combinations that, instead of transforming as the identity irrep, must transform as the complex conjugate of the irrep of the vibration. Therefore the fitting process is the same, but a different set of parameters must be fitted for transitions corresponding to each vibrational mode. Reid and Richardson (1984c) and Crooks et al. (1997) have performed such fits for octahedral complexes, where the non-vibronic electric-dipole transitions are forbidden.

The vibronic intensities are absorbed into the Ω_λ parametrization of total intensities between J-multiplets. It is therefore impossible to distinguish vibronic from non-vibronic intensity with this parametrization.

2.3.6 Circular Dichroism

Molecules or crystals that are chiral (posses a definite handedness) may exhibit differential absorption of left and right circularly polarized light. This is known as circular dichroism (CD). Circular dichroism arises from an interference between electric dipole moments and high-order moments (e. g. magnetic dipole, electric quadrupole). The reader is referred to the literature for details (Piepho and Schatz, 1983). The oxydiacetate systems exhibit CD and have been extensively studied by Richardson and co-workers (May et al., 1987a; Berry et al., 1988; Hopkins et al., 1998).

For an axial geometry, the differential absorption (left - right in the chemists' convention) is related to a rotatory strength that is given by (May et al., 1987a)

$$R_{Ffi}(\text{axial}) = -\frac{3}{2}\text{Im}\sum_i \sum_f \sum_{q=\pm 1} \langle Ff| - eD_q^{(1)} | Ii\rangle \langle Ff| M_q^{(1)} | Ii\rangle^*, \tag{2.39}$$

where Im means the imaginary part. Note the negative sign that appears because we have rearranged the expression of (May et al., 1987a) to place the initial states to the right of the dipole moment operators. The $D_q^{(1)}$ may be replaced by our A_{tp}^λ or $B_{l\pi/\sigma}^\lambda$ parametrized effective operator. The parametrized model has been quite successful in reproducing experimental data for the oxydiacetate systems (May et al., 1987a; Berry et al., 1988; Burdick et al., 2003b). Note that Eq. (2.39) is a signed expression and that the intensity parameters appear linearly. Thus, there is more information in the CD spectra than in normal absorption spectra, and in principle one could determine the absolute signs of the intensity parameters by using this expression. Simultaneous use of CD and intensity data should allow better determinations of intensity parameters. Recent work using the B_{lq}^λ parametrization has addressed this possibility (Crooks et al., 2000; Burdick et al., 2002, 2003b).

2.3.7 Parameter Fits

The one-electron multiplet-multiplet Ω_λ or crystal-field level A_{tp}^{λ} or B_{lq}^{λ} effective operator parametrizations, plus the magnetic dipole operator, can explain most aspects of rare earth transition intensities within the $4f^N$ configuration.

Both of these parametrizations have some shortcomings. The Ω_λ parametrization involves the drastic assumption that all states in the initial multiplet are equally populated and some of the inaccuracies in such fits may be attributed to this assumption. In the case of the A_{tp}^{λ} and B_{lq}^{λ} the non-linearity of the fitting process makes a unique determination of the parameters difficult (Crooks et al., 2000; Burdick et al., 2000, 2003b).

2.3.7.1 Transitions Between Crystal-field Levels

To extract the maximum information from rare earth spectral intensities it is necessary to measure transition intensities between crystal field levels. In contrast to the Ω_λ parametrization, fits using the A_{tp}^{λ} parameters are highly non-linear, since the line strengths contain squares of sums of products of A_{tp}^{λ} parameters with matrix elements. This leads to many local minima and it is difficult and time consuming to exhaustively search the parameter space for the global minimum. Furthermore, small uncertainties in the crystal-field parameters (and therefore the eigenvectors) or measured intensities lead to large uncertainties in the fitted parameters. Therefore, the fitted parameters in the literature should be approached with some caution.

Many workers (including the present author) have carried out least squares fits that minimize

$$\sum_{i=1}^{n} \frac{1}{n - n_p} \left| \frac{e_i - c_i}{e_i + c_i} \right|^2, \tag{2.40}$$

where e_i and c_i are the experimental and calculated dipole strengths respectively, n is the number of data points, and n_p is the number of parameters. The rationale behind using this function is to avoid having the fit dominated by the most intense transitions. However, by effectively giving identical weight to all measurements, it is possible that very weak transitions, which may have large uncertainties, are overemphasized. Also, Eq. (2.40) is not a standard statistical function. The more usual definition of the variance,

$$\sum_{i=1}^{n} \frac{1}{n - n_p} \left| \frac{e_i - c_i}{\sigma_i} \right|^2, \tag{2.41}$$

where the σ_i are the uncertainties of the measurements, is generally a more

appropriate function to minimize (Crooks et al., 2000; Burdick et al., 2003b). Equal weighting of all transitions may be accomplished by setting the σ_i proportional to the e_i.

The first fits to crystal-field level intensity measurements were carried out by Axe (1963). During the 1960s and early 1970s there were only a small number of phenomenological analyses of crystal-field level intensity measurements. Since the late 1970s there have been a number of fits by Porcher and various coworkers (Porcher and Caro, 1978a), many on emission transitions of Eu^{3+} ions, Richardson and coworkers (Dallara et al., 1984; Burdick et al., 1994), and Görller-Walrand and co-workers (Görller-Walrand and Binnemans, 1998). The Richardson group has carried out extensive analyses of the spectra of rare-earth oxydiacetate (ODA) crystals that display the interesting property of circular dichroism (May et al., 1987a; Hopkins et al., 1998). These crystals also provide a model system for which the superposition model appears to be invalid (Dallara et al., 1984).

In many cases the superposition model does appear to hold (Chan and Reid, 1989; Burdick et al., 1994) so there are two categories of crystal to consider:

(1) Crystals for which the superposition model is a good approximation;

(2) Crystals containing complex ligands for which the superposition model is invalid.

Restricting the parameter set to only the superposition-allowed (odd t) parameters removes the problem of multiple solutions for the A_{tp}^{λ} parameters. The superposition approximation seems to be satisfactory for most inorganic crystals (Chan and Reid, 1989; Burdick et al., 1994) so in this case the A_{tp}^{λ} parameters are the most appropriate and we shall concentrate on that parametrization here. For the second class of crystal, where it is essential to use the full parameter set it is advantageous to use the B_{lq}^{λ} parameter set (Crooks et al., 2000; Reid, 2000; Burdick et al., 2002, 2003b).

2.3.7.2 Eu^{3+} in KY_3F_{10}

The emission spectrum of Eu^{3+} ions in KY_3F_{10} provides an excellent example of the use of the one-photon intensity parametrization model. Porcher and Caro (1976) analyzed the emission spectrum and obtained crystal-field parameters. In later work they performed fits to the intensity data to obtain parameters equivalent to our A_{tp}^{λ} (Porcher and Caro, 1978a). Absolute intensities were obtained by normalizing the measurements against calculated magnetic dipole transitions. Finally, they used these parameters to calculate radiative rates for all radiative decay pathways from the $^5D_0$ and $^5D_1$ multiplets, and used these rates, along with experimental lifetimes, to calculate non-radiative decay rates for the $^5D_1$ states (Porcher and Caro, 1978b).

Though the experimental spectra were obtained using powders, and so contain no polarization information, selection rules may be used to understand several aspects of the spectrum. The Eu^{3+} ions substitute for Y^{3+} ions in sites of C_{4v} symmetry. In Table 2.1 we give the JM basis functions for C_{4v} irreps

contained in O_3 irreps 0^+, 1^+, 1^- and 2^+. As discussed in Section 2.2.2 the electric dipole operator transforms as 1^- and the magnetic dipole operator as 1^+. In Table 2.1 we have indicated the functions corresponding to π and σ polarization. Since the $4f^6$ configuration of Eu^{3+} has an even number of 4f electrons the electronic states have even parity.

Table 2.1 Transformation properties of selected kets with C_{4v} symmetry labels (Butler, 1981). Functions relevant to magnetic dipole (MD) and electric dipole (ED) polarization are indicated. Note that the E irreps are doubly degenerate

C_{4v}	JM	Polarization
$\|0^+A_1\rangle$	$\|0^+0\rangle$	
$\|1^+A_2\rangle$	$\|1^+0\rangle$	MDσ
$\|1^+E\rangle$	$\|1^+\pm1\rangle$	MDπ
$\|1^-A_1\rangle$	$\|1^-0\rangle$	EDπ
$\|1^-E\rangle$	$\|1^-\pm1\rangle$	EDσ
$\|2^+A_1\rangle$	$\|2^+0\rangle$	
$\|2^+B_1\rangle$	$(\|2^+2\rangle+\|2^+-2\rangle)/\sqrt{2}$	
$\|2^+B_2\rangle$	$(\|2^+2\rangle-\|2^+-2\rangle)/\sqrt{2}$	
$\|2+E\rangle$	$\|2^+\pm1\rangle$	

In Table 2.2 the intensity data of Porcher and Caro (1978a) for which the initial state is $^5D_0$ are shown. This initial state transforms as the irrep A_1 so the only electric-dipole transitions that are allowed are to final states labeled by the irreps A_1 and E, in π and σ polarization respectively. The only magnetic-dipole transitions that are allowed are to final states labeled by the irreps A_2 and E, in σ and π polarization respectively. Thus transitions to the B_1 and B_2 states of $^7F_2$ have zero intensity (transitions to these states from the E state of $^5D_1$ are allowed).

Table 2.2 Experimental and calculated transition rates from the $^5D_0$ multiplet to the $^7F_0$, $^7F_1$ and $^7F_2$ multiplets of Eu^{3+} in KY_3F_{10} (Porcher and Caro, 1978a). Units are s^{-1}

multiplet	irrep	A_{ED}	A_{MD}	A_{expt}
$^7F_0$	A_2	0.48	0.00	0.00
$^7F_1$	A_2	0.00	15.44	15.44
	E	0.04	29.72	29.74
$^7F_2$	E	7.29	0.78	11.36
	B_1	0.00	0.00	0.00
	A_1	34.70	0.00	34.95
	B_2	0.00	0.00	0.00

The data that are shown have been normalized to the calculated intensity of the transition to the A_2 state of $^7F_1$, which is predicted to be purely magnetic dipole. Note that the predicted magnetic dipole intensity of the transition to the E state of $^7F_1$ is almost exactly twice that of the transition to the A_2 state. If there were no crystal-field mixing between $^7F_1$ and other multiplets then the ratio would be exactly 2. The magnetic dipole moments for the transitions may be calculated using the Wigner-Eckart theorem (Appendix B) and we find that transitions to all states of $^7F_1$ are equally probable, and the factor of two arises from the degeneracy of the E state.

For the transitions to the $^7F_2$ multiplet the relevant part of the effective electric-dipole transition operator (Eq. (2.28)) is

$$A^{\lambda}_{10}U^{(2)}_q(-1)^q\langle 2q, 1-q \mid 10\rangle + A^{\lambda}_{30}U^{(2)}_q(-1)^q\langle 2q, 1-q \mid 30\rangle. \tag{2.42}$$

It is clear from this expression that no $U^{(2)}_{\pm 2}$ operators arise. Therefore, from the Wigner-Eckart theorem selection rules (Appendix B) the final states cannot have $M = \pm 2$. From Table 2.1 we see that the B_1 and B_2 states of the $^7F_2$ multiplet have $M = \pm 2$. This gives us an alternative way of determining that the transition intensities for these transitions must be zero. The polarization selection rules for the allowed transitions can also be investigated. For example, for π transitions $q = 0$ and the operators in Eq. (2.42) can only connect the $^5D_0$ initial state to final states with $M = 0$, i.e., only the A_1 state of $^7F_2$.

Porcher and Caro (1978a) fitted 21 emission intensities to obtain intensity parameters. In Table 2.3 we give the parameters, translated into our A^{λ}_{tp} notation. The overall sign of the parameter set cannot be determined from the transition intensities and we have chosen signs for the parameters that are consistent with our *ab initio* calculation (Section 2.3.8). From Table 2.2, and the full data set (Porcher and Caro, 1978a) we can see that the calculated intensities give a good match to the experimental data.

In the absence mixing of the multiplets by the even-parity crystal field the only non-zero electric-dipole transitions listed in Table 2.2 would be to $^7F_2$ and the only magnetic-dipole transitions to $^7F_1$. However, we see that the crystal field mixing gives small electric-dipole contributions to transitions from $^5D_0$ to $^7F_0$ and $^7F_1$ that obey the point-group selection rules.

Given the intensity parameters of Table 2.3 it is straightforward to use the coordinates of the ligands to evaluate the sum on the right hand side of Eq. (2.35) and hence to determine the intrinsic intensity parameters (Reid et al., 1983). The parameters are given in Table 2.4. These will be discussed in the next Section.

Table 2.3 Intensity parameters for Eu^{3+} in KY_3F_{10} (Porcher and Caro, 1978a). Units are 10^{-13} cm. Signs have been chosen for consistency with Table 2.6

Parameter	Value	Parameter	Value
A^2_{10}	−534	A^6_{50}	902
A^2_{30}	2060	A^6_{54}	2270
A^4_{30}	−493	A^6_{70}	107
A^4_{50}	900	A^6_{74}	638
A^4_{54}	1930		

Table 2.4 Phenomenological intrinsic intensity parameters $\bar{A}^\lambda_t$ (in units of 10^{-13} cm) for various systems. Signs have been chosen for consistency with Table 2.6

System	$\bar{A}^2_1$	$\bar{A}^2_3$	$\bar{A}^4_3$	$\bar{A}^4_5$	$\bar{A}^6_5$	$\bar{A}^6_7$
Pr^{3+}: $LiYF_4$ [a]	–	−950	1050	150	−1790	−260
Pr^{3+}: $LaAlO_3$ [b]	–	−310	1870	1620	−3900	−8000
Nd^{3+}: YAG [c]	–	−1100	1920	2710	−4290	−1030
Eu^{3+}: KY_3F_{10} [b]	−1600	−3000	710	1700	1900	370
Eu^{3+}: $LiYF_4$ [d]	–	−3000	1000	1200	−400	17800

(a) Reid and Richardson, 1984a; (b) Reid et al., 1983; (c) Burdick et al., 1994; (d) Reid (1987).

2.3.7.3 Superposition-model Analysis of A^λ_{tp} Parameters

Intrinsic intensity parameters for a selection of ions and crystals are summarized in Table 2.4. More examples may be found in the literature (Reid et al., 1983; Reid, 1987, 1993; Görller-Walrand and Binnemans, 1998). The overall sign of the parameter sets are not determined by the data and the signs in Table 2.4 which have been chosen to agree with the calculations discussed in Section 2.3.8. We see that the relative signs of the parameters for $\lambda = 2$ and $\lambda = 4$ are quite consistent, but the $\lambda = 6$ parameters are less consistent. In the case of the Eu^{3+} parameters this is most likely because those fits do not include any transitions that are strongly dependent on the $\lambda = 6$ parameters. Note that the ratio of the $\bar{A}^2_3$ and $\bar{A}^4_3$ is negative for all of these cases. We discuss the significance of this in Section 2.3.8.

The number of intrinsic parameter determinations is so small that it is difficult to make systematic comparisons. It is particularly unfortunate that only one of the site symmetries admits an A^2_{1p} parameter so that only one determination of the intrinsic parameter $\bar{A}^2_1$ has been made. Comparing the magnitudes of the parameters in Table 2.4, it can be seen that the $\lambda = 2$, 4 intrinsic parameters for Eu^{3+} ions with F^- ligands, in KY_3F_{10} and $LiYF_4$, are quite similar (both experimental sets were obtained by Porcher and co-workers (Porcher and Caro, 1978a; Görller-Walrand et al., 1985)). However, other parameters in the table

vary widely. Not only have these parameters been derived from analyses by several different experimental groups, using very different techniques, but for practical reasons intensity measurements only sample a small number of the possible $4f^N$ transitions, often from only one initial state (typically the ground state). This restriction to a small subset of the possible transitions may explain some of the discrepancies in Table 2.4. Another source of uncertainty is that, for some parameters, the contributions to the sum in Eq. (2.35) cancel strongly. Unlike the crystal field case (Newman and Ng, 1989a, 2000) there are no systems for which the power law exponents τ_t^λ can be reliably determined. To derive the $\bar{A}_t^\lambda$ it is necessary to assume values for the τ_t^λ.

2.3.7.4 Vibronic Transitions

Vibronic transitions rare-earth ions in the octahedral elpasolite crystals Cs_2NaYCl_6 have been extensively studied. Faulker and Richardson (1977) modeled these vibronics using a point-charge plus ligand-polarization model. Parametrization of vibronics was discussed by Reid and Richardson (1984c) and applied to octahedral uranium complexes. Other approaches may be found in Satten et al. (1983), Acevedo et al. (1990).

Crooks et al. (1997) modeled extensive absorption data for Er^{3+} in Cs_2NaYCl_6. Four sets of intensity data were treated independently. Since the site symmetry is centrosymmetric (O_h) zero-phonon lines are electric-dipole forbidden, but magnetic-dipole transitions are allowed. There are three odd-parity vibrations that can couple to the electronic states, giving rise to allowed vibronic transitions. The ν_3 vibronics are displaced from the origins by 245 – 265 cm^{-1} and the vibration transforms as T_{1u}. The ν_4 vibronics are displaced from the origins by $100 - 115\ cm^{-1}$ and the vibration transforms as T_{2u}. The ν_6 vibronics are displaced from the origins by $70 - 90\ cm^{-1}$ and the vibration transforms as T_{1u}. Each set of vibronic transitions was fitted to a separate set of intensity parameters, with linear combinations of the A_{tp}^λ parameters transforming as T_{1u} or T_{2u}. Crooks et al. (1997) had difficulty performing fits using the full set of parameters, so they reduced the number of free parameters by using ratios predicted by the superposition model. These restrictions were derived by differentiating the superposition-model expression Eq. (2.35) with respect to the normal modes. The quality of these fits was not as good as the example discussed in Section 2.3.7.2. This may be because the vibrations are not purely local modes, but mix with lattice modes.

2.3.7.5 Multiplet-multiplet Transitions

The fitting of multiplet-multiplet experimental intensity data using Eq. (2.36) is relatively straightforward, since the expression is linear in the three Ω_λ parameters. A large number of fits with Ω_λ parameters have appeared in the literature (Peacock, 1975; Görller-Walrand and Binnemans, 1998) and the

parametrization has been a useful aid in the design of lasers and phosphors (Kaminskii, 1996; Shionoya and Yen, 1999; Henderson and Bartram, 2000).

The focus of many of these studies has been on the "hypersensitive" transitions, with $\Delta J = 2$, that are most strongly affected by the Ω_2 parameters. Strong hypersensitive transitions and large Ω_2 parameters appear to be correlated with the polarizability of the ligands. However, this analysis does not take into account the effect of the site symmetry. In Table 2.5 we show a few parameter sets for Nd^{3+} in different host crystals. It is true that the Ω_2 parameters for the hosts with F^- ligands are small and that the Ω_2 parameter for Y_2O_3, with more polarizable O^{2-} ligands, is larger. However, the Ω_2 parameter for YAG, which also has O^{2-} ligands, is not particularly large. The explanation is that the geometry of the site also plays a role. For the D_2 site symmetry in YAG there are no A_{tp}^{λ} parameters with $t = 1$, whereas such parameters are allowed in the C_2 site symmetry of Y_2O_3. Also, superposition-model calculations (Burdick et al., 1994) show that there is considerable cancellation in the contributions to the A_{32}^2 parameter in YAG.

Table 2.5 Phenomenological Ω_λ parameters for various Nd^{3+} systems(in units of $10^{-20}cm^2$)

System	Ω_2	Ω_4	Ω_6
Nd^{3+}: YAG[(a)]	0.2	2.7	5.0
Nd^{3+}: Y_2O_3[(b)]	8.6	5.3	2.9
Nd^{3+}: LaF_3[(b)]	0.35	2.6	2.5
Nd^{3+}: $LiYF_4$[(c)]	0.36	4.0	4.8

(a) Krupke, 1971; (b) Krupke, 1966; (c) Ryan and Beach, 1992.

The Ω_λ parametrization has been useful in laser and phosphor design (e. g. Kaminskii, 1996; Shionoya and Yen, 1999; Henderson and Bartram, 2000). However, the approach does have limitations. The assumption that the parametrization is based on, i. e. that there is an equal occupation of the states of the ground multiplet, is a poor approximation, even at room temperature. Since measurements are performed at room temperature, vibronic processes add to the zero-phonon processes, making comparison with *ab initio* calculations inconclusive.

2.3.8 Comparison with First-principles Calculations

The phenomenology discussed above is not just an end in itself. The goal is to use the parameters to understand the fundamental physics of the rare-earth systems.

Unfortunately many calculations of intensity parameters have concentrated on the point-charge crystal-field mixing with excited rare-earth states and dipolar

interactions involving the ligand ("ligand polarization" or "dynamic coupling" mechanism). In fact, some authors consider only the point-charge crystal field mixing, despite the fact that the earliest determinations of phenomenological parameters (Axe, 1963) revealed the shortcomings of this model. There have been only a few attempts to treat the ligands in a realistic manner including ligand excitations and covalent (charge transfer) effects (Henri et al., 1976; Poon and Newman, 1984; Reid and Ng, 1989; Kotzian et al., 1995).

Given an *ab initio* calculation of the effective dipole moments, the A_{tp}^{λ} parameters may be calculated by comparing Eq. (2.24) to Eq. (2.28). Most of the calculations discussed below are from Reid and Ng (1989), for a single Cl^- ligand. These calculations will be compared to experimental intrinsic intensity parameters from Table 2.4. As discussed above, intrinsic parameters for a variety of systems are broadly similar, at least for $\lambda = 2$ and 4, so the fact that Table 2.4 contains no data for Cl^- ligands should not be seen as a difficulty.

Note that there was an overall sign error in earlier calculations (see Xia and Reid, 1993) and all the parameters reported here have had their signs changed. This change has no effect on calculated intensities.

2.3.8.1 Crystal Field Mixing

We begin by considering the mechanism used in the original work of Judd (1962) and Ofelt (1962). The odd-parity crystal field mixes $4f^{N-1}$ *n*d and $4f^{N-1}$ *n*g configurations into $4f^N$, leading to the contribution

$$A_{tp}^{\lambda} = -A_{tp}\Xi(t, \lambda)\frac{(2\lambda + 1)}{(2t + 1)^{1/2}}, \qquad (2.43)$$

for $\lambda = 2,\ 4,\ 6$ and $t = \lambda \pm 1$. The A_{tp} are interconfigurational (e. g., f – d) crystal-field parameters and the $\Xi(t, \lambda)$ factors, defined by Judd (1962), contain radial integrals between the f and d orbitals.

Experience with the crystal field parameters (Ng and Newman, 1987; Newman and Ng, 2000) suggests that a more elaborate calculation, taking into account the overlap of ligand orbitals, will give contribution of the same sign, but different magnitudes, and this is indeed what is found (see Section 2.3.8.3).

The crystal field mechanism can contribute to parameters with $t = 1$ (Judd, 1966). If the crystal field is thought of as a purely external electrostatic potential then this would imply a dipolar potential that would move the ion to a different equilibrium position. Since the crystal field is not merely an external electrostatic potential this poses no difficulty in a realistic calculation.

Eq. (2.43) may be used to predict ratios between parameters with the same t and p but different λ. Crystal field contributions to intensity parameters for a single Cl^- ligand are given in Table 2.6, in the row labeled the "crude point charge". From the earliest fits using the A_{tp}^{λ} (or equivalent) parametrizations (Axe, 1963) calculations of this sort have been incapable of explaining the

relative signs of the intensity parameters. In all cases shown in Table 2.4 $\bar{A}_3^2/\bar{A}_3^4$ is negative, whereas the crude point charge calculation (Table 2.6) gives a positive ratio.

Table 2.6 *Ab initio* calculations of intrinsic intensity parameter $\bar{A}_t^\lambda$ (in units of 10^{-13} cm) for the system $Pr^{3+} - Cl^-$. The calculation is from Reid and Ng (1989), with the sign correction of Xia and Reid (1993). For a detailed discussion of the contributions see the text

Contribution	$\bar{A}_1^2$	$\bar{A}_3^2$	$\bar{A}_3^4$	$\bar{A}_5^4$	$\bar{A}_5^6$	$\bar{A}_7^6$
a: First order	−70	53	99	−45	−107	27
b: Crystal field	−2104	163	369	−125	−516	115
c: Covalency	155	165	280	−150	−286	124
d: Ligand polarization	397	−2927	99	144	−68	15
e: Ligand polarization exchange	−125	93	2	11	27	−66
a + *b* + *c*	−2019	381	748	−320	−909	266
d + *e*	−272	−2834	101	155	−41	−50
Crude point charge	−4630	260	610	−50	−170	20
Crude ligand polarization	0	−4276	0	738	0	−294

2.3.8.2 Ligand Polarization

This mechanism (also called "dynamic coupling" (Mason et al., 1974)) may be viewed in two different ways (Judd, 1979). The first is that the radiation field dynamically polarizes the ligand, and this excitation is transferred to the rare earth *via* the coulomb interaction between the 4f and ligand electrons. The other view is that the 4f electrons polarize the ligand and it is this dipole that interacts with the radiation. The latter view leads us to expect that the ligand polarization mechanism will give contributions that are generally of opposite sign to the contribution from the crystal-field mechanism (in which the ligand electrons polarize the 4f electrons).

For a ligand with isotropic polarizability the ligand polarization mechanism (line "crude ligand polarization" of Table 2.6) only gives contributions to parameters for which $t = \lambda + 1$. The contributions are, indeed, of opposite sign to the contributions from the crystal-field mechanism, for those parameters that the ligand-polarization mechanism contributes to. If the ligand polarization mechanism is assumed to dominate for parameters with $t = \lambda + 1$ then the signs of the parameters agree with the experimental values for $\lambda = 2$ and 4 (Table 2.4).

In the case of complex organic ligands, such as the oxydiacetate systems (May et al., 1987a; Berry et al., 1988; Hopkins et al., 1998), parameters with $t = \lambda$ may arise. Dallara et al. (1984) calculated contributions to these parameters from anisotropic ligand polarization. While these calculations are rather crude they do confirm the importance of effects that do not obey the

superposition model, and are thus outside of the standard Judd-Ofelt model.

2.3.8.3 Overlap and Covalency

Reid and Ng (1989) carried out extensive *ab initio* calculations of the A^{λ}_{tp} parameters based on the calculations of crystal field and correlation crystal field parameters by Ng and Newman (1987). Results are summarized in lines $(a-e)$ of Table 2.6.

Contributions b and d arise primarily from crystal field and ligand polarization contributions, which are roughly equivalent to the crude point-charge and crude ligand polarization calculations. Contribution e is a contribution to ligand polarization arising from the exchange part of the Coulomb interaction between the 4f electrons and ligand electrons. In addition, there is a small first order contribution, a, due to the basis states being molecular orbitals of mixed parity. The other significant contribution, c, is primarily a covalent effect – excitations from ligand orbitals to 4f orbitals. These covalent contributions were also considered by Henri et al. (1976) and Poon and Newman (1984).

In calculations of the phenomenological crystal field in insulating materials all major contributions to the intrinsic parameters (apart from screening) are positive (Ng and Newman, 1987; Newman and Ng, 2000). In contrast, the major contributions to the intensity parameters can have different signs, with ligand polarization effects generally being of opposite sign to the other contributions. If these calculations are compared to the phenomenological intrinsic intensity parameters (Table 2.4) we see that the calculation does appear to explain the experimental signs of the $\bar{A}^2_1$, $\bar{A}^2_3$, and $\bar{A}^4_3$ parameters. We suspect that the ligand polarization contribution to $\bar{A}^4_5$ is underestimated, and if it were larger then we would have agreement for that parameter. The experimental signs of the other parameters are not well determined, so no detailed comparison is possible.

The cancellation between the ligand polarization and other contributions has implications for the dependence of the intensity parameters on the distance to the ligands. In the case of the phenomenological crystal field, as all contributions (apart from screening) have the same sign, the crystal-field power law exponents t_k are always positive, corresponding to a monotonic reduction of the interaction strength with ligand distance (Newman and Ng, 1989b, 2000). It is possible that, over certain distance ranges, the intensity parameter power law exponents τ^{λ}_t may not be positive since the different contributions have opposing signs and could have very different distance dependences. This has implications in the analysis of phenomenological parameters using the superposition model (Section 2.3.7.3).

It is our hope that routine quantum chemistry calculations will soon be capable of realistic calculations of $4f^N$ transition intensity parameters. An example of progress in this direction is the calculations of (Kotzian et al., 1995). Those calculations were not designed to determine the phenomenological parameters,

but a determination of the parameters from such a calculation would not be particularly difficult.

2.3.9 Extensions to the Models

The first-principles calculations described in the previous section only go to first order in the perturbation. If the calculation is extended to higher order, i. e. with two or more potential operators V (Appendix A, Eq. (A. 14)) in the expansion leading to Eq. (2. 24), there is the possibility of two-electron operators (i. e. correlation effects) and spin-dependent operators. In the former case the second V includes the Coulomb interaction, in the latter the spin-orbit interaction. The higher order effects also modify the one-electron spin-independent A^{λ}_{tp} (or B^{λ}_{lq}) parameters.

There is not enough information in the available experimental data to test a truly general parametrization. A general parametrization would modify Eq. (2. 28), supplementing the $\boldsymbol{U}^{(\lambda)}$ operators by two-body $(\boldsymbol{U}^{(k_1)}\ \boldsymbol{U}^{(k_2)})^{(K)}$ operators, as in the case of the correlation crystal field, and spin-dependent $\boldsymbol{V}^{(1k_1)(K)}$ operators. We do not propose to discuss the details of such a parametrization here (see, for example, (Wybourne, 1968; Reid, 1993; Smentek, 1998)). The number of parameters is so great that we cannot hope to determine them experimentally. However, if transitions involving only a few multiplets are considered then the extra operators will simply be proportional to the one-electron operators, as in the case of correlation crystal field operators (Newman, 1971; Newman and Ng, 1989b, 2000).

In cases where Ω_{λ} fits are poor some authors have extended the parametrization to include odd-λ parameters. We believe that these attempts are technically incorrect. Since the effective transition operator should be Hermitian λ must be even (like k in the crystal field calculation) for one-electron spin-independent operators. However, as in the case of the correlation crystal field, one can have odd rank two-electron operators (but not rank 1 (Newman, 1971)). Although adding odd-rank one-electron operators is not technically correct it has been attempted for some Pr^{3+} systems (Eyal et al., 1985). The success of such fits might be interpreted to suggest that two-body (correlation) operators of odd rank might be important.

Extensive calculations of correlation effects have been carried out by Smentek and co-workers (reviewed by Smentek (1998)). Though these calculations use a point-charge approach to the crystal field the evaluation of the correlation effects is very sophisticated. These calculations demonstrate that correlation is very important, although in many cases it merely modifies the one-electron parameters.

Burdick et al. (1989) have extended the Ω_{λ} parametrization to include spin-dependent operators. Their fits are considerably better than the standard ones for cases where the standard operators have very small matrix elements. This is

particularly apparent for Gd^{3+}. These extensions were first developed by Judd and Pooler (1982) for two-photon transitions. The reason why spin-dependent operators are important is that many transitions are "spin forbidden" ($\Delta S \neq 0$), obtaining intensity because of spin-orbit mixing in the $4f^N$ configuration. If this mixing is small the spin-dependent operators (which take into account spin-orbit mixing in the excited states) provide a means to increase the intensity of transitions that otherwise would be very weak.

There have also been attempts to extend the basis set to include the $4f^{N-1}5d$ states explicitly. Since this configuration is very close to the $4f^N$ configuration it is a major source of correlation and spin-orbit effects (Garcia and Faucher, 1992; Burdick et al., 1995). It should be noted that in making such extensions care must be taken to not count the same contribution twice.

Another type of extension is to allow for the presence of slightly different sites in the crystal. Molecular dynamics methods have been used to estimate inhomogeneous broadening effects on optical spectra (Klintenberg et al., 1997; Klintenberg and Thomas, 1997; Liu et al., 2000).

2.4 Higher-energy Transitions

While most infra-red and visible rare-earth electronic transitions are predominantly within the $4f^N$ configuration, UV and VUV transitions can also involve $4f^{N-1}5d$ or charge-transfer states.

2.4.1 $4f^N \leftrightarrow 4f^{N-1}5d$ Transitions

There has recently been intense interest in transitions involving the $4f^{N-1}5d$ states, since a detailed understanding of these states is needed for development of new phosphor technology, involving VUV xenon discharges (Wegh et al., 1999; Wegh and Meijerink, 1999).

Though an enormous amount of experimental data exists (Dorenbos, 2000), until recently there had been little quantitative treatment of these states. However, detailed calculations are now possible (Laroche et al., 2000; Reid et al., 2000). Comparisons between experiment and theory have been carried out for most of the trivalent rare-earth ions in $LiYF_4$, and several ions in CaF_2 and YPO_4. Both absorption (van Pieterson et al., 2002c, a, b) and emission (van Pieterson et al., 2001) transitions have been studied and a satisfactory understanding of these excited states has now been achieved (Reid et al., 2002). There are two steps to these calculations: (1) Calculation of the $4f^{N-1}5d$ energies and eigenstates; (2) Calculation of the transition intensities, including detailed modeling of the vibronics.

Calculation of the $4f^{N-1}5d$ energies and eigenstates is discussed in Chapter 1. These calculations are a straight-forward extension to the crystal-field

calculations for $4f^N$, with additional operators to take into account the crystal-field and spin-orbit interactions for the 5d electron and the Coulomb interaction between the 4f and 5d electrons. However the large number of $4f^{N-1}5d$ states makes the calculations time-consuming for some ions.

The modeling of transition intensities requires us to consider transitions for both electronic and vibrational states, since the spectra typically consist of sharp zero-phonon lines and broad vibronic bands because the 5d electrons couple strongly to the lattice (Section 2.2.3.2). The electronic part is straightforward. In contrast to transitions within the $4f^N$ configuration the dipole moment operator $D_q^{(1)}$ of Eq. (2.1) does not vanish between states of the $4f^N$ and $4f^{N-1}5d$ configurations. Once the $4f^N$ and $4f^{N-1}$ 5d eigenstates are obtained it is straightforward to calculate the matrix elements of this operator. However, a detailed treatment of the vibronic part is more difficult. The spectra (van Pieterson et al., 2002c) indicate that progressions involving more than one vibration are present in the bands. A detailed calculation of the band shapes has not yet been attempted and we have made use of a simple Gaussian to model the bands (Reid et al., 2000; van Pieterson et al., 2002c, a).

Sharp zero-phonon lines, and identifiable vibronic structure, are usually only observed for states in which the 5d electron is in the lowest crystal-field state. For higher energy states photoionization into the conduction band broadens the lines and only a broad band is observed. In a few cases sharp features have been observed at much higher energies (van Pieterson et al., 2002b). In these cases the $4f^{N-1}$ core has a high energy arrangement but the 5d electron is still in the lowest crystal-field state, and so fast photoionization is not possible.

Since the spectra consist largely of broad vibronic bands detailed comparisons between theory and experiment for $4f^N \leftrightarrow 4f^{N-1}$ 5d transitions are more difficult than for transitions within the $4f^N$ configuration. Since there are a very large number of states, and broad bands, it is not generally possible to compare the spectra with calculations line by line. Instead, comparison of experimental and simulated spectra is necessary. Unfortunately, few experiments have been carried out with polarized light, so the information that might be obtained from polarization selection rules is generally not available.

2.4.2 Charge Transfer

Charge-transfer bands are often observed in rare-earth materials. These bands are associated with excitations of a ligand electron into a 4f orbital. For some ions, especially Eu^{3+}, the charge transfer bands in many host crystals lie at lower energy than the $4f^{N-1}5d$ states (van Pieterson et al., 2002c). This is, of course, relevant to our discussion in Section 2.3.8.3 on covalent effects, i.e., mixing of the $4f^N$ configuration with charge transfer states. Extensive measurements of charge-transfer absorption and emission have been carried out by van Pieterson et al. (2000). For these transitions the vibronic coupling in the excited states is

very large and the transitions are completely dominated by vibronics. The excited state has one more 4f electron and a hole in the ligand orbitals. While it should be possible to formulate a phenomenological model analogous to the other models discussed in this chapter detailed modeling does not appear to have been attempted.

2.5 Two-photon Processes

As well as one-photon transitions, two-photon processes including two-photon absorption, Raman scattering, and second-harmonic generation are possible. A review may be found in Downer (1989) and more recent references in Nguyen (1997) and Görller-Walrand and Binnemans (1998).

For two-photon processes, the expression analogous to the matrix elements of the electric dipole moment operator (see Eq. (2.1)) is

$$-e^2\left(\sum_k \frac{\langle f \mid D^{(1)}_{q_2} \mid k\rangle\langle k \mid D^{(1)}_{q_1} \mid i\rangle}{E_i - E_k + \hbar\omega_1} + \sum_k \frac{\langle f \mid D^{(1)}_{q_1} \mid k\rangle\langle k \mid D^{(1)}_{q_2} \mid i\rangle}{E_i - E_k + \hbar\omega_2}\right), \tag{2.44}$$

where q_1 and q_2 and $\hbar\omega_1$, $\hbar\omega_2$ are the polarizations and energies of the two photons. For this formula to be applied to Raman scattering a minus sign must be associated with the $\hbar\omega$ of the outgoing photon. The summation runs over all possible intermediate states (including $4f^N$), so resonance effects are possible (Huang et al., 1989). The transition rate is proportional to the square of Eq. (2.44).

It is important to note that the states and denominators in Eq. (2.44) are exact and the denominators arise from the time-dependent perturbation theory derivation of Fermi's golden rule. To derive an effective operator (time-independent) perturbation theory must be used to expand both the states and the denominators. For a discussion of these issues see Bryson and Reid (1998), Duan and Reid (2002).

2.5.1 $f^N \leftrightarrow f^N$ Transitions

A phenomenology based on Eq. (2.44) may be developed in much the same way as the analysis of one-photon crystal-field assisted transitions (Axe, 1963; Downer, 1989; Nguyen, 1997). The analogous equation to Eq. (2.25) or Eq. (2.28) is

$$D_{\text{TPA, effective}} = \sum_{\lambda=0,1,2} F_\lambda (-1)^\lambda U^{(\lambda)} \cdot (e^{(2)} e^{(1)})^{(\lambda)}. \tag{2.45}$$

In this expression the e are the polarization vectors for the electric fields of the photons. The F_λ may be treated as phenomenological parameters, or calculated as a function of radial integrals and other factors (Axe, 1963; Downer, 1989; Nguyen, 1997). A detailed discussion of polarization effects in multiphoton processes from a more general point of view may be found in Stedman(1985, 1990).

The intensities of different polarizations are calculated by expanding the coupled product of polarization vectors and transforming to a cartesian basis. In a cartesian basis the $\lambda = 0$ term contains the totally symmetric function $x_2x_1 + y_2y_1 + z_2z_1$, the $\lambda = 1$ term contains functions antisymmetric in the polarization vectors, such as $x_2y_1 - y_2x_1$, and the $\lambda = 2$ term contains functions symmetric in the polarization vectors, such as $x_2y_1 + y_2x_1$.

The $\lambda = 0$ term can only contribute to Rayleigh scattering. This is because this operator cannot change the electronic state.

Since the $\lambda = 1$ term involves antisymmetric functions it cannot contribute to two-photon absorption with identical photons. Therefore, for a single-beam experiment, only the $\lambda = 2$ parameter is non-zero, and at this lowest order of perturbation, where any mixing of the states via the potential, V, is omitted, there are no free parameters in a calculation of relative intensities (Axe, 1964). Dagenais et al. (1981) found that this model gave a very poor reproduction of experimental data for Gd^{3+}. Judd and Pooler (1982) were able to explain the measurements by extending the model to include spin-orbit interactions in the excited states. Subsequent work by Downer and co-workers also included crystal-field effects in the excited states (Downer, 1989). These higher-order contributions are important in Gd^{3+} because the lowest order contributions are so small for this ion. The influence of electron correlation effects has been discussed by Smentek (1998) and by Burdick and Reid (1993), Burdick et al. (1993). In their study of Eu^{2+} Burdick et al. (1993) found that a perturbation expansion failed to converge, since the $4f^6 5d$ configuration substantially overlaps the $4f^7$ configuration, and it was necessary to include the $4f^6 5d$ configuration as part of the model space. More complete calculations, based on the work on the $4f^6 5d$ configuration described in Section 2.4.1 are now being carried out (Duan et al., 2002; Burdick et al., 2003a).

Some two-photon experiments have concentrated on the variation in intensity as the polarization of the incoming light is rotated. These variations are more complex than in the case of one-photon absorption. In some cases the variations fit the model very well (Gâcon et al., 1993). However, some experiments are not well explained by the theory (Murdoch et al., 1997).

Raman scattering is also an interesting test of the formalism. In this case the very different denominators in the two terms of Eq. (2.44) allow effective operators with $\lambda = 1$ (time-reversal and Hermiticity arguments do not rule out $\lambda = 1$ operators, since, in contrast with Eq. (2.24) the denominators are not identical), in addition to the $\lambda = 2$ operators allowed in single-beam two-photon absorption. This leads to interesting polarization effects due to the interference between $\lambda = 1$ and $\lambda = 2$ terms. In some cases the theoretical predictions explain

the experimental results (Nguyen et al., 1997), whereas in other cases there are difficulties rationalizing the experimental ratios of the $\lambda = 1$ and $\lambda = 2$ parameters with calculations (Becker et al., 1985).

2.5.2 $4f^N \leftrightarrow 4f^{N-1}5d$ Transitions

Two-photon transitions from the $4f^N$ configuration to the $4f^{N-1}5d$ states are parity forbidden, and, like one-photon electric dipole transitions between $4f^N$ states, require an odd-parity crystal field. The principle is similar to the one-photon $4f^N$ transitions discussed in Section 2. 3. 2 (Gayen and Bartram, 1986; Leavitt, 1987; Sztucki and Strek, 1990; Daoud and Kibler, 1992).

2.6 Conclusions

Though the parametrization of crystal-field energy levels (Chapter 1) is well developed, the parametrization of transition intensities between these energy levels is still a difficult problem. Nevertheless, it is becoming possible to not only carry out detailed parametrizations but also explain the results in terms of *ab initio* calculations.

While two-photon processes have limited practical applications, they have provided some of the more stringent tests of the assumptions underlying the one-photon calculations. In fact, it was in the two-photon case that high-order expansions were first developed.

Transitions outside of the $4f^N$ configuration, such as $4f^N \leftrightarrow 4f^{N-1}\,5d$ transitions and charge-transfer transitions, are parity allowed. In those cases there are challenges in (1) calculating the excited eigenstates, and (2) treating the vibronic effects realistically. For the case of $4f^N \leftrightarrow 4f^{N-1}\,5d$ transitions quite satisfactory calculations can now be made.

References

Acevedo, R., G. Diaz, J. R. Letelier, and C. D. Flint. Mol. Phys. **71**, 1063 (1990).
Altmann, S. L., P. Herzig. *Point-group theory tables* (Clarendon Press, Oxford, 1994).
Axe, J. D. J. Chem. Phys. **39**, 1154 (1963).
Axe, J. D. Phys. Rev. A **136**, 42 (1964).
Becker, P. C., N. Edelstein, G. M. Williams, J. J. Bucher, R. E. Russo, J. A. Koningstein, L. A. Boatner, and M. M. Abraham. Phys. Rev. B **31**, 8102 (1985).
Berry, M. T., C. Schweiters, and F. S. Richardson. Chem. Phys. **122**, 105 (1988).
Brandow, B. H. Rev. Mod. Phys. **39**, 771 (1967).
Bryson, A. R., M. F. Reid. J. Alloys Comp., **275 – 277**, 284 (1998).
Burdick, G. W., A. Burdick, C. K. Duan, M. F. Reid (2003a). In Preparation.
Burdick, G. W., S. M. Crooks, M. F. Reid. Phys. Rev. B **59**, 7789 (1999).
Burdick, G. W., M. C. Downer, D. K. Sardar. J. Chem. Phys. **91**, 1511 (1989).
Burdick, G. W., C. K. Jayasankar, F. S. Richardson, M. F. Reid. Phys. Rev. B **50**, 16,

309 (1994).
Burdick, G. W., H. J. Kooy, M. F. Reid. J. Phys.: Condens. Matter **5**, L323 (1993).
Burdick, G. W., E. S. LaBianca, D. L. Binus. J. Alloys Comp. **344**, 327 (2002).
Burdick, G. W., M. F. Reid. Phys. Rev. Lett. **70**, 2491 (1993).
Burdick, G. W., F. S. Richardson, M. F. Reid, and H. J. Kooy. J. Alloys Comp. **225**, 115 (1995).
Burdick, G. W., R. L. Summerscales, S. M. Crooks, M. F. Reid, F. S. Richardson. J. Alloys Compounds **303 – 305**, 376 (2000).
Burdick, G. W., Y. Yim, and E. S. LaBianca. Mol. Phys. **101**: 909(2003).
Butler, P. H. *Point Group Symmetry Applications* (Plenum Press, 1981).
Chan, D. K. T., M. F. Reid. J. Less Common Metals **148**, 207 (1989).
Crooks, S. M., M. F. Reid, and G. W. Burdick. J. Alloys Compounds **303 – 305**, 383 (2000).
Crooks, S. M., M. F. Reid, P. A. Tanner, and Y. Y. Zhao. J. Alloys Comp. (1997). In Press.
Dagenais, M., M. Downer, R. Neumann, and N. Bloembergen. Phys. Rev. Lett. **46**, 561 (1981).
Dallara, J. J., M. F. Reid, and F. S. Richardson. J. Phys. Chem. **88**, 3587 (1984).
Daoud, M., M. Kibler. Laser Phys. **2**, 704 (1992).
Dorenbos, P. J. Luminescence **91**, 155 (2000).
Downer, M. C. In: *Laser Spectroscopy of Solids II* ed. W. M. Yen (Springer-Verlag, Berlin, 1989), pp. 29 – 75.
Duan, C. K., M. F. Reid. J. Alloys. Comp. **344**, 272 (2002).
Duan, C. K., M. F. Reid, G. W. Burdick. Phys. Rev. B **66**, 155, 108 (2002).
Duan, C. K., M. F. Reid. J. Alloys Comp. **323 – 324**, 726 (2001).
Eyal, M., E. Greenberg, R. Reisfeld, and N. Spector. Chem. Phys. Lett. **117** 108 (1985).
Faulker, T. R., F. S. Richardson. Mol. Phys. **35**, 1141 (1977).
Gâcon, J. C., G. W. Burdick, B. Moine, and H. Bill. Phys. Rev. B **47**, 11, 712 (1993).
Garcia, D., M. Faucher. J. Alloys Comp. **180**, 239 (1992).
Gayen, S. K., D. S. H. and R. H. Bartram. Phys. Rev. B **34**, 7517 (1986).
Görller-Walrand, C., M. Behets, P. Porcher, O. K. Moune-Minn, and I. Laursen. Inorganica Chimica Acta **109**, 83 (1985).
Görller-Walrand, C., K. Binnemans. In: *Handbook on the Physics and Chemistry of the Rare Earths* eds. K. A. Gschneidner, Jr., and L. Eyring (North Holland, Amsterdam, 1998), volume 25, p. 101.
Henderson, B., R. H. Bartram. *Crystal-Field Engineering of Solid-State Laser Materials* (Cambridge University Press, 2000).
Henderson, B., G. F. Imbusch. *Optical Spectroscopy of Inorganic Solids* (Clarendon Press, Oxford, 1989).
Henri, D. E., R. L. Fellows, and G. R. Choppin. Coord. Chem. Rev. **18**, 199 (1976).
Hopkins, T. A., D. H. Metcalf, and F. S. Richardson. Inorg. Chem. **37**, 1401 (1998).
Huang, J., G. K. Liu, and R. L. Cone. Phys. Rev. B **39**, 6348 (1989).
Hüfner, S. *Optical Spectra of Transparent Rare Earth Compounds* (Academic Press, 1978).
Judd, B. R. Phys. Rev. **127**, 750 (1962).
Judd, B. R. J. Chem. Phys. **44**, 839 (1966).
Judd, B. R. J. Chem. Phys **70**, 4830 (1979).
Judd, B. R, D. R. Pooler. J. Phys. C **15**, 591 (1982).
Kaminskii, A. A. *Crystalline lasers: physical processes and operating schemes* (CRC Press, Boca Raton, Florida, 1996).
Kibler, M., J. C. Gâcon. Croatica Chemica Acta **62**, 783 (1989).

Klintenberg, M., S. Edvardsson, and J. O. Thomas. Phys. Rev. B **55**, 10,369 (1997).
Klintenberg, M., J. O. Thomas. Phys. Rev. B **56**, 13,006 (1997).
Koster, G. F., J. O. Dimmock, R. G. Wheeler, and H. Statz. *Properties of the Thiry-two Point Groups* (MIT Press, Cambridge, MA, 1963).
Kotzian, M., T. Fox, and N. Rösch. J. Phys. Chem. **99**, 600 (1995).
Krupke, W. F. Phys. Rev. **145**, 325 (1966).
Krupke, W. F. IEEE J. Quantum Electron. QE**7**, 153 (1971).
Laroche, M., J.-L. Doualan, S. Girard, J. Margerie, and R. Moncorgé. J. Opt. Soc. Am. B **17**, 1291 (2000).
Leavitt, R. C. Phys. Rev. B **35**, 9271 (1987).
Liu, G. K., V. V. Zhorin, S. T. Li, and J. V. Beitz. J. Chem. Phys. **112**, 373 (2000).
Mason, S. F., R. D. Peacock, and B. Stewart. Chem. Phys. Lett. **29**, 149 (1974).
May, P. S., M. F. Reid, and F. S. Richardson. Mol. Phys. **62**, 341 (1987a).
May, P. S., M. F. Reid, and F. S. Richardson. Mol. Phys. **61**, 1471 (1987b).
Murdoch, K. M., A. D. Nguyen, and J. C. Gâcon. Phys. Rev. B **56**, 3038 (1997).
Newman, D. J. Adv. Phys. **20**, 197 (1971).
Newman, D. J., G. Balasubramanian. J. Phys. C: Solid State Phys. **8**, 37 (1975) (In this paper the sense of σ and π polarization is reversed from the convention used in Chapter 10).
Newman, D. J., B. Ng. J. Phys.: Condens. Matter **1**, 1613 (1989a).
Newman, D. J., B. Ng. Rep. Prog. Phys. **52**, 699 (1989b).
Newman, D. J., B. K. C. Ng. *Crystal Field Handbook* (Cambridge University Press, Cambridge, 2000).
Ng, B., D. J. Newman. J. Chem. Phys. **87**, 7110 (1987).
Nguyen, A. D. Phys. Rev. B **55**, 5786 (1997).
Nguyen, A. D., K. Murdoch, N. Edelstein, L. A. Boatner, and M. M. Abraham. Phys. Rev. B **56**, 7974 (1997).
Ofelt, G. S. J. Chem. Phys. **37**, 511 (1962).
Peacock, R. D. Struct. Bonding **22**, 83 (1975).
Piepho, S. B., P. N. Schatz. *Group Theory in Spectroscopy, with Applications to Magnetic Circular Dichroism* (Wiley, New York, 1983).
Poon, Y. M, D. J. Newman. J. Phys. C: Solid State Phys. **17**, 4319 (1984).
Porcher, P., P. Caro. J. Chem. Phys. **68**, 4176 (1978a).
Porcher, P., P. Caro. J. Chem. Phys. **68**, 4183 (1978b).
Porcher, P., P. Caro. J. Chem. Phys. **65**, 89 (1976).
Reid, M. F., L. van Pieterson, and A. Meijerink. J. Alloys. Comp. **344**, 240 (2002).
Reid, M. F., L. van Pieterson, R. T. Wegh, and A. Meijerink. Phys. Rev. B **62**, 14,744 (2000).
Reid, M. F. In: Crystal Field Handbook ed., D. J. Newman, B. Ng (Cambridge University Press, 2000), chapter 10, pp. 193 – 230.
Reid, M. F. J. Alloys Comp. **193**, 160 (1993).
Reid, M. F., B. Ng. Mol. Phys. **67**, 407 (1989).
Reid, M. F. J. Chem. Phys. **87**, 6388 (1987).
Reid, M. F., F. S. Richardson. J. Luminescence **31/32**, 207 (1984a).
Reid, M. F., F. S. Richardson. J. Phys. Chem. **88**, 3579 (1984b).
Reid, M. F., F. S. Richardson. Mol. Phys. **51**, 1077 (1984c).
Reid, M. F., J. J. Dallara, F. S. Richardson. J. Chem. Phys. **79**, 5743 (1983).
Reid, M. F., F. S. Richardson. Chem. Phys. Lett. **95**, 501 (1983).
Ryan, J. R., R. Beach. J. Opt. Soc. Am. B **9**, 1883 (1992).
Satten, R. A., C. L. Schreiber, and E. Y. Wong. J. Chem. Phys. **78**, 79 (1983).

Shionoya, S., W. M. Yen, *Phosphor Handbook* (CRC Press, Boca Raton, 1999).
Smentek, L. Phys. Rep. **297**, 155 (1998).
Stedman, G. E. Adv. Phys **34**, 513 (1985).
Stedman, G. E. *Diagram Techniques in Group Theory* (Cambridge University Press, Cambridge, 1990).
Sztucki, J., W. Strek. Chem. Phys. **143**, 347 (1990).
Tanner, P. A., G. G. Siu. Mol. Phys. **75**, 233 (1992).
van Pieterson, L., M. F. Reid, G. W. Burdick, and A. Meijerink. Phys. Rev. B **65**, 045, 114 (2002a).
van Pieterson, L., M. F. Reid, and A. Meijerink. Phys. Rev. Lett. **88**, 067,405 (2002b).
van Pieterson, L., M. F. Reid, R. T. Wegh, S. Soverna, and A. Meijerink. Phys. Rev. B **65**, 045,113 (2002c).
van Pieterson, L., R. T. Wegh, A. Meijerink, and M. F. Reid. J. Chem. Phys. **115**, 9382 (2001).
van Pieterson, L., M. Heeroma, E. de Heer, and A. Meijerink. J. Lumin **91**, 177 (2000).
Wegh, R. T., H. Donker, K. D. Oskam, and A. Meijerink. Science **283**, 663 (1999).
Wegh, R. T., A. Meijerink. Phys. Rev. B **60**, 10,820 (1999).
Weissbluth, M. *Atoms and Molecules* (Academic Press, New York, 1978).
Wybourne, B. G. J. Chem. Phys. **48**, 2596 (1968).
Wybourne, B. G. *Spectroscopic Properties of Rare Earths* (Wiley-Interscience, New York, 1965).
Xia, S. D., M. F. Reid. J. Phys. Chem. Sol. **54**, 777 (1993).

3 Ion-phonon Interactions

B. Z. Malkin

3.1 Introduction

The main objective of this chapter is to present the basis for the description of the electron-phonon interaction and the effects of this interaction on spectral features and dynamics of excitations in nonmetallic crystals containing impurity lanthanide ions. In the application of fiber amplifiers, laser and scintillator materials activated by lanthanide ions, electron-phonon interaction plays an important role. Many hundreds of papers devoted to different problems in the theory of the electron-phonon interaction and to experimental manifestations of this interaction have been published during the second half of the 20th century. A brief but comprehensive description of the interaction between lanthanide ions and crystal lattice vibrations was presented by Ovsyankin (1987).

This chapter contains mainly physical concepts expressed in the form of mathematical formulae, that are necessary to understand and to interpret experimental data concerning primarily different processes in the ground $4f^n$ electron configuration of the impurity lanthanide ion. It start with the adiabatic Born-Oppenheimer approximation. The Hamiltonian of the ion-phonon interaction is derived in the framework of basic concepts of the crystal field theory reviewed in Chapter 1. Explicit expressions of coupling constants relevant to the exchange charge model of the dynamical crystal field are presented. Experimental methods used to determine coupling constants, and systematic trends in the strength of the ion-lattice interaction over the lanthanide series are considered. A brief review of the quantum theory of relaxation based on the density matrix formalism serves as a background for a derivation of expressions, that determine relaxation rates of electronic excitations and zero-phonon line shifts. Processes of the resonance absorption and emission, of the elastic and nonelastic scattering of phonons on rare earth ions are discussed in connection with the mechanisms of the spectral line shifts and line broadening. The detailed discussion of the one-phonon sidebands in the f – f transitions, of comparative roles of the linear and nonlinear mechanisms of multiphonon transitions is presented. The main attention is paid for the derivation of expressions allowing to compute the electron-phonon interaction effects on the spectral and kinetic properties of activated crystals using the real vibrational spectrum of the host crystal lattice. Some examples of simulations of thermal line shifts, line widths and nonradiative transition rates, based on the realistic models of lattice dynamics

in $LiYF_4$ and $CsCdBr_3$ crystals doped with different rare earth ions, are given. The novel interpretation of the exponential gap law in the phenomenological theory of multiphonon relaxation rates is proposed. The content of the chapter demonstrates the modern state of the art in the theory of dynamical ion-lattice interactions. Not only are experimental data being interpreted, but it is also possible to forecast spectral properties of new promising laser crystals. The thermal broadening and shift of the sharp laser line, the multiphonon relaxation rate have profound significance because their values are closely related to gain, output frequency stability, and thermal tunability of the laser. Some challenging problems mainly connected with proceedings of theoretical analysis of the ion-phonon interaction effects in real systems are emphasized in the conclusion.

3.2 Basic Concepts: Hamiltonian of the Ion-phonon Interaction, Adiabatic and Nonadiabatic Terms

In order to gain some insight into the treatment of the electron-phonon interaction effects, I would like to begin from the Schrodinger equation of the solid. The total crystal Hamiltonian, neglecting spin-dependent terms, is the sum of the electronic (T_e) and nuclear (T_N) kinetic energies, and of the potential (electron-electron, electron-nucleus, nucleus-nucleus) energy $U(\boldsymbol{r}, \boldsymbol{R})$. The symbols $\boldsymbol{r}$ and $\boldsymbol{R}$ will be used to denote the sets of electronic and nuclear coordinates, respectively. Following the Born-Oppenheimer approach (Born and Oppenheimer, 1927), we can expand eigenfunctions of the Schrodinger equation for the electron-nuclear system

$$[T_e + U(\boldsymbol{r}, \boldsymbol{R}) + T_N]\,\Phi(\boldsymbol{r}, \boldsymbol{R}) = E\Phi(\boldsymbol{r}, \boldsymbol{R}). \tag{3.1}$$

in eigenfunctions of the Schrodinger equation of the electronic subsystem:

$$\Phi(\boldsymbol{r}, \boldsymbol{R}) = \sum_{\Gamma} \chi_{\Gamma}(\boldsymbol{R})\,\Psi_{\Gamma,\boldsymbol{R}}(\boldsymbol{r}), \tag{3.2}$$

where the $\Psi_{\Gamma,\boldsymbol{R}}(\boldsymbol{r})$ satisfy the equation

$$[T_e + U(\boldsymbol{r}, \boldsymbol{R})]\,\Psi_{\Gamma,\boldsymbol{R}}(\boldsymbol{r}) = \varepsilon_{\Gamma}(\boldsymbol{R})\,\Psi_{\Gamma,\boldsymbol{R}}(\boldsymbol{r}) \tag{3.3}$$

and the normalization condition

$$\int \Psi^*_{\Gamma,\boldsymbol{R}}(\boldsymbol{r})\,\Psi_{\Gamma'\boldsymbol{R}}(\boldsymbol{r})\,\mathrm{d}\boldsymbol{r} = \delta_{\Gamma\Gamma'}. \tag{3.4}$$

The Eq. (3.2) with the condition Eq. (3.4) is called the adiabatic representation, and the $\varepsilon_{\Gamma}(\boldsymbol{R})$ is the adiabatic potential for the nuclear subsystem.

Inserting Eqs. (3.2) and (3.3) into Eq. (3.1), we obtain coupled equations for the nuclear wavefunctions $\chi_\Gamma(\boldsymbol{R})$

$$[\,T_N + \varepsilon_\Gamma(\boldsymbol{R})\,]\chi_{\Gamma p}(\boldsymbol{R}) = E_{\Gamma p}\chi_{\Gamma p}(\boldsymbol{R}) + \hat{L}(\boldsymbol{R})\chi_{\Gamma p}(\boldsymbol{R}), \tag{3.5}$$

where $E_{\Gamma p}$ is the total energy of the crystal, and

$$\hat{L}(\boldsymbol{R})\chi_{\Gamma p}(\boldsymbol{R}) = \sum_{Ls,\,\Gamma' p'} \frac{\hbar^2}{2m_s} \int d\boldsymbol{r}\Psi^*_{\Gamma,\boldsymbol{R}}(\boldsymbol{r}) \times \left[\Delta_{\boldsymbol{R}_{Ls}}\Psi_{\Gamma',\boldsymbol{R}}(\boldsymbol{r}) + 2\ \nabla_{\boldsymbol{R}_{Ls}}\Psi_{\Gamma',\boldsymbol{R}}(\boldsymbol{r})\ \nabla_{\boldsymbol{R}_{Ls}}\right]\chi_{\Gamma' p'}(\boldsymbol{R}). \tag{3.6}$$

where $\nabla_{\boldsymbol{R}_{Ls}} = \boldsymbol{i}\frac{\partial}{\partial X_{Ls}} + \boldsymbol{j}\frac{\partial}{\partial Y_{Ls}} + \boldsymbol{k}\frac{\partial}{\partial Z_{Ls}}$, $\boldsymbol{i}, \boldsymbol{j}, \boldsymbol{k}$ are the basis vectors in the Cartesian system of coordinates, and $\nabla_{\boldsymbol{R}_{Ls}} = (\nabla_{\boldsymbol{R}_{Ls}})^2$. (the index L is the three-dimensional vector that determines the position of a unit cell in the Bravais sublattice, and the index s of a sublattice determines the position of ions within the cell, m_s is the mass of a nucleus at the site s.) Both $\Psi_{\Gamma,\boldsymbol{R}}(\boldsymbol{r})$ of nuclei at the fixed positions $\boldsymbol{R}$ and $\chi_{\Gamma p}(\boldsymbol{R})$ form complete sets of eigenfunctions (the label $\boldsymbol{p}$ determines different nuclear states in the fixed adiabatic potential). Let us consider now possible simplifications of the exact Eqs. (3.3) and (3.5). The contribution of the operator $\hat{L}(\boldsymbol{R})$ depends on the relation between velocities of electrons and nuclei. Taking into account the difference between electron (m_e) and nucleus (m_s) masses, and the corresponding difference between their velocities, we can neglect the terms Eq. (3.6) and consider the stationary electronic state $\Psi_{\Gamma,\boldsymbol{R}}(\boldsymbol{r})$ with the energy $\varepsilon_\Gamma(\boldsymbol{R})$ parametrically depending on the nuclear positions $\boldsymbol{R}$. The nuclear wave function in turn depends not on the electronic positions, but only on the electronic energy that plays a role of the effective potential in the Eq. (3.5). In this case, the total wave function is separated into electronic and nuclear factors:

$$\Phi_{\Gamma p}(\boldsymbol{r}, \boldsymbol{R}) = \Psi_{\Gamma,\boldsymbol{R}}(\boldsymbol{r})\chi_{\Gamma p}(\boldsymbol{R}), \tag{3.7}$$

the movement of nuclei does not induce transitions between different states of the electronic subsystem, electrons adiabatically follow after nuclei.

This zero adiabatic approximation cannot be used when we deal with degenerate (or quasi-degenerate) electronic states. If frequencies of electronic transitions $\omega_{\Gamma\Gamma'} = (\varepsilon_\Gamma - \varepsilon_{\Gamma'})/\hbar$ are comparable with frequencies of nuclear vibrations, the linear combinations Eq. (3.2) are to be considered as the wave functions of the electron-nuclear system. Considering the terms of Eq. (3.6) as a perturbation, we can include the diagonal matrix elements $L_{\Gamma\Gamma}$ into the effective adiabatic potential $\varepsilon_\Gamma(\boldsymbol{R})$ of the nuclear subsystem. The nondiagonal elements

$L_{\Gamma\Gamma'}(\Gamma \neq \Gamma')$ that are called as nonadiabaticity operators describe the coupling between different electronic states, they cause mixing of electronic wave functions Ψ_Γ and $\Psi_{\Gamma'}$.

Let us suppose that the adiabatic potential ε_Γ has a minimum at $\boldsymbol{R}_{0\Gamma}$ representing equilibrium nuclear positions for the electronic state Γ, and expand the adiabatic electronic energy $\varepsilon_\Gamma(\boldsymbol{R}_{0\Gamma} + \boldsymbol{u})$ in a Taylor series in dynamical nuclear displacements $\boldsymbol{u}$:

$$\varepsilon_\Gamma(\boldsymbol{R}) = \varepsilon_\Gamma(\boldsymbol{R}_{0\Gamma}) + \frac{1}{2}\boldsymbol{u}\,\nabla_{\boldsymbol{R}}\,\nabla_{\boldsymbol{R}}\varepsilon_\Gamma(\boldsymbol{R})\mid_{\boldsymbol{R}=\boldsymbol{R}_{0\Gamma}}\boldsymbol{u} + \cdots. \tag{3.8}$$

In the harmonic approximation, saving in Eq. (3.8) terms of the second order in nuclear displacements, we can transform the nuclear Eq. (3.5) into a set of harmonic oscillator equations relative lattice normal cordinates q_f. The frequencies $\omega_f^{(\Gamma)}$ of the lattice normal coordinates are determined by second derivatives $\partial^2\varepsilon_\Gamma/\partial q_f^2$, and the differences between their equilibrium positions $q_{\Gamma' f} - q_{\Gamma f}$ for different electronic states are determined by (we use the Hellmann-Feynman theorem) (Hellmann, 1937; Feynman, 1939; Fowler and Dexter, 1968)

$$\left.\frac{\partial\varepsilon_{\Gamma'}(\boldsymbol{R})}{\partial q_f}\right|_{\boldsymbol{R}=\boldsymbol{R}_{0\Gamma}} = \left\langle \Psi_{\Gamma',\boldsymbol{R}_{0\Gamma}}(\boldsymbol{r}) \mid \partial U(\boldsymbol{r},\boldsymbol{R})/\partial q_f \mid_{\boldsymbol{R}=\boldsymbol{R}_{0\Gamma}} \mid \Psi_{\Gamma',\boldsymbol{R}_{0\Gamma}}(\boldsymbol{r}) \right\rangle. \tag{3.9}$$

Thus, we can develop the potential U in the electronic Eq. (3.3) in a power series in nuclear displacements relative to their equilibrium positions $\boldsymbol{R}_{0\Gamma}$

$$U(\boldsymbol{r},\boldsymbol{R}) = U(\boldsymbol{r},\boldsymbol{R}_{0\Gamma}) + (\boldsymbol{R} - \boldsymbol{R}_{0\Gamma})\ \nabla_{\boldsymbol{R}}U(\boldsymbol{r},\boldsymbol{R})\mid_{\boldsymbol{R}=\boldsymbol{R}_{0\Gamma}} + \cdots, \tag{3.10}$$

and the average value of the linear term in Eq. (3.10) in the electronic state $\Psi_{\Gamma',\boldsymbol{R}_{0\Gamma}}(\boldsymbol{r})$ defines the equilibrium positions of lattice oscillators $\boldsymbol{R}_{0\Gamma'}$. The second order terms define the effect of electronic state on frequencies of lattice oscillators.

We shall confine ourselves to nondegenerate electronic states. However, this restriction does not prevent to use results drawn below in a case of degenerate electronic states if the electron-phonon coupling is weak compared with the lattice excitation energy, so that the Jahn-Teller energy (a shift of the electronic energy due to the electron-phonon interaction) is much less than the maximum energy of lattice vibrations (Koloskova and Kochelaev, 1967). The further simplification is possible if we neglect the dependence of electronic wave functions $\Psi_{\Gamma,\boldsymbol{R}}(\boldsymbol{r})$ on the nuclear movement. Considering the difference $U(\boldsymbol{r},\boldsymbol{R}) - U(\boldsymbol{r},\boldsymbol{R}_0)$ as a perturbation in the electronic Eq. (3.3), and making use of eigenfunctions of the Hamiltonian $H_{\mathrm{el}} = T_{\mathrm{e}} + U(\boldsymbol{r},\boldsymbol{R}_0)$, we obtain the following multiplicative wave

functions of a crystal with a single impurity optical center (in this case vectors $\boldsymbol{R}_0$ can correspond to the equilibrium nuclear positions in the perfect host lattice, the lattice Hamiltonian defined below is considered in the harmonic approximation):

$$\Phi_{\Gamma,n_f}(\boldsymbol{r},\boldsymbol{R}) = \Psi_{\Gamma,\boldsymbol{R}_0}(\boldsymbol{r})\prod_f \chi_{\Gamma,n_f}(q_f - q_{f\Gamma}), \tag{3.11}$$

where $\Psi_{\Gamma,\boldsymbol{R}_0}(\boldsymbol{r})$ are the wave functions of localized electrons, n_f are occupation numbers of lattice oscillators, and χ_{Γ,n_f} is the oscillator wave function. The Eq. (3.11) of a wave function of the electron-nuclear system corresponds to the crude adiabatic approximation. The lattice wave functions depend on the electronic state through the first order correction to the electronic energy in Eq. (3.5),

$$\varepsilon_\Gamma(\boldsymbol{R}) = \varepsilon_\Gamma(\boldsymbol{R}_0) + \int \Psi^*_{\Gamma,\boldsymbol{R}_0}(\boldsymbol{r})[U(\boldsymbol{r},\boldsymbol{R}) - U(\boldsymbol{r},\boldsymbol{R}_0)]\Psi_{\Gamma,\boldsymbol{R}_0}(\boldsymbol{r})\,\mathrm{d}\boldsymbol{r},$$

that is included into the zeroth -order lattice Hamiltonian $H_{\mathrm{ph}} = \sum_\Gamma |\Gamma\rangle H^\Gamma_{\mathrm{ph}}\langle\Gamma|$ (Basiev et al., 1997), where

$$\begin{aligned} H^\Gamma_{\mathrm{ph}} &= \langle\Gamma|\, T_N + U(\boldsymbol{r},\boldsymbol{R}) - U(\boldsymbol{r},\boldsymbol{R}_0)\,|\,\Gamma\rangle \\ &= \langle\Gamma|\, U(\boldsymbol{r},\boldsymbol{R}_{0\Gamma}) - U(\boldsymbol{r},\boldsymbol{R}_0)\,|\,\Gamma\rangle + \sum_f \hbar\,\omega_f^{(\Gamma)}\left(n_f + \frac{1}{2}\right). \end{aligned} \tag{3.12}$$

Normal modes of a perfect lattice in the framework of the harmonic approximation are characterized by the wave vector $\boldsymbol{q}$ and the number j of the branch of the lattice vibrational spectrum, $\{f\} \equiv \{\boldsymbol{q}j\}$. Let us expand dynamical ion displacements in terms of dimensionless lattice normal modes $q_f - q_{f\Gamma} = (a_{\boldsymbol{q}j} + a^+_{-\boldsymbol{q}j})/\sqrt{2}$:

$$u_\alpha(Ls) = \frac{1}{\sqrt{Nm_s}}\sum_{j\boldsymbol{q}}\left[\frac{\hbar}{2\omega_j(\boldsymbol{q})}\right]^{1/2} e_\alpha(\boldsymbol{q}j\,|\,s)\exp(\mathrm{i}\boldsymbol{q}\boldsymbol{R}_{Ls})(a_{\boldsymbol{q}j} + a^+_{-\boldsymbol{q}j}). \tag{3.13}$$

Here N is the number of unit cells in a crystal lattice, vectors $\boldsymbol{R}_{Ls}$ with the coordinates $X_{Ls\alpha}$ define equilibrium positions of ions in the lattice, $\boldsymbol{e}(\boldsymbol{q}j|s)$ is the polarization vector, $\omega_j(\boldsymbol{q})$ is the frequency of a phonon (the dependence of polarization vectors and frequencies on the electronic state Γ is neglected here and below), $a_{\boldsymbol{q}j}$ and $a^+_{\boldsymbol{q}j}$ are the phonon annihilation and creation operators. The polarization vectors are solutions of the $3r$-dimensional dynamic equation of the lattice, that gives $3r$ branches of the frequency spectrum (r is the number of ions in the unit cell) ($s = 1, \cdots, r$).

As we shall see below, evolution of excitations in the coupled electron-

phonon system may be described in terms of time dependent correlation functions. Correlation functions for dynamical ion displacements can be written as

$$\langle u_\alpha(Ls,t)\,u_\beta(L's',0)\rangle = \frac{\hbar}{\pi}\int_0^\infty \mathrm{Im}G^0_{\alpha\beta}(Ls,L's'\mid\omega) \times[\mathrm{e}^{-\mathrm{i}\omega t}(n(\omega)+1)+\mathrm{e}^{\mathrm{i}\omega t}n(\omega)]\,\mathrm{d}\omega, \quad (3.14)$$

where

$$G^0_{\alpha\beta}(Ls,L's'\mid\omega) = \frac{1}{N\sqrt{m_s m_{s'}}}\sum_{jq}\frac{e_\alpha(qj\mid s)e_\beta(qj\mid s')^*}{\omega^2-\omega_j(q)^2-\mathrm{i}\varepsilon} \times\exp[\mathrm{i}q(R_{Ls}-R_{L's'})] \quad (3.15)$$

is the advanced Green's function with poles in the upper half plane ($\varepsilon\to 0^+$) of the complex variable ω (Bottger, 1983). The imaginary part of the Green's function

$$\mathrm{Im}\,G^0_{\alpha\beta}(Ls,L's'\mid\omega) = \frac{\pi}{N\sqrt{m_s m_{s'}}}\sum_{qj}e_\alpha(qj\mid s)e_\beta(qj\mid s')^* \times\exp[\mathrm{i}q(R_{Ls}-R_{L's'})]\,\delta(\omega^2-\omega_j(q)^2) \quad (3.16)$$

presents a spectral density of ion displacements, it satisfies the normalization constraint

$$\frac{\sqrt{m_s m_{s'}}}{\pi}\int \mathrm{Im}\,G^0_{\alpha\beta}(Ls,L's'\mid\omega)\,\mathrm{d}\omega^2 = \delta_{\alpha\beta}\delta_{ss'}\delta_{LL'}. \quad (3.17)$$

The Green's function matrix G for the locally perturbed crystal can be put down through the Green's function G^0 of the perfect crystal. When considering crystals activated by rare earth ions, we are interested only in local dynamical properties of the lattice perturbed due to a substitution of an impurity ion for the host lattice ion. In this case,

$$G(\omega) = [1-G^0(\omega)V(\omega)]^{-1}G^0(\omega), \quad (3.18)$$

where the perturbation V is determined by changes of the ion mass and of the force constants equal to derivatives of the crystal potential energy relative to ion coordinates $\Phi_{\alpha\beta}(Ls,L's')=\partial^2\varepsilon_T(R)/\partial X_{Ls\alpha}\partial X_{L's'\beta}$. In the site representation, if the impurity ion is at the site $L=0$, $s=0$,

$$V_{\alpha\beta}(Ls,L's') = \Delta\Phi_{\alpha\beta}(Ls,L's') - \Delta m\delta_{Ls,L's'}\delta_{\alpha\beta}\delta_{Ls,00}\omega^2, \quad (3.19)$$

where Δm is the difference between the impurity and host ion masses. In the frequency range, where Im G^0 is nonzero, the imaginary part of the Green's function of the perturbed lattice equals

$$\text{Im } \boldsymbol{G}(\omega) = \boldsymbol{F}(\omega)\,\text{Im } \boldsymbol{G}^0(\omega) + \boldsymbol{D}^{-1}(\omega)\,\text{Im } \boldsymbol{G}^0(\omega)\,\boldsymbol{V}(\omega)\,\boldsymbol{F}(\omega)\,\text{Re}\boldsymbol{G}^0(\omega), \tag{3.20}$$

where $\boldsymbol{F}(\omega) = \boldsymbol{D}(\omega) + \text{Im } \boldsymbol{G}^0(\omega)\,\boldsymbol{V}(\omega)\,\boldsymbol{D}^{-1}(\omega)\,\text{Im } \boldsymbol{G}^0(\omega)\,\boldsymbol{V}(\omega)$, and

$$\boldsymbol{D}(\omega) = 1 - \text{Re } \boldsymbol{G}^0(\omega)\,\boldsymbol{V}(\omega). \tag{3.21}$$

The redistribution of the spectral density of lattice vibrations due to a lattice perturbation may suppress essentially the spectral density of a perfect lattice and induce sharp peaks (resonant vibrations) at frequencies satisfying the equation det $\boldsymbol{D}(\omega) = 0$. In the frequency range, where Im $\boldsymbol{G}^0(\omega) = 0$, Im $\boldsymbol{G}(\omega)$ may have singular points at frequencies of local vibrations ω_1, that satisfy the equation

$$\det[\boldsymbol{D}(\omega_1)] = \det[1 - \boldsymbol{G}^0(\omega_1)\,\boldsymbol{V}(\omega_1)] = 0. \tag{3.22}$$

In this case,

$$\text{Im } \boldsymbol{G}(\omega) = \pi \lim_{\omega \to \omega_1} \left(\frac{\boldsymbol{D}(\omega)^{-1}\boldsymbol{G}^0(\omega)}{\dfrac{\mathrm{d}}{\mathrm{d}\omega} \ln [\det \boldsymbol{D}(\omega)]} \right) \delta(\omega - \omega_1), \tag{3.23}$$

and the normalization constraint for the Green's function of the perturbed lattice takes the following form (Malkin et al., 2001):

$$\frac{(m + \Delta m)^{1/2}}{\pi} \left[\int \text{Im } \boldsymbol{G}(\omega)\,\mathrm{d}\omega^2 + 2\pi \sum_l \omega_l \right.$$
$$\left. \times \lim_{\omega \to \omega_1} \left(\frac{\boldsymbol{D}(\omega)^{-1}\boldsymbol{G}^0(\omega)}{\dfrac{\mathrm{d}}{\mathrm{d}\omega} \ln [\det \boldsymbol{D}(\omega)]} \right) \right] (m + \Delta m)^{1/2} = 1, \tag{3.24}$$

where Im $\boldsymbol{G}(\omega)$ is determined in Eq. (3.19). To present results of calculations in the compact form, it is useful to define linear combinations of phonon Green' s functions for differences between displacements of lattice ions and that of the impurity rare-earth ion $\boldsymbol{u}(Ls, 0) = \boldsymbol{u}(Ls) - \boldsymbol{u}(00)$. We shall use below the corresponding spectral densities:

$$g_{\alpha\beta}(Ls, L's' \mid \omega) = \text{Im } [G_{\alpha\beta}(Ls, L's' \mid \omega) - G_{\alpha\beta}(Ls, 00 \mid \omega)$$
$$- G_{\alpha\beta}(00, L's' \mid \omega) + G_{\alpha\beta}(00, 00 \mid \omega)]. \tag{3.25}$$

In the range of low frequencies, where only acoustical branches of the vibrational spectrum contribute to the spectral densities of correlation functions, and the linear dispersion law is approved ($\omega_j(\boldsymbol{q}) = qv_j(\boldsymbol{q}/q)$, $v_j(\boldsymbol{q}/q)$ is the velocity of sound propagation in a crystal), the spectral densities of relative displacements can be approximated by

$$g_{\alpha\beta}(Ls, L's' \mid \omega \to 0) \sim \omega^3. \tag{3.26}$$

After this brief deviation into the field of lattice dynamics, let us return to the consideration of electrons localized at open electronic shells (4f or 5d, in particular) of rare earth ions and interacting with phonons. In accordance with the multiplicative form of Eq. (3.11) of the wave functions, it is possible to introduce the effective Hamiltonian for the electron-lattice system

$$\hat{H} = H_{\text{el}} + H_{\text{ph}} + H_{\text{el-ph}}, \tag{3.27}$$

where H_{el}, H_{ph}, and

$$H_{\text{el-ph}} = \sum_{\Gamma\Gamma'} \mid \Gamma\rangle\langle\Gamma \mid [U(\boldsymbol{r}, \boldsymbol{R}) - U(\boldsymbol{r}, \boldsymbol{R}_0)](1 - \delta_{\Gamma\Gamma'}) \mid \Gamma'\rangle\langle\Gamma' \mid \tag{3.28}$$

stand for the Hamiltonian terms for the electrons localized at the isolated lanthanide dopant ion, for the phonon field, and for the electron-phonon interaction, respectively. The nonadiabaticity operator of Eq. (3.6) in this case, that is usually named as static coupling approximation, vanishes exactly, and time evolution of the non-stationary states Eq. (3.11) is totally determined by the operator of Eq. (3.28). When the dependence of the electronic wave functions on the lattice coordinates is taken into account, the explicit form of the operator that connects different electronic states and leads to a redistribution of the crystal energy between electronic and vibrational subsystems becomes more complicated. Relations between different approaches to this problem have been thoroughly considered by Peuker et al. (1982). The electron-phonon interaction Eq. (3.28) is the time-even operator in the space of electronic variables, additional time-odd terms containing scalar products of the electron momentum and nuclear velocities can be included when taking into account relativistic corrections (Aminov, 1978). These additional terms in the electron-phonon interaction may be of interest when dealing with real or virtual transitions between configurations of opposite parity ($4f^n$ and $4f^{n-1}5d^1$, in particular). Some effects due to the time-odd electron-phonon coupling were considered by Moore and Stedman (1990), Johnsson and Stedman (1999).

The electronic Hamiltonian of a rare earth ion can be presented as follows:

$$H_{el} = H_{FI} + H_{CF}, \tag{3.29}$$

where the first term corresponds to the free ion energy, and the second term defines the energy of localized electrons in the static crystal field (see Chapter 1). Following the Van Vleck model of electron-lattice coupling (Van Vleck, 1940), we single out from the potential energy of the electronic subsystem terms corresponding to the interaction of the electrons on the unfilled shell of the impurity ion with the host ions (actually, we use the second adiabatic approximation considering the electrons on the closed shells of the impurity and host ions as a fast subsystem), and expand these terms in powers of relative displacements of the host and impurity ions $\boldsymbol{u}(Ls, 0)$ relative to their quasi-equilibrium positions $\boldsymbol{R}_0$ in the perfect lattice (under the assumption that $\boldsymbol{u}(Ls)$ are much smaller than distances between ions). The zero-order term in this expansion, averaged over the radial 4f- or 5d-electron wave function, presents the corresponding crystal field Hamiltonian

$$H_{CF} = \sum_{pk} B_k^p C_k^{(p)}, \quad B_k^p = \sum_{Ls} B_k^p(\boldsymbol{R}_{Ls}), \tag{3.30}$$

where $C_k^{(p)} = \left(\frac{4\pi}{2p+1}\right)^{1/2} Y_{pk}(k = -p, -p+1, \cdots, p)$, are spherical electronic operators defined within the manifold of states of the unfilled electron shell, complex crystal field parameters satisfy the conditions Eq. (1.44) (we neglect in Eq. (3.30) two-particle operators that correspond to changes of the intraion electrostatic coupling in the crystal field). When considering a structure of the energy spectrum of a lanthanide ion having the unfilled $4f^n$ shell, we need only even components of the static crystal field ($p = 2, 4, 6$), odd components of the crystal-field mix electronic states of opposite parity (4f – 5d, 5g, $\cdots$) and determine a response of a lanthanide ion on the electric component of the radiation field (see Chapter 2 and Section 3. 6 below). The static lattice deformation due to the substitution of the rare earth ion for the host ion can be taken into account in simulations of the crystal field parameters when the functions $B_k^p(\boldsymbol{R}_{Ls})$ are determined explicitly.

The Hamiltonian of the electron-phonon interaction can be written as a power series in dynamical displacements of ions from their equilibrium positions in the lattice:

$$H_{el\text{-}ph} = \sum_{\alpha, Ls} V_\alpha(Ls)\, u_\alpha(Ls, 0) + \frac{1}{2}\sum_{\alpha\beta, Ls} V_{\alpha\beta}(Ls)\, u_\alpha(Ls, 0)\, u_\beta(Ls, 0) + \cdots$$
$$+ \frac{1}{n!}\sum_{\alpha_1 \cdots \alpha_n, Ls} V_{\alpha_1 \cdots \alpha_n}(Ls)\, u_{\alpha_1}(Ls, 0) \cdots u_{\alpha_n}(Ls, 0) + \cdots \tag{3.31}$$

where

$$V_\alpha(Ls) = \sum_{pk} B^p_{k,\alpha}(Ls)\, C^{(p)}_k, \quad V_{\alpha\beta}(Ls) = \sum_{pk} B^p_{k,\alpha\beta}(Ls)\, C^{(p)}_k, \cdots \quad (3.32)$$

are the electronic operators, and $B^p_{k,\alpha}(Ls)$, $B^p_{k,\alpha\beta}(Ls)\cdots$ are the coupling constants (Cartesian components of vectors are labeled by Greek indices). In accordance with the definition Eq. (3.28), we have to consider only nonadiabatic (nondiagonal in respect the electronic states) terms in Eq. (3.31) that mix different electronic states.

3.3 Coupling Constants

In the Eq. (3.32), constants of the electron-phonon interaction $B^p_{k,\alpha\beta\cdots\gamma(Ls)}$ are the derivatives of the crystal-field parameters in respect to relative coordinates $X_{Ls\alpha}$ of the host lattice ion in the site Ls and the lanthanide ion. Up to the moment, the developement of theoretical models to determine these constants presents one of most challenging problems. We shall restrict ourselves here by an examining of modulated crystal field energy, but it should be mentioned that modulation of intraion interactions by lattice vibrations can also contribute to the electron-phonon interaction due to the nephelauxetic effect (reduction of the free ion electrostatic parameters and the spin-orbit interaction constant in solids). Direct information about coupling constants can be obtained from piezospectroscopic experiments by measuring shifts of the impurity ion energy levels as functions of displacements of the host lattice ions under the external pressure. It should be noted that differences between bulk and local elastic constants are to be taken into account (Ivanenko and Malkin, 1969; Tovar et al., 1983) when analysing results of piezospectroscopic measurements. Holzapfel and his coworkers have fulfilled a series of hydrostatic high-pressure studies of the optical spectra of crystals containing lanthanide ions: MFCl: Sm^{2+} (M = Ba, Sr, Ca), LaOCl: Eu^{3+} (Shen and Holzapfel, 1995), $PrCl_3$ (Gregorian et al., 1989), $LaCl_3$: Pr^{3+}, $LaCl_3$: Nd^{3+} (Troster et al., 1993), PrOCl (Bungenstock et al., 2000). The measured relative changes of Slater integrals and of the spin-orbit constant of an order of -0.1% per GPa correspond to absolute shifts of the multiplet centres of gravity comparable with shifts of the crystal field sublevels induced by changes of the crystal field parameters with relative variations of $1\% - 3\%$ per GPa. Some indications on the essential role of the long-range electrostatic contributions to crystal field parameters and coupling constants were obtained from the analysis of the crystal field parameters under high pressure in terms of the superposition model (SM) (Newman, 1978, see Chapter 1) using structural data from the X ray diffraction. Bungenstock et al. (2000) marked that to resolve certain deviations between experimental data and concepts of the SM, modifications of the SM, possibly related to long-range electrostatic or ligand-ligand interactions,

are required. Shen et al. (1997) obtained the shift of $-13/(\text{kbar} \cdot \text{cm})$ (1 bar = 100 kPa) in the Sm^{2+} $4f^5 5d^1$ configuration in SrFCl under hydrostatic pressure. This shift is much larger than in the $4f^n$ states and clearly shows a stronger coupling of the 5d state with a lattice. Effect of high hydrostatic pressure on the Slater parameters, the spin-orbit coupling constant and the crystal-field strength was studied for Eu^{3+} in Gd_2O_2S (Yuanbin et al., 1998), GdOBr (Yuanbin et al., 1997), YOCl (Yuanbin et al., 2001). The Slater parameters and the spin-orbit interaction decrease by less than 0.05% per GPa due to increasing covalency and the corresponding expansion of the 4f shell. Absolute values of different crystal field parameters change with pressure in different directions, and the value of the crystal-field strength parameter S (see Chapter 1, Eq. (1.43)), that is an invariant under arbitrary rotations of the crystal lattice, was found to increase (Ln_2O_2S, YOCl) or decrease (LnOBr, LaOCl) in the range -0.45% to $+0.74\%$ per GPa. Relative changes of the electrostatic Slater parameters are about an order of magnitude smaller than relative changes of the crystal field parameters, but absolute values of contributions from both effects to the effective linear coupling constants may be of comparable magnitude (typical values of matrix elements of operators $V_\alpha(Ls)$ in the space of $|4f^n JJ_z\rangle$ states are in the range $10-100/(\text{Å} \cdot \text{cm})$). However, no detailed studies of the electron-phonon interaction due to modulations of the inter-electron electrostatic coupling have been presented in the literature.

To calculate the electron-phonon coupling constants $B^p_{k,\alpha\beta\cdots\gamma}(Ls)$, we need to know the explicit dependence of the crystal field parameters on coordinates of the host lattice ions relative to the impurity lathanide ion. Different crystal field models based on the assumption of additive interactions between the localized 4f (5d) electrons and the lattice ions were considered in Chapter 1. In the framework of the electrostatic model of the point electric multipoles localized at the host lattice sites (in this case the infinite lattice sums can be evaluated with the Ewald method (Born and Huang, 1954)), a number of fitting parameters is not large (effective ion charges and polarizabilities), but very important terms corresponding to non-Coulomb interactions with ligand ions are ignored. On the contrary, in the framework of a quasimolecular center containing the lanthanide ion and its nearest neighbors only (in particular, in the earlier variant of the Superposition Model (Newman, 1971)), the role of the long-range Coulomb interaction was underestimated.

The exchange charge model (see Chapter 1, Section 1.5.4.2) was derived with the main goal to describe electron-phonon interaction effects without introducing any additional fitting parameters, other than those that are necessary to interprete the crystal field splittings in the optical spectra of paramagnetic ions (Malkin et al., 1970). Let us consider here the Hamiltonian of electron-phonon interaction operating within the manifold of 4f-states in the framework of the exchange charge model. According to Eqs. (1.51) and (1.56), contributions to

the crystal field parameters Eq. (3.30) related to the electrostatic field of the point charge eq_s of the lattice ion with spherical coordinates R_{Ls}, θ_{Ls}, φ_{Ls} (the origin of coordinates is at the lanthanide ion), and to the field of the exchange charge that approximates a redistribution of the electronic density of this ion (having the outer filled $n''s^2$ and $n''p^6$ electron shells) due to overlap and covalency effects equal

$$B_k^p(\boldsymbol{R}_{Ls}) = e^2\left[-q_s(1-\sigma_p)\langle 4f|\, r^p \,|4f\rangle + \frac{2(2p+1)}{7} \times R_{Ls}^p S_p(R_{Ls})\right](-1)^k C_{-k}^{(p)}(\theta_{Ls}, \varphi_{Ls})/R_{Ls}^{p+1} \tag{3.33}$$

we drop superscripts (4f, 4f) in the shielding factors σ_p and in the quadratic forms of the overlap integrals $S_p(R_{Ls})$ (see Eq. (1.53)). Explicit expressions for all coupling constants $B^p_{k,\alpha_1\cdots\alpha_n}(Ls)$ of any order n for each ligand (Ls) can be obtained using the functional dependences of overlap integrals on the interion distance R (these dependences can be approximated very well by the exponential functions; see Table 3.1) and the recurrent relations for the spherical functions. In particular,

$$\frac{\partial}{\partial X_\alpha}\left(\frac{C_k^{(p)}}{R^{p+1}}\right) = -\frac{W^k_{p,\alpha}}{R^{p+2}}, \tag{3.34}$$

where the uniform spherical polynomials $W^k_{p,\alpha}$ of the $(p+1)$ power are linear combinations of spherical tensors $C_{k'}^{(p+1)}$ (Faucher and Garcia, 1982):

$$W^k_{p,x} = \frac{1}{2}[(p+1-k)^{1/2}(p+2-k)^{1/2}C_{k-1}^{(p+1)} - (p+1+k)^{1/2}(p+2+k)^{1/2}C_{k+1}^{(p+1)}], \tag{3.35}$$

$$W^k_{p,y} = \frac{i}{2}[(p+1-k)^{1/2}(p+2-k)^{1/2}C_{k-1}^{(p+1)} + (p+1+k)^{1/2}(p+2+k)^{1/2}C_{k+1}^{(p+1)}], \tag{3.36}$$

$$W^k_{p,z} = [(p+1)^2 - k^2]^{1/2}C_k^{(p+1)}. \tag{3.37}$$

As an example, we present here linear coupling constants related to the crystal field parameters in Eq. (3.33):

$$B^p_{k,\alpha}(Ls) = B^{(\mathrm{pc})p}_{k,\alpha}(Ls) + B^{(\mathrm{ec})p}_{k,\alpha}(Ls). \tag{3.38}$$

here $B^{(\mathrm{pc})p}_{k,\alpha}(Ls)$, $B^{(\mathrm{ec})p}_{k,\alpha}(Ls)$ are the contributions due to the modulation of even components of the point charge and exchange charge fields by lattice vibrations,

Table 3. 1 Values of parameters (atomic units) used in simulations of electron-phonon coupling constants[a]

		Pr^{3+} (X = Br)	Nd^{3+} (X = F)	Ho^{3+} (X = F)	Er^{3+} (X = F)	Tm^{3+} (X = F)
$1-\sigma_2$		0.11	0.208	0.421	0.44	0.45
$\langle 4f\|r^2\|4f\rangle$		1.086	1.001	0.695	0.666	0.646
$\langle 4f\|r^4\|4f\rangle$		2.822	2.401	1.219	1.126	1.067
$\langle 4f\|r^6\|4f\rangle$		15.726	12.396	4.502	3.978	3.647
$S_\sigma(Ln^{3+}-X^-)$	*a*	0.04610	0.67099	0.653535	0.69080	0.72463
	b	0.03733	1.52452	1.66766	1.72285	1.77597
	c	3.06620	1.01612	1	1	1
$S_\pi(Ln^{3+}-X^-)$	*a*	0.39635	2.24840	1.32391	1.31210	1.29235
	b	0.87514	2.44679	2.19139	2.22703	2.26048
	c	1.30253	0.89619	1	1	1
$S_s(Ln^{3+}-X^-)$	*a*	0.09988	1.72827	2.22980	2.30970	2.37567
	b	0.20882	2.12148	2.37229	2.43112	2.48764
	c	2.17238	0.93651	1	1	1
Compound		$CsCdBr_3$	$LiYF_4$	$LiYF_4$	$LiYF_4$	$LiYF_4$
$G_s; G_s; G_\pi$		5.4; 6.1; 6.1	2.5; 4; 2	5.6; 5.6; 2.85	7; 7; 7	8; 8; 4

(a) Overlap integrals have been computed using the radial 4f wave functions of trivalent lanthanide ions (Freeman and Watson, 1962; Synek and Corsiglia, 1968) and the 2s, 2p (4s, 4p) wave functions of the F^- (Br^-) ion presented by Clementi and McLean, 1964 (Clementi and Roetti, 1974). Dependences of the overlap integrals on the interionic distance R (in Angstrems) are approximated by the analytical function (Garcia and Faucher, 1985) $S = a\exp[-bR^c]$.

$$B_{k,\alpha}^{(pc)p}(Ls) = e^2 q_s(1-\sigma_p)\langle 4f|\, r^p \,|4f\rangle(-1)^k \frac{W_{p,\alpha}^{-k}(\theta_{Ls},\varphi_{Ls})}{R_{Ls}^{p+2}}, \quad (3.39)$$

$$B_{k,\alpha}^{(ec)p}(Ls) = -\frac{2(2p+1)}{7}(-1)^k e^2 R_{Ls}^{-2}\left\{W_{p,\alpha}^{-k}(\theta_{Ls},\varphi_{Ls})S_p(R_{Ls}) - X_{Ls\alpha}C_{-k}^{(p)}(\theta_{Ls},\varphi_{Ls})\left[p\frac{S_p(R_{Ls})}{R_{Ls}} + \frac{d}{dR_{Ls}}S_p(R_{Ls})\right]\right\}, \quad (3.40)$$

respectively. Coupling constants of higher order can be obtained by differentiating successively Eqs. (3.39), (3.40) and making use of Eqs. (3.34) – (3.37).

The number of independent coupling constants $B_{k,\alpha\beta\cdots\gamma}^{p}(Ls)$ that differ by sets of n coordinate indices equals $Z_n = (n+1)(n+2)/2$ for each lattice ion Ls. In particular, there are 3 linear coupling constants $B_{k,\alpha}^{p}(Ls)$ ($\alpha = x, y, z$), 6

independent second order coupling constants that correspond to a set of indices *xx*, *yy*, *zz*, *xy*, *xz*, *yz*, 10 and 15 independent third order and fourth order coupling constants, respectively. A detailed discussion of these coupling constants in $LiYF_4$: Ln^{3+} crystals is given below in Section 3.7.1.

At low temperatures (in particular, at the liquid helium temperature), only low frequency acoustic vibrations are excited in a crystal, and the interaction of rare earth ions with these long wave vibrations plays the dominant role in different relaxation processes. It is worth noting that values of constants of the linear interaction with the long wave acoustic vibrations can be obtained directly from strain derivatives of the crystal field parameters determined from spectroscopic data under uniaxial pressure. Displacements of ions from the equilibrium positions at the uniform lattice deformation may be presented as

$$u_\alpha(Ls) = \sum_\beta u_{\alpha\beta} X_{Ls\beta} + w_\alpha(s), \tag{3.41}$$

where $u_{\alpha\beta} = e_{\alpha\beta} + \omega_{\alpha\beta}$ are the components of the displacement tensor, $e_{\alpha\beta}$ are components of the symmetric infinitesimal deformation tensor, $\boldsymbol{w}(s)$ is the sublattice displacement vector, and components $\omega_{\alpha\beta} = (u_{\alpha\beta} - u_{\beta\alpha})/2$ of the antisymmetric tensor determine the rotation vector $\boldsymbol{\theta} = \mathrm{rot}\,\boldsymbol{u}/2$. Under the uniaxial pressure p along the unit vector $\boldsymbol{n}$, $e_{\alpha\beta} = -p \sum_{\gamma\delta} S_{\alpha\beta\gamma\delta} n_\gamma n_\delta$, where $\boldsymbol{S}$ is the elastic compliance tensor, and macroscopic and microscopic lattice deformations are linearly coupled (Born and Kun Huang, 1954): $w_\alpha(s) = \sum_{\beta\gamma} \Gamma_{\alpha,\beta\gamma}(s) e_{\beta\gamma}$. The crystal field Hamiltonian of the rare earth ion in the deformed lattice includes in the linear approximation the following terms that correspond to electron-deformation and electron-rotation interactions (the deformational and rotational interactions of second order in the displacement tensor were considered by Dohm and Fulde (1975), the electron-rotation interaction is important in the presence of the external magnetic field, in particular):

$$H_\mathrm{d} = \sum_{pk} \sum_{\alpha\beta} B^{(e)p}_{k,\alpha\beta} e_{\alpha\beta} C^{(p)}_k + \mathrm{i}[H_\mathrm{CF}, \boldsymbol{L\theta}], \tag{3.42}$$

where $\boldsymbol{L}$ is the orbital momentum of the rare earth ion, and parameters of the electron-deformation interaction are related to the linear coupling constants of Eq. (3.38) in the Hamiltonian of Eq. (3.31) by the lattice sums

$$B^{(e)p}_{k,\alpha\beta} = \frac{1}{2} \sum_{Ls} [B^p_{k,\alpha}(Ls) X_{Ls\beta} + B^p_{k,\beta}(Ls) X_{Ls\alpha}] + \sum_{Ls} B^p_{k,\gamma}(Ls) [\Gamma_{\gamma,\alpha\beta}(s) - \Gamma_{\gamma,\alpha\beta}(0)]. \tag{3.43}$$

The same Hamiltonian of Eq. (3.42) can be used when examining effects due to the interaction of the rare earth ion with the longwave acoustic vibrations, it is enough to substitute the corresponding expansions in phonon creation and annihilation operators for the deformation tensor and the rotation angle:

$$e_{\alpha\beta} = \frac{\mathrm{i}}{2}\sum_{j_{\mathrm{ac}}q}\sqrt{\frac{\hbar}{2Nm\omega_{j_{\mathrm{ac}}}(\boldsymbol{q})}}\,[e_{\alpha}(\boldsymbol{q}j_{\mathrm{ac}})q_{\beta} + e_{\beta}(\boldsymbol{q}j_{\mathrm{ac}})q_{\alpha}](a_{\boldsymbol{q}j} + a^{+}_{-\boldsymbol{q}j}), \tag{3.44}$$

where m is the unit cell mass, j_{ac} is the acoustic branch index, $e(\boldsymbol{q}j_{\mathrm{ac}})$ is the unit polarization vector, and the rotation angle θ_{γ} is given by the same Eq. (3.44) with the minus sign in the square brackets. The essential role of the renormalization of the interaction with the macroscopic deformations (this interaction is determined by the first term in the right hand side of Eq. (3.42)) due to the interaction with the sublattice displacements was demonstrated by Malkin et al. (1970), Ivanenko and Malkin (1972) in the analysis of piezospectroscopic data and spin-lattice relaxation rates in the fluorite type crystals activated by rare earth ions. In particular, the change in sign of a splitting Δ of the Sm^{2+} multiplet $^7F_1$ into doublet and singlet states under the applied stress along the trigonal symmetry axis ($\Delta > 0$ in CaF_2 and $\Delta < 0$ in SrF_2, BaF_2, Kaplyanskii and Przhevusski, 1966), and the anomalous increase of the interaction of the impurity Tm^{2+} ion with dynamical trigonal deformations along the homological series of fluorite type crystals with the increasing lattice constant were explained as a result of the competition between contributions to the coupling constants due to macroscopic and microscopic strains.

The total number of independent parameters $B^{(e)p}_{k,\alpha\beta}$ of electron-deformation interaction is determined by the symmetry of the static crystal field affecting the impurity rare earth ion. Let us consider, for example, impurity Ln^{3+} ions substituting for Y^{3+} ions with the local S_4 symmetry in the $LiYF_4$ crystal. In this case, there are 14 parameters $B^{(e)p}_{k,A_gi}$ ($i = 1, 2$; p, $k = 2, 0; 4, 0; 6, 0; 4, \pm 4; 6, \pm 4$), 16 parameters $B^{(e)p}_{k,B_gi}$ ($i = 1, 2$; p, $k = 2, \pm 2; 4, \pm 2; 6, \pm 2; 6, \pm 6$), and 12 parameters $B^{(e)p}_{k,xz}$ (p, $k = 2, \pm 1; 4, \pm 1; 4, \pm 3; 6, \pm 1; 6, \pm 3; 6, \pm 5$) that describe the interaction with the totally symmetric deformations $e(A^1_g) = e_{zz}$, $e(A^2_g) = e_{xx} + e_{yy}$, with the axial deformations $e(B^1_g) = e_{xy}$, $e(B^2_g) = e_{xx} - e_{yy}$, and with deformations e_{xz}, e_{yz} corresponding to the twofold irreducible E-representation of the lattice factor group C_{4h}. By having chosen a proper geometry of the pizospectroscopic experiment, and measuring shifts and splittings of different spectral lines, it is possible to obtain a volume of information sufficient to estimate all parameters in the Hamiltonian of Eq. (3.42). In particular, Vinokurov et al. (1986, 1988) determined the total number of 16 parameters $B^{(e)p}_{k,B_gi}$ for the Tm^{3+} ion from measured splittings of the 9 singlet-doublet

transitions in the optical spectra of $LiYF_4$: Tm^{3+} crystal under uniaxial pressure in the basis plane of the lattice, and all 14 parameters $B^{(e)p}_{k,A_{gi}}$ for the Er^{3+} ion from measured shifts of 15 optical transitions in $LiYF_4$: Er^{3+} crystal under uniaxial pressure parallel or perpendicular to the lattice symmetry axis. Values of parameters calculated in the framework of the exchange charge model agree satisfactorily with the experimental data. The exchange charge model was used also successfully to describe different effects due to the linear electron-phonon interaction in the concentrated double lithium-rare earth fluorides $LiRF_4$ (R = Tm, Er, Tb, Ho, Dy), namely, forced magnetostriction (Bumagina et al., 1981), magneto-acoustic phenomena (Aminov et al., 1996) and spectra of the mixed electron-phonon excitations (Kupchikov et al., 1987).

3.4 Density Matrix Formalism in the Quantum Theory of Relaxation

The description of different effects due to the ion-phonon interaction may be presented in the framework of the approach used in the general theory of magnetic relaxation almost half a century ago (Wangsness and Bloch, 1953; Bloch, 1956; Abragam, 1961; Redfield, 1965). The close connection between the theory of magnetic resonance spectra and spin-lattice relaxation and the theory of optical sharp-line spectra of impurity ions was emphasized by McCumber (1964a).

We consider the isolated impurity ion in the phonon bath with a short relaxation time τ_c that is supposed much less than relaxation times in the electronic subsystem. The dynamics of the system with the Hamiltonian of Eq. (3.27) is determined by the density matrix $\boldsymbol{\rho}$ that satisfies the equation of motion

$$i\hbar\frac{\partial\boldsymbol{\rho}}{\partial t} = [\hat{H}, \boldsymbol{\rho}]. \tag{3.45}$$

In this section, we assume that the electron-phonon interaction is so weak that it is possible to neglect the dependences of lattice characteristics on the electron subsystem state. In the interaction representation, the density matrix

$$\boldsymbol{\rho}(t) = e^{i(H_{el}+H_{ph})t/\hbar}\boldsymbol{\rho}e^{-i(H_{el}+H_{ph})t/\hbar} \tag{3.46}$$

slowly evolves due to the interaction between the electron and phonon subsystems:

$$i\hbar\frac{\partial\boldsymbol{\rho}(t)}{\partial t} = [H_{el-ph}(t), \boldsymbol{\rho}(t)]. \tag{3.47}$$

Considering the right hand side of Eq. (3.47) as a perturbation, and using the iteration procedure, we obtain a series expansion of $\rho(t)$ in powers of $H_{\text{el-ph}}$:

$$\rho(t_0+\Delta t) = \rho(t_0) - \frac{\mathrm{i}}{\hbar}\int_{t_0}^{t_0+\Delta t}[H_{\text{el-ph}}(t'),\rho(t_0)]\,\mathrm{d}t' - \left(\frac{1}{\hbar^2}\right)\int_{t_0}^{t_0+\Delta t}\mathrm{d}t'\int_{t_0}^{t'}\mathrm{d}t''[H_{\text{el-ph}}(t')],[H_{\text{el-ph}}(t''),\rho(t_0)] + \cdots \tag{3.48}$$

where explicit time dependences of operators are determined similarly to Eq. (3.46). Taking into account in Eq. (3.48) terms up to fourth order in $H_{\text{el-ph}}$, for $\Delta t \gg \tau_c$, it is possible to obtain the following kinetic equations for the diagonal and nondiagonal elements of the density matrix

$$\frac{\mathrm{d}\rho(t)_{ff}}{\mathrm{d}t} = \frac{2\pi}{\hbar}\sum_i \left| H_{\text{el-ph},fi} + \sum_d \frac{H_{\text{el-ph},fd}H_{\text{el-ph},di}}{E_i - E_d} + \cdots \right|^2 \times \delta(E_i - E_f)[\rho(t)_{ii} - \rho(t)_{ff}] + \cdots \tag{3.49}$$

$$\frac{\mathrm{d}\rho(t)_{fi}}{\mathrm{d}t} = -\frac{\mathrm{i}}{\hbar}(\Delta E_f - \Delta E_i)\rho(t)_{fi} - \frac{\pi}{\hbar}\sum_d [|H_{\text{el-ph},fd}|^2\delta(E_f - E_d) + |H_{\text{el-ph},di}|^2\delta(E_i - E_d)]\rho(t)_{fi} + \frac{2\pi}{\hbar}\sum_{dd'} H_{\text{el-ph},fd}\rho(t)_{dd'}H_{\text{el-ph},d'i}\delta(E_f - E_d)\delta(E_i - E_{d'}) + \cdots \tag{3.50}$$

where

$$\Delta E_f = H_{\text{el-ph},ff} + P\sum_d \frac{H_{\text{el-ph},fd}H_{\text{el-ph},df}}{E_f - E_d} + \cdots = P(H^{\text{eff}}_{\text{el-ph}})_{ff}, \tag{3.51}$$

P denotes the principal part of the integral. Here E_f, E_i, E_d are eigenvalues of the operator $H_{\text{el}} + H_{\text{ph}}$. The derivation of Eqs. (3.49) – (3.51), as presented by Beck et al. (1998), is based, in particular, on the Fourier transforms of the Heaviside function

$$\mathrm{e}^{\mp\mathrm{i}\omega_d t}\theta(t) = \lim_{\varepsilon\to 0+}\left(\pm\frac{\mathrm{i}}{2\pi}\int_{-\infty}^{\infty}\frac{\mathrm{e}^{\mp\mathrm{i}\omega t}\mathrm{d}\omega}{\omega - \omega_d \pm \mathrm{i}\varepsilon}\right), \tag{3.52}$$

that is inserted into the integrands in Eq. (3.48) to perform integrations over intermediate time variables from $-\infty$ to $+\infty$.

Let E_Γ, E_Γ, $\cdots$, and E_λ, E_μ, $\cdots$ be eigenvalues of the operators H_{el} and H_{ph}, respectively. In a case of very fast thermalization of the phonon subsystem,

we can use, in the zero approximation, the factorization of the density matrix $\rho(t) = \rho_{el}(t)\rho_{ph}$, where ρ_{ph} is the equilibrium density matrix of the phonon bath, $\rho_{ph,\lambda\mu} = \delta_{\lambda\mu}p_\lambda$, and p_λ is the probability that λ state is occupied. Making use of a definition of the density matrix of the electron subsystem $\rho_{el}(t) = Sp_{ph}\rho(t) = \sum_\lambda \langle\lambda|\rho(t)|\lambda\rangle$, we obtain from Eq. (3.49) the master equation for populations of the electron subsystem

$$\frac{d\rho_{el}(t)_{\Gamma\Gamma}}{dt} = \sum_{\Gamma'}[W_{\Gamma'\to\Gamma}\rho_{el}(t)_{\Gamma'\Gamma'} - W_{\Gamma\to\Gamma'}\rho_{el}(t)_{\Gamma\Gamma}], \tag{3.53}$$

and from Eq. (3.50) the rate of the coherence change

$$\frac{d\rho_{el}(t)_{\Gamma\Gamma'}}{dt} = -\Big[\frac{1}{2}\sum_{\Gamma''}(W_{\Gamma'\to\Gamma''} + W_{\Gamma\to\Gamma''}) + \gamma_{\Gamma\Gamma'} + \frac{i}{\hbar}(\Delta E_\Gamma - \Delta E_{\Gamma'})\Big]\rho_{el}(t)_{\Gamma\Gamma'}, \quad \Gamma \neq \Gamma'. \tag{3.54}$$

where

$$\Delta E_\Gamma = Sp_{ph}[\Delta E_f\rho_{ph}] = \sum_\lambda p_\lambda\langle\Gamma\lambda|H^{eff}_{el-ph}|\Gamma\lambda\rangle \tag{3.55}$$

is the shift of the energy E_Γ of the electron subsystem due to the electron-phonon interaction, $W_{\Gamma\to\Gamma'}$ is the transition probability between the states Γ and Γ' of the electron subsystem with the energy gap $E_\Gamma - E_{\Gamma'} = \hbar\omega_{\Gamma\Gamma'}$, it has the following form

$$W_{\Gamma\to\Gamma'} = \frac{2\pi}{\hbar}\sum_{\lambda\mu}|\langle\Gamma'\mu|H^{eff}_{el-ph}|\Gamma\lambda\rangle|^2 p_\lambda\delta(\hbar\omega_{\Gamma\Gamma'} + E_\lambda - E_\mu), \tag{3.56}$$

that is equivalent to a more general expression

$$W_{\Gamma\to\Gamma'} = \frac{2\pi}{\hbar}\Big\langle\sum_f|\langle f|H^{eff}_{el-ph}|i\rangle|^2\Big\rangle_i\delta(E_i - E_f), \tag{3.57}$$

where the initial state of the lattice is averaged, and the sum is over all possible final lattice states. When the interaction Hamiltonian has a form of a product of an operator A acting on the electronic variables, and a function F of dynamical ion displacements,

$$H_{el-ph} = AF(u), \tag{3.58}$$

the transition probability Eq. (3.56) takes a well known multiplicative form

$$W_{\Gamma\to\Gamma'} = \frac{1}{\hbar^2} | A_{\Gamma\Gamma'} |^2 K(\omega_{\Gamma\Gamma'}), \tag{3.59}$$

where

$$K(\omega) = \int_{-\infty}^{+\infty} Sp[F(u(0))F(u(\tau))\rho_{ph}]e^{i\omega\tau}d\tau \tag{3.60}$$

is the spectral density of the lattice correlation function.

According to Eq. (3.54), the time evolution of the coherence between electronic states with lifetimes τ_Γ and $\tau_{\Gamma'}\left(\tau_\Gamma^{-1} = \sum_{\Gamma''} W_{\Gamma\to\Gamma''}\right)$ is defined by the effective decay time T_2 that contains a contribution from the adiabatic modulation of the electronic energy levels $\gamma_{\Gamma\Gamma'} = 1/T^*_{2,\Gamma\Gamma'}$:

$$\frac{1}{T_{2,\Gamma\Gamma'}} = \frac{1}{2}(\tau_\Gamma + \tau_{\Gamma'}) + \frac{1}{T^*_{2,\Gamma\Gamma'}}. \tag{3.61}$$

The corresponding zero-phonon line has a Lorentzian lineshape with the full width at half height (FWHH) of $2/2\pi T_2$ in units of Hz for T_2 measured in seconds. The explicit expression of the adiabatic broadening is easily obtained from Eq. (3.50):

$$\gamma_{\Gamma\Gamma'} = \frac{\pi}{\hbar}\sum_{\lambda\mu} | \langle\Gamma\mu | H^{eff}_{el-ph} | \Gamma\lambda\rangle - \langle\Gamma'\mu | H^{eff}_{el-ph} | \Gamma'\lambda\rangle |^2 p_\lambda \delta(E_\lambda - E_\mu), \tag{3.62}$$

and, for the interaction Eq. (3.58), it can be presented through the spectral density of the lattice correlation function at zero frequency,

$$\gamma_{\Gamma\Gamma'} = \frac{1}{2\hbar^2} | A_{\Gamma\Gamma} - A_{\Gamma'\Gamma'} |^2 K(0). \tag{3.63}$$

The more detailed discussion of spectral line shifts and line widths induced by the electron-phonon interaction in the f – f spectra of rare-earth ions is presented below and in the next Chapter.

In the formulae presented above, we have neglected the electron subsystem effect on the lattice vibrations. The generalization can be carried out by making use of the wave functions Eq. (3.11) when calculating matrix elements of the perturbation Eq. (3.28). In particular, using the integral representation for the δ-function, we can write the transition probability Eq. (3.57) as the Fourier transform

$$W_{\Gamma\Gamma'} = \frac{1}{\hbar^2}\int_{-\infty}^{\infty} I_{\Gamma\to\Gamma'}(t)\exp(-i\omega_{\Gamma\Gamma'}t)\,dt, \tag{3.64}$$

of the generating function

$$I_{\Gamma\to\Gamma'}(t) = Sp_{ph}[(H_{el-ph})_{\Gamma\Gamma'}\exp(itH_{ph}^{\Gamma'}/\hbar)(H_{el-ph})^{\dagger}_{\Gamma\Gamma'}\exp(-itH_{ph}^{\Gamma}/\hbar)\rho_{ph}^{\Gamma}], \tag{3.65}$$

where ρ_{ph}^{Γ} is the equilibrium density matrix corresponding to the phonon subsystem with the Hamiltonian of Eq. (3.12). The formalism of generating functions to obtain expressions for optical lineshapes and nonradiative transition probabilities was worked out by Lax (1952), Pekar (1953), Krivoglaz and Pekar (1953), Kubo and Toyozawa (1955), and Perlin (1963). Accounting only for the linear electron-phonon coupling (the first term in Eq. (3.31)) and neglecting changes in phonon frequencies in different electronic states, it is possible to obtain the following form of the generating function Eq. (3.65) (Perlin and Tzukerblat, 1974)

$$I_{\Gamma\to\Gamma'}(t) = \sum_{\alpha\beta LL'ss'}\langle\Gamma\mid V_\alpha(Ls)\mid\Gamma'\rangle\langle\Gamma'\mid V_\beta(L's')\mid\Gamma\rangle \times\langle u_\alpha(Ls,0\mid 0)\,u_\beta(L's',0\mid t)\rangle\exp[M_\Gamma^{\Gamma'}(t) - M_\Gamma^{\Gamma'}(0)], \tag{3.66}$$

where the correlation function of ion displacements is determined in Eq. (3.14), and

$$M_\Gamma^{\Gamma'}(t) = \frac{1}{\pi\hbar}\int D_{\Gamma\Gamma'}(\omega)\{e^{i\omega t}[n(\omega)+1] + e^{-i\omega t}n(\omega)\}\,d\omega/\omega^2 \tag{3.67}$$

$$D_{\Gamma\Gamma'}(\omega) = \sum_{\alpha\beta LsL's'}(\langle\Gamma\mid V_\alpha(Ls)\mid\Gamma\rangle - \langle\Gamma'\mid V_\alpha(Ls)\mid\Gamma'\rangle) \times g_{\alpha\beta}(Ls,L's'\mid\omega)(\langle\Gamma\mid V_\beta(L's')\mid\Gamma\rangle - \langle\Gamma'\mid V_\beta(L's')\mid\Gamma'\rangle). \tag{3.68}$$

A probability of any transition between electronic states Γ and Γ' contains the Debye-Waller factor $\exp[-M_\Gamma^{\Gamma'}(0)]$ that accounts for the overlap between oscillator wave functions related to different adiabatic potentials. The corresponding Franck-Condon integrals (Franck, 1925) equal (see Eq. (3.11))

$$\begin{aligned} I_{jm}^{(\Gamma\Gamma')}(a_f^{\Gamma\Gamma'}) &= \int\chi_{\Gamma,j}(q_f - q_{f\Gamma})\chi_{\Gamma',m}(q_f - q_{f\Gamma'})\,dq_f \\ &= (-1)^m(2^m j!\,2^j m!)^{1/2}(a_f^{\Gamma\Gamma'}/2)^{m-j}\exp[-(a_f^{\Gamma\Gamma'}/2)^2] \\ &\quad\times L_m^{m-j}([a_f^{\Gamma\Gamma'}]^2/2)/m!,\ j<m, \\ &= (-1)^m(2^m j!/2^j m!)^{1/2}(a_f^{\Gamma\Gamma'}/2)^{m-j}\exp[-(a_f^{\Gamma\Gamma'}/2)^2]L_j^{m-j} \end{aligned}$$

$$\times ([a_f^{\Gamma\Gamma'}]^2/2)/m!, \quad j < m, \tag{3.69}$$

where $a_f^{\Gamma\Gamma'} = q_{f\Gamma'} - q_{f\Gamma}$ is the equilibrium displacement of the lattice oscillator f due to the electronic transition $\Gamma \rightarrow \Gamma'$, $L_m^{m-j}(x)$ is the generalized Laguerre polynomial (Kemble, 1937). At low temperatures, the probability for the vibrational transition ($L_m^m = (-1)^m m!$)

$$[I_{0m}^{(\Gamma\Gamma')}(a_f^{\Gamma\Gamma'})]^2 = (1/m!)[(a_f^{\Gamma\Gamma'})^2/2]^m \exp[-(a_f^{\Gamma\Gamma'})^2/2]. \tag{3.70}$$

In accordance with Eq. (3.70), the product of exponents leads to the factor $e^{-S(\Gamma\Gamma')}$ in the transition probability, where $S(\Gamma\Gamma') = M_\Gamma^{\Gamma'}(0, T = 0)$ is the Huang-Rhys parameter (Huang and Rhys, 1950).

The lattice relaxation is negligible at f – f transitions, and the Huang-Rhys parameter is very small ($S \leqslant 0.01$). For example, calculated values of the Huang-Rhys parameter for the transitions between the lowest sublevel of the $^4G_{5/2}$ multiplet and the six crystal field sublevels of the $^2H_{11/2}$ multiplet of the impurity Nd^{3+} ion in the $LiYF_4$ crystal are in the range $(2.6 - 4.3) \times 10^{-4}$, for the transition between the lowest sublevel of the $^4F_{5/2}$ multiplet and the upper sublevel of the $^4F_{7/2}$ multiplet of the Er^{3+} ion in the same crystal $S = 2.8 \times 10^{-3}$ (details of simulations are discussed below in Section 3.7.1). So low values provide the sufficient justification to substitute unity for the exponential factor in the generating function Eq. (3.66). In such an event of very weak electron-phonon interaction, Eqs. (3.64) and (3.66) may be used to calculate probabilities of one-phonon transitions only.

The form-function of the optical spectrum related to the radiative transition between the nondegenerate electronic states Γ and Γ' is given by the same Fourier integral of Eq. (3.64),

$$F_{\Gamma\Gamma'}(\Omega) = \frac{1}{\hbar^2}\int_{-\infty}^{\infty} I_{\Gamma\rightarrow\Gamma'}^R(t) \exp[-i(\omega_{\Gamma\Gamma'} - \Omega)t]\,dt, \tag{3.71}$$

where Ω is the frequency of the emitted light ($\omega_{\Gamma\Gamma'} > 0$), and the generating function has the same form as Eq. (3.65) with the operator of the effective electric dipole or magnetic dipole moment of the electronic subsystem substituted for the Hamiltonian H_{el-ph}. If we neglect the dependence of this operator, responsible for the interaction of electrons with the electromagnetic field, on lattice variables (in the framework of the Condon approximation (Condon, 1928)), the dependence of the generating function $I_{\Gamma\rightarrow\Gamma'}^R(t)$ on its argument is determined by the factor $\exp[M_\Gamma^{\Gamma'}(t) - M_\Gamma^{\Gamma'}(0)]$. Expanding the exponent in a power series in $M_\Gamma^{\Gamma'}(t)$, and collecting terms with 1, $e^{\pm i\omega t}$, $e^{\pm i(\omega_1 t \pm \omega_2 t)}$, $\cdots$, it is possible to present the form function as a sum of spectra corresponding to the

zero phonon transition, one phonon, two phonon, and multiphonon optical transitions. The value of $\Omega = \omega_{\Gamma\Gamma'}$ presents a singular point of the form function that corresponds to the zero phonon line with the integral intensity determined by the Debye-Waller factor (Krivoglaz and Pekar, 1953). As it has been mentioned above, the Debye-Waller factor is very close to unity in the f – f transitions, and the phonon sidebands appear only due to nonadiabatic terms in the Hamiltonian of Eq. (3.31). However, in the 5d state, the ion-lattice interaction is stronger than in the 4f state by more than an order of magnitude, and the interconfigurational electron-vibrational f – d spectra consist of broad bands with widths up to a thousand of wave numbers even at the liquid helium temperature contrary to the sharp zero phonon lines with widths less than ten wave numbers in the intraconfigurational f – f spectra.

3.5 Thermal Shifts of Zero-phonon Line Positions

The temperature shift of the zero-phonon line equals the difference between the shifts of the initial (Γ) and final (Γ') levels of a transition. These shifts may be as large as 30 cm^{-1} in the temperature range of 4 – 300 K for f – f transitions in the optical spectra of rare earth ions (CaF_2: Tm^{2+}, Kiss, 1962). Effects due to dependences of the spin-orbit constant and Slater integrals as well as of static crystal field parameters on the lattice constants are to be taken into account also when analysing thermal shifts of the optical lines. In particular, increase of spin-orbit coupling constant and electrostatic Slater parameters may be expected with the increasing temperature due to decreasing overlapping between wave functions of a rare earth ion and the nearest anions and contraction of the 4f shell in the expanding crystal lattice.

In accordance with Eqs. (3.51) and (3.55), the main contributions to the shift of the electronic energy due to the electron-phonon interaction have their origin from linear and second order terms in ion displacements in the Hamiltonian H_{el-ph}:

$$\begin{aligned}\Delta E(\Gamma) = & \frac{1}{\pi}\sum_{\Gamma'}\sum_{LsL's'\alpha\beta}\langle\Gamma \mid V_\alpha(Ls) \mid \Gamma'\rangle\langle\mid \Gamma' V_\beta(L's') \mid \Gamma\rangle \\ & \times P\int\left[\frac{n(\omega)+1}{\omega_{\Gamma\Gamma'}-\omega}+\frac{n(\omega)}{\omega_{\Gamma\Gamma'}+\omega}\right] g_{\alpha\beta}(Ls, L's' \mid \omega)\,\mathrm{d}\omega \\ & + \frac{\hbar}{2\pi}\sum_{Ls\alpha\beta}\langle\Gamma \mid V_{\alpha\beta}(Ls) \mid \Gamma\rangle\int[2n(\omega)+1]\, g_{\alpha\beta}(Ls, Ls \mid \omega)\,\mathrm{d}\omega. \end{aligned} \tag{3.72}$$

where $n(\omega)$ is the phonon occupation number, and $g_{\alpha\beta}(Ls, L's' \mid \omega)$ are the linear combinations of the imaginary parts of lattice Green's functions for differences between displacements of ligands and the lanthanide ion, defined in Eq. (3.25). To obtain reasonable estimates, it is enough to sum in Eq. (3.72) over the

intermediate crystal field states Γ' within the manifold containing the energy level Γ under consideration. The shift in Eq. (3.72) contains temperature independent term ($n(\omega)=0$) that contributes to the crystal field energy of the sublevel Γ, and the temperature dependent term. At low temperatures ($kT < \hbar\omega_{\Gamma\Gamma'}$, $kT < \hbar\omega_M$, ω_M is the maximum frequency of the lattice vibrations), only low frequency vibrations contribute to integrals in Eq. (3.72), the spectral densities of the correlation functions of the relative ion displacements are proportional to ω^3, and temperature dependent shifts of the energy levels are proportional to T^4 (McCumber and Sturge, 1963). The static crystal field diminishes with the thermal lattice expansion, and the corresponding changes of the crystal field energies (proportional to T^4 at low temperatures as well) in a general case are opposite to dynamical shifts induced by the "repulsion" of the energy levels through the phonon field.

Ignat'ev and Ovsyankin (1997) calculated shifts of Tm^{2+} ion crystal field levels in fluorite-type crystals using parameters of the Coulomb electron-phonon interaction (checked by their studies of vibronic sidebands) and the realistic models of the crystal lattice dynamics. Taking into account only linear terms in the Hamiltonian of the electron-phonon interaction, they obtained the zero temperature shifts of the crystal field sublevels of an order of 10 cm^{-1}, these shifts increase the crystal field splittings of the ground $^2F_{7/2}$ and excited $^2F_{5/2}$ multiplets by 5% (20 cm^{-1}) and 10% (50 cm^{-1}), respectively. These results have shown unambigously that contributions to the crystal field energies due to the dynamical ion-lattice interactions are to be taken into account when comparing any theoretical model of the static crystal field with the experimental data or when estimating results of the fitting of crystal field parameters.

Sardar and Stubblefield (1999) measured the temperature dependence of the shifts of transitions between the crystal field sublevels of the $^4F_{3/2}$ (the lowest doublet) – $^4I_{9/2}$, $^4I_{11/2}$ manifolds in $Sr_5(VO_4)_3F$: Nd^{3+} in the temperature range 10 – 300 K. In this temperature range, thermal shifts of the transitions mentioned above are equal (–7) – (–14) cm^{-1}. All lines were found to shift towards longer wavelength (redshift) with increasing temperature. The so-called redshift is generally observed in most crystalline solids, but the blueshift was also observed (Chen and Di Bartolo, 1993; Sardar and Yow, 1998; Sardar et al., 2001). Pelle et al. (2000) reported a blue shift of absorption transitions to the $^3P_0$ and $^1D_2$ states of Pr^{3+} dopant ions in $CsCdCl_3$ (up to 5 cm^{-1} in the range of temperatures 4 – 100 K) that was assumed as a result of the lattice thermal expansion effect on crystal field energies. The combined effect due to a repulsion between crystal field levels through the phonon field, relative shifts of rare earth ion terms and diminishing of the static crystal field with the lattice temperature expansion, may govern both red- and blue-shifts of different spectral lines with the increasing temperature.

3.6 Non-radiative Transitions Between Crystal Field Energy Levels

3.6.1 One- and Two-phonon Transition Rates

In accordance with the general formula Eq. (3.54), the probability of the one-phonon transition between the electronic initial (Γ) and final (Γ') states with the energy gap $\hbar\omega_{\Gamma\Gamma'} > 0$ can be presented as

$$W_{\Gamma\to\Gamma'} = \frac{2}{\hbar}\sum_{Ls\alpha L's'\beta}\langle\Gamma' \mid V_\alpha(Ls) \mid \Gamma\rangle g_{\alpha\beta}(Ls, L's' \mid \omega_{\Gamma\Gamma'}) \times \langle\Gamma \mid V_\beta(L's') \mid \Gamma'\rangle(n(\omega_{\Gamma\Gamma'}) + 1). \tag{3.73}$$

The probability of the spontaneous emission of two phonons contains three terms that correspond to the first order contribution from the nonlinear (quadratic) electron-phonon interaction

$$W^{(2a)}_{\Gamma\to\Gamma'} = \frac{1}{\pi}\sum_{\substack{Ls\alpha\beta\\ L's'\gamma\delta}}\langle\Gamma' \mid V_{\alpha\beta}(Ls) \mid \Gamma\rangle\langle\Gamma \mid V_{\gamma\delta}(L's') \mid \Gamma'\rangle \times \iint g_{\alpha\gamma}(Ls, L's' \mid \omega_1) g_{\beta\delta}(Ls, L's' \mid \omega_2)\delta(\omega_{\Gamma\Gamma'} - \omega_1 - \omega_2)\,\mathrm{d}\omega_1\mathrm{d}\omega_2, \tag{3.74}$$

to the second order contribution from the linear electron-phonon interaction

$$W^{(2b)}_{\Gamma\to\Gamma'} = \frac{2}{\pi\hbar^2}\sum_{jl}\iint\left[\frac{M^{\Gamma' j}_{l\Gamma'}(\omega_1) M^{j\Gamma}_{\Gamma l}(\omega_2)}{(\omega_{\Gamma j} - \omega_1)(\omega_{\Gamma l} - \omega_1)} + \frac{M^{\Gamma' j}_{\Gamma l}(\omega_1) M^{j\Gamma}_{l\Gamma'}(\omega_2)}{(\omega_{\Gamma j} - \omega_1)(\omega_{\Gamma l} - \omega_2)}\right] \times \delta(\omega_{\Gamma\Gamma'} - \omega_1 - \omega_2)\,\mathrm{d}\omega_1\mathrm{d}\omega_2, \tag{3.75}$$

where

$$M^{fj}_{lm}(\omega_n) = \sum_{LsL's'\alpha\beta}\langle f \mid V_\alpha(Ls) \mid j\rangle \times g_{\alpha\beta}(Ls, L's' \mid \omega_n)\langle l \mid V_\beta(L's') \mid m\rangle,$$

and to the combined action of the first and second order transition amplitudes:

$$W^{(2c)}_{\Gamma\to\Gamma'} = \frac{2}{\pi\hbar}\sum_{\substack{LsL's'\\ \alpha\beta\gamma\delta}}[\langle\Gamma' \mid V_{\alpha\beta}(Ls) \mid \Gamma\rangle\langle\Gamma \mid V_\delta(L's') \mid j\rangle$$

$$\times \langle j \mid V_\gamma(L's') \mid \Gamma' \rangle + c.c.] \cdot \iint g_{\alpha\gamma}(Ls, L's' \mid \omega_1)$$
$$\times g_{\beta\delta}(Ls, L's' \mid \omega_2) \frac{1}{\omega_{\Gamma j} - \omega_1} \delta(\omega_{\Gamma\Gamma'} - \omega_1 - \omega_2)\, d\omega_1 d\omega_2. \quad (3.76)$$

The two-phonon emission by rare earth ions was first considered by Malkin (1963a) and Orbach (1964) who estimated the probability of a transition between the $^7F_1$ and $^7F_0$ states of Sm^{2+} ion in the cubic crystal field of CaF_2 by making use of linear electron-phonon coupling in second order via the intermediate $^7F_2$ multiplet (direct $^7F_1 \rightarrow {}^7F_0$ one- and two-phonon transitions are forbidden).

The transition probability due to Raman scattering of phonons by the impurity ion (the first phonon induces the virtual transition of the lanthanide ion from the initial state Γ to the intermediate state p, and the second phonon induces the transition to the final state Γ'), may be written as

$$W^{(Ra)}_{\Gamma\to\Gamma'} = \frac{2}{\pi\hbar^2} \int n(\omega - \omega_{\Gamma\Gamma'}) [n(\omega) + 1] Sp[\boldsymbol{K}^{(\Gamma'\Gamma)}(\omega)$$
$$\times \boldsymbol{g}(\omega - \omega_{\Gamma\Gamma'}) \boldsymbol{K}^{(\Gamma'\Gamma)+}(\omega) \boldsymbol{g}(\omega)]\, d\omega, \quad (3.77)$$

where integration over ω from $\omega_{\Gamma\Gamma'}$ to the maximum phonon frequency is supposed, and

$$K^{(\Gamma'\Gamma)}_{\alpha\beta}(Ls, L's' \mid \omega) = \sum_p \left[\frac{\langle \Gamma' \mid V_\beta(L's') \mid p \rangle \langle p \mid V_\alpha(Ls) \mid \Gamma \rangle}{\omega_{\Gamma' p} + \omega - i\gamma_p} \right.$$
$$\left. + \frac{\langle \Gamma' \mid V_\alpha(Ls) \mid p \rangle \langle p \mid V_\beta(L's') \mid \Gamma \rangle}{\omega_{\Gamma p} - \omega - i\gamma_p} \right]. \quad (3.78)$$

γ_p is the inverse lifetime of the intermediate ion state p, matrices $\boldsymbol{K}(\omega)$ and $\boldsymbol{g}(\omega)$ in Eq. (3.77) have dimensions of $3L_0 \times 3L_0$, where L_0 is the number of ligand ions which contribute to the electron-phonon interaction Eq. (3.31). The nonelastic phonon scattering can be also induced by terms in the Hamiltonian of Eq. (3.31) which are quadratic in dynamical ion displacements, the corresponding transition probability

$$W^{(Rb)}_{\Gamma\to\Gamma'} = \frac{2}{\pi} \sum_{\substack{\alpha\beta Ls \\ \gamma\delta L's'}} \langle \Gamma \mid V_{\alpha\beta}(Ls) \mid \Gamma' \rangle \langle \Gamma' \mid V_{\gamma\delta}(L's') \mid \Gamma \rangle$$
$$\times \int g_{\alpha\gamma}(Ls, L's' \mid \omega) g_{\beta\delta}(Ls, L's' \mid \omega - \omega_{\Gamma\Gamma'}) [n(\omega) + 1] n(\omega - \omega_{\Gamma\Gamma'})\, d\omega \quad (3.79)$$

is similar to Eq. (3.74), and the contribution due to cross terms is similar to Eq. (3.76).

In most cases energy gaps between multiplets of the $4f^n$ electron shell of a rare earth ion are essentially larger than the maximum phonon frequency, and one and two phonon transitions are allowed only between the crystal field sublevels belonging to a fixed multiplet. Results of calculations of transition probabilities can be compared with parameters, which are obtained from optical and EPR experiments, such as homogeneous spectral linewidths and spin-lattice relaxation times. Some examples of these calculations will be discussed below in this and the next Chapters.

3.6.2 Phonon Contributions to Linewidths

According to Kiel (1962), mechanisms that cause broadening of zero-phonon spectral lines of rare earth ions in solids may be divided into two classes. (1) The first class includes all those mechanisms that reduce the lifetimes of the states connected by the optical transition. This includes such familiar line broadening causes as the natural lifetime and the nonradiative transitions. The natural radiative linewidth in f – f spectra of rare earth ions is almost always negligible. (2) The second class includes all those interactions that change the frequency of the radiative transition due to different shifts of the upper and the lower energy levels without affecting their lifetimes. The statistical strain broadening, the broadening in the nonuniform external magnetic field, the hyperfine unresolved structure, due to the interaction of the magnetic moment of the rare earth ion with the nuclear magnetic moments of ligand ions, present the corresponding examples. The slow (adiabatic) variations in energy of the rare earth ion in the crystal field modulated by phonons belong to this second class as well (adiabatic broadening). The adiabatic condition requires that the change of the optical transition frequency ν during the period $1/\nu$ to be less than the average frequency ν: $(1/\nu)(\mathrm{d}\nu/\mathrm{d}t) < \nu$, and this condition is fulfilled for $\mathrm{d}\nu/\mathrm{d}t = \nu\nu_0$, where $\nu_0 \ll \nu$ is the phonon frequency. The explicit expressions of the adiabatic electron-phonon contributions to the linewidth of the $\Gamma \rightarrow \Gamma'$ transition are obtained from Eq. (3.62). Taking into account quadratic and linear terms in the electron-phonon interaction Eq. (3.31), we obtain, respectively,

$$\gamma_{\Gamma\Gamma'}^{(a)} = \frac{1}{\pi} \sum_{\substack{\alpha\beta Ls \\ \gamma\delta L's'}} (\langle \Gamma | V_{\alpha\beta}(Ls) | \Gamma \rangle - \langle \Gamma' | V_{\alpha\beta}(Ls) | \Gamma' \rangle) \times (\langle \Gamma | V_{\gamma\delta}(L's') | \Gamma \rangle - \langle \Gamma' | V_{\gamma\delta}(L's') | \Gamma' \rangle) \times \int g_{\alpha\gamma}(Ls, L's' | \omega) g_{\beta\delta}(Ls, L's' | \omega) [n(\omega) + 1] n(\omega) \mathrm{d}\omega, \quad (3.80)$$

$$\gamma_{\Gamma\Gamma'}^{(b)} = \frac{1}{\pi \hbar^2} \int n(\omega)[n(\omega) + 1] Sp\{[\boldsymbol{K}^{(\Gamma\Gamma)}(\omega) - \boldsymbol{K}^{(\Gamma'\Gamma')}(\omega)] \times g(\omega)[\boldsymbol{K}^{(\Gamma\Gamma)}(\omega) - \boldsymbol{K}^{(\Gamma'\Gamma')}(\omega)]^+ \boldsymbol{g}(\omega)\} \mathrm{d}\omega \quad (3.81)$$

and the contribution due to cross terms has a similar form

$$\gamma^{(c)}_{\Gamma\Gamma'} = \frac{1}{\pi\hbar} \sum_{\substack{\alpha\beta Ls \\ \gamma L's', \delta L''s''}} (\langle\Gamma | V_{\alpha\beta}(Ls) | \Gamma\rangle - \langle\Gamma' | V_{\alpha\beta}(Ls) | \Gamma'\rangle)$$
$$\times [K^{\Gamma\Gamma}_{\gamma\delta}(L's', L''s'' | \omega) - K^{\Gamma'\Gamma'}_{\gamma\delta}(L's', L''s'' | \omega)] \int g_{\alpha\gamma}(Ls, L's' | \omega)$$
$$\times g_{\beta\delta}(Ls, L''s'' | \omega)[n(\omega) + 1] n(\omega)\, d\omega + c.c., \qquad (3.82)$$

where elements of the matrix $\boldsymbol{K}(\omega)$ are defined in Eq. (3.78).

At low temperatures, only acoustic phonons contribute to integrals in Eqs. (3.80) – (3.82), and the adiabatic broadening is proportional to T^7. Because of this strong temperature dependence, the adiabatic broadening is suppressed at liquid helium temperature, and the observed residual linewidths are chiefly due to strains in real crystals and the spontaneous nonradiative relaxation (when the energy separations are favorable). The thermal broadening is homogeneous and therefore yields a Lorentzian line shape (McCumber, 1964b) that is really observed (Beck et al., 1998; Sardar et al., 2001). The applicability of the formulae that determine temperature dependences of the one- and two-phonon transition probabilities to the behavior of sharp line spectra from dopant rare-earth ions in solids was first demonstrated by Yen et al. (1964).

The clear evidence for direct process dominated relaxation between the two lowest crystal field singlets of the $^3H_6$ multiplet of Tm^{3+} in YAG with a gap of 27 cm^{-1} was presented by Macfarlane (2000) from measurements of the temperature dependent linewidth of the transition between the lowest crystal field states in the excited $^3H_4$ and the ground $^3H_6$ manifolds fulfilled with spectral hole burning and free induction decay methods. The spontaneous rate of phonon emission of 318 MHz was obtained. The important role of the direct one-phonon relaxation was also emphasized by Sardar and Yow (1998).

Sardar and Stubblefield (1999) measured the temperature dependence of the line broadening of the transitions between the sublevels of the $^4F_{3/2}$ (the lowest doublet) – $^4I_{9/2}$, $^4I_{11/2}$ manifolds in $Sr_5(VO_4)_3F$: Nd^{3+}. The spontaneous phonon emission contribution of an order of 10 cm^{-1} to the linewidth of the transition terminated on the excited crystal field sublevel of the ground manifold was obtained at low temperatures. Changes in the linewidths (FWHH) as the temperature increases from 10 to 300 K are in the range 4 – 30 cm^{-1}.

On the basis of measurements of the temperature dependent linewidths in the spectra of nine trivalent rare earth ions (Ce, Pr, Nd, Eu, Gd, Tb, Er, Tm, Yb) in $LiYF_4$ in the temperature range 4 – 300 K, Ellens et al. (1997a, b) came to the conclusion about the symmetric behavior (strong in the beginning and the end of the series, and weak in the middle) of the electron-phonon coupling strength in lanthanide compounds that was suggested earlier by Hellwege (1941) and Krupke (1966). However, it should be noted that actually only the strength of the effective coupling could be estimated from the experimental data, and

without the detailed analysis, no statements about the parameters of the one-electron interaction with lattice vibrations could be presented. The arguments of Ellens et al. (1997b) based on the lanthanide contraction (that diminishes the crystal-field effects in the end of the series) and variation of the screening of the electrostatic quadrupole component of the crystal field (the shielding constant σ_2 diminishes through the series, and correspondingly this crystal field component increases in the end of the lanthanide series) are limited by neglect of overlap contributions that vary monotonically through the series and exceed pure electrostatic terms. Based on the lanthanide contraction, one would expect a gradual decrease of the electron-phonon coupling strength through the lanthanide series similar to the systematic variation of the crystal field parameters (in particular, see Table 3.2).

Table 3.2 Crystal field parameters (cm^{-1}) in $LiYF_4$: Ln^{3+} crystals in the crystallographic system of coordinates

Ln^{3+}	B_0^2	B_0^4	$-\lvert B_4^4\rvert$, ReB_4^4, ImB_4^4	B_0^6	$-\lvert B_4^6\rvert$, ReB_4^6, ImB_4^6	Reference
Pr^{3+}	433	−1068	−1319	−67	−1187	(a)
Nd^{3+}	372	− 974	−1266, −1116, −598	−20	−1039, −1020, −200	(b)
	360	− 814	−1128, −979, − 560	−55	−672, −620, −259	(ECM)
Sm^{3+}	368	−755	−938	−64	−898	(c)
Eu^{3+}	348	−749	−1054	−93	−778	(d)
Tb^{3+}	388	−766	−1055	−57	−754	(e)
Dy^{3+}	330	−704	−937	−70.4	−616	(f)
Ho^{3+}	379	−626	−831	−52	−608	($LiHoF_4$g)
	308	−712	−955, −669, −682	−33	−594, −459, −378	(ECM)
	513	−600	−824, −575, −590	−44.2	−561, −439, −350	(ECMc)
Er^{3+}	323	−754	−1052	−43.6	−624	(h)
	380	−640	−975	−36.8	−607	(f)
	328	−723	− 975, −683, −696	−41.1	−512, −395, −325	(ECM)
	520	−619	−854, −595, −612	−35.5	−471, −368, −294	(ECMc)
Tm^{3+}	323	−626	−907	−63	−600	(i)
	320	−682	−919, −644, −656	−40	−482, −372, −306	(ECM)
	510	−582	−803, −560, −576	−41.1	−581, −454, −362	(ECMc)
Yb^{3+}	380	−600	−780	−35.2	−485	(j)

(a) Lee et al., 2001;
(b) De Leebeeck et al., 1999;
(c) Wells et al., 1999;
(d) Gorller-Warland et al., 1993;
(e) Liu et al., 1994;
(f) Davidova et al., 1977;
(g) Christensen, 1979;
(h) Couto dos Santos et al., 1998;
(i) Chen Xueyan and Luo Zundu, 1997;
(j) Malkin, unpublished;
ECM: calculated in the framework of the exchange charge model;
ECMc: contributions from interactions with the nearest eight fluorine ions.

Vink et al. (2001) have found similar values of effective electron-phonon coupling constants in the comparative measurements of temperature-dependent line broadening in the spectra of isoelectronic divalent and trivalent lanthanides (Eu^{2+} and Gd^{3+} ($4f^7$), Sm^{2+} and Eu^{3+} ($4f^6$)). The slightly stronger coupling in divalent ions is in agreement with the larger crystal field splittings.

Some peculiarities in the lineshapes of the zero-phonon transitions are possible if the phonon density of states has narrow maxima at the frequencies of electronic transitions between the energy levels involved in the transition and other sublevels of the ion multiplets. In particular, if the excited state Γ can relax due to a single phonon process, the absorption lineshape is given by (Lupei, 2001)

$$I(\Omega) = w(\Omega_0)\frac{(\gamma + W(\Omega))/\pi}{[\Omega - \Omega_0 - \delta E(\Gamma, \Omega)/\hbar]^2 + [\gamma + W(\Omega)]^2}, \quad (3.83)$$

where

$$\delta E(\Gamma, \Omega) = \sum_{\Gamma'} \sum_{LsL's'\alpha\beta} \langle \Gamma \mid V_\alpha(Ls) \mid \Gamma' \rangle \langle \Gamma' \mid V_\beta(L's') \mid \Gamma \rangle \times P\int \left[\frac{n(\omega) + 1}{\Omega - \Omega_0 + \omega_{\Gamma\Gamma'} - \omega} + \frac{n(\omega)}{\Omega - \Omega_0 + \omega_{\Gamma\Gamma'} + \omega}\right] \times g_{\alpha\beta}(Ls, L's' \mid \omega)\, d\omega, \quad (3.84)$$

$$W(\Omega) = \frac{2}{\hbar} \sum_{Ls\alpha L's'\beta\Gamma'} \langle \Gamma \mid V_\alpha(Ls) \mid \Gamma' \rangle g_{\alpha\beta}(Ls, L's' \mid \Omega - \Omega_0 + \omega_{\Gamma\Gamma'}) \times \langle \Gamma' \mid V_\beta(L's') \mid \Gamma \rangle \times [n(\Omega - \Omega_0 + \omega_{\Gamma\Gamma'}) + 1], \quad (3.85)$$

$w(\Omega_0)$ is the integral intensity of the zero-phonon transition to the Γ state at the frequency Ω_0, and γ is the linewidth in absence of the electron-phonon coupling. Asymmetries or splittings may be observed , obtained from solutions of the equation $\Omega - \Omega_0 - \delta E(\Gamma, \Omega)/\hbar = 0$.

If the spectral functions $g(\omega)$ have a peak at frequency ω_m close to $\omega_{\Gamma\Gamma'}$, and the electron-phonon coupling is strong enough, the line is split into two Lorentz components, whose intensities depend on the resonance degree $|\omega_m - \omega_{\Gamma\Gamma'}|$. In a case of weak coupling, and smooth shape of phonon correlation functions, we have a single Lorentz line with the width $W(\Omega_0)$ and the shift, determined by Eq. (3.72).

3.6.3 Multiphonon Relaxation

A total rate of de-excitation of the metastable emitting state of the lanthanide ion can be written as

$$1/\tau = 1/\tau_{rad} + W. \tag{3.86}$$

The first term in the right hand side of Eq. (3.86) is the radiative rate (that accounts for all transitions induced by the interaction with the electromagnetic field) and the second term corresponds to the nonradiative energy transfer to the lattice. As it has been verified by many authors, the nonradiative decay rate between crystal field energy levels belonging to different manifolds is predominantly determined by the energy gap and the particular host crystal lattice. The energy gap law for the nonradiative rate at low temperatures was introduced: (Riseberg and Moos, 1968; Moos, 1970; Weber, 1973)

$$W = (1/\tau_0)\exp(-a\Delta E/\hbar\omega_M) \tag{3.87}$$

where a and τ_0 are empirically fitted parameters, ω_M is related to the highest phonon frequency of the host medium, and ΔE is the energy gap between the populated state and the next lower lying energy level of the lanthanide ion (usually this gap is considered as the difference between energies of the lowest crystal field state of the upper multiplet and the highest crystal field state of the lower multiplet). The minimum number of phonons p needed to bridge the gap ($\Delta E = \hbar\omega_{\Gamma\Gamma'} = \hbar[(p-1)\omega_M + \Omega]$, $\Omega < \omega_M$) denotes the order of the process. For large p ($p > 4$), the contribution of radiative processes to the fluorescence lifetime may be large enough and has to be accounted for. The existing theoretical derivation of the energy gap law in the framework of linear mechanism of the electron-phonon interaction (Miyakawa and Dexter, 1970) based on the substitution of an exponent e^{-ap} for $1/p!$ (where p is the number of phonons emitted by the ion) is not satisfactory. However, the simple expression Eq. (3.87) is used to describe experimental data varying over several orders of magnitude. Payne and Bibeau (1998) reported the nonradiative decay rates of $^4G_{7/2}$ state of Nd^{3+} in 26 different crystals and glasses with the relevant energy gaps ($^4G_{7/2} - {}^4G_{5/2}$, $^2G_{7/2}$) in the range $1100 - 1500\ cm^{-1}$. The corresponding lifetimes depend strongly on the order of the process and vary in the wide range from 70 ps for $Ca_5(PO_4)_3F$ ($\Delta E = 1141\ cm^{-1}$, $\omega_M = 1080\ cm^{-1}$) to 41 ns for LaF_3 ($\Delta E = 1542\ cm^{-1}$, $\omega_M = 414\ cm^{-1}$), with the reasonably good adherence to the energy gap low. The rate of phonon assisted decay of excited states may be essentially enhanced in hosts containing molecular groups with high effective phonon energy as is usual for silicates, phosphates and vanadates due to the vibration modes of the covalently bonded (MO_4) tetrahedra (M = Si, P, V). In the YPO_4 crystal with the boundary of the phonon spectrum at $1058\ cm^{-1}$, the relaxation rate for the energy gap as large as $4000\ cm^{-1}$ (the $^3P_0 - {}^1D_2$ transition) is so fast as $1.5 \times 10^6\ s^{-1}$ because the gap is bridged with only four phonons (Lian et al., 2000).

The energy-gap law for multiphonon relaxation assumes that the multiphonon transition probabilities depend only on the required number of

phonons to bridge the energy gap between two crystal field levels of the lanthanide ion. This means that there is no difference in electron-phonon coupling strength for the different lanthanide ions. It is obvious that parameters depending on the lanthanide ion, the host matrix, and the specified transition are to be introduced. Basiev et al., (1996) marked the strong experimental dependence of multiphonon relaxation rates on crystal and lanthanide ion dopant type.

In the framework of the first order perturbation theory, accounting for the linear electron-phonon interaction only, in accordance with Eqs. (3.64) – (3.68), the probability of the nonradiative n-phonon transition $\Gamma \rightarrow \Gamma'$ at zero temperature equals

$$W^{(n)}_{\Gamma\rightarrow\Gamma'} = \frac{2}{\hbar^n}\left(\frac{1}{\pi}\right)^{n-1}\frac{1}{(n-1)!}\exp(-S_{\Gamma\Gamma'})\sum_{\alpha\beta Ls L's'}\int d\omega_1 \cdots$$
$$\times d\omega_n \delta\Big(\omega_{\Gamma\Gamma'} - \sum_{k=1}^{n}\omega_k\Big)\frac{D_{\Gamma\Gamma'}(\omega_1)\cdots D_{\Gamma\Gamma'}(\omega_{n-1})}{\omega_1^2\cdot\cdots\cdot\omega_{n-1}^2}\cdot\langle\Gamma' \mid V_\alpha(Ls)\mid\Gamma\rangle$$
$$\times g_{\alpha\beta}(Ls, L's' \mid \omega_n)\langle\Gamma \mid V_\beta(L's')\mid\Gamma'\rangle. \qquad (3.88)$$

This expression includes the multiple ($n-1$ times) product of the one-phonon spectral densities projected on the adiabatic lattice deformations (promoting phonons) and the only one factor corresponding to the nonadiabatic deformation (accepting phonon). Because of a continuous phonon spectrum in real solids, and in accordance with the definition of the Huang-Rhys parameter (see Eq. (3.67) for $t=0$ and $n(\omega)=0$), we have to consider $n=p+1$ in Eq. (3.88), and the transition rate may be approximated by the following

$$W^{(p+1)}_{\Gamma\rightarrow\Gamma'} \approx W^{(1)}_{\Gamma\rightarrow\Gamma'} e^{-S(\Gamma\Gamma')} S(\Gamma\Gamma')^p/p!, \qquad (3.89)$$

where the first factor in the right hand side stands for the virtual one-phonon transition probability at the average phonon frequency. In the case of intraconfiguration f – f transitions, the interaction with the adiabatic deformations is extremely weak (see Section 3.3.), and the real nonradiative transition rates are greatly underestimated by Eqs. (3.88) – (3.89).

Pukhov and Sakun (1979) worked out the microscopic model of nonradiative multiphonon transitions using terms of n-th order in the Hamiltonian of electron-phonon interaction Eq. (3.31) to calculate the probability of a process that involved n phonons. We shall consider here this so called nonlinear mechanism of nonradiative transitions in the framework of a cluster model taking into account interactions between the rare earth ion and a finite number (denoted below by L_0) of its ligand ions in the first coordination shell.

At the zero temperature, for the n-phonon process, taking the n-th order term in the expansion Eq. (3.31) as the time dependent perturbation, we obtain from Eq. (3.56) the following expression for the transition probability

(symmetry of the coupling constants $B^{k}_{p,\alpha\beta\cdots\gamma}(Ls)$ under the permutations of the indices $\alpha\beta\cdots\gamma$ is taken into account)

$$W^{(n)}_{\Gamma\to\Gamma'} = \frac{2}{\hbar}\left(\frac{\hbar}{\pi}\right)^{n-1}\frac{1}{n!}\sum_{pp'kk'} M^{kk'}_{pp'}(\Gamma\Gamma')\,D^{kk'}_{pp'}(\omega_{\Gamma\Gamma'}), \tag{3.90}$$

where

$$M^{kk'}_{pp'}(\Gamma\Gamma') = \langle\Gamma'\mid C^{(p)}_{k}\mid\Gamma\rangle\langle\Gamma\mid C^{(p')}_{k'}\mid\Gamma'\rangle, \tag{3.91}$$

$$D^{kk'}_{pp'}(\omega) = \sum_{Ls,\,\alpha\beta\cdots\gamma}\sum_{L's',\,\lambda\mu\cdots\nu} B^{p}_{k,\alpha\beta\cdots\lambda}(Ls)\,B^{p'}_{k',\lambda\mu\cdots\nu}(L's')\,J^{\lambda\mu\cdots\nu}_{\alpha\beta\cdots\gamma}(Ls, L's'\mid\omega), \tag{3.92}$$

$$J^{\lambda\mu\cdots\nu}_{\alpha\beta\cdots\gamma}(Ls, L's'\mid\omega) = \int\cdots\int \mathrm{d}\omega_1\cdots\mathrm{d}\omega_n\,\delta\Big(\omega-\sum_{i=1}^{n}\omega_i\Big)\,g_{\alpha\lambda} \times(Ls, L's'\mid\omega_1)\cdots g_{\gamma\nu}(Ls, L's'\mid\omega_n). \tag{3.93}$$

The multiple summation in Eq. (3.92) can be simplified by introducing a matrix $\boldsymbol{J}_n$ of the symmetrized spectral densities with dimensions of $D_n\times D_n(D_n = Z_nL_0$, Z_n is the number of different sets of n indices $\alpha\beta\cdots\gamma$ considered in Section 3.2):

$$J_{n,ab}(Ls, L's'\mid\omega) = \sum_{P} J^{\lambda\mu\cdots\nu}_{\alpha\beta\cdots\gamma}(Ls, L's'\mid\omega) = \int\cdots\int \mathrm{d}\omega_1\cdots\mathrm{d}\omega_n\,\delta\Big(\omega-\sum_{i=1}^{n}\omega_i\Big) \times S_{n,ab}(Ls, L's'\mid\omega_1,\omega_2,\cdots,\omega_n), \tag{3.94}$$

where

$$S_{n,ab}(Ls, L's'\mid\omega_1,\omega_2,\cdots,\omega_n) = \sum_{P} g_{\alpha\lambda}(Ls, L's'\mid\omega_1)\cdots g_{\gamma\nu}(Ls, L's'\mid\omega_n) \tag{3.95}$$

(the sum is over permutations between different $\alpha\beta\cdots\gamma$, $\lambda\mu\cdots\nu$; $a = 1: Z_n$, $Ls = 1: L_0$) The transition probability (see Eq. (3.90)) takes the following form

$$W^{(n)}_{\Gamma\to\Gamma'} = \frac{2}{\hbar}\left(\frac{\hbar}{\pi}\right)^{n-1}\frac{1}{n!}\,Sp[\,\boldsymbol{V}^{(n)}_{\Gamma\Gamma'}\boldsymbol{J}_n(\omega_{\Gamma\Gamma'})\,\boldsymbol{V}^{(n)+}_{\Gamma\Gamma'}], \tag{3.96}$$

where vectors $\boldsymbol{V}^{(n)}_{\Gamma\Gamma'}$ have D_n components corresponding to matrix elements of operators $V_{\alpha\beta\cdots\gamma}(Ls) = V_a(Ls)$ (see Eq. (3.32)).

The explicit expressions of probabilities of one- and two-phonon processes

have been given in the previous Section 3.5.1. Now we shall consider relaxation processes that involve from 3 to 5 phonons. The minimum number p of phonons participating in the relaxation process is determined by the energy conservation law. The first nonzero contribution to the transition probability comes from the p-th-order terms in Eq. (3.31), and the corresponding convolution of the lattice correlation functions Eq. (3.94) takes the form

$$J_{p,ab}(Ls, L's' \mid \omega_{\Gamma\Gamma'}) = \int_{\Omega}^{\omega_M} d\omega_1 \int_{\Omega+\omega_M-\omega_1}^{\omega_M} d\omega_2 \cdots \int_{\Omega+\sum_{k=1}^{p-2}(\omega_M-\omega_k)}^{\omega_M} d\omega_{p-1} S_{p,ab} \times \left(Ls, L's' \mid \omega_1, \omega_2, \cdots, \omega_{p-1}, \omega_p = \omega_{\Gamma\Gamma'} - \sum_{k=1}^{p-1} \omega_k\right). \tag{3.97}$$

For $T \neq 0$, each spectral density $g_{\alpha\beta}(Ls, L's' \mid \omega)$ is to be multiplied by $[1 + n(\omega)]$, where $n(\omega)$ is the phonon occupation number, if emission of phonons is considered. At finite temperatures, the combination processes with the annihilation and creation of phonons may give a remarkable contribution to the transition probability as well. In particular, for the $(p+1)$ – phonon process, that involves annihilation of one phonon, the corresponding integrand contains an additional factor $K_{p+1}(\omega_1, \cdots, \omega_{p+1}) = (p+1)n(\omega_1) \prod_{k=2}^{p+1} [1 + n(\omega_k)]$, and we obtain (we omit below labels Ls, $L's'$ of ligand ions in elements of matrices $\boldsymbol{J}_n$ and $\boldsymbol{S}_n$):

$$J_{p+1,ab}(\omega_{\Gamma\Gamma'}) = \int_0^{\omega_M-\Omega} d\omega_1 \int_{\Omega+\omega_1}^{\omega_M} d\omega_2 \cdots \int_{\Omega+\omega_1+\sum_{k=2}^{p-1}(\omega_M-\omega_k)}^{\omega_M} d\omega_p \times K_{p+1}(\omega_1, \cdots, \omega_{p+1}) S_{p+1,ab}\left(\omega_1, \cdots, \omega_p, \omega_{p+1} = \omega_1 + \omega_{\Gamma\Gamma'} - \sum_{k=2}^{p} \omega_k\right). \tag{3.98}$$

When Ω is close to ω_M, only the upper part of the phonon spectrum is active in generating the nonradiative transitions, and the convolution Eq. (3.97) drastically diminishes with Ω approaching ω_M. In this case, the $(p+1)$ – phonon process may become more effective due to a larger volume in the frequency space that contributes to the corresponding convolution of spectral densities $g_{\alpha\beta}(Ls, L's' \mid \omega)$.

Let us consider the case when $\omega_{\Gamma\Gamma'} = \omega_M + \Omega (0 < \Omega < \omega_M)$. For the transitions with the creation of three or four phonons, the effective spectral densities at the transition frequency take the following forms:

$$J_{3,ab}(\omega_{\Gamma\Gamma'}) = \left[\int_0^{\Omega} d\omega_1 \int_{\Omega-\omega_1}^{\omega_M} d\omega_2 + \int_{\Omega}^{\omega_M} d\omega_1 \int_0^{\Omega+\omega_M-\omega_1} d\omega_2\right]$$

$$\times S_{3,ab}(\omega_1, \omega_2, \omega_3 = \omega_{\Gamma\Gamma'} - \omega_1 - \omega_2), \tag{3.99}$$

$$J_{4,ab}(\omega_{\Gamma\Gamma'}) = \Big[\int_0^{\Omega} d\omega_1 \Big(\int_{\Omega-\omega_1}^{\omega_M} d\omega_2 \int_0^{\Omega+\omega_M-\omega_1-\omega_2} d\omega_3 + \int_0^{\Omega-\omega_1} d\omega_2 \int_{\Omega-\omega_1-\omega_2}^{\omega_M} d\omega_3\Big) + \int_{\Omega}^{\omega_M} d\omega_1 \int_0^{\Omega+\omega_M-\omega_1} d\omega_2 \int_0^{\Omega+\omega_M-\omega_1-\omega_2} d\omega_3\Big] \times S_{4,ab}(\omega_1, \omega_2, \omega_3, \omega_{\Gamma\Gamma'} - \omega_1 - \omega_2 - \omega_3). \tag{3.100}$$

If $\omega_{\Gamma\Gamma'} = 2\omega_M + \Omega (0 < \Omega < \omega_M)$, the three-phonon spectral density can be obtained from Eq. (3.97), and the four-phonon spectral density has the following form:

$$J_{4,ab}(\omega_{\Gamma\Gamma'}) = \Big[\int_0^{\Omega} d\omega_1 \int_{\Omega-\omega_1}^{\omega_M} d\omega_2 \int_{\Omega+\omega_M-\omega_1-\omega_2}^{\omega_M} d\omega_3 + \int_{\Omega}^{\omega_M} d\omega_1 \times \Big(\int_0^{\Omega+\omega_M-\omega_1} d\omega_2 \int_{\Omega+\omega_M-\omega_1-\omega_2}^{\omega_M} d\omega_3 + \int_{\Omega+\omega_M-\omega_1}^{\omega_M} d\omega_2 \int_0^{\Omega+2\omega_M-\omega_1-\omega_2} d\omega_3\Big)\Big] \times S_{4,ab}(\omega_1, \omega_2, \omega_3, \omega_4 = \omega_{\Gamma\Gamma'} - \omega_1 - \omega_2 - \omega_3). \tag{3.101}$$

The five-phonon process can play a dominant role when $\omega_{\Gamma\Gamma'} = 3\omega_M + \Omega$ ($0 < \Omega < \omega_M$), the corresponding spectral density

$$J_{5,ab}(\omega_{\Gamma\Gamma'}) = \Big\{\int_0^{\Omega} d\omega_1 \int_{\Omega-\omega_1}^{\omega_M} d\omega_2 \int_{\Omega+\omega_M-\omega_1-\omega_2}^{\omega_M} d\omega_3 \int_{\Omega+2\omega_M-\omega_1-\omega_2-\omega_3}^{\omega_M} d\omega_4 + \int_{\Omega}^{\omega_M} d\omega_1 \Big[\int_0^{\Omega+\omega_M-\omega_1} d\omega_2 \int_{\Omega+\omega_M-\omega_1-\omega_2}^{\omega_M} d\omega_3 \int_{\Omega+2\omega_M-\omega_1-\omega_2-\omega_3}^{\omega_M} d\omega_4 + \int_{\Omega+\omega_M-\omega_1}^{\omega_M} d\omega_2 \Big(\int_0^{\Omega+2\omega_M-\omega_1-\omega_2} d\omega_3 \int_{\Omega+2\omega-\omega_1-\omega_2-\omega_3}^{\omega_M} d\omega_4 + \int_{\Omega+2\omega_M-\omega_1-\omega_2}^{\omega_M} d\omega_3 \int_0^{\Omega+3\omega_M-\omega_1-\omega_2-\omega_3} d\omega_4\Big)\Big]\Big\} \times S_{5,ab}(\omega_1, \omega_2, \omega_3, \omega_4, \omega_5 = \omega_{\Gamma\Gamma'} - \omega_1 - \omega_2 - \omega_3 - \omega_4). \tag{3.102}$$

The transition probability (see Eq. (3.96)) contains a number of terms (for example, in a case of the 4-phonon process in the rare earth ion interacting with eight ligand ions, we have to calculate 120^2 convolutions determined in Eq. (3.101)), and the question remains why experimental data on multiphonon relaxation rates in different lanthanide ions, at least in the fixed host crystal lattice and in the limited range of energy gaps, can be nicely fitted by a single exponential gap law (Ermeneux et al., 2000). An answer may be obtained from the following considerations that allow to simplify the general expression Eq. (3.96). Each term in the Hamiltonian of electron-phonon interaction contains relative displacements of the fixed ligand ion and the rare earth ion. Correspondingly, in the framework of the first order perturbation theory, the

transition probability contains only products of the positive spectral densities of autocorrelation functions $g_{\alpha\beta}(Ls, Ls \mid \omega)$ or products of spectral densities of correlation functions for two different ligand ions ($Ls \neq L's'$) with alternating signs that satisfy the inequality $g_{\alpha\beta}(Ls, L's' \mid \omega) < g_{\alpha\beta}(Ls, Ls \mid \omega)$. Thus, it is possible, at least in the case of a large enough order n of a relaxation process, to neglect nondiagonal (in respect to ligand labels) elements of the matrix $J_{n,ab}(Ls, L's' \mid \omega)$. The next simplifying step may be done by neglecting nondiagonal elements in the blocks $J_{n,ab}(Ls, Ls \mid \omega)$. We restrict our attention to the spontaneous multiphonon relaxation. Then, we can approximate the transition probability by the expression

$$W^{(n)}_{\Gamma\to\Gamma''} = \frac{2\pi}{\hbar^2}\frac{1}{n!}\langle V^{(n)2}_{\Gamma\Gamma''}\rangle_{Av} Sp\left[\left(\frac{\hbar}{\pi}\right)^n \boldsymbol{J}_n(\omega_{\Gamma\Gamma''})\right], \tag{3.103}$$

where the mean square value of coupling constants is defined through the scalar product

$$\boldsymbol{V}^{(n)}_{\Gamma\Gamma''} \cdot \boldsymbol{V}^{(n)+}_{\Gamma\Gamma''} = D_n \langle \boldsymbol{V}^{(n)2}_{\Gamma\Gamma''}\rangle_{Av}. \tag{3.104}$$

As we shall see below (see Section 3.7.1), the dependence of the lattice factor in Eq. (3.103) on the energy gap $\omega_{\Gamma\Gamma''}$ really can be approximated in the fixed crystal by a single exponential function.

The traces of the matrices Eq. (3.95) of the symmetrized products of phonon spectral densities $S_{n,ab}(Ls, Ls \mid \omega_1, \cdots, \omega_n)$ can be expressed through the invariant forms of one-phonon spectral densities $g_{\alpha\beta}(Ls, Ls \mid \omega) = g_{L,\alpha\beta}(\omega)$. In particular, for $n = 1, \cdots, 5$, we define

$$g_{L,1}(\omega) = g_{L,xx}(\omega) + g_{L,yy}(\omega) + g_{L,zz}(\omega)$$

(the spectral density of the scalar product of relative displacements between the rare earth ion and a ligand L),

$$\begin{aligned}
g_{L,2}(\omega_1, \omega_2) &= g_{L,xy}(\omega_1) g_{L,yx}(\omega_2) + g_{L,xz}(\omega_1) g_{L,zx}(\omega_2) \\
&\quad + g_{L,yz}(\omega_1) g_{L,zy}(\omega_2); \\
g_{L,3}(\omega_1, \omega_2, \omega_3) &= g_{L,xy}(\omega_1) g_{L,yz}(\omega_2) g_{L,zx}(\omega_3) \\
&\quad + g_{L,xz}(\omega_1) g_{L,zy}(\omega_2) g_{L,yx}(\omega_3); \\
g_{L,4}(\omega_1, \omega_2, \omega_3, \omega_4) &= g_{L,xy}(\omega_1) g_{L,yx}(\omega_2) [g_{L,yz}(\omega_3) g_{L,zy}(\omega_4) \\
&\quad + g_{L,xz}(\omega_3) g_{L,zx}(\omega_4)] \\
&\quad + g_{L,yz}(\omega_1) g_{L,zy}(\omega_2) g_{L,xz}(\omega_3) g_{L,xz}(\omega_4).
\end{aligned}$$

Traces of correlators that are necessary to evaluate transition probabilities of n-phonon processes ($n=2, \cdots, 5$) equal

$$
\begin{aligned}
Sp\boldsymbol{J}_2(\omega) &= \sum_{L=1}^{L_0} \iint \delta(\omega-\omega_1-\omega_2)[g_{L,1}(\omega_1)g_{L,1}(\omega_2) \\
&\quad + 2g_{L,2}(\omega_1,\omega_2)]\,\mathrm{d}\omega_1\mathrm{d}\omega_2; \\
Sp\boldsymbol{J}_3(\omega) &= \sum_{L=1}^{L_0} \iiint \delta(\omega-\omega_1-\omega_2-\omega_3)[g_{L,1}(\omega_1)g_{L,1}(\omega_2)g_{L,1}(\omega_3) \\
&\quad + 6g_{L,1}(\omega_1)g_{L,2}(\omega_2,\omega_3) \\
&\quad + 6g_{L,3}(\omega_1,\omega_2,\omega_3)]\,\mathrm{d}\omega_1\mathrm{d}\omega_2\mathrm{d}\omega_3; \\
Sp\boldsymbol{J}_4(\omega) &= \sum_{L=1}^{L_0} \iiiint \delta(\omega-\omega_1-\omega_2-\omega_3-\omega_4) \\
&\quad \times [g_{L,1}(\omega_1)g_{L,1}(\omega_2)g_{L,1}(\omega_3)g_{L,1}(\omega_4) \\
&\quad + 6g_{L,2}(\omega_1,\omega_2)g_{L,2}(\omega_3,\omega_4) + 12g_{L,4}(\omega_1,\omega_2,\omega_3,\omega_4) \\
&\quad + 12g_{L,1}(\omega_1)g_{L,1}(\omega_2)g_{L,2}(\omega_3,\omega_4) \\
&\quad + 24g_{L,1}(\omega_1)g_{L,3}(\omega_2,\omega_3,\omega_4)]\,\mathrm{d}\omega_1\mathrm{d}\omega_2\mathrm{d}\omega_3\mathrm{d}\omega_4; \\
Sp\boldsymbol{J}_5(\omega) &= \sum_{L=1}^{L_0} \iiiiint \delta(\omega-\omega_1-\omega_2-\omega_3-\omega_4-\omega_5) \\
&\quad \times [g_{L,1}(\omega_1)g_{L,1}(\omega_2)g_{L,1}(\omega_3)g_{L,1}(\omega_4)g_{L,1}(\omega_5) \\
&\quad + 20g_{L,1}(\omega_1)g_{L,1}(\omega_2)g_{L,1}(\omega_3)g_{L,2}(\omega_4,\omega_5) \\
&\quad + 30g_{L,1}(\omega_1)g_{L,2}(\omega_2,\omega_3)g_{L,2}(\omega_4,\omega_5) \\
&\quad + 60g_{L,1}(\omega_1)g_{L,4}(\omega_2,\omega_3,\omega_4,\omega_5) \\
&\quad + 60g_{L,1}(\omega_1)g_{L,1}(\omega_2)g_{L,3}(\omega_3,\omega_4,\omega_5) \\
&\quad + 60g_{L,2}(\omega_1,\omega_2)g_{L,3}(\omega_3,\omega_4,\omega_5)]\,\mathrm{d}\omega_1\mathrm{d}\omega_2\mathrm{d}\omega_3\mathrm{d}\omega_4\mathrm{d}\omega_5.
\end{aligned}
$$

Examples of simulations of multiphonon transition rates in the frameworks of linear and nonlinear theories of the ion-lattice interaction are given in Section 3.7.1.

It should be noted that all explicit expressions for the relaxation rates presented above are obtained under the assumption that lattice correlation times are short enough, and the isolated excited rare earth ion interacts with the equilibrium phonon subsystem. At high excitation level and finite concentration of optical centers, a bottleneck effect in the relaxation of the excited lattice modes coupled to the optical centers may reduce the non-radiative decay probabilities. Auzel and Pelle (1997) have found a remarkable influence of the excitation density on the multiphonon transition rates in a rare earth doped germanate glass due to the local spatial saturation of the lattice modes. In this case the single ion approximation is not valid, but the study of the cooperative behaviour of the excited rare earth ions is beyond the scope of this review.

3.7 Vibrational Structure of the Optical Spectra

Lanthanide ions in solids interact with two bosonic fields of photons and phonons. Along with pure nonradiative and radiative transitions considered above and in Chapter 2 of this book, respectively, electron – vibrational transitions that induce changes in populations of electronic, lattice and electromagnetic field states may be of primarily interest when interpreting spectral properties and dynamical phenomena in activated crystals. We consider first the vibronic sidebands in the f – f spectra. Lattice vibrations may induce crystal field changes of odd and even parity. In the f – f spectra, the odd components of the electron-phonon interaction induce forced electric dipole vibronic transitions (VanVleck mechanism of electron-vibrational transitions), and the even components of the dynamical crystal field are responsible for magnetic dipole vibronic transitions, or, in absense of inversion symmetry, for electric dipole transitions as well (Herzberg-Teller mechanism). The forced electric dipole transitions induced by nonadiabatic terms in the Hamiltonian of the ion-lattice interaction are known as a result of M-process, phonon replicas due to relative shifts in the equilibrium positions of lattice normal coordinates in the lanthanide ion states involved in the optical transition are known as a result of Δ-process. The intensity of the Franck-Condon replicas induced by adiabatic phonons is determined by the m-th power of the spectral density $D_{\Gamma\Gamma'}(\omega)/\omega^2$ of the Huang-Rhys parameter (see Eq. (3.68)), m gives the number of phonons involved. The Huang-Rhys parameter in f – f transitions is very small, and usually only one-phonon transitions dominate in the vibronic sidebands in the intraconfigurational spectra.

Neglecting effects due to finite lifetimes of electronic and lattice excited states, the spectral distribution of the radiation corresponding to the double-quantum transitions between the crystal field energy levels Γ and Γ' that involve the spontaneous emission of a photon at the frequency Ω with the simultaneous emission or absorption of a phonon with the frequency $\omega = |\omega_{\Gamma\Gamma'} - \Omega|$ can be written as (in the case of absorption of a photon, the spectral distribution may be easily obtained by changing some signs in expressions given below)

$$I_{\Gamma\Gamma'}(\Omega) = W^{-}_{\Gamma\Gamma'}(\omega_{\Gamma\Gamma'} - \Omega)\,\theta(\omega_{\Gamma\Gamma'} - \Omega) + W^{+}_{\Gamma\Gamma'}(\Omega - \omega_{\Gamma\Gamma'})\,\theta(\Omega - \omega_{\Gamma\Gamma'}), \tag{3.105}$$

where probabilities of the one-phonon radiative transitions are given by the following formulae (Malkin, 1963b, 1965)

$$W^{\pm}_{\Gamma\Gamma'}(\omega) = \frac{4(\omega_{\Gamma\Gamma'} \pm \omega)^3}{3\hbar c^3} A^{\pm}(\omega), \tag{3.106}$$

$$A^{\pm}(\omega) = \frac{\hbar}{\pi}\left[n(\omega) + \frac{1}{2} \mp \frac{1}{2}\right] \sum_{LsL's'\alpha\beta\delta} \sigma_{\alpha,\delta}^{\pm\Gamma\Gamma''}(Ls \mid \omega)\, \sigma_{\beta,\delta}^{\pm\Gamma\Gamma''*} \times (L's' \mid \omega)\, g_{\alpha\beta}(Ls, L's' \mid \omega), \tag{3.107}$$

$$\sigma_{\alpha,\delta}^{\pm\Gamma\Gamma''}(Ls \mid \omega) = \sum_{\Gamma''} \left[\frac{\langle\Gamma' \mid V_\alpha(Ls) \mid \Gamma''\rangle\langle\Gamma'' \mid d_\delta \mid \Gamma\rangle}{\Delta(\Gamma', \Gamma'') \mp \hbar\omega + i\gamma_{\Gamma''}} + \frac{\langle\Gamma' \mid d_\delta \mid \Gamma''\rangle\langle\Gamma'' \mid V_\alpha(Ls) \mid \Gamma\rangle}{\Delta(\Gamma, \Gamma'') \pm \hbar\omega + i\gamma_{\Gamma''}}\right]. \tag{3.108}$$

where $\gamma_{\Gamma''}$ is the inverse lifetime of the intermediate ion state Γ'', and d_δ is the component of the effective electric or magnetic dipole moment of the rare earth ion. Additional factors in the transition probability Eq. (3.106) caused by the difference between local and macroscopic electric or magnetic components of the radiation field in a crystal (Aminov et al., 1986) are dropped.

If we study optical intraconfigurational $4f^n - 4f^n$ electric dipole transitions, we have to consider states of opposite parity ($4f^{n-1}5d$, in particular) as the intermediate states of the two-quantum transition in the sums (see Eq. (3.108)). In this case, we can neglect phonon frequencies in the denominators, and the spectral distribution of the one-phonon sideband presents a sum of weighted spectral distributions of the displacement-displacement correlation functions. To get a correct description of vibronic sidebands, it is essential to have a reasonable approximation for the Green's function of the real crystal. The problem of the one-phonon sideband shape was formulated in terms of Green's functions by Buchanan and Woll (1969) in the analysis of the Sm^{2+} f – f spectra in alkali halides. In computer simulations, we can proceed directly with the Eq. (3.107) using Green's functions in the site representation, but it may be more convenient to use the Hamiltonian of the electron-phonon interaction expanded in powers of linear combinations $Q_\lambda(\Gamma_\alpha)$ of ligand ion displacements that transform according to the row λ of the irreducible representation Γ of the point symmetry group (if this symmetry is high enough). It should be noted that, in a general case, the spectral distributions of correlation functions $\langle Q_\lambda(\Gamma_\alpha \mid t)\, Q_\lambda(\Gamma_\beta \mid 0)\rangle$ that determine the structure of vibronic sidebands and correspond to odd irreducible representations of the cubic group, for example, are not the same distributions (corresponding to even irreducible representations) that determine phonon-induced line shifts and relaxation rates. It should be emphasized that in a general case no correlations between positions of peaks in the vibronic structure, that resembles peculiarities in the projected phonon densities, and frequencies of vibrations with the zero wave-vector, active in Raman and infrared absorption lattice spectra, exist. Search for such correlations is approved only if the dispersion of phonon branches is very narrow, in general, it may bring about misleading results (Lupei et al., 1999).

Operators $V_\alpha(Ls)$ in Eq. (3.108) determine changes of the crystal field due to relative displacements of the lanthanide ion and surrounding ions. Values of

corresponding linear coupling constants $B^p_{k,\alpha}(Ls)$ (see Eq. (3.32)) for odd p depend on the intermediate ion state Γ''' involved in matrix elements in Eq. (3.108), and can be obtained in the framework of the exchange charge model with the formulae similar to Eqs. (3.38) – (3.40).

Interaction with photons through the alternating dipoles induced by the radiation field at the host lattice ions (Judd, 1980) becomes important when considering the f – f transitions in absence of the inversion symmetry at the rare earth ion site (see Chapter 2, Section 2.3.8.2). In this case, the operator of the effective electric dipole moment of the rare earth ion contains both odd and even terms, and the vibronic electric dipole transitions may be induced by the even component of the dynamical crystal field.

Vibronic structures of electric dipole and magnetic dipole transitions may be of comparable intensity relative to the zero-phonon line. The ratio I_V between integral intensity of the one-phonon vibronic sideband to the integral intensity of the zero-phonon line can be estimated from the general expressions Eqs. (3.106) – (3.108). For the forced electric dipole f – f transitions, this ratio is determined by $|\partial \ln V/\partial R|^2 (\hbar/m\omega)$, where V is the 4f – 5d matrix element of the odd component of the crystal field, m is the reduced mass of a ligand ion, and ω is the average frequency of the lattice vibrations. For the magnetic dipole f – f transitions, the phonon sidebands can be described with the Eqs. (3.106) – (3.108) as well (with the magnetic dipole moment substituted for the electric dipole moment), and we obtain the same expression for the ratio I_V with V as the matrix element of the even component of the crystal field. Assuming the crystal-field parameter dependences on interion distances as R^{-10}, in both cases the considered ratio has a value of an order of unity. Experimental data for the f – f transitions give the ratio I_V in the range from 0.01 to 2, and in common with the measured lifetimes ($10^{-5} - 10^{-3}$ s), it is possible to estimate the integral vibronic transition probabilities as $10^2 - 10^5$ s^{-1}. In particular, Ellens et al. (1997c) obtained integral intensities of vibronic sidebands of 100 s^{-1} (Pr^{3+}, $^3P_0 - {}^3H_4$) and for Tm^{3+} 250 s^{-1} ($^1D_2 - {}^3F_4$), 650 s^{-1} ($^1D_2 - {}^3H_6$) in emission and excitation spectra in $LiYF_4$, these sidebands resemble the phonon density of states of the perfect lattice. For Tm^{3+} spectra in YOCl, $Na_5La(WO_4)_4$ the ratio I_V for different multiplet-multiplet transitions changes in a wide range of 0.006 – 1.7, and the integrated vibronic transition probabilities were estimated to be 250 – 2500 s^{-1} (Ellens et al., 1996).

Large variation (up to two orders of magnitude) of the vibronic transition probability for the fixed multiplet-multiplet transition (in particular, in the excitation spectrum of Pr^{3+} ($^3H_4 - {}^3P_0$)) is observed in different crystals due to differences in crystal field parameters, and in crystals of the same structure but of different composition due to local lattice deformations induced by the impurity ion (De Mello Donega et al., 1992).

Due to small energy gap between $4f^n$ and $4f^{n-1}5d$ configurations with the opposite parity in divalent lanthanide ions, vibronic sidebands in spectra of

divalent ions are stronger than that in spectra of isoelectronic trivalent ions. Ignat'ev and Ovsyankin (1996a, 1996b) thoroughly studied vibronic sidebands in emission and excitation spectra of Tm^{2+} and Sm^{2+} ions in crystals with the fluorite structure (CaF_2, SrF_2, BaF_2). Only slight deviations from the mirror symmetry in absorption and luminescence were observed. Authors have found that the interaction with odd vibrations is primarily determined by short-range interactions with neighboring fluorine ions, but the long-range Coulomb coupling is responsible for vibronic structure of magnetic dipole transitions that is formed by even vibrations. The ratio $I_V = 3.65 \pm 0.5$ is approximately the same in the spectra of Tm^{2+} in all crystals and agrees with the results of calculations by Voron' ko et al. (1976) carried out in the framework of the exchange charge model.

Calculations of integrated intensities of vibronic intermultiplet transitions for the isoelectronic lanthanide ions ($^6P_{7/2} - {}^8S_{7/2}$ transitions in Eu^{2+} and Gd^{3+}, $^5D_0 - {}^7F_2$ transitions in Sm^{2+} and Eu^{3+}), performed by Campos et al. (2000), have demonstrated the stronger effective electron-phonon coupling in divalent ions in fluoride host lattices ($LiYF_4$ and $LiBaF_3$). These calculations accounting for static and dynamic mechanisms of radiative f-f transitions (see Chapter 2) reproduced also successfully the experimental trend of the ion-lattice coupling strength through the lanthanide trivalent ion series: stronger in the beginning (Pr^{3+}) and the end of the series (Tm^{3+}) and weaker at the center (Gd^{3+}, Eu^{3+} in $LiYF_4$, YOCl and $Na_5La(WO_4)_4$ host crystals). However, we have to distinguish real and effective strengths of the electron-phonon interaction. A comparison of the effective coupling constants used to describe data of measurements and obtained from fitting procedures based on the simplified formulae may bring about misleading conclusions in discussions of the relations between coupling constants in different hosts and lanthanide ions. The weak intensity of vibronic sidebands of magnetic dipole transitions in the spectra of Eu^{3+} ($J = 0 - J' = 0, 1$) and Gd^{3+} ($L = 0 - L' = 1$), as compared with that of vibronic sidebands in the spectra of lanthanide ions at the beginning and the end of the lanthanide series has been already explained by Ignat'ev and Ovsyankin (1983) as a result of a suppression of the dynamical odd crystal field effect due to selection rules for the effective even multipole moments representing the combined action of photons and phonons.

The more detailed information about phonon modes active in the formation of spectral sidebands in optical spectra of rare earth ions, especially in sites with high point symmetry, may be obtained when studying morphic effects on vibrational structure due to lowering of symmetry in external fields. Induced changes of the selection rules, of the equilibrium positions of the lattice ions cause changes in the shape of the vibronic bands. For example, from the polarized spectra in the external magnetic field, the symmetry of active vibrations in the f – f and f – d spectra of Sm^{2+}, Eu^{2+} in SrF_2 was determined by Cohen and Guggenheim (1968). The relative intensities of vibronic lines with different polarization properties may be used to obtain information on dynamical

interactions between the rare earth ion and ligand ions.

During last years, parity allowed 4f – 5d spectra and electronic relaxation in the $4f^{n-1}$ – 5d manifold are widely studied (van Pieterson et al., 2002a, 2002b), the renewed researches are connected with the development of new efficient solid-state emitters in the vacuum ultraviolet spectral range for both laser and scintillation techniques. Due to strong electron-phonon interaction in the 5d state, the 4f – 5d spectra consist of broad electron-vibrational bands. The first theoretical analysis of widths of these bands in CaF_2: Ce^{3+} was performed by Perlin et al. (1966) who estimated moments of generating functions for the 4f – 5d transitions in the cubic crystal field and interpreted the fine structure of the spectra as the Franck-Condon replicas of local vibrations.

The shape of interconfigurational $4f^n - 4f^{n-1}5d$ vibrational spectra of alkali halides with impurity Eu^{2+} ($4f^7 - 4f^6 5d$) and Yb^{2+} ($4f^{14} - 4f^{13} 5d$) ions was studied by Wagner and Bron (1965) and Bron and Wagner (1965). Wagner (1964) has shown that if the squared equilibrium displacement of the lattice oscillator due to the electronic transition has a maximum at ω_0, a series of equidistant vibronic lines at $m\omega_0$ appear with the half-widths increasing with the line number m. The series is displaced asymmetrically against the maximum of a continuous background to the low-energy tail in absorption and the high-energy tail in emission. The sharp line vibronic series were observed on the high-energy side of the broad emission bands and the low-energy side of absorption bands in accordance with the theoretical predictions (Wagner, 1964). Long series of sharp vibronic structure are observed at low temperatures. The general finding is that local modes change their frequencies during the electronic transition, but lattice modes are changed only in their equilibrium positions.

3.8 Simulations of the Ion-phonon Interaction Effects

The aim of this section is to present examples of realistic theoretical studies of the relaxation rates in the lanthanide ions in ionic crystals. The lithium-yttrium double fluorides activated by Tm, Ho, Er and Nd, and the Pr-doped cesium-cadmium bromide are selected as model objects of these studies because experimental data on relaxation rates in these crystals are available, and the crystal field effects and the vibrational spectra of the crystal lattices have been investigated earlier. In the case of the homovalent substitution of rare earth ions for Y^{3+} in $LiYF_4$, we can neglect the lattice perturbation. However, in the case of the heterovalent substitution of trivalent rare earth ions for Cd^{2+} ions in $CsCdBr_3$, impurity dimer centers are preferentially formed that essentially change the local structure and dynamics of the lattice. We demonstrate that taking into account these effects is very important to obtain reasonable estimates of relaxation rates. The non-linear mechanism of the electron-phonon interaction (Pukhov and Sakun, 1979) is employed to calculate probabilities of multiphonon nonradiative transitions in the first order of the time-dependent perturbation theory. The

exchange charge model is used to obtain values of coupling constants that determine the electron-phonon interaction similarly to some previously published treatments of this problem (Orlovskii et al., 1995; Basiev et al., 1997), but our approach differs substantially from the all preceding investigations because of avoiding any procedure of averaging over the multiplet states (probabilities of the transitions between the crystal field states are considered), and because the computed phonon spectral densities are used to describe dynamical properties of the real crystal lattices.

3.8.1 Impurity Rare Earth Single Ion Centers in the $LiYF_4$ Crystal

3.8.1.1 Spectral Densities of Correlation Functions of the Ion Displacements

$LiYF_4$ crystals belong to the C_{4h}^6 space group, the lattice constants a = 0.5164 nm, c = 1.0741 nm (T = 295 K, Garcia and Ryan, 1993). Rare earth ions substitute for Y^{3+} ions in sites with the S_4 point symmetry. The nearest surroundings of the Y-site include eight fluorine ions which form two deformed tetrahedra. In the crystallographic system of coordinates with its origin on the rare-earth ion, ligand coordinates are (x_k, y_k, z_k), $(-x_k, -y_k, z_k)$, $(y_k, -x_k, -z_k)$, $(-y_k, x_k, -z_k)$, $k = 1, 2$. In the perfect lattice, four fluorine ions are at the distance R_1 = 2.297 nm from the rare earth ion (x_1 = 0.1645a, y_1 = 0.2183a, $z_1 = -0.1687c$), and four other fluorine ions are at the distance R_2 = 2.244 nm ($x_2 = x_1 - 0.5a$, $y_2 = y_1$, $z_2 = -z_1 - 0.25c$).

The vibrational spectrum of the $LiYF_4$ crystal lattice was studied by Salaun et al. (1997a, 1997b). Results of optical and neutron inelastic scattering experiments were described successfully in the framework of the rigid-ion model. The maximum phonon frequency ω_M of this crystal equals 560 cm^{-1}. Using parameters of this model, Popova et al. (2000) computed frequencies and polarization vectors of vibrations for 8870 wave vectors distributed uniformly over the irreducible part of the Brillouin zone. Thus the database corresponding to 36 × 64,000 normal modes of the lattice was obtained. Imaginary parts of the lattice Green's functions Eq. (3.16) were calculated at the equally spaced 1120 points $\omega_f (0 \leqslant \omega_f \leqslant \omega_M)$ on the frequency axis by numerical integration over the Brillouin zone, and real parts were obtained with the Caushy relations. Examples of the calculated spectral densities of the displacement-displacement correlation functions $g_{\alpha\beta}(pk \mid \omega)$ defined in Eq. (3.25) and corresponding to relative displacements of Y^{3+} ion and its nearest neighbors in the perfect $LiYF_4$ crystal lattice ($p, k = 1:8$ are the labels of F^- ligands) are given in Figs. 3.1 and 3.2. It should be noted that the diagonal elements of the matrix $g_{\alpha\alpha}(pp \mid \omega)$ (presented for the two nonequivalent ligands F_1^- and F_5^- in Fig. 3.1) are remarkably larger

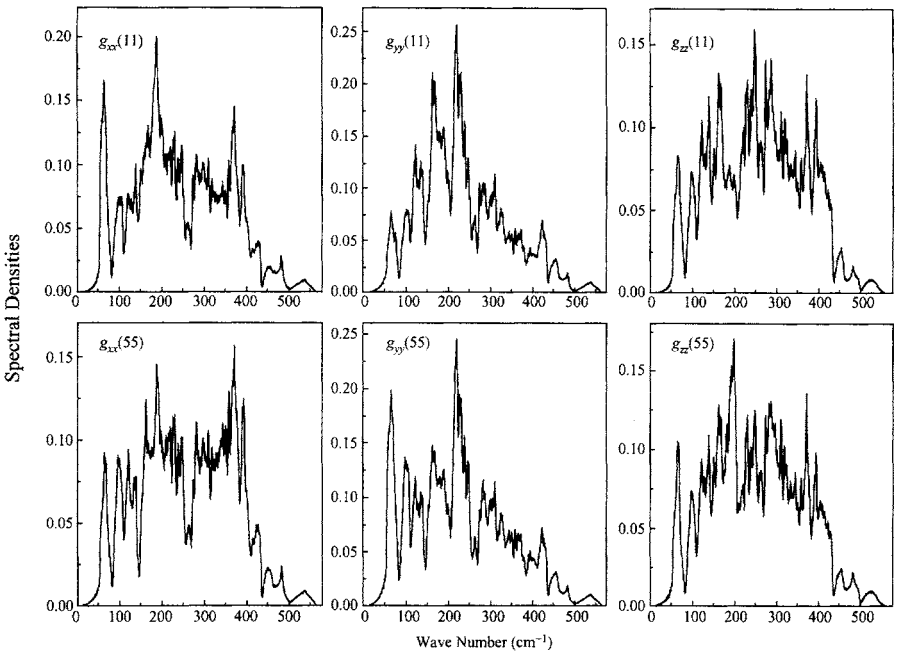


Figure 3.1 Spectral densities of autocorrelation functions of differences between displacements of Y^{3+} ion and its nearest neighbors $F_1^-(x_1, y_1, z_1)$ and $F_5^-(x_2, y_2, z_2)$ in $LiYF_4$ (in units of 0.2121 m^2/J)

than absolute values of the nondiagonal elements corresponding to different ligands (see Fig. 3.2). As a consequence of this fact, one may expect that elements $J_{n,ab}(Ls, Ls \mid \omega)$ of the diagonal blocks of the multiphonon correlation functions Eq. (3.94) are substantially larger than elements of nondiagonal blocks $J_{n,ab}(Ls, L's' \mid \omega)$ with $Ls \neq L's'$. The matrices of multiphonon spectral densities $\boldsymbol{J}_n(\omega)$ in the space of relative displacements of ions within the complex containing the Y^{3+} ion and its eight ligands for $n = 2, 3, 4, 5$ with dimensions of $4(n+1)(n+2)$ were simulated as functions of a discrete variable $\omega = \omega_f (f = 1:1120)$. The calculated dependences of dimensionless traces of symmetrized correlators $Sp[\alpha_n \boldsymbol{J}_n(\omega)]$ (where $\alpha_n = [\hbar/(\pi \text{Å}^2)]^n/\delta t$ and $\delta t = 1$ second) on the frequency ω are given as the semilogarithmic plot in Fig. 3.3. This plot shows that the multiphonon spectral densities $Sp[\alpha_n \boldsymbol{J}_n(\omega)]$ have maximum values at the frequencies $\omega = n\omega_{\text{eff}}$, and the frequency $\omega_{\text{eff}} = 225$ cm^{-1} can be considered as the frequency of the most effective lattice vibration; it should be noted that ω_{eff} is much smaller than the maximum phonon frequency $\omega_M = 560$ cm^{-1}. The curves $Sp[\alpha_n \boldsymbol{J}_n(\omega)]$ and $Sp[\alpha_{n+1} \boldsymbol{J}_{n+1}(\omega)]$ intersect at the points $\omega_{n,n+1}$ that equal 990 cm^{-1} ($n = 2$), 1400 cm^{-1} ($n = 3$) and 1800 cm^{-1} ($n = 4$). Beginning from the value of the energy gap $\hbar\omega_{\Gamma\Gamma'} > \hbar\omega_{n,n+1}$, the contribution of the $(n+1)$-

phonon process definitely dominates in the corresponding nonradiative transition $\Gamma \rightarrow \Gamma'$. Such a process becomes the most effective one at the gap value essentially less than $n\omega_M$.

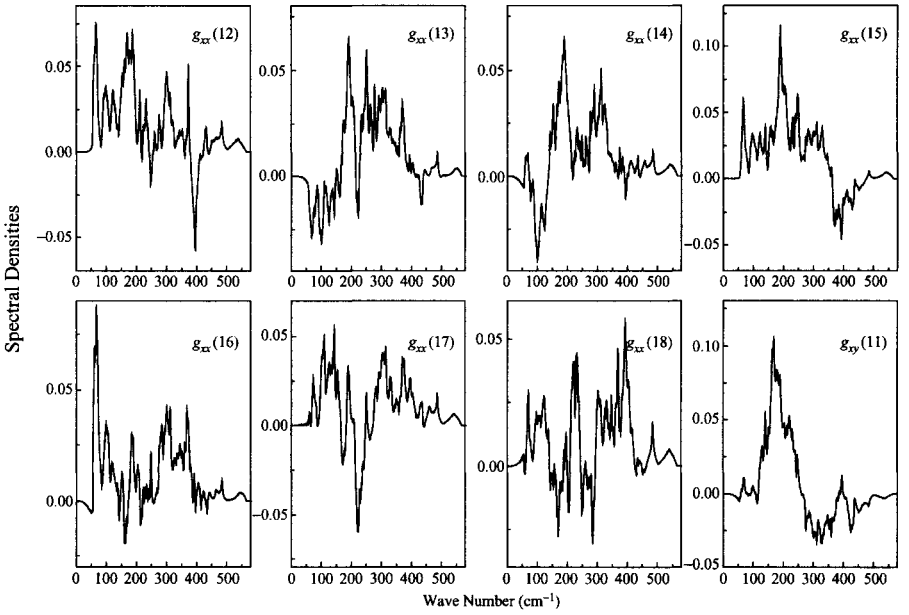


Figure 3.2 Spectral densities of nondiagonal correlation functions of differences between displacements of Y^{3+} ion and its nearest neighbors in $LiYF_4$ (in units of 0.2121 m^2/J). Ligand coordinates equal (see also Fig. 3.1): $F_2^-(-x_1, -y_1, z_1)$, $F_3^-(-y_1, x_1, -z_1)$, $F^{-4}(y_1, -x_1, -z_1)$, $F_6^-(-y_2, x_2, -z_2)$, $F_7^-(y_2, -x_2, -z_2)$, $F_8^-(-x_2, -y_2, z_2)$

The direct line AB in Fig. 3.3 presents an approximation of a common tangent to curves $\log_{10}[Sp\alpha_n J_n(\omega)]$. This line may serve as a good approximation for the dependence of the multiphonon spectral density on a gap $\hbar\omega$ between electronic states in the case of the spontaneous phonon emission.

3.8.1.2 Relaxation Broadening of Spectral Lines and Multiphonon Relaxation

The Hamiltonian of Eq. (3.30) of rare earth ions in the static crystal field of S_4 symmetry is specified by seven independent parameters B_0^2, B_0^4, Re B_4^4, Im B_4^4, B_0^6, Re B_4^6, Im B_4^6. Values of the crystal field parameters obtained by different authors from fitting the eigenvalues of the Hamiltonian of Eq. (3.29) to the measured frequencies of radiative transitions in the optical spectra of impurity Nd^{3+}, Ho^{3+}, Er^{3+} and Tm^{3+} ions are presented in Table 3.2. It should be noted that

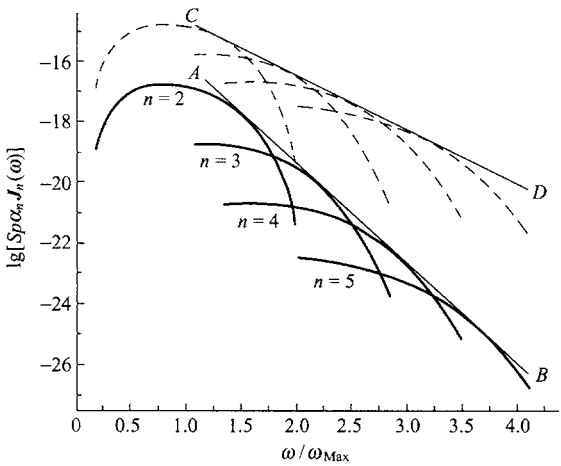


Figure 3.3 Simulated traces (solid curves) of the n-phonon spectral density matrices at zero temperature in $LiYF_4$ with the maximum phonon frequency ω_{Max} = 560 cm^{-1}. The dotted curves present the same traces with the additional factors 10^n

analysis of the experimental spectra gives only three constraints on the four parameters ReB_k^p and ImB_k^p with $k = 4$; and the total set of crystal field parameters, corresponding to the crystallographic system of coordinates, has been determined only for the neodymium doped $LiYF_4$ by De Leebeeck et al. (1999) from the polarized absorption and magnetic circular dichroism spectra.

The crystal field energy levels are labeled according to the corresponding irreducible representations of the S_4 point symmetry group. Multiplets of the electronic $4f^n$ shell of a non-Kramers ion (n is an even number) split into singlets Γ_1, Γ_2 and doublets Γ_{34}, energy levels of Kramers ions are Γ_{56} and Γ_{78} doublets. Dynamical perturbations of the crystal field can be also classified by their symmetry properties (as it has been already fulfilled for the electron-deformational interaction in Section 3.2.). The electron-phonon interaction that involves, similarly to the crystal field Hamiltonian, the electronic operators $C_k^{(p)}$ with $k = 0, \pm 4$ corresponds to the identical irreducible representation $\Gamma_1(A_g)$ of the S_4 group (the corresponding irreducible representation of the lattice C_{4h} factor group is given in brackets), it induces transitions between the electronic states with the same symmetry properties ($\Gamma_i \rightarrow \Gamma_i$). The rhombic part of the electron-phonon interaction, that corresponds to the $\Gamma_2(B_g)$ representation and involves eight electronic operators $C_k^{(p)}$ with $k = \pm 2, \pm 6$, allows transitions of the type $\Gamma_1 \leftrightarrow \Gamma_2$, $\Gamma_{34} \leftrightarrow \Gamma_{34}$, $\Gamma_{56} \leftrightarrow \Gamma_{78}$. The electron-phonon interaction expressed through the twelve electronic operators $C_k^{(p)}$ with $k = \pm 1, \pm 3, \pm 5$ corresponds to the $\Gamma_{34}(E_g)$ representation and induces transitions $\Gamma_1 \leftrightarrow \Gamma_{34}$, $\Gamma_2 \leftrightarrow \Gamma_{34}$, $\Gamma_{56} \leftrightarrow \Gamma_{56}$, $\Gamma_{56} \leftrightarrow \Gamma_{78}$, $\Gamma_{78} \leftrightarrow \Gamma_{78}$.

Our goal here is to calculate the low temperature relaxation rates of excited

states of impurity rare earth ions on the basis of the known patterns of electronic energy levels and dynamical properties of the crystal lattice considered in the previous subsection. The solution of this task is possible in the framework of the exchange charge model. The crystal field parameters determined from the experimental data are well described by the exchange charge model with the reasonable trends in variations of the model phenomenological parameters G_s, G_σ, G_π (see Table 3.1) along the lanthanide series. The calculated crystal field parameters are compared with the literature data in Table 3.2. It should be noted that calculated values of the B_0^2 parameter contain large contributions from electrostatic fields of point dipoles and quadrupoles induced by the internal electric field at the host lattice ions (Bumagina et al., 1981; Eremin, 1989). The adequate description of the neodymium spectrum has been achieved assuming that the complex including the impurity ion and its nearest eight F^- ions rotates around the S_4 symmetry axis by an angle of 4° and radially expands by 2.2% due to the essential difference between the Nd^{3+} and Y^{3+} ionic radii. The interaction of the localized 4f electrons with the nearest neighbors (eight F^- ions) of the rare earth ion is responsible for the major contributions to the crystal field parameters (these contributions are also presented in Table 3.2). By taking into account interactions of the lanthanide ion with its nearest neighbors only, we can avoid calculations of infinite number of the lattice correlation functions. This greatly simplifying approach is used in what follows. Given parameters of the exchange charge model as determined from the crystal field splittings, it was not a difficult problem to calculate the coupling constants in the Hamiltonian of Eq. (3.31) (from first to fifth order) using the formulae presented in Section 3.2. To obtain the transition probabilities, matrix elements of operators of Eq. (3.32) were calculated with the eigenfunctions of the Hamiltonian of Eq. (3.29) in the total space of 364 $|4f^n\ \gamma LSJJ_z\rangle$ states of $Nd^{3+}(4f^3)$ and $Er^{3+}(4f^{11})$, and of 91 states of $Tm^{3+}(4f^{12})$, the restricted basis of 100 states with the total spin $S=2$ and the orbital angular momenta $L=6$ and $L=3$ was used in the case of $Ho^{3+}(4f^{10})$.

Let us start with the simplest case of the one-phonon transitions. At liquid helium temperatures these spontaneous intramultiplet transitions determine the lower bounds of the linewidths in the optical spectra of rare earth ions.

In Table 3.3 the computed probabilities of the one-phonon transitions within the manifolds of $^4I_{11/2}$ and $^4I_{13/2}$ multiplets, as well as from the first excited sublevels to the lowest sublevel in the ground state ($^4I_{15/2}$) and in the $^4F_{9/2}$ multiplet, of the impurity Er^{3+} ion in $LiYF_4$ are compared with the linewidths measured by Popova et al. (2000) in the high-resolution absorption spectra at the temperature of 5 K and with the dephasing rates of the optical free induction measured at low temperatures by Wannemacher et al. (1989) (see also Chapter 4). Calculations were carried out according to the Eq. (3.73) using model parameters given in Table 3.1 and phonon spectral densities of the perfect lattice (the mass defect perturbation of the lattice due to the substitution of Er^{3+} for Y^{3+} induces relatively small (up to 10%) increase of the one-phonon

Table 3. 3 Measured linewidths in the absorption spectra (Popova et al., 2000, 2001), dephasing rates and calculated one-phonon transition probabilities in $LiYF_4$: Er^{3+} and $CsCdBr_3$: Pr^{3+} ($T = 5$ K)

Multiplet, crystal-field level		E (cm^{-1})	Gap (cm^{-1})	W($\times 10^{10}$ s^{-1})	
				experiment	theory
1		2	3	4	5
			$LiYF_4$: Er^{3+}		
$^4F_{9/2}$	$\Gamma_{56}^{(1)}$	15,324	17	0.008[a]	0.014
	$\Gamma_{78}^{(1)}$	15,307	0	–	–
$^4I_{11/2}$	$\Gamma_{78}^{(3)}$	10,312	6, 17, 35, 80, 94	0.35	0.30
	$\Gamma_{78}^{(2)}$	10,306	11, 29, 74, 88	0.76	0.41
	$\Gamma_{56}^{(3)}$	10,295	18, 63, 77	0.21	0.44
	$\Gamma_{56}^{(2)}$	10,277	45, 59	0.20	0.76
	$\Gamma_{56}^{(1)}$	10,232	14	0.018	0.007
	$\Gamma_{78}^{(1)}$	10,218	0	0.016	–
$^4I_{13/2}$	$\Gamma_{56}^{(4)}$	6738	14, 42, 66, 159, 200, 204	7.0	6.22
	$\Gamma_{78}^{(3)}$	6724	28, 52, 145, 186, 190	2.7	2.58
	$\Gamma_{56}^{(3)}$	6696	24, 117, 158, 162	2.5	4.11
	$\Gamma_{78}^{(2)}$	6672	93, 134, 138	2.0	2.89
	$\Gamma_{56}^{(2)}$	6579	41, 45	0.07	0.10
	$\Gamma_{56}^{(1)}$	6538	4	0.017	0.0003
	$\Gamma_{78}^{(1)}$	6534	0	0.015	–
$^4I_{15/2}$	$\Gamma_{78}^{(2)}$	28	11, 28	0.032[a]	0.069
	$\Gamma_{78}^{(1)}$	17	17	0.005[a]	0.014
	$\Gamma_{56}^{(1)}$	0	0	0	0
			$CsCdBr_3$: Pr^{3+}		
$^3F_3$	$\Gamma_2^{(2)}$	6526	23, 30, 43, 53	–	57.0
	$\Gamma_3^{(2)}$	6503	7, 20, 30	5.85	4.2
	Γ_1	6496	13, 23	3.20	0.80
	$\Gamma_3^{(1)}$	6483	10	0.75[c]	0.13
	$\Gamma_2^{(1)}$	6473	0	–	0
$^3F_2$	Γ_1	5153	5, 80	52.8	30.9
	$\Gamma_3^{(2)}$	5148	75	–	19.4
	$\Gamma_3^{(1)}$	5073	0	0.94[c] (1.32[b])	0
$^3H_5$	$\Gamma_3^{(4)}$	2620[d]	27, 73, 288, 303, 359, 385	–	52.0
	$\Gamma_2^{(2)}$	2593[d]	46, 261, 276, 332, 358	–	77.5
	$\Gamma_3^{(3)}$	2547	215, 230, 286, 312	13.2	18.2[e]
	Γ_1	2332	15, 71, 97	62.2	48.7
	$\Gamma_3^{(2)}$	2317	56, 82	56.6	116.4
	$\Gamma_3^{(1)}$	2261	26	5.65(6.4[b])	1.9
	$\Gamma_2^{(1)}$	2235	0	0.94[c]	0

(a) dephasing rate $2/T_2$ (Wannemacher et al., 1989);
(b) total width of the unresolved hyperfine structure;
(c) inhomogeneous width;
(d) calculated crystal field energy;
(e) two-phonon relaxation rate.

relaxation rates). For each crystal field sublevel, the sum of transition probabilities to all lower sublevels and the corresponding gaps are presented. It is seen that despite many simplifying approximations, there is a good correlation between the experimental data and the estimated relaxation rates (up to a factor of 3).

Once the model (specifically, values of the linear coupling constants) has been approved with some degree of certainty, we can consider more complicated multiphonon nonradiative transitions. Experimental data on multiphonon relaxation rates in metastable states of impurity rare earth ions in $LiYF_4$ corresponding to gaps that are bridged by phonons in the range from 1000 to 2000 cm^{-1} (from 1.8 to 3.6 ω_M) are collected in Table 3.4 (volumn 6). Results of calculations of probabilities $W^{(n)}_{\Gamma\to\Gamma'}$ of spontaneous 2-, 3-, 4- and 5-phonon transitions between the crystal field sublevels (see volumn 2 in Table 3.4) of Nd^{3+}, Er^{3+}, Tm^{3+} and Ho^{3+} are given in column 4, and the total relaxation rate that may be compared with the measured lifetime of the corresponding upper sublevel is presented in column 5. Because the available from literature experimental data were taken mainly at the nitrogen temperature, the relaxation rates were calculated not only for the lowest sublevel of the upper multiplet, but also for some excited sublevels that might be populated. All calculations were carried out in accordance with Eq. (3.96) in the framework of approximations introduced above using the model parameters from Table 3.1 and simulated spectral densities of the lattice correlation functions.

A comparison of calculated and measured relaxation rates shows that there is a good agreement only for small enough energy gaps ($\omega_{\Gamma\Gamma'} \leqslant 2.8\omega_M$) if the processes that involve no more than five phonons are considered. On no account can the order of the most effective process be estimated from the ratio between the gap and the maximum phonon frequency. In particular, in the case of $^4G_{5/2}\rightarrow {}^2H_{11/2}$ nonradiative transition in Nd^{3+} ($\omega_{\Gamma\Gamma'} \leqslant 1.9\omega_M$), the two-phonon processes are allowed, but the corresponding probability is about an order of magnitude less than the probability of the three phonon transition. Similarly, in the case of nonradiative relaxation of the $^4F_{5/2}$ multiplet of Er^{3+} ion ($\omega_{\Gamma\Gamma'} \geqslant 2.83\omega_M$) and of the $^3F_3$ multiplet of Tm^{3+} ion ($\omega_{\Gamma\Gamma'} \geqslant 2.81\omega_M$), three-phonon transitions to the crystal field states of the nearest $^4F_{7/2}$ and $^3H_4$ multiplets, respectively, are possible, but the transition probabilities of these processes are much less than probabilities of the four-phonon transitions (see Table 3.4).

Calculated values of the transition rates as compared with the measured lifetimes of the excited states are underestimated up to two orders of magnitude if the gap exceeds $3.3\omega_M$. The disagreement is too large to be related to possible errors in estimations of coupling constants, processes involving emission of five and even six phonons are to be accounted for to obtain reasonable theoretical description of relaxation rates in the range of $10^4 - 10^6\ s^{-1}$. The harmonic approximation is likely to be invalid when the lattice excitation involves creation of more than three phonons, however, so far no detailed study of lattice anharmonicity effects in the theory of multiphonon relaxation has been carried out.

Table 3.4 Multiphonon relaxation rates in rare earth-doped $LiYF_4$ crystals

Ion References	Transition: Initial level Γ — Final level Γ' Symmetry, energy (cm^{-1})[a]	Energy gap (cm^{-1})	Relaxation rate $\sum_{\Gamma'} W_{\Gamma\to\Gamma'}$ (s^{-1}): Theory ($T = 0$ K) — Transition probabilities $W^{(2)} + W^{(3)} + W^{(4)} + W^{(5)}$	Theory ($T = 0$ K) — Total rate	Eperiment (Temperature)
1	2	3	4	5	6
Nd^{3+} (b)	$^4G_{5/2}(\Gamma_{56}\ 17{,}163)\to{}^2H_{11/2}(\Gamma_{56}\ 16{,}147)$	1016	$(0.5+3.4+0.2+0)\times10^7$	10.4×10^7	22.2×10^7 (77 K)
	$^4G_{5/2}(\Gamma_{56}\ 17{,}163)\to{}^2H_{11/2}(\Gamma_{78}\ 16{,}136)$	1027	$(0.4+5.0+0.4+0)\times10^7$		
(c),(d)	$^4G_{7/2}(\Gamma_{78}\ 19{,}072)\to{}^2G_{7/2}(\Gamma_{56}\ 17{,}653)$	1419	$(0+0.1+0.1+0)\times10^7$	7.7×10^7	8.3×10^7 (77 K)
	$^4G_{7/2}(\Gamma_{56}\ 19{,}082)\to{}^2G_{7/2}(\Gamma_{56}\ 17{,}653)$	1429	$(0+1.9+5.8+0)\times10^7$	$[4.6\times10^7]$	11.0×10^7 (300 K)
Er^{3+} (d)	$^4F_{5/2}(\Gamma_{56}\ 22{,}255)\to{}^4F_{7/2}(\Gamma_{78}\ 20{,}671)$	1584	$(0+0.103+10.24+2.3)\times10^5$	0.3×10^7	1.88×10^7 (77 K)
	$^4F_{5/2}(\Gamma_{56}\ 22{,}255)\to{}^4F_{7/2}(\Gamma_{56}\ 20{,}662)$	1593	$(0+0.072+8.42+2.7)\times10^5$	$[0.24\times10^7]$	
	$^4F_{5/2}(\Gamma_{56}\ 22{,}255)\to{}^4F_{7/2}(\Gamma_{78}\ 20{,}573)$	1682	$(0+0+1.66+0.9)\times10^5$		
	$^4F_{5/2}(\Gamma_{56}\ 22{,}255)\to{}^4F_{7/2}(\Gamma_{56}\ 20{,}571)$	1684	$(0+0+2.28+0.9)\times10^5$		
(d)	$^4G_{11/2}(\Gamma_{56}\ 26{,}393)\to{}^2G_{9/2}(\Gamma_{78}\ 24{,}756)$	1637	$(0+0.03+7.8+2.6)\times10^5$	0.16×10^7	2.05×10^7 (77 K)
	$^4G_{11/2}(\Gamma_{56}\ 26{,}393)\to{}^2G_{9/2}(\Gamma_{56}\ 24{,}703)$	1690	$(0+0+1.8+0.9)\times10^5$	$[0.11\times10^7]$	
	$^4G_{11/2}(\Gamma_{56}\ 26{,}393)\to{}^2G_{9/2}(\Gamma_{78}\ 24{,}645)$	1748	$(0+0+0.40+0.74)\times10^5$		
	$^4G_{11/2}(\Gamma_{56}\ 26{,}393)\to{}^2G_{9/2}(\Gamma_{56}\ 24{,}610)$	1783	$(0+0+0.34+0.58)\times10^5$		
	$^4G_{11/2}(\Gamma_{56}\ 26{,}393)\to{}^2G_{9/2}(\Gamma_{78}\ 24{,}531)$	1862	$(0+0+0.03+0.20)\times10^5$		
(e)	$^2G_{9/2}(\Gamma_{78}\ 24{,}531)\to{}^4F_{3/2}(\Gamma_{78}\ 22{,}653)$	1878	$(0+0+0.065+0.584)\times10^4$	0.98×10^4	
	$^2G_{9/2}(\Gamma_{78}\ 24{,}531)\to{}^4F_{3/2}(\Gamma_{56}\ 22{,}622)$	1909	$(0+0+0.044+0.282)\times10^4$		8.0×10^4 (14 K)
	$^2G_{9/2}(\Gamma_{56}\ 24{,}610)\to{}^4F_{3/2}(\Gamma_{78}\ 22{,}653)$	1957	$(0+0+0.017+0.29)\times10^4$	0.48×10^4	7.4×10^4 (80 K)
	$^2G_{9/2}(\Gamma_{56}\ 24{,}610)\to{}^4F_{3/2}(\Gamma_{56}\ 22{,}622)$	1988	$(0+0+0.008+0.16)\times10^4$		

continue

Ion References	Transition Initial Level Γ — final level Γ' Symmetry, energy (cm^{-1})[a]	Energy gap (cm^{-1})	Relaxation rate $\sum_{\Gamma'} W_{\Gamma\to\Gamma'}$ (s^{-1}) Theory ($T = 0$ K) Transition probabilities $W^{(2)} + W^{(3)} + W^{(4)} + W^{(5)}$	Total rate	Eperiment (Temperature)
1	2	3	4	5	6
Tm^{3+} (d)	$^3F_3(\Gamma_{34}\ 14{,}520)\to{}^3H_4(\Gamma_2\ 12{,}946)$	1574	$(0+0.091+16.8+4.01)\times10^5$	0.45×10^7	1.28×10^7 (77 K)
	$^3F_3(\Gamma_{34}\ 14{,}520)\to{}^3H_4(\Gamma_{34}\ 12{,}835)$	1685	$(0+0+9.98+5.83)\times10^5$	[0.56×10^7]	1.85×10^7 (300 K)
	$^3F_3(\Gamma_{34}\ 14{,}520)\to{}^3H_4(\Gamma_1\ 12{,}835)$	1685	$(0+0+2.04+1.36)\times10^5$		
	$^3F_3(\Gamma_{34}\ 14{,}520)\to{}^3H_4(\Gamma_1\ 12{,}745)$	1777	$(0+0+0.44+0.91)\times10^5$		
	$^3F_3(\Gamma_{34}\ 14{,}520)\to{}^3H_4(\Gamma_{34}\ 12{,}643)$	1879	$(0+0+0.25+1.88)\times10^5$		
	$^3F_3(\Gamma_{34}\ 14{,}520)\to{}^3H_4(\Gamma_1\ 12{,}624)$	1898	$(0+0+0.13+0.95)\times10^5$		
	$^3F_3(\Gamma_{34}\ 14{,}520)\to{}^3H_4(\Gamma_2\ 12{,}599)$	1923	$(0+0+0.06+0.68)\times10^5$		
Ho^{3+} (d)	$^5F_5(\Gamma_2\ 15{,}485)\to{}^5I_4(\Gamma_1\ 13{,}532)$	1953	0 + 0 + 10 + 89	3.5×10^2	1.61×10^4 (77 K)
	$^5F_5(\Gamma_2\ 15{,}485)\to{}^5I_4(\Gamma_{34}\ 13{,}405)$	2080	0 + 0 + 0 + 134		3.57×10^4 (300 K)
	$^5F_5(\Gamma_2\ 15{,}485)\to{}^5I_4(\Gamma_2\ 13{,}339)$	2146	0 + 0 + 0 + 21		
	$^5F_5(\Gamma_2\ 15{,}485)\to{}^5I_4(\Gamma_1\ 13{,}337)$	2148	0 + 0 + 0 + 106		
	$^5F_5(\Gamma_{34}\ 15{,}491)\to{}^5I_4(\Gamma_1\ 13{,}532)$	1959	0 + 0 + 20 + 285	6.4×10^2	
	$^5F_5(\Gamma_{34}\ 15{,}491)\to{}^5I_4(\Gamma_{34}\ 13{,}405)$	2086	0 + 0 + 0 + 229		
	$^5F_5(\Gamma_{34}\ 15{,}491)\to{}^5I_4(\Gamma_2\ 13{,}339)$	2152	0 + 0 + 0 + 18		
	$^5F_5(\Gamma_{34}\ 15{,}491)\to{}^5I_4(\Gamma_1\ 13{,}337)$	2154	0 + 0 + 0 + 92		

(a) crystal field energies are given according to (De Leebeeck et al., 1999) (Nd^{3+}), (Couto dos Santos et al., 1998) (Er^{3+}), (Hehlen et al., 2000), (Dulick et al., 1991) (Tm^{3+}), (Karayianis et al., 1976) (Ho^{3+});

(b) Orlovskii et al., 1998;

(c) Payne and Bibeau, 1998;

(d) Basiev et al., 1996;

(e) Orlovskii et al., 2001.

The excited state lifetimes usually shorten with temperature due to increase of the relaxation rates. The temperature dependence of the n-phonon transition probability may be approximated by the factor $(1 - e^{-\hbar\omega_{eff}/kT})^{-n}$ that does not differ too much from unity for $T < 100$ K. Neglecting contributions from the radiative processes, and assuming the equilibrium distribution of the excited ions among the crystal field sublevels of the populated multiplet J, we can write the corresponding lifetime τ_J through probabilities of multiphonon transitions from all J-states to each sublevel of the lower J'-multiplet:

$$\frac{1}{\tau_J(T)} = \sum_{\Gamma\subset J}\sum_{\Gamma'\subset J'} p(\Gamma \mid T)\, W_{\Gamma\to\Gamma'}(T), \qquad (3.109)$$

where $p(\Gamma \mid T) = \exp(-\varepsilon_\Gamma/kT) / \sum \exp(-\varepsilon_\Gamma/kT)$ is the relative population of the corresponding sublevel. Nonmonotonic temperature dependence of the lifetime may be observed due to lower deexcitation rates in the upper J-states than in the lowest J-sublevel (in particular, such a dependence of the luminescence lifetime of the $^2G_{9/2}$ multiplet of Er^{3+} (see Table 3.4) was measured by Orlovskii et al. (2001)). Strong temperature dependence of the lifetime of the $^4G_{7/2}$ multiplet of Nd^{3+} might be observed at low temperatures because theory predicts very different relaxation rates for two lower closely spaced sublevels (Table 3.4).

Contributions due to the n-th order terms in the electron-phonon interaction prevail in the n-phonon transition rate, but the total contribution of all lower order terms may play a comparable role. When considering two-phonon processes in Section 3.5.1, we have already obtained exact expressions of the transition probabilities that include along with the first order terms due to quadratic electron-phonon interaction also the second order and the cross terms from the linear coupling. Similarly, the transition amplitude for the n-phonon process contains different higher order terms along with the first order term presented by Eq. (3.90). In particular, the 4-phonon process can be realized through two-step (2+2)- or (1+3)-processes. Calculations of the probability of the 4-phonon transition $^4F_{5/2}(\Gamma_{56}) \to {}^4F_{7/2}(\Gamma_{78})$ at the gap of 1584 cm^{-1} in Er^{3+} have shown (the sum over intermediate ion states included only sublevels of the multiplets involved into the transition) that the positive second order terms of the type (1+3)·(1+3) and the negative cross terms (4)·(1+3) diminish the first order term (the total contribution of the second order terms is approximately −10% of the main term). The calculated contribution into the relaxation rate of the $^4F_{5/2}(\Gamma_{56})$ state of Er^{3+} caused by the linear mechanism of nonradiative transitions (Eq. (3.88)) is about three orders of magnitude less than the measured rate.

Before closing this section, let us return to the approximate multiplicative form of the n-phonon transition probability of Eq. (3.103). This expression may be presented through the dimensionless trace of the matrix $\alpha_n J_n$ (see Fig. 3.3),

$$W^{(n)}_{\Gamma\to\Gamma'} = \frac{2\pi}{n!}\left\langle\left(\frac{\tilde{V}^{(n)}_{\Gamma\Gamma'}}{\hbar}\right)^2\right\rangle_{\mathrm{Av}} \delta t Sp[\alpha_n J_n(\omega_{\Gamma\Gamma'})], \tag{3.110}$$

where the renamed coupling constants of n-th order $\tilde{V}^{(n)}_{\Gamma\Gamma'} = V^{(n)}_{\Gamma\Gamma'}(\text{Å})^n$ are measured in energy units, and $\delta t \cdot \alpha_n = [\hbar/(\pi \text{Å}^2)]^n$. As it follows from simple physical arguments, and has been confirmed by our calculations, the averaged squares of coupling constants increase with the order n of a process (at least, by an order of magnitude with n increased by unity). The semilogarithmic plots of gap dependences of the traces $10^n Sp[\alpha_n J_n(\omega)]$ are presented by dotted curves in Fig. 3.3. The gap dependence of the sum of these traces may be well approximated by the direct line CD. Substituting the equation of this line for the trace of the multiphonon correlation functions, we obtain the nonradiative transition probability at low temperatures ($kT \ll \hbar\omega_{\mathrm{M}}$) in the form of the exponential gap law (see Eq. (3.87))

$$W^{(n)}_{\Gamma\Gamma'} = (1/\tau^{(n)}_{0,\Gamma\Gamma'})\exp(-a\omega_{\Gamma\Gamma'}/\omega_{\mathrm{M}}), \tag{3.111}$$

where $a = 4.15$, and

$$(1/\tau^{(n)}_{0,\Gamma\Gamma'}) = 3.25\times 10^{10}\left\langle(\hat{V}^{(n)}_{\Gamma\Gamma'})^2\right\rangle_{\mathrm{Av}}\frac{1}{n!}s^{-1} \tag{3.112}$$

($\hat{V}^{(n)}_{\Gamma\Gamma'}$ stands for coupling constants vector $V^{(n)}_{\Gamma\Gamma'}$ in units of $10^{-n/2}(\mathrm{cm}^{-1}/\text{Å}^n)$), the rate factor (see Eq. (3.112)) becomes a constant if $\langle(\hat{V}^{(n)}_{\Gamma\Gamma'})^2\rangle_{\mathrm{Av}} \propto \frac{1}{n!}$. Actually, the order n of the transition (and the corresponding rate factor) is determined by the condition $\omega_{n-1,n} < \omega_{\Gamma\Gamma'} < \omega_{n,n+1}$, where $\omega_{n,n+1}$ are the intersection points of the dotted curves in Fig. 3.3. It should be noted that Payne and Bibeau (1998) found $a = 3.1$ and $\tau_0 = 3.3$ ps from the analysis of relaxation rates measured in different compounds.

Relaxation rates estimated according to the approximate expression Eq. (3.110) and given in square brackets in Table 3.4, column 5, agree well with the results of exact calculations. So, the multiplicative form of the multiphonon transition probability can be used to simplify simulations. For the majority of transitions considered in Table 3.4, the averaged squares of coupling constants that characterize interactions with deformations of different symmetry (Γ_1, Γ_2, Γ_{34}) have comparable values, and the calculated ratios $\langle(V^{(n+1)}_{\Gamma\Gamma'})^2\rangle_{\mathrm{Av}}/\langle(V^{(n)}_{\Gamma\Gamma'})^2\rangle_{\mathrm{Av}}$ are in the range 8.5 – 14 if $n = 2$ or 3. For this reason, we may suppose that the intersections of the dotted curves in Fig. 3.3 actually determine ranges of transition frequencies where the n-phonon processes dominate ($\omega_{n+1,n} =$

860, 1200, 1560 cm^{-1} for $n=2,3,4$, respectively). In particular, the probability of the 5-phonon process exceeds the probability of the 4-phonon process by at least an order of magnitude, and moreover, the 6-phonon process may be already of importance at the gap value less than 3.4 ω_M (see Table 3.4).

3.8.2 Relaxation Broadening of Optical Transitions in Pr^{3+} Dimer Centers in $CsCdBr_3$

To illustrate the significant impact of local lattice perturbations due to the heterovalent impurity rare earth ions on the manifestations of the electron-phonon interaction, we present one more example of detailed calculations of one- and two-phonon transition probabilities between the crystal field states of Pr^{3+} dimer centers in the quasi-one-dimensional bromide $CsCdBr_3$.

The crystal structure of $CsCdBr_3$ belongs to the D_{6h}^4 space group. It consists of linear chains of opposite face-sharing slightly deformed $[CdBr_6]^{4-}$ octahedra arranged along the crystallographic c-axis and connected through the Cs^+ ions. Impurity trivalent rare earth ions in $CsCdBr_3$ mainly form symmetrical dimer centers substituting for three adjacent Cd^{2+} ions in the chain (in this case the condition of electric neutrality of a lattice is fulfilled). The central Cd^{2+} site is vacant, and the rare earth ions at both sides of the vacancy are brought together due to the Coulomb attraction to the effective vacancy charge, the distance between impurity ions diminishes from the lattice constant c value of 0.72 nm down to 0.59 – 0.60 nm (Popova et al., 2001). Both Ln^{3+} ions are equivalent, the local symmetry at the position of the impurity ion is C_{3v}.

The rigid ion model of the $CsCdBr_3$ lattice dynamics was derived by Malkin et al. (2001) on the basis of measured Raman scattering and infrared reflectivity spectra. Phonon frequencies and polarization vectors were calculated over the evenly spaced mesh of sample wave vectors in the irreducible part of the Brillouin zone (8844 points). Examples of simulated spectral densities of the correlation functions for relative displacements of the Cd^{2+} ion and its six nearest neighbor Br^- ions in the perfect $CsCdBr_3$ lattice are given in Fig. 3.4. The substitution of a pair of trivalent rare earth ions for three Cd^{2+} ions leads to the strong lattice perturbation. The Green's functions of Eq. (3.18) of the locally perturbed lattice were calculated taking into account mass defects at the three adjacent Cd^{2+} sites and changes of the force constants within the cluster containing the impurity $(Pr^{3+})_2$ dimer and the twelve nearest neighbor Br^- ions located at the vertexes of the two deformed octahedra. The simulated spectral densities of correlation functions of ion displacements in the perturbed lattice (see Fig. 3.4) are essentially suppressed, and local vibrations are induced outside the boundary of the continuous phonon spectrum ($\omega_M = 180\ cm^{-1}$) with frequencies 193.7(A_{2u}), 195.8 (A_{1g}), 199.9 (E_g), 203.8 (E_u) cm^{-1} (local vibrations are labeled with irreducible representations of the dimer D_{3d} point symmetry group).

The relative weights of local vibrations in the spectral distributions of the impurity Pr^{3+} ion vibrations along the dimer symmetry axis z (A_{1g} and A_{2u} vibrations) and in the (x, y)-plane (twofold E_g and E_u vibrations) have been estimated as 40% and 50%, respectively. The localized modes are represented in the spectral distributions of the correlation functions in Fig. 3.4 by Lorentzians (of the 2 cm^{-1} FWHH estimated from the relative intensities of the vibronic structure components in the optical spectra of $CsCdBr_3$: Ln^{3+} crystals), with the proper weights, substituted for δ functions in the Eq. (3.23). Figure 3.4 demonstrates the essential redistribution of phonon spectral densities induced by impurity rare earth dimers in $CsCdBr_3$. The most remarkable specific feature of the simulated spectral densities is the intensive doublet line that appears near the boundary of the phonon spectrum of a regular lattice. In the praseodymium dimer, the doublet is formed mainly by the localized modes of E_g and E_u symmetry.

An experimental evidence for a localized mode appearance in the Raman

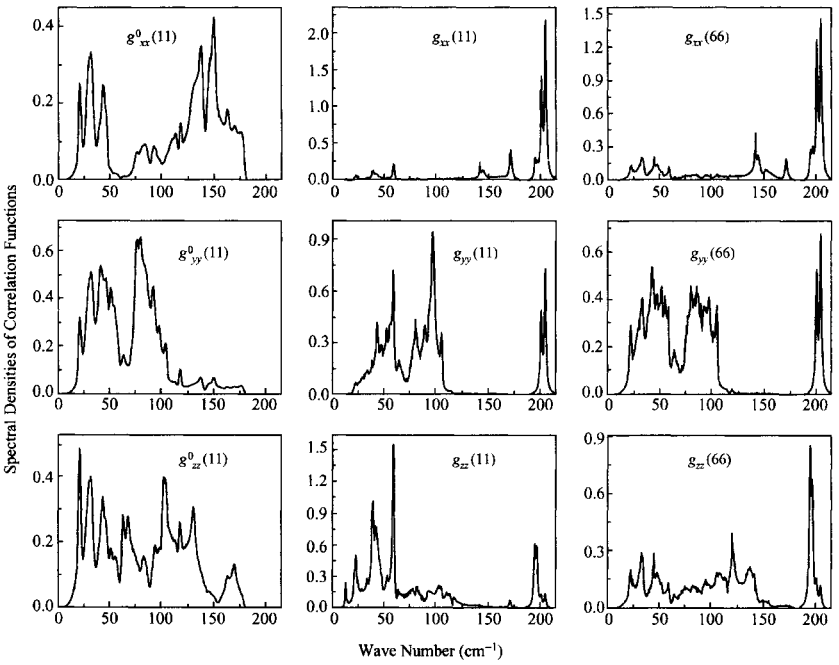


Figure 3.4 Spectral densities $g^0_{\alpha\alpha}(11)$ of correlation functions of differences between displacements of Cd^{2+} ion and the nearest neighbor Br_1^- ion in the perfect $CsCdBr_3$ lattice, and spectral densities $g_{\alpha\alpha}(pp)$ of differences between displacements of the impurity Pr^{3+} ion and its nearest neighbors Br_p^- from the external ($p=6$) and internal (bridging, $p=1$) bromine triangles in the symmetric dimer center (in units of 0.2454 m^2/J). Ligand crystallographic coordinates relative to the Pr^{3+} (Cd^{2+})-site equal ($\pm x$, 0, $\mp c/4$) with the upper and lower signs for Br_1^- and Br_6^-, respectively; $x=0.2201$ nm, and $c=0.6722$ nm is the lattice constant

spectrum and in the luminescence excitation sideband in $CsCdBr_3$: Yb^{3+} was firstly communicated by Hehlen et al. (1997). The specific features of the simulated spectral densities of correlation functions are well seen in the vibrational structure of optical spectra in $CsCdBr_3$: Yb^{3+} and $CsCdBr_3$: Pr^{3+} crystals (Malkin et al., 2001; Neukum et al., 1994).

In the crystal field of the C_{3v} symmetry, multiplets of Pr^{3+} split into singlets Γ_1, Γ_2 and doublets Γ_3. Popova et al. (2001) have studied the low temperature high-resolution absorption spectra of $CsCdBr_3$: Pr^{3+} in the region between 2000 and 7000 cm^{-1} that corresponds to transitions from the ground state ($\Gamma_1(^3H_4)$ singlet) to the crystal field sublevels of the $^3H_5$, $^3H_6$, $^3F_J(J=2,3,4)$ multiplets. The measured relaxation broadening of spectral lines is the subject of our attention here. The crystal field parameters $B_0^2 = -140(-145)$, $B_0^4 = -1125$ (-1030), $B_0^6 = 242$ (239), Re $B_3^4 = -1417$ (-1391), Re $B_3^6 = -218$ (-128), Re $B_6^6 = 106$ (243) cm^{-1} were obtained from the analysis of the experimental crystal field splittings and the hyperfine structure of the transitions to electronic doublet states (the nuclear spin of ^{141}Pr, 100% abundant, $I=5/2$). Values of these parameters calculated in the framework of the exchange charge model are given in brackets (parameters of the model are presented in Table 3.1). It should be mentioned that remarkable differences between the theoretical estimates and the fitted values of B_6^3 and B_6^6 are most likely caused by uncertainties in the dimer local structure. The first- and second-order coupling constants in the Hamiltonian H_{el-ph} were calculated using the same parameters of the exchange charge model and taking into account interactions of the Pr^{3+} ion with the nearest six bromine ions.

The probabilities (see Eq. (3.73)) of one-phonon spontaneous transitions, allowed by the energy conservation law, from each crystal field sublevel of the $^3F_3$, $^3F_2$ and $^3H_5$ multiplets to all lower sublevels were calculated. The corresponding inverse lifetimes of the crystal field sublevels $\tau_{\Gamma_i}^{-1} = W_{\Gamma_i} = \sum_j W_{\Gamma_i \to \Gamma_j}$ are compared with the measured linewidths in Table 3.3. The agreement is satisfactory, and it should be emphasized that similar calculations but with the correlation functions of the perfect lattice result in essentially (up to an order of magnitude) overestimated relaxation rates. The measured width of the doublet $\Gamma_3^{(3)}$ ($^3H_5$) is five times larger than the estimated total hyperfine splitting, though the one-phonon relaxation broadening of this level is not possible at low temperatures. This level, and two upper levels $\Gamma_2^{(2)}$ and $\Gamma_3^{(4)}$ are essentially broadened due to the two-phonon relaxation processes. In particular, the calculated sum of probabilities of two-phonon spontaneous transitions from the doublet $\Gamma_3^{(3)}$ ($^3H_5$) to all lower sublevels of the $^3H_5$ multiplet (see Table 3.3) agrees satisfactorily with the measured linewidth. It consists of three terms that correspond to the first order contribution from the second order coupling (Eq. (3.74), $1.8 \times 10^{10}\ s^{-1}$), to the second order contribution from linear

coupling (Eq. (3.75), $20.5 \times 10^{10}\ s^{-1}$), and to the contribution from "crossed" terms (Eq. (3.76), $-4.1 \times 10^{10}\ s^{-1}$). It should be noted that relaxation processes that involve excitations of localized modes of E_u and E_g symmetry dominate providing more than a half of the total relaxation rate.

3.9 Conclusions

General theory of ion-lattice interaction effects on optical properties of rare earth compounds has been developed in the past century. Characteristics of these effects depend on parameters of the both electronic and lattice subsystems. Electronic properties of impurity ions in real crystals have been thoroughly studied, but there is only a limited number of examples when direct calculations are carried out by making use of real spectral properties of lattice vibrations. Different simplifying approximations that have played an important role in establishing the main regularities in causes and effects of the ion-lattice coupling (in particular, Einstein single frequency model or Debye model of elastic waves) are often used. However, to provide quantitative understanding and meaningful estimates of physical properties of optical centers in solids, it is necessary to work with vibrational modes of a real system under consideration. The fast development of *ab initio* methods of simulations of vibrational spectra in crystals may provide in near future the expanded databases that allow to check the existing theory and to construct more elaborated models of the ion-lattice interaction in specific compounds. One of main goals of this Chapter involved a derivation of some explicit expressions for spectral characteristics of the rare earth ions in crystals that might be used in simulations based on the computed spectral densities of multiphonon correlation functions.

The one-particle mechanism of electron-phonon coupling considered in the present Chapter dominates in the most cases. The physically justified estimation of coupling constants (especially, of higher order) in the Hamiltonian of the electron-phonon interaction is a difficult problem. Of course, the exchange charge model gives only a crude description of a large number of contributions to crystal field energies with different dependences on the interion distances. However, as it has been shown above, this model allows to obtain reasonable values of spectroscopic and kinetic parameters of the coupled ion-lattice system. The presented approach has the advantage of expressing characteristics of effects due to the electron-phonon interaction in terms of a limited number of model parameters that have a precise physical meaning and that are easily obtained from crystallographic information and crystal field splittings.

This Chapter may by no means pretend on a complete review of all phenomena where the dynamical ion-lattice interactions play the dominant role. In particular, the phonon assisted energy transfer, cross-relaxation processes, and the phonon spectroscopy of the rare earth compounds (Eisenmenger and Kaplyanskii, 1986, Abramov et al., 1987; Rump et al., 1996) appear worthy of

special consideration, as well as the optical spectroscopy of insulating nanocrystals containing rare earth ions that quickly develops during last years. Contrary to bulk crystals with the quasi-continuous spectrum of lattice modes, the longwave low-frequency lattice excitations are absent in nanocrystals due to the quantization of wavelengths. The confinement effect on the phonon density of states provides changes in temperature dependences of optical linewidths and lifetimes of electronic excitations because of slowing down (or total absence) of direct relaxation that depends on the finite particle size. Some peculiarities of relaxation rates and line broadening mechanisms caused by the electron-phonon interaction in insulating nanoparticles containing impurity lanthanide ions, when the phonon density of states is sufficiently sparse and phonon-phonon interactions are hindered, are discussed in the next Chapter.

Finally, I would like to point out that some problems mentioned in this Chapter (such as the theory of the correlated crystal field interactions, the dynamical nepheloxeutic effect and its role in the electron-phonon interaction) are still need further comprehensive treatment.

References

Abragam, A. *The Principles of Nuclear Magnetism* (Clarendon Press, Oxford, 1961), ch. VIII.

Abramov, A. P., I. N. Abramova, K. L. Aminov, I. Ya. Gerlovin, B. Z. Malkin, I. K. Razumova. Fiz. Tverd. Tela **29**, 2725 (1987).

Aminov, L. K., B. Z. Malkin, M. A. Teplov. Magnetic properties of nonmetallic lanthanide compounds. In: *Handbook on the Physics and Chemistry of the Rare-Earths*, V. **22**, eds. K. A. Gschneidner, and LeRoy Eyring (North-Holland, Amsterdam, 1996), p. 295.

Aminov, L. K., A. A. Kaminskii, B. Z. Malkin. In: *Physics and Spectroscopy of Laser Crystals* (Moscow, Nauka, 1986), p. 84.

Aminov, L. K. Adiabatic and nonadiabatic one-particle mechanisms of spin-lattice relaxation, In: *Spectroscopy of crystals* (Leningrad, Science, 1978), p. 116.

Auzel, F., F. Pelle. Opt. Mat. **8**, 15 (1997).

Basiev, T. T., Yu. V. Orlovskii, K. K. Pukhov, F. Auzel. Laser Physics **7**, 1139 (1997).

Basiev, T. T., Yu. V. Orlovskii, K. K. Pukhov, V. B. Sigachev, M. E. Doroshenko, I. N. Vorobév. J. Luminesc. **68**, 241 (1996).

Beck, W., D. Ricard, and C. Flytzanis. Phys. Rev. B **57**, 7694 (1998).

Bloch, F. Phys. Rev. **102**, 104 (1956).

Born, M., and Kun Huang. *Dynamical Theory of Crystal Lattices* (Clarendon Press, Oxford, 1954).

Born, M., and J. R. Oppenheimer Ann. Physik **84**, 457 (1927).

Bron, W. E., M. Wagner. Phys. Rev. **139**, A 233 (1965).

Bottger, H. *Principles of the Theory of Lattice Dynamics* (Academie-Verlag, Berlin, 1983).

Buchanan, M., E. J. Woll, Jr., Canad. J. Phys. **47**, 1757 (1969).

Bumagina, L. A., V. I. Krotov, B. Z. Malkin, A. Kh. Khasanov. Zh. Eksp. Teor. Fiz. **80**, 1543 (1981); Sov. Phys. JETP **53**, 792 (1981).

Bungenstock, C., Th. Troster, and W. B. Holzapfel. Phys. Rev. B **62**, 7945 (2000).

Campos, A. F., A. Meijerink, C. de Mello Donega, O. L. Malta. J. Phys. Chem. Sol. **61**,

1489 (2000).
Chen, X., B. Di Bartolo. J. Lumin. **54**, 309 (1993).
Chen Xueyuan, Luo Zundu. J. Phys.: Condens. Matter **9**, 4197 (1997).
Christensen, H. P. Phys. Rev. B **19**, 6564 (1979).
Clementi, E., C. Roetti. Atomic Data and Nuclear Data Tables **14**, 177 (1974).
Clementi, E., A. D. McLean. Phys. Rev. A **133**, 419 (1964).
Cohen, E., H. J. Guggenheim. Phys. Rev. **175**, 354 (1968).
Condon, E. U. Phys. Rev. **32**, 858 (1928).
Couto dos Santos, M. A., E. Antic-Fidancev, J. Y. Gesland, J. C. Kroupa, M. Lemaitre-Blaise, P. Porcher. J. Alloys Comp. **275 – 277**, 435 (1998).
Davidova, M. P., S. B. Zdanovitch, B. N. Kazakov, S. L. Korableva, A. L. Stolov. Opt. & Spectrosk. **42**, 577 (1977).
De Leebeeck, H., K. Binnemans, C. Gorller-Warland. J. Alloys Compounds **291**, 300 (1999).
De Mello Donega, C., A. Meijerink, G. Blasse. J. Phys.: Condens. Matter **4**, 8889 (1992).
Dohm, V., P. Fulde. Z. Physik B **21**, 369 (1975).
Dulick, M., G. E. Faulkner, N. J. Cockroft, D. C. Nguyen. J. Luminesc. **48 – 49**, 512 (1991).
Eisenmenger, W., A. A. Kaplyanskii. *Nonequilibrium Phonons in Nonmetallic Crystals* (Elsevier Science B. V., Amsterdam, 1986).
Ellens, A., H. Andres, A. Meijerink and G. Blasse. Phys. Rev. B **55**, 173 (1997a).
Ellens, A., H. Andres, M. L. H. Heerdt, R. T. Wegh, A. Meijerink, and G. Blasse. Phys. Rev. B **55**, 180 (1997b).
Ellens, A., S. Schenker, A. Meijerink, and G. Blasse. J. Luminesc. **72 – 74**, 183 (1997c).
Ellens, A., S. Schenker, A. Meijerink, and G. Blasse. J. Luminesc. **69**, 1 (1996).
Eremin, M. V. In: *Spectroscopy of Crystals*, ed. A. A. Kaplyanskii (Nauka, Leningrad, 1989), p. 30.
Ermeneux, F. S., C. Goutaudier, R. Moncorge, Y. Sun, R. L. Cone, E. Zannoni, E. Cavalli, M. Bettinelli. Phys. Rev. B **61**, 3915 (2000).
Faucher, M., D. Garcia. Phys. Rev. B **26**, 5451 (1982).
Feynman, R. P. Phys. Rev. **56**, 340 (1939).
Fowler, W. B., D. L. Dexter. Phys. Rev. **128**, 2154 (1968).
Franck, J. Trans. Faraday Soc. **21**, 536 (1925 – 1926).
Freeman, A. J., R. E. Watson. Phys. Rev. **127**, 2058 (1962).
Garcia, E., R. R. Ryan. Acta crystallogr. C **49**, 2053 (1993).
Garcia, D., M. Faucher. J. Chem. Phys. **82**, 5554 (1985).
Gorller-Warland, C., K. Binnemans, L. Fluyt. J. Phys.: Condens. Matter **5**, 8359 (1993).
Gregorian, T., H. d' Amour-Sturm, and W. B. Holzapfel. Phys. Rev. B **39**, 12, 497 (1989).
Hehlen, M. P., A. Kuditcher, A. L. Lenef, H. Ni, Q. Shu, S. C. Rand, J. Rai, S. Rai. Phys. Rev. B **61**, 1116 (2000).
Hehlen, M. P., A. Kuditcher, S. C. Rand, M. A. Tischler. J. Chem. Phys. **107**, 4886 (1997).
Hellmann, H. In: *Einfuhrung in Die Quanten Chemie*, ed., B. G. Teubner (Leipzig, 1937), p. 285.
Hellwege, K. H. Ann. Phys. **40**, 529 (1941).
Huang, K., A. Rhys. Proc. Roy. Soc. (London), A **204**, 406 (1950).
Ignat'ev, I. V., V. V. Ovsyankin. J. Luminesc. **72 – 74**, 679 (1997).

Ignat'ev, I. V., V. V. Ovsyankin. Proc. SPIE **2706**, 142 (1996a).
Ignat'ev, I. V., V. V. Ovsyankin. Optika i spectrosk. **81**, 68 (1996b).
Ignat'ev, I. V., V. V. Ovsyankin. *Spectroscopy of crystals* (Leningrad, Nauka, 1983), p. 36.
Ivanenko, Z. I., B. Z. Malkin. Fiz. Tverd. Tela **14**, 153 (1972); Sov. Phys. Solid State **14**, 122 (1972).
Ivanenko, Z. I., B. Z. Malkin. Fiz. Tverd. Tela **11**, 1859 (1969); Sov. Phys. Solid State **11**, 1498 (1969).
Johnsson, M. T., G. E. Stedman. J. Phys.: Condens. Matter **11**, 787 (1999).
Judd, B. Phys. Scr. **21**, 543 (1980).
Kaplyanskii, A. A., A. K. Przhevusski. Optika i spectrosk. **20**, 1045 (1966).
Karayianis, N., D. E. Wortman, H. P. Jenssen. J. Phys Chem. Sol. **37**, 675 (1976).
Kemble, E. C. *The Fundamental Principles of Quantum Mechanics* (McGraw-Hill Book Company, New York, 1937), p. 585.
Kiel, A. Phys. Rev. **126**, 1292 (1962).
Kiss, Z. J. Phys. Rev. **127**, 718 (1962).
Koloskova, N. G., B. I. Kochelaev. Fizika Tverd. Tela **9**, 2948 (1967).
Krivoglaz, M. A., S. I. Pekar. Proc. Institute of Physics AS USSR **4**, 37 (1953).
Krupke, W. F. Phys. Rev. **145**, 325 (1966).
Kubo, R., Y. Toyozawa. Progr. Theor. Phys. **13**, 160 (1955).
Kupchikov, A. K., B. Z. Malkin, A. L. Natadze, A. I. Ryskin. Fiz. Tverd. Tela **29**, 3335 (1987).
Lax, M. J. Chem. Phys. 20, 1752 (1952).
Lee, M. J., M. F. Reid, M. D. Faucher, G. W. Burdick. J. Alloys Compounds **323 – 324**, 636 (2001).
Lian, R., M. Yin, W. Zhang, L. Lou, J. C. Krupa. J. Alloys Compounds **311**, 97 (2000).
Liu, G. K., W. T. Carnall, R. P. Jones, R. L. Cone, J. Huang. J. Alloys Compounds **207 – 208**, 69 (1994).
Lupei, A. Optic. Mater. **16**, 153 (2001).
Lupei, A., V. Lupei, C. Presura, V. N. Enaki, and A. Petraru. J. Phys.: Condens. Matter **11**, 3769 (1999).
Macfarlane, R. M. J. Luminesc. **85**, 181 (2000).
Malkin, B. Z., A. I. Iskhakova, S. Kamba, J. Heber, M. Altwein, G. Schaack. Phys. Rev. B **63**, 0107 (2001).
Malkin, B. Z. In: *Spectroscopy of Solids Containing Rare-Earth Ions*, eds. A. A. Kaplyanskii, R. M. Macfarlane (Elsevier Science Publishers, Amsterdam, 1987), ch 2, p. 13.
Malkin, B. Z., Z. I. Ivanenko, I. B. Aizenberg. Fiz. Tverd. Tela **12**, 1873 (1970); Sov. Phys. Solid State **12**, 1491 (1970).
Malkin, B. Z. Zh. Eksp. Teor. Fiz. **48**, 1637 (1965); Sov. Phys. JETP **21**, 1101 (1965).
Malkin, B. Z. Fiz. Tverd. Tela **5**, 1062 (1963a).
Malkin, B. Z. Fiz. Tverd. Tela **5**, 3088 (1963b).
McCumber, D. E. Phys. Rev. **133**, A163 (1964a).
McCumber, D. E. Phys. Rev. **135**, A1676 (1964b).
McCumber, D. E. M. D. Sturge. J. Appl. Phys. **34**, 1682 (1963).
Miyakawa, T., D. L. Dexter. Phys. Rev. B **1**, 2961 (1970).
Moore, D. J., G. E. Stedman. J. Phys.: Condens. Matter **2**, 2559 (1990).
Moos, H. W. J. Luminesc. **1**, 106 (1970).
Neukum, J., N. Bodenschatz. J. Heber. Phys. Rev. B **50**, 3536 (1994).

Newman, D. J. Aust. J. Phys. **31**, 79 (1978).
Newman, D. J. Adv. Phys. **20**, 197 (1971).
Orbach, R. Phys. Rev. **133** A, 34 (1964).
Orlovskii, Yu. V., T. T. Basiev, I. N. Vorob' ev, E. O. Orlovskaya, N. P. Barnes, S. B. Mirov. Optic. Mater. **18**, 355 (2001).
Orlovskii, Yu. V., T. T. Basiev, S. A. Abalakin, I. N. Vorob' ev, O. K. Alimov, A. G. Papashvili, K. K. Pukhov. J. Luminesc. **76 – 77**, 371 (1998).
Orlovskii, Yu. V., K. K. Pukhov, T. T. Basiev, T. Tsuboi. Optic. Mater. **4**, 583 (1995).
Ovsyankin, V. V. In: *Spectroscopy of Solids Containing Rare-Earth Ions*, eds. A. A. Kaplyanskii, R. M. Macfarlane (Elsevier Science Publishers, Amsterdam, 1987), ch. 7, p. 343.
Payne, S. A., C. Bibeau. J. Luminesc. **79**, 143 (1998).
Pekar, S. I. Uspekhi Fiz. Nauk **50**, 197 (1953).
Pelle, F., N. Gardant, R. Pelletier, N. Pelletier-Allard. Optic. Mat. **14**, 49 (2000).
Perlin, Yu. E., B. S. Tzukerblat. *Electron-vibrational Interaction Effects on Optical Spectra of Impurity Paramagnetic Ions* (Kishinev, Stiintza, 1974).
Perlin, Yu. E., Yu. B. Rosenfeld, B. S. Tzukerblat. Fiz. Tverd. Tela **8**, 3490 (1966).
Perlin, Yu. E. Usp. Fiz. Nauk **80**, 553 (1963); Soviet Phys. Usp. **6**, 542 (1964).
Peuker, K., R. Enderlein, A. Schenk, E. Gutsche. Phys. Stat. Sol. (b) **109**, 599 (1982).
Popova, M. N., E. P. Chukalina, B. Z. Malkin, A. I. Iskhakova, E. Antic-Fidancev, P. Porcher, J. P. Chaminade. Phys. Rev. B **63** (2001).
Popova, M. N., E. P. Chukalina, B. Z. Malkin, and S. K. Saikin. Phys. Rev. B **61**, 7421 (2000).
Pukhov, K. K., V. P. Sakun. Phys. Stat. Sol. (b) **95**, 391 (1979).
Redfield, A. G. Adv. Magn. Reson. **1**, 1 (1965).
Rump, P. J., A. F. M. Arts, H. W. de Wijn, M. Nielsen. Physica B **219 – 220**, 760 (1996).
Riseberg, L. A., H. W. Moos. Phys. Rev. **174**, 429 (1968).
Salaun, S., M. T. Fornoni, A. Bulou, M. Rousseau, P. Simon, J. Y. Gesland. J. Phys. Condens. Matter **9**, 6941 (1997a).
Salaun, S., A. Bulou, M. Rousseau, B Hennion, J. Y. Gesland. J. Phys. Condens. Matter **9**, 6957 (1997b).
Sardar, D. K., R. M. Yow, F. S. Salinas. Opt. Mater. **18**, 301 (2001).
Sardar, D. K., S. C. Stubblefield. Phys. Rev. B **60**, 14724 (1999).
Sardar D. K., R. M. Yow. Opt. Mater. **10**, 191 (1998).
Shen, Y. R., K. L. Bray, W. B. Holzapfel. J. Luminesc. **72 – 74**, 266 (1997).
Shen, Y., W. B. Holzapfel. Phys. Rev. B **52**, 12618 (1995).
Synek, M., L. Corsiglia. J. Chem. Phys. **48**, 3121 (1968).
Tovar, M., C. A. Ramos, C. Fainstein. Phys. Rev. B **28**, 4813 (1983).
Troster, Th., T. Gregorian, and W. B. Holzapfel. Phys. Rev. B **48**, 2960 (1993).
Van Pieterson, L., M. F. Reid, R. T. Wegh, S. Soverna, A. Miejerink. Phys. Rev. **65**, 045113 (2002a).
Van Pieterson, L., M. F. Reid, G. W. Burdick, A. Miejerink. Phys. Rev. **65**, 045114 (2002b).
Van Vleck. J. H. Phys. Rev. **57**, 426(1940).
Vink, A. P., M. A. Rejme, A. Meijerink. J. Luminesc. **92**, 189 (2001).
Vinokurov, A. V., B. Z. Malkin, A. I. Pominov, A. L. Stolov. Fiz. Tverd. Tela **30**, 801 (1988); Sov. Phys. Solid State **30**, 459 (1988).
Vinokurov, A. V., B. Z. Malkin, A. I. Pominov, A. L. Stolov. Fiz. Tverd. Tela **28**, 381 (1986); Sov. Phys. Solid State **28**, 211 (1986).

Voron' ko, Yu. K., A. L. Larionov, B. Z. Malkin. Optika i spectroscopia **40**, 86 (1976).
Wagner, M., W. E. Bron. Phys. Rev. **139**, A223 (1965).
Wagner, M. J. Chem. Phys. **41**, 3939 (1964).
Wangsness, R. K., F. Bloch. Phys. Rev. **89**, 728 (1953).
Wannemacher, R., D. Boye, Y. P. Wang, R. Pradhan, W. Grill, J. E. Rives, and R. S. Meltzer. Phys. Rev. B **40**, 4237 (1989).
Weber, M. J. Phys. Rev. B **8**, 54 (1973).
Wells, J. -P. R., M. Yamaga, T. P. J. Han, H. G. Gallagher, M. Honda. Phys. Rev. B **60**, 3849 (1999).
Yen, W. M., W. C. Scott, A. L. Schawlow. Phys. Rev. **136**, A271 (1964).
Yuanbin, C., L. Shenxin, P. Yuewu. J. Alloys Compounds **325**, 95 (2001).
Yuanbin, C., L. Shenxin, A. Qiuping, W. Lizhong. Physica B **245**, 293 (1998).
Yuanbin, C., L. Shenxin, L. Hongnian, Z. Xuyi, W. Lizhong. J. Alloys Compounds **256**, 1 (1997).

Acknowledgements
The author thanks L. K. Aminov, M. N. Popova and K. K. Pukhov for valuable discussions of problems considered in this Chapter and acknoledges the support by RFBR (Grant 03-02-16449).

4 Line Broadening Mechanisms and Their Measurement

R. S. Meltzer

4.1 Introduction

The subjects of this chapter are the mechanisms and measurement of line broadening. Macfarlane and Shelby (1987) provided an excellent review on coherent transient and hole burning spectroscopy which examines line broadening in a large number of rare earth systems. Many of the ideas presented in that seminal work apply to work done in the following 15 years and the reader is encouraged to consult that source as well. In this chapter we will reexamine the subject emphasizing examples of scientific results published in the last 15 years. Advances have come on a number of fronts. The limits of high resolution non-linear laser spectroscopy techniques have been pushed ahead orders of magnitude with resolution limits in the frequency domain down to 100 Hz. Non-linear laser spectroscopy has been applied to a number of new classes of materials that include nanostructured and disordered materials. Some of these developments will be described in Chapter 8 as well. Important developments are being made to apply non-linear optical techniques to current technologies of optical storage and optical processing. These applications are described in Chapter 5 to 7.

The scale of optical linewidths of rare earth ions in solids is extremely broad. Homogeneous linewidths in dilute systems, when the host has negligibly small nuclear moments, are limited by excited state lifetimes, which for trivalent rare earth ions can be 10 ms or more; this results in linewidths of only ~100 Hz. On the other extreme, at room temperature, or for excited states that are strongly coupled by phonons to lower states, homogeneous linewidths can be as large as 1 THz. This represents a range of ten orders of magnitude. A smaller but still large range is found for inhomogeneous linewidths. The narrowest observed inhomogeneous linewidth for a rare earth ion occurs for Nd^{3+} ions in $YLiF_4$ where for very low doping levels are ~10 MHz. These same Nd ions or any other trivalent rare earth ion ($4f^n$ configuration) in an amorphous material such as a glass, can have inhomogeneous linewidths larger than 1 THz and for divalent rare earth ions ($4f^{n-1}d$ configuration) this may be even greater. This represents a span of five or six orders of magnitude. If it should be possible to perform spectroscopy on a single ion, as has recently been accomplished for organic molecules (Ambrose et al., 1991), then the inhomogeneous contribution

to the linewidth would disappear, except to the extent that environmental dynamics occurs on a timescale shorter than the measurement time. Although two recent claims of single rare earth ion detection have been reported (Barnes et al., 2000) (Rodrigues-Herzog et al., 2000), no spectrally resolved zero-phonon lines were described.

A study of the linewidths of rare earth ions in solids requires one to separate the homogeneous and inhomogeneous contributions so that the mechanisms that control the linewidths can be determined. Conventional spectroscopy does not readily allow this to be accomplished, although a number of nice examples of temperature dependent studies exist in the literature. When the inhomogeneous linewidths are relatively small, it is possible to observe the growth of the homogeneous linewidth as the temperature is increased. For example, in a recent study using conventional spectroscopy to compare the homogeneous linewidths of isoelectronic Sm^{2+} and Eu^{3+} ions (Vink et al., 2001), it was shown that the line broadening of 4f $\rightarrow$4f transitions resulting from two-phonon Raman scattering did not depend on the proximity of the 5d bands that are much closer to the $4f^6$ excited state for Sm^{2+}. However, in cases where conventional spectroscopy is inadequate, non-linear spectroscopy allows one to easily separate the inhomogeneous and homogeneous contributions. These techniques operate in two general modes. With frequency domain techniques, a subset of ions with a certain transition frequency are selected or marked by the laser and their optical properties are observed. In the second method, referred to as the time domain, the sample is coherently excited with pulses of light and the coherence of the ensemble is followed in time.

In order to present the concepts of homogeneous and inhomogeneous broadening, let us begin by considering a group or ensemble of isolated rare earth atoms or ions that are at rest, (say in the gas phase). One would observe a series of optical transitions involving a change in the electronic atomic or ionic state. These states are characterized by their angular moment, J, and have a degeneracy $2J + 1$ as described in Chapter 1. Each transition would have a linewidth determined by the lifetimes of the initial and final states participating in the transition. This is referred to as homogeneous broadening; in solids there can be a number of other dynamical processes that influence the effective lifetime appropriate to determining the linewidths of optical transitions. When both the electronic states and nuclear states of the isolated atom or ion have a magnetic moment, there are additional hyperfine splittings on the scale of MHz or GHz which may or may not be resolved depending on the relative size of these splittings compared to the homogeneous linewidths of the electronic transitions.

If we now consider a group of identical non-interacting atoms or ions, they would then all have identical transition frequencies and homogeneously broadened linewidths. However, if we set these atoms into random motion, then the observer in the laboratory would see each atom's transition frequency shifted by the Doppler effect such that the resulting lineshape of the ensemble would now be broadened; this is referred to as inhomogeneous broadening. If, in addition, the

atoms interact, there are further contributions to the linewidth that can be either homogeneous or inhomogeneous depending on the time scale of the experiment relative to the time scale of the dynamic processes. In a very fast experiment, the atoms may be viewed as fixed and the linewidths would be determined by the environmental perturbations at that moment; i. e. it is inhomogeneous. However, in a slow experiment where the environment changes during the time scale of the experiment or where energy is exchanged between atoms, the lineshape would also have homogeneous contributions. It is therefore not always a simple matter to categorize the description of linewidths.

For rare earth ions in solids, similar ideas apply. Inhomogeneous broadening is always present in real solids since no material is so perfect that all ions experience identical environments. Defects such as missing or misplaced neighbors, substitutional defects of another chemical species, or trapped charges and alternative charge states are always present. In addition, there are static interactions between the optical center and its crystallographically correct neighbors that occur when the electronic states have magnetic moments and the neighbors themselves have either electronic or nuclear magnetic moments. Since there are many configurations of these moments that occur with some statistical distribution and since the frequency of the optical center depends on the particular surrounding configuration of moments, the ensemble of optical centers exhibits a distribution of transition frequencies leading to inhomogeneous broadening.

As for the gas, there are mechanisms for homogeneous broadening which are experienced (usually equally) by all the ions due to dynamical perturbations on the optical transition frequencies. The most important of these is interactions with phonons which are always present, although at liquid helium temperatures they are often inconsequential to the linewidths, at least for transitions that occur between the lowest electronic state in the ground and excited state manifolds of states (i. e. what are termed metastable states). In addition, there are dynamical interactions with both the electronic and nuclear moments of the neighboring ions which can contribute to the homogeneous linewidths. In disordered, non-crystalline or amorphous materials (e. g. glasses) interactions with the two-level systems which arise from the myriad of metastable configurational states of the systems also contribute to the homogeneous linewidths. However, as for the atomic examples, the interaction with neighbors can contribute both to homogeneous and inhomogeneous broadening, depending on the time scale of the experiment.

This chapter will first treat the line broadening mechanisms, both inhomogeneous and homogeneous, that occur for rare earth ions in condensed matter. Then the various techniques that enable a determination of optical linewidths will be reviewed, citing examples which illustrate their application. Finally some selected examples of linewidth measurements in disordered and nanostructured materials will be described in more detail, with an emphasis on new results in the last 15 years.

4.2 Inhomogeneous Broadening

Inhomogeneous broadening arises due to the fact that each ion in a solid experiences a different local environment. Inhomogeneous broadening has been reviewed by Macfarlane (1987a, 1990). Since the optical transition frequency of an ion depends on the strain, local electric and magnetic fields acting on the ion, these environmental differences lead to a distribution of these frequencies for a particular type of ion. The distribution of these frequencies produce an inhomogeneously broadened line whose lineshape depends on the details of this distribution. In crystalline materials where an ion sits at a regular lattice site, these differences arise because of defects in the lattice produced by vacancies, interstitials, impurities, ions in different valence states or trapped electrons or holes. In some crystalline materials, where the homogeneous linewidths are quite narrow and where a certain defect occurs with some regularity about the optical center, distinct resolved optical transitions can be observed and selectively probed with techniques such spectral hole burning and optically detected magnetic resonance. For transitions where the electronic states have magnetic moments, inhomogeneous broadening can also occur as a result of interactions of the optical center with the many possible arrangements of the spins of the nearby ions due to their electronic or nuclear moments. These surrounding ions produce local magnetic fields or electronic exchange fields that alter the optical transition frequencies of the optical centers.

4.2.1 Zero-phonon Linewidths of 4f→4f and 4f→5d Transitions

Rare earth ions usually exist in their trivalent state. However certain ions occur in divalent (Sm^{2+}, Eu^{2+}, Dy^{2+}, Yb^{2+}) or tetravalent (Ce^{4+}, Pr^{4+}) charge states. For the trivalent ions, transitions in the infrared and visible occur between electronic states of the f^n configuration. Because the f-electrons are well-shielded from the electronic distributions of the neighboring ion, due to their small radial distribution shielded by the outer 5s and 5p bonding electrons, they are relatively insensitive to external perturbations. As a result, inhomogeneous linewidths are relatively narrow as compared to transitions which involve the f^{n-1} 5d configurations. For example, for f – f transitions the Stark effect coefficients are typically in the range of $10-100\ \mathrm{kHz/(V \cdot cm^{-1})}$ (Vink et al., 2001; Macfarlane, 1993b) and uniaxial stress coefficients are of the order $\approx$ $1\ \mathrm{GHz/(kg \cdot mm^{-2})}$ (Reeves and Macfarlane, 1989). However, the d-electron has a much larger radial extent and is less shielded so it is much more sensitive to the presence of defects as indicated by the corresponding Stark and stress

coefficients which are typically an order of magnitude greater than that for 4f – 4f transitions. For the divalent and tetravalent species, the f^{n-1} – d configurations are often much closer in energy from the ground state so that these transitions, with much broader inhomogeneous zero-phonon linewidths, occur in the visible. However the f^{n-1} – d configuration of the trivalent rare earths can be accessed in the ultraviolet and studies of their spectroscopy have become of great interest recently as discussed in Chapter (Meijerink).

To estimate the effect of a defect on the optical transition frequency of an ion, consider the electric field produced by an unshielded unit charge defect sitting at a nearest neighbor cation site. The electronic energy levels of the rare earth ion are determined by the local crystal field at the site. The local field of the charge defect will occur in addition to the crystalline fields determined by the nearby host ions. This field is $e/\varepsilon r^2$ where ε is the dielectric constant, typically about 5, and acts in addition to the normal unperturbed crystalline field. To crudely estimate its effect consider a single charge at a typical nearest neighbor cation distances (3 Å), this amounts to a local field of 10 MV/cm. Based on the typical Stark coefficients described above, frequency shifts for states in the f^n and f^{n-1} – d configurations are therefore 0.1 – 1 THz (3 – 30 cm^{-1}) and 1 – 10 THz (30 – 300 cm^{-1}), respectively. Of course the actual effect of a charge defect must consider the total charge density surrounding the rare earth ion and therefore the macroscopic dielectric constant is only a crude approximation to any shielding effects associated with the rearrangement of the charge distribution of the surrounding ions in response to the presence of the defect charge.

The case of charge compensation of trivalent rare earth ions in CaF_2 offers an excellent opportunity to compare the relative sensitivities of 4f→4f and 4f→5d optical transitions to perturbing fields. All the trivalent rare earths substitute for a Ca^{2+} ion. The most common mode of charge compensation occurs with an extra F^- ion at a nearby interstitial position producing an additional local electric field with symmetry $C_{4v}(100)$ or $C_{3v}(111)$. The effect of that field can be compared for the zero-phonon line of the lowest energy 4f→5d transition of a Ce^{3+} ion and the 4f→4f transitions for Eu^{3+}. In each case the transition energy shift(splitting) of the perturbed ion relative to the "cubic site" are known. Whereas for Ce^{3+} the shift of one of the f – d transitions is 403 cm^{-1} relative to that of the cubic site, (McClure et al., 1989), the values for Eu^{3+} are 50 cm^{-1} for the splitting of the $^5D_1$ by the axial C_{4v} field and 19 cm^{-1} for the shift of the center of gravity relative to the cubic site (Olsen et al., 1996). Thus the effect of the interstitial fluorine is about an order of magnitude less for the f – f transition compared to the f – d transition as expected from measurements of Stark coefficients.

4.2.2 Line Broadening from Defects and Disorder

The transition frequencies of the optical centers are perturbed by the presence of defects in their surroundings. These defects occur with a probability distribution for the nearest distance of the defect from the optical center. For low defect

concentrations and random statistics, only a small number of rare earth ions will be so perturbed that their transition frequencies are sufficiently different from those of the majority that a well-resolved distinct site can be identified. However, in certain materials, for example when a trivalent rare earth ion replaces a divalent cation, charge compensation is required and distinct perturbed sites are the rule rather than the exception. For the case of a random distribution of defects, where the perturbative effect of the defect falls off with distance (i. e. $1/r^2$ for a charge defect) small perturbations are most probable and the statistical distribution of distance of the defects from the rare earth ion produces an inhomogeneously broadened lineshape. The theory of the lineshapes resulting from the presence of defects have been considered by Orth et al. (1993, 1994) and references therein which suggest that both Gaussian and Lorentzian lineshapes are possible for zero-phonon lines.

For highly disordered crystalline or amorphous materials, all optical centers experience quite different local environments and as a result these systems have very large inhomogeneous linewidths, in some cases approaching $\sim 100\ cm^{-1}$ or more even for 4f – 4f transition. The measurement of these linewidths can be an important tool with which to characterize the disorder of the material. In nanostructured materials, inhomogeneous broadening can result from interactions with the environment external to the nanoparticle or film due to the distribution of positions of the optical centers with respect to the surface of the nanomaterial. Thus each optical center will experience a different interaction with the surrounding material. This will be considered in more detail later.

An illustration of the effect of substitutional disorder is shown in Fig. 4. 1 where the inhomogeneously broadened zero-phonon line for the $^6H_{15/2} \rightarrow {}^5F_{9/2}$ transition of Er^{3+} in the solid solution mixed crystal system Y_2O_3/Sc_2O_3 is shown as a function of composition (Tissue et al., 1991). These two materials are isostructural in their pure forms and Y^{3+} and Sc^{3+} have nearly identical radii. As a result, they can be expected to form a good solid solution. In unmixed Y_2O_3, with an Er^{3+} doping level of 1%, the inhomogeneous linewidth of the $^4I_{15/2} \rightarrow {}^4S_{3/2}$ transition is only about $5\ cm^{-1}$. This gradually broadens as Sc_2O_3 is added, reaching a maximum value of $30\ cm^{-1}$ for a 50/50 mixture of these two materials. Linewidths have been examined as a function of concentration in a number of other mixed crystal systems and these will be discussed in Section 4. 6. 1.

Inhomogeneous broadening can also arise in a much more subtle way due to the statistical distribution of isotopes of the host ions. In the insert of Fig. 4. 2, the lineshapes of three hyperfine transitions of the $^5I_8 \rightarrow {}^5I_7$ transition of Ho^{3+} are shown for samples with different distributions of the Li isotopes. (Agladze and Popova, 1993). Note that the sample with the pure ^7Li has no structure. The structure results from the many possible statistical distributions of Li isotopes in the eight nearest neighbor positions as explained in Section 4. 2. 4. Similar effects have been described for Er^{3+} in $YLiF_4$ with shifts of 480 and 570 MHz for the replacement of ^7Li by ^6Li in the nearest Li site Chukalina (2000).

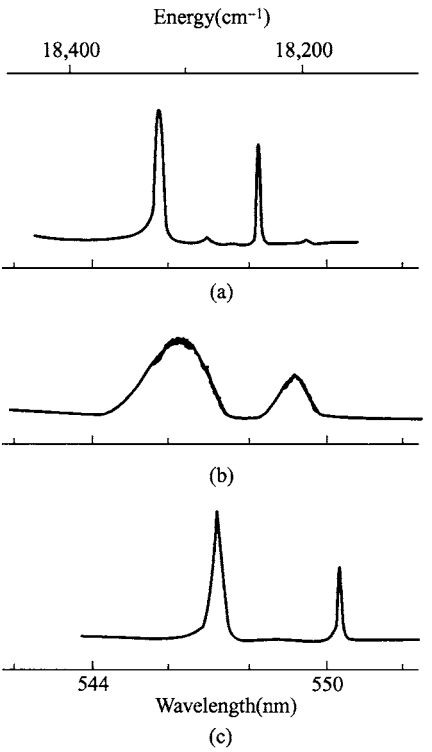


Figure 4.1 $^4I_{15/2} \rightarrow {}^4S_{3/2}$ excitation spectra monitoring direct fluorescence at 14 K of (a) 1% $Er^{3+}:Y_2O_3$, (b) 1% $Er^{3+}:YScO_3$, and (c) 1% $Er^{3+}:Sc_2O_3$ (Tissue et al., 1991)

The measurement of the inhomogeneous linewidths of rare earth ions doped into a wide range of materials have been used to characterize their properties. For example, Eu^{3+} has been used in silica-gels to monitor their dehydration (Piazza et al., 1994). Pr^{3+} linewidths have been used to determine the Li deficit level of $LiTaO_3$ (Rybaromanowski et al., 1997) and $LiNbO_3$ (Gill et al., 1996). Dy^{3+} has been used as a probe to follow the disorder on the cation sites of the scheelite structured $KY(WO_4)_2$ (Macalik et al., 1998), and linewidth measurements have provided a means to characterize the effect of annealing SBN films prepared with laser deposition (Liu et al., 1999) and (Li et al., 2000).

4.2.3 Site-selective Spectroscopy

When the number density of defects is small such as in the case of lightly doped materials, it may be possible to observe and study ions with a specific environment. Often the spectrum of a single electronic transition is accompanied

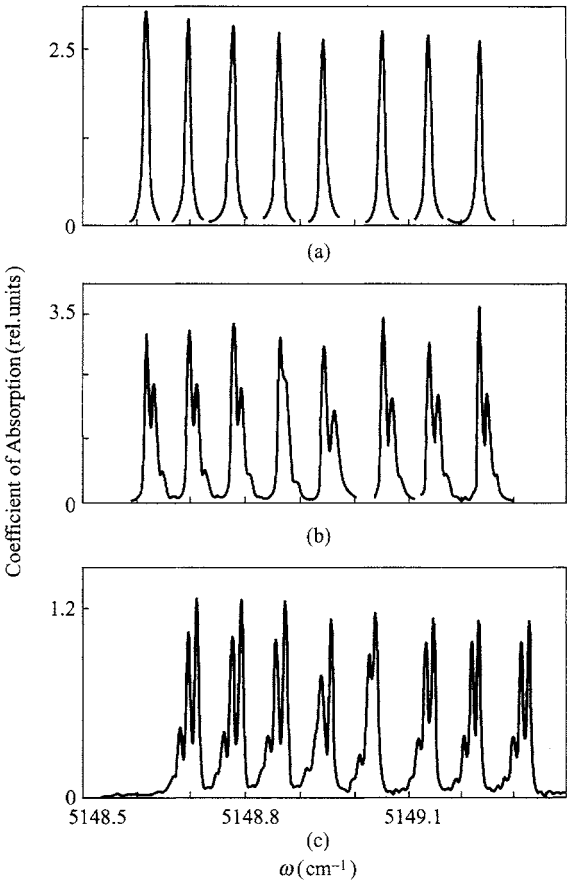


Figure 4. 2 Hyperfine structure obtained in absorption at liquid helium temperatures of the $^5I_8(\Gamma_2^1) \rightarrow {}^5I_7(\Gamma_{34}^1)$ transition of Ho^{3+} (0.1%) in $^6Li_x{}^7Li_{1-x}YF_4$ with polarization $\boldsymbol{E}$, $\boldsymbol{H} \perp c$. (a) $x=0$, (b) $x=0.0742$, (c) $x=0.9$ (Agladze et al., 1993)

by one or many satellite lines, each of which is resolved and represents a transition for an ion in a particular environment. Such a spectrum obtained by Yamaguchi et al. (1998, 1999) for Eu^{3+} in $YAlO_3$ for three different dopant concentrations is reproduced in Fig. 4.3. While the inhomogeneous width of the central peak does not change very much in the dopant range from 0.001mol% to 0.1mol%, a large number of satellite lines appear over a frequency range of up to 400 GHz and strengthen relative to the main central absorption as the Eu^{3+} concentration is increased. By studying the integrated area of the lines as a function of concentration it was possible to identify which lines result from perturbations by nearby Eu^{3+} ions and which arise from intrinsic defects. Jaaniso

et al. (1994) were able to identify all of the nearest neighbor sites in the mixed crystal $SrFCl_xBr_{1-x}$: Sm^{2+} system. Cone et al. (1993) have identified over 40 satellite lines in flux-grown stoichiometric $EuVO_4$ and they have characterized many of these with spectral hole burning and optically detected nuclear quadrupole resonance techniques (Hansen et al., 1997) and for some sites, their symmetry can be determined. Using optical RF double resonance techniques in $YAlO_3$, it was possible to measure the hyperfine splittings in the $^7F_0$ ground state of Eu^{3+} of many of the 60 observed satellites and show that the hyperfine splittings and crystal field splittings exhibit a strong correlation (Yamaguchi et al., 1998).

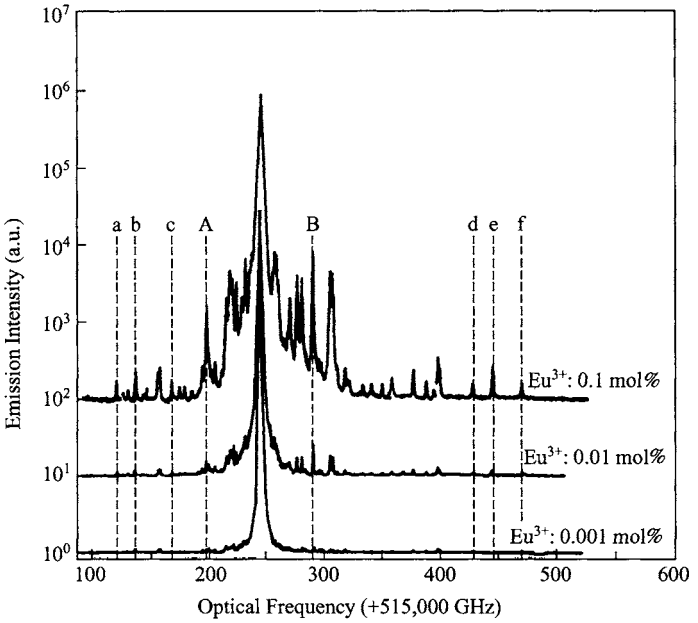


Figure 4.3 Logarithmic display of the excitation spectrum of the $^7F_0 \rightarrow {}^5D_0$ transition of Eu^{3+}: $YAlO_3$ (0.1 mol%, 0.01 mol%, 0.001 mol%) showing the growth of weak satellite lines with concentration (Yamaguchi et al., 1999)

The concentration distribution of these different sites is a complicated problem in defect equilibria. Wright and co-workers have shown that site-selective spectroscopy is a very useful tool to characterize the defect equilibria in CaF_2 (Cirillo-Penn and Wright, 1990), (Olsen et al., 1996). In Fig. 4.4 the concentration of the various sites, which have been identified with site-selective spectroscopy, are followed as a function of annealing time, t (in hours), in a sample of CaF_2 with 0.19% Eu^{3+}. Aggregate sites, such as the Q (trimer) site, tend to become dominant at long annealing times. Similarly they have performed

similar studies in the $SrTiO_3$ (Knott et al., 1995) and $LiNbO_3$ (Gill et al., 1996) systems.

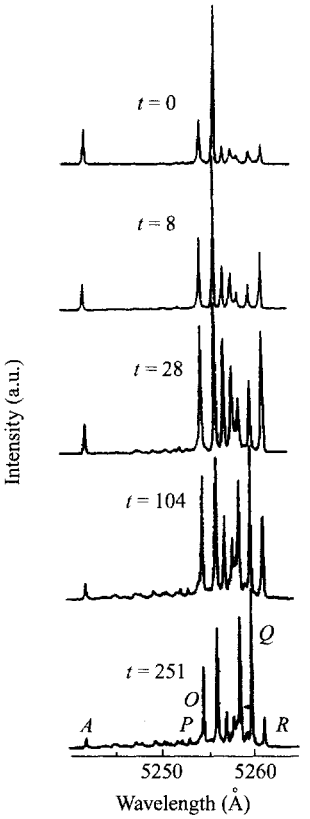


Figure 4. 4 Excitation spectra of the $^7F_0 \rightarrow {}^5D_1$ transition of Eu^{3+} (0.19%) in a CaF_2 sample annealed (followed by quenching) at 562 ℃ for a time, *t*, in hours (Cirillo-Penn and Wright, 1990)

A number of site selective studies have examined the dependence of certain optical properties on the excitation energy within inhomogeneously broadened optical transitions. These include the electronic magnetic moment (Sox et al., 1985; Pelletier Allard and Pelletier, 1986), quadrupole resonance spectrum in LaF_3: Pr^{3+} (Wald et al., 1992), unresolved crystal field splittings in glasses (Schmidt et al., 1994; Piazza et al., 1994), fluorescence lifetime (Tissue et al., 1991), homogeneous linewidth (Shelby and Macfarlane, 1980), energy transfer (Lupei et al., 1996), and spectral hole width. Some of these will be discussed in discussions of spectrally selective techniques later in this chapter.

4.2.4 Ultranarrow Inhomogeneous Linewidths

The narrowest inhomogeneous linewidths that have been seen in a rare earth doped solid are found in $YLiF_4$. Using Nd^{3+} probe ions, linewidths as small as 10 MHz or 0.0003 cm^{-1} have been reported by Macfarlane et al. (1998) in the presence of an external magnetic field. Somewhat broader, but still very narrow linewidths of 40 MHz were previously reported for Er^{3+} in this host (Macfarlane et al., 1992; Chukalina et al., 2000). To achieve these linewidths, the rare earth probe ion concentration must be extremely low, despite the fact that it is substitutional for Y with the same valence state and similar ionic radius. In fact the samples were not intentionally doped but contained only the residual rare earth concentrations present in the starting materials ($1-10$ ppm, $1\text{ppm}=10^{-6}$). In this case, the remaining inhomogeneous broadening, several 100 MHz, resulted from the random distribution of the Li isotopes (7% ^{6}Li, 93% ^{7}Li), which produced mass-dependent shifts of the optical transition frequencies. This has been unambiguously demonstrated by Agladze et al. (1991) as described in Section 4.2.2 (see Fig. 4.2). These result from a small dependence of the crystal field on the mass of the neighboring ions since their average distance from the rare earth increases with decreasing mass due to the enhanced zero-point vibrational motion. To obtain the narrowest linewidths in the pure ^{7}Li samples containing Nd^{3+}, a large magnetic field was applied in order to suppress homogeneous contributions to the linewidths due to the spin dynamics of these Kramers ions. An excitation spectrum of an "undoped" isotopically pure sample containing Nd^{3+} is shown in Fig. 4.5. The residual broadening results from the interaction of the Nd^{3+} ions, which have a large electronic magnetic moment, with the magnetic moment of the neighboring F nuclear spins whose two $S=1/2$ spin states occur with statistically random probabilities producing an inhomogeneous broadening through the superhyperfine interaction. As a result of these ultranarrow linewidths, the Nd^{3+} ($^4I_{9/2}\rightarrow{}^4F_{3/2}$) and Er^{3+} ($^4I_{15/2}\rightarrow{}^4F_{9/2}$) isotope shifts of 115 and 76 MHz/unit mass were directly measured in their respective excitation spectra. In addition, for Nd^{3+} a 30 MHz splitting of the inhomogeneously broadened lines were resolved for the even mass Nd^{3+} isotopes due to the superhyperfine interaction (Macfarlane et al., 1998). Isotope shifts of Eu in $EuCl_3:6H_2O$ have also been identified (Martin et al., 1998a).

In an elegant technique, even much narrower absorption lines have been produced by exciting a sample of Y_2SiO_5: Eu^{3+} with two oppositely phased coherent pulses of light, one long and one short (Sellars et al., 2000). This essentially burns out a hole in a inhomogeneously broadened line, but leaves a 50 kHz wide narrow absorption at the center.

4.3 Non-inhomogeneous Sources of Line Structure

Line structure is not always caused by inhomogeneous sources. There are a variety of intrinsic sources of line structure that occur even for an ideal defect-free crystal. It is important to realize this fact when analyzing optical spectra. One such example occurs in a magnetically ordered material, where at very low temperature, all ions experience the same local fields (dipolar or exchange) producing shifts and splittings of the optical transitions as discussed by Cone and Meltzer (1987). A recent example is the study of Er_2BaNiO_3 which illustrates how the magnetic order is manifested in the structure of the Er^{3+} spectra and can provide information on the Ni-Ni, Ni-Er and Er-Er magnetic interactions (Popova et al., 2003).

4.3.1 Hyperfine Structure and Isotope Shifts

For many of the rare earth ions, when the homogeneous linewidths and defect-induced contributions to the inhomogeneous linewidths are small, the lineshapes observed in absorption, emission and spectral hole burning spectroscopy are determined by hyperfine interactions involving coupling of the electrons and nucleus of a single ion. The hyperfine interaction is described in Chapter 1. The interaction splits the ground and excited electron-nuclear coupled states into components characterized by different values of the nuclear spin which have slightly different energies. Transitions occur among the ground and excited state hyperfine levels, the strongest ones conserving the nuclear spin. The result is a spectrum with a lineshape structure reflecting these splittings. Ho^{3+}, which typically has large hyperfine splittings, was the first rare earth ion to reveal (in $LaCl_3$) the hyperfine splitting in solids (Dieke and Pandey, 1964). Since then the hyperfine splittings of Ho^{3+} in CaF_2 have been observed in absorption for the C_{4v} site (Martin et al., 1992) or the C_{3v} site (Manson et al., 1992), and in $YLiF_4$ (Agladze et al., 1991) and (Martin et al., 1995). Hyperfine structure is also pronounced for the odd atomic mass isotopes of Er^{3+} (Macfarlane et al., 1992) and (Popova et al., 2000) and Nd^{3+} (Macfarlane et al., 1998) in $YLiF_4$ (see Fig. 4.5). The hyperfine structure of Pr^{3+} in $LaCl_3$ was also obtained using fluorescence line-narrowing (Pelletier Allard and Pelletier, 1979). In a high resolution infrared absorption study by Popova et al. (2001), hyperfine structure has been clearly resolved on a number of transitions for Pr^{3+} existing as Pr^{3+}-Cd^{2+} vacancy-Pr^{3+} symmetric pairs in $CsCdBr_3$. A crystal field calculation of the electronic energies and hyperfine splittings, including the relaxation of the pair, is in good agreement with experiment. From the measured linewidths, it was possible to obtain the homogeneous broadening of several transitions, which,

based on comparison with calculations, led to the identification of both one-phonon and two-phonon contributions to the relaxation.

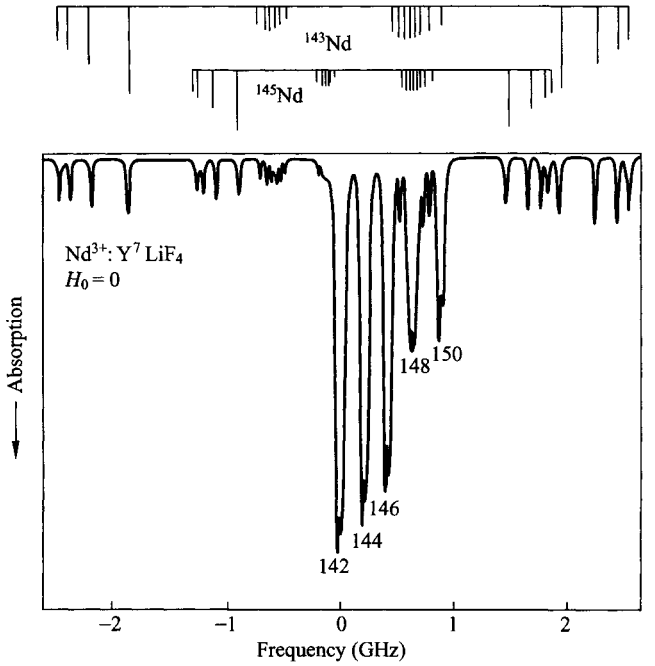


Figure 4.5 Fluorescence excitation spectrum of Nd isotopes in "undoped" Y^7LiF_4, isotopically pure in ^7Li at 1.6 K and zero magnetic field. Even Nd isotopic mass numbers are labeled. The calculated hyperfine structure for the two odd isotopes is shown at the top of the figure (Macfarlane et al., 1998)

It is important to recognize that the structure associated with these hyperfine transitions is not inhomogeneous in nature because all equivalent optical centers behave identically. The characterization of the shifts of the optical transition frequencies of the even isotopes of Nd^{3+} and Er^{3+} described earlier for $YLiF_4$ is not as obvious a situation since the different isotopes do experience slightly different crystal fields as described earlier. However all ions of a single isotope do have the same spectrum; thus each isotope should be considered as a different species with its own slightly different unique crystal field and spectrum.

4.3.2 Vibronic Sidebands

One other important source of line broadening and structure which is not inhomogeneous is the vibronic sideband which accompanies zero-phonon lines. While most of the 4f→4f transitions of trivalent rare earth ions have spectra

dominated by the zero-phonon lines, transition also occur in which one or more quanta of vibrational excitation are created or destroyed in conjunction with the electronic excitations. For $4f \rightarrow 5d$ transitions, the vibronic sidebands can dominate the spectrum. In absorption, this gives rise to an anti-Stokes sideband (phonon creation) on the high energy side or a Stokes sideband (phonon destruction) on the low energy side of the zero-phonon line. In emission these anti-Stokes and Stokes sidebands are associated with the creation or destruction of vibronic excitations, respectively.

The phonon sidebands involve all of the phonon modes of the host. The contribution of each phonon mode depends on the coupling of the phonon modes to the electronic transition moments of the rare earth ion and on the phonon density of states. The phonon sidebands vary from broad structureless band to continuous bands with structure as for Eu^{2+} in $KMgF_3$ (Ellens et al., 1994). In some cases, such as Sm^{2+} in $LiBaF_3$ the sidebands appear as sharp transitions associated with specific vibrational modes of the host lattice (Meijerink and Dirksen, 1995).

For $4f \rightarrow 5d$ transitions, the lineshapes are usually dominated by the vibronic sidebands and often the zero-phonon lines may be completely absent even at the lowest temperatures. The subject of vibronic sidebands is presented here for completeness but a full discussion can be found in Chapter 3.

4.4 Homogeneous Broadening

Dynamical processes, which persist even to very low temperatures, govern the homogeneous linewidths in solids. A study of these homogeneous linewidths provides a wealth of information about the physics of these dynamical processes. Any process which produces a real transition out of either the initial or final electronic state of the optical transition will contribute to the homogeneous linewidth. For example, the existence of an ion in an excited state is inherently transient with the ultimate decay to the ground state or some lower level through the emission of photons or phonons. In addition thermally available phonons interact with an ion in either its ground or excited state producing real transitions among the crystal field levels within a manifold. Virtual transitions involving two-phonon processes will destroy the phase of the transition dipoles also leading to homogeneous broadening. Transitions among the electron or nuclear spin states of an ion are constantly occurring; these processes occur for both the optical center itself, limiting the lifetimes of the initial or final states and for its surrounding neighbors leading to pure dephasing processes. Here the dynamics of the neighbors modulate the optical frequency of the optical center producing a dephasing of the transition dipole moments.

At room temperature and above, for most crystalline materials with low defect concentrations, homogeneous broadening dominates the optical lineshapes of the metastable excited states. As the temperature is reduced, the phonon

occupation is decreased such that inhomogeneous broadening tends to become dominant in the absorption or emission spectrum of a rare earth ion. However, a number of techniques are available, to probe within the inhomogeneous linewidth in order to extract information on the dynamical processes which govern the homogeneous linewidths. These methods such as fluorescence line-narrowing, spectral hole burning and coherent transient spectroscopy will be discussed in Section 4. 5. We first focus on the physical processes that determine these homogeneous linewidths.

The homogeneous linewidth Γ_h, is determined by the dephasing time T_2, which consists of contributions from real transitions, termed T_1 processes, and pure dephasing processes, governed by a relaxation time T_2^*. The relationship among these quantities is

$$\Gamma_h = (\pi T_2)^{-1} = (2\pi T_1)^{-1} + (\pi T_2^*)^{-1} \qquad (4.1)$$

The excited state decay always contributes to the T_1 processes. The lifetime contains contributions from both radiative and non-radiative processes. For excited states of the f^n configuration, radiative rates are typically in the millisecond and submillisecond time scale since these are parity forbidden, and often spin forbidden as well. These optical selection rules are described in Chapter 2. As a result, contributions to the homogeneous linewidth due to radiative decay are in the kHz or sub kHz regime. Lifetime-limited homogeneous linewidths as small as 122 Hz have been observed for Eu^{3+} in Y_2SiO_5 at low temperature using the two-pulse photon echo (Equall et al., 1994). For the $4f^n5d$ configuration, lifetimes are in the nanosecond to microsecond time regime which limit linewidths to the MHz range.

Non-radiative processes usually involve phonons to provide the energy conservation between the initial and final states involved in the population relaxation process. However processes such as autoionization, which can be quite fast, are a non-radiative process which will contribute to the homogeneous linewidth, often rendering the zero-phonon line so broad that it cannot be observed as a spectrally resolved feature. This can occur if the excited state of the rare earth ion lies in the conduction band of the host. In the case of Eu^{2+} in BaF_2 photoionization occurs with the formation of an impurity trapped exciton which is the emitting state (Moine et al., 1991).

4.4.1 Ion-phonon Interactions

The various electron-phonon interactions which contribute to relaxation are described in detail in Chapter 3. They will be briefly summarized here. As shown in Fig. 4. 6, the ground and excited crystal field multiplets consist of a number of electronic states separated by tens to hundreds of wavenumbers. The direct process, shown on the lower left of the figure, occurs when a phonon-

induced transition occurs between two crystal levels within either the ground or excited state manifold resulting in the absorption or emission of a single phonon. The downward relaxation process occurs spontaneously through the emission of a phonon with a rate T_{1d}^{-1}. If the transition involves such an excited crystal field level, this a relaxation will make a contribution to the homogeneous linewidth

$$\Gamma_{hd} = (2\pi T_{1d})^{-1}(p + 1) \tag{4.2}$$

where p is the occupation number of the phonons of frequency ω whose energy, $\hbar\omega = \Delta$, is the energy separation between the two crystal field levels since this is a resonant process. If the transition involves a higher-lying level in the manifold, like level c in the figure, one must consider all phonon processes which couple that level to all other levels in the manifold; these contribute additively to the homogenous linewidth. If the transition involves the lowest, metastable level in the manifold (level a) then only stimulated direct processes can occur and the homogeneous linewidth is

$$\Gamma_{hd} = (2\pi T_{1d})^{-1} p(\text{lowest level in manifold}). \tag{4.3}$$

These considerations apply to both the initial and final states of the transition and they are additive in their contributions to the homogeneous linewidth.

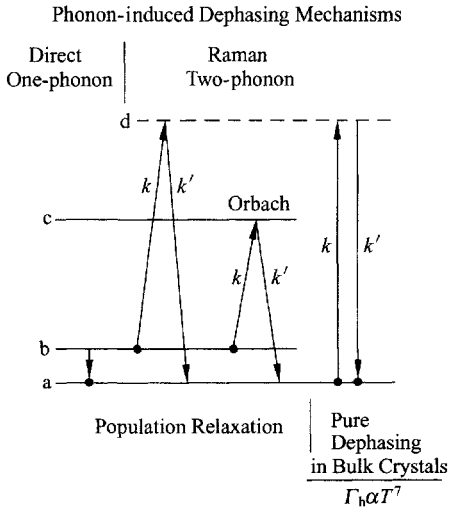


Figure 4. 6 Schematic showing phonon-induced dephasing mechanisms. Three crystal-field levels are labeled by a, b, and c. On the lower left is the direct one-phonon process between levels b and a. On the right are three two-phonon processes which are, from left to right, a Raman process coupling b and a through the virtual state d, the Orbach process involving two resonant phonons, and a two-phonon pure dephasing process

The rate, T_{1d}^{-1}, is proportional to the square of an electron-phonon matrix element for the particular crystal field levels involved in the phonon-mediated transition. It also is proportional to the phonon density of states at the resonant frequency ω. In the Debye limit where $kT \ll T_{Debye}$ such that in most materials only acoustic phonon modes are populated, this is proportional to the square of the frequency and it' s magnitude is host-dependent. It therefore follows that generally, $T_{1d}^{-1} \sim \omega^3$ (Meltzer and Rives, 1977). As a result, transitions that involve higher-lying levels in a manifold, in either emission or absorption, are more severely broadened. The electron-phonon matrix elements are usually an order of magnitude bigger in the $4f^{n-1}$ 5d configurations than in the $4f^n$ configurations because of the larger radial extent of the d-electron which results in greater sensitivity of the transition frequency to the motion of the neighbors.

Higher order processes involving two or more phonons also occur. The first and third of these two-phonon processes, shown to the right in Fig. 4.6 are non-resonant processes that involve all the phonon modes. The two-phonon Raman rate follows the form (McCumber and Sturge, 1963)

$$(T_{2R}^*)^{-1} = \int M^2 p(\omega)[p(\omega) + 1]\rho(\omega)^2 d\omega \qquad (4.4)$$

where M is the two-phonon electron-phonon matrix element and $\rho(\omega)$ is the phonon density of states. For transitions involving the lowest levels in both the ground and excited state manifolds, where only stimulated direct one-phonon processes are possible, it is often found, at low temperatures where the phonon occupation numbers coupling these metastable levels to higher levels are very small, that these two-phonon processes can dominate the homogeneous linewidths. When one integrates the contribution of Eq. (4.4) over all the phonon modes for low temperatures ($T \ll T_{Debye}$), the two-phonon Raman process contributes a T^7 temperature dependence to the homogeneous. Fig. 4.7 shows the T^7 temperature dependence of the $^7F_0 \rightarrow {}^5D_0$ homogeneous linewidth for Eu^{3+} in $YAlO_3$ and Y_2SiO_5 (Altner et al., 1996b). Two-phonon Raman processes are expected to dominate the dephasing in Eu^{3+} due to the isolation of the singlet ground ($^7F_0$) and excited ($^5D_0$) states associated with the transition. Two-phonon processes also become important at high temperatures where they can dominate the direct process because of the fact that they utilize all of the phonon modes. As shown by McCumber and Sturge (1963), in the high temperature limit, Eq. (4.4) yields a T^2 temperature dependence to the homogeneous linewidths. Resonant two-phonon processes, such as the Orbach process, occur when there are more than two levels in the ground or excited manifolds. It exhibits an exponentially activated temperature dependence (Yen et al., 1965) and often controls the relaxation time in electron spin resonance experiments.

In magnetically ordered materials, such as MnF_2, magnons can also take up the energy mismatch in a non-radiative electronic transition (Jongerden et al., 1985). In this case it was shown that transitions between Er^{3+} crystal field levels occur through the generation of magnons of the antiferromagnetic MnF_2 host.

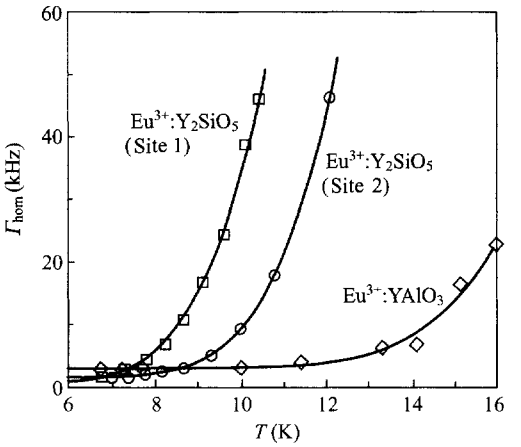


Figure 4.7 Temperature dependence of the homogeneous linewidth of the $^7F_0 \rightarrow {}^5D_0$ transition of Eu^{3+} measured by the two-pulse photon echo. The symbols are the experimental values and the full lines are fitted according to the T^7 law for two-phonon Raman scattering (Altner et al., 1996b)

4.4.2 Ion-ion Interactions

Any process that alters the frequency of the optical center, even if this occurs only briefly, will cause a dephasing of the transition dipole moment and therefore contribute to the homogeneous linewidth. Thus any dynamic interaction with the surrounding ions can play such a role. Important processes include electron spin-spin interactions, electron spin-nuclear spin interactions, excitation-induced frequency shifts, and energy transfer processes.

When the rare earth ions have electronic magnetic moments, electron spin-spin interactions occur between the dopant rare earth ions which contain magnetic dipolar and, if the ions are close to one another, exchange contributions. As the surrounding electron spins flip, this interaction modulates the frequencies of each of the optical centers, the magnitude of which depends on their separation. Where the initial and final spin states of the neighboring electron spin system have different energies, phonons will be required to conserve energy. However, energy conserving processes also occur whereby the surrounding ions undergo mutual spin flip. Because the two spins are not symmetrically placed with regard

to the optical center, the mutual spin flips produce a change in the frequency of the optical center. In some cases, one of the spins involved in the mutual spin flips may be the optical center itself, and this is referred to as a direct process for spin-spin interactions.

For Kramers rare earth ions all the states have magnetic moments. As a result, the electron spin-spin interaction plays a dominant role in the dephasing processes even at fairly low concentrations. For the case of two ions with a moment of the free electron spin ($g=2$) the magnetic dipole-dipole interaction at a typical nearest neighbor distance of 3 Å is about 10 GHz. Since the dipolar field falls off as $1/r^3$, even at impurity concentrations of 0.1%, these interactions produce optical frequency shifts of some 10 MHz. Therefore, for Kramers ions, if one wishes to observe radiative lifetime limited dephasing (<1 kHz), it will be necessary to study samples with impurity concentrations much smaller than 10 ppm. It is for this reason, in part, that radiative lifetime-limited dephasing has been observed predominantly for non-Kramers rare earth ions such as Eu^{3+}. However, in very large magnetic fields at low temperature, where the excited electron spin states are frozen out, very long dephasing times have been observed for Er^{3+} (a Kramers ion) in Y_2SiO_3 at 1.5 μm (Macfarlane et al., 1997). This technique has been used to observe the weaker electron-nuclear spin-spin interactions in several Kramers systems (Ganem et al., 1991b) and will be described in more detail later in Section 4.5.

It has been observed that the measured dephasing times are sometimes power dependent. Although laser experiments can cause transient thermal processes to occur (Bai and Kachru, 1992), often this mechanism for increased dephasing can be ruled out. It was shown that the enhanced dephasing resulted from a pure dephasing process associated with frequency shifts of the optical center caused by excitation of the neighboring ion to an excited state that has a different electronic dipole moment than that of the ground state (Taylor and Hessler, 1974; Huang et al., 1989; Liu and Cone, 1990). In this case, the dipole-dipole interaction of one rare earth with another causes a redistribution of optical frequencies that is "instantaneous", i.e. it occurs on the time scale of the optical excitation process. In principle, any change in the electronic distribution surrounding the optical center will produce a modification of the local fields and therefore will alter the energy level structure, ever so slightly. While these effects are small, in high resolution experiments they are important and can determine the dephasing rate. Graf et al. (1998) have done an exhaustive analysis of these excitation-induced frequency shifts (EFS) for Eu^{3+} and Pr^{3+} ions in Y_2SiO_5. EFS show up very readily in this system because of its very small homogeneous linewidths. In Fig. 4.8 the results of one of their experiments is shown in which the homogeneous linewidth obtained from the decay of the two-pulse photon echo (see Section 4.5.3.2) is plotted as a function of laser intensity as the laser is tuned across the inhomogeneous line profile. Γ_h depends linearly on the laser intensity and on the absorption coefficients at the laser frequency. The density of excited ions in the system depends linearly on both of these quantities. When the

results are divided by the absorption coefficient (or inhomogeneous line profile) they all fall on the same straight line (insert of Fig. 4.8) as predicted from the theory of EFS. These effects can be related quantitatively to the differences between the ground and excited state dipole moments.

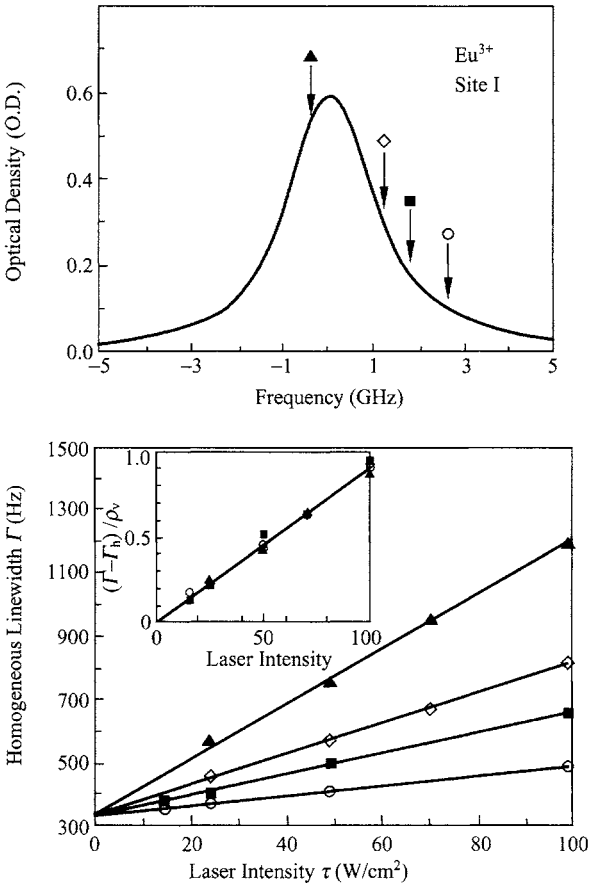


Figure 4.8 Line broadening based on the two-pulse photon echo as a function of position within the inhomogeneously broadened $^7F_0 \rightarrow {}^5D_0$ transition of Eu^{3+} (0.1%) in Y_2SiO_5 co-doped with 0.01% Pr^{3+} and 0.01% Nd^{3+}. The upper figure shows the location of the experiments within the absorption line profile while the lower figure shows the measured homogeneous linewidths as a function of laser intensity. The inset shows the same data, with the extrapolated zero intensity linewidth subtracted, divided by the line profile. The data collapse indicates that the broadening depends solely on the excitation density. The straight lines are linear fits (Graf et al., 1998)

Energy transfer can also lead to dephasing for two reasons. Energy transfer to a site with slightly different transition energy changes the optical frequency. In

addition, transfer processes among the neighboring ions results in a change in the dipole moments of these ions as one neighboring ion is excited and another is de-excited. The ion-ion interaction then causes shifts in the frequencies of all nearby ions, even if they have not been involved in the energy transfer. Although energy transfer-induced dephasing is difficult to confirm experimentally, it has been identified in the stoichiometric $LiTbF_4$ (Liu et al., 1990). This process gives rise to a spectral diffusion whereby the transition energies of the ensemble of optical centers evolve in time.

It should be noted that when the optical center is one of the host constituents in a stoichiometric material, ion-ion interactions lead to the formation of energy bands and the resulting quantum states are cooperative states of the system; these are referred to as excitons. The interactions responsible for the formation of these bands is identical to that which leads to energy transfer, namely multipole-multipole or exchange interactions. These states are delocalized and are characterized by their wavevector, $\boldsymbol{k}$, the pseudo momentum vector of the reciprocal space of the crystal lattice. These exciton bands have characteristic dispersion relations which describe the relationship between their energy and wavevector. The resulting transitions between these exciton bands have lineshapes which are determined by these dispersion relationships and their corresponding densities of states as has been described in detail in a previous review article (Cone and Meltzer, 1987). These lineshapes are neither inhomogeneously nor homogeneously broadened as they exist in the absence of any defects or disorder and are stationary states of the crystal. When transitions occur among these different exciton states within a band, contributions to the homogeneous linewidths do occur. For example, all transitions from the ground state ($\boldsymbol{k}=0$ state) can only go to $k=0$ excitons of the excited state since the optical photon connecting these states has a nearly zero $\boldsymbol{k}$-value of $\boldsymbol{k}=2\pi/\lambda$ where λ is the optical photon wavelength. These transitions between $\boldsymbol{k}=0$ states may be homogeneously broadened as a result of phonon-induced transitions out of the $\boldsymbol{k}=0$ state to other exciton states. These exciton dynamics have been described by Chen and Meltzer (1980).

Transitions among excited states are band-to-band transitions that include contributions from all wavevectors, subject of course to the condition that the wavevector is conserved in the transition because of the nearly zero wavevector of the optical photon. Their lineshapes are determined by the combined density of states of the initial and final exciton bands and the exciton dispersion relations. A very clear example of these unusual lineshapes observed in the $^5D_4 \rightarrow {}^7F_5$ band-to-band transitions is shown in Fig. 4. 9 for the ferromagnet, $Tb(OH)_3$. On the lower left in the figure is plotted the dependence of the energy of the exciton states as a function of $\boldsymbol{k}$ (dispersion relation). The band-to-band transition lineshapes occur vertically in $\boldsymbol{k}$ space because of the near zero momentum of the photon and their probability is proportional to the combined density of states of the initial (excited) and final (ground) states, weighted by the thermal occupancy of the exciton states in the upper band. Because the interactions

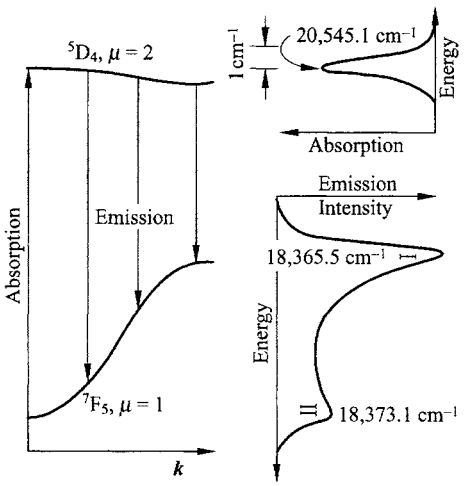


Figure 4. 9 One-dimensional ($\boldsymbol{k}/\!/c$) dispersion curves and absorption ($^5D_4$, $\mu = 2$) and emission ($^5D_4$, $\mu = 2 \rightarrow {}^7F_5$, $\mu = 1$) line shapes in $Tb(OH)_3$ at 1.5 K and with $H = 30$ kG $/\!/c$. Band-to-band emission occurs vertically at all k-values and the intensity contribution from each k-value is proportional to the population of the different $^5D_4$, $\mu = 2$ $\boldsymbol{k}$ states (Chen and Meltzer, 1980)

among Tb^{3+} ions occur almost exclusively between the ions located along the c-axis, these exciton bands are nearly purely one-dimensional. For one-dimensional excitons, the density of states is a maximum at the Brillouin zone boundaries (i. e. $\boldsymbol{k} = 0$ and the maximum $\boldsymbol{k}$-value) which accounts for the double peaked structure in emission. The ability to resolve the different $\boldsymbol{k}$ states spectrally made it possible to study the dynamics of relaxation in the excited exciton band which occurs at a rate of $\sim 10^6\ s^{-1}$. Thus the T_1 contribution to the homogeneous broadening of the exciton states in this system at 1.5 K due to phonon processes is about 1 MHz. More recently, Salem et al. (1990) have described the exciton lineshapes in the fluorescence of $Gd(OH)_3$.

A special case of these cooperative states occurs for the case of isolated pairs of identical rare earth ions. In that case, each ion has the same energy levels, aside from slight differences resulting from asymmetrically placed defects which affect the two ions differently. A pair of energy levels arises from each single ion state and the energy states of the pair are linear combinations of the states of the isolated ions. Their exact wavefunctions and energies depend on the ratio of the slight energy mismatch and the coupling between the ions due to exchange and multipolar interactions. When the pair is excited, the energy is shared between the two ions and oscillates between the two ions coherently. As in the case of exciton bands, the transition lineshapes reflect the fact that each single ion state is

split by the Davidov splitting and one must consider the details of the selection rules which govern transitions among these split pair states. One of the best materials to study rare earth pairs is $CsCdCl_6$ since the rare earth ions preferentially enter as pairs consisting of two rare earth ions substituting for three Cd ions forming a RE^{3+}-vacancy-RE^{3+} pair along the *c*-axis. Charge compensation then occurs naturally within the pair without the need for any additional defects. Nd^{3+} pairs have been studied by Barthem et al. (1989) and Ramaz et al. (1992) while Chaminade et al. (1991) have described the case of Pr^{3+} pairs and have set a limit of 2 MHz on the Davidov splitting for the pair. Homogeneous broadening can then modify the lineshapes further, usually masking the pair interaction if it much greater than the energy mismatch and ion-ion interactions.

The occurrence of rare earth pairs is quite frequent in all rare earth doped systems as the concentration is increased simply by the statistical occupancy of two ions in nearby sites. These pairs are usually difficult to characterize exactly because so many different pairs are possible. The most exhaustively studied material is CaF_2 where pairs as well as trimers and even more complicated aggregates have been identified (Olsen et al., 1996, Cirillo-Penn and Wright, 1990 and references therein). An interesting example, in which coherently excited pairs have now been reported is Nd^{3+} doped CaF_2 (Basiev et al., 1999) (Fedorov et al., 2000; Basiev et al., 2001; Orlovskii et al., 2002) and the problem has been discussed theoretically (Bodenschatz and Heber, 1996) where it was shown that optical bistability can occur. Optical bistability has been observed in $CsCdBr_3$: RE^{3+} (Hehlen et al., 1999). Ferromagnetically coupled Nd^{3+} pairs have also been reported in $YLiF_4$ and YVO_4 (Guillot-Noel et al., 2000).

4.4.3 Ion-nuclear Spin-spin Interactions

Dynamical processes involving the surrounding nuclear spins can make important contributions to the homogeneous linewidths when phonon-induced processes are suppressed. The various possible configurations of surrounding nuclear spins create local magnetic fields acting on the electron-nuclear states of the optical center. Spin flips of these surrounding nuclei produce a constantly fluctuating magnetic field at the optical centers, thereby modulating their optical transition frequencies by an amount $\Delta\nu$. This interaction is of the form

$$\Delta\nu = \mu_e \mu_n / r^3, \tag{4.5}$$

where μ_e and μ_n are the electron and nuclear magnetic moments, respectively, r is the distance between the optical center and the surrounding nuclear spin. The interaction of a free-electron spin and a nuclear spin of one nuclear Bohr magneton produces a frequency shift of ~ 10 MHz for typical nearest neighbor

cation distances of 3 Å. Since nuclear spin flip Zeeman energies are about of ~1 MHz/kG and because the hyperfine splittings are usually less than 1 GHz, it is not possible to freeze out these spin flips except at ultra-low temperatures (i. e., mK to μK).

A proper understanding of the effect of these superhyperfine interactions on homogeneous broadening must take into account the factor of the "frozen core" (Mims, 1972; Wald et al., 1992) which arises in the following manner. Nuclear spin flips must conserve energy and so the dominant nuclear spin-flip process involves the mutual spin flips of two or more nuclei. The optical center however produces a local field acting on the surrounding nuclei, whose magnitude is proportional to the electronic magnetic moment of the optical center. Because of the asymmetrical placement of the nuclei with respect to the optical center, this local field causes an energy difference in the splittings of the nuclear states of different ions making energy conserving mutual spin-flip processes more difficult. As a result, the nearby nuclei that produce the largest transition frequency shifts of the optical center flip much more slowly than the more distant nuclei that have much smaller dephasing effects. This was directly observed in Pr^{3+}: LaF_3 where a resonance condition is established between transitions of the Pr and F nuclear spins. The resonance leads to the refilling of the Pr^{3+} nuclear spin states which were emptied by the hole burning and, as a result, to the depopulation of the nearby F nuclear spins in the frozen core. NMR studies of the bulk spins demonstrate the greatly reduced coupling of the perturbed F spins from the bulk spins (Wald et al., 1992). As a result of the frozen core one cannot define a unique dephasing time because the transition frequency shift is small at short times and much larger at longer times when the nearby spins have had time to flip. The "melting" of the core gradually inward toward the optical center leads to spectral diffusion. Beautiful examples of these effects have been observed and will be discussed in more detail later in this chapter. Even for rare earth ions that have no electronic magnetic moment, homogeneous broadening and spectral diffusion can occur because of the interaction of the nuclear quadrupole moments of the optical center with the surrounding nuclei.

4.5 Measurement of Line Broadening and Examples

While conventional spectroscopy can provide a wealth of information on inhomogeneous broadening, or at high temperatures when dynamical processes limit the linewidth, about homogeneous broadening, information about homogeneous linewidths are often buried within the inhomogeneously broadened lineshape. To extract information about homogeneous broadening, two approaches have been developed. One operates in the frequency domain and selectively excites a subset of ions from within the inhomgeneously broadened lineshape. Such techniques include fluorescence line narrowing (FLN), first described in solids by Denisov and Kizel (1967) and Szabo (1970), and spectral

hole burning, initially performed in the solid state by Szabo (1975). In the second method, referred to as the time domain, the sample is coherently excited with pulses of light and the coherence of the ensemble is followed in time. Examples of time domain techniques include the photon echo, demonstrated for the first time by Kurnit et al. (1964), and optical free induction as described in a solid by Genack et al. (1976). The resolution capabilities of these different techniques are limited in various ways. For FLN, the resolution is limited by the band width of the detection system, usually some tens of MHz. spectral hole burning (SHB) and Optical free induction techniques are limited by the laser band width. Recent development have produced ultra narrow laser bandwidths in the kHz (Sellars et al., 1994a; Manson et al., 1995) and sub-kHz regimes (Sellin et al., 1999), although commercial CW lasers are usually limited to about 1 MHz. The PE does not suffer from these limitations.

4.5.1 Fluorescence Line-narrowing

The technique of fluorescence line-narrowing(FLN) was first described in solids by Szabo (1970). Earlier reviews have described the FLN technique and provide many examples of its applications (Selzer, 1986). A laser or other light source whose bandwidth is less than the inhomogeneous linewidth, is used to selectively excite a subset of rare earth ions from within the inhomogeneously broadened absorption. The fluorescence is then selected for detection with some sort of spectrally selective device. Even the best grating spectrometers are limited in resolution to about 1 GHz. Thus high resolution FLN experiments often utilize a Fabry-Perot interferometer as the spectrum analyzer. These can easily provide resolution in the tens of MHz. In addition, they typically have a much higher throughput than grating spectrometers. However, one must be careful to limit the detected light to the one optical transition that one is investigating. Thus a secondary spectrally selective device is usually needed to block these other wavelengths such as an absorbing glass filter, interference filter, or a low resolution high throughput spectrometer.

In the usual case, it is the emitted light resonant with the excitation source which is of interest. This resonant FLN provides the best means of removing inhomogeneous contributions, allowing the extraction of the homogeneous linewidth. Because the detector will then see the exciting light, which is much more intense than the emission, it is necessary to design the experiment in such a way as to eliminate or minimize the excitation light from reaching the light detector. This is accomplished by choosing a geometry, usually such that the source illuminates the sample at right angles to the viewing direction, so that only a minimal amount of scattered exciting light reaches the detector. In strongly scattering materials, or where this geometrical arrangement is not possible, it may be necessary to gate the excitation and detection so that they are open at mutually exclusive times. Thus one can use a chopper or acousto-optic modulator

to turn on the source, and an appropriately timed shutter (mechanical, acousto-optic, or electro-optic) to open the optical path from the sample to the spectral analyzing system and light detector, only during the time interval when the excitation source is blocked from the sample. This optical gating system also has the advantage that one can do time-resolved FLN experiments. Choppers and mechanical shutters are limited to time windows of some tens of microseconds, which can be inadequate for short-lived luminescence or for fast time resolution. Acousto-optic and electro-optic devices can operate in the nanosecond time domain.

If one looks at non-resonant fluorescence, many of the technical problems of separating the source from the emission are not present. However, non-resonant fluorescence is still subject to inhomogeneous broadening. This follows from the fact that while a subset of ions has been selected by the laser which has the same transition energy for that one chosen transition, there may still be a distribution of frequencies for transitions to other levels. The accidental degeneracy of the ions which are excited by the source is not matched for other transitions which have not been site selected for other transitions. As a result, the non-resonant transitions may exhibit some line-narrowing because there has been some selectivity, but generally they will not be greatly line-narrowed.

An exception to this occurs when there is a strong correlation among the energy levels in a manifold. An example of this occurs when the sublevels of a given crystal field level are split by an external field such as a magnetic field. The Zeeman sublevels are then all split by nearly the same amount, as long as the g-values are not inhomogeneous. Thus when one excites one Zeeman transition between the ground and excited crystal field levels, all other transitions among the Zeeman levels of those crystal field levels will be strongly line-narrowed. This provides an effective means to obtain similar information to that of excited state electron-spin resonance but without a microwave source (Sox et al., 1985; Pelletier Allard and Pelletier, 1986). FLN spectroscopy is also an effective means of looking at small unresolved splittings that exist in the ground or excited states when these splittings are much less sensitive to the environment that the electronic transition energy between the ground and excited states. For example, using FLN spectroscopy, the hyperfine splitting of Pr^{3+} in $LaCl_3$ can be extracted from within the inhomogeneously broadened line as shown in Fig. 4.10. The strong lines are the emission at the laser excitation frequency in two orders of the interferometer while the non-resonant lines involve transitions to other hyperfine levels in the ground state (Delsart et al., 1976). FLN can also be utilized to great advantage in rare earths to look at the small crystal field splittings in the ground state as has been done for Cr^{3+} in a number of hosts; the first example was ruby (Szabo, 1970).

FLN spectroscopy is restricted to systems that luminesce. The technique can also become difficult if the excited state lifetime is very short since it becomes difficult to separate the fluorescence from the excitation source, at least when detecting resonantly. While FLN spectroscopy is a powerful tool of site-selective

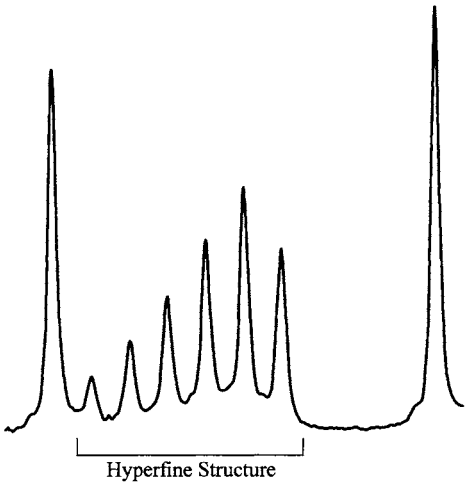


Figure 4. 10 Fluorescence line narrowing for the $^3H_4(E_2) \rightarrow {}^1D_2(A_1)$ transition of Pr^{3+} in $LaCl_3$ in a magnetic field of $H = 17.35$ kG$//c$. The two largest lines show the free spectral range of the Fabry-Perot interferometer. The six line pattern results from the nuclear Zeeman effect for the $S = 5/2$ nuclear spin of Pr (Pelletier-Allard, 1977)

spectroscopy, a number of high resolution techniques are available and so it has received its greatest use in disordered and amorphous systems as discussed later.

Because the fluorescence continues for the lifetime of the excited state, it can evolve in time due to dynamical processes. As a result, the measured fluorescence spectrum records the time-average spectrum and includes these dynamical processes. Thus, in using FLN to measure homogeneous linewidths, one must remember that the measurement may not record the "true" homogeneous linewidth, but rather one which includes the broadening resulting from dynamics which occurs over the time scale of the FLN experiment. However, if one detects the fluorescence as a function of time one can study dynamical processes such as resonant energy transfer or spectral diffusion associated with dynamics of the environment. Time-resolved fluorescence line narrowing (TRFLN) was reviewed by Yen (1979) and Yen and co-workers have shown the power of this technique for near-resonant energy transfer studies (Selzer et al., 1977; Flach et al., 1977). More recently, TRFLN has been applied to study energy transfer in glasses. Two of the many recent examples are the studies of Eu^{3+}-doped fluorophosphate glass (Balda et al., 1996) or in Yb^{3+}-doped fluoroindate glasses (Martin et al., 1998b). However, line broadening in glasses will not be considered extensively in this chapter. A good review of the subject can be found in a special issue of the Journal of Luminescence (Weber, 1987).

Near-resonant fluorescence will also evolve in time due to changes in the environment of the optical center. Examples of such changes include slight rearrangements of the atoms in amorphous materials, or changes in the electronic or magnetic moments of the neighboring spins. Because of the spectral resolution limits of FLN spectroscopy, many of these processes are better addressed with hole burning techniques.

4.5.2 Spectral Hole Burning

Spectral hole burning (SHB) spectroscopy has the advantage that it is not limited to systems that luminesce since it can be applied in absorption as well as excitation spectroscopy and its resolution capabilities are the linewidth of the laser, not that of the spectrometer or interferometer. The process was first described by Szabo (1975) for ruby. The technique is based on ones ability to remove the absorption of some subset of ions through selective excitation. This requires that the selectively excited ions remain for a sufficient time in some state other than the original ground state. The reduced ground state population of those ions leads to a reduction in absorption at the excitation frequency for the period of time it takes for those ions return to their original ground state. This creates a "hole" in the absorption spectrum. If the ion population is stored in some state other than the original ground state for some short period of time, we refer to the process as transient spectral hole burning (TSHB). Examples of population reservoirs for TSHB include the originally excited electronic state, referred to as saturation spectroscopy, the method used in the original work of Szabo (1975), hyperfine levels in the ground electronic state (Erickson, 1977), Zeeman sublevels when the ions are placed in a magnetic field (Macfarlane and Vial, 1988), or even the superhyperfine levels which result from the interaction of the ion with its surrounding nuclei (Macfarlane et al., 1981; Hasan et al., 1990).

4.5.2.1 Transient Spectral Hole Burning

The transient hole burning spectrum of Eu: Y_2SiO_5, shown in Fig. 4.11, exhibits the characteristics of populations storage in the hyperfine levels of the ground state(Yano et al., 1991). The mechanism is described in Fig. 4.12. For those ions for which the laser is resonant with one of the transitions between a particular set of hyperfine levels of the ground and excited states, as indicated by transition A, population is removed from that ground state hyperfine level. This occurs because when the ion relaxes back to the ground state, there is a probability that it will return to some other hyperfine level than the one from which it was excited. After many cycles of excitation and relaxation, population will be moved from the initial ground state hyperfine level to one of the other hyperfine levels for a period equal to the nuclear spin relaxation time. When the laser frequency is scanned about the initial burn frequency, a hole will be found at the original burn frequency (A in Fig. 4.12) and all other transition frequencies from this initial level to the various excited state hyperfine levels,

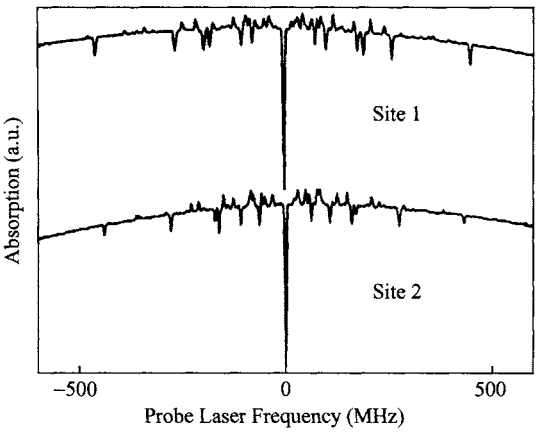


Figure 4. 11 Hole burning spectra in absorption for the $^7F_0 \rightarrow {}^5D_0$ transition of Eu^{3+} (0.1%) in Y_2SiO_5 at the two crystallographically inequivalent sites at 6 K. Note the six sideholes (3 for each isotope of Eu) and the larger number of antiholes (Yano et al., 1991)

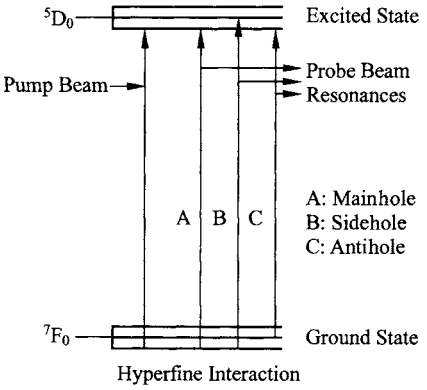


Figure 4. 12 Schematic of the transient hole burning mechanism of Eu^{3+} by population redistribution among the hyperfine levels of the ground state. Hole burning occurs for those ions for which the laser beam is resonant with one of the hyperfine transitions since when these excited ions relax, they may return to one of the other ground state hyperfine levels leaving a hole in the absorption at the pump frequency A. Side holes B appear at frequencies from the depleted ground state level to other excited state hyperfine levels and antiholes (increased absorption) appear at transition originating from other ground state hyperfine levels C (Meltzer et al., 1997)

one of which is indicated by transition B. For Eu^{3+} the hyperfine structure in the ground state contains three levels so that three sideholes should be observed for

each of the two Eu isotopes, producing a total of six sideholes, as seen in Fig. 4.11, on each side of the main hole. Antiholes, or increased absorption, will occur at frequencies such as C where the absorption originates from some other ground state hyperfine levels that have had their population enhanced. These will occur at all combinations of excited and ground state hyperfine splittings and thus there are many more antiholes as seen in Fig. 4.11.

In some cases when the selectively excited ions (actually it is the nearly equivalent ions that remain in their original ground state) have their frequencies altered only slightly, as was the case for FLN, the hole spectrum may change continuously in time and the bandwidth of the spectral hole may gradually increase; this is referred to as spectral diffusion. This may arise from rearrangements of the surroundings as in glasses or it can occur from dynamics of the electron or nuclear spins surrounding the optical center. The broadening is limited by the interaction strength of the electron spin on the optical center and the neighboring spins. This is GHz for electron spin-electron interactions involving Kramers ions with permanent electronic magnetic moments. For interactions with the nearby nuclear spins this ranges from tens of MHz for Kramers ions to sub-MHz for ions without permanent electronic magnetic moments. An example of time-resolved SHB is shown in Fig. 4.13 for Er^{3+}, a Kramers ion, interacting with the surrounding fluorine nuclei (Wang et al., 1992). The $^4I_{15/2} \rightarrow {}^4F_{9/2}$ transition (lowest crystal field level) in $YLiF_4$, 0.02% Er^{3+}, in a magnetic field of 26.5 kG to suppress the effect of electron spin flips of the surrounding Er^{3+} ions, is observed to broaden with time as the fluorine nuclear spins flip. The broadening is proportional to the difference in the magnetic moments of the ground and excited electronic states, 4.69 MHz/G in the present example. Computer simulations of the time-resolved broadening indicate that it is not the mutual spin flips of pairs of F nuclei that produce the broadening, because these are suppressed by the frozen core effect, but rather it is the slow spin flips of the Er^{3+} electron spins which induce spin flips of the nearby F spins. The case of Pr^{3+}: LaF_3 illustrates the case of broadening for non-Kramers systems, although here the broadening is greater than that predicted for simple magnetic dipole-dipole coupling between the F^- and Pr^{3+} magnetic moments (Sellars et al., 1994b).

4.5.2.2 Persistent Spectral Hole Burning

If the optical transition frequencies are altered permanently (or practically speaking, a long time) then the system is said to undergo persistent spectral hole burning (PSHB). This occurs, for examples, when those ions resonant with the laser are photoionized, producing a new valence state whose optical absorption is totally different. The removal of the original absorption gives rise to a spectral hole. Divalent rare earth ions such as Eu^{2+} and Sm^{2+} are prone to this process. Sm^{2+} frequently exhibits photoionization PSHB in both ordered and disordered

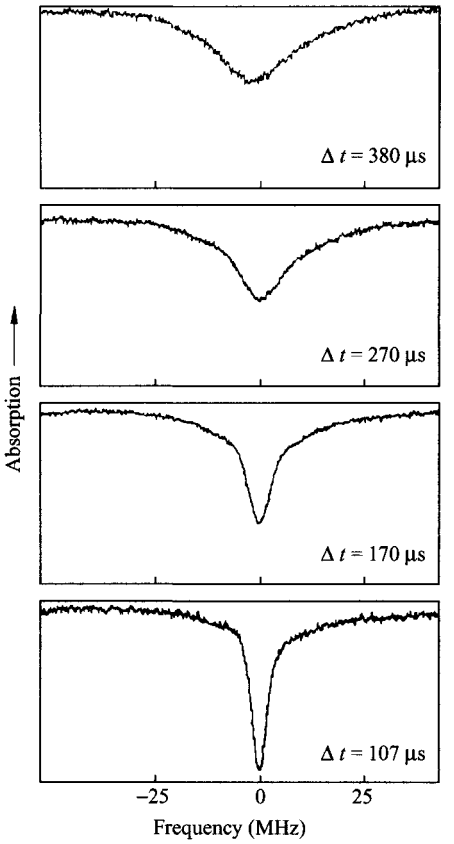


Figure 4. 13 Time dependence of the shape of a spectral hole showing spectral diffusion for the lowest crystal-field components of the $^4I_{15/2} \rightarrow {}^4F_{9/2}$ transition of Er^{3+} in $YLiF_4$. The spectrum was detected in absorption and was scanned by ramping a magnetic field in a coil surrounding the samples at a scan rate of 0.5 MHz/μs. The time delay between burning and scanning is indicated by Δt and the sample was in a DC magnetic field $H = 28.6$ kG//c (Wang et al., 1992)

crystalline systems and in glasses. The cases of disordered crystals are discussed in Section 4. 6. In well-ordered crystalline systems, PSHB of Sm^{2+} has been observed in CaF_2 (Macfarlane and Shelby, 1984; Beck et al., 1998), SrF_2 (Macfarlane and Meltzer, 1985), CaClF (Oppenlander et al., 1989), SrFCl (Zhang et al., 1992), $KLaF_4$ (Kodama et al., 1998) and Sr_2MgSiO_7 (Mikhail et al., 1999). For Eu^{2+} PSHB has been used to obtain the $^8S_{7/2}$ ground state structure (Boye et al., 1996a) as shown in Fig. 4. 14 where the hole spectrum is shown at zero magnetic field. The ground state is split into a closely-spaced triplet in the cubic field. Hyperfine interactions between the Eu^{2+} electron and F

nuclear spin produce a further structure. It was possible to calculate the expected hole lineshape based on the known parameters of the ground state obtained from previous electron spin resonance experiments obtained in a magnetic field and the agreement with the zero-field experiments is seen to be very good (Fig. 4.14). Eu^{2+} PSHB has also been studied in CaS (Basun et al., 1997; Kaplyanskii et al., 1998; Hasan et al., 1998a) and in MgS (Hasan et al., 1998b; Biyikli and Hasan, 1999). Because of the nature of the process, holes burned through PSHB often broaden as the hole is continuously burned. As additional ions have their charge states altered and the resulting released electrons migrate and become trapped, time varying electric fields are experienced by the remaining ions. The hole results from the absorption of the remaining ions that have not been photoionized. As the local electric field that they experience changes, their transition frequencies change and thereby modify the hole spectrum as a function of time (Biyikli and Hasan, 1999). As a result, the photoionization-induced spectral holes have linewidths which are usually some tens of MHz to GHz, even for shallow holes. These time varying Coulomb fields can even lead to hole burning of ions which were not originally in resonance with the laser producing broad spectral holes as discussed for Eu^{2+}: CaS by Basun et al. (1997).

PSHB also can occur without a photochemical change of the optical center. If the optical excitation induces some change in the environment, a non-photochemical persistent hole burning can occur. Perhaps the clearest example involving rare earths occurs for hydrogenated CaF_2 containing rare earth ions. The H^- (D^-) can provide charge compensation, like F^-, by going into a nearest interstitial position forming a site with C_{4v} symmetry. This site does not show PSHB. However, more complicated sites with one or two additional H^- (D^-) replacing F^- occur as well. Upon optical excitation of the rare earth ion in these more complicated sites, the H^- (D^-) perform a coordinated move to different positions, altering the environment about the rare earth and changing the absorption frequency; hence a spectra hole is formed (Macfarlane et al., 1987). These holes can be erased by illuminating with another polarization, thereby exciting the new center that had been formed and returning the H^- (D^-) ions to their original place (Reeves et al., 1989). This system has recently been used as a frequency reference for ultra-stable lasers using Tm^{3+} (Sellin et al., 1999). In a number of disordered crystalline or amorphous materials, rearrangements of the surroundings can also occur during optical excitation of the rare earth ion, generating a hole. These processes occur more frequently for ions which couple more strongly to their environment like Pr^{3+} than those like Eu^{3+} which couple rather weakly (Yugami et al., 1995; Schmidt et al., 1994). Hole burning in disordered systems will be considered later in Section 4.6.1.

For applications of materials exhibiting PSHB, such as frequency domain optical memories, one would like to have stable holes (Hasan et al., 1998a). However, this is generally not the case as discussed above. Not only does the hole spectrum evolve as additional burning is performed, but the holes can be erased by further light-induced effects associated with both the writing and

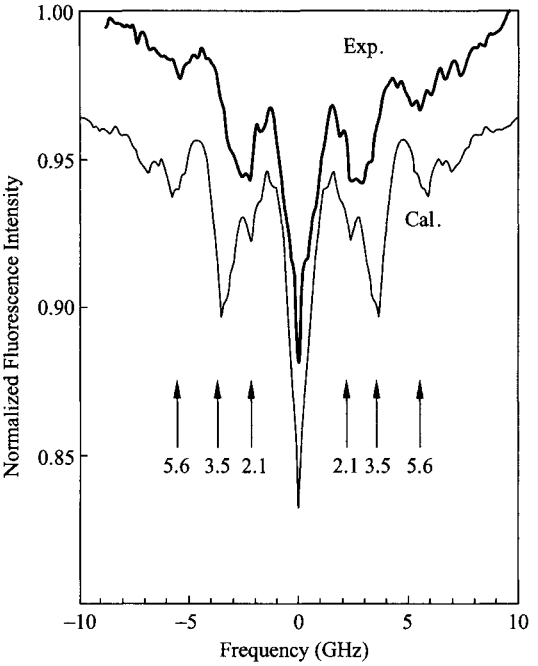


Figure 4. 14 Absorption spectrum of the hole burned in 75 min at an intensity of 50 W/cm^2 in the $4f^7(^8S_{7/2}) \rightarrow 4f^6 5d(\Gamma_8)$ zero-phonon transition of Eu^{2+} (0. 001% in CaF_2 at 1. 5 K). The experiment (dark curve) is compared with a calculation (light curve). The numbers indicate the frequency splittings in the ground state based on the known crystal-field splittings from ESR experiments. The narrow central feature has a width of 200 MHz (Boye et al., 1996a)

reading steps. One solution is the use of photon-gated spectral hole burning which was first described by Macfarlane (1987b). In this scheme, two photons are used to photoionize the hole burning system. The first performs a frequency-selective excitation which selects some subset of ions from within the inhomogeneously broadened line. The second, or gating step, at the same or preferably a different and lower frequency, induces the production of the hole. For photoionization-induced processes, this usually happens when the first excited state prepared by the first photon lies below the conduction band of the host while the second step performs an excited state absorption that carries the ion to a state above the edge of the conduction band edge. Ionization and migration of the released electron then occur until it is trapped. The process was first demonstrated by Winnacker et al. (1985) for Sm^{2+} in BaClF and has since been observed in a number of other systems involving mainly the divalent rare earths Sm^{2+} and Eu^{2+}. In at least one case of trivalent rare earth ions, photon-gated

PSHB due to selective photoionization of Pr^{3+} has been reported in Pr^{3+}: YAG (Macfarlane and Wittman, 1996) where hole burning, with a gating ratio in excess of 10^4, was observed in the absorption lines to the two lowest components of the $^1D_2$ manifold.

A novel hole burning mechanism has been reported by Kurita et al. (1999) in clusters of Sm^{2+}: ZnS nanoscrystals which has potential application in optical storage. The mechanism operates in strongly scattering media and it is both frequency selective and directionally selective so it has the properties of both hole burning and holography. The hole results from photoionization of the Sm^{2+} at any place in the absorption band, not necessarily the zero-phonon line, but a frequency selective feature appears when the probe light is incident on the sample from the same direction as the original bleaching beam. The effect occurs due to the interference pattern produced in the multiply scattering medium, somewhat analogous to coherent backscattering.

The availability of stable holes greatly simplifies the high resolution spectroscopic investigation of these materials since one can easily apply stress, or electric and magnetic fields after the holes are burned. One can also burn the holes at one temperature and study the hole spectrum as a function of temperature to examine effects of thermal broadening on the homogeneous linewidths or on thermal shifts of the optical transitions. Oppenlander et al. (1991) have measured a T^4 dependence of the hole position with temperature in Sm^{2+}: $BaFCl_{0.5}Br_{0.5}$ and have followed a temperature-induced hole broadening from 86 MHz to over 10 GHz from 1.5 to 77 K. Beck et al. (1998) found an unusual non-monotonous temperature shift of the hole frequency and a thermal broadening which they attribute to one-phonon coupling to a level 45 cm^{-1} above the T_{1u} resonant level of Sm^{2+} in CaF_2. Nonlinear Zeeman effects have been studied by Macfarlane and Shelby (1984) in CaF_2: Sm^{2+} and electronic Zeeman and Stark spectroscopy has been performed in BaClF: Sm^{2+} (Macfarlane et al., 1985) and in Sm^{2+}: SrF_2 (Macfarlane and Meltzer, 1985) using photon-gated hole burning. Pseudo Stark splittings of Eu^{2+} in CaS were measured and used to demonstrate the lack of inversion symmetry of the Eu^{2+} sites (Kaplyanskii et al., 1999). Hydrostatic pressure effects were studied by Oppenlander (1989) for Sm^{2+}: CaClF.

4.5.2.3 Hole Burning Measurement Techniques

The measurement of spectral hole burning is performed almost exclusively with a laser source. The laser promotes only those ions with which it is in resonance to some excited level. At some later time, the laser is scanned through the region which includes the original frequency, usually at a much lower power level so as not to alter the population distribution of the optical centers any further. In transmission detection, the transmitted laser light will increase when the laser frequency passes through that of the original burning frequency. If the absorption is very weak, then very sensitive detection techniques are required, as described

by Huston and Moerner (1984). If the lifetime of the population reservoir is very short, it may be possible to measure the hole spectrum using two frequency sources either by generating a sideband (Szabo, 1975) or with two different lasers where one laser is maintained at fixed frequency to continuously burn the hole while the absorption is monitored with a second laser passing through the same volume of the sample to measure the reduced transmission (Manson et al., 1992). Alternatively, when the optical centers fluoresce, the reduced absorption may be observed using excitation spectroscopy where the fluorescence intensity is monitored as the laser is scanned through the original frequency region. Because fluorescence detection can be quite sensitive, this can be applied in cases where the original absorption is very weak, even below the absorption detection limit. The disadvantage of excitation spectroscopy is that it usually is not possible to reduce the laser power during scanning as much as in a transmission measurement and one must be concerned that the laser further modifies the population distribution of the optical centers during scanning of the hole. A further disadvantage is that the scanning rate must be slower than the fluorescence lifetime or else the spectrum of the hole will be distorted by the slow response time of the ions.

While in most cases the hole spectrum is obtained by scanning the frequency of the laser, the scanning speed is limited, typically to about 100 MHz/ms for commercial single frequency tunable dye laser or Ti/sapphire laser systems. The scanning rate can be increased by several orders of magnitude by inserting a phase modulator in the laser cavity (Wannemacher et al., 1990). More rapid scanning, which is useful in cases where the hole lifetime is shorter than the time it would take the laser to scan the hole spectrum, or where rapid time-resolved hole burning is required to examine the hole refilling process or spectral diffusion, can sometimes be accomplished by scanning the spectrum of the ions. For example, usually the optical transition undergoes a linear Stark shift such that an electric field can be used to scan the spectrum of all the ions within the inhomogeneously broadened line together in unison. In this case, the spectral features of the hole will remain in tact and will be preserved. However, if the electric field distorts the spectrum because all the ions do not respond in the same way to the field, then this may not be a viable option. This can occur if the ions are inequivalent either because they sit at sites which are crystalographically equivalent but orientationally inequivalent, or if the defects producing the inhomogeneous broadening influence the Stark coefficients inhomogeneously. Alternatively, a tunable diode laser can be used to rapidly burn and scan the hole (Wannemacher et al., 1992).

If the electronic states involved in the optical transition have magnetic moments, a rapidly ramped magnetic field can also be utilized to scan the spectrum (Wang et al., 1992). In Fig. 4. 15, a hole spectrum for Er^{3+} in $YLiF_4$ is obtained by ramping a current in a small coil surrounding the sample. First the

hole is burned with a constant current in the coil, followed by ramping the current from zero to a current value which is twice that of the burn current, thereby using the Zeeman tuning to sweep the transition frequency of the ions through the laser frequency. The spectrum shows the central hole and nuclear spin-flip sideholes. In this case, the excitation of the Er ions can also produce nuclear spin flips on the surrounding F and Li nuclear spins. Because of the large DC magnetic field (19.8 kG, $\perp c$-axis), these double excitations which absorb a photon of laser energy share the energy between the electronic and nuclear transitions. As a result, when the hole is detected some ions whose electronic transitions energies differ from those of the laser by the nuclear spin flip energy have also been excited, thereby providing sideholes. The sideholes are labeled by the nuclei which are involved in the spin flip. While the eight Li nuclei are equivalent and produce one sidehole, the eight nn fluorine nuclei produce two inequivalent sets of Er^{3+} nuclei, each with four fluorine nuclei, labeled F1 and F2 in the Fig. 4.15. In addition there are sideholes produced by the flipping of more than one of the surrounding nuclei in a single electronic excitation.

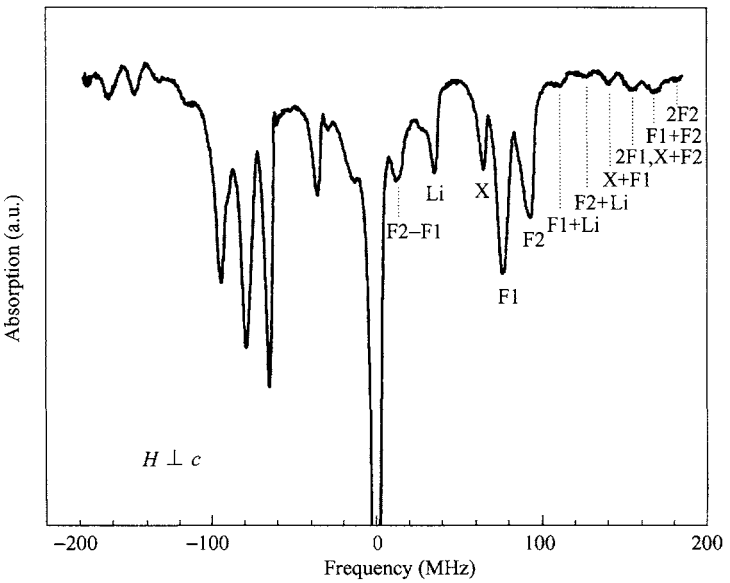


Figure 4.15 Hole spectrum in absorption using Zeeman scanning of the optical transition for the lowest crystal field components of the $^4I_{15/2} \rightarrow {}^4F_{9/2}$ transition of Er^{3+} in $YLiF_4$ at 1.6 K and $H = 19.8$ kG $\perp c$. The side holes result from nuclear spin-flip sidebands in which one of the two sets of F nuclei (F1 or F2), Li nuclei, or combinations of nuclei are flipped along with the electronic transition

In some cases, a modulated acoustic field applied with a transducer can be used to modulate the hole through the laser frequency, producing very sensitive detection. The resulting AC signal can be analyzed to determine the spectrum (Huston and Moerner, 1984).

4.5.3 Coherent Transient Spectroscopy

Frequency domain spectroscopy is limited in resolution by the capability of either the detector (FLN) or laser (SHB). In addition, these frequency domain experiments require a certain minimum time for excitation and detection. In many systems, dynamics can occur between the preparation and detection phase. While coherent transient spectroscopy (time-domain spectroscopy) still requires a finite time interval, it is generally much shorter, limited by T_2, the transverse relaxation time. It is an elegant technique, with characteristics analogous to pulsed NMR techniques. For an excellent description of optical coherent transient techniques, see Levenson and Kano (1988).

Time domain spectroscopy requires that the ensemble of optical centers be prepared in a coherent superposition of the ground and excited state. The time evolution of the coherence of the ensemble can then be described, to a first approximation, by the optical Bloch equations (Bloch, 1946) whose general applicability has been described by Muramoto et al. (1992). While the system remains in a coherent state, the light emitted will contain coherence and this coherence can be detected in a variety of ways. As the phase relationship among the ions becomes uncorrelated due to dynamical processes the coherence of the ensemble decays and so does the coherent emission. By following the decay of the coherence in time, the processes that cause the ensemble to dephase can be examined. The homogeneous linewidth is obtained from the observed dephasing time, T_2 through Eq. (4.1).

4.5.3.1 Optical Free Induction Decay

The method of optical free induction decay (FID) was first developed in magnetic resonance and it has proved to be an extremely important technique for extracting spin dynamics. The method was first applied in the optical frequency regime for rare earths by Genack et al. (1976). The FID signal is obtained by exciting the optical centers with a narrow bandwidth laser pulse of bandwidth $\Delta\nu$ and pulse duration Δt. The first order FID is analogous to the ringing of a bell and the coherence decays in a time given by the inverse of the inhomogeneous linewidth. For practical purposes, this is in the sub-nanosecond regime for most systems. It is the third order FID that is usually detected in rare earth systems. In this processes the exciting light begins to saturate the transition creating a hole in the optical spectrum. The third order FID is proportional to the third power of the Rabi frequency of the driving transition where the Rabi frequency is $\chi = \mu_{12}E/\hbar$.

Here μ_{12} is the optical transition dipole moment and E is the electric field of the laser radiation. The ensemble of excited optical centers begins radiating but because of their coherence with the original excitation source, the propagation characteristics of the FID signal are the same as the original excitation source. As the ions become out of phase with one another, the coherence of the ensemble decreases and the component of the coherent radiation diminishes while the incoherent component takes over. The intensity of the coherent emission decays exponentially in time and the $1/e$ decay time yields the value of $T_2/4$. However one must recognize that the bandwidth of the saturated absorption feature produced by the initial excitation pulse is instrument limited by the laser frequency jitter, $\Delta\nu$ (integrated over the preparation time), and the inverse of the excitation pulse width, $1/\Delta t$. As a consequence, the decay time of the FID is also laser limited. Reducing Δt can reduce the laser jitter but at some point the value of $1/\Delta t$ will exceed the time-integrated laser jitter. For commercial single frequency lasers, the FID signal will decay due to instrumental limitations in the microsecond time domain. However with some of the newer highly stable laser sources, long FID signals are possible.

To enhance the detection ability of the FID, the laser frequency can be shifted immediately after excitation of the coherence. The interference of the FID signal at the original laser frequency with the light from the frequency shifted laser will give an oscillatory beat signal enabling heterodyne detection of the amplitude of the FID signal. The signal can be detected with a photomultiplier, photodiode, or avalanche photodiode. The frequency shifting is usually accomplished with an electro-optic element in the cavity of a single frequency dye or Ti: sapphire laser or more recently, by current switching a diode laser (Macfarlane and Zhu, 1997). An alternative which has advantages for systems with short values of T_2 is phase switching whereby the phase of the laser is shifted by π through the application of a short pulse to a phase modulator inside the laser cavity (Genack et al., 1980). The amplitude of the heterodyne signal decays exponentially with a characteristic time, $T_2/2$, in the absence of instrumental limitations and under weakly saturating conditions when there is no power broadening, i. e. $\chi^2 T_1 \ll T_2^{-1}$, where T_1 is the excited state population lifetime. As was described for hole burning experiments, an alternative to shifting the laser frequency is to shift the transition frequency of the excited ions as has been done with electric (Shelby and Macfarlane, 1978) and magnetic fields (Wannemacher et al., 1989; Boye et al., 1990). An illustration of an heterodyne-detected FID response based on Zeeman field-switching for the lowest crystal field components of the $^4I_{15/2} \rightarrow {}^4F_{9/2}$ transition of Er^{3+} in $YLiF_4$ is shown in Fig. 4. 16 (Wannemacher et al., 1989). Both the ground and excited Kramers levels are split into a pair of Zeeman levels by the large field ($H = 29.5$ kG // c-axis) producing a total of four transitions. Each transition yields a different heterodyne beat frequency based on the magnetic moment differences between the ground and excited states involved in the transitions, which are therefore determined by the beat frequency in the FID signal. The decay time of the FID yields the

dephasing time which is determined by direct and indirect contributions of $Er^{3+} - Er^{3+}$ interactions due to mutual spin flips.

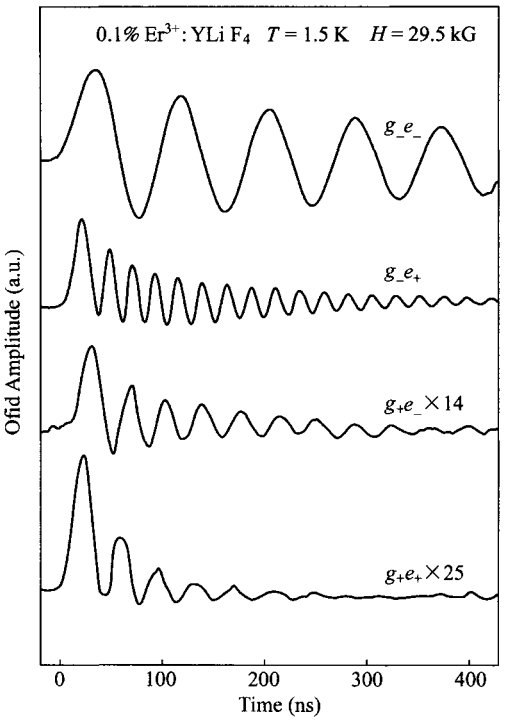


Figure 4. 16 Zeeman-switched optical free induction decay signals for each of the four Zeeman transitions of the $^4I_{15/2} \rightarrow {}^4F_{9/2}$ transition of Er^{3+} (0.1%) in $YLiF_4$ at about 1.5 K and for $H = 29.5$ kG//c. Here $g_{\pm}$ and $e_{\pm}$ identify the lower and upper Zeeman levels of the ground and excited electronic states. Note that the beat frequency is proportional to the magnetic moment difference between the ground and excited states (Wannemacher et al., 1989)

When there is sublevel structure within either the ground or excited state that falls within the bandwidth of the laser source, the laser excites more than one transition into a coherent superposition state. As a result, the coherence of the ensemble exhibits interference so that the coherent emission produces a heterodyne signal. This is referred to as quantum beat interference and is a method to obtain the sublevel energy level structure buried within the inhomogeneously broadened line by Fourier analyzing the interference to determine the frequencies responsible for the observed temporal behavior (Shelby et al., 1983; Shelby and Macfarlane, 1984). A short pulse of light of width Δt, is applied such that $1/\Delta t$ exceeds the sublevel splittings. The coherent Raman scattering of a weak beam at the same frequency is then modulated by the

sublevel coherence. For quantum beat interference to occur, the sublevel structure must exist in the spectrum of each ion since it is the sublevel coherence within each ion that causes the modulation of the FID. This structure can result from hyperfine, or superhyperfine interactions, and by splittings produced by external electric, magnetic or strain fields that remove the degeneracy and thereby produce the sublevel structure.

FID experiments also provide a means to measure spectral diffusion. Since the third order FID is generated from the saturation hole, the hole may be interrogated at a later time, limited by the hole lifetime, by a short pulse which generates a delayed FID. The decay time of the FID is determined by the width of the hole that can be interrogated as a function of time delay. This is then equivalent to time-resolved SHB. The decay of the FID under the influence of spectral diffusion has been treated theoretically (Malinovsky, 1995). It is also possible to use the delayed FID to characterize the frequency stability of a laser since if the laser frequency shifts between the first and second pulses, the heterodyne detected FID will exhibit a beat frequency showing the frequency shift of the laser (Pryde, 1999).

4.5.3.2 Photon Echo

The photon echo (PE) is a method of obtaining homogeneous linewidth information contained within the inhomogeneously broadened line that is not limited by the spectral bandwidth of the source or detector. In this method, two co-Linear laser pulses resonant with one of the optical transitions of the rare earth ion are applied to a volume of the sample as first described by Kurnit et al. (1964) in ruby. Each pulse produces an optical FID but the coherence decays in a time equal to the inverse laser bandwidth. The application of the second pulse at a time t_{12} after the first pulse, termed a π-pulse, effectively produces a reversal in the time evolution of the phases of the different ions as shown in Fig. 4.17 (after Levenson and Kano, 1988). The first pulse excites the ions either within the inhomogeneous linewidth or the effective laser bandwidth, whichever is greater. The different isochromats, resulting from the fact that each ion has a slightly different resonant frequency, get out of phase. At a time, t_{12}, a second pulse of pulse area, π, reverses the phase angles of all the ions by exchanging to some degree the amplitudes of the ground and excited states in the coherent superposition state. Their phase angles continue to evolve as before such that at time $2t_{12}$ all the ions rephase. At this moment, a coherent optical pulse, called the photon echo (PE), is generated by the coherent emission of the optical centers, co-linear with the excitation pulses.

Photon echoes can be generated with a number of different types of laser systems. Because the laser must be resonant with some particular transition of the rare earth ion, they usually require some sort of tunable laser. The first echoes were performed using short pulse tunable dye lasers pumped by N_2 lasers which

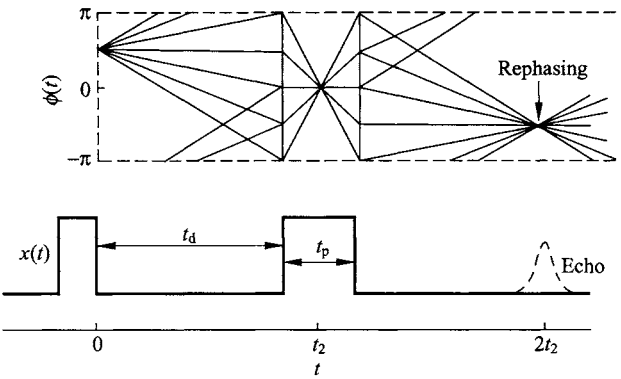


Figure 4. 17 Two-pulse photon echo indicating the phase evolution of the different ions with slightly different resonant frequencies. After the first $\pi/2$ pulse, which prepares a coherent superposition of the ground and excited state, the different ions get out of phase as indicated by the different lines in the figure describing $\phi(t)$. The second π pulse at time t_2 causes a reversal of all phases. The phase of each ion then continues to evolve as before until at a time $2t_2$, all ions rephase producing the echo (Levenson and Kano, 1988)

produced 10 ns pulses. Pump lasers now are usually Nd^{3+}: YAG or excimer lasers. When T_2 values are more than some tens of nanoseconds, gated CW tunable lasers such as dye or Ti: sapphire lasers pumped by gas lasers are used. More recently diode lasers, which are also tunable, have been successfully applied.

It is sometimes difficult to observe the echo, which is much weaker than the excitation pulses, because the detector has been saturated by the preparation pulses. One means to circumvent this problem is to propagate the two preparation pulses at an angle, θ, with respect to one another. Phase matching conditions, $\boldsymbol{k} = 2\boldsymbol{k}_2 - \boldsymbol{k}_1$, where $\boldsymbol{k}_1$, $\boldsymbol{k}_2$ and $\boldsymbol{k}$ are the wavevectors of the first, second and echo beams, respectively, dictate that the echo will appear in a direction 2θ with respect to the first pulse, on the other side of the second pulse. Spatial filters can then be used to mask the two preparation pulses so that only the echo is transmitted to the detector. It may still be necessary to further reduce the scattered light produced by the preparation pulses. Thus some sort of shutter (acousto-optic or electro-optic) is used to gate the transmission between the sample and detector such that the shutter is closed during the preparation pulses. In practice, two of these shutters in series may be necessary for rare earth ions. In cases where the PE is extremely weak, heterodyne detection techniques can be used enhance the echo relative to any background signal (Macfarlane et al., 1979). As the angle, θ, is increased, the echo signal decreases because the optical path of beam overlap is reduced and phase matching is incomplete. Wang et al. (1990) have shown that, for a paramagnetic ion, a pulsed non-uniform magnetic field can be used to restore much of the lost phase matching by

producing a spatially dependent phase correction to improve the phase matching and thereby enhance the echo signal.

Information on the homogeneous linewidth is obtained by measuring the echo intensity as a function of pulse delay, t_{12}. In the simplest case, the echo decays exponentially with a characteristic decay time of $T_2/4$. An example for the $^7F_0 \rightarrow {}^5D_0$ transition of Eu^{3+} in Y_2SiO_5 is shown in Fig. 4.18 (Equall et al., 1994) which shows the echo intensity as a function of t_{12}. While very narrow

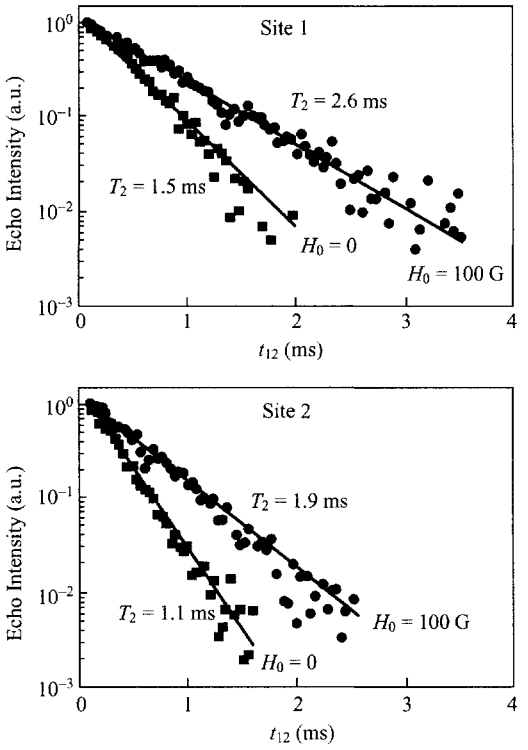


Figure 4.18 Photon echo decays on the $^7F_0 \rightarrow {}^5D_0$ transition for the two crystallographically inequivalent sites of Eu^{3+} in Y_2SiO_5 at 1.4 K and for a field H_0 = 100G. The excitation density was 6 W/cm^2 and the straight lines are exponential fits to the decays yielding the decay times, T_2, shown in the figure (Equall et al., 1994)

linewidths had previously been reported for this system (Yano et al., 1992) these results carry the effort even further. They represent the narrowest homogeneous linewidths seen in a solid, made possible by the fact that the host ions have zero or very small nuclear magnetic moments. To obtain these ultranarrow linewidths the sample had to be placed in a small magnetic field of 100G to limit the effects of dephasing due to flipping of the ^{89}Y nuclear spins and at the minimum pulse

intensities to reduce excitation-induced frequency effects (i.e., EFS or instantaneous diffusion). After correction for EFS, based on measurements as a function of intensity, linewidths of 105 Hz, nearly equal to the population lifetime-limited values, were obtained for both crystallographically inequivalent sites. Very narrow homogeneous linewidths have also been reported for the $^3H_4 \rightarrow {}^1D_2$ transition of Pr^{3+} (Equall et al., 1995) and the $^4I_{15/2} \rightarrow {}^4I_{13/2}$ transition of Er^{3+} in Y_2SiO_5 (Macfarlane et al., 1997) and for the $^5F_0 \rightarrow {}^5D_0$ transition of Eu^{3+} in $YAlO_3$ (Yano et al., 1992).

Spectral diffusion processes, such as those described for time resolved SHB, that occur during the time evolution of the echo, can lead to non-exponential decay. in situations for which ions are gradually removed from the coherent ensemble at a constant rate, as occurs for phonon-induced processes, an exponential decay is expected in contrast, interactions that lead to very small frequency shifts which grow with time will tend to produce a rate of dephasing which increases with time as the initial frequencies of ions in the coherently prepared ensemble spread from their initial values. Non-exponential decays have been clearly observed for ruby (Ganem et al., 1991a) and Kramers rare earth ions such as Er^{3+} (Macfarlane et al., 1991), and Tm^{3+} (Macfarlane, 1993a) at very low concentrations and in large magnetic fields which serve to suppress the effects of ion-ion interactions among the electronic spins of the paramagnetic ions (Ganem et al., 1991b). The remaining interactions with the host nuclear spins produce a slow spectral diffusion that leads to the non-exponential decay. For low concentrations (0.02%) of Er^{3+}, the echo decay time increases and becomes more non-exponential as the magnetic field is increased, finally saturating with a characteristic form, $I = I_0 \exp(-4t_{12}/T_m)^x$. For $x = 1$, the decay would be exponential; however for all these systems $x = 2.4$. This is shown in Fig. 4.19 for Er^{3+} ions in several hosts and for Cr^{3+} ion ruby. It is seen that when the decay of each system is scaled by the T_m, the phase memory time, the behavior of all systems is essentially identical indicating a universal behavior. Computer simulations of the echo decay behavior (Meltzer and Landau, 1992) successfully describe the experiments using the concept of the frozen core whereby the Er^{3+} magnetic moment perturbs the nearby F nuclear spin resonance energies such that mutual spin-spin flip-flops among the F nuclear spins near the Er^{3+} ion are greatly slowed since they are non energy conserving. As a result, F nuclear spins far from the Er^{3+} ions flip rapidly producing small changes in the optical frequencies of the ions. However, as time evolves, F spins closer to the Er^{3+} become more likely to flip. This produces the gradual broadening of the frequency distribution of the ensemble, leading to dephasing rates that increase with time. Simulations based on this model predict non-exponential decay with $x = 2.8$, close to that observed in the experiments. Calculations based on a bivalued random-telegraph process for the nuclear spin flips yield similar agreement with experiment (Huang and Szabo, 1996; Wang and Huang, 1997).

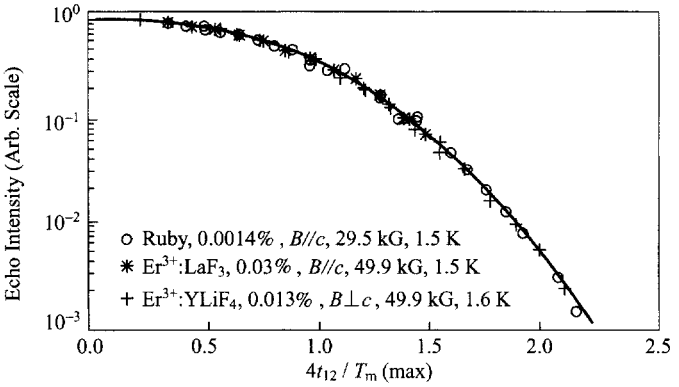


Figure 4. 19 Photon echo intensities in the superhyperfine limit for ruby (^{2}E), Er^{3+} in $YLiF_4$($^4F_{9/2}$) and LaF_3($S_{3/2}$). The data is plotted as a function of $4t_{12}/T_m$ where T_m is a parameter for each sample obtained by fitting the time decay of the echo (solid curve) to the form $\exp(-4t_{12}/T_m)^x$ where $x=2.4$ for all samples. Note the universality of the echo decay in the superhyperfine limit (Ganem et al., 1991b)

As for the case of the OFID, small splittings buried within the inhomogeneously broadened line can be observed as an oscillation of the two-photon echo intensity as a function of t_{12} as first demonstrated for rare earth ions in solids by Chen et al. (1980) where both the Pr^{3+} ground ($^3H_4$) and excited ($^3P_0$) state hyperfine interactions were extracted by a Fourier analysis of the echo modulations in Pr^{3+}: LaF_3; this work was followed by that of Whittaker and Hartmann (1982) on the $^1D_2$ excited state. Two-photon echo modulation studies have also been carried out for the $^3H_4 \rightarrow {}^1D_2$ transition of Pr^{3+} in YAG (Kim and Kachru, 1989).

Modulation of the echo intensity by time-dependent electric fields can also be used to obtain Stark coefficients which describe the pseudo-splitting resulting from the orientationally inequivalence of the sites whose transition dipole moments lie in different directions relative to the applied field. The effect of applying a pulsed electric field somewhere between the first echo preparation pulse and the echo produces different phase accumulations for the orientationally inequivalent sites. As a result an interference occurs between the echoes from the two sites. This is shown for Er^{3+} in $YAlO_3$ in Fig. 4. 20 where a voltage pulse produces an electric field along the a-axis between the first pulse and the echo that distinguishes two groups of sites (Wang and Meltzer, 1992). The phase accumulation depends on the product of the electric field (proportional to V, the voltage applied to the sample) and the width of the pulse (Δt) and therefore the intensity is modulated as a function of either Δt or V. Other examples of the

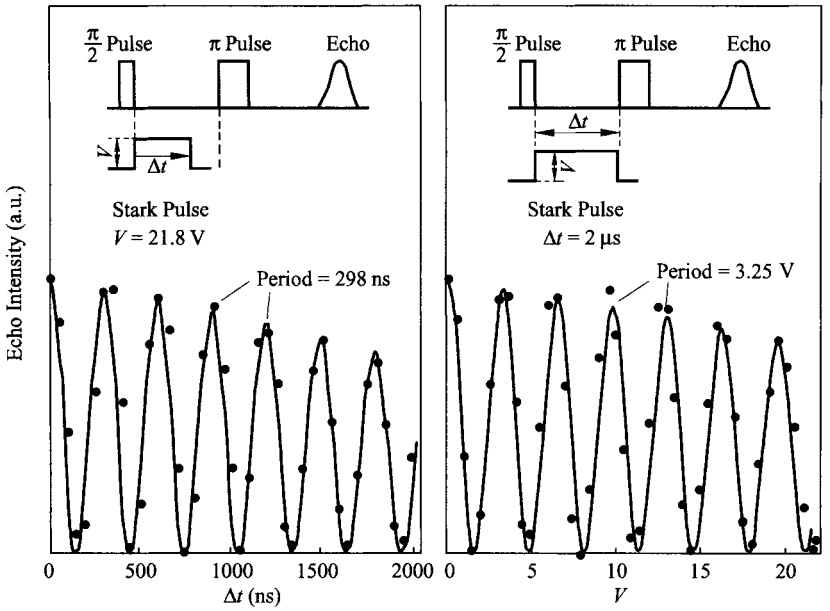


Figure 4.20 Photon echo intensity for the lowest crystal field components of the $^4I_{15/2} \rightarrow {}^4F_{9/2}$ transition of Er^{3+} in $YAlO_3$ as a function of (left figure) the width at fixed amplitude (21.8 V) and (right figure) the amplitude at fixed width (2 μs) of an electric field pulse applied to the sample along the *a*-axis between pulses one and two. The period of the oscillations yields the pseudo-Stark splitting due to the orientational inequivalence of two groups of sites in the field (Wang and Meltzer, 1992)

effect include studies of Eu^{3+} (Meixner et al., 1992; Graf et al., 1997) and Pr^{3+} in $YAlO_3$ (Macfarlane and Meixner, 1994; Graf et al., 1997a) and Pr^{3+} in LaF_3 (Lisin et al., 1996). Application of two Stark pulses, one during the time interval between the two echo preparation pulses and one between the second pulse and the formation of the echo can lead to a total rephasing of the echo and this makes it possible to study non reversible Stark interactions (Graf et al., 1997b).

In an interesting CW photon echo scheme, first proposed for the optical regime by Mitsunaga and Brewer (1985) and realized in $YAlO_3$ for Eu^{3+} by Mitsunaga et al. (1989) and Pr^{3+} by Mitsunaga (1990), where it was analyzed theoretically, the first pulse is replaced by a very long pulse. In this case the echo appears also as a long pulse whose intensity is modulated by the hyperfine splittings. Here all the information about the sublevel structure is contained in each echo event rather than in the time dependence of the echo intensity which must be obtained by varying the delay.

The decay of the photon echo is very sensitive to excitation-induced

frequency shifts (EFS) as discussed earlier under ion-ion interactions. This was first demonstrated by Huang et al. (1989). Dephasing from EFS has also been observed in two-pulse echoes for Pr^{3+} in $YAlO_3$ (Kroll et al., 1991), LaF_3 (Zhang and Mossberg, 1993) and Y_2SiO_5 (Altner et al., 1996; Graf et al., 1998). Theoretical treatments of this dephasing mechanism were performed by Altner and Mitsunaga (1996) and Altner et al. (1996).

Important information can also be obtained with other multipulse schemes. The stimulated echo is used to obtain information on dynamics, spectral diffusion and sublevel structure in the ground and excited states. In the stimulated photon echo, two pulses, separated by t_{12} are applied as in the two pulse echo. At a later time, t_{23}, after the second pulse, a third pulse is applied. This induces a new echo at time t_{12} after the third pulse. The stimulated photon echo occurs when there are population storage reservoirs to hold population in states other than the ground state and is therefore closely related to SHB. The first pulse, a $\pi/2$ pulse, coherently prepares the ions which then dephase according to their different frequencies as described in Fig. 4.17. The second $\pi/2$ pulse moves population into the excited or ground states for ions in-phase, or 180° out of phase with that of the first pulse, respectively. As a consequence of the first two pulses, ground state population is selectively removed from subsets of ions at certain resonant frequencies such that a structured hole spectrum is generated in the absorption. This frequency grating resulting from the frequency selective reduced ground state population can be stored for long time periods through the various processes described for spectral hole burning in Section 4.5.2. The third short pulse, also of area $\pi/2$, whose bandwidth exceeds the width of this hole structure, again prepares a coherence. Ions corresponding to peaks in the population grating will all have phase differences of 2π at a time t_{12} after the third pulse since their enhanced population was so selected by the first two pulses. As a result, this rephasing will lead to the generation of the stimulated echo. Both the phase relaxation time, T_2, and the population reservoir relaxation times can be obtained from measurements of the stimulated echo intensity as a function of t_{12} and t_{23}.

Frequency sublevel structure in the ground and excited states can be obtained through studies of the modulation of the stimulated echo intensity as a function of t_{12} and t_{23}. For the $^3H_4 \rightarrow {}^1D_2$ transition of Pr^{3+} in $YAlO_3$, Glaser et al. (1985) obtained the hyperfine splittings from the intensity of the stimulated photon echo as a function of t_{23}. The hyperfine structure of Pr^{3+} in a number of hosts including LaF_3 and YAG (Kim and Kachru, 1989, 1991) were obtained by varying t_{12}. Theoretical treatments of the stimulated echo have been provided by Mitsunaga et al. (1986), Levenson and Kano (1988) and Kim and Kachru (1991). The information about sublevel structure obtained with the stimulated PE is complementary to that obtained through the two-pulse PE but there are differences and additional information can obtained from the two experiments

(Kim and Kachru, 1991). In an exhaustive study of the $^3H_4 \rightarrow {}^1D_2$ transition of Pr^{3+} in $YAlO_3$, Mitsunaga et al. (1992a) analyzed both the two pulse and stimulated PEs as a function of both t_{12} and t_{23}. Large sublevel splittings are accessible by varying t_{12} in either echo scheme but smaller splittings require a study of the stimulated PE as a function of t_{23} because of the coherence lifetime limit imposed by T_2. The experimental and theoretical modulation patterns as a

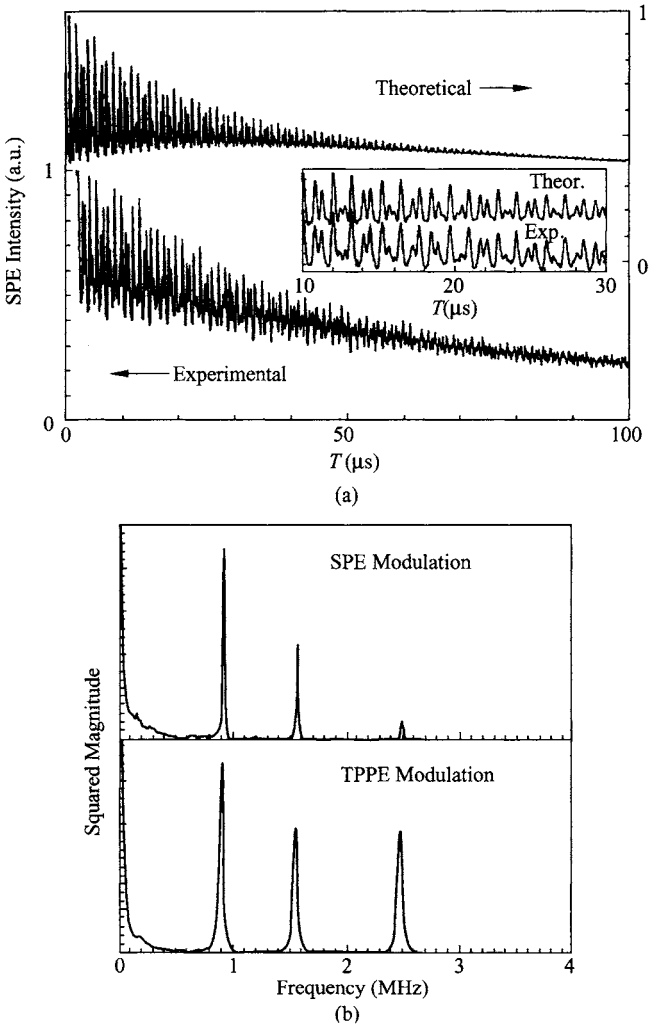


Figure 4. 21 Stimulated photon echo intensities for the $^3H_4 \rightarrow {}^1D_2$ transition of Pr^{3+} in $YAlO_3$. Shown are the theoretical (upper) and experimental (lower) results as a function of time delay, T or t_{23}, between the second and third excitation pulses. Insert is a portion of the temporal signal on an expanded time scale (Mitsunaga et al., 1992a)

function of t_{23} are compared in Fig. 4.21 for the $^3H_4 \rightarrow {}^1D_2$ transition of Pr^{3+} in $YAlO_3$. In this experiment, t_{12} was fixed at 2 μs while t_{23} (T in figure) was varied. The Fourier transform of the stimulated photon echo intensity vs t_{23} yields the small excited state splittings.

In addition, information on slow spectral diffusion can be obtained from the stimulated echo intensity as a function of t_{23} since spectral diffusion will broaden the population grating, thereby reducing the echo intensity. Yano et al. (1992) showed that in Eu^{3+}: $YAlO_3$ the homogeneous linewidth broadens from 1.2 to 7.2 kHz as t_{23} increases from microseconds to milliseconds due to spin flips of the nearby Al nuclei which perturb the optical frequencies. With the application of a small magnetic field, these can be slowed, resulting in an even further narrowing of the linewidth.

Excitation-induced frequency shifts can also be important in stimulated photon echo experiments. For example, it was demonstrated that excitation of one crystallographic site at the same time that a stimulated echo is performed on a different crystallographically inequivalent site, leads to a change in the decay of the stimulated echo that can be accounted for with a stochastic theory of EFS (Manykin et al., 1991; Mitsunaga et al., 1992b). There are instantaneous effects associated with the excitation of the ions by the echo preparation pulses and slow effects associated with the relaxation of the population of the ions that occur on a time scale of the relaxation time back to the ground state.

The stimulated echo can serve as the read out pulse for additional echoes (Erickson, 1992) and in optically dense media quite complicated multiple echo sequences can be observed (Khasanov et al., 1997a) and described theoretically (Khasanov et al., 1997b).

In situations where T_2 is extremely short but where there is an intermediate level to store population, the technique of the accumulated photon echo (APE) can be applied to studies of homogeneous linewidths. The technique was first demonstrated in glasses by Shelby (1983) and Macfarlane and Shelby (1983). In this method, a train of picosecond optical pulses is used to form a frequency grating in the ground state population. Each successive pulse increases the depth of the grating while at the same time it produces a stimulated echo. Using two beams which make a small angle with respect to one another, the echo is angularly separated from the preparation beam as described for the two-pulse photon echo. Because the APE is most useful in systems with short values of T_2, it has been applied mainly in amorphous and disordered systems.

4.6 Disordered, Low-dimensional and Nanostructure Crystalline Materials

For many technological applications, it is not well-ordered single crystals that are required, but rather, materials that have a high degree of disorder such as mixed

crystals or glasses, or materials with special dimensionality or nanoscale size. Applications include waveguides, frequency domain memories, special types of lasers, etc. In this section we address issues of inhomogeneous and homogeneous broadening in such rare earth-doped systems. While some aspects of line broadening remain unchanged, new features appear in these materials and this will be the emphasis of the present discussion.

4.6.1 Disordered Materials

For applications involving SHB memories, it is desirable to maximize the ratio of the inhomogeneous to the homogeneous linewidths. In this way it is possible to achieve the maximum number of distinct memory bits in the frequency domain, since the hole width is limited by the homogeneous linewidth. A great deal of effort has been expended by a number of groups to achieve this end.

Mixed crystals and glasses provide the largest inhomogeneous linewidths. Here one looks for materials which can be produced in solid solution over much or all of the concentration range. For mixed crystals the neighbors still form a regular crystalline array but the environment of the optical center is highly variable as the distribution of the mixed species, A and B, about the optical centers spans all possible combinations of the two species at the nearest neighbor positions. Since the crystal field levels are a function of these surroundings, a wide range of transition energies is provided. Variations of the neighbors in the second or third nearest neighbor positions provide a more subtle effect on the transition energies of the optical center. For glasses, not only the identity of the nearest neighbors, but also their positions form a distribution for the ensemble of optical centers, providing the line broadening. It is the dynamics of the environment that determines the homogeneous line broadening and this might be quite different in disordered crystalline and amorphous systems.

Amorphous systems or glasses exhibit a different type of dynamical behavior that is not observed in well-ordered crystals and which is described by the model of two-level systems (Anderson et al., 1972). As we shall see, however, disordered crystalline systems can exhibit dynamical behavior similar to that of amorphous systems. In amorphous systems, the ions do not sit on lattice sites; therefore they do not exhibit long range order. The ions on average maintain certain typical distances and arrangements with respect to one another, producing some degree of short range order, but many similar arrangements exist with only slightly different energies. The total energy of the systems depends of course on the exact location of all the ions in the system but many of these possible arrangements have similar energies with a large number of local energy minima. Displacements of the ions allow the system to move among these different local minima with potential energy barriers impeding these movements. At very low temperatures, the system is frozen in some local minimum with insufficient thermal energy to traverse the barriers but tunneling among these potential

minima can still occur. As the temperature is raised, more and more of these local minima are accessible and the system becomes more dynamically active.

The electronic energies of the optical rare earth centers depend on their local environment and as a result, the transition energies of the ions change as the system moves among these metastable configurations. Hence, the dephasing rate of the rare earth ions increases with temperature. Detailed models, which work rather well, have been presented to describe the dynamics. While it is not the purpose here to review or evaluate this work, it is important to state the central idea that involves the two-level systems (TLS).

It is assumed that the ions couple to these TLS such that the transition energy of the ions changes as the system undergoes a transition among two energy minima due to phonon-assisted tunneling across the potential energy barrier. Of course there is not one TLS but many to which the ion is coupled. As a result, the models consider a distribution of energy minima differences, a distribution of barrier heights, tunneling rates and coupling strengths, as well as different distributions of densities of states for the TLS. Because of the many parameters involved, the results may also depend on the way the averages are performed over these parameters. However, all the models lead to a power law behavior for the homogeneous linewidth which is nearly linear (slightly superlinear) at low temperatures with a T^2 behavior at higher temperatures. This behavior has been observed experimentally in a large number of both inorganic and organic glasses using FLN, SHB and coherent transient techniques and it is the accepted model for dephasing in glasses. For a comprehensive discussion see Weber (1987).

Mixed crystalline systems are ones in which one or more new types of ion (cation or anions) are added to a crystalline material such that the new species can replace the original one at the original lattice site in a random fashion. Three examples of mixed crystalline systems will be described in detail: yttrium oxide, alkaline earth fluorides, and the lead halide structure of mixed crystals containing mixtures of different alkaline earths and halides.

4.6.1.1 Yttria-based Mixed Crystalline Systems

Inhomogeneous linewidths in highly disordered mixed crystalline systems are of course very large, the more so for $4f-5d$ than for $4f-4f$ transitions as discussed in Section 4.2. The relationship between homogeneous and inhomogeneous linewidths have been extensively studied in yttria (Y_2O_3) containing high concentrations of other ions. Even in nominally pure material containing low concentrations of rare earth ions, the inherent defect presence shows up as an increased homogeneous linewidth that grows nearly linearly with temperature, similar to the behavior in glasses where it is the interaction with the TLS that dominate the dephasing. Two-pulse PE experiments on Pr^{3+} in fibers produced by laser-heated pedestal growth (Flinn et al., 1994) show a non-exponential echo decay with a decay rate which grows near linearly with temperature. Similarly,

PSHB and FLN experiments on two different samples of Pr^{3+}-doped Y_2O_3 shows that in one of the two samples , produced by flame fusion growth, the hole widths which grow as $T^{1.2}$ (Okuno et al., 1994a) while the second, higher quality sample, exhibited the T^7 Raman behavior expected for a defect free material.

Experiments on highly disordered mixed crystals of Eu^{3+}-doped $Y_{2-2x}Sc_{2x}O_3$ for which the Y_2O_3 and Sc_2O_3 components are identical in structure and contain cations of the same valence state show a rather surprising result. A comparison of the compositional dependence of the inhomogeneous and homogeneous linewidths is shown in Fig. 4. 22 (Jang and Meltzer, 1995). Samples with different values of x and containing different levels of Eu^{3+} ions are compared with one another and with yttria-stabilized zirconia (YSZ) and Eu^{3+}-doped glass. While the inhomogeneous linewidths grow monotonically with the degree of mixing, no such systematic variation of the homogeneous linewidth was observed. Evidently the mixing of two such similar materials does not increase the density of two-level systems associated with the intrinsic disorder.

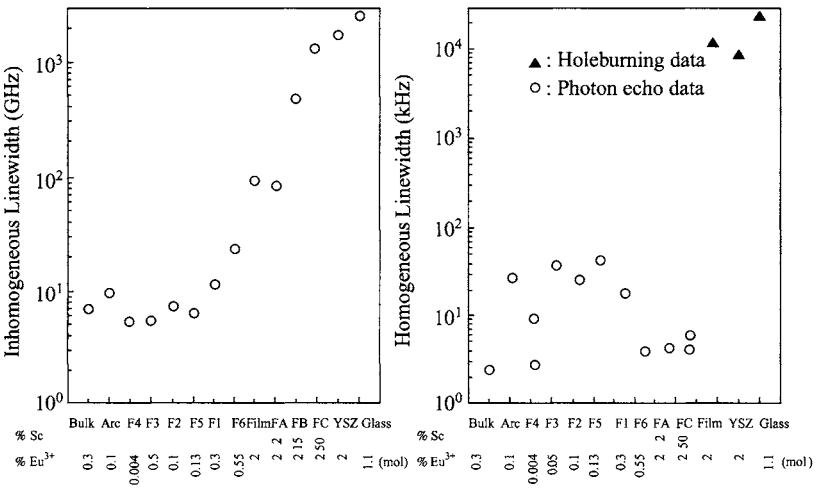


Figure 4. 22 Inhomogeneous and homogeneous linewidths for the $^7F_0 \rightarrow {}^5D_0$ transition of Eu^{3+} in Y_2O_3 (bulk, arc, F1 – F6), $Y_{2-2x}Sc_{2x}O_3$: Eu^{3+} 2% ($x = 0.02$, 0.15, 0.5), YSZ and silicate glass. Data from transient hole burning at 1. 5 K except for the glass ($T = 77$ K) (Jang and Meltzer, 1995)

The addition of divalent ions such as Mg^{2+} to Y_2O_3 enables PSHB of Pr^{3+}, which does not occur for samples with no Mg^{2+}, thereby producing a new hole burning mechanism. Unlike the case of transient holeburning by population redistribution among the ground state hyperfine levels, the holes have no

associated antihole structure, are much broader, the burning rate depends on the Mg^{2+} concentration and the hole width is a function of the light fluence (Okuno et al., 1996). The dependence of hole growth rate on light fluence and the observation that the homogeneous linewidths increase nearly linearly with Mg^{2+} concentration is consistent with a model in which the Pr^{3+} ions interact with TLS associated with the disorder introduced by the addition of Mg^{2+}, probably associated with oxygen vacancies (Okuno and Suemoto, 1999). Similar effects have been observed for Pr^{3+} in YAG containing MgO (Suemoto et al., 1998) and in $LiNbO_3$ and $Sr_{0.6}Ba_{0.4}Nb_2O_6$ (SBN), two materials known for having high levels of defects associated with vacancies (Macfarlane et al., 2000).

Further evidence for the role of different valence states on the dephasing rate comes from PSHB experiments on Pr^{3+} in yttria-stabilized zirconia or YSZ, a mixture of ZrO_2 and Y_2O_3 which preserves the Y_2O_3 phase (Tanaka et al., 1991) and Eu^{3+} (Jang and Meltzer, 1995), which show that the homogeneous linewidths are much larger than those found in $Y_{2(1-x)}Sc_{2x}O_3$ and that they exhibit a nearly linear temperature dependence. The additional dephasing may result from tunneling motion of the mobile vacancies which contribute to the ionic conductivity of YSZ (Tanaka et al., 1991). The inhomogeneous linewidths in YSZ result from disorder but buried within these broad lines are the crystal field splittings which have a distribution of values depending on the local environment. These splittings are revealed in FLN experiments which contain Stokes and anti-Stokes sidebands whose temperature dependences can be used to obtain the ground state crystal field splittings for Pr^{3+} in YSZ (Okuno et al., 1994b).

Thus it is seen that while the addition of ions which do not enhance the crystal defect structure do not in general lead to an increase in the dephasing rates, the addition of other ions, especially those of different valence states than that of the host, which promote the increase of the density of these defects (vacancies in this case) will give rise to behavior like that found in glasses where the dynamics is governed by the presence of two-level systems.

4.6.1.2 Mixed Fluorides

The alkaline earth fluorites are another interesting system to investigate the effects of disorder. Mixed crystals can be prepared from the different alkaline earth fluorides, MF_2 (M = Ca, Sr, Ba) which have identical valence states but different sizes. In addition trivalent fluorides such as LaF_3 and YF_3 can be mixed with MF_2 to produce solid solutions over a large range of concentrations. Both divalent and trivalent RE ions can be incorporated for optical studies. Trivalent RE ions require charge compensation and this occurs both by nearby compensation of the monomer dopant forming sites of C_{4v} and C_{3v} symmetry in addition to O_h symmetry sites where the charge compensation is quite distant. Even for relatively low lanthanide concentrations, pairs, trimers and more extended clusters form. At higher concentrations large defect structures are prevalent

(Catlow et al., 1989 and references therein).

The effect of the addition of small amounts of SrF_2 (up to 0.3%) to CaF_2 on the inhomogeneous linewidths of hyperfine transitions of Pr^{3+} have be studied and it was found that the removal of the axial symmetry of the C_{4v} charge-compensated site due to impurity-induced strain has large effects on the optical lineshapes (Martin et al., 1994). Laser selective excitation of Pr^{3+} centers in CaF_2 containing up to 1% SrF_2 or BaF_2 and similar samples of SrF_2 containing small amounts of CaF_2 and BaF_2 have identified up to nine sites exhibiting three site symmetries (Khong et al., 1993). Site-selective experiments of the $^4I_{9/2} - {}^4F_{3/2}$ transition of Nd^{3+} in CaF_2 containing a high (12%) concentration of YF_3 showed the presence of two classes of sites and allowed the determination of the ground state crystal field levels of each of the two classes as a function of excitation within each of their overlapping absorption profiles. Although studies of the spectral hole linewidth of the $^4I_{9/2} \rightarrow {}^4G_{5/2}(^2G_{7/2})$ transition of Nd^{3+} in the mixed crystal CaF_2/YF_3 were performed (Beck et al., 2000), the dynamics of this transition are dominated by single-phonon relaxation and did not allow for studies of TLS dominated dephasing. However, a number of optical studies of other rare earth ions in mixed crystals of MF_2 with LaF_3 or YF_3 have indicated the presence of TLS as described below.

Evidence for the presence of TLS in $Ba_{1-x}La_xF_{2+x}$ was first presented by Cahill and Pohl (1989) with the observation of glasslike behavior of the low temperature specific heat, thermal conductivity and internal friction. Far IR absorption measurements in $Ca_{1-x}La_xF_{2+x}$ (Fitzgerald et al., 1994) and $Ca_{1-x}La_xF_{2+x}$ (Karasik et al., 1998) and Raman scattering (Tu et al., 1996) indicated the presence of a continuous distribution of TLS like those found in glasses. The first optical evidence from rare earth spectroscopy appeared in the mid-IR where PSHB was performed in $Ba_{1-x}La_xF_{2+x}$ for the $^7F_6 \rightarrow {}^7F_5$ transition of Tb^{3+} (Love et al., 1992). The holes showed highly nonexponential decay over a time period from minutes to hours and a broad distribution of barrier heights observed in thermal cycling studies indicating that the hole burning results from a photophysical rearrangement as in glasses. Temperature dependent studies of the hole linewidth of the $^3H_4 \rightarrow {}^1D_2$ transition of Pr^{3+} in CaF_2 containing up to 30% YF_3 showed that the transient holes, produced by population redistribution among the hyperfine levels, broaden nearly linearly with temperature from 1 to 8 K (Jang et al., 1995). This result is similar to the temperature dependence of the hole linewidth observed in many glasses providing further evidence for the presence of TLS-like excitations in these disordered crystals; for a comparison to glasses see Schmidt et al. (1994) which discusses hole burning of Pr^{3+} in silicate glass.

4.6.1.3 Mixed Crystals Based on Sm^{2+}: BaClF

For applications in frequency domain optical storage, where some subset of ions are marked as a data bit, it is important to maximize the ratio of the

inhomogeneous linewidth, Γ_{inh}, to homogeneous linewidth, Γ_h, since the number of bits that can be stored at a particular location is $\sim \Gamma_{inh}/\Gamma_h$. One method to accomplish this is to use mixed crystals because of their large values of Γ_{inh}. The material which has received the most attention in this regard is the family of compounds related to BaFCl, where the disorder is introduced by mixing other halides or other alkaline earths into the crystal. The material is especially useful since when Sm^{2+} is doped into the crystal, two-photon gated spectral hole burning, with the holes stable up to 300 K, occurs by two-photon ionization (Winnacker et al., 1985), as described in Section 4.5.2. In BaClF, the lowest excited state of Sm^{2+} in the optical regime is the $^5D_0$ level of the $4f^6$ configuration which in the pure crystal gives sharp optical transitions from the $^7F_0$ ground state.

Wei et al. (1989) first demonstrated in $BaFCl_xBr_{1-x}$ that for $x=0.5$, Γ_{inh} could be increased by an order of magnitude relative to pure BaClF to about 26 cm^{-1} for transitions to $^5D_0$ and 40 cm^{-1} for transitions to $^5D_2$ and that these were nearly identical at 77 K and 300 K, proving that these linewidths were predominantly inhomogeneously broadening. Two-photon hole burning in the $^7F_0 \rightarrow {}^5D_2$ transition occurred at 77 K with a hole width of about 1 cm^{-1} yielding a ratio of Γ_{inh}/Γ_h of nearly 100. It was shown that this ratio is greatest in the concentration range $x=0.5$ to 0.8 and for the $^7F_0 \rightarrow {}^5D_2$ (Zhang et al., 1990). Two maxima are observed in the FLN spectra which are assigned to ions sitting at sites with the two most probably distributions of nearest neighbor halides assuming random statistics of site occupancy. Oppenlander et al. (1991) demonstrated that holes burned in the $^7F_0 \rightarrow {}^5D_2$ transition of an $x=0.5$ samples survived to 183 K and that their width at 1.5 K, 86 MHz, was only a factor of three larger than for samples with $x=0$. Even at 77 K the hole widths were only about 10 GHz so that 50 – 100 permanent holes could be burned simultaneously. Gating can be accomplished with a second non-resonant laser at 514.5 nm but the gating ratio is only three. The holes can be erased with 488 nm excitation. However the burning of subsequent holes partially erases previous holes because the burning irradiation also photoionizes the Sm^{2+} ions which resulted from the trapping of the released electrons at Sm^{3+} sites, converting them to Sm^{2+} in the process. To address the problem of erasure of holes upon the burning of new holes, Yb was added to Sm^{2+}: SrFCl to form a new electron trap that replaces the Sm^{3+} trap so that the Yb-induced trap is not photoionized by additional burning fluence (Zhang et al., 1993). Gating with a second laser source was found to be essential for selective excitation by the first laser to $^5D_0$ but only mildly effective at increasing the burning rate for excitation to $^5D_1$ and $^5D_2$ (Wei et al., 1991), indicating that the location of the Sm^{2+} ground state is such that two photons from the selective laser is below the energy threshold for reaching the host conduction band, consistent with previous results on the $x=0$ samples. Holes were observed after cycling to 300 K but significant refilling occurs. Studies of the temperature dependence of the hole width indicate a slightly superlinear

behavior below 20 K with a near T^3 dependence from 20 to 90 K, but as noted by the authors, no theory satisfactorily accounts for this behavior. The role of TLS is suggested by the low temperature behavior but the data is not sufficient to claim this with any confidence.

Jaaniso and Bill (1991) demonstrated room temperature PSHB of Sm^{2+} in $SrFCl_{0.5}Br_{0.5}$. Homogeneous widths as narrow as 1.3(2.4) cm^{-1} for selective excitation into the $^5D_0$ ($^5D_1$) state were observed while the inhomogeneous linewidth was 30 cm^{-1} making the ratio of $\Gamma_{inh}/\Gamma_h \approx 10-20$. Room temperature hole burning was also accomplished in even more disordered samples obtained by mixing the alkaline earth cations as well as the halide component forming materials of composition $M_yM'_{1-y}FCl_{0.5}Br_{0.5}$ (Holliday et al., 1992; Zhang et al., 1993). While mixing of the cation component did not appreciably increase the inhomogeneous linewidths, Zhang et al. (1993) found that forming a composite made of samples with different values of y yielded a powder for which Γ_{inh} was increased to over 60 cm^{-1}. Homogeneous linewidths at room temperature were about 7 cm^{-1}. The temperature dependence of the hole widths are shown in Fig. 4.23 for the $^7F_0 \rightarrow ^5D_1$ transition of Sm^{2+} in $Sr_{0.65}Ba_{0.35}FCl_{0.5}Br_{0.5}$ and is similar to that of a sample of $Sr_{0.5}Mg_{0.5}FCl_{0.5}Br_{0.5}$ and $BaFCl_{0.5}Br_{0.5}$ (Holliday et al., 1992). The data above 15 K fits a model based on two-phonon Raman scattering with little contribution from single-phonon processes. Another mechanism, which may be due to TLS dominates below 15 K but its magnitude is small perhaps because all the cation and the anion ions which are mixed have the same valence states tending not to introduce defects such as vacancies.

A systematic investigation of this mixed crystal family was carried out by Jaaniso and Bill (1995) by varying both the cation and halide anion composition. In Fig. 4.24 the excitation spectrum for the $^7F_0 \rightarrow ^5D_1$ transition of Sm^{2+} in different unmixed materials (Fig. 4.24c) and various mixed samples (Fig. 4.24a) are shown. It is seen that the transition frequency varies by almost 200 cm^{-1} across the series (Fig. 4.24c) and that cation mixing further increases Γ_{inh} (Fig. 4.24a). A theoretical model for the lineshape in these mixed crystals, based on work by Orth et al. (1993) and Jaaniso et al. (1994), which takes into account the statistical distribution of near neighbor configurations, was parameterized to describe the observed lineshapes in this family of mixed crystals. A series of holes burned at room temperature are shown in Fig. 4.24b. Studies of the decay of the holes above room temperature indicate that anionic diffusion broadens the holes. In fact, in samples with only cation disorder, the holes were quite stable even at 430 K.

Other disordered materials have also been examined for room temperature hole burning with large inhomogeneous linewidths. Kodama et al. (1995) found that the system $MALnF_6$ with M = Ca, Sr; A = Na, K, Rb; and Ln = Y, La exhibited room temperature holeburning of Sm^{2+}. The largest values of Γ_{inh} was 110 cm^{-1} for Ca/Sr/K/La samples. Additional attempts to increase Γ_{inh} were

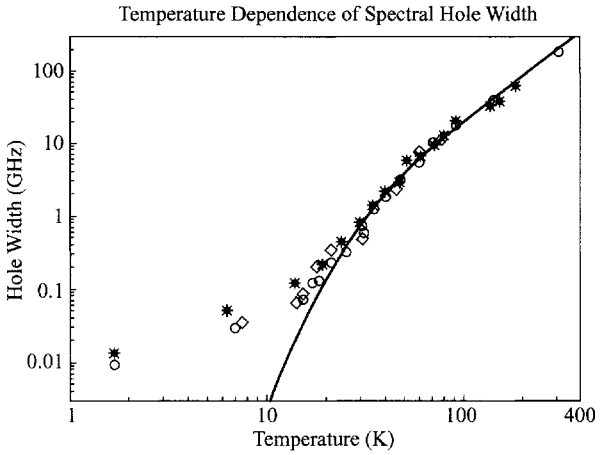


Figure 4. 23 Temperature dependence of the holewidths of PSHB of the $^7F_0 \rightarrow {}^5D_1$ transition of Sm^{2+} in $BaFCl_{0.5}Br_{0.5}$ (*), $Sr_{0.5}Mg_{0.5}FCl_{0.5}Br_{0.5}$ (°), $Sr_{0.65}Ba_{0.35}FCl_{0.5}Br_{0.5}$ (◇). The line is a fit assuming a two-phonon Raman scattering. An additional dephasing mechanism dominates below 15 K (Holliday et al., 1992)

made using thin films but this will be discussed later.

4.6.2 Low Dimensional Systems

Two-dimensional structures doped with rare earth ions are of interest for waveguide applications such as amplifiers or lasers and for fundamental studies of reduced dimensionality. Since waveguides containing rare earths are the subject of Chapter 8 (Jacquier), here we will focus on nanometer scale two-dimensional films and the effect of reduced dimensionality and epitaxial control of crystal growth on the optical lineshapes for rare earth ions in these films.

Epitaxial growth of fluoride films were first obtained by Farrow et al. (1981). High quality films of alkaline earth and lanthanide fluoride containing rare earth ions have been prepared by a number of groups. The optical properties of the rare earth ions serve as an excellent probe for film structure, strain and defect content. Although the 4f – 4f transitions of trivalent rare earths have very small oscillator strengths, ultra-sensitive techniques have been developed to measure absorption of the films through reflectance spectroscopy (Jones et al., 1990; Shortt et al., 1991). For films of NdF_3 as thin as 50 Å on GaAs, asymmetric lineshapes were observed due to the effect of narrow resonances on both the optical thickness and on the Fresnel coefficients. For films thinner than 50 Å, a much thicker LaF_3 buffer layer was grown on the GaAs before growing the NdF_3 film. Absorption lines in these thinner films were broadened and shifted

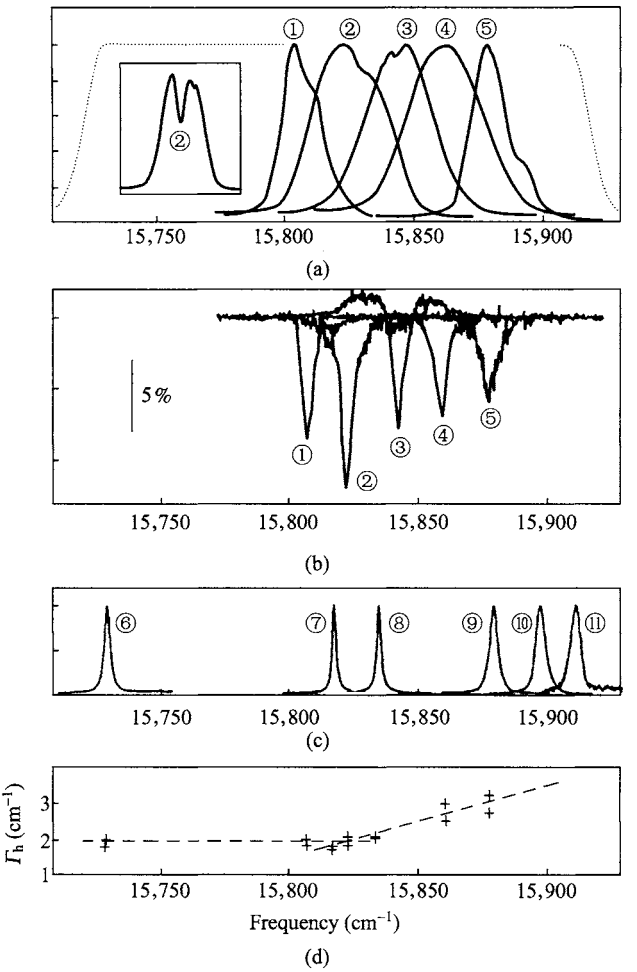


Figure 4. 24 Room temperature excitation (a), (c) and PSHB (b) spectra for the $^7F_0 \rightarrow {}^5D_1$ transition of Sm^{2+} in ① $Ca_{0.2}$ $Sr_{0.8}$ FCl; ② $SrFCl_{0.5}$ $Br_{0.5}$; ③$Sr_{0.8}Ba_{0.2}FCl_{0.2}Br_{0.8}$; ④ $Sr_{0.5}$ $Ba_{0.5}$ $FCl_{0.5}$ $Br_{0.5}$; ⑤ $BaFCl_{0.5}$ $Br_{0.5}$; ⑥ CaFCl; ⑦SrFCl; ⑧SrFBr; ⑨BaFCl; ⑩BaFBr; ⑪BaFI. Inset in (a) shows ~ 40% hole in spectrum ②; (d) shows the homogeneous linewidth for the different compounds as a function of transition frequency (Jaaniso and Bill, 1995)

relative to the thicker films due to the distortion of the film by the lattice mismatch between LaF_3 and NdF_3.

Sokolov and his co-workers have utilized the divalent rare earth ions, Sm^{2+} and Eu^{2+} which have well-defined zero-phonon lines in their 4f – 5d transitions as a very sensitive probe of strain in epitaxial layers of CaF_2 on Si substrates.

Using low temperature photoluminescence spectroscopy, the shift and broadening of the $4f^7\ (^8S_{7/2}) \rightarrow 4f^6 5d$ transition was easily seen as the thickness of the pseudomorphic film grown on Si (111) was increased as shown in Fig. 4.25 (Sokolov et al., 1989). For the thinnest film (12 nm), the peak position is

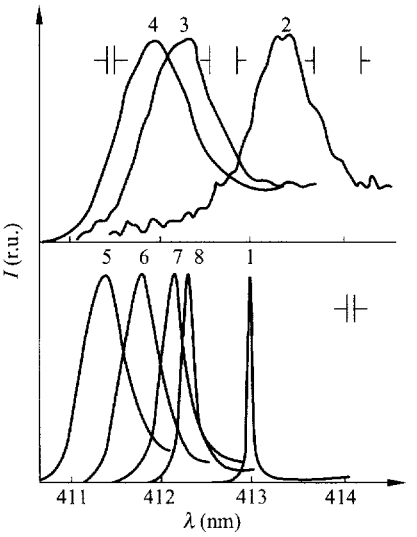


Figure 4.25 Photoluminescence spectra at 1.8 K of the $4f^7\ (^8S_{7/2}) \rightarrow 4f^6 5d(\Gamma_8)$ zero-phonon transition of Eu^{2+} in CaF_2: (1) bulk single crystal, (2–8) epitaxial films of CaF_2/Si(111) grown at 560℃: (2) 12 nm, (3) 17 nm, (4) 33 nm, (5) 59 nm, (6) 120 nm, (7) 295 nm, (8) 1100 nm (Sokolov et al., 1989)

shifted 0.4 nm to longer wavlength, but as the film thickness increases, the zero-phonon line moves to the shorter wavelength side of the bulk emission. For films thicker than about 60 nm, the line sharpens and moves back toward the bulk emission wavelength. Since the CaF_2 lattice constant is greater than that of Si at all temperatures, for thin layers there exists in plane compression. Compression is known to produce a long wavelength shift in the emission, consistent with the experimental result on the 12 nm film. For thick films, point defects and dislocations appear to relieve the stress due to lattice mismatch and enable an unstressed film to form at the growth temperature. As a result of the dislocations, the line broadens. These are frozen in after growth and therefore, upon cooling to the 1.8 K temperature of the experiment, differential contraction of the Si and CaF_2 lattices leads to in plane dilatation and thus a shift toward shorter wavelengths. Thus it is seen that the zero-phonon line position can be used to ascertain the strain in thin films and the linewidth can serve as a measure of the defect content. Monnier et al. (1995) have also examined the linewidth as a function of film thickness for possible applications in hole burning optical

storage.

A theory for the lineshapes in two-dimensional films where the elastic strain fields are distributed in a narrow surface layer has been developed by Averkiev et al. (1992, 1996). The theory considers edge dislocations in films and the role of compensating image forces in a quasi two-dimensional geometry in the limit that both the distance between defects and the distance between optical probe centers is greater than the film thickness. Because of the long range character of the perturbation, non standard lineshapes will occur. The theory leads to the prediction of asymmetric lineshapes in the case where only one type of dilatation center exists such as only vacancies. Where two types exist, a symmetric lineshape can occur but it will have wings which are much greater than that of Lorentzian lineshapes. The theory has been used to describe experimental lineshapes for the $4f^6 \rightarrow 4f^5 5d$ zero-phonon lines of Sm^{2+} in thin films (Averkiev et al., 1994). The theory has also been applied to very thin Sm^{2+} doped CaF_2 layers contained within a thicker undoped CaF_2 film in order to examine the lineshapes as a function of depth within the film (Yakovlev et al., 1997).

The spectroscopy of much thicker films CaF_2 (Bausa and Munoz-Yague, 1991) and LaF_3 (Lahoz et al., 1999) containing Nd^{3+}, prepared by molecular beam epitaxy, have also been described. The $4f \rightarrow 4f$ line positions and lineshapes of the trivalent rare earths are much less sensitive to strains and defects. It was found that the photoluminescence spectra depend on the type of substrate, where the distribution of different types of charge compensated centers is affected by the substrate (Bausa et al., 1992). Heteroepitaxial layers of Nd: LaF_3 grown on CaF_2 showed a dependence of the emission line positions on the selected surface orientation of the CaF_2 substrate (Bausa and Munoz-Yague, 1991) but homoepitaxial layers grown on LaF_3 exhibited spectra nearly identical to that of the bulk (Lahoz et al., 1999).

SHB studies of CaF_2 films containing Eu^{2+} show that only transient spectral hole burning occurs in films prepared by molecular beam epitaxy (Boye et al., 1996b), in contrast to bulk samples where PSHB results from photoionization of the Eu^{2+} centers. Evidently, in the MBE films, Eu^{3+} trapping centers do not form so that after excitation from the excited state by a second photon, the electron returns to the original Eu^{2+} ion. The hole spectrum as a function of magnetic field for a Eu^{2+} (0.1%) : CaF_2 on Si (111) is shown in Fig. 4.26. Holes and antiholes are observed due to the hyperfine splittings in the ground and excited states. The sideholes at 0.6 and 1.4 GHz are the excited state hyperfine splittings of ^{153}Eu and ^{151}Eu, respectively. The magnetic field dependent feature, labeled NSF, results from nuclear spin flip sidebands as discussed in Section 4.5. The central hole, under weak burning conditions has a width of 40 MHz ($H > 5$ T) which sets an upper limit on the homogeneous linewidth of 20 MHz. However, the slow time scale of the experiment (100 ms) implies that part of this linewidth results from spectral diffusion associated with superhyperfine interactions between the electron magnetic moment of the Eu^{2+} and the F nuclear

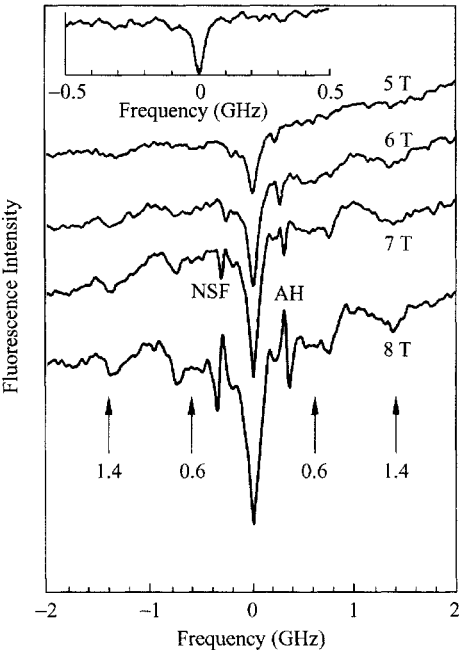


Figure 4. 26 Transient hole spectra at 2. 5 K burned in the $4f^7(^8S_{7/2}) \rightarrow 4f^6 5d(\Gamma_8)$ zero-phonon transition of Eu^{2+} in a 1100nm epitaxial MBE film of CaF_2 as a function of magnetic field. AH and NSF indicate antiholes and nuclear spin-flip sidebands of the F nuclei. The arrows at 0. 6 GHz and 1. 4 GHz show the excited state hyperfine splittings for the ^{153}Eu and ^{151}Eu isotopes, respectively. The inset shows the narrow central hole (40 MHz) at 7 T (Boye et al., 1996b)

spins. Spin flips of the nuclear spins occur with time as the frozen core, created by the large Eu^{2+} electronic magnetic moment "melts".

However, for heterostructures of Eu^{2+}: CaF_2 and CdF_2 on Si(111) bleaching and PSHB is again observed (Boye et al., 1997). Studies of the hole burning as a function of the CaF_2 layer thickness, sandwiched between the CdF_2 layers demonstrate that the electron trapping occurs by transfer through the thin CaF_2: Eu^{2+} to the CdF_2 (Sokolov et al., 1999). This tunneling is made possible by the band offset between the CaF_2 and CdF_2 conduction bands such that the $4f^6 5d$ excited state of Eu^{2+} lies above the conduction band of CdF_2. Tunneling of the electron to the CdF_2 layer can then occur for thin films. The observation of a predicted logarithmic decay of the luminescence and the successful application of this model to superlattices with undoped buffer layers of variable thickness located between the Eu^{2+}: CaF_2 and CdF_2 confirm this tunneling model (Suturin et al., 2000).

Thin films have also been examined for frequency domain optical storage applications. Asatsuma et al. (1995) prepared micron polycrystalline films of Sm^{2+}: $SrFCl_x Br_{1-x}$ on quartz with a gas flow apparatus. Room temperature holeburning with antihole structure was observed, indicating that the Sm^{3+} ions act as traps. Monnier et al. (1997) prepared sub-micron polycrystalline films of Sm^{2+}: $Sr_xCa_{1-x}FCl$ using a molecular beam deposition technique and investigated PSHB and the possibility to use films to increase the inhomogeneous linewidth. The inhomogeneous linewidths of these mixed crystal films were similar to that found for bulk crystals. However multiple layer films, where each layer contained a different Sr/Ca mixture (value of x) did almost double the linewidth compared to that of single layers ($\Gamma_{inh} \approx 70\ cm^{-1}$).

4.6.3 Nanocrystalline Materials

The optical properties of nanocrystalline materials can be quite different than those of bulk materials. Strong confinement effects have been observed in semiconductor quantum dots and the inhomogeneous broadening can be completely eliminated by studying the spectroscopy of individual quantum dots. While the spectroscopy of semiconductor quantum dots is determined by the delocalized extended electronic states which are confined by the quantum dot boundaries, the situation for rare earth doped insulator nanoparticles is quite different. The electronic states of rare earth ions are quite localized to dimensions much smaller than the size of the nanocrystals. Nonetheless, the crystal structure of nanoparticles is not necessarily identical to that of the bulk and as a result the nanoparticles may have quite different spectra than bulk material.

While there had been considerable interest in the report that ZnS: Mn nanoparticles exhibited dramatic enhancements of the Mn^{2+} radiative rates (Bhargava et al., 1994), with the expectation that this might be a general property also of rare earth-doped nanoparticles, it was later shown that the fast luminescence arises from the tail of the intrinsic luminescence of ZnS (Bol and Meijerink, 1998). In at least one case, the confinement effects of the electronic states of the host in Eu-doped ZnS were used to advantage to obtain rare earth luminescence (Chen et al., 2000). Whereas in bulk Eu: ZnS, no Eu^{2+} emission is seen due to the fact that the $4f^6 5d$ excited state lies above the conduction band edge, confinement effects in nanoparticles increase the band edge so that the Eu^{2+} excited state now lies below the bottom of the conduction band and it can now emit. In addition, changes in the radiative rate have been demonstrated for nanoscale particles, due to modifications of the effective index of refraction of the surroundings of the nanoparticle and its matrix, averaged over dimensions of the wavelength of light (Meltzer et al., 1999).

Although the electronic states of the rare earth ions are quite localized, the vibrational states of the nanoparticles are extended states, and therefore they are subject to the affects of confinement and this has important consequences on the

electron-phonon interaction. In addition, because of their proximity to the boundary of the nanoparticle the rare earth ions may interact with defects at the surface or with the medium in which they are imbedded altering both their inhomogeneous and homogeneous linewidths.

A number of rare earth-doped nanocrystalline materials have been prepared and their optical properties are receiving considerable attention. Two examples will be focused on here: yttria (Y_2O_3) nanoparticles and LaF_3 nanocrystals that can form in certain oxyfluoride glasses. While a number of other interesting rare earth-doped nanocrystals have been prepared and characterized optically, including YVO_4 and $LaPO_4$ (Haase et al., 2000; Huignard et al., 2000) and Y_2SiO_5 (Duan et al., 2000), detailed spectroscopic investigations of their linewidths and lineshapes have not been reported.

4.6.3.1 Y_2O_3 Nanocrystals

Rare earth doped Y_2O_3 (and rare earth oxide) nanoparticles (< 50 nm) can be prepared in number of ways including colloidal chemical preparation (Bhargava et al., 1994; Wakefield et al., 1999), gas phase condensation (Eilers and Tissue, 1995), sonochemically (Patra et al., 1999) and by reverse microemulsion techniques (Lee et al., 2000). While in most cases, the nanoparticles form in the bulk cubic phase with two crystallographically inequivalent sites, for gas phase condensation, the monoclinic phase, which can also be prepared in microcrystalline size under high pressure, is formed (Eilers and Tissue, 1996). In this phase there are three crystallographically inequivalent sites at which the rare earth ions reside. The sonochemical preparation yields amorphous material with glass like inhomogeneous linewidths. Much of the interest in these materials has centered on increased luminescence and not the details of the linewidths and line shapes.

For monoclinic samples of the gas phase synthesis, high resolution laser spectroscopy has been performed. These nanoparticles exhibit good crystalline properties as indicated by X-ray diffraction and their sharp optical transitions whose transition frequencies and intensities are nearly identical to those found for micron powders in the monoclinic phase. It appears that their spectra are significantly inhomogeneously broadened relative to the corresponding bulk material due to the presence of defects in the nanoparticles and the perturbation by the surface and any adsorbed constituents on that surface which affect the rare earth ions differently depending on their location with respect to the particle boundary. This inhomogeneous broadening is to be expected and depends on the material and particular sample, but in good crystalline nanoparticles containing low concentrations of rare earth ions (< 1%) it is typically a few cm^{-1}. The fluorescence excitation spectrum of Eu_2O_3 and Eu^{3+} (0.1%) : Y_2O_3 for the $^7F_0 \rightarrow {}^5D_0$ transition as a function of average particle size is shown in Fig. 4.27 (Hong, 1999). As the particle size decreases, the inhomogeneous linewidths broaden for all three of the crystallographically inequivalent sites, with the A site

showing the greatest sensitivity to particle size. For Eu_2O_3 (Fig. 4.27a) at about 5 nm, the sites become indistinguishable indicating that the material is becoming disordered. In fact X-ray studies support this suggestion showing that the nanoparticles consist of a disordered cubic phase.

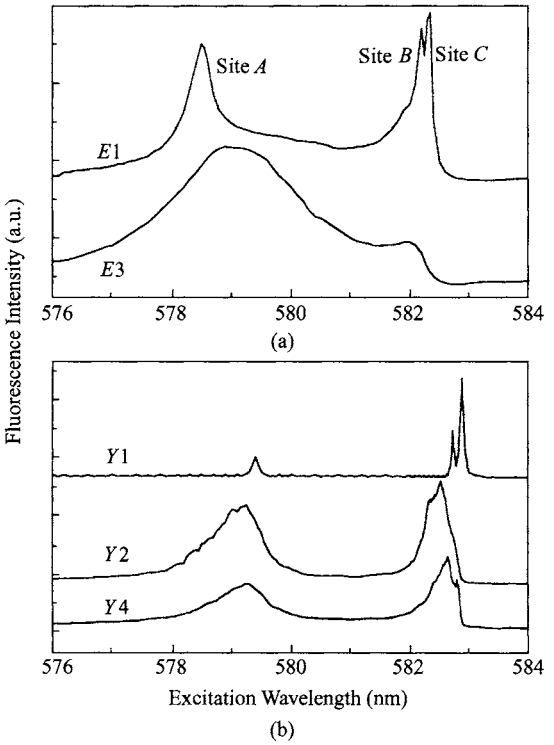


Figure 4.27 Excitation spectra for the $^7F_0 \rightarrow {}^5D_0$ transition of Eu^{3+} in nanoparticles of (a) Eu_2O_3 ($T = 10$ K) and (b) Eu^{3+} (0.1%) : Y_2O_3 ($T = 1.5$ K). Average particle size is $E1 = 11.6$ nm, $E3 = 5.6$ nm, $Y1 \approx 500$ nm, $Y2 = 23$ nm, and $Y4 = 12$ nm (Hong, 1999)

Measurements of the homogeneous linewidths in monoclinic Y_2O_3 have utilized Eu^{3+} as the probe in both dilute material and in stoichiometric Eu_2O_3. Transient spectral hole burning indicates that in the nanoparticles at low temperatures the hole widths are much larger than in both single crystals and in micron powders (Hong et al., 1998). In single crystal Eu^{3+}: Y_2O_3, two-phonon Raman scattering dominates the homogeneous linewidth and at low temperatures its temperature dependence is $\Gamma_h \sim T^7$. However in Eu^{3+}: Y_2O_3 and Eu_2O_3 nanoparticles, the temperature dependence of the hole width is found to be $\Gamma_h \sim T^3$. This is shown for Eu_2O_3 in Fig. 4.28 (Meltzer and Hong, 2000). The open

points are the observed hole widths for samples with three different particle size distributions after subtracting a small low temperature contribution. This is a behavior quite distinct from that of the bulk. In addition, for a fixed temperature, the hole widths depend on the particle diameter, d, with an approximate behavior $\Gamma_h \sim d^{-2}$.

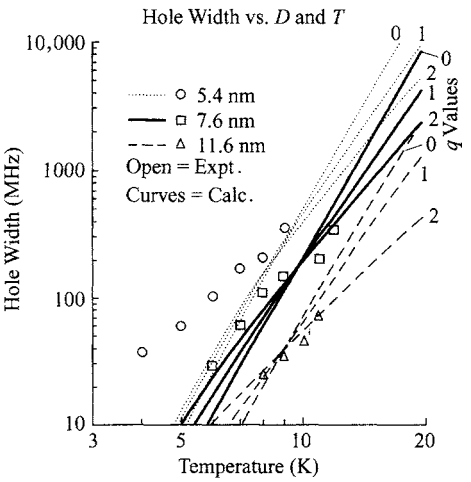


Figure 4. 28 Temperature dependence of the transient hole linewidth for the $^7F_0 \rightarrow {}^5D_0$ transition of Eu^{3+} in a series of nanoparticles of different size distributions. The low temperature behavior $\Gamma_{hole} = \Gamma_0 + aT$ has been subtracted to show the dominant contribution. The dashed, solid and dotted curves are the result of a calculation of the two-phonon Raman scattering including the effects of confinement on the phonons. The three curves for each particle size labeled by the q value show the effect of the frequency dependence of the broadening of the phonon modes as described in the text (Meltzer and Hong, 2000)

The explanation for the strong deviation from bulk-like behavior is based on confinement effects on the electron-phonon interaction. Confinement leads to a gap in the acoustic phonon spectrum and to the formation of discrete phonon modes above the gap. As a result, the phonon density of states is strongly modified from that in the bulk. In addition, confinement leads to an enhancement of the amplitudes of atomic vibrations in the modes as the particle size is reduced. When these confinement effects are included in a calculation of the two-phonon Raman scattering, the resulting prediction for the temperature and particle size dependence of the hole width is shown by the dashed, solid and dotted lines in Fig. 4. 28. The three curves for each particle size are results based on a different assumption about the broadening of the low frequency phonon modes which are assumed to be $\Delta\omega \sim \omega^q$ with $q = 0, 1,$ or 2, as labeled in the figure. The best fit occurs for $q = 2$ and provides information on the phonon

broadening and phonon relaxation rates which increase as the square of the phonon energy in the nanoparticles.

The direct process, which can control homogeneous linewidths in bulk materials when two nearby crystal field levels are coupled by the phonons, is also severely modified in nanoparticles. The formation of a low frequency gap in the acoustic phonon spectrum and the discrete nature of the low-lying modes above the gap imply that it may be difficult for phonons to provide the energy relaxation pathways among crystal field levels in nanoparticles. The resulting slow-down of the direct phonon process has indeed been reported for relaxation among the three levels of $^5D_1$ of Eu^{3+} in Y_2O_3 nanoparticles (Yang et al., 1999). Anomalous thermalization effects have been observed for Er^{3+} in Y_2O_2S nanophosphors that have also been attributed to the absence of low energy phonon modes based on calculations of phonon-induced relaxation rates (Liu et al., 2002, 2003).

4.6.3.2 LaF_3 Nanocrystals in Oxyfluoride Glasses

It has been discovered that materials consisting of insulating nanocrystals doped with rare earth ions imbedded into glassy matrices possess spectral properties like those of bulk crystals of LaF_3 including nearly identical sharp line optical spectra and efficient fluorescence (Dejneka, 1998). X ray characterization confirm the fact that LaF_3 nanocrystals form in the glass during annealing. The particle size distribution can be controlled by the duration and temperature of the annealing. The sharp line nature of the transitions allow one to spectrally isolate the rare earth ions in the nanoparticle from those that remain in the glass.

Transient spectral hole burning can be performed in the nanocrystals just as they have been done in the bulk. As for the Y_2O_3 nanocrystals, the temperature dependence of the hole linewidth is different from that of the bulk. In addition, the hole width at a given temperature was found to increase with a decrease in particle size, approaching that of the ions contained directly in the glass host which could also be examined. This is shown for the $^7F_0 \rightarrow {}^5D_0$ transition of Eu^{3+} in Fig. 4. 29 (Meltzer et al., 2001). However, the resulting temperature dependence cannot be explained either by the direct process or the electron-phonon interaction known for the bulk or observed in isolated Y_2O_3 nanocrystals. Rather the linear temperature dependence suggests that the dephasing is governed by interaction with the TLS of the surrounding glass matrix. A similar result was found for Y_2O_3: Eu^{3+} nanocrystals embedded in polymer amorphous matrices where the T^3 behavior of the isolated nanoparticles became nearly linear when the nanocrystals were placed in the polymer. Effects of interaction with the surrounding glass have also be observed as an increase in the single-phonon direct process relaxation rates of Ho^{3+} in these oxyfluoride glass ceramics due to coupling to the higher density of phonon modes in a glass than in a crystal whose contribution to the relaxation increases with a decrease in particle size (Meltzer et al., 2002).

Dephasing in glasses is described theoretically by a long range interaction

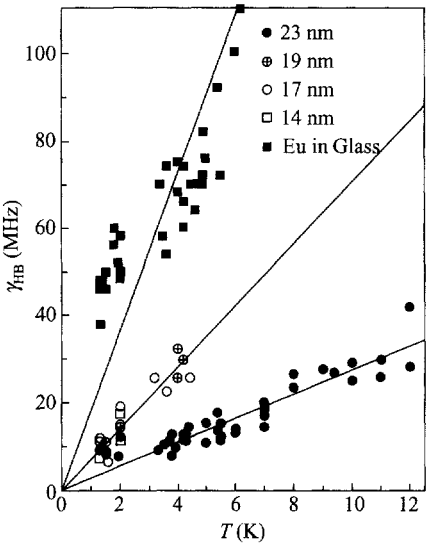


Figure 4. 29 Temperature dependence of the transient hole linewidth for the $^7F_0 \rightarrow {}^5D_0$ transition of Eu^{3+} in LaF_3 nanocrystals embedded in oxyfluoride glass ceramics and for Eu^{3+} ions in the glass matrix (solid squares). The temperature dependence is approximately linear in temperature for all samples (Meltzer et al., 2001)

between the rare earth ions and the TLS (Huber et al., 1984, 1986; Silbey and Kassner, 1987). A calculation of the interaction following the approach of Lyo (1982) and Molenkamp and Wiersma (1985), allowing one to exclude the nanocrystal volume that surrounds the rare earth ions and which contain no TLS, results in a size dependence that is consistent with experiment. This provides further support for the idea that this interaction is long range and that it plays the dominant role of dephasing for nanocrystals embedded in amorphous matrices. Recent photon echo measurements on the $^3H_4 \rightarrow {}^3P_0$ transition of Pr^{3+} in these LaF_3 nanocrystals contained in oxyfluoride glass ceramics confirm the dominant role of the interaction with the TLS (Zheng and Meltzer, 2004). The strong temperature dependence of the homogenous linewidths seen above 5 K for Pr^{3+} and Tm^{3+} in hole burning is absent for Pr^{3+} in the the photon echo experiments. The rapid time scale (< 100 ns) of the photon echo experiment provides evidence that this $\sim T^6$ temperature dependent contribution to the dephasing seen above 5 K results from a spectral diffusion process.

4.7 Conclusions

The purpose of this chapter has been to summarize the subject of linewidths of rare earth ions in solids within the framework of examples of work done during the past 15 years. In this period, the frequency regime of linewidths has been pushed in two directions. Measurements of radiative lifetime-limited homogeneous linewidths down to 100 Hz have been performed in the time domain using photon echo spectroscopy. Inhomogeneous linewidths of 10 MHz have been demonstrated in $YLiF_4$ by removing the inhomogeneous broadening due to the random distribution of Li isotopes in isotopically pure material. Sub-kHz ultra narrow bandwidth lasers have been devised for the highest frequency resolution studies. On the other extreme, highly disordered mixed crystalline materials have been prepared to provide the maximum inhomogeneous linewidths for applications in optical memories.

Time and frequency domain spectroscopy have been directed towards the study of new classes of materials that have come on the scene in the last 15 years including ultra thin films prepared by molecular beam epitaxy and rare earth-doped nanocrystals. Their inhomogeneous and homogeneous linewidths exhibit behavior that is different from that of bulk materials. MBE films show transition frequencies and linewidths which depend on the film preparation because of strains that result from lattice mismatch between the film and substrate. Nanoparticles have inhomogeneous linewidths of rare earth ions that are broadened by their proximity to the surface and in some cases totally different spectra from those of the bulk because of the appearance of different crystal structures. Their homogeneous linewidths behave very differently from that of the bulk because of confinement effects on the phonons and on the electron-phonon interactions and because of interactions with their surroundings such as TLS when they are embedded in an amorphous matrix.

This chapter is certainly not complete in its coverage. It does not treat all of the work done in this arena in the last fifteen year. For example, it does not deal with the extensive amount of research done on rare earth-doped glasses nor does it deal much with double resonance techniques which combine optical and radio- or microwave fields. It also suffers from an emphasis on the author' s own work, a weakness which is difficult to avoid because of its familiarity. Hopefully the extended bibliography will partially make amends for this bias.

References

Agladze, N. I., M. N. Popova, M. A. Koreiba, B. Z. Malkin, and V. R. Pekurovskii. JETP **77**, 1021 (1993).

Agladze, N. I., M. N. Popova, G. N. Zhizhin, V. J. Egorov, and M. A. Petrova. Phys.

Rev. Letts. **66**, 477 (1991).
Altner, S. B., M. Mitsunaga. G. Zumhofen and U. P. Wild Phys. Rev. Lett. **76**, 1747 (1996).
Altner, S. B., G. Zumofen, U. P. Wild, and M. Mitsunaga. Phys. Rev. B **54**, 17,493 (1996b).
Ambrose, W. P., T. Basche, and W. E. Moerner. J. Chem. Phys. **95**, 7150 (1991).
Anderson, P. W., B. I. Halperin, and C. M. Varma. Phil. Mag. **25**, 1 (1972).
Asatsuma T., N. Umezu, Y. Takemoto, and M. Kaneko. J. Lumin. **64**, 201 (1995).
Averkiev N. S., V. S. Vikhnin, and N. I. Sablina. Fiz. Tverd. Tela **38**, 138 (1996).
Averkiev N. S., V. S. Vikhnin, N. S. Sokolov, and N. L. Yakovlev. Fiz. Tverd. Tela **36**, 1087 (1994).
Averkiev N. S., V. S. Vikhnin, N. S. Sokolov, and N. L. Yakovlev. JETP Lett. **56**, 9 (1992).
Bai, Y. S., R. Kachru. Phys. Rev. B **46**, 13735 (1992).
Balda, R., J. Fernandez, J. L. Adam, and M. A. Arriandiaga. Phys. Rev. B **17**, 12, 076 (1996).
Barnes, M. D., A. Mehta, T. Thundat, R. N. Bhargava, V. Chhabra, and B. Kulkarni, J. Phys. Chem. **104**, 6099 (2000).
Barthem, R. B., R. Buisson, and R. L. Cone. J. Chem. Phys. **91**, 627 (1989).
Barthem, R. B., R. Buisson, F. Madeore, J. C. Vial, and J. P. Chaminade. J. de Physique **48**, 379 (1987).
Basiev, T. T., Y. V. Orlovskii, A. G. Papashivili, M. E. Doroshenko, F. Pelle, J. Heber. J. Lumin. 94, 123(2001).
Basiev, T. T., V. V. Fedorov, A. Y. Karasik, and K. K Pukhov. J. Lumin. **81**, 189 (1999).
Basiev, T. T., A. Ya. Karasik, and R. L. Shubochkin. J. Lumin. **64**, 259 (1995).
Basun, S. A., M. Raukas, U. Happek, A. A. Kaplyanskii, J. C. Vial, J. Rennie, W. M. Yen, and R. S. Meltzer. Phys. Rev. B **56**, 12, 992 (1997).
Bausa, L. E., C. Fontaine, E. Daran, and A. Munozyague. J. Appl. Phys. **72**, 499 (1992).
Bausa, L. E., A. Munoz-Yague. Appl. Phys. Lett. **59**, 3511 (1991).
Beck, W., A. Karasik, J. Arvanitidis, T. Basiev, and C. Flytzanis. J. Lumin. **86**, 289 (2000).
Beck, W., D. Ricard, and C. Flytzanis. Phys. Rev. B **58**, 11, 996 (1998).
Bhargava, R. N., D. Gallagher, X. Hong, and A. Nurmikko. Phys. Rev. Lett. **72**, 416 (1994).
Bill, H., R. Jaaniso, H. Hagemann, D. Lovy, A. Monnier, and M. Schnieper. Opt. Eng. **34**, 2333 (1995).
Biyikli, L., Z. Hasan. J. Lumin. **83**, 373 (1999).
Bloch, F. Phys. Rev. **70**, 460 (1946).
Bodenschatz, N., J. Heber. Phys. Rev. A **54**, 4428 (1996).
Bol, A. A., A. Meijerink. Phys. Rev. B **58**, R15, 997 (1998).
Boye, D. M., S. P. Feofilov, and R. S. Meltzer. J. Lumin. **76**, 60 (1998).
Boye, D. M., Y. Sun, R. S. Meltzer, S. P. Feofilov, N. S. Sokolov, A. Khilko, and J. C. Alvarez. J. Lumin. **72/4**, 290 (1997).
Boye, D. M., R. M. Macfarlane, Y. Sun, and R. S. Meltzer. Phys. Rev. B **54**, 6263 (1996a).
Boye, D. M., Y. Sun, R. S. Meltzer, N. S. Sokolov, and J. C. Alvarez. J. Lumin. **66/67**, 29 (1996b).
Boye, D. M., R. Wannemacher, Y. P. Wang, W. Grill, J. E. Rives, and R. S. Meltzer. J.

Lumin. **45**, 431 (1990).
Cahill, D. G., and R. O. Pohl. Phys. Rev. B **39**, 10,477 (1989).
Catlow, C. R. A., A. V. Chadwick, J. Corish, L. M. Moroney, and A. N. Oreilly. Phys. Rev. B **39**, 1897 (1989).
Chaminade, J. P., R. M. Macfarlane, F. Ramaz, and J. C. Vial. J. Lumin. **48/49**, 531 (1991).
Chen, H. T., R. S. Meltzer. Phys. Rev. Lett. **44**, 599(1980).
Chen, W., J. O. Malm, V. Zwiller, Y. N. Huang, S. M. Liu, R. Wallenberg, J. O. Bovin, and L. Samuelson. Phys. Rev. B **61**, 11, 021 (2000).
Chen, Y. K., K. Chiang, and S. R. Hartmann. Phys. Rev. B **21**, 40 (1980).
Chukalina, E. P., M. N. Popova, S. L. Korableva, R. Yu. Abdulsabirov. Phys. Lett. A **269**, 348(2000).
Cirillo-Penn, K. and J. C. Wright. Phys. Rev. B **41**, 10, 799 (1990).
Cone, R. L., P. C. Hansen, M. J. M. Leask, and B. M. Wanklyn. J. Phys. Condens. Mat. **5**, 573 (1993).
Cone, R. L., and R. S. Meltzer, In: *Spectroscopy of Solids Containing Rare Earth Ions*, eds. A. A. Kaplyanskii, R. M. Macfarlane (North-Holland, Amsterdam, 1987), p. 481.
Dejneka, M. J. J. Non-Cryst. Sol. **239**, 147 (1998).
Delsart, C., N. Pelletier-Allard, and R. Pelletier. Opt. Commun. **16**, 114 (1976).
Denisov, Yu. V. and V. A. Kizel. Opt. & Spectrosc. **23**, 251 (1967).
Dieke, G. H., B. Pandey. J. Chem. Phys. **41**, 1952 (1964).
Duan, C. K., M. Yin, K. Yan, and M. F. Reid. J. Alloys and Cmpds. **303**, 371 (2000).
Eilers, H., B. M. Tissue. Chem. Phys. Lett. **251**, 74 (1996).
Eilers, H., B. M. Tissue. Mater. Lett. **24**, 261 (1995).
Ellens, A., A. Meijerink, and G. Blasse. J. Lumin. **59**, (1994).
Equall, R. W., R. L. Cone, and R. M. Macfarlane. Phys. Rev. B **52**, 3963 (1995).
Equall, R. W., Y. Sun, R. L. Cone, and R. M. Macfarlane. Phys. Rev. Lett. **72**, 2179 (1994).
Erickson, L. E. Phys. Rev. A **46**, 5899 (1992).
Erickson, L. E. Phys. Rev. B **16**, 4731 (1977).
Farrow, R. F. C., P. W. Sullivan, G. M. Williams, G. R. Jones, and D. C. Cameron. J. Vacuum Sci. & Tech. **19**, 415 (1981).
Fedorov, V. V., W. Beck, T. T. Basiev, A. Ya. Karasik, and C. Flytzanis. Chem. Phys. **257**, 275 (2000).
Fitzgerald, S. A., J. A. Campbell, A. J. Sievers. Phys. Rev. Lett. **73**, 3105 (1994).
Flach, R., D. S. Hamilton, P. M. Selzer, and W. M. Yen. Phys. Rev. B **15**, 1248 (1977).
Flinn, G. P., K. W. Jang, J. Ganem, M. L. Jones, and R. S. Meltzer. Phys. Rev. B **49**, 5821 (1994).
Ganem, J., Y. P. Wang, R. S. Meltzer, and W. M. Yen. Phys. Rev. **43**, 8599 (1991a).
Ganem, J., Y. P. Wang, D. Boye, R. S. Meltzer, W. M. Yen, and R. M. Macfarlane. Phys. Rev. Lett. **66**, 695 (1991b).
Genack, A. Z., D. A. Weitz, R. M. Macfarlane, and R. M. Shelby. Phys. Rev. Lett. **45**, 438 (1980).
Genack, A. Z., R. M. Macfarlane, and R. G. Brewer. Phys. Rev. Lett. **37**, 1078 (1976).
Gill, D. M., L. McCaughan, J. C. Wright. Phys. Rev. B **53**, 2334 (1996).
Glaser, S., G. Wackerle, K. P. Dinse. Chem. Phys. Lett. **121**, 267 (1985).
Graf, F. R., A. Renn, G. Zumofen, and U. P. Wild. Phys. Rev. B **58**, 5462 (1998).
Graf, F. R., A. Renn, U. P. Wild, and M. Mitsunaga. Phys. Rev. B **55**, 11, 225 (1997a).
Graf, F. R., B. H. Plagemann, A. Renn, U. P. Wild, and M. Mitsunaga. Opt. Lett. **22**, 181 (1997b).

Guillot-Noel, O., V. Mehta, V. Viana, and D. Gourier. Phys. Rev. B **61**, 15,338 (2000).
Haase, M., K. Riwotzki, H. Meyssamy, A. Kornowski. J. Alloys and Cmpds. **303**, 191 (2000).
Hansen, P. C., M. J. M. Leask, B. M. Wanklyn, Y. Sun, R. L. Cone, and M. M. Abraham. Phys. Rev. B **56**, 7918 (1997).
Hasan, Z., M. Solonenko, P. I. Macfarlane, L. Biyikli, V. K. Mathur, and F. A. Karwacki. Appl. Phys. Lett. **72**, 2373 (1998a).
Hasan, Z., L. Biyikli, and P. I. Macfarlane. Appl. Phys. Lett. **72**, 3399 (1998b).
Hasan, Z., H. Ghafoori Fard, N. B. Manson. J. Lumin. **45**, 304 (1990).
Hehlen, M. P., A. Kuditcher, S. C. Rand, and S. R. Luthi. Phys. Rev. Lett. **82**, 3050 (1999).
Holliday, K., C. J. Wei, M. Croci, and U. P. Wild. J. Lumin. **53**, 227 (1992).
Hong, K. S., Thesis (University of Georgia, unpublished, 1999), p. 66.
Hong, K. S., R. S. Meltzer, B. Bihari, D. K. Williams, and B. M. Tissue. J. Lumin. **76**, 234 (1998).
Huang, J., J. M. Zhang, A. Lezama, and T. W. Mossberg. Phys. Rev. Lett. **63**, 78 (1989).
Huang, S. H., A. Szabo. J. Lumin. **68**, 291 (1996).
Huber, D. L., M. M. Broer, and B. Golding. Phys. Rev. Lett. **52**, 2281 (1984); Phys. Rev. B **33**, 7297 (1986).
Huignard, A., T. Gacoin, J. P. Boilot. Chem Mater. **12**, 1090 (2000).
Huston, A. L., W. E. Moerner. J. Opt. Soc. Am. B **1**, 349 (1984).
Jaaniso, R., H. Bill. J. Lumin. **64**, 173 (1995).
Jaaniso, R., H. Hagemann, and H. Bill. J. Chem. Phys. **101**, 10,323 (1994).
Jaaniso, R., H. Bill. Europhys. Lett. **16**, 569 (1991).
Jang, K. W., R. S. Meltzer. Phys. Rev. B **52**, 6431 (1995).
Jang, K. W., K. S. Hong, T. T. Basiev, and R. S. Meltzer. J. Lumin. **66**, 8 (1995).
Jones, M. L., D. W. Shortt, A. L. Schawlow. Phys. Rev. B **42**, 132 (1990).
Jongerden, G. J., A. J. Kil, J. I. Dijkhuis, A. F. M. Arts, and H. W. de Wijn. J. Phys. - Paris **46** (C – 7) 241 (1985).
Kaplyanskii, A. A., S. A. Basun, U. Happek, and R. S. Meltzer. J. Lumin. **83**, 335 (1999).
Kaplyanskii, A. A., S. A. Basun, M. Raukas, U. Happek, J. Rennie, J. C. Vial, W. M. Yen, and R. S. Meltzer. J. Lumin. **76**, 292 (1998).
Karasik, A. Ya., T. T. Basiev, A. A. Volkov, and G. A. Komandin. Opt. & Spec. **85**, 548 (1998).
Khasanov, O. K., T. V. Smirnova, and O. M. Fedotova. Opt. Spektrosk. **82**, 285 (1997a).
Khasanov, O. K., T. V. Smirnova, and O. M. Fedotova. Appl. Magn. Reson. **12**, 299 (1997b).
Khong, Y. L., G. D. Jones, and R. W. G. Syme. Phys. Rev. B **48**, 672 (1993).
Kim, M. K., R. Kachru. Phys. Rev. B **44**, 9826 (1991).
Kim, M. K., R. Kachru. Phys. Rev. B **40**, 2082 (1989).
Knott, L. J., N. J. Cockroft, and J. C. Wright. Phys. Rev. B **51**, 5649 (1995).
Kodama, N., T. Takahashi, and K. Hirao. Appl. Phys. Lett. **72**, 1548 (1998).
Kodama, N., S. Hara, Y. Inoue, et al. J. Lumin. **64**, 181 (1995).
Kroll, S., E. Y. Xu, and R. Kachru. Phys. Rev. B **44**, 30 (1991).
Kurita, A., Y. Kanematsu, M. Watanabe, K. Hirato, and T. Kushida. Phys. Rev. Lett. **83**, 1582 (1999).
Kurnit, N. A., I. D. Abella, and S. R. Hartmann. Phys. Rev. Lett. **13**, 567 (1964).
Lahoz, F., E. Daran, X. Zhang, A. Munoz-Yague, R. Cases, R. Alcala. J. Appl. Phys.

8, 3699 (1999).
Lee, M. H., S. G. Oh, S. C. Yi, D. S. Seo, J. P. Hong, C. O. Kim, Y. K. Yoo, and J. S. Yoo. J. Electrochem. Soc. **147**, 3139 (2000).
Levenson, M. D., S. S. Kano. *Introduction To Nonlinear Laser Spectroscopy* (Academic Press, London, 1988), Chapter 6.
Li, S. T., G. K. Liu, H. Liu, and F. E. Fernandez. J. Alloy Compd. **303**, 360 (2000).
Lisin, V. N., V. A. Zuikov, A. M. Shegeda, V. V. Samartsev, and B. M. Khabibullin. Laser Phys, **6**, 195 (1996).
Liu, G. K., H. Z. Zhuang, X. Y. Chen. Nano. Lett. 2, 535 (2002).
Liu, G. K., X. Y. Chen, H. Z. zhuang, R. S. Niedbala. J. Sol. State Chem. 171, 123 (2003).
Liu, G. K., R. L. Cone. Phys. Rev. B **41**, 6193 (1990).
Liu, G. K., R. L. Cone, M. F. Joubert, B. Jacquier, and J. L. Skinner. J. Lumin. **45**, 387 (1990).
Liu, H., S. T. Li, G. K. Liu, W. Jia, and F. E. Fernandez. J. Lumin. **83**, 367 (1999).
Love, S. P., C. E. Mungan, A. J. Sievers, and J. A. Campbell. J. Opt. Soc. Am. B **9**, 794 (1992).
Lupei, V., A. Lupei, and G. Boulon. Phys. Rev. B **53**, 14,818 (1996).
Lyo, S. K. Phys. Rev. Lett. **48**, 688 (1982).
Macalik, L., J. Hanuza, B. Macalik, W. Ryba-Romanowski, S. Golab, and A. Pietraszko. J. Lumin. **79**, 9 (1998).
Macfarlane, R. M., and M. J. Dejneka. Opt. Lett. 26, 429(2001).
Macfarlane, R. M., F. Konz, Y. Sun, and R. L. Cone. J. Lumin. **86**, 311 (2000).
Macfarlane, R. M., R. S. Meltzer, and B. Z. Malkin. Phys. Rev. B **58**, 5692 (1998).
Macfarlane, R. M., T. L. Harris, Y. Sun, R. L. Cone, R. W. Equall Opt. Lett. **22**, 871 – 873 (1997).
Macfarlane, R. M., M. Zhu. Opt. Lett. **22**, 248 (1997).
Macfarlane, R. M., G. Wittmann. Opt. Lett. **21**, 1289 (1996).
Macfarlane, R. M., A. J. Meixner. Opt. Lett. **19**, 987 (1994).
Macfarlane, R. M. Opt. Lett. **18**, 1958 (1993a).
Macfarlane, R. M. Opt. Lett. **18**, 829 (1993b).
Macfarlane, R. M., A. Cassanho, and R. S. Meltzer. Phys. Rev. Lett. **69**, 542 (1992).
Macfarlane, R. M. R. Wannemacher, D. Boye, Y. P. Wang, R. S. Meltzer. J. Lumin. **48/9**, 313 (1991).
Macfarlane, R. M., J. Lumin. **45**, 1 (1990).
Macfarlane, R. M., J. C. Vial. J. Lumin. **40**, 505 (1988).
Macfarlane, R. M., In: *Lasers, Spectroscopy and New Ideas*, eds. W. M. Yen, M. D. Levinson (Springer Verlag, 1987a), p. 205.
Macfarlane, R. M., R. M. Shelby. J. Lumin. **36**, 179 (1987a).
Macfarlane, R. M. J. Lumin. **38**, 20 (1987b).
Macfarlane, R. M., R. J. Reeves, and G. D. Jones. Opt. Lett. **12**, 660 (1987).
Macfarlane, R. M., R. M. Shelby, and A. Winnacker. J. Phys. Paris **46**, 537 (1985).
Macfarlane, R. M., R. S. Meltzer. Opt. Commun. **52**, 320 (1985).
Macfarlane, R. M., R. M. Shelby. Opt. Lett. **9**, 533 (1984).
Macfarlane, R. M., R. M. Shelby, Opt. Commun. **45**, 46 (1983).
Macfarlane, R. M., R. M. Shelby, and D. P. Burum. Opt. Lett. **6**, 593 (1981).
Macfarlane, R. M., R. M. Shelby, and R. L. Shoemaker. Phys. Rev. Lett. **43**, 1726 (1979).
Malinovsky, V. S. Phys. Rev. A **52**, 4921 (1995).
Manson, N. B., M. J. Sellars, P. T. H. Fisk, and R. S. Meltzer. J. Lumin. **64**, 19 (1995).

Manson, N. B., N. Rigby, B. Lou, and J. P. D. Martin. J. Lumin. **53**, 251 (1992).
Manykin, E. A., N. V. Znamenskii, D. V. Marchenko, and E. A. Petrenko. JETP. Lett. **54**, 168 (1991).
Martin, J. P. D., M. J. Sellars, P. Tuthill, N. B. Manson, G. Pryde, and T. Dyke. J. Lumin. **78**, 19 (1998a).
Martin, I. R., V. D. Rodriguez, U. R. Rodriquez-Mendoza, and V. Lavin. Phys. Rev. B **57**, 3396 (1998b).
Martin, J. P. D., T. Boonyarith, and N. B. Manson. J. Lumin. **63**, 297 (1995).
Martin, J. P. D., T. Boonyarith, N. B. Manson, and Z. Hasan. J. Phys. -Condens. Mat. **4**, L411 (1992).
Martin, J. P. D., T. Boonyarith, N. B. Manson, Y. L. Khong, and G. D. Jones. Phys. Rev. B **49**, 15,495 (1994).
McCumber, D. E., M. D. Sturge. J. of Appl. Phys. **34** (1963).
Meijerink, A. and G. J. Dirksen. J. Lumin. **63**, 189 (1995).
Meixner, A. J., C. M. Jefferson, and R. M. Macfarlane. Phys. Rev. B **46**, 5912 (1992).
Meltzer, R. S., W. M. Yen, H. Zheng, S. P. Feofilov, M. J. Dejneka. Phys. Rev. B **66**, 224,202 (2002).
Meltzer, R. S., W. M. Yen, H. Zheng, S. P. Feofilov, M. J. Dejneka, B. M. Tissue, and H. B. Yuan. Phys. Rev. B **64**, 100,201 (2001).
Meltzer, R. S., K. S. Hong. Phys. Rev. B **61**, 3396 (2000).
Meltzer, R. S., S. P. Feofilov, B. Tissue, and H. B. Yuan. Phys. Rev. B **60**, R14, 012 (1999).
Meltzer, R. S., K. W. Jang, K. S. Hong, Y. Sun, and S. P. Feofilov. J. Alloys and Compounds **250**, 279 (1997).
Meltzer, R. S., and D. P. Landau. In: *Computer Simulation Studies in Condensed-Matter Physics V*, eds. D. P. Landau, K. K. Mon, and H. B. Schuttler (Springer-Verlag, Berlin, 1992), p. 191.
Meltzer, R. S., J. E. Rives. Phys. Rev. B **15**, 2442 (1977).
Meltzer, R. S. Solid State Commun. **20**, 553 (1976).
Mikhail, P., M. Schnieper, H. Bill, and J. Hulliger. Phys. Status Solidi B **215**, R17 (1999).
Mims, W. B. In: *Electron Paramagnetic Resonance*, ed. S. Geschwind (Plenum, New York, 1972), p. 263.
Mitsunaga, M., R. Yano, and N. Uesugi. Phys. Rev. B **45**, 12,760 (1992a).
Mitsunaga, M., T. Takagahara, R. Yano, and N. Uesugi. Phys. Rev. Lett. **68**, 3216 (1992b).
Mitsunaga, M. Phys. Rev. A **42**, 1617 (1990).
Mitsunaga, M. R. Kachru, E. Xu, and M. K. Kim. Phys. Rev. Lett. **63**, 754 (1989).
Mitsunaga, M., K. Kubodera, and H. Kanbe. Opt. Lett. **11**, 339 (1986).
Mitsunaga, M., R. G. Brewer. Phys. Rev. A **32**, 1605 (1985).
Moine, B., C. Pedrini, and B. Courtois. J. Lumin. **53**, 31 (1991).
Molenkamp, L. W., D. A. Wiersma. J. Chem. Phys. **83**, 1 (1985).
Monnier, A., M. Schnieper, R. Jaaniso, H. Bill. J. Appl. Phys. **82**, 536 (1997).
Monnier, A., M. Schnieper, R. Jaaniso, and H. Bill. Rad. Effects and Defects in Solids **135**, 751 (1995).
Muramoto, T., Y Takahashi, and T. Hashi. J. Lumin. **53**, 84 (1992).
Okuno, T., T. Suemoto. Phys. Rev. B **59**, 9078 (1999).
Okuno, T., K. Tanaka, and T. Suemoto. Opt. Commun. **123**, 512 (1996).
Okuno, T., K. Tanaka, K. Koyama, N. Namiki, and T. Suemoto. J. Lumin. **58**, 184 (1994a).

Okuno, T., K. Tanaka, K. Koyama, and T. Suemoto. J. Lumin. **60**, 85 (1994b).
Olsen, L. R., A. O. Wright, and J. C. Wright. Phys Rev. B **53**, 14,135 (1996).
Oppenlander, A., F. Madeore, J. C. Vial, and J. P. Chaminade. J. Lumin. **50**, 1 (1991).
Oppenlander, A., J. C. Vial, R. M. Macfarlane, and J. P. Chaminade. J. Lumin. **42**, 331 (1989).
Orlovskii Y. V., T. T. Basiev, A. G. Papashvili, I. N. Vorob' ev, O. K. Alimov, V. V. Osiko, J. Heber. J. Lumin. **99**, 223(2002).
Orth, D. L., and J. L. Skinner. J. Phys. Chem. 30, 7342 (1994).
Orth, D. L., R. J. Mashl, and J. L. Skinner. J. Phys. Condens. Mat. **5**, 2533 (1993).
Pack D. W., W. J. Manthey, and D. S. McClure. Phys. Rev. **40**, 9930 (1989).
Patra, A., E. Sominska, S. Ramesh, Y. Koltypin, Z. Zhong, H. Minti, R. Reisfeld, and A. Gedanken. J. Phys. Chem. B **103**, 3361 (1999).
Pelletier-Allard, N., R. Pelletier. J. Less-Common Met. **126**, 277 (1986).
Pelletier-Allard, N., R. Pelletier. J. Phys. Chem. **12**, 4647 (1979).
Pelletier-Allard, N. Colloq. Int. CNRS **255**, 289 (1977).
A. Piazza, A. Bouajaj, M. Ferrari, M. Montagna, R. Campostrini, Popova, M. N., S. A. Klimin, E. P. Chukalina, and G. Carturan. J. Phys. **4**, 569 (1994).
Popova, M. N., E. P. Chukalina, B. Z. Malkin, and S. K. Saikin. Phys. Rev. B **61**, 7421 (2000).
Pryde, G. J., M. J. Sellars, and N. B. Manson. Phys. Rev. Lett. **84**, 1152 (2000).
Pryde, G. J. Thesis (Australian National University, Unpublished, 1999), p. 21.
Ramaz, F., J. C. Vial, and R. M. Macfarlane. J. Lumin. **53**, **244** (1992).
Raukas, M., S. A. Basun, W. van Schaik, W. M. Yen, and U. Happek. Appl. Phys. Letts. **69**, 3300 (1996).
Reeves, R. J., R. M. Macfarlane. Phys. Rev. B **39**, 5771 (1989).
Reeves, R. J., G. D. Jones, and R. W. G. Syme. Phys. Rev. B **40**, 6475 (1989).
Rodrigues-Herzog, R., F. Trotta, H. Bill, J. M. Segura, B. Hecht, and H. J. Guntherodt. Phys. Rev. B **62**, 11,163 (2000).
RybaRomanowski, W., I. Sokolska, S. Golab, and T. Lukasiewicz. Appl. Phys. Lett. **70**, 686 (1997).
Salem, Y., B. Jacquier, and R. L. Cone. Phys. Rev. B **41**, 1735 (1990).
Schmidt, T., R. M. Macfarlane, and S. Volker. Phys. Rev. B **50**, 15,707 (1994).
Sellars, M. J., R. S. Meltzer, P. T. H. Fisk, and N. B. Manson. J. Opt. Soc. Am. B **11**, 1468 (1994a).
Sellars, M. J., P. T. H. Fisk, and N. B. Manson. J. Lumin. **58**, 188 (1994b).
Sellin, P. B., N. M. Strickland, J. L. Carlsten, and R. L. Cone. Opt. Lett. **24**, 1038 (1999).
Selzer, P. M., In *Laser Spectroscopy Of Solids, 2nd edition*, eds. W. M. Yen, P. M. Selzer (Springer-Verlag, Heidelberg, 1986), p. 113.
Selzer, P. M., D. S. Hamilton, and W. M. Yen. Phys. Rev. Lett. **38**, (1977).
Shelby, R. M., R. M. Macfarlane. J. Lumin. **31**, 839 (1984).
Shelby, R. M. Opt. Lett. **8**, 88 (1983).
Shelby, R. M., A. C. Tropper, R. T. Harley, and R. M. Macfarlane. Opt. Lett. **8**, 304 (1983).
Shelby, R. M., R. M. Macfarlane. Phys. Rev. Letts. **45**, 1098 (1980).
Shelby, R. M., R. M. Macfarlane. Opt. Commun. **27**, 399 (1978).
Sellars, M. J., G. J. Pryde, N. B. Manson, E. R. Krausz. J. Lumin. **87 – 89**, 833(2000).
Shortt, D. W., M. L. Jones, A. L. Schawlow, R. M. Macfarlane, and R. F. C. Farrow. J. Opt. Soc. Am. B **8**, 923 (1991).
Silbey, R. and K. Kasner. J. Lumin. **36**, 283 (1987).

Sokolov, N. S., S. V. Gastev, A. Y. Khilko, S. M. Suturin, I. N. Yassievich, J. M. Langer, and A. Kozanecki. Phys. Rev. B **59**, R2525 (1999).
Sokolov, N. S., E. Virgilio, S. V. Gastev, S. V. Novikov, and N. L. Yakovlev. Sov. Phys. Solid State **31**, 216 (1989).
Sox, D. J., S. Majetich, J. E. Rives, and R. S. Meltzer. J. Phys. -Paris **46**, 493 (1985).
Suemoto, T., T. Okuno, and D. Nakano. Opt. Commun. **145**, 113 (1998).
Suturin, S. M., S. A. Basun, S. V. Gastev, J. M. Langer, R. S. Meltzer, and N. S. Sokolov. Appl. Surf. Sci. **162**, 474 – 478 (2000).
Szabo, A. Phys. Rev. B **11**, 4512 (1975).
Szabo, A. Phys. Rev. Lett. **25**, 924 (1970).
Tanaka, K., T. Okuno, H. Yugami, M. Ishigame, and T. Suemoto. Opt. Commun. **86**, 45 (1991).
Taylor, D. R., J. P. Hessler. Phys. Lett. A **50**, 205 (1974).
Tissue, B. M., N. J. Cockroft, L. Z. Lu, D. C. Nguyen, and W. M. Yen. J. Lumin. **48**, 477 (1991).
Tu, J., S. A. Fitzgerald, J. A. Campbell, and A. J. Sievers. J. Non-Cryst. Sol. **203**, 153 (1996).
van Pieterson, L., M. F. Reid, R. T. Wegh, S. Soverna, A. Meijerink. Phys. Rev. B **65**, 045, 113 (2002a).
van Pieterson, L., M. F. Reid, G. W. Burdick, A. Meijerink. Phys. Rev. B **65**, 045, 114 (2002b).
Vink, A. P., M. A. Reijne, and A. Meijerink. J. Lumin. **92**, 189 (2001).
Wakefield G., H. A. Keron, P. J. Dobson, and J. L. Hutchison. J. Colloid and Interface Sci. **215**, 179 (1999).
Wald, L. L., E. L. Hahn, and M. J. Lukac. Opt. Soc. Am. B **9**, 784 (1992).
Wang, H. Y., S. H. Huang. Physica B **239**, 261 (1997).
Wang, Y. P., R. S. Meltzer. Phys. Rev. B **45**, 10, 119 (1992).
Wang, Y. P., D. P. Landau, R. S. Meltzer, and R. M. Macfarlane. J. Opt. Soc. Am. B **9**, 946 (1992).
Wang, Y. P., D. M. Boye, J. E. Rives et al. J. Lumin. **45**, 437 (1990).
Wannemacher, R., H. E. Smorenburg, Th. Schmidt and S. Völker. J. Lumin. **53**, 266 (1992).
Wannemacher, R., R. S. Meltzer, and R. M. Macfarlane. J. Lumin. **45**, 307 (1990).
Wannemacher, R., D. Boye, Y. P. Wang, R. Pradhan, W. Grill, J. E. Rives, and R. S. Meltzer. Phys. Rev. B **40**, 4237 (1989).
Weber, J. J. Lumin. **36** (1987).
Wei, C. J., K. Holliday, A. J. Meixner, M. Croci, and U. P. Wild. J. Lumin. **50**, 89 (1991).
Wei, C. J., S. H. Huang, and J. Q. Yu. J. Lumin. **43**, 161 (1989).
Whittaker, E. A., S. R. Hartmann. Phys. Rev. B **26**, 3617 (1982).
Winnacker, A., R. M. Shelby, and R. M. Macfarlane. J. Phys. -Paris **46**, 543 (1985).
Yakovlev, N. L., G. T. Warren, R. S. Meltzer, W. M. Yen, and W. M. Dennis. J. Lumin. **72**, 578 (1997).
Yamaguchi, M., T. Suemoto. J. Phys. Soc. Jap. **72**, 429 (2003).
Yamaguchi, M., K. Koyama, T Suemoto. J. Lumin. **87 – 79**, 1099(2000).
Yamaguchi, M., K. Koyama, T. Suemoto, and M. Mitsunaga. Phys. Rev. B **59**, 9126 (1999).
Yamaguchi, M., K. Koyama, T. Suemoto, and M. Mitsunaga. J. Lumin. **76**, 681 (1998).
Yang, H. S., S. P. Feofilov, D. K. Williams, J. C. Milora, B. M. Tissue, R. S. Meltzer, and W. M. Dennis. Physica B **263**, 476 (1999).

Yano, R., M. Mitsunaga, and N. Uesugi. Phys. Rev. B **45**, 12,752 (1992).
Yano, R., M. Mitsunaga, and N. Uesugi. Opt. Lett. **16**, 1884 (1991).
Yen, W. M. J. Lumin. **18/9**, 639 (1979).
Yen, W. M., W. C. Scott, and P. L. Scott. Phys. Rev. **137**, A1009 (1965).
Yugami, H., S. Matsuo, and M. Ishigame. Solid State Ionics **77**, 195 (1995).
Zhang, J. H., S. H. Huang, and J. Q. Yu. J. Lumin. **56**, 51 (1993).
Zhang, J. H., S. H. Huang, W. P. Qin, D. K. Gao, and Y. Q. Yu. J. Lumin. **53**, 275 (1992).
Zhang, J. M., T. W. Mossberg. Phys. Rev. B **48**, 7668 (1993).
Zhang, L. F., J. Yu, and S. Huang. J. Lumin. **45**, 301 (1990).
Zumofen, G., F. R. Graf, A. Renn, and U. P. Wild. J. Lumin. **83**, 379 (1999).

Acknowledgements
I wish to express my appreciation to my colleagues who have played a pivotal role in my own contributions to this field. I especially want to acknowledge the numerous fruitful collaborations with Roger M. Macfarlane who has been a tremendous stimulus and to William M. Yen for his constant encouragement over the many years. Gratitude is also due to the students and post doctoral associates who played an essential part in my research efforts. I also wish to thank the National Science Foundation for their support over many years.

5 Up-conversion in RE-doped Solids

F. Auzel

Abstract

As for other fluorescence light emitters, rare-earth-doped solids usually follow the well known principle of the Stokes law which simply states that excitation photons are at higher energy than emitted ones, or in other words that out put photon energy is weak, less than input photon energy. Such a principle is valid of course only when one ion system is considered.

In this chapter, we want to discuss the "unconventional case" where the above principle is not respected in its simple statement. It will be shown that RE-doped solids may deviate rather easily from the above principle giving rise, under moderate to strong excitation density, to unconventional emissions of the anti-Stokes types.

Four mechanisms may be involved in up-conversion: Besides (1) multistep excitation due to classical excited state absorption (ESA), there is (2) the very efficient process of up-conversion by sequential energy transfers due to the fact that in many RE-doped solids, ions may be connected energetically by energy transfer diffusion. This last phenomenon has to be distinguished from (3) a third process, namely cooperative up-conversion either between two ions or between a pair of ions and a third one. Though some of their theoretical behaviors are rather analogous to those of up-conversion by energy transfers, their efficiencies are usually much lower because they involve virtual levels which have to be described in a higher order of perturbation. (4) A fourth process, the photon avalanche effect, will also be considered. It is also based on sequential energy transfers but of the down-conversion type (usually called cross-relaxation), whereas the up-conversion step itself is due to ESA.

Various experimental techniques that allow distinctions to be made between the behaviors of these various processes will be analyzed.

Finally, perspectives for applications of these processes in various types of RE-doped solids such as crystals and glasses in bulk or fiber form are given, and recent advances are encompassed and described.

At any rate this chapter is not intended to be a review; its purpose is to be a didactic description of the various processes that may be involved together with selected typical examples that may help in understanding further developments.

5.1 Introduction and Historical Background

Before the twenty sixties, all anti-Stokes emissions which were known to exist, involved energies above excitation energies not higher than about kT. They were linked to thermal populations of energy states above excitation states by about such an energy difference. It was the well-known case of the fluorescence anti-Stokes emission for the so-called thermal bands, or in Raman effect for the well-known anti-Stokes bands. Also thermoluminescence, where traps are emptied by excitation energies of the order of kT, also constituted a field of anti-Stokes emission of its own. "Superexcitation", that is raising an already excited electron to a still higher level, was also known but with very weak emissions. All these types of well-known anti-Stokes processes have been reviewed in classical textbooks on luminescence (Leverenz, 1968).

In this chapter we discuss anti-Stokes emissions or up-conversion processes for which emission is found to exceed excitation energies by 10 to 100 times kT.

This research can be traced back to an idea of Bloembergen in 1959 (Bloembergen, 1959), proposing that infrared (IR) photons could be detected and counted through sequential absorption within the levels of a given ion in a solid. This was a short proposal for a detector called an infrared quantum counter (IRQC). In fact, because there was little chance that the same single doping ion would receive two photons in sequence at its given position during the first excited state lifetime, the experimental demonstration of such an effect had to wait for laser excitations and fiber local confinement. Some of the first experimental observations (Brown et al., 1969) have been proved later to be due to energy diffusion through energy transfers between identical ions (Auzel, 1984).

The role of energy transfers in up-conversion processes was not recognized until 1966 when it was suggested by Auzel that energy transfers between RE ions could take place between two ions, both of them being in an excited state for the initial energy transfer step (Auzel, 1966). Until then, all energy transfers were assumed to take place from a first ion in an excited state to a second one in its ground state (Van Uitert and Johnson, 1966). Because up-conversion by sequential energy transfers or the APTE effect (French acronym for addition de photons par transfert d'énergie) is so efficient, it could first be induced through blackbody excitation or spontaneous diode emission before the common availability of laser sources.

Principles and applications of such up-conversion phosphors were presented in several reviews by the 1970s by Auzel(1973), Mita and Nagazawa(1974), Garlick(1976) and Wright (1976). Since then, laser excitation in the IR and the use of fibers have become so easy that up-conversion has become a pervasive effect in all RE doped materials under high-density IR excitation. Also another type of up-conversion, namely the photon avalanche process, has been widely investigated in recent years. In this chapter, both the basic processes of energy transfer and their application to up-conversion together with their more recent

evolution and selected examples of applications are presented.

5.2 Energy Transfers Between RE Ions; Role of Energy Diffusion in Up- and Down-conversion

In previous chapters of this book, properties of isolated ions have been considered. In the following their mutual interactions are the key feature.

When the concentration of active ions is increased, long before the appearance of new lines due to pairs or modifications in radiative transition probabilities, a migration of energy between the centers is found. We are going to study this now, assuming that multiphonon decays and the radiative transitions remain one-center processes.

Single ion properties having been reviewed in Chapters 1 to 4, now in this Chapter 5, multi-ion processes, namely energy transfers, are dealt with. Energy transfer occurs in a system when absorption and emission do not take place within the same center. It may occur without charge transport. Then one may distinguish between radiative and non-radiative, resonant and phonon-assisted energy transfer. Theoretical approaches start from a microscopic point of view with a macroscopic result averaged over all the centers in the sample. In fact an energy transfer between two given ions cannot by itself increase efficiency; it can only provide a new excitation wavelength range with a reduced efficiency since the product of two processes with intrinsic efficiency less or equal to 1 is then considered. Overall efficiency improvement by energy transfers is gained only from the spatial averaging of the macroscopic process of diffusion.

5.2.1 Recall of Basics of Energy Transfer with Activator in Its Ground State

In a schematic way, the different microscopic energy transfer processes between two ions can be presented as in Fig. 5.1. One usually distinguishes radiative transfer (Fig. 5.1a), non-radiative energy transfer (Fig. 5.1b, c, d), and multiphonon assisted energy transfer (Fig. 5.1c). S ions and A ions may also be identical ions and non-radiative transfer may give rise to self-quenching by cross-relaxation (Fig. 5.1d).

When energy transfer is radiative (Fig. 5.1a), real photons are emitted by the sensitizer ions and are then absorbed by any activator ions within a photon travel distance. Because of this fact, such transfer depends on the shape of the sample.

Moreover, according to the degree of overlap between the emission spectrum of the sensitizer (S) and the absorption spectrum of the activator (A), the structure of the emission spectrum of the sensitizer will change with activator concentration. Since photons are emitted anyway, the sensitizer lifetime is

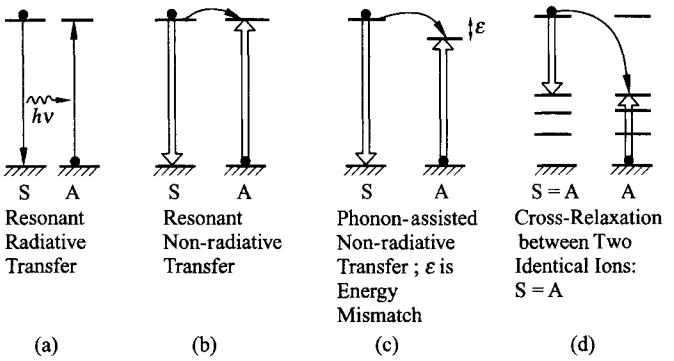


Figure 5.1 Various basic energy transfer processes between two ions considered before 1966: note that activator ion (A) receiving the energy from the sensitizer (S) is initially in its ground state. Cross-relaxation is the special case where S is identical to A. Doubled arrows symbolize the Coulomb interaction. (a) resonant radiative transfer; (b) resonant non-radiative transfer; (c) phonon-assisted non-radiative transfer; (d) is the cross-relaxation special case of non-radiative transfer

independent of the activator concentration. These three facts are the criteria used to distinguish between radiative and non-radiative resonant energy transfer.

The probability of such transfer between two ions at a sufficiently large distance R is found to be (Auzel, 1980)

$$p_{SA}(R) = \frac{\sigma_A}{4\pi R^2}\frac{1}{\tau_S}\int g_S(\nu)\, g_A(\nu)\, d\nu, \qquad (5.1)$$

where τ_S is the sensitizer lifetime, and σ_A the integrated absorption cross section. The integral represents the spectral overlap between A and S. It should be noted that the distance dependence goes as R^{-2}. Such resonant radiative transfer may permit long-range energy diffusion between identical ions and gives rise to photon trapping effects of the same type as observed long time ago in gas(Milne, 1926). Trapping effects increase the apparent experimental lifetime and τ_S has to be measured on thin and lightly doped samples. These effects are particularly strong in Cr^{3+} and Yb^{3+} (Varsanyi and Schawlow, 1959; Auzel, 1969).

Let us consider the simple case of two ions, each with one excitable electronic state separated from its electronic ground state by nearly equal energy; it is the case described in Fig. 5.1b. With suitable interaction between the two electronic systems, the case for non-radiative energy transfer, the excitation will jump from one ion S to A before S is able to emit a quantum of fluorescence. The mutual interactions are the Coulomb interactions of the Van der Waals type between the two ions. Förster(1948), who first treated such a case theoretically by quantum-mechanical theory, considered the dipole-dipole interactions. He assumed that the interaction is strongest if for both transitions electric-dipole

transitions are permitted (Förster, 1948). The interaction energy is then proportional to the inverse of the third power of the interionic distance and the transfer probability is given by

$$p_{SA} = \frac{2\pi}{h} | \langle S^* A^0 | H_{SA} | S^0 A^* \rangle |^2 \rho_E, \tag{5.2}$$

H_{SA} is electric dipole – dipole interaction Hamiltonian, proportional to the inverse third power of the ion separation, ρ_E is density of states provided by the vibrational motion, which contributes to line broadening of the transition. p_{SA} is proportional to the inverse sixth power of the ion separation. The wavefunctions to be considered for the matrix element describe an initial state of the system with the sensitizer in its excited state and the activator in its ground state, the final state having the sensitizer in its ground state and the activator in its excited state.

Therefore, the transfer probability can be written as

$$p_{SA} = \frac{1}{\tau_S}\left(\frac{R_0}{R}\right)^6 \tag{5.3}$$

where τ_S is the actual lifetime of the sensitizer excited state, including multiphonon radiative decay, and R_0 is the critical transfer distance for which excitation transfer and spontaneous deactivation of the sensitizer have equal probability.

However, Dexter (1953) pointed out that this theory should be extended to include higher multipole and exchange interactions. In fact, for an isolated atom, one can consider the transition probability as decreasing as $(a_0/\lambda)^{2n}$, where a_0 is the Bohr radius, λ the wavelength, and n an integer. On the other hand in an energy transfer process with a dependence on near-zone interactions, the transition probabilities drop off as $(a_0/\rho)^{2n}$, where ρ is the separation of the interacting ions. ρ can be as much as three orders of magnitude smaller than λ, so that the energy transfer effects tend to be more pronounced in systems with forbidden transitions (Dexter, 1953). This holds true for ions with transitions forbidden to first order, such as transition metal and lanthanide ions.

The energy transfer probability for electric multipole interactions can be more generally written as (Dexter, 1953)

$$p_{SA} = \frac{(R_0/R)^S}{\tau_S}, \tag{5.4}$$

where S is a positive integer taking the following values: $S = 6$ for dipole – dipole interactions; $S = 8$ for dipole – quadrupole interactions; $S = 10$ for quadrupole – quadrupole interactions.

It should be noted that for dipole – dipole interactions, the differences

between radiative and non-radiative resonant transfer are essentially that for radiative transfer there is no critical R_0; they depend only upon concentration. The variation goes as R^{-2} instead of R^{-6}, and the sensitizer lifetime does not depend upon the distance R.

Now, to be able to calculate p_{SA} effectively, Eq. (5.4) is not very useful, because R_0 cannot be easily obtained theoretically. Applying Racah tensorial methods straightaway at the beginning of the calculation of Dexter, Eq. (5.2), permits one to develop calculations analogous to Judd's theory for radiative transitions (see Chapter 2). The case of multipole interactions was treated in this way by Kushida(1973) and extended by Pouradier and Auzel to magnetostatic and exchange interactions (Pouradier and Auzel, 1978), showing that a single general formula could be used for all types of energy transfers.

The general form obtained is then

$$p_{SA}(R) = \frac{2\pi}{\hbar}\frac{I}{g_{S^*}g_{A^0}}\sum_{l_1l_2}|C_{l_1l_2}\langle S^*\|U^{(l_1)}\|S^0\rangle\langle A^0\|U^{(l_2)}\|A^*\rangle|^2, \quad (5.5)$$

with

$$I = \int\gamma_S(E)\Gamma_A(E)\,dE, \quad (5.6)$$

where $g_{S^*}(g_{A^0})$ is the degeneracy of the $S^*(A^0)$ level, and $\gamma_S(E)[\Gamma_A(E)]$ is the normalized line shape function of the emission (absorption) spectrum. $U^{(l)}$ are the tensorial operators already seen for Judd theory. $|C_{l_1l_2}|^2$ can be considered as a parameter analogous to Judd $T_\lambda(\Omega_\lambda)$ for oscillator strength.

This expression of the transfer probability has the following advantages:

(1) Radial and orbital parts have been separated.

(2) Only a few reduced matrix elements need to be calculated. They are the same for the three interactions we consider (for any interaction leaving spins unchanged).

(3) Comparison between two different interactions can be made through comparison of $C_{l_1l_2}$ coefficients. They are independent of the states involved in the transfer and we call them $E_{l_1l_2}$, $M_{l_1l_2}$, and $X_{l_1l_2}$ for electrostatic, magnetostatic, and exchange interactions, respectively.

(4) Forced electric-dipole transitions, as calculated by the Judd method, can be included in Eq. (5.5).

(5) This expression also yields a single mathematical form regardless of the interaction, which is a convenient result. The somewhat complicated expressions for the different $C_{l_1l_2}$ of 4f electrons are given in (Pouradier and Auzel, 1978). But we can note that:

For electrostatic interaction, $E_{l_1l_2}$, the $l_1=1$ and $l_2=1$ term, corresponding to dipole – dipole interaction, being zero in first order, the introduction of T_λ

parameters is needed. The $E_{l_1 l_2}$ values are typically between $E_{22} \approx 30\ \mathrm{cm}^{-1}$ for quadrupole – quadrupole intensities to $E_{66} \approx 3 \times 10^{-1}\ \mathrm{cm}^{-1}$, but all contain some dipole – dipole part due to the T_λ.

For magnetostatic interactions ($M_{l_1 l_2}$) only terms with $l_i = 1, 3, 5$ are nonzero and have the following order of magnitude: $M_{11} \approx 1\ \mathrm{cm}^{-1}$, $M_{55} \approx 2 \times 10^{-7}\ \mathrm{cm}^{-1}$.

For exchange interactions ($X_{l_1 l_2}$) we have $1 \leqslant l_1 \leqslant 6$, giving estimates of 1 to $10^{-1}\ \mathrm{cm}^{-1}$ for the coefficients.

These results show that exchange or magnetostatic interactions can be found in cases of small dipole – dipole and quadrupole electrostatic interactions if the matrix elements allow them.

If now we consider two ions with excited states of different energies (Fig. 5.1c), the probability for energy transfer should drop to zero where the overlap integral $\int g_S(\nu) g_A(\nu) \mathrm{d}\nu$ vanishes. However, it is experimentally found that energy transfer can take place without phonon-broadened electronic overlap provided that overall energy conservation is maintained by production or annihilation of phonons with energies approaching $k\Theta_d$, where Θ_d is the Debye temperature of the host matrix (Axe and Weller, 1964). Then for small energy mismatch ($\approx 100\ \mathrm{cm}^{-1}$) energy transfer assisted by one or two phonons can take place (Orbach, 1975). However, in energy transfer between rare earths, energy mismatches as high as several thousand reciprocal centimeters are encountered. This is much higher than the Debye cut off frequency found in normally encountered hosts, so that multiphonon phenomena have to be considered here.

Miyakawa and Dexter (Miyakawa and Dexter, 1971) have shown that it is still legitimate to write the probability of energy transfer in the form of Eq. (5.2), where ρ_E is taken as S_{SA}, the overlap of the lineshape functions for emission in ion S and absorption of ion A, including theoretically the phonon sidebands in the lineshape. It is necessary to consider each partial overlap between the m-phonon emission line shape of ion S and the n-phonon absorption lineshape of ion A. A physical meaning to this mathematical assumption has been given by Auzel's experimental demonstration (Auzel, 1976) of the existence of multiphonon sidebands for trivalent rare earth ions; even though they had not be seen by usual absorption spectroscopy because of their very small electron – phonon coupling. They could be revealed by laser excitation spectroscopy.

Along the same lines as for vibronic – sideband studies, S_{SA} can be expressed as follows:

$$S_{SA} = \sum_N \mathrm{e}^{-(S_{OS}+S_{OA})} \frac{(S_{OS} + S_{OA})^N}{N!} \sigma_{SA}(0, 0; E) \delta(N, \Delta E/\hbar\omega), \qquad (5.7)$$

where S_{OS} and S_{OA} are the respective lattice coupling constants for the S and A ions, N is the order of the multiphonon process with $N = \Delta E/\hbar\omega_m$, ΔE the

energy mismatch between both ions, and $\hbar\omega_m$ the phonon cutoff frequency. $\sigma_{SA}(0, 0; E)$ is the zero-phonon overlap integral between S and A. Eq. (5.7) contains a "Pekar" function of the type described in Chapter 3.

The expression for S_{SA} with an energy mismatch of ΔE for small S_0 constants and for an occupation number $\bar{n} = [\exp(\hbar\omega/kT) - 1]^{-1}$ not exceeding unity at the operating temperature can be approximated with Stirling's formula by

$$S_{SA}(\Delta E) = S_{SA}(0)\,e^{-\beta\Delta E}, \tag{5.8}$$

where $S_{SA}(0)$ is the zero-phonon overlap between S and A in the case where there is no energy mismatch between the two ions. β is given by

$$\beta = (\hbar\omega)^{-1}\log N/S_0(\bar{n} + 1) - \log\left(1 + \frac{S_{OA}}{S_{OS}}\right) \equiv \alpha_S - \gamma \approx \alpha_S - \log 2 \tag{5.9}$$

involving α_S the non-radiative decay parameters, and assuming identical electron-phonon coupling for ions A and S. This exponential dependence on energy mismatch agrees well with experiments (Yamada et al., 1972).

Up to this point we have been dealing with the microscopic case of two ions interacting with one another. To discuss the case of real macroscopic samples with many ions and to obtain a link with experimental facts, a statistical analysis of the energy transfer is necessary.

We have then to think about the overlap integrals that arise in all transfer between two ions as already seen. In the microscopic case we are sure that involved lineshapes can only be due to some homogeneous broadening, even for transfer between two identical ions in different lattices sites.

In the macroscopic case, we can measure absorption and emission spectra taking into account all broadening processes averaged over the whole sample, for instance the inhomogeneous broadening process due to emission and absorption at centers in different lattice sites. Then the overlap integral measured experimentally from the usual spectra is a measure in excess of the real overlap since we take into account emission and absorption of centers at all distances, even those which cannot interact. The error is the largest for processes at the shortest interacting distances (exchange), and in contrast is certainly negligible for radiative transfer, since photons can travel a much larger distance than the spread of spatial disorder. The error is also smaller for systems with small inhomogeneous broadening having centers in only one type of lattice site, that is, without disorder.

Fluorescence line-narrowing techniques (FLN) (see Chapter 4) could give some idea about the homogeneous part of an emission line, but statistical analysis should still be performed for the whole sample. Supposing only a sensitizer – activator interaction, an average transfer efficiency can be calculated (Dexter, 1953). This was studied in some detail by Inokuti and Hirayama (Inokuti and

Hirayama, 1965). They considered the number of activators situated at random in a sphere around a sensitizer such that the activator concentration is constant when the volume of the sphere and the number of activator ions considered goes to infinity. Then the average probability for transfer from one sensitizer to any acceptor is

$$W_{SA} = N_A \int_{R_{min}}^{\infty} p_{SA}(R) 4\pi R^2 dR. \tag{5.10}$$

Introducing Eq. (5.2) into the expression for the intensity emitted by all sensitizers, each with different activator neighborhood, they obtained the following relation for the intensity decay of the emission of the sensitizer surrounded by many activators

$$I(t) = \exp -\frac{t}{\tau_{SO}} - \Gamma\left(1 - \frac{3}{S}\right)\frac{C}{C_0}\left(\frac{t}{\tau_{SO}}\right)^{3/S}, \tag{5.11}$$

where τ_{SO} is the decay constant of the sensitizer in the absence of activators, C is the activator concentration, C_0 is the critical activator concentration, and S the parameter of the multipole interaction. The comparison between experiment and this theoretical expression has been widely used to determine the index of the multipole interaction involved. This theory is valid only when there is no sensitizer-to-sensitizer transfer or activator-to-activator transfer. This formulation, therefore, has to be modified for high concentrations of sensitizers and activators. Then, due to the perfect resonance conditions of such cases, rapid energy migration between sensitizers or between activators is possible. The general result is complicated (Yokota and Tanimoto, 1967) but Weber has shown, that for large t, $I(t)$ decays exponentially (Weber, 1971),

$$I(t) = \exp\left(-\frac{t}{\tau_S} - \frac{t}{\tau_D}\right). \tag{5.12}$$

Then, two cases can be distinguished.

(1) In one case, spontaneous decay of excited sensitizers, diffusion among sensitizers, and energy transfer between sensitizers and activators are of about the same order of magnitude.

For sufficiently long time and dipole – dipole interactions one has (Weber, 1971)

$$\tau_D^{-1} = V N_S N_A, \tag{5.13}$$

where $V = 8\pi C^{1/4} C_{SS}^{3/4}$ with C is the sensitizer – activator energy transfer constant, such as $C = (R_0)^S/\tau$; C_{SS} is the sensitizer – sensitizer transfer constant. N_S is the sensitizer concentration, N_A the activator concentration.

(2) For high sensitizer concentration, the diffusion rate can be greater than that of spontaneous sensitizer decay or sensitizer – activator energy transfer. The limiting step is no longer diffusion, and D appears to saturate with increased donor concentration; each activator experiences the same excited sensitizer neighborhood. We take R as the minimum distance between sensitizers permitted by the lattice ($R = R_{min}$). One has

$$\tau_D^{-1} = UN_A, \tag{5.14}$$

with U a constant that depends on the type of interaction as discussed earlier in this section through Eq. (5.5).

Another approach to the macroscopic case is the use of the well-known rate equations that deal with the population of ions in a given state. This was used as a phenomenological approach in studies of lasers. The applicability of those equations in relation to the Inokuti and Hirayama statistics has been discussed by Grant (1958). The basic result of Grant is that the energy transfer probability is proportional to the activator concentration

$$W_t = UN_A. \tag{5.15}$$

This result is the same as obtained for fast-diffusion studies (see Eq. (5.14)). The practical interest in considering diffusion is that the decays are again exponential, as when ions are not interacting. This validates the use of rate equations.

"Cross-relaxation" terminology usually refers to all types of down-conversion energy transfer between identical ions. In such a case the same kind of ion is both a sensitizer and an activator.

As shown in Fig. 5. 1d, cross-relaxation may give rise to the diffusion process already considered between sensitizers when the levels involved are identical or to self-quenching when they are different. In the first case there is no loss of energy, whereas in the second there is a loss or a change in the energy of the emitted photons.

Theoretically the same treatment is valid as for the more general case of energy transfer, however, experimentally it may be more difficult to distinguish between sensitizers and activators. So any of the microscopic processes discussed above may happen with a maximum overlap when an identical pair of levels are involved. From the macroscopic point of view, the diffusion-limited case predicts from Eq. (5.13) that

$$\tau_D^{-1} = VN^2 \tag{5.16}$$

for

$$N_S = N_A = N,$$

and in the fast-diffusion case

$$\tau_D^{-1} = UN. \tag{5.17}$$

A typical illustration of this is found for the self-quenching behavior of Nd^{3+} ($^4F_{3/2}$). In weak quenching materials such as $La_{1-x}Nd_xP_5O_{14}$, self-quenching is found to behave linearly with ion concentration whereas for strong quenching ones such as $Y_3Al_5O_{12}$(YAG), quadratic behavior is obtained. This respectively reflects the fast diffusion before the quenching step in the first type and the limited diffusion before quenching in the second type of material (Auzel, 1980, 1979).

5.2.2 Up-conversion Processes by Sequential Energy Transfers; Comparison with ESA and Typical Examples

As mentioned in introduction, up to 1966 all identified energy transfers between rare-earth ions were of the types summarized in Fig. 5.1. That is, the activator ion receiving the energy from a nearby sensitizer (S) was in its ground state. Then Auzel proposed to consider cases where activators (A) were already in an excited state (Auzel, 1966) as shown in Fig. 5.2. Because activator ions usually have several (n) excited states but a single ground state, one can understand why n-photons may be summed up through this new consideration. This is evident afterwards because one has to realize that only energy differences and not absolute energy can be exchanged between ions.

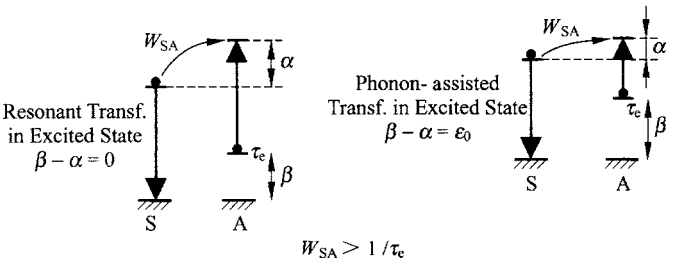


Figure 5.2 APTE basic step: energy transfer to an ion already in an excited state. Non-radiative energy transfer is either resonant or phonon-assisted with energy mismatch $\varepsilon_0 \neq 0$

The reason for proposing such upward transfer was to point out that energy transfers then used (Snitzer and Woocock, 1965) to improve the laser action of Er^{3+} by pumping Yb^{3+} in a glass matrix could also have the detrimental effect of increasing reabsorption (Auzel, 1966, 1969). The simple proof of such an effect was to look for an up-converted green emission (from $^4S_{3/2}$ of Er^{3+}) while pumping Yb^{3+} ($^2F_{7/2} - {}^2F_{5/2}$) transition, which was effectively observed (Auzel,

1966; Auzel and Deuschbein, 1969). Of course the situation in Fig. 5.2 could repeat itself several times at the activator. This means that n-photon up-conversion by energy transfer was possible, as demonstrated by the 3-photon up-conversion of 0.97 μm into blue light (0.475 μm) in the Yb^{3+}-Tm^{3+} couple (Auzel, 1966). Independently such IR→blue up-conversion was interpreted by Ovsyankin and Feofilov (Ovsyankin and Feofilov, 1966) as a 2-photon effect connected with cooperative sensitization of Tm^{3+}, initially in its ground state, by two cooperatively excited Yb^{3+} ions. This interpretation originated from the quadratic law obtained for output versus excitation instead of the cubic one found in (Auzel, 1966). The later discrepancy probably resulted from a saturation in an intermediate step in the APTE process (Hewes and Sarver, 1969). Cooperative processes will be discussed in the next paragraph.

In order to make the terminology clearer, a schematic comparison between the APTE effect and other 2-photon up-conversion processes, namely 2-step absorption, cooperative sensitization, cooperative luminescence, second harmonic generation (SHG), and 2-photon absorption excitation is presented in Fig. 5.3, together with their respective typical efficiency.

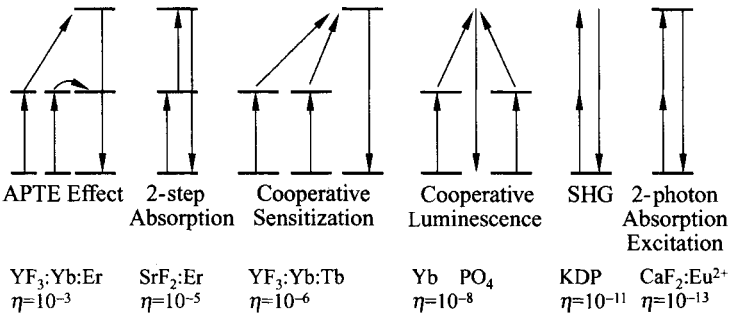


Figure 5.3 Various two-photon up-conversion processes with their relative efficiency in considered materials

Since we are dealing with nonlinear processes, the usual efficiency, as defined in percent, has no meaning because it depends linearly on excitation intensity. Values are then normalized for incident flux and given in cm^2/W units.

A simple inspection of involved energy schemes shows that they differ at first sight by the resonances involved for in- and out-going photons: for highest efficiency, photons have to interact with the medium for a longer time, which in practice derives from the existence of resonances. As shown, the APTE effect is the most efficient because it most closely approaches the full resonance case.

However reality is sometimes not so simple, and different up-conversion processes may exist simultaneously, or their effects can be tentatively reinforced reciprocally. For instance two-photon absorption and cooperative absorption have been theoretically investigated (Rios Leite and de Araujo, 1980). Also SHG and

cooperative luminescence have been considered simultaneously in order to increase SHG by the partial resonance of cooperative luminescence (Bonneville and Auzel, 1976; Ovsyankin and Fedorov, 1981).

Let us consider now the role of macroscopic energy diffusion in both APTE and ESA up-conversion second-order processes.

The probability for ESA in a two-step absorption (W_{13}) connecting a state E_1 to E_3 by the intermediate state E_2 is just given by the product of the probabilities for each step (Fig. 5.4):

$$W_{13} = W_{12} \cdot W_{23}. \qquad (5.18)$$

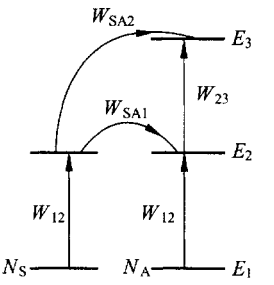


Figure 5.4 Simplified energy level scheme and symbols used in Eqs. (5.18) – (5.22)

In order to obtain the same result by an APTE effect we have also to consider the product of two energy transfer probabilities and to calculate the equivalent rate for populating E_3 by APTE, yielding

$$N_A W_{13} \equiv (N_A N_S^* W_{SA1}) N_S^* W_{SA2} \qquad (5.19)$$

or

$$W_{13} \equiv N_S^{*2} W_{SA1} W_{SA2}, \qquad (5.20)$$

where W_{SA} are the energy transfer probabilities for each step, and N_S^* the concentration of excited sensitizers given by

$$N_S^* = N_S W_{12}.$$

Assuming all W_{ij} to have the same magnitude, and all W_{SA} also, as is typical for rare earth ions, we have to compare

$$W_{13} \approx W_{12}^2 \qquad (5.21)$$

for single-ion ESA with

$$W_{13} \approx N_S^{*2} W_{SA}^2 = N_S^2 W_{12} W_{SA}^2 \qquad (5.22)$$

for two APTE ions. Clearly the gain by APTE over one-ion ESA comes from the product $N_S^2 W_{SA}^2$ which has to be as large as possible.

This points to an increase in sensitizer concentration (N_S), which leads to "fast diffusion" (Weber, 1971), and allows the use of rate equations in such

multi-ions systems (Grant, 1958). This a posteriori validates the implicit use of rate equation for establishing Eqs. (5.18) – (5.22).

Besides nonradiative diffusion at the sensitizer level, it has been observed that radiative diffusion also plays a role in APTE up-conversion. The measured time constants for the Er^{3+} or Tm^{3+} emission have been observed to be correlatively lengthened by the photon trapping lengthening of the Yb^{3+} lifetime, reflecting the radiative diffusion at the sensitizer level (Auzel and Pecile, 1973). Also reducing to powder form a single crystal doped with Yb-Er or Tm usually shows an intensity reduction when grain size is reduced below 100 μm. This shows that the effective radiative diffusion length is of this order of magnitude in this experiment.

Many times in the literature, when ESA is not advocated, up-conversion involving coupled ions is referred to as cooperative effects without proof, when in fact as can be guessed from their relative efficiencies, APTE effects are involved. The fact that the APTE effect and cooperative ones are often mistaken one for the other is linked with a number of common properties (Auzel, 1973). For instance, for two-photon up-conversion, both processes show a quadratic increase with excitation and with absorber concentration; both show an emission lifetime equal to half the absorber lifetime. However, they show different rise-times; cooperative rise-time is instantaneous as for any absorption, whereas APTE rise-time reflects population accumulation in the sensitizer excited state. However as shown below the difference is more basic, though sometime difficult to establish experimentally except in special cases: when single-ion resonances clearly do not exist or when diffusion between ions is prohibited by too small a concentration while an interaction is still in progress, as in clusters.

The basic distinction between both up-conversion processes is the purpose of the next paragraph.

5.3 Up-conversion in Single-ion and Pair-level Level Description; Theoretical and Experimental Discrimination

When active ions are situated at sufficiently short distance for interactions between them to take place, two types of up-conversion processes may occur: summation of photon energy through energy transfers (Auzel, 1973) (APTE effect) and cooperative effects either by sensitization (Ovsyankin and Feofilov, 1966) or emission as found by Nakazawa and Shionoya (Nakazawa and Shionoya, 1970). Both APTE effects and cooperative ones are often mistaken one for the other because both present several similarities and may simultaneously occur in a given system for a given excitation. In particular both processes reflect the n-photon order versus excitation density and sensitizer concentration in the same manner.

As seen in the introduction, up-conversion by energy transfers is just a generalization of Dexter's energy transfer (Dexter, 1953) to the case of the activator being in a metastable state instead of being in its ground state; this requires that the interaction between S and A (H_{SA}) be smaller than the vibronic interaction of S and A in order that both ions be described by single-ion levels coupled to the lattice. It is generally the case, since for fully concentrated rare earth crystals or for clusters, pair-level splitting is of the order of $0.5\ cm^{-1}$ (Ovsyankin, 1987). In a host with smaller concentration this interaction can even be weaker, whereas one-phonon or multi-phonon sidebands may modulate the level positions by several $100\ cm^{-1}$. Further, up-conversion requires that the transfer probability for the second step (W_{SA}) be faster than radiative and non-radiative decay from the metastable level, that is $W_{SA} > \tau^{-1}$, with τ the measured intermediate state lifetime for ion A. W_{SA} is obtained from

$$W_{SA} = \frac{2\pi}{\hbar} | \langle \Psi_S^e \Psi_A^0 | H_{SA} | \Psi_S^0 \Psi_A^e | ^2 \rho(E), \tag{5.23}$$

where the wave functions are simple products of single-ion wave functions, and $\rho(E)$ describes the dissipative density of states due to the coupling with the lattice.

All cooperative processes including up-conversion can be considered as transitions between pair level for both ions as a whole. A dipole electric transition would be forbidden for such two-center transitions and one needs product wave functions corrected to first order to account for interactions between electrons of different centers (Stavola and Dexter, 1979):

$$\Psi_{pair} = \Psi^0(S)\Psi^0(A) - \sum_{s''\neq 0}\sum_{a\neq 0} \frac{\langle s''a'' | H_{SA} | 00\rangle}{\delta_{s''} - 0 + \varepsilon_{a''} - 0} \Psi_{s''}(S)\Psi_{a''}(A), \tag{5.24}$$

for example for the ground state, s'', a'' denote intermediate states for S and A; $\delta_{s''}$, $\varepsilon_{a''}$ denote their corresponding energies. Then any one-photon transition in the cooperative description already involves four terms in the matrix element, which cannot be reduced to Eq. (5.5), that contains only single ion wavefunctions and not pair wavefunctions as in Eq. (5.24).

APTE up-conversion corresponds to a lower order of perturbation than a cooperative process, which has to be considered in practice only when the first type cannot take place.

Such is the case when real levels do not exist to allow energy transfers; it is the case for $Yb^{3+} - Tb^{3+}$ up-conversion (Ovsyankin, 1987; Livanova et al., 1969; Ostermayer and Van Uitert, 1970) or when concentration is too small to allow efficient transfer by energy diffusion between sensitizers. Then cooperative up-conversion is likely within clusters (Vial et al., 1979; Auzel et al., 1994a). One may also look for crystal structures where the pair clustering is built in

(Cockroft et al., 1989).

Until the 1980s, few unquestionable experimental examples of cooperative up-conversion were demonstrated besides the Yb-Tb cooperative sensitization quoted above and the cooperative luminescence in Yb^{3+} described in detail below (Nakazawa and Shionoya, 1970).

Since then, two more cases have been described (Rand et al., 1982; Lee et al., 1984):

(1) The cooperative luminescence in the UV (from 405 nm to 270 nm) coming from two $(^2P_0)Pr^{3+}$ excited ions in PrF_3.

(2) In $Pr^{3+}:LaF_3$, APTE cooperative sensitization of the $^1S_0$ state of one Pr^{3+} ion already in its excited state ($^3P_0$) due to the energy annihilation of two other Pr^{3+} ions also in their $^2P_0$ excited state, as for the cooperative luminescence case. Overall this is a 3-ion, 3-photon effect which, from 477 nm blue excitation, yields an up-conversion in the UV region (400 – 250 nm). Figure 5.5 describes the energy schemes and the mechanisms for both processes. However, for some unclear reason the cubic law which should be present for emission intensity versus excitation is not observed in the $^1S_0$ level emission (Rand et al., 1982) and a quadratic law is obtained as for the cooperative luminescence case. The cooperative effects were clearly discriminated from other processes through excitation spectra investigations.

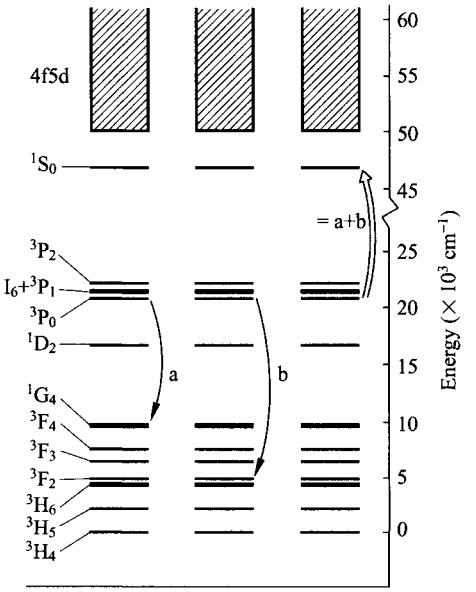


Figure 5.5 Cooperative luminescence and APTE (activator ion already in an excited state). Cooperative sensitization in $Pr^{3+}:LaF_3$ system (Lee et al., 1984)

Generally, experimental discrimination between APTE and cooperative processes is not straightforward apart from the trivial cases where no real intermediate energy level, even due to unwanted impurities, exists for the APTE effect to take place. The weak ion concentration level alone is not a good argument to eliminate APTE up-conversion, knowing that RE ion clusters may exist, for instance in glasses, even at level of doping as low as 70 ppm (Blixt et al., 1991).

In order to illustrate the experimental difference between APTE and cooperative up-conversion, we shall discuss an example of excitation line-narrowing effect in n-photon summation as a means to distinguish the two processes (Auzel, 1984, 1985). Irradiating Er^{3+} doped samples with IR radiation at 1.5 μm leads to various visible emissions.

Room temperature IR F-center laser excitation between 1.4 and 1.6 μm of 10% Er^{3+} doped vitroceramics and of Er: YF_3 leads to emission bands from near IR to UV. Such emission may be ascribed to multiphoton excitation respectively of order 1 to 5, either of the APTE or of the cooperative type as depicted respectively with energy levels of single ions (APTE) or with pair levels (Fig. 5.6).

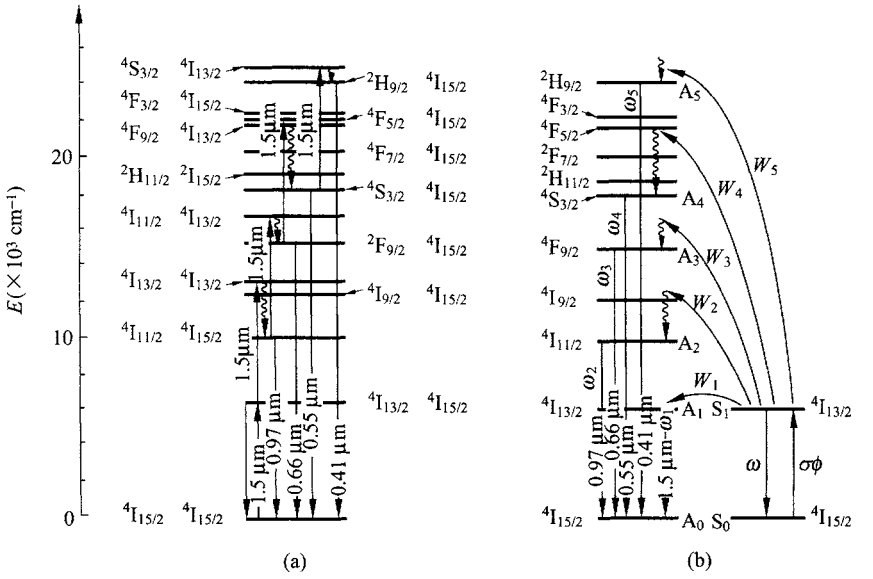


Figure 5.6 Cooperative (a) and APTE (b) energy scheme for n-photon ($n = 1 - 5$) up-conversion in Er^{3+}-doped hosts (Auzel, 1984)

Successive absorptions in Fig. 5.6a involve a combination of several J states. The APTE effect, because of self-matching by multiphonon processes, involves (Fig. 5.6b) only $J = 15/2$ and $J = 13/2$ states.

Excitation spectra (Fig. 5.7) show a striking behavior: each spectrum

presents the same spectral structure with clearly an increasing narrowing with process order. The structure reproduces the Stark structure of the $^4I_{15/2} - {}^4I_{13/2}$ first excited terms as can be obtained by a diffuse reflectance spectrum. Then this is a direct proof of the validity of the APTE explanation, since a cooperative effect should show the convolution of all J states involved in the multiple absorption between pair levels (Auzel, 1984).

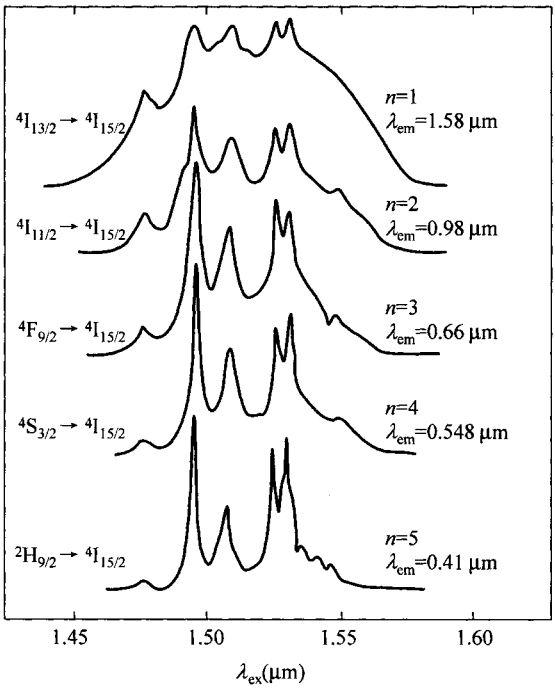


Figure 5.7 Excitation spectra for n-photon ($n = 1 - 5$) up-conversion in Er^{3+}-doped YF_3 (Auzel, 1990)

The spectral narrowing can be understood by a rate equation treatment where higher excited populations are neglected meaning unclear – rephrase the lower ones in order to obtain a tractable development (weak excitation assumption).

The emitted power from an n-photon summation is then given by

$$P_n(\lambda) = \frac{W_n \cdots W_2}{(\omega_{n-1} \cdots \omega_2)} P_1^n(\lambda) \tag{5.25}$$

with symbols of Fig. 5. 5b and $P_1(\lambda)$ the line shape of $^4I_{15/2} - {}^4I_{13/2}$ absorption (Auzel, 1984).

5.3.1 Application of Cooperative Luminescence; Theory and Examples

Because cooperative processes are less effective than APTE by 4 to 5 orders of magnitude, very few applications of such processes exist except, as we shall see, the detection of RE ion clusters. We have proposed that the simplest cooperative process, the cooperative luminescence of Yb^{3+} (Nakazawa and Shioonoya, 1970), be used as a probe of the existence of Yb^{3+} ion clusters in glasses (Auzel et al., 1994).

Cooperative luminescence (or its opposite cooperative absorption) is the simplest cooperative phenomenon, and the corresponding two-center matrix element is

$$\langle \Psi^{g}_{pair} \mid D^{(1)}_{1} + D^{(1)}_{2} \mid \Psi^{e}_{pair} \rangle , \qquad (5.26)$$

where the operator is the sum of the electric dipole operators for ion 1 and ion 2. The wave functions for both ions in their excited state Ψ^{e}_{pair} and in their ground state Ψ^{g}_{pair} are derived from expressions given by Eq. (5.24). The calculation of Eq. (5.26) gives four terms that are represented in Fig. 5.8; terms III and IV provide the cooperative emission at twice the energy of the single-ion excited state.

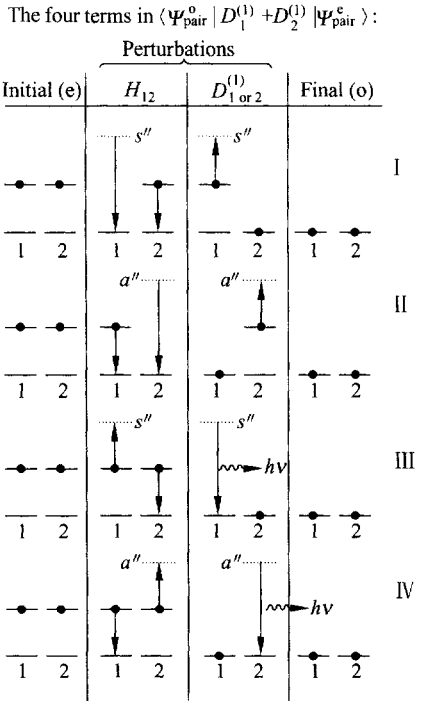


Figure 5.8 The four terms for cooperative luminescence in a two-level ion system (the Yb^{3+} case)

Because nearest neighbor ions have analogous chemical properties along the RE series, we assumed that Yb^{3+} would behave chemically for the clustering process like Er^{3+}, the ion generally used in optical amplifiers (see Chapter 8). Since Yb^{3+} ions have only two spin – orbit states, they are good examples of the simple situation schematized in Fig. 5.8. It is one of the reasons of its use as a cluster probe. The other reason is the following.

In optical amplifier applications, the basic limitation associated with the existence of the so-called clustering of RE ions was addressed. "Clusters" of RE dopant, as found in the literature from direct fiber amplification experiments (Blixt et al., 1991; Delevaque et al., 1993; Maurice et al., 1995), are related to what could be called "interaction clusters" with size much larger than for "chemical clusters". Because of spatial diffusion as shown in Section 5.2.1, such "interaction clusters" could have spatial extent of more than 20 to 100 Å for non radiative interaction clusters and up to 100 μm for radiative ones. Clearly such "clusters" have nothing to do with "chemical clusters" which are the only ones that depend on the chemical processes of glass preparation. The existence of "chemical clusters" of spatial extent of a few Å would increase tremendously ion – ion interactions of all kinds. One needs to obtain signature of such clusters that are the only ones that chemistry could eventually modify. Cooperative luminescence of Yb^{3+} has been proposed as a signature of the existence of chemical clusters in glasses (Auzel et al., 1994).

Cooperative luminescence (Auzel et al., 1990, 1994; Goldner et al., 1997a, 1997b) is a phenomenon which, requesting very close proximity of interacting RE ions in order to be experimentally observable, is a very good signature of clusters constituted by ions at practical distances of less than about 5 Å. Such distances, or shorter ones, between interacting ions are also of the order of the magnitude of the size of chemical clusters. Figure 5.9 presents the cooperative

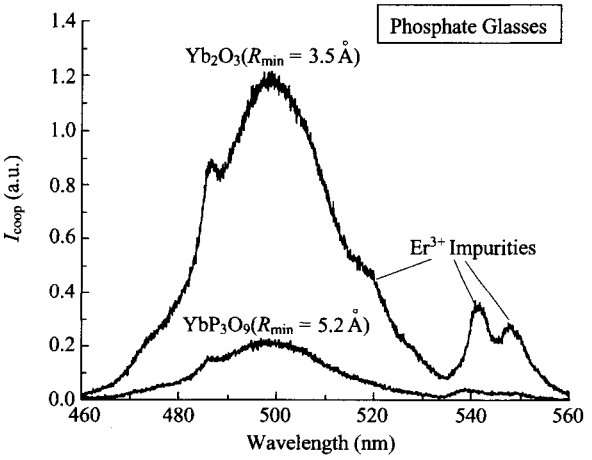


Figure 5.9 Normalized cooperative emission spectra for Yb^{3+} in a phosphate glass for two doping precursors with different Yb – Yb shortest distance R_{min} (Auzel and Goldner, 2001)

luminescence of Yb^{3+} in a phosphate glass doped with Yb^{3+} introduced through various precursors with different Yb – Yb shortest distances (Auzel and Goldner, 1999, 2001). It is shown that the normalized cooperative intensities depend on such distances. Also it can be noted that unwanted impurities (Er^{3+}, Tm^{3+}) introduced with Yb^{3+} oxide are revealed at ppm level by the much more efficient APTE effect (Auzel and Goldner, 1999, 2001; Schaudel et al., 2000).

5.3.2 Some Experimental Results for APTE Effect and Their Implications in Various Field

5.3.2.1 APTE for Display and IR Detection Applications

In display technology, the light emitting material is always in powder form, traditionally called a "phosphor". Because of various inclinations of the crystallite external surfaces reducing total internal reflection, more light output is extracted in a wider view angle from crystallites than from an equivalent single crystal. The up-conversion phosphor field has recently been reinvestigated (Page et al., 1998; Mita et al., 1995; Yen et al., 1988; Cases and Chamaro, 1990; Kermaoui et al., 1994). For the now well known two-photon and three-photon phosphors based respectively on Er-Yb and Tm-Yb co-doped materials. Besides the older light emitting incoherent sources (Auzel, 1973) renewed interest stems from potential applications ranging from simple hand-held devices used to find IR laser beams (Auzel, 1968; Tokin IR Catcher, 1987; Photo-Turkey-1, 1994) to visible enhanced detection of IR emissions, X-rays reusable memory plates (Breteau et al., 1990) and 3D display technologies (Downing et al., 1996).

In particular, with now available tunable lasers and fiber beam homogenizers, the various efficiencies have been recently revisited in Krupke's group (Page, et al., 1998) with more refined experiments than pioneering ones (Auzel and Pecile, 1973, 1976; Sommerdijk and Jager, 1974). Results essentially confirm the previously measured efficiencies below saturation; normalized efficiency of 10^{-2} to 2×10^{-4} cm^2/W, for 2-photons, have been obtained respectively for the fluoride hosts $NaYF_4$ and $Na_2Y_3F_{11}$, instead of 10^{-3} cm^2/W as shown in Fig. 5.3 for YF_3. In the case of the Yb^{3+}-Tm^{3+} couple the initial energy level diagram depicting the involved processes as shown in Fig. 5.10 (Auzel, 1966) is confirmed (Page, 1998) against the cooperative sensitization scheme (Ovsyankin and Feofilov, 1966) of Fig. 5.3. In $NaYF_4$, efficiency as high as 2% is reached under pump excitation of 6 W/cm^2 at 960 nm 1though a saturation density of 4 W/cm^2 is estimated for the first intermediate step ($^4H_4$). In the Yb^{3+}-Er^{3+} case the saturation is found at about 100 W/cm^2 for fluoride hosts $NaYF_4$ and $Na_2Y_3F_{11}$ (Page et al., 1998); observed saturation is explained by excitation trapping into the long lifetime $^4I_{13/2}$ state. These more recently obtained results in fact confirm the theoretical prediction (Auzel, 1985; Auzel and Pecile, 1976) that fluorides should be the ideal hosts for green and blue emissions

with the Yb^{3+}-Er^{3+} and Yb^{3+}-Tm^{3+} couples (see Fig. 5.11).

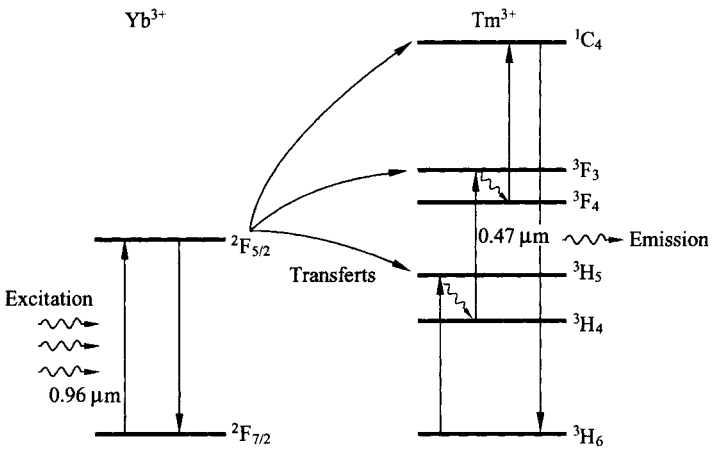


Figure 5.10 The three-photon APTE up-conversion energy scheme in Yb^{3+}-Tm^{3+} couples (Auzel, 1966)

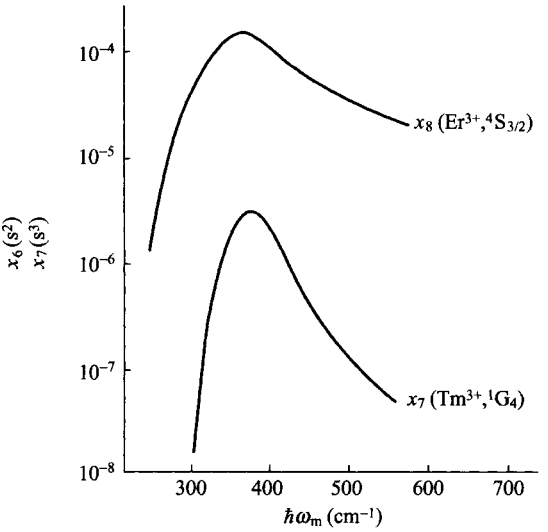


Figure 5.11 Theoretical effective phonon energy optimization for Yb^{3+}-Er^{3+} (green emission, black line) and Yb^{3+}-Tm^{3+} (blue emission) up-conversion (Auzel, 1985); x_6 and x_7 are respective relative population of levels $^4S_{3/2}$ and $^1D_4$

In this respect, Quimby et al. studied heavy metal fluoride glasses (Quimby et al., 1987) and Auzel et al. (Auzel et al., 1976) proposed and studied particularly efficient composite APTE up-conversion materials in which the RE

ions were substituted into a crystalline matrix (PbF_2) itself embedded into an oxygen-based glass material. By such means, the multiphonon processes were optimized in the fluoride crystals whereas the overall sample was obtained through classical oxygen glass techniques. This pioneering work has recently been extended to transparent glass ceramics by Ohwaki's group (Wang and Ohwaki, 1993a). Transparency was obtained by reducing the crystallite ($Pb_{0.5}Cd_{0.5}F_2$) size to about 20 nm.

The same group has also recently investigated Er^{3+}-doped $BaCl_2$ (Wang and Ohwaki, 1993b) and ErX_3 (X = Br, I) (Ohwaki and Wang, 1994a) polycrystalline phosphors for 1.5 μm detection cards (Photo-Turkey-1, 1994) which follows the up-conversion processes described in Fig. 5.6b. More recently, they have demonstrated (Ohwaki and Wang, 1994b) a 1.3 μm to visible detection in a Dy^{3+}-Er^{3+} co-doped $BaCl_2$ phosphor. The involved APTE scheme is given on Fig. 5.12. As can be seen, Dy^{3+} is the sensitizer while Er^{3+} is the activator; It should be noted that some back transfer from Er to Dy is taking place and that shall be a basic limitation, as it has been known for years that Dy^{3+} is a quencher for the Er^{3+} emissions (Auzel, 1973).

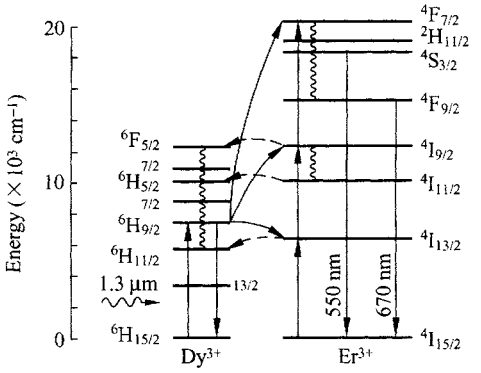


Figure 5.12 APTE scheme for 1.3 μm to visible up-conversion in Dy^{3+}-Er^{3+} doped $BaCl_2$ (Ohwaki and Wang, 1994)

Besides equal energy photon summation as just seen, different energy photons may be summed up by APTE so producing an effective IRQC with visible enhanced IR detection (Auzel, 1985). With again the Yb-Er couple, embedded in vitroceramics of general composition, PbF_2-GeO_2-YbF_3-ErF_3, an IRQC has been obtained for 1.5 μm, using an additive pump flux at 0.96 μm. Final detection at 0.66 μm is obtained by summations as shown in Fig. 5.13a. The experimental test scheme is presented in Fig. 5.13b; the pump flux is produced by an IR GaAs: Si light emitting diode (Mullard GAL-10), the signal is produced by a filtered tungsten lamp; a GaAs photocathode photomultiplier provides the final detection at 0.66 μm. A noise equivalent power of

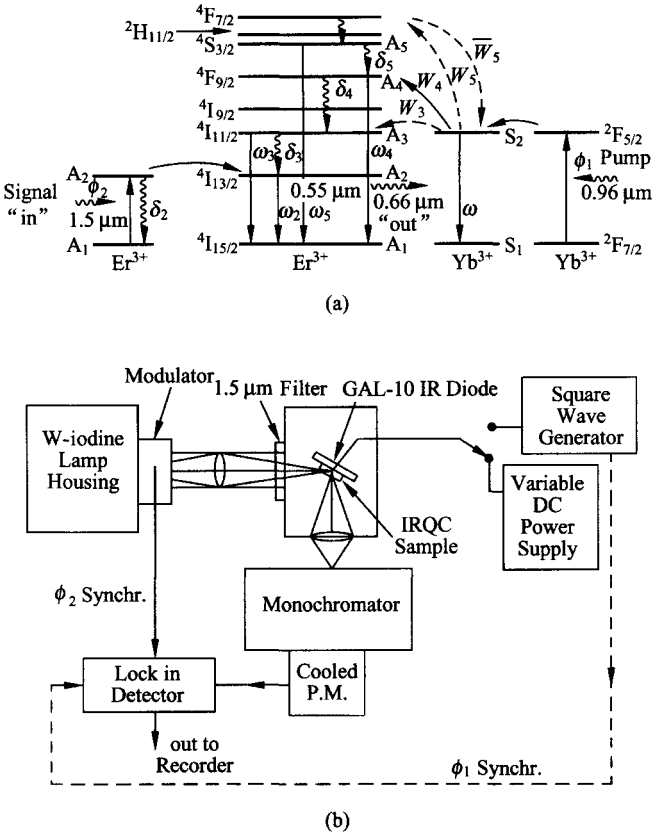


Figure 5.13 (a) Experimental scheme for a 0.96 μm diode pumped IRQC at 1.55 μm with energy transfers; (b) experimental setup for IRQC detection at 1.55 μm (Auzel et al., 1985)

10^{-11} $WHz^{-1/2}$ has been obtained for 3 mW of pumping at 0.96 μm and useful concentration of 10% (Yb^{3+}) and 5% (Er^{3+}). As always in APTE effects, it can be noted that the sensitizer concentration is greater than the activator in accordance with the prediction of Eq. (5.22). Of course, if instead of a photomultiplier the detection is made through an electronic image intensifier, an imaging IRQC can be obtained for IR visualization purposes. This approach has recently been systematically considered in Smirnov's group (Kurokin et al., 1992a) in order to make an IR image converter at wavelengths beyond the usual S1 or GaAS photocathode limits. Here IR(1.5 – 1.6 μm)-to-IR(0.8 – 0.9 μm) up-conversion phosphors have been developed with the addition of microchannel image intensifiers. Based on $Y_{0.85}Er_{0.15}O_2S$ phosphors and an image intensifier with a GaAs photocathode, an IR sensitivity of 10^{-11} W/cm^2 is anticipated for an image converter screen illuminance of 0.1 cd/m^2 (Kurokin et al., 1992b).

In another direction, reusable X-ray memory detection plates have been

made from a screen based on the same type of vitroceramics as mentioned above. X-rays are then the source of defect centers that reduce the Yb lifetime which in turn reduces the APTE up-conversion efficiency. After X-ray irradiation is the object to be investigated, the X-ray latent image is revealed in the visible spectrum by IR irradiation at 0.96 μm, the Yb^{3+} excitation wavelength. The sensitivity is increased via higher-order up-conversion processes. An image so produced in the blue spectrum is shown in Fig. 5.14 for a 3-photon APTE process in a Yb-Tm doped vitroceramic screen revealed under IR after a 90 kV, 5 mA, 1 min, 45 s X-ray irradiation (Breteau et al., 1990). The screen may be reused after a heating procedure, which bleaches the defect centers.

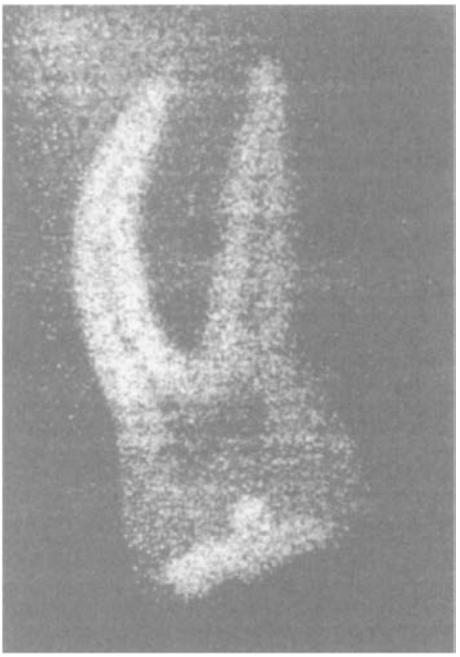


Figure 5.14 Latent X-ray image of a tooth in a Yb-Tm doped vitroceramic, revealed by blue emission under IR irradiation at 0.96 μm (Breteau et al., 1990)

The inherent nonlinearity of the APTE process had been considered as an incoherent optical amplifier since the first days of APTE (Auzel, 1966). Its principle, given in Fig. 5.15, is based on a two-beam scheme: one of them, the pump beam, is broadband and CW, and it fixes the "bias point" of the sample; the other beam (narrow-band and modulated) is the signal beam, which is tuned through the excitation band to be investigated. Practical gain of a few factors of ten can be so obtained. This procedure has been effectively used to obtain the excitation spectra for up-conversion both in 4f systems (Auzel, 1966) and 5f systems (U^{4+} in $ThBr_4$ and $ThCl_4$) (Hubert et al., 1986).

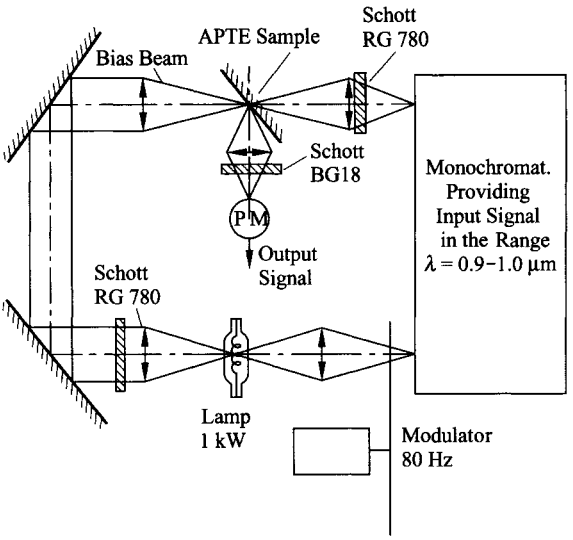


Figure 5.15 Incoherent amplifier scheme with an APTE sample (Auzel, 1966)

The first proposed use of APTE phosphors has been the hand held laser modes visualization screen (Auzel, 1968) and since then proposed again for visualization of both 0.96 and 1.5 μm spectral regions (Tokin IR Catcher, 1987; Photo-Turkey-1, 1994).

5.3.2.2 General Negative Roles Brought up by Undesired APTE Effects

APTE being an anti-Stokes process does induce reabsorption from excited states. Because it is so efficient when concentration and excitation density are high, it is sometimes an undesired, pervasive effect. Historically this effect takes its roots in a study on reabsorption from population-inverted states in Yb-Er laser glass studies (Auzel, 1969): all visible light obtained by up-conversion is at the expense of the 1.5-μm laser transition. In high concentration Nd^{3+} laser materials, the so-called stoichiometric lasers, APTE effect may induce reabsorption (Blätte et al., 1973). Because up-converted energy feeds nonradiative states, this is a direct loss for the laser output. In NdP_5O_{14} such effect begins to be seen when population inversion reaches 10%, whereas in Nd^{3+}: $Y_3Al_5O_{12}$ where concentration of RE ions is much lower, it cannot be seen even at high pumping levels (Danielmeyer and Blätte, 1973).

This type of APTE effect is also the process that has been advocated to take place within Er^{3+}-clusters and which limits the gain in optical fiber amplifiers (Blixt et al., 1991; Delevaque et al., 1993; Maurice, 1995), providing the so-called non-saturable ground state absorption (see Chapter 8 and Section 5.3.1 above). Its involved energy scheme is given in Fig. 5.16a.

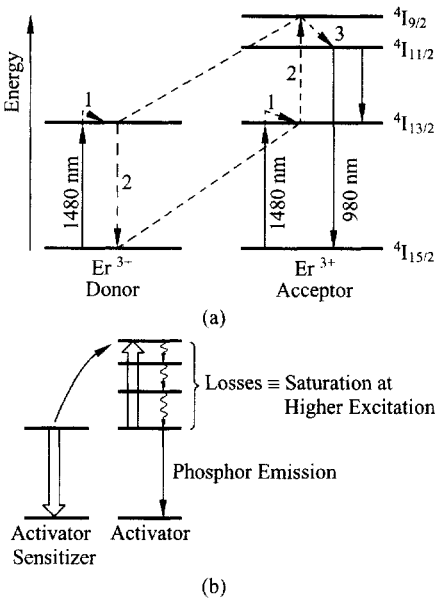


Figure 5.16 (a) Energy scheme for cluster quenching in an Er^{3+}-doped amplifier(Blixt et al., 1991); (b) energy scheme for APTE saturation in a cathode ray tubes phosphor, note analogy (de Leeuward and' t Hooft, 1983)

In CW 2.7-μm Er^{3+} lasers, it had first been thought that APTE had the positive effect of emptying the final $^4I_{13/2}$ laser state, avoiding "self-terminating" or self-saturation behavior (Deutschbein and Auzel, 1963) due to the long lifetime of this final laser state (Bagdasarov et al., 1983). An investigation of the various up-converted emission in Er^{3+}: $LiYF_4$ during the laser action at 2.7 μm brought some proof that APTE was in fact emptying the laser emitting level $^4I_{11/2}$, thus being a drawback rather than an advantage (Auzel et al., 1989). So the laser CW action was essentially linked to direct reabsorption from $^4I_{13/2}$ of the pumping laser towards higher states.

Another important field in the phosphor domain is the availability of high-intensity projection cathode ray tubes which are presently universally used for large-screen television displays. At high excitation, density saturation appears that has been partially attributed to APTE for higher doping concentration (Van der Weg and Van Tol, 1981; de Leeuward and' t Hooft, 1983); in Fig. 5.16b, the clear analogy with the clustering role in Er^{3+}-doped amplifiers is shown. This has also has been the explanation for Mn: Zn_2SiO_4, Eu^{3+}: Y_2O_2S, and Tb: $Y_3Al_5O_{12}$. Furthermore, in electroluminescence phosphors such as Mn: ZnS, up-conversion has been advocated to explain saturation (Smith, 1981).

5.3.2.3 APTE or ESA Pumped Lasers

Very early, the APTE effect was demonstrated to be a new method of laser pumping. For example, in Er^{3+}: $Ba(Y, Yb)_2F_8$ and Ho^{3+}, even with IR flash pumping (Johnson and Guggenheim, 1971), respective pulsed emissions have been obtained at 0.67 μm and 0.55 μm, as shown in Fig. 5.17 in a three-level laser configuration at room temperature. Availability now of powerful CW IR laser diodes has rejuvenated this field. Because powerful blue laser diodes are still lacking for Stokes laser pumping, there are still many opportunities for APTE anti-Stokes pumping.

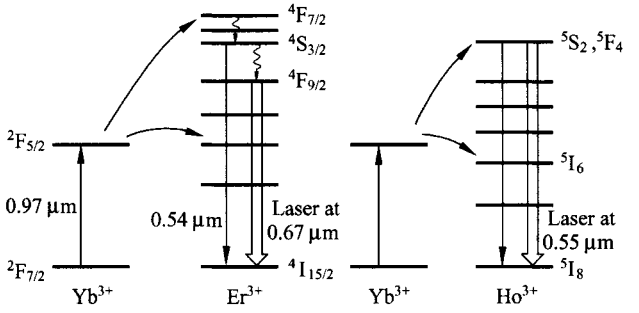


Figure 5.17 The first operating APTE up-conversion pulsed laser pumping schemes in Yb-Ho and Yb-Er couples (Johnson and Guggenheim, 1971)

By using the two first steps described in Fig. 5.18, APTE has been used to excite the $^4I_{11/2}$ level of Er^{3+} in CaF_2, in order to obtain a pulsed laser at 2.8 μm between that level and $^4I_{13/2}$ (Pollack and Chang, 1988). Shortly afterwards and for the first time, CW up-conversion lasers in the green for the $^4S_{3/2} - {}^4I_{15/2}$ transition of Er at 0.551 μm have been obtained in $LiYF_4$ under laser diode pumping at 0.791 μm at 40 K (Tong et al., 1989); this was followed by obtaining laser blue emission at 0.470 μm with a 10-mW threshold under the same conditions (Hebert et al., 1990).

Up-conversion, attributed to the ESA type, has even provided violet emission at 0.380 μm in Nd^{3+}: LaF_3 by summing an IR and a yellow laser pump or two yellow dye laser pumps (Macfarlane et al., 1988), however only at low temperature (at 90 K). Low temperature has been a general drawback for CW up-conversion lasers. In solids, a three-level scheme at room temperature generally becomes a quasi four-level scheme at lower temperature. This explained why the first up-conversion lasers were working in a pulsed mode at room temperature and continuous operation could only be obtained at lower temperature. This drawback has recently been overcome by using glass fibers or higher density laser pumping to providing ground state quasi-saturation. In particular, the versatile tunable Ti-Sapphire laser has helped a lot in this matter.

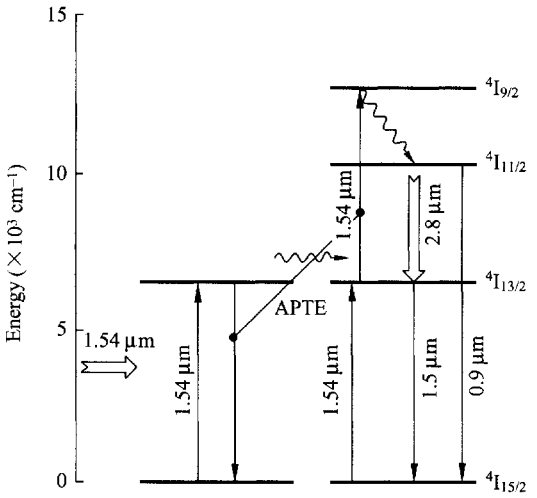


Figure 5.18 Up-conversion APTE pumping in an Er^{3+} laser at 2.8 μm (Pollack and Chang, 1988)

In recent years, Huber's group in Hamburg has obtained many new up-conversion laser results. After initial pulsed laser operation in Er: KYF_4 at 0.551 μm at room temperature (Brede et al., 1993), the CW function has been achieved (Heine et al., 1994), in both cases with an attributed ESA up-conversion pumping by a Ti-Sapphire laser; for CW operation, the laser threshold has however the large value of 2.2 – 2.4 W. On the other hand, a very efficient CW laser effect has recently been achieved in a 3 mm long single crystal of Yb(3%)-Er(1%): $LiYF_4$; pumping at 0.966 μm at a level of 1.6 W was provided by a Ti-sapphire. An up-conversion laser threshold of 418 mW was obtained and nature of the pumping was proved to be of the APTE type both by the laser excitation spectrum analysis replicating the Yb absorption spectrum and by a nonlinearity narrowing as described in Section 5.3.1. The laser useful output at 0.551 μm is 40 mW with 5% output coupling (Möbert et al., 1997).

Because of their inherent small core diameter, glass fibers easily enable high pumping density over long lengths. Such high densities over long lengths cannot be provided by any lens focusing system. Ground state depletion of any doped fiber can be easily reached with less than 100 mW pumping (Auzel, 1993) (see Chapter 8). In particular, fluoride fibers favor anti-Stokes lasers for three reasons:

(1) the existence of long-lived metastable states coupled to the low energy phonons of the fluoride matrix;

(2) ground state saturation enabling CW laser function even in a three-level laser energy scheme;

(3) the advantage of nonlinear pumping, associated again with the optical confinement of the fiber medium.

Since the first demonstration in 1986 (Mears et al., 1986) of the feasibility of CW room-temperature three-level lasers in the Er^{3+}-doped glass fibers, one could think that an up-conversion pumped "three-level scheme" could also be used in CW operation at room temperature for Er^{3+} emission at 540 nm (Monerie et al., 1989). After preliminary results, obtained first at 77 K with Tm^{3+}-doped fluorozirconate fiber lasing at 455 nm and 480 nm (Allain et al., 1990a), the very first CW room temperature up-conversion laser was demonstrated at CNET by Allain et al. (1990b) in a three-level scheme of the Ho^{3+}-doped fluoride fiber laser (Fig. 5.19). Because of the weak Ho^{3+} concentration (1200 ppm) it was believed that within the single-ion levels system, ESA was taking place. However, since clustering with subsequent APTE effect may sometimes occur at much lower concentration (70 ppm in (Blixt et al., 1991)), some doubt is cast upen about the effective pumping process, as in many of the subsequent up-conversion pumped fiber lasers.

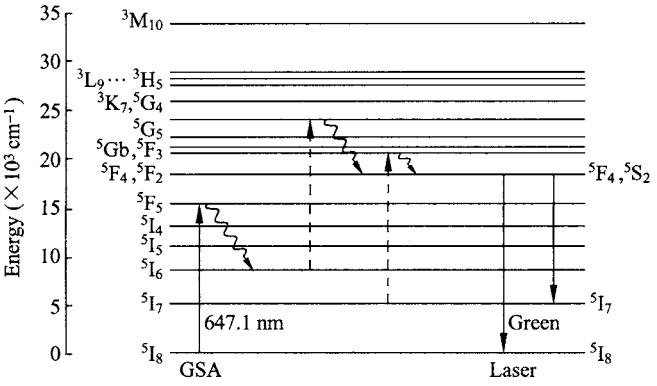


Figure 5.19 Energy scheme for the first visible CW up-conversion Ho^{3+}-doped fiber laser (Allain et al., 1990b)

Er^{3+}-doped glass fibers have also shown CW room-temperature three-level laser emission at 540 nm when pumped at 801 nm (Whitley et al., 1991). Because the pumping wavelength is in the diode laser range, there was some hope that a compact fiber laser could be obtained.

Besides these two-photon up-conversion pumped lasers, a three-photon pumped two pumping has been demonstrated in a Tm^{3+}-doped ZBLAN fiber (Grubb et al., 1992): pumping at 1.12 μm, a room temperature CW laser emitting at 480 nm with a differential efficiency of 18% has been obtained with the rather low threshold of 30 mW.

Pr^{3+}-doped fluoride fibers, because of their low phonon energy with respect to Pr^{3+} emitting levels energy differences, have allowed CW room temperature

anti-Stokes lasers at blue, green, and red wavelengths in a single fiber (Smart et al., 1991). More detailed results on such recent evolution up-conversion laser may be found in Section 8.3.

However, concluding this section, it is worth mentioning the possibility of up-conversion lasers with multiphonon pumping in the electronic rare-earth ion sideband transitions described in(Auzel, 1976) and in Chapter 3. It presents the advantage of the self-adaptation of ESA absorption to a single pump wavelength. Up-conversion pumping is successful through multiphonon sideband pumping with energy mismatches as large as 1000 cm^{-1}. This was the case for a Tm^{3+} fluoride fiber laser pumped at 1.06 μm in a three-photon ESA process and lasing at 1.47 μm (Komukai et al., 1992). This provides an efficient four-level laser scheme that allows CW oscillation with a differential efficiency of 27% at room temperature. On the other hand this opens the door to long (km) distributed amplifiers where the losses per unit length are compensated at each point by the gain; the transmission line is then turned into an active lossless line.

Multiphonon pumping is also one process involved in the avalanche up-conversion process described in the next section.

5.4 Cross-relaxation and the Photon Avalanche Effect

The most recently considered up-conversion process is the photon avalanche effect. Since it was not considered in the review of 1973 (Auzel, 1973), more detailed attention will be paid to it here.

While looking for two-step absorption (ESA) in Pr^{3+}-doped $LaCl_3$ and $LaBr_3$ at low temperature (<40 K) as a means of detecting an IR photon by its energy summation with a more energetic photon (IRQC) so performing excited state absorption (ESA), it was found that the higher-energy photon alone could, at the same time, give rise to up-conversion and reduce the transmission of the sample above a given intensity threshold (Chivian et al., 1979) (see Fig. 5.20). The effect was attributed to an enhanced population of an excited state resulting from a cross-relaxation process. The starting process was initially not completely determined. In the Pr^{3+} case, the $^3H_5 \rightarrow {}^3P_1$ absorption is initially very weak at low temperature because $^3H_5$ is about 2000 cm^{-1} above ground state (see Fig. 5.21); however above about 1 mW of excitation, this transition is increased; the cross-relaxation process $(^3H_6, {}^3H_4) \rightarrow (^3H_5, {}^3H_5)$ increases the $^3H_5$ population, which in turn reduces the transparency of the sample at the $(^3P_1 - {}^3H_5)$ energy. Since the more the $(^3P_1 - {}^3H_5)$ energy is absorbed, the more the $^3H_5$ population is increased, the process was termed "photon avalanche" (Chivian et al., 1979). It is clearly a way to increase ESA in a sample.

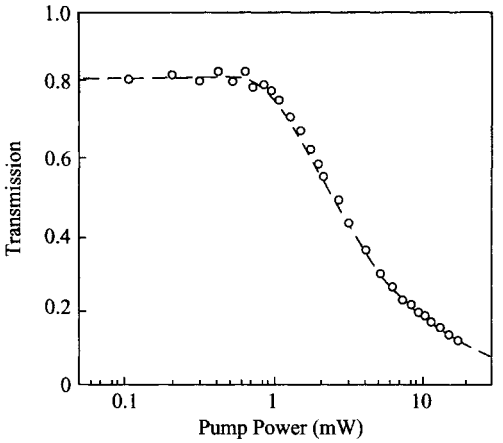


Figure 5.20 Decrease of transmission in a Pr^{3+}: $LaCl_3$ sample under $^3H_5 - {}^3P_1$ pumping (Chivian et al., 1979)

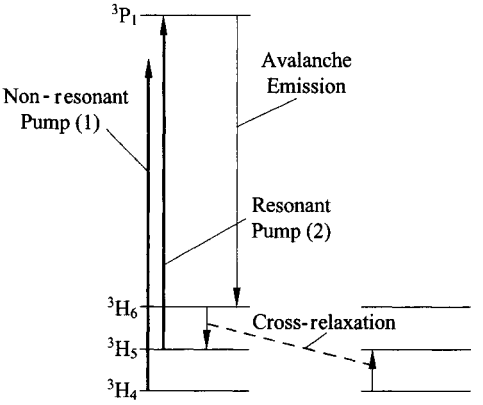


Figure 5.21 Pr^{3+}: $LaCl_3$ energy scheme for the avalanche mechanism (Chivian et al., 1979)

Afterwards, similar effects were observed in Sm^{3+}, Nd^{3+}, Ni^{2+}, Tm^{3+} doped halide crystals (Krasutsky, 1983; Lenth and Macfarlane, 1990; Oetliker et al., 1992; Ni and Rand, 1992). Recently the photon avalanche effect was obtained at room temperature for the Er^{3+} ion in a ZBLAN glass both in bulk and in fiber form (Auzel et al., 1994; Auzel and Chen, 1995; Chen and Auzel, 1994, 1995) and in a $LiYF_4$ crystal (Auzel and Chen, 1995).

The photon avalanche process is characterized by three distinct nonlinear behaviors: (1) transmission, (2) emission, and (3) rise time as a function of pump intensity, generally with the existence of a critical pump threshold.

Particularly long rise times, from seconds to minutes (Auzel and Chen, 1995; Pelletiek-Allard and Pelletier, 1987), have been observed.

At this point it is worth discussing the notion of threshold for avalanche. Because of the complexity of the phenomenon, it has usually been modeled by a simplified three-level system (Joubert et al., 1993; Kueny et al., 1993; Goldner and Pellé, 1995).

5.4.1 The Avalanche Process as a Positive Feedback System

Using the three-level simplified model of (Joubert et al., 1993) or (Kueny et al., 1993) and adding to the initial ground state absorption ($\sigma_1\Phi = R_1$) auxiliary direct feeding into the metastable state $\sigma_0\Phi_{IR}$, we may write the following set of equations; see Fig. 5.22 for explanation of symbols, which except for the trigger $\sigma_0\Phi_{IR}$ are the same as in (Joubert et al., 1993).

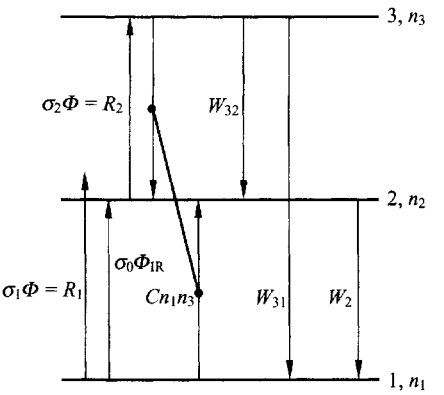


Figure 5.22 The simplified three-level avalanche scheme: C is the cross-relaxation coefficient; W_{ij} are the spontaneous emission terms

Being interested in the steady state initial step of avalanche, we assume

$$\frac{dn_1}{dt} = \frac{dn_2}{dt} = \frac{dn_3}{dt} = 0,$$
$$n_1 = 1 - n_2 - n_3 \approx 1,$$

then the rate equations are simplified to

$$0 = -R_1 - \sigma_0\Phi_{IR} + bW_3n_3 + W_2n_2 - Cn_3, \tag{5.27}$$
$$0 = (1-b)W_3n_3 - W_2n_2 + 2Cn_3 + R_1 + \sigma_0\Phi_{IR} - R_2n_2, \tag{5.28}$$
$$0 = R_2n_2 - W_2n_3 - Cn_3. \tag{5.29}$$

Here C is the cross-relaxation parameter and b the branching ratio. The following relationships exist between the transition probabilities:

$$(1-b)W_3 = W_{32}; \quad bW_3 = W_{31}; \quad W_3 = W_{32} + W_{31}.$$

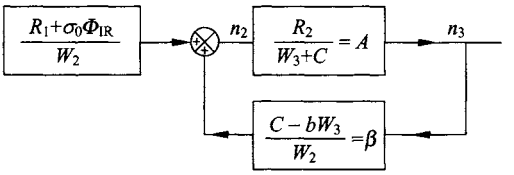
Equation(5.29) can be written

$$n_2 \frac{R_2}{W_3 + C} = n_3. \tag{5.30}$$

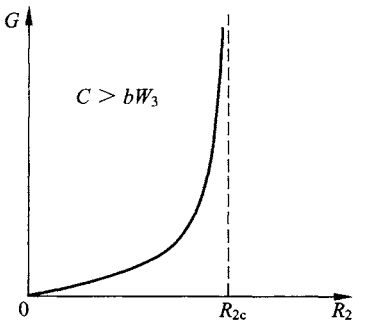
Or considering amplitude and using the symbolic representation for feedback systems, Eq. (5.30) gives block A of Fig. 5.23a. In the same way Eq. (5.27) is can be written

$$n_2 = \frac{R_1 + \sigma_0 \Phi_{IR}}{W_2} + \frac{C - bW_3}{W_2} n_3 \tag{5.31}$$

which can be symbolized in Fig. 5.23a by block β and an adder with input source $(R_1 + \sigma_0 \Phi_{IR})/W_2$. Combining Eqs. (5.31) and (5.30) gives the classical



(a)



(b)

Figure 5.23 (a) Positive feedback model for avalanche. (b) Gain behavior of the model versus R_2: positive feedback condition is $b > CW_3$. The asymptote R_{2c} corresponds to the avalanche threshold

feedback systems scheme of Fig. 5.23a.

Such systems are known to be unstable when $A\beta = 1$. One can define the "gain" of the closed loop feedback system, G, to be the ratio of the green output to a pump-related input signal (R_1) plus an eventual trigger (Φ_{IR}):

$$G = \frac{n_3}{(R_1 + \sigma_0 \Phi_{IR})/W_2} \tag{5.32}$$

It is well known that in term of the A and β of Fig. 5.23a, one has

$$G = \frac{A}{1 - A\beta}. \tag{5.33}$$

The stability condition is then

$$\frac{R_2}{W_3 + C} \frac{C - bW_3}{W_2} < 1, \tag{5.34}$$

and its limit is just the threshold condition given by Joubert et al. (1993), obtained here in a simplified way as

$$R_{2c} = \frac{W_2(W_3 + C)}{C - bW_3}, \tag{5.35}$$

with $C > bW_3$ for positive feedback.

The behavior of our feedback system below threshold can be described by the behavior of $G(R_2)$; see Fig. 5.23b.

The "black box" feedback approach has also been considered in studying the dynamics of the above three-level system (Brenier et al., 1993). It is based on the fact that general linear feedback theory can solve time varying differential equation systems algebraically by using the Laplace transform of the time dependent functions.

5.4.2 Conditions for Observing an Avalanche Threshold

Neglecting the first nonresonant absorption step (R_1) and taking into account only the second resonant absorption step (R_2) when calculating the population of the third level (n_3) versus R_2 (the pumping excitation) leads to a well-defined nonlinearity in n_3 for the asymptotic curve ($R_1/R_2 = 0$), as shown in Fig. 5.24.

When the first step (R_1) is explicitly taken into account (Goldner and Pellé, 1995), the "threshold" nonlinearity is progressively smoothed out with increasing ratio R_1/R_2 as shown in Fig. 5.24. This corresponds to a progressively more

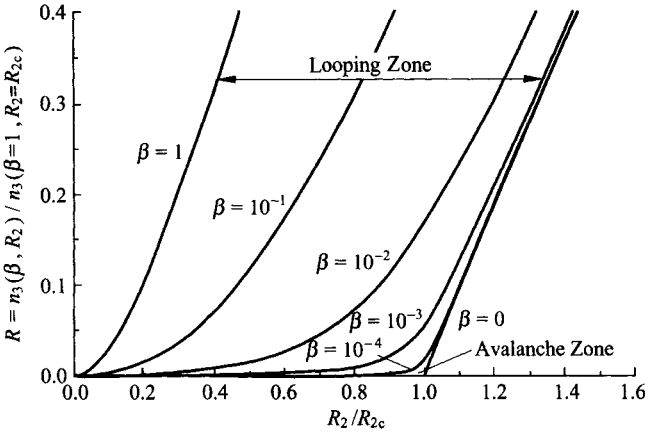


Figure 5.24 The third level normalized population, $R = n_3(\beta, R_2)/n_3(\beta = 1, R_2 = R_{2c})$, versus pumping term ($R_2$) with β as a parameter (Goldner and Pellé, 1995)

resonant first step. As shown by Goldner and Pellé (Goldner and Pellé, 1995), a clear avalanche threshold can be expected in practice only for R_1/R_2 ratios $\ll 10^{-4}$.

Some of the features of the avalanche effect have been observed at room temperature in Tm^{3+}: $YAlO_3$ (Ni and Rand, 1992) and in Pr^{3+} in silica glass fibers (Gomes et al., 1993). The lack of a clear threshold in these two systems can certainly be related to the above prediction.

The region in Fig. 5.24 where $10^{-4} \ll R_1/R_2 < 1$ corresponds to cases for which the losses in the feedback loop may exceed the loop gain for R_2 values below R_{2c}, so that after a number of "loops" of the excited population between level 3 and the metastable level 2, the system neither diverges nor maintains n_3 independently of R_1. Such cases have been called the "looping mechanism" (Brenier et al., 1994). We also believe that some of the reported cases of quasi-zero threshold avalanche cases in the literature (Gomes et al., 1993; Dyson et al., 1994) belong to large $10^{-3} \ll R_1/R_2 \ll 1$ cases for which, as shown in Fig. 5.24, it is very difficult to distinguish between avalanche and sequential two photon absorption (ESA), which occurs strictly for $\beta = 1$. Sometimes such cases have been termed "quasi-avalanche"(Goldner and Pellé, 1995).

Up to now, only Er^{3+} with $(R_1/R_2) \approx 10^{-6}$ has shown, at room temperature, all three characteristic features of avalanche when doping a $LiYF_4$ crystal or a ZBLAN fluoride glass both in bulk and in a fiber shape (see Sections 5.4.3 and 5.4.4); a long delay of several seconds to minutes has even been observed (Auzel and Chen, 1995a, 1995b; Chen and Auzel, 1995). For comparison the following values have been given for the critical parameter β: for Nd^{3+}-$LiYF_4$, $(R_1/R_2) = 1.7 \times 10^{-4}$ for avalanche at $T \leqslant 40$ K (Lenth and Macfarlane, 1990; Joubert et al., 1993); for Tm^{3+}-Ho^{3+}-$Gd_2Ga_5O_{12}$,

$(R_1/R_2) = 3.6 \times 10^{-2}$ for the two-ion looping process (Brenier et al., 1994); for a Tm^{3+}-BIGaZYTZr glass, $(R_1/R_2) = 1.2 \times 10^{-2}$ (Guy, 1995) for what was claimed to be "avalanche" at 100 K (Joubert et al., 1995). In this last case since the delay reaches only 16 times (Guy, 1995) the metastable state lifetime (W_2^{-1}), it looks more like a "looping process" case. In Er^{3+}, will be seen in Sections 5.4.3 and 5.4.4, the avalanche delay reaches 6×10^2 to 10^4 times W_2^{-1}, respectively, for Er^{3+}-doped fluoride glass and crystal.

5.4.3 Er^{3+}: $LiYF_4$ as an Avalanche Model Experiment

In the case of Er^{3+}, the first step for photon avalanche has been clearly identified and attributed to anti-Stokes multiphonon sideband absorption (Auzel et al., 1994; Auzel and Chen, 1995) (see Fig. 5.25). Calculating the (R_1/R_2) ratio from mutiphonon absorption makes it possible to estimate a value of 5×10^{-6} (Chen and Auzel, 1995; Auzel and Chen, 1995), as shown in Fig. 5.26 which displays the multiphonon side-band absorption in the avalanche excitation region. As observed, such experimental situations provide marked threshold behavior in erbium (Auzel et al., 1994).

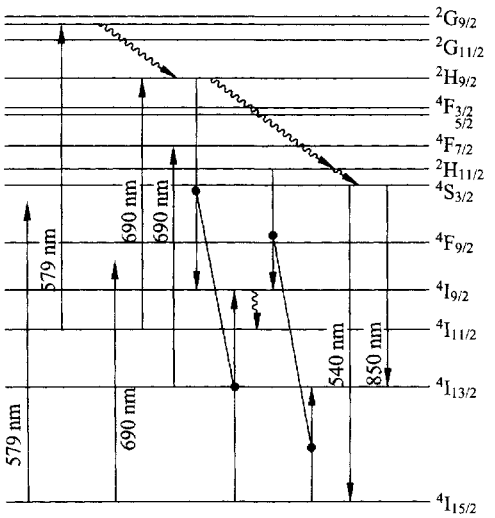


Figure 5.25 Energy scheme of Er^{3+} and principal mechanisms responsible for photon avalanche cycles under excitation at 579 nm and 690 nm (Auzel and Chen, 1995)

The simple theory of Section 5.4.1 has been verified by experimentally measuring $G(R_2)$. This was done using the following method (see the experimental setup in Fig. 5.27): having obtained a given green output for a

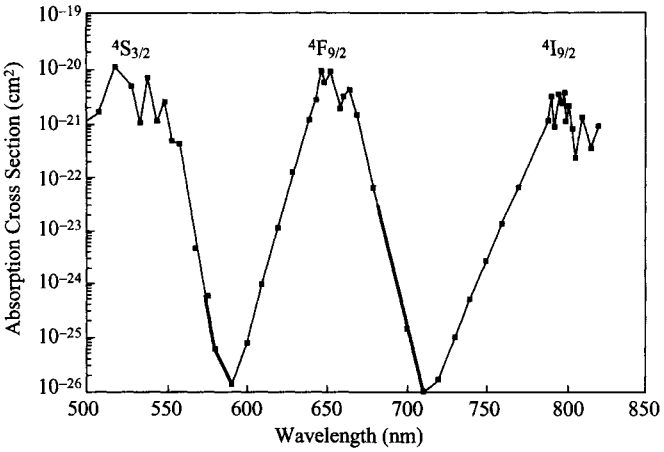


Figure 5.26 Absorption cross section for Er^{3+} : $LiYF_4$ taking into account the multiphonon contribution; the heavier lines show the anti-Stokes zones which contribute to W_1 for the avalanche processes in erbium (Auzel and Chen, 1995)

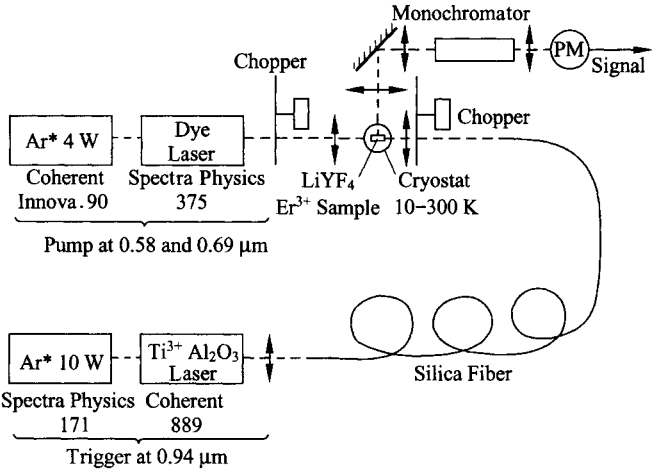


Figure 5.27 Experimental scheme for measuring the positive feedback gain

pump R_2 with $\Phi_{IR=0}$, R_2 is reduced while increasing Φ_{IR} in order to maintain a constant green output. Φ_{IR} is an infrared signal at 0.94 μm in resonance with the metastable state 2 (here $^4I_{11/2}$) absorbing with a cross section σ_0.

Each point is obtained after waiting for a steady state. Because of the large ratio σ_0/σ_1 this experiment provides a good description of $G(R_2)$, as shown by results in Fig. 5.28 for three temperatures. One can define an R_{2C} asymptote only at 300 K and 220 K, respectively 120 mW and 240 mW. At 163 K one cannot

reach an asymptote (threshold) at the maximum available power of 250 mW in that experiment. So the effect of lowering temperature is essentially to increase R_{2c}.

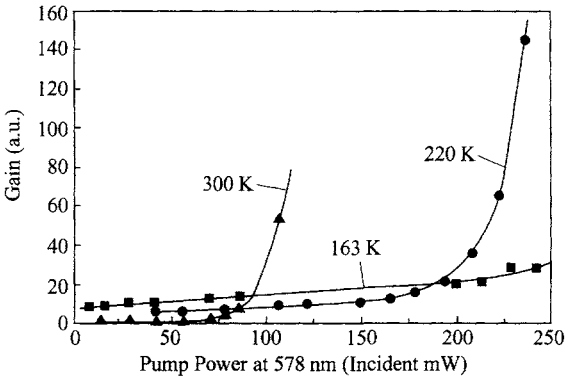


Figure 5.28 Experimental $G(R_2)$ for three temperatures: 300 K, 220 K, 163 K. Residual signal near $R_2 = 0$ comes from direct up-conversion under 0.94 μm excitation (Auzel and Chen, 1995)

The part in R_{2c} which is most sensitive to temperature is C because it is related to phonon energies of only 100 cm^{-1}, whereas W_2 and W_3 are related to phonons covering the energy gap below level 3 and 2, that is energies greater than 2000 cm^{-1}. However this requires that C be of same order as W_3 or bW_3; otherwise, as long as $C \gg W_3$, bW_3, one has $R_{2c} \approx W_2$ and its temperature dependence is just the same as W_2.

Comparing the theoretical threshold as given by Eq. (5.35) with experimental conditions, one can verify the simple feedback model.

Assuming level 1 to be $^4I_{15/2}$, level 2 to be $^4I_{11/2}$, and level 3 to be the aggregation of levels between $^2G_{9/2}$ and $^4S_{3/2}$ with the emission properties of $^4S_{3/2}$ (see Fig. 5.25), and taking the room temperature data given by (Rubin et al., 1986; Hubert et al., 1991) the following parameters are found:

$$W_3 = 2500\ s^{-1};\ b = 0.5;\ C = 0.5 \times 10^6\ s^{-1};\ W_2 = 140\ s^{-1}.$$

Because corresponding oscillator strength are about equals ($\approx 0.4 \times 10^{-6}$) (Hubert et al., 1991), one can also assume $\sigma_2 = \sigma_0 = 4 \times 10^{-21}$ cm^2.

Using reduced population units (pure numbers), $R_{2c} = 141\ s^{-1} \approx W_2$ (at room temperature), from which it can be estimated

$$\Phi_{\text{threshold}} = 141/4 \times 10^{-21} = 3.5 \times 10^{22}(s^{-1} \cdot cm^{-2}).$$

At 0.578 μm this yields, for a 50-μm diameter spot, a threshold power of P_{th} =

222 mW; this value is of the same order as observed threshold values for 0.578-μm pumping.

$G(R_2)$ shows (Fig. 5.23b) that the Er^{3+}-doped solid constitutes a "marginally stable" positive feedback system: even below the R_{2c} asymptote, it is known from feedback theory that a strong input signal can drive a system that is otherwise stable into instability (existence of a "gain stability margin").

In order to experimentally verify this behavior, a pulsed trigger of amplitude $\sigma_0 \Phi_{IR}/W_2$ is added to the input signal R_1/W_2 given by the pump; the experimental setup is again presented in Fig. 5.27. The results at room temperature are given in Fig. 5.29a – c. In the absence of a trigger, with P_p = 114 mW at 578 nm incident on sample, threshold is reached after a very long time (>50 s) (Fig. 5.29a). With the same pump intensity (P_p = 114 mW) and a short trigger of 0.6 s, the avalanche state is obtained quickly and maintained after trigger extinction (Fig. 5.29b). With same the trigger but a reduced pump (P_p = 99 mW), the avalanche state cannot be reached. Such behaviors as depicted in Fig. 5.29a – c are obtained down to 180 K.

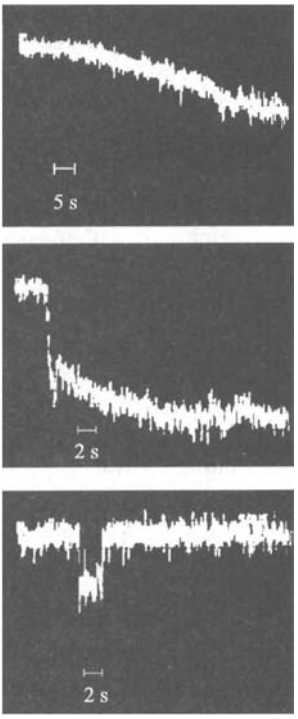


Figure 5.29 Avalanche behavior just below threshold without (a) and with (b) a trigger feeding the metastable state, and (c) much below threshold (Auzel and Chen, 1995a)

Below 180 K, the observed threshold increases as shown in Fig. 5.28. However, due to the temperature scan cycle's relatively short time constant (3 s/K from 10 to 50 K, then 21 s/K from 50 to 150 K), it was not certain that threshold could not be reached for avalanche delay times $\geqslant$50 s.

From this experiment, it is understood that measuring an avalanche threshold depends on the time one is ready to wait before its observation. This time depends not only on excited state pumping but also on the ground state absorption conditions. In any case, below 180 K, being then limited by the pump laser at a much lower power than threshold, the result of Fig. 5.29c is obtained. Such a triggering effect constitutes an optical analog of a thyratron, providing intrinsic material-based optical bistability.

The time delay behavior of the avalanche process has been studied theoretically quite recently within the general model of Landau for phase transitions (Guy, 1995). The time delay at threshold, in fact a "critical slowing time" t_c, proved itself to be the most sensitive experimental data when looping or avalanche takes place. It has been shown to be given by (Guy, 1995)

$$t_c = K\sqrt{\sigma_2/\sigma_1}, \tag{5.36}$$

where K depends on other spectroscopic parameters. Equation (5.36) is rather well verified in the above experiments, for which avalanche delay times have been determined for two different excitation wavelengths of known multiphonon anti-Stokes cross sections: at $\lambda = 688$ nm, with $\sigma_1 = 10^{-24}$ cm^2, the delay is found to be 0.4 s; whereas at $\lambda = 579$ nm, with $\sigma_1 = 2 \times 10^{-26}$ cm^2, the observed delay is 4s. Assuming for σ_2 the same value in both cases of excitation, the ratio of the delays is 0.1, which is in rather good agreement with the value of 0.14 as given by Eq. (5.36).

Above threshold, the delay for avalanche is given by (Case et al., 1990) as

$$t_c = kW_2^{-1}/(\Phi/\Phi_c - 1) \tag{5.37}$$

with $k = W_3^{-1}/(1 + b)(2C + W_3)$, where $\Phi_c = R_c/\sigma_2$ is the pumping flux at threshold and Φ, the effective pumping flux.

5.4.4 Photon Avalanche in Er^{3+}-doped Fluoride Glasses in Fibre and Bulk Shape

Recently, the photon avalanche effect has been observed at room temperature in a Pr^{3+}-doped silica fiber (Gomes et al., 1993) and in an Er^{3+}-doped fluoride glass fiber (Chen and Auzel, 1994, 1995). In the first case, only a nonlinearity of the transmission is observed and not the up-conversion emission threshold. It was believed that the threshold was so low that it could not be observed. We think that this is explained by the too-strong nonresonant to resonant absorption ratio as mentioned in Section 5.4.2. On the contrary in the second case, clear thresholds at 5 mW and at 4 mW of incident power at respectively 579 nm and

690 nm (Chen and Auzel, 1995) are observed because in these two cases, the first step is a weak anti-Stokes multiphonon absorption giving again a (R_1/R_2) ratio of about 10^{-6}, much below the critical value of 10^{-4}. The involved energy scheme for both excitations is essentially the same as in Fig. 5.25; it shows both pumping routes and the two types of cross-relaxations involved. In Fig. 5.30, the typical threshold behavior for avalanche up-conversion emission is displayed. The long delay behavior is displayed in Fig. 5.31 showing, near threshold, the very long time (3.5 s), widely in excess of any of the lifetimes of the metastable states of erbium. The observed delay follows the behavior predicted by Eq. (5.37) rather well.

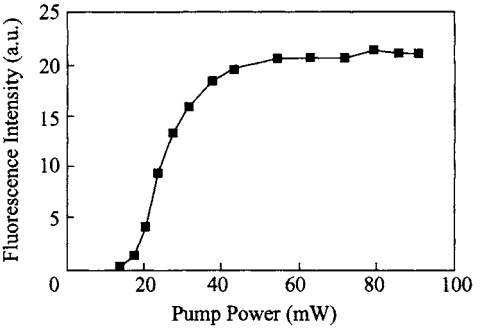


Figure 5.30 Up-conversion emission at 550 nm showing the existence of the avalanche threshold in a Er^{3+}: ZBLAN fibre observed from its extremity (Chen and Auzel, 1995)

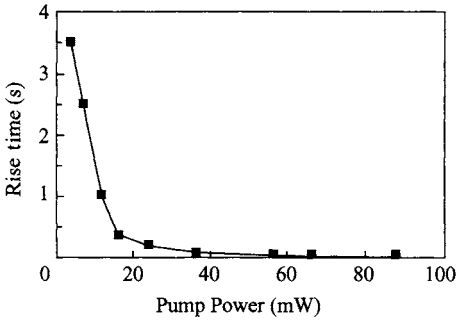


Figure 5.31 Time delay for the avalanche establishment versus incident pump power at 579 nm in a Er^{3+}: ZBLAN fibre (Chen and Auzel, 1994b)

Same results can be obtained for glass fibers and bulk samples (Auzel et al., 1994; Chen and Auzel, 1994b). Because the first absorption step is of a multiphonon nature and is featureless, the excitation spectrum for avalanche directly provides the ESA spectrum of the resonant second absorption with a single excitation beam as shown in Fig. 5.32 for the $^4I_{11/2} - {}^2G_{9/2}$ transition of

Er^{3+} this gives a new method (Auzel and Chen, 1995) to reach ESA spectra otherwise difficult to obtain without double-beam excitation.

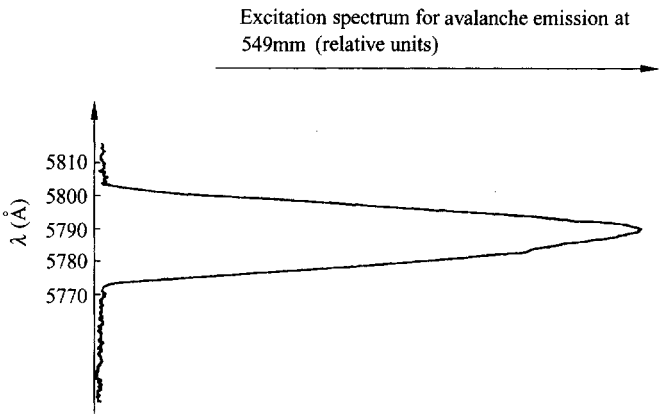


Figure 5. 32 Excitation spectrum for the avalanche emission at 549 nm in a Er^{3+}: ZBLAN glass showing the spectrum for the $^4I_{11/2} - {}^2G_{9/2}$ ESA transition (Auzel, 1985)

The main difference with bulk samples, is that in the fluoride fiber case, up-conversion spatial domains appear with periodic structures with periods ranging from a few cm to mm, themselves containing substructures of period about 100 μm (Chen and Auzel, 1994b, 1995), as shown in Fig. 5. 33. This behavior has been explained by the high contrast provided by the avalanche effect; it then optically reveals the internal electric field modes structure of the fiber waveguide (Chen and Auzel, 1994b; Goldner et al., 1998).

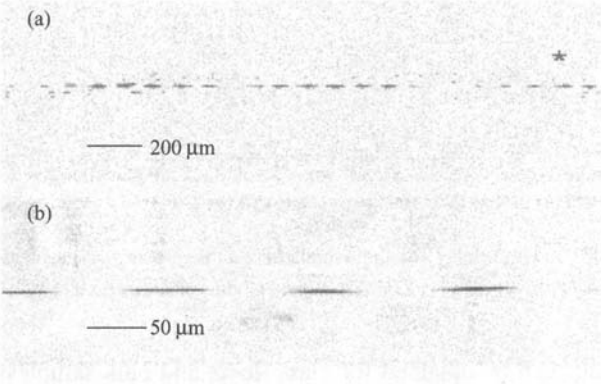


Figure 5. 33 Spatial domains observed along the fiber above the photon avalanche threshold: (a) dot separation is about 1 mm; (b) microscope view of a 1-mm avalanche dot; the scale is 100 μm per division (Goldner et al., 1998)

5.4.5 Avalanche in Co-doped Systems

Up to this point, avalanche has been described within a single type of ions. As far as energy transfers in general are concerned, the sensitizer and the acceptors may be either of the same or of a different nature. So in the avalanche process, instead of having two ions of the same nature participating in the cross-relaxation step, as has been described until now, cross-relaxation has also been considered between two ions of a different type. This was the case in the first study of avalanche involving $Tm^{3+} - Ho^{3+}$ (Brenier et al., 1994). A complex process of cross-relaxation within two Tm^{3+} ions together with a back transfer from Ho^{3+} to Tm^{3+} has been proposed. The first excitation step was out of resonance with the $^3H_6 - {}^3H_4$ absorption of Tm^{3+}, it is followed by cross-relaxation within two Tm^{3+} ions, which populates the $^4F_4(Tm^{3+})$ state, transferring its own energy to the $^5I_7(Ho^{3+})$ state, from which the resonant second step of excitation towards $^5S_2(Ho^{3+})$ takes place. Then another "cross-relaxation" (energy back-transfer) between Ho^{3+} and Tm^{3+} of the type $^3H_6(Tm^{3+}) + {}^5S_2(Ho^{3+}) \Rightarrow {}^3H_4(Tm^{3+}) + {}^5I_7(Ho^{3+})$ provides the feedback loop; see Fig. 5.34. However, the avalanche threshold was not reached and, calculating the R_1/R_2 ratio from the data in (Brenier et al., 1994), parameter

$$\beta = 6.16 \times 10^{-22} / 1.73 \times 10^{-20} = 3.6 \times 10^{-2}$$

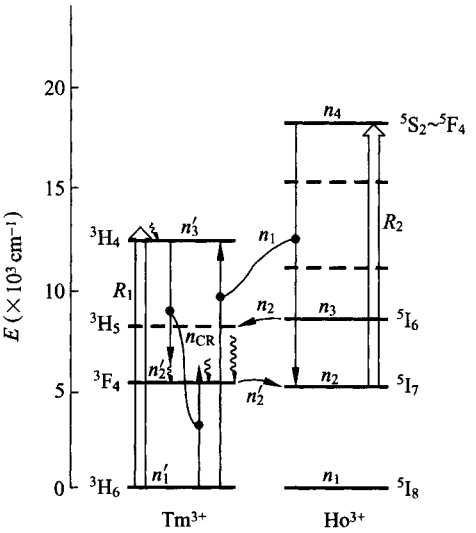


Figure 5.34 Energy scheme and mechanism for "looping effect" in the $Ho^{3+} - Tm^{3+}$ co-doped system (Brenier et al., 1994)

is determined. This clearly confirms what the authors have found, that the behavior of this system is in the "looping region" of Fig. 5.24. The "looping process" is different from avalanche in the sense that it has a reversible character that "real" avalanche doesn't have. In the case of the co-doped $Yb^{3+} - Pr^{3+}$ system, "real" avalanche has been reached (Kük et al., 2000). In this system (see Fig. 5.35), the first nonresonant excitation step is in the Yb^{3+} ion, which transfers its excitation to the metastable state $^1G_4(Pr^{3+})$, from which the resonant second step up to $^3P_0(Pr^{3+})$ takes place. The cross-relaxation step within two Pr^{3+} ions feeds the metastable state $^1G_4(Pr^{3+})$, and the back transfer to Yb^{3+} again feeds the $^1G_4(Pr^{3+})$ metastable state. The ratio β from the nonresonant to resonant pumping was estimated to be 10^{-6} to 10^{-8} (Kük et al., 2000) well within the condition to observe a real avalanche threshold.

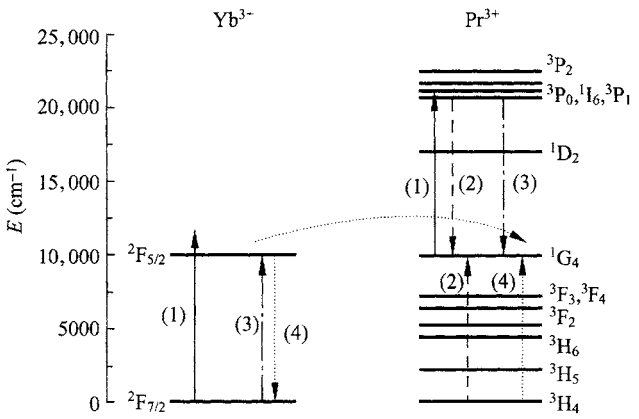


Figure 5.35 Energy scheme and mechanisms for the co-doped $Yb^{3+} - Pr^{3+}$ avalanche system: (1) pumping at 0.85 μm into Yb^{3+} sideband and in resonance by ESA into Pr^{3+}; (2) cross-relaxation within Pr^{3+}; (3) $Yb^{3+} - Pr^{3+}$ cross-relaxation; (4) $Pr^{3+} - Yb^{3+}$ back-transfer (Kük et al., 2000)

5.4.6 Up-conversion Laser with Multiphonon-assisted Pumping Scheme and Photon Avalanche

Besides pumping in the electronic RE ions transitions, we have also seen that up-conversion laser pumping can be attempted in multiphonon sidebands with energy mismatch as large as 1000 cm^{-1} (Komukai et al., 1992); see Section 5.3.2.3.

Of course, most of the avalanche-pumped lasers also belong to this category because of the required weak first-step absorption. It is worth mentioning the first avalanche laser in $Pr^{3+}:LaCl_3$ (Koch et al., 1990). CW emission in a four-level scheme was obtained at 0.644 μm through an up-conversion avalanche process under 0.677 μm pumping, which corresponds to ESA pumping for the second step and probably to multiphonon absorption for the first step, as recently

observed for amplified spontaneous emission at 0.850 μm in a Er^{3+}: ZBLAN fiber in an avalanche pumped regime (Chen and Auzel, 1994a). Powerful avalanche-pumped up-conversion lasers have been obtained in the CW regime, at low temperature (7 K) in Er^{3+}: YALO (Scheps, 1994, 1995); and 33 mW of output at 0.549 μm has been reached with an optical efficiency of 3.5%. Interestingly, the same crystal system may provide lasing under APTE up-conversion pumping simply by tuning-in the first excitation step (0.8069 μm). The laser threshold is then lowered (~100 mW) in comparison with the avalanche regime (~380 mW at 0.7913 μm); the output law is quadratic versus pumping in the APTE regime, while for the avalanche regime it has a much higher power law above threshold, saturating towards a square law at about 1 W of incident pump power. In the APTE regime, the laser output is 166 mW with an optical conversion efficiency of 17%.

As already mentioned in Section 5.3.2.3, fiber optical confinement may make it possible to obtain CW four-level lasers even at room temperature. This has also been the case for avalanche-pumped lasers. A high-power up-conversion laser has been demonstrated in a Pr, Yb: ZBLAN double-clad fiber (see Chapter 8) under avalanche pumping (Sandrock et al., 1997). The energy scheme and avalanche process involved are the ones described in the previous subsection for the avalanche process with Yb-Pr co-doping (Kük et al., 2000). Laser emission is from the $^3P_0 - {}^3F_2$ transition of Pr^{3+} at 0.635 μm with a record output of 1020 mW. The pumping is from two Ti-Sapphire lasers providing 5.51 W at 0.850 μm. This last wavelength, being detuned from the maximum Yb^{3+} absorption at 0.96 μm but tuned with the $^1G_4 - {}^1I_6$ Pr^{3+} absorption, provides the condition for the avalanche regime of a weak $\beta(10^{-8} - 10^{-6})$, as seen above.

5.5 Perspectives and Future Advances

From the most recent studies and their respective aim as described in above sections, and from some emerging new researches, one can try to derive some future trends and perspectives. In the following they are divided into three main directions that can be anticipated:

(1) up-conversion pumped lasers;
(2) new materials for low level IR visualization;
(3) intrinsic material optical bistability.

5.5.1 Up-conversion UV Tunable Lasers

Because optically pumped lasers are originally based on a Stokes pumping process, one of their basic problems is to obtain a high density-pumping source at a shorter wavelength than their emitting wavelength. With the tendency to go all-solid state there will be a continuous race between the shortest wavelength of the

pumping semiconductor-based source and the shortest solid state laser emitting wavelength.

A few years ago, the anticipated pumping diode emitted only in the near IR; now that blue semiconductor laser have begun to appear, one can theoretically anticipate that at some point blue diodes might pump visible solid state lasers. However, because there do not yet exist powerful red semiconductor lasers that can be used for solid state laser pumping, one can also anticipate that for many years to come there will exist no UV CW semiconductor or even frequency-multiplied semiconductor laser powerful enough to usefully pump tunable UV CW solid state lasers.

There, clearly, up-conversion pumping of tunable UV solid state lasers has a role to play. So much the better that presently available gas UV lasers are not tunable. Recent results give hints for that (see Chapter 9).

As already shown in Section 5.3.2.3, UV emission has been obtained from LaF_3: Nd^{3+} at 380 nm through a somewhat complicated anti-Stokes pumping scheme (Macfarlane et al., 1988). On the other hand, very efficient tunable UV lasers using Ce^{3+}: $LiLuF_4$ have recently been obtained from 305 nm to 333 nm under Stokes pumping provided by a frequency-doubled copper vapor laser (McGonigle et al., 1999); the slope efficiency was 51%. This result has to be connected to recent results (Nicolas et al., 2001) on up-conversion and energy transfers from Pr^{3+} ($4f-5d$) to Ce^{3+} ($5d$) to see that a tunable UV laser by anti-Stokes pumping can be imagined. The very recently issued collection of selected papers on up-conversion lasers (Gosnell, 2000) certainly confirms this trend.

5.5.2 New Materials for Low-intensity IR Imaging

As pointed out in Section 5.3.2.1, an interesting point of view is the IR – IR up-conversion for low-intensity IR viewing. Though it is basically the old IRQC concept to up-convert IR out of the photocathode range to the photocathode detection range (GaAs and S1, from 760 to 1200 nm), few investigations had used the more recent understanding of RE-doped materials for this application. It has recently been proposed to use low phonon energy glasses such as chalcogenide glasses ($GeS_2 - Ga_3S_3$) as 1500 to 1000 nm converters, with most of the up-converted energy at the latter wavelength (Tverjanovich et al., 2001). Of course other low phonon energy materials such as the stable $CsCdBr_3$ (which is well known in this respect) together with strong RE – RE pair coupling might be applied to yet more remote IR ranges.

5.5.3 Up-conversion Material Intrinsic Bistability

This is certainly the hottest and most recent subject in the up-conversion field. A few years ago, it was found by Güdel's group (Hehlen et al., 1994) that the ion

cooperative luminescence (see Section 5.3) of Yb^{3+} in $Cs_3Y_2Br_9$ clearly displays a hysteresis loop in up-conversion emission under variable excitation density and fixed temperature between 11 K and 31 K. A corresponding hysteresis loop was also observed when excitation was kept constant and the temperature was varied, as shown in Fig. 5.36. A physical explanation was given in the framework of the optical coherent field coupling between two ions in a solid that had been theoretically proposed (Heber, 1987) by Heber. The problem with such a model is the extent to which it can describe RE-doped systems realistically. This can be questioned.

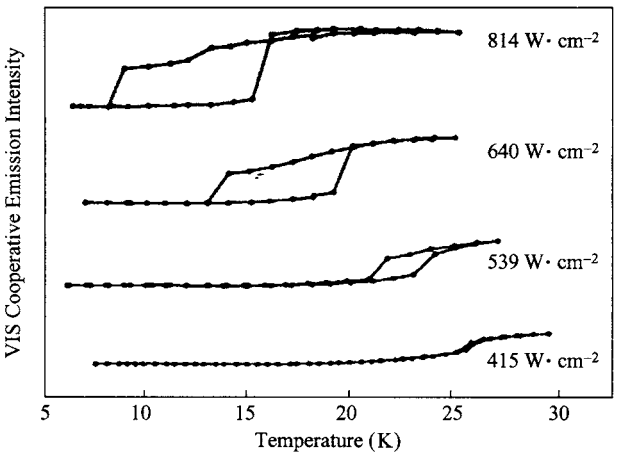


Figure 5.36 Thermal hysteresis loop for cooperative luminescence in Yb^{3+}: $Cs_3Y_2Br_9$ (Hehlen et al., 1994)

It has been recognized for a long time now that optical bistability within a cavity can originate from optical cooperative coupling between cavity modes and the atomic system in a way similar to optical cooperative coupling between atomic systems giving rise to superfluorescence (Bonifacio and Lugiato, 1982). However, obtaining superfluorescence in RE-doped systems is very difficult because it requires long dephasing times (T_2) (see Chapter 7) which are impossible to obtain in a solid at high doping concentration due to ion – ion and ion – phonon dephasing. Observation of superfluorescence in Er: $LiYF_4$ required both low T (<30 K) and very weak concentration (0.3%) (Auzel et al., 1988) and a threshold of 842 W · cm^{-2}. The rather high concentration used here in the Yb^{3+} experiment certainly requires that the Rabi frequency be less than the ion linewidth at the considered excitation density of 800 W · cm^{-2}, which is also about the threshold for the observed hysteresis loop (Hehlen et al., 1994). This rules out significant coherent field coupling.

Interestingly, in the very first experiment on APTE up-conversion, thermal hysteresis loops had been observed at high temperature (Auzel, 1967); see

Fig. 5.37. Clearly at such high temperatures it has nothing to do with coherent field coupling. Also the bistability observed in avalanche systems (see Section 5.4.1) has been described within the framework of population rate equations. Then it appears more in accord with physical reality not to consider coherent field coupling as the root of observed bistability. This is implicitly recognized for $Cs_3Y_2Br_9$: Yb in a later paper (Hehlen et al., 1996) pointing out the analogy with avalanche bistability and describing the effect in terms of population rate equations. As the temperature changes, so do the overlap integrals governing the RE – RE energy transfers, which provide the necessary nonlinear feedback effect. Clearly this can also be the only explanation for the high-temperature (430 K) hysteresis loops, which had initially been observed in $WO_4Na_{0.5}Yb_{0.5}$: 2% Er (Auzel, 1967).

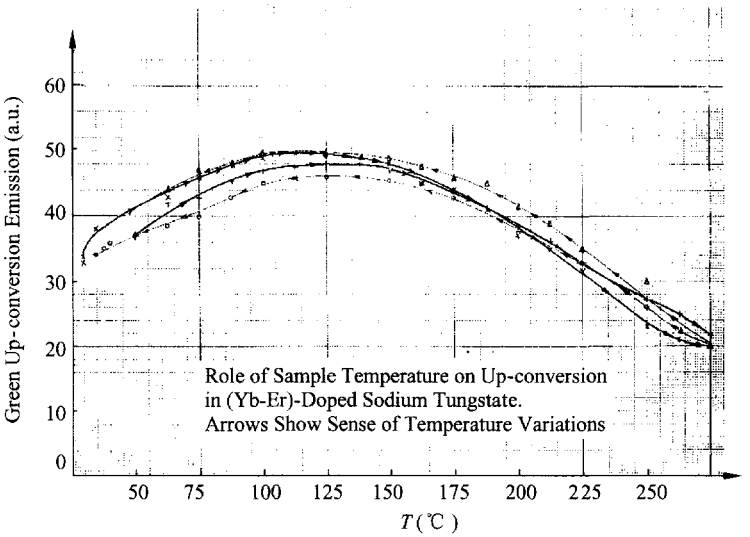


Figure 5. 37 First observation (from 1967 unpublished original document) of thermal hysteresis loops for APTE up-conversion in 2% Er^{3+}: $WO_4Na_{0.5}Yb_{0.5}$. Arrows show sense of temperature variations for two sets of experiments (Hehlen et al., 1996)

5.6 Conclusions

The general principles of up-conversion have been presented in a self-contained way together with typical examples. Because these effects are now so generally observed with the general use of laser excitations, it was thought important to distinguish them in precise ways in order that future researchers start from well-established definitions and speak a common language.

Besides a didactic approach we have tried to present some selected recent important results – certainly not all of them in an exhaustive review, but at least with all important turning points.

If we had some general philosophy to espouse, we could say that up-conversion is an endless field and that features not really exploited at some times may become important with more refined experiments and new available technologies. Also the implied processes may help understand other aspects of optical processes in RE-doped solids. Two examples might be the presently considered down-conversion: "photon-cutting effect" (Wegh et al., 1999) – just the opposite of APTE up-conversion – which may open the way to new efficient lighting systems; also cooperative quenching, the reverse of cooperative luminescence, has just been shown to be practically one to two orders of magnitude larger than cooperative luminescence because of its intrinsically larger number of final states (Basiev et al., 2000).

References

Allain, J.-Y., M. Monerie, and H. Poignant. Electron. Lett. **26**, 261 (1990a).

Allain, J.-Y., M. Monerie, and H. Poignant. Electron. Lett. **26**, 166 (1990).

Auzel F., and P. Goldner. Opt. Mat. **16**, 93 (2001).

Auzel, F., Y. H. Chen. J. Lumin. **65**, 45 (1995a).

Auzel, F., Y. H. Chen. J. Non-Crystal. Sol. **184**, 57 (1995b).

Auzel, F., D. Meichenin, F. Pellé, and P. Goldner. Opt. Mat. **4**, 35 (1994).

Auzel, F., Y. H. Chen, and D. Meichenin J. Lumin. **60/61**, 692 (1994).

Auzel, F. In: *Defects in Insulating Materials* (World Scientific, Singapore, 1993), p. 43.

Auzel, F., J. Lumin. **45**, 341 (1990).

Auzel, F., S. Hubert, and D. Meichenin. Appl. Phys. Lett. **54**, 681 (1989).

Auzel, F., S. Hubert, and D. Meichenin. Europhys. Lett. **7**, 459 (1988).

Auzel, F., In: *Rare-Earth Spectroscopy* (World Scientific, Singapore, 1985), p. 502.

Auzel, F., P. A. Santa-Cruz, and G. F. de Sa. Rev. Phys. Appl. (France) **20**, 273 (1985).

Auzel, F. J. Lumin. **31/32**, 759 (1984).

Auzel, F. In: *Radiationless Processes,* eds. B. DiBartolo and V. Goldberg (Plenum Publishing Co., New York, 1980), p. 213.

Auzel, F., Mat. Res. Bull. **14**, 223 (1979).

Auzel F. Phys. Rev. B **13**, 2809(1976).

Auzel F., D. Pecile. J. Lumin. **11**, 321 (1976).

Auzel, F., C. R. Acad. Sci. (Paris) **262**, 1016 (1966), and **263**, 819 (1966).

Auzel F., D. Pecile. J. Lumin. **11**, 321(1976).

Auzel F., D. Pecile. *De l'influence de la matrice sur l'addition de photons par transferts d'energie (APTE) dans les couples* $Yb^{3+} - Er^{3+}$ *et* $Yb^{3+} - Tm^{3+}$ (Thèse, Université P. et M. Curie, Paris, 1976).

Auzel, F., Pecile, and D. Morin. J. Electrochem. Soc. **122**, 101 (1975).

Auzel, F. Proc. IEEE, **61**, 758 (1973).

Auzel F., and D. Pecile. J. Lumin. **8**, 32 (1973).

Auzel F., D. Pecile, and C. R. Acad. Sc. Paris B **155**, 277 (1973).

Auzel F., and O. Deuschbein. Z. Naturfosch **24a**, 1562 (1969).

Auzel, F. Ann. Telecom. (France) **24**, 363 (1969).

Auzel, F. French Patent N°1.532.609 (1968).

Auzel, F. *Document de Travail "PCM.* 171". *Utilisation du transfert d'energie entre ions de terres-rares pour leur application eventuelles aux compteurs quantiques; addition de deux et trois photons,* CNET, Issy-les Moulineaux (France), 13 Mars(1967), unpublished.

Axe, J. D., P. F. Weller. J. Chem. Phys. **40**, 3066 (1964).
Bagdasarov, K. S., V. I. Zhekov, V. A. Lobachev, J. M. Murina, and A. M. Prokhorov. Sov. J. Quantum Electron. **13**, 262 (1983).
Basiev, T. T., M. E. Doroshenko, and V. V. Osiko. JETP Letters **71**, 8 (2000).
Blätte, M., H. G. Danielmeyer, and R. Verich. Appl. Phys. (German.) **1**, 275 (1973).
Blixt, P., J. Nilsson, J. Carlknäs, and B. Jaskorzynska. IEEE Trans. Photon. Techn. **3**, 996 (1991).
Bloe mbergen. N. Phy S. Rev. Lett. **2**, 84(1959).
Bonifacio R., L. A. Lugiato. In: *Dissipative Systems in Quatum Optics* (Springer-Verlag, Berlin, 1982), p. 2.
Bonneville R., and F. Auzel. Opt. Commun. **18**, 51 (1976).
Brede, R., E. Heumann, J. Koltke, T. Danger, and G. Huber. Appl. Phys. Lett. **63**, 2030 (1993).
Brenier, A., L. C. Courrol, C. Pédrini, C. Madej, G. Boulon. J. Lumin. **58**, 285 (1994a).
Brenier, A., L. C. Courrol, C. Pédrini, C. Madej, G. Boulon. Opt. Mat. **3**, 25 (1994b).
Brenier, A., G. Boulon, C. Madej, C. Pédrini, and L. Lou. J. Lumin. **54**, 271 (1993).
Breteau, J. M., J. L. Ayral, F. Micheron, and F. Auzel. J. Appl. Phys. **67**, 1102 (1990).
Bril, A., J. L. Sommerdijk, and A. W. de Jager. J. Electrochem. Soc. **121**, 660 (1974).
Brown M. R., H. Thomas, J. M. Williams, and R. J. Woodwards. J. Chem. Phys. **51**, 3321 (1969).
Case, W. E., M. E. Koch, and A. W. Kueny. J. Lumin. **45**, 351 (1990).
Chamaro M. A., and R. Cases. J. Lumin. **46**, 59 (1990).
Chen, Y. H., F. Auzel. J. Phys. D: Appl. Phys. **28**, 207 (1995).
Chen, Y. H., F. Auzel. Electron. Lett. **30**, 1602 (1994a).
Chen, Y. H., F. Auzel. Electron. Letters **30**, 323 (1994b).
Chivian, J. S., W. E. Case, and D. D. Eden. Appl. Phys. Lett. **35**, 124 (1979).
Cockroft, N. J., G. D. Jones, and R. W. G. Syme. J. Lumin. **43**, 275 (1989).
Danielmeyer H. G., M. Blätte. Appl. Phys. (German.) **1**, 269 (1973).
de Leeuward, D. M., and G. W.'t Hooft. J. Lumin. **28**, 275 (1983).
Delevaque, E., T. Georges, M. Monerie, P. Lamouler, and J. F. Bayon. IEEE Photon. Techn. Lett. **5**, 73 (1993).
Deutschbein O., F. Auzel. In: *Quantum Electronics*, eds. P. Grivet, and N. Bloembergen (Dunod, Paris and Columbia Univ. Press, NYC, 1963), p. 85.
Dexter, D. L. J. Chem. Phys. **21**. 836 (1953).
Downing, E., L. Hesselink, J. Ralston, and R. Macfarlane. Science **273**, 1185 (1996).
Dyson, J. M., S. M. Jaffe, H. Eilers, M. L. Jones, W. M. Dennis, and W. M. Yen. J. Lumin. **60/61**, 668 (1994).
Förster, T. Ann. Physik **2**, 55 (1948).
Garlick, G. F. J. Contemp. Phys. **17**, 127 (1976).
Goldner, P., F. Pellé, and F. Auzel. J. Lumin. **72/74**, 901 (1997).
Goldner, P., F. Pellé, D. Meichenin, and F. Auzel. J. Lumin. **71**, 137 (1997).
Goldner, P., and F. Pellé. Opt. Mat. **5**, 239 (1995).
Gosnell, T. R. *Selected papers on Up-conversion Lasers, SPIE Milestone Series MS* 161 (SPIE Optical Engineering Press, Bellingham, Washington, 2000).
Grant, W. J. C. Phys. Rev. **109**, 648 (1958).
Grubb, S. G., K. W. Bennett, R. S. Cannon, and W. F. Humer. Electron. Lett. **28**, 1243 (1992).
Goldner, P., M. Fesquet, and F. Auzel. J. Opt. Soc. Am. B **15**, 2688 (1998).
Gomes, A. S. L., G. S. Maciel, R. E. de Araujo, L. H. Acioli, and C. B. de Araujo. Opt.

Comm. **103**, 361 (1993).
Guy, S. L. Avalanche de photons; application à l'ion Tm^{3+} dans differents matériaux, Thèse, Université Claude-Bernard-Lyon I, 14 Décembre(1995).
Heber, J. Z. Phys. B- Condensed Matter **68**, 115 (1987).
Hebert, T., R. Wannemacher, W. Lenth, and R. M. Macfarlane. Appl. Phys. Lett. **57**, 1727 (1990).
Hehlen, M. P., H. U. Güdel, Q. Shu, S. C. Rand. J. Chem. Phys. **104**, 1232 (1996).
Hehlen, M. P., H. U. Güdel, Q. Shu, S. Rai, S. C. Rand. Phys. Rev. Lett. **73**, 1103 (1994).
Heine, F., E. Heumann, T. Danger, T. Schweizer, and G. Huber. Appl. Phys. Lett. **65**, 383 (1994).
Henderson, B., G. F. Imbusch. *Optical Spectroscopy of Inorganic Solids* (Clarendon Press, Oxford, 1989), p. 445.
Hewes R. A., and J. F. Sarver. Phys. Rev. **182**, 427 (1969).
Hubert, S., Chong Li Song, M. Genet, and F. Auzel. J. Solid State Chem. **61**, 252 (1986).
Hubert, S., D. Meichenin, B. Zhou, and F. Auzel. J. Lumin. **50**, 7 (1991).
Inokuti M., and F. Hirayama. J. Chem. Phys. **43**, 1978 (1965).
Joubert, M. F., S. Guy, C. Linares, B. Jacquier, and J. L. Adam. J. of Non-crystal. Sol. **184**, 98 (1995).
Joubert, M. F., S. Guy, and B. Jacquier. Phys. Rev. B **48**, 10,031 (1993).
Johnson, L. F., H. J. Guggenheim. Appl. Phys. Lett. **19**, 44 (1971).
Kermaoui, A., G. Özen, P. Goldner, J. P. Denis, and F. Pellé. J. Phys. Chem. Solids **55**, 677 (1994).
Koch, M. E., A. W. Kueny, and W. E. Case. Appl. Phys. Lett. **56**, 1083 (1990).
Komukai, T., T. Yamamoto, T. Sugawa, and Y. Miyajima. Electron. Lett. **28**, 830 (1992).
Krasutsky, N. J. J. Appl. Phys. **54**, 1261 (1983).
Kueny, A. W., W. E. Case, and M. E. Koch. J. Opt. Soc. Am. B **10**, 1834 (1993).
Kük, S., A. Diening, E. Heumann, E. Mix, T. Sandrock, K. Sebald, and G. Huber. J. Alloys and Compounds **300/301**, 65 (2000).
Kurochkin. A. V., O. Ya. Manshisrov, D. K. Sattarov, V. B. Smirnov, and O. V. Tsyurupa. Svetotekhnika **5**, 4 (1992) (Tranlated by Allerton Press Inc., 1993).
Kurokin, A. V., L. M. Mailibaeva, O. Ya. Manashirov, D. K. Sattarov, and V. B. Smirnov. Part 1, Opt. Spectrosc. **73**, 442 (1992); and Part 2, ibidem, 447.
Kushida, T. J. Phys. Soc. Jpn. **34**, 1318 (1973).
Lee, L. S., S. C. Rand, and A. L. Schawlow. Phys. Rev. B **29**, 6901 (1984).
Lenth, W., and R. M. Macfarlane. J. Lumin. **45**, 346 (1990).
Livanova, L. D., I. G. Saitkulov, and A. L. Stolov. Sov. Phys. Solid State **11**, 750 (1969).
Leverenz, H. W. *Introduction to Luminescence of Solids* (Dover Publications, NYC, 1968).
Macfarlane, R. M., F. Tong, A. J. Silversmith, and W. Lenth. Appl. Phys. Lett. **52**, 1300 (1988).
Maurice, E., G. Monnom, B. Dussardier, and D. B. Ostrowsky. Optics Lett. **20**, 2487 (1995).
McGonigle, A. J. S., S. Girard, D. W. Coutts, and R. Moncorgé. Electon. Lett. **35**, 1640 (1999).
Mears, R. J., L. Reekie, S. B. Poole, and D. N. Payne. Electron. Lett. **22**, 159 (1986).
Milne, E. A. Lond. Math. Soc. **1**, 1 (1926).
Mita, Y., H. Yamamoto, K. Katayanagi, and S. Shionoya. J. Appl. Phys. **78**, 1219 (1995).
Mita, Y., E. Nagasawa. NEC Research and Development, **33**, 61 (1974).
Miyakawa, T., Dexter, D. L. Phys. Rev. B **1**, 70 (1971).

Möbert, P. E. -A., E. Heumann, and G. Huber. Opt. Lett. **22**, 1412 (1997).
Monerie, M., J. -Y. Allain, H. Poignant, and F. Auzel. Fluorescence, Up-conversion, and lasing in Er-doped quasi-single mode fluorozirconate fibres, In: *Proceedings of ECOC'89* (Gothenburg, Sweden, 1989), paper TuB12-6.
Nakazawa E., S. Shionoya. Phys. Rev. Lett. **25**, 1710 (1970).
Ni, H., S. C. Rand. Opt. Lett. **17**, 1222 (1992).
Nicolas, S., E. Descroix, Y. Guyot, M. -F. Joubert, R. Yu. Abdulsabirov, S. L. Korableva, A. K. Naumov, and V. V. Semashko. Optical Materials, Fev, 2001.
Oetliker, U., M. J. Riley, P. S. May, and H. U. Güdel. J. Lumin. **53**, 553 (1992).
Ohwaki J., Y. Wang. Appl. Phys. Lett. **65**, 129 (1994a).
Ohwaki J., Y. Wang. Jpn. J. Appl. Phys. **33**, L334 (1994b).
Orbach, R. In: *Optical Properties of Ions in Solids,* ed. B. DiBartolo (Plenum Press, New York, 1975), p. 445.
Ostermayer, F. W., Jr. and L. G. Van Uitert. Phys. Rev. B **1**, 4208 (1970).
Ovsyankin, V. V. In: *Spectroscopy of Solids Containing Rare-Earth Ions*, ed. A. A. Kaplyanskii R. M. MacFarlane (North Holland, Amsterdam, 1987), p. 405.
Ovsyankin V. V., and A. A. Fedorov. Opt. Spectrosc. **50**, 565 (1981).
Ovsyankin V. V., and P. P. Feofilov. Sov. Phys., JETP Lett. **4**, 317 (1966).
Page, R. H., K. I. Schaffers, P. A. Waide, J. B. Tassano, S. A. Payne, W. F. Krupke, W. K. Bischel. J. Opt. Soc. Am. B **15**, 996 (1998).
Pelletier-Allard, N., R. Pelletier. Phys. Rev. B **26**, 4425 (1987).
"Photo-Turkey-1" (Sumita Optical Glass Inc., 4-7-25 Harigaya, Urawa-City, Saitama, Japan, 1994).
Pollack, S. A., D. B. Chang. J. Appl. Phys. **64**, 2885 (1988).
Pouradier, J. F., F. Auzel. J. Phys. (France) **39**, 825 (1978).
Quimby, R. S., M. G. Drexhage, and M. J. Suscavage. Electron. Lett. **23**, 32 (1987).
Rand, S. C., L. S. Lee, and A. L. Schawlow. Opt. Comm. **42**, 179 (1982).
Rois Leite J. R., and C. B. de Araujo. Chem. Phys. Lett. **73**, 71 (1980).
Rubin, J., A. Brenier, R. Moncorgé, and C. Pédrini. J. Lumin. **36**, 39 (1986).
Sandrock, T., H. Scheife, E. Heuman, and G. Huber. Opt. Lett. **22**, 808 (1997).
Schaudel, B., P. Goldner, M. Prassas, and F. Auzel. J. Alloys and Compounds **300/301**, 443 (2000).
Scheps, R. IEEE QE**31**, 309 (1995).
Scheps, R. IEEE QE**30**, 2914 (1994).
Smart, R. G., D. C. Hanna, A. C. Tropper, S. T. Davey, S. F. Carter, and D. Szebesta. Electron. Lett. **27**, 1308(1991).
Smith, D. J. Lumin. **23**, 209 (1981).
Snitzer, E., and R. Woocock. Appl. Phys. Lett. **6**, 5 (1965).
Stavola M., and D. L. Dexter. Phys. Rev. B **20**, 1867 (1979).
"Tokin IR Catcher" (Tokin America, 155 Nicholson Lane, San Jose, Calif. 95134, USA, 1987).
Tong, F., W. P. Risk, R. M. Macfarlane, and W. Lenth. Electron. lett. **25**, 1389 (1989).
Tverjanovich, A., Ya. G. Grioriev, S. V. Degtyarev, A. V. Kurochkin, A. A. Man' shina, and Yu. S. Tver' yanovich. J. Non-Cryst. Sol. **286**, 89(2001).
Van der Weg W. F., M. W. Van Tol. Appl. Phys. lett. **38**, 705 (1981).
Van Uitert L. G., L. F. Johnson. J. Chem. Phys. **44**, 3514 (1966).
Varsanyi, F., D. L. Wood, and A. L. Schawlow. Phys. Rev. Lett. **3**, 544 (1959).
Vial, J. C., R. Buisson, F. Madeore, and M. Poirier. J. Phys. (France) **40**, 913 (1979).
Wang Y., and J. Ohwaki. Appl. Phys. Lett. **63**, 3268 (1993a).

Wang Y., and J. Ohwaki. J. Appl. Phys. **74**, 1272 (1993b).
Weber, M. J. Phys. Rev. B **4**, 2932 (1971).
Wegh, R. T., H. Donker, K. D. Oskam, and A. Meijerink. Science **283**, 663 (1999).
Whitley, T. J., C. A. Millar, R. Wyatt, M. C. Brierley, and D. Szebesta. Electron. Lett. **27**, 1785 (1991).
Wright, J. In: *Radiationless Processes in Molecules and Condensed Phases, Topics in Applied Physics* **15**, ed. F. K. Fong (Springer, NYC, 1976), p. 239.
Yamada, N., S. Shionoya, and T. Kushida. J. Phys. Soc. Jpn. **32**, 1577 (1972).
Yeh, D. C., W. A. Sibley, and M. J. Suscavage. J. Appl. Phys. **63**, 4644 (1988).
Yokota M., and O. Tanimoto. J. Phys. Soc. Jpn. **22**, 779 (1967).

Acknowledgments
It is a pleasure to acknowledge a number of researchers who have kindly sent me their preprints and reprints and have thus help me in the writing of this chapter. I would like to mentioned particularly Dr. Junichi Owaki (NTT), Pr. Günter Huber (Hambourg University), Pr. Johann Heber (Darmstadt University of Technology), Drs. Valery Smirnov and Alina Man'shina (Russian Center for Laser Physics), Pr. Georges Boulon and Dr. Marie – France Joubert (Université de Lyon). I would also like to thank Dr. Fabienne Pellé (CNRS – Bellevue), my colleague, for a careful reading of the manuscript. Last but not least, thanks are due to my wife, Odile, for having accepted my diversion of much leisure time to this work.

6 Current Topics in Rare-earth Lasers

R. Moncorgé

6.1 Introduction

Although semiconductor diode lasers, thanks to their high light/current conversion efficiency, the diversity of their emission domains, and their extreme compactness, gain more ground every day over other systems, their beam quality remain somewhat limited. They can often be improved at the price of rather complex technologies, but they remain difficult to scale up to high powers, and their very short upper-state emission lifetimes do not permit the storage of energy to produce high peak powers, which are useful in many applications. Thus, it is still desirable to seek systems in which simplicity, compactness, energy storage, and (for some uses) wavelength tunability can be combined more optimally. From this point of view, rare-earth doped materials pumped with semiconductor diode lasers and eventually associated (to reach more extended spectral ranges) with various types of nonlinear devices such as optical paramagnetic oscillators's (OPO's) are already very attractive laser systems, and will be certainly developed in the future for various types of applications.

Although the history of solid state lasers based on rare-earth doped materials started in the early sixties with $Sm^{2+}: CaF_2$ and $Sm^{2+}: SrF_2$ (Kaiser et al., 1961; Sorokin et al., 1962) using crystals doped with a divalent rare earth ion, most laser materials discovered and developed subsequently were materials doped with trivalent rare earth ions. Moreover, among all these materials, it is clear that only a few of them, even after all these years, really represent a big market. They are, first, the Nd^{3+}-doped laser crystals such as $Nd^{3+}: Y_3Al_5O_{12}$ (YAG) (see Appendix 6. E) and $Nd^{3+}: YVO_4$ (to a lesser extent) for the high-power and compact laser systems, respectively, and the Nd^{3+} doped phosphate and silicate glasses for the high-power laser amplifiers operating around 1 μm. On the other hand, they also include Er^{3+} doped phosphate and silicate glasses for optical fiber amplifiers and microlasers used in optical telecommunications and for telemetry. However, many other laser sources operating from the near UV to the far infrared and based on different types of materials doped with other rare earth ions are presently being studied very actively and may address, in the future various types of scientific, medical, biological, and industrial applications with non-negligible markets.

The purpose of this chapter is first to familiarize the reader with the vocabulary and the various methods of optical characterization used by the

scientific community working in the field of rare-earth based solid state laser materials. It is also intended to give a short overview of the most recently explored laser systems, restricting, however, the presentation to the less exotic ones, i. e., to those which already lead to remarkable laser performance.

Thus, the second section will first be devoted to a presentation of the basic spectroscopic and laser parameters necessary to understand or predict the laser performance of various laser systems. Particular attention will be paid the theoretical and experimental methods which can be used for that purpose.

The third section will treat of two very special types of UV visible laser sources, those based on crystals doped with rare-earth ions such as Ce^{3+}, which provide very efficient and tunable laser radiation in the near UV, and those based on Nd^{3+} and (to a lesser extent) Yb^{3+} ions in nonlinear crystals, leading to frequency-doubled radiation in the green spectral domain. The reader who requires a more extended overview of the laser systems operating in this UV visible spectral domain can find it in another very recent review article (Moncorgé, 1999).

Finally, in the last section, three types of infrared laser materials are described: (1) Yb^{3+} doped crystals, since they provide a very interesting alternative to Nd^{3+} based laser systems for high-power applications, and also because of their potential in the generation of ultra-short laser pulses; (2) Er^{3+} and, more particularly, Tm^{3+} doped materials for their interest in telecommunications and eye-safe laser applications around 1.5 μm; and (3) Tm^{3+} and Er^{3+} doped crystals, for their efficient laser radiation around 2 and 2.8 μm, respectively.

6.2 Spectroscopic and Laser Parameters

Depending on the nature of the laser system, more or less sophisticated models can be used and different expressions for the threshold pump power, and the laser efficiency can be obtained. In fact, in most practical cases, there are so many parameters to account for that only numerical solutions are possible.

Since the goal here is to present and discuss the main parameters which contribute to the laser performance of a given rare earth doped material, we will not enter into the details of laser theory, which is already perfectly done in a number of excellent books (Siegman, 1986; Svelto, 1998; Miloni and Eberly, 1988; Koechner, 1988; etc.). For example, important aspects such as inhomogeneous broadening, spatial hole burning, and amplified spontaneous emission (ASE) will not be discussed at all. Consequently, only simple expressions which can be handled without too many calculations will be given, returning sometimes, however, to the basics when it is judged necessary.

6.2.1 Basic Laser Parameters

The laser output power of a laser operating in the continuous wave (CW) regime is usually given by

$$P_{out} = \eta_{slope}(P_{in} - P_{th}), \tag{6.1}$$

where P_{in} and P_{th} are the input and threshold pump powers, P_{out} the laser output power, and η_{slope} the laser efficiency above threshold or laser slope efficiency.

It is clear that the same expression can be written in the pulsed regime by replacing powers by energies. η_{slope} can also be replaced by $\eta_{slope}^{abs} = \eta_{slope}/\eta_p$ with $\eta_p = [1 - \exp(-\sigma_p N l)]$ when absorbed (P_{in}^{abs} and P_{th}^{abs}) instead of input pump powers are used. σ_p is the absorption cross section at the pump frequency ν_p, l the length of the laser medium, and N the total active ion density (cm^{-3}).

The specifics of the different systems enter into the expressions for η_{slope} and P_{th}, the simplest being written (see Appendix 6. A)

$$\eta_{slope} = \eta_q \eta_e \varepsilon_p \eta_p \frac{\ln R}{\ln R - L} \tag{6.2}$$

and

$$P_{th} = \frac{h\nu_e S}{2\eta_q \sigma_e \eta_e \tau_r \eta_r \varepsilon_p \eta_p}(L - \ln R), \tag{6.3}$$

where the factor 2 applies to a standing wave situation and is replaced by 1 in case of ring conditions. In pulsed operation, P_{th} and $\tau_r \eta_r$ must be replaced by E_{th} and $\eta_d = \frac{\tau_f}{\tau_p}\left[1 - \exp\left(-\frac{\tau_p}{\tau_f}\right)\right]$, respectively, the latter expressing the overlap between the pump pulse duration τ_p and the fluorescence lifetime τ_f of the emitting level, which is linked to the purely radiative lifetime τ_r of this emitting level by the radiative quantum efficiency

$$\eta_r = \frac{\tau_f}{\tau_r}.$$

In the above expressions, the other ingredients have the following meaning: S stands for the cross sectional overlap integral of the pump and laser cavity beams (Fan and Byer, 1987; Risk, 1988); for longitudinal pumping and gaussian beams with pump and cavity beam waists $\tilde{\omega}_p$ and $\tilde{\omega}_c$, S is approximately given by $\pi(\tilde{\omega}_p^2 + \tilde{\omega}_c^2)/2$, ν_e is the laser emission frequency, σ_e is the spectroscopic stimulated emission cross section (see Section 6.2.3). L is the round-trip loss;

In ground and excited state absorption with cross section σ_a and σ_e^{esa} at the laser wavelength, L must be replaced by $L+2\frac{\sigma_{esa}}{\sigma_e}\cdot\sigma_a Nl$ in Eq. (6.2) and by $L+2\sigma_a Nl$ in Eq. (6.3). $T\approx -\ln R$ (for small T values) is the output mirror transmission, $\eta_q=\frac{h\nu_e}{h\nu_p}$ is the quantum conversion (defect) efficiency, ε_p is the pump efficiency, i.e., the fraction of absorbed pump photons in the laser level, and $\eta_e=\frac{\sigma_e^{eff}}{\sigma_e}$, where $\sigma_e^{eff}=(\sigma_e+\sigma_a-\sigma_e^{esa})$ is the effective stimulated emission cross section.

Based on these fairly general expressions, several remarks can be made. It is immediately clear, whatever the nature of the laser system, that the best laser performance, i.e., the lowest threshold pump power (energy) and the highest laser slope efficiency will be obtained, first, for large pump efficiencies ε_p, large absorption cross sections σ_p, and large effective stimulated emission cross sections σ_e^{eff}, i.e., for large spectroscopic values σ_e as well as reduced excited state absorption (ESA) σ_e^{esa}. A long radiative lifetime τ_r and high radiative quantum efficiency, thus a long emission lifetime τ_f, are only desirable, however, to obtain a low laser threshold. Indeed, efficient lasing (high slope efficiency) is possible even for short lifetimes and low quantum efficiencies (see for example Manaa et al., 1993).

A long emission lifetime τ_f also means a low saturation pump intensity $I_p^{sat}=\frac{h\nu_p}{\sigma_p\tau_f}$, a laser parameter which plays a very important role, especially in the case of quasi three-level laser systems. Indeed, I_p^{sat} gives a measure of the minimum pump intensity I_p^{min} necessary to compensate for ground-state reabsorption losses and to reach transparency at the laser wavelength. For example, if $\beta=\frac{N_e}{N}$ stands for the fraction of excited ions, then for moderate pump powers $\beta\approx\frac{\varepsilon_p I_p}{I_p^{sat}}$ (see Appendix 6. A). Then ground state absorption losses, with cross section σ_a at the laser wavelength, will be exactly balanced (assuming no other losses) by stimulated emission of cross section σ_e when $\beta=\beta_{min}$, β_{min} being given (see Appendix 6. B) by $\beta_{min}\sigma_e-(1-\beta_{min})\sigma_a=0$; thus,

$$\beta_{min}=\frac{\sigma_a}{\sigma_e+\sigma_a}, \tag{6.4}$$

and the minimum pump intensity I_p^{min} will be given by

$$I_p^{min}=\beta_{min}I_p^{sat}. \tag{6.5}$$

These relations can be easily deduced from Eq. (6.3) for the threshold pump power P_{th}, in which (1) we neglect the output coupling term $-\ln R$ and restrict the loss term L to the reabsorption loss term $2\sigma_a Nl$; (2) we assume no ESA; and (3) we approximate $\eta_p = [1 - \exp(-\sigma_p Nl)]$ by $\sigma_p Nl$ and assume $\varepsilon_p = 1$. Then P_{th} transforms as

$$P_{th}^{min} = \frac{h\nu_p S}{2(\sigma_e + \sigma_a)\tau_f \varepsilon_p \sigma_p Nl}(2\sigma_a Nl) = \frac{\sigma_a}{\sigma_e + \sigma_a}\frac{h\nu_p S}{\sigma_p \tau_f},$$

with

$$I_p^{min} = \frac{P_{th}^{min}}{S}.$$

A long emission lifetime τ_f – thus a small saturation pump intensity I_p^{sat} – is also desirable for good energy storage, especially when high powers are needed. If N_e is the density of excited ions, $V(=S \cdot l)$ the excited volume, and ν_e the laser emission frequency, this stored energy takes the form

$$E_{sto} = \beta_0 N h\nu_e V \tag{6.6}$$

with the initial fraction of excited ions $\beta_0 = \frac{N_e}{N}$.

In amplification of short pulses or Q-switching, where the stored energy is extracted very rapidly compared with the emission lifetime of the laser level, This also implies extraction efficiency

$$\eta_{ext} = \frac{E_{out} - E_{in}}{E_{sto}} = \frac{\beta_0 - \beta}{\beta_0} = 1 - \frac{\beta}{\beta_0}, \tag{6.7}$$

where β is for the fraction of ions left in their excited state after amplification. Thus, in principle, according to Eq. (6.7), all the stored energy can of course be extracted, when $\beta = 0$. However, the maximum limit for extraction efficiency η_{max} will in fact be obtained for $\beta = \beta_{min}$, the minimum fraction of excited ions that will remain in the gain medium after extraction, thus (Chase et al., 1991),

$$\eta_{max} = 1 - \frac{\beta_{min}}{\beta_0}. \tag{6.8}$$

This means in turn that the greatest fraction of stored energy that can be extracted is

$$f_{max} = 1 - \beta_{min} = \frac{\sigma_e}{\sigma_e + \sigma_a}. \tag{6.9}$$

Since this situation is in fact realized not only when all ions are pumped into their excited state, i. e., $\beta_0 = 1$, but also when the fluence of the extraction beam is much greater than the emission saturation fluence, i. e. $F_e^{in} = \frac{E_{in}}{S} \gg F_e^{sat} = \frac{h\nu_e}{\sigma_e + \sigma_a}$, i. e., $E_{in} \gg E_{sat} = F_{sat} \cdot S$, the best extraction conditions will be obtained for large stimulated emission cross sections σ_e. This is well illustrated by relating the extraction efficiency η_{ext} to the expression for the gain as proposed by Frantz and Nodvik (1963) to describe short pulse amplification

$$G = \frac{E_{out}}{E_{in}} = \frac{E_{sat}}{E_{in}} \ln \left\{ 1 + \left[\exp\left(\frac{E_{in}}{E_{sa}}\right) - 1 \right] G_0 \right\}, \tag{6.10}$$

where $G_0 = \exp(\beta_0 \sigma_e N l) = \exp\left(\frac{E_{sto}}{E_{sat}}\right)$ is the small-signal gain, i. e., by writing

$$\eta_{ext} = \frac{(G-1)(E_{in}/E_{sat})}{E_{sto}/E_{sat}}, \tag{6.11}$$

the three essential parameters being the stored, input, and saturation energies (or fluences). From Fig. 6. 1, it is clear that the gain will be the highest as the input fluence is reduced and when the stored energy is large. However, Fig. 6. 1 also tells us that reduced input and/or high saturation energies lead to reduced extraction efficiencies. It is thus preferable to work with systems with a large energy storage capability and a reasonably high stimulated emission cross section σ_e, thus a low saturation energy E_{sat}, both to keep the gain high and to work with input fluences two to three times the saturation fluence to get good extraction efficiencies while not exceeding the limit of optical damage of the laser material.

Of course, in many cases not all the ions are in their excited state with $\beta_0 < 1$. Indeed, during the pumping process and depending on the systems, energy can be lost due to different mechanisms, the most detrimental ones in rare-earth doped materials being ESA at the pump wavelength and up-conversion and migration type energy transfers, at high dopant concentrations.

In ESA at the pump wavelength, we have to solve rate equations of the type

$$\frac{\partial N_e}{\partial t} = (\varepsilon_p \sigma_p N_g - \sigma_p^{esa} N_e) \frac{I_p}{h\nu_p} - \frac{N_e}{\tau_f}, \tag{6.12}$$

where σ_p^{esa} denotes the ESA absorption cross section at the pump wavelength λ_p. Assuming that $N_g + N_e \approx N$ (quasi three-level laser system), and using the definition for the fraction of excited ions $\beta = \frac{N_e}{N}$, Eq. (6.12) can also be written

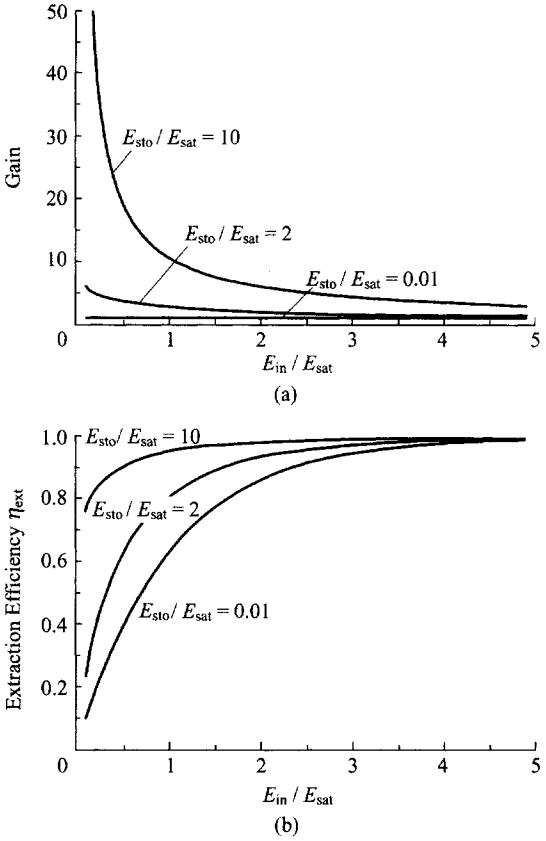


Figure 6.1 Gain (upper curves) and extraction efficiency (lower curves) versus reduced input energy (E_{in}/E_{sat}) for different values of the reduced stored energy (E_{sto}/E_{sat})

$$\frac{\partial \beta}{\partial t} = \frac{\varepsilon_p \sigma_p I_p}{h\nu_p} - \left[\frac{1}{\tau_f} + \left(1 + \frac{\sigma_p^{esa}}{\varepsilon_p \sigma_p}\right)\frac{\varepsilon_p \sigma_p I_p}{h\nu_p}\right]\beta, \tag{6.13}$$

which can be solved very easily either analytically in special cases, such as a square pump pulse of duration τ_p (see Appendix 6. C) or numerically for any pump profile $I_p(t)$.

As an illustration, Fig. 6.2a shows the time dependance of β obtained for different ratios $\frac{\sigma_p^{esa}}{\sigma_p}$ using the input parameters $\varepsilon_p = 1$, $h\nu_p = 2.5 \times 10^{-19}$ J, $\sigma_p = 1.5 \times 10^{-21}$ cm^2, $\tau_f = 300$ μs, and $I_p(t) = F_p \frac{t}{\tau_p^2}\exp\left(-\frac{t}{\tau_p}\right)$ with $F_p = 80$ J/cm^2 and $\tau_p = 35$ μs (parameters close to those describing the fraction of excited population reached in Nd doped glasses after alexandrite laser excitation pumping around 780 nm (Descamps, 1997)).

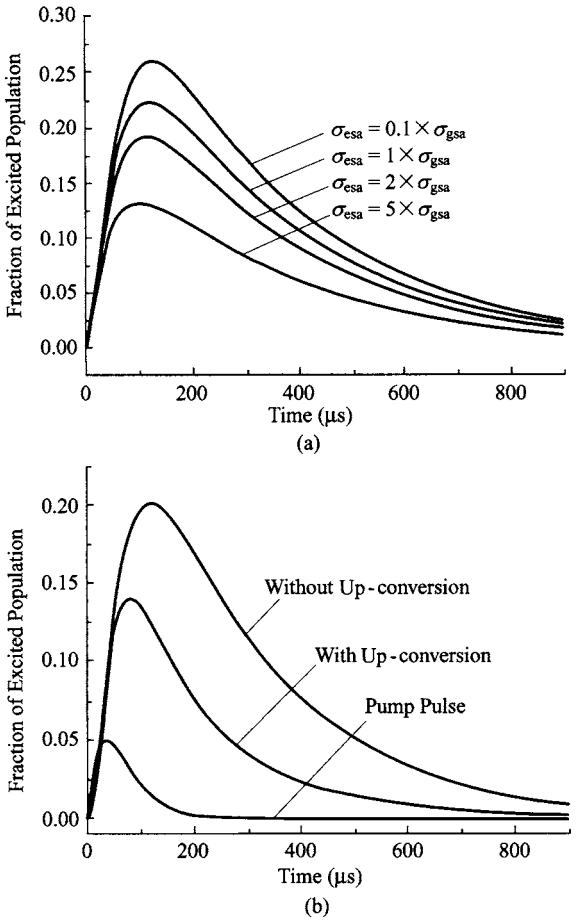


Figure 6.2 Fraction of excited population with and without up-conversion losses (lower curves), and for excited-state absorption (ESA), losses at the pump wavelength for different values of the corresponding ESA cross section (upper curves)

As mentioned above, up-conversion, migration, and cross-relaxation type energy transfers may also reduce the fraction of excited ions very strongly. In this case, we have to solve a rate equation of the form (Doualan et al., 2000)

$$\frac{\partial N_e}{\partial t} = \varepsilon_p \sigma_p I_p N - \left(\varepsilon_p \sigma_p I_p + \frac{1}{\tau_f}\right) N_e - 2W_\uparrow N_e^2, \qquad (6.14)$$

where the up-conversion transfer rate $W_\uparrow$, for example, may depend on two types of transfer mechanisms: direct (or static) Forster – Dexter energy transfers and migration-assisted Burstein (hopping model) energy transfers, the associated transfer rates in dipole – dipole inter-ion interactions being proportional (see Appendix 6. C) to overlap integrals of the type

$$C_{FD} = \frac{3c}{8\pi^4 n^2}\int \sigma_e(\lambda)\sigma_e^{esa}(\lambda)\,d\lambda \qquad (6.15)$$

and

$$C_{mig} = \frac{3c}{8\pi^4 n^2}\int \sigma_e(\lambda)\sigma_a(\lambda)\,d\lambda, \qquad (6.16)$$

which can be determined spectroscopically. This matter is illustrated in Fig. 6.2b, which shows the time dependence of the fraction of excited ions $\beta = \frac{N_e}{N}$ reached in the absence or presence of up-conversion (UC) energy transfer losses as predicted (Descamps, 1997; Doualan, 2000) in the case of a Nd doped glass pumped with the aid of an alexandrite (Cr: $BeAl_2O_4$) laser. Clearly, up-conversion may be responsible for very significant pumping losses.

From the above presentation, it becomes clear that the laser potential of any rare-earth doped material will depend on several parameters, among them the minimum pump intensity I_p^{min} and saturation fluence at the emission wavelength F_e^{sat}, and that prediction and optimization of their laser performance will not be possible without detailed knowledge of the spectroscopic and dynamical properties of the active ions within the considered host lattice.

It is immediately recognized that the absorption and emission cross sections at the pump (σ_p) and laser wavelengths (σ_a and σ_e) as well as the radiative and fluorescence lifetimes τ_r and τ_f of the laser level play the most important roles and thus must be considered first. However, ESA at the pump wavelength (cross section σ_p^{esa}) and ESA at the laser wavelength (cross section σ_e^{esa}), either within the same excited ion or between adjacent excited ions linked by energy transfers, must be considered almost at the same time. They are generally the main limiting parameters and it is absolutely useless to compare two laser systems without considering these very detrimental effects. We are then concerned with the methods which can be used to derive reliable values for these various parameters.

6.2.2 Determination of Absorption Cross Sections

The absorption cross sections at the pump and laser wavelengths are generally obtained without any difficulty. They only require recording an absorption spectrum, and the absorption cross sections $\sigma_{p(a)}$ are immediately derived from the measured absorption coefficients $\alpha_{p(a)}$ by using the relation $\alpha_{p(a)} = \sigma_{p(a)} N$. However, the total active ion density N must be known or estimated very accurately, which is not always evident. It can be estimated fairly accurately when the segregation coefficient of the dopant active ions in a particular material is itself a well-defined parameter. It can be measured chemically with the aid of methods such as induction coupled plasma (ICP). It can be obtained by

comparison with absorption spectra found in the literature and assumed to be themselves accurately calibrated, but that may be risky.

Another method consists in recording, at a particular absorption wavelength, the transmission T of a laser pump beam passing through the sample as a function of its incident intensity or fluence, and fitting the data, when the pump pulse duration satisfies $\tau_p \ll \tau_f$ (slow saturable absorber), with an expression such as the one given by the modified Frantz-Nodvik relation (Frantz and Nodvik, 1963), and similar to the gain expression given by Eq. (6.10), i.e.,

$$T = \frac{F_p^{out}}{F_p^{in}} = \frac{F_p^{sat}}{F_p^{in}} \ln\left\{1 + \left[\exp\left(\frac{F_p^{in}}{F_p^{sat}}\right) - 1\right] T_0\right\}, \tag{6.17}$$

with $F_p = \int_0^{\tau_p} I_p(t)\,dt$, $F_p^{sat} = \frac{h\nu_p}{\sigma_p}$ and $T_0 = \exp(-\sigma_p N l)$ or, for ESA at the pump wavelength and again when $\tau_p \ll \tau_f$, by integrating an expression such as (Kuo et al., 1995)

$$\frac{dF_p}{dz} = -(\sigma_p - \sigma_p^{esa}) N F_p^{sat}\left[1 - \exp\left(-\frac{F_p}{F_p^{sat}}\right)\right] - (\sigma_p^{esa} N) F_p, \tag{6.18}$$

a procedure which only involves three fit parameters, σ_p, σ_p^{esa}, and N, and often gives good results. At low pump fluences $F_p \ll F_p^{sat}$, by integrating over the length l of the active medium, one obtains $T \approx T_0$. On the other hand, at high pump fluences, Eq. (6.18) transforms like (Lenévé, 1996)

$$T = T_{sat} + \left(1 - \frac{\sigma_p}{\sigma_p^{esa}}\right)(1 - T_{sat}) \frac{F_p^{sat}}{F_p^{in}}, \tag{6.19}$$

with

$$T_{sat} = T_0^{\gamma} \quad \text{and} \quad \gamma = \frac{\sigma_p^{esa}}{\sigma_p}, \tag{6.20}$$

and T asymptotically approaches T_{sat}.

We must not forget, however, that such simplified expressions only rigorously apply for a pump pulse with an uniform "top-hat" profile. A more elaborate numerical procedure is generally needed for typical laser pulses.

6.2.3 Determination of Emission Cross Sections

Two kinds of methods can be used to determine the stimulated emission cross section σ_e:

(1) spectroscopic methods called McCumber or reciprocity (RM) (McCumber, 1964; Aull and Jenssen, 1982; Payne et al., 1992) and

Fuchtbauer-Ladenburg methods (FL) (Krupke et al., 1986; Moulton, 1986) which bear upon a perfect knowledge of the energy level structure of the emitting ion and measurements of absorption and emission spectra, respectively; and (2) laser methods involving small signals (Payne et al., 1991) or saturated, laser threshold and laser slope efficiency measurements (Martin and Milam, 1982).

6.2.3.1 Spectroscopic Methods

Going back to the definition of the Einstein coefficients (Appendix 6.D), the absorption and emission cross coefficients at a frequency ν between two atomic energy levels i and j with degeneracies g_i and g_j, respectively, the latter being the higher-lying one, are given by

$$g(\nu) = -\alpha(\nu) = \sigma(g_i N_j - g_j N_i), \tag{6.21}$$

with

$$\sigma = \frac{c^2}{8\pi\nu^2}\frac{A_{ji}}{g_i}\Phi(\nu) \quad \text{and} \quad \sigma = \frac{\sigma_{ji}}{g_i} = \frac{\sigma_{ij}}{g_j}. \tag{6.22}$$

Assuming that level i is some Stark level of the ground state manifold g of a given rare-earth ion and j some Stark level of the excited manifold e between which transition at the wavelength λ is considered (see in Fig. 6.3), the spectroscopic cross sections $\sigma_a(\lambda)$ and $\sigma_e(\lambda)$ of the absorption and emission transitions at this wavelength λ are obtained, at a temperature T, by summing the above individual cross sections σ_{ij} and σ_{ji} weighted by the fractional thermal occupation $f_i = \frac{N_i}{N_g}$ and $f_j = \frac{N_j}{N_e}$ of the levels i and j, respectively, according to the expressions

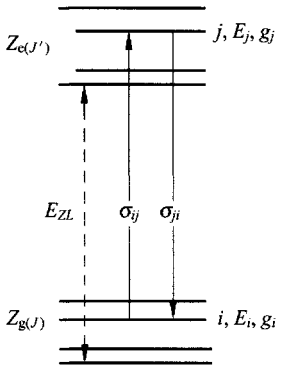


Figure 6.3 Crystal field Stark sublevels i and j of two multiplets g and e with quantum numbers J and J' for a rare-earth ion

$$\sigma_a(\lambda) = \sum_{i,j} f_i \sigma_{ij}(\lambda) \quad \text{and} \quad \sigma_e(\lambda) = \sum_{i,j} f_j \sigma_{ji}(\lambda), \tag{6.23}$$

with

$$f_{i(j)} = \frac{g_{i(j)} \exp(-E_{i(j)}/kT)}{Z_{g(e)}}, \tag{6.24}$$

$E_{i(j)}$ being the energies of the levels i and j measured from the lowest Stark level of each ground and excited multiplet, and

$$Z_{g(e)} = \sum_{i(j)} g_{i(j)} \exp(-E_{i(j)}/kT) \tag{6.25}$$

the partition functions of the ground (g) and excited (e) manifolds.

At this point, several remarks can be made.

(1) If only one pair of Stark sublevels i and j leads to a transition at a particular wavelength λ, then

$$\sigma_a(\lambda) = f_i \sigma_{ij}(\lambda) \quad \text{and} \quad \sigma_e(\lambda) = f_j \sigma_{ji}(\lambda) \tag{6.26}$$

which gives, according to Eq. (6.22)

$$\frac{\sigma_e}{\sigma_a} = \frac{f_j}{f_i}\frac{g_i}{g_j}. \tag{6.27}$$

(2) When none of the positions of the possible Stark sublevels of a given rare-earth ion multiplet of quantum number J can be determined experimentally (especially in the case of amorphous systems), the associated partition function Z_J can be estimated either by using theoretical level positions resulting from more or less sophisticated calculations, or by using the approximate relation

$$Z_J = \frac{N^J_{\text{predicted}}}{N^J_{\text{observed}}}, \tag{6.28}$$

where the predicted number of sublevels $N^J_{\text{predicted}}$ depends on the crystal field splitting of the particular multiplet, knowing that this number cannot exceed $2J+1$ when J is even and $J+1/2$ when J is odd.

(3) $\beta_{\min}$, the minimum fraction of excited ions necessary to reach transparency, is given (assuming $N_g + N_e = N$) when the absorption (gain) coefficient α (g) satisfies (see also in Appendix 6. B)

$$\begin{aligned}\alpha &= \sigma_a N_g - \sigma_e N_e = \sigma(g_j f_i N_g - g_i f_j N_e) \\ &= \sigma[g_j f_i N - (g_j f_i + g_i f_j) N_e] = 0,\end{aligned}$$

thus

$$\beta = \beta_{\min} = \frac{N_e}{N} = \frac{\sigma_a}{\sigma_a + \sigma_e} = \frac{g_j f_i}{g_j f_i + g_i f_j}. \tag{6.29}$$

when $g_i = g_j$, $$\beta = \beta_{\min} = \frac{f_i}{f_i + f_j}. \tag{6.30}$$

Note that the present notation slightly differs from that used in the article by Payne et al. (1992), in which the individual cross sections σ_{ij} and σ_{ji} are both

equal to our σ value.

Introducing the zero-line energy separation E_{ZL} between the lowest Stark components of the ground and excited states (see Fig. 6.3) and writing $E_j - E_i = \frac{hc}{\lambda} - E_{ZL}$, one obtains the well known "reciprocity" relation

$$\sigma_e(\lambda) = \sigma_a(\lambda) \frac{Z_g}{Z_e} \exp\left[\left(E_{ZL} - \frac{hc}{\lambda}\right)\Big/ kT\right]. \tag{6.31}$$

From this relation, it is clear that the stimulated emission cross section spectrum $\sigma_e(\lambda)$ can be easily constructed from the absorption cross section band shape $\sigma_a(\lambda)$, at least when this absorption band shape is not too noisy, especially in the emission wavelength region. This very convenient method was extensively used for Nd^{3+}, Er^{3+}, Tm^{3+}, Ho^{3+} and Yb^{3+} mid-infrared quasi-three-level laser transitions $^4I_{9/2} \leftrightarrow {}^4F_{3/2}$, $^4I_{15/2} \leftrightarrow {}^4I_{13/2}$, $^3H_4 \leftrightarrow {}^3F_4$, $^5I_8 \leftrightarrow {}^5I_7$ and $^2F_{7/2} \leftrightarrow {}^2F_{5/2}$ around 0.94, 1.55, 1.9, 2 and 1.03 μm, respectively. It was also used, however, in the case of four-level laser transitions (Shinn et al., 1989) to determine, for instance, the stimulated emission cross section of Nd: $Y_3Al_5O_{12}$ at 1.064 μm. In this case, the considered transition ($^4I_{11/2} \leftrightarrow {}^4F_{3/2}$) takes place between the $^4F_{3/2}$ metastable level and the high lying (2000 cm^{-1}) ground state multiplet $^4I_{11/2}$, and very weak absorption (absorption coefficients $\alpha \approx 10^{-4} - 10^{-3}$ cm^{-1}) had to be measured.

While the above reciprocity method is probably the most accurate one to determine stimulated emission cross sections, another, known as the Fuchtbauer-Ladenburg (FL) spectroscopic method, is also very convenient, at least to corroborate the previous one. The corresponding equation is

$$\sigma_e^p(\lambda) = \frac{3\lambda^5 \beta_r}{8\pi c \tau_r n_p^2} \frac{I_e^p(\lambda)}{\int \sum_p \lambda I_e^p(\lambda) d\lambda}, \tag{6.32}$$

where I_e^p is for the p-polarized emission intensity, n_p the corresponding refractive index of the host material at the wavelength λ, and β_r the radiative branching ratio of the considered multiplet-multiplet transition for emission from a particular metastable level down to several multiplets ($^4F_{3/2}$ down to levels $^4I_{9/2}$, $^4I_{11/2}$, $^4I_{13/2}$ and $^4I_{15/2}$ for instance in Nd^{3+}).

Although Eq. (6.32) does not require any detailed description of the energy level scale of the active ion, it requires however, accurate determination of the radiative emission lifetime and branching ratio τ_r and β_r, respectively, which has often proved difficult. The most direct way to determine τ_r is to measure the associated fluorescence lifetime τ_f and make the assumption that $\tau_r = \tau_f$, which

applies when the radiative quantum yield $\eta_r = \frac{\tau_f}{\tau_r} = 1$. Unfortunately, there are many situations for which this assumption is not valid and the measured fluorescence decay is shortened or lengthened due to nonradiative multiphonon relaxation, quenching by unwanted impurities and defects, nonradiative energy transfer processes to neighboring active ions of the same species as the emitting one (for high doping concentrations), and reabsorption or trapping effects (in three-level type laser systems). On the other hand, an accurate determination of β_r necessitates very careful calibration of all emission bands associated with the various emission transitions from the considered emitting level to the various multiplets, which may be difficult when broad spectral domains are to be investigated and changes of detectors and monochromators are necessary.

Several remarks can be made concerning Eq. (6.32)

(1) For an uniaxial system with optical axis (ao), emission is π-polarized for a polarization vector $\boldsymbol{E}//(\text{ao})$ and a propagation vector $\boldsymbol{k} \perp (\text{ao})$; σ-polarized for $\boldsymbol{E} \perp (\text{ao})$ and $\boldsymbol{k} \perp (\text{ao})$; α-polarized for $\boldsymbol{E} \perp (\text{ao})$ and $\boldsymbol{k}//(\text{ao})$. Moreover, for electric dipole transitions, α-and σ-polarized spectra are equivalent, whereas in the case of magnetic dipole transitions, α-polarized spectra are equivalent to π's.

(2) For an electric dipole transition and a uniaxial host crystal

$$\sum_p I^p = I^\pi + 2I^\sigma \tag{6.33}$$

and

$$\frac{\beta_r}{\tau_r} = A_r = \frac{1}{3}A_\pi + \frac{2}{3}A_\sigma \tag{6.34}$$

and if the emission is strongly π-polarized ($A_\pi \gg A_\sigma$), then according to Eq. (6.32) the product $\sigma_e^\pi \tau_r$ will be approximately 3 times greater than in the unpolarized case. This means that relatively large emission cross sections are usually found in uniaxial systems that exhibit strongly π-polarized optical transitions. This is the case, for example, in the Nd doped vanadates YVO_4, $GdVO_4$ and $LuVO_4$ (Maunier et al., 2001) with a record π-polarized emission cross section at 1.065 μm of about 13.5×10^{-19} cm^2 at room temperature (see Table 6.1 for a comparison with other well-known Nd doped laser systems).

Table 6.1 Key parameters for the most important Nd doped laser systems

	Nd: $Y_3Al_5O_{12}$	Nd: YLF	Nd: YVO_4
σ_e ($\times 10^{-19}$ cm^2)	2.6	1.8(π) 1.4(σ)	13.5(π)
$\Delta\nu_e$(cm^{-1})	6	13	9
τ_r(μs)	230	520	75
$\sigma_e \cdot \tau_r 10^{-24}$(cm^2 · s)	60	90	100
n	~1.81	~1.48	~2

(3) For biaxial crystals, the absorption and emission spectra are usually measured with light polarized along each of the three optical indicatrix axes, denoted by x, y, and z. In this case, Eq. (6.32) can be used with $p = x$, y, and z. Then, from the values $\sigma_{e,x}$, $\sigma_{e,y}$ and $\sigma_{e,z}$, the stimulated emission cross section can be estimated for any polarization direction. This is especially important in nonlinear crystals, for which the direction of light propagation and polarization must follow some phase-matching conditions to produce some particular radiation (frequency-doubling, frequency-mixing). If the direction of polarization makes an angle θ with the z axis and if its projection in the xy plane makes an angle φ with the x axis, the stimulated emission cross section can be calculated by using the equation (Maunier et al., 2000)

$$\sigma(\theta, \varphi) = \frac{\sigma_x \sigma_y \sigma_z}{[\sigma_x^2 \sigma_y^2 \cos^2(\theta) + \sigma_y^2 \sigma_z^2 \sin^2(\theta) + \sigma_x^2 \sigma_z^2 \sin^2(\varphi) \sin^2(\theta)]^{1/2}}. \tag{6.35}$$

(4) Equation (6.32) also tells us that the emission cross section is inversely proportional to the product of the emission linewidth, radiative lifetime, and square of the refractive index. This means first that larger cross sections will be found, in general, in homogeneouly broadened, single-site systems, for which linewidths are usually narrow, and in materials with a relatively low index of refraction such as fluorides. However, as shown in Table 6.1, this cannot be considered as a rule. The second point concerns laser threshold, stored energy and power extraction efficiency which, according to the previous subsection, should be optimized for large $\sigma_e \cdot \tau_f$ thus for a large $\sigma_e \cdot \tau_r$ product. This means that some compromise will have to be found, and will depend on the considered mode of laser operation. For high-power systems, for example, and within a certain limit, a long fluorescence lifetime will be privileged over a large stimulated emission cross section; indeed, then, more energy can be stored and amplified spontaneous emission (ASE) losses (Lowenthal and Eggleston, 1986) are reduced.

6.2.3.2 Gain and Laser Methods

These methods of course need special experimental arrangements, in particular adequate pump and probe lasers, which are not always available. Moreover, they are more risky since the result of these measurements may not only depend on the experimental conditions and the quality of the materials but also on the complexity of the model used to analyze the data. On the other hand, they remain interesting since they constitute the ultimate step of verification of the spectroscopically derived parameters.

Small-signal gain measurements consist in measuring the amplification of a weak probe laser beam at the considered emission wavelength λ passing through a sample while it is pumped with another laser at some particular absorption

frequency ν_p. For example, assuming that the pump and the probe beam overlap in a region of section S and length l in the direction z, the small-signal gain will be given, with the notation used in the beginning, by

$$G = \frac{F_e^{out}}{F_e^{in}} = \exp \int_0^l [\beta(\sigma_e - \sigma_{esa}) - (1 - \beta)\sigma_a] N dz, \tag{6.36}$$

with $$\beta(z) = \frac{N_e(z)}{N}.$$

In the case of a four-level laser system, thus for $\sigma_a = 0$, Eq. (6.36) becomes

$$G = \frac{F_e^{out}}{F_e^{in}} = \exp \int_0^l \beta(\sigma_e - \sigma_{esa}) N dz \approx \exp(\sigma_e - \sigma_{esa}) \frac{\varepsilon_p I_p}{I_p^{sat}} Nl,$$

thus $$G \approx \exp(\sigma_e - \sigma_{esa}) \frac{\varepsilon_p P_{abs} \tau_f}{S h \nu_p}. \tag{6.37}$$

Therefore, gain measurements can directly provide the effective emission cross section $\sigma_e^{eff} = \sigma_e - \sigma_{esa}$.

An alternative method consists in measuring gain saturation as a function of input energy E_{in} or input fluence F_e^{in}, as given by Eq. (6.10).

The third method consists in using laser threshold and laser slope efficiency measurements. However, as indicated by Eqs. (6.2) and (6.3), the round-trip losses, radiative lifetime, and several efficiency factors must be evaluated, which can be difficult to do with high accuracy. Moreover, as above, ESA can affect the results. A related method was recently proposed (Nostrand and Page, 2001) to overcome these difficulties when the laser threshold pump power P_{th} and laser slope efficiency η_{slope} have been measured for different output mirror transmissions $T \approx -\ln R$. Indeed, Eqs. (6.2) and (6.3) give the relation

$$P_{th} \cdot \eta_{slope} = \frac{h\nu_l S}{2\sigma_e \tau_r \eta_r} T \tag{6.38}$$

and the spectroscopic emission cross section σ_e can be simply derived from a plot of the product $P_{th} \cdot \eta_{slope}$ versus T, provided that the pump and laser beam profiles inside the material, thus S and the emission lifetime $\tau_f = \tau_r \eta_r$, are known.

It is worth noting that the above product is also directly given by the intercept of the laser output versus input power curve with the ordinate axis (see Eq. (6.1)), i.e. for $P_{in} = 0$, since then $P_{out} = -P_{th} \cdot \eta_{slope}$.

6.2.4 Determination of Radiative Lifetimes and Branching Ratios

The radiative emission lifetime and branching ratio τ_r and β_r, respectively, can be determined, alternatively, by using the Judd-Ofelt formalism (Judd, 1962; Ofelt, 1962). This formalism is based on an analysis of room temperature absorption spectra, with the assumption (among others which will not be examined here) that all the Stark sublevels of each multiplet are equally populated. This is a crude assumption. However, the method usually gives rather good results, especially for moderate crystal field splitting and when some precautions are taken, such as eliminating hypersensitive transitions (Gorller and Binnemans, 1998) from the fitting procedure.

The method involves first recording polarized absorption cross section spectra $\sigma_a^p(\lambda)$ around several absorption wavelengths corresponding to a number q of distinct $J \rightarrow J'$ multiplet-to-multiplet transitions. Then these spectra are used to determine the polarization averaged electric-dipole (ED) transition strengths:

$$S_{ED}^{meas}(J \rightarrow J') = \frac{9n}{(n^2+2)^2}\left[\frac{3h(2J+1)}{8\pi^3 e^2 \bar{\lambda}}\int \sigma_a(\lambda)\,d\lambda - nS_{MD}(J \rightarrow J')\right], \tag{6.39}$$

where S_{MD} is the magnetic-dipole (MD) contribution to each inter-multiplet transition, given by

$$S_{MD}(J \rightarrow J') = \left(\frac{h}{4\pi nc}\right)^2 |\langle \Psi_J \| L + 2S \| \Psi_{J'} \rangle|^2. \tag{6.40}$$

Indeed, a particular transition can be both electric- and magnetic-dipole allowed. It is ED allowed when it satisfies the selection rules $\Delta J \leqslant 6$ and $J = 0 \leftrightarrow J' = 0$ or J' odd forbidden, and it can be MD allowed when $\Delta J = 0, \pm 1$. This is not the case, for example, for the $^4I_{9/2} \leftrightarrow {}^4F_{3/2}$ transition of Nd^{3+}, which is strictly ED, but it is for the $^4I_{15/2} \leftrightarrow {}^4I_{13/2}$ transition of Er^{3+}.

It is to be noted here that various polarization averaging procedure can be used. One of them simply consists in directly averaging the measured polarized spectra, i. e., writing

$$\sigma_a = \frac{1}{3}\sum_p \sigma_a^p \quad \text{and} \quad n = \frac{1}{3}\sum_p n_p,$$

thus

$$\sigma_a = \frac{1}{3}(2\sigma_a^\sigma + \sigma_a^\pi) \quad \text{and} \quad n = \frac{1}{3}(2n_\sigma + n_\pi)$$

in the case of a uniaxial system.

Once this is done, the resulting polarization-averaged values S_{ED}^{meas} can be combined with the transition strengths which can be calculated, within the Judd-Ofelt formalism, with the aid of the equation

$$S_{ED}^{calc}(J \rightarrow J') = \sum_{t=2,4,6} \Omega_t |\langle \Psi_J \| U^{(t)} \| \Psi_{J'} \rangle|^2. \qquad (6.41)$$

In this equation, the Ω_t are the so-called Judd-Ofelt (JO) parameters, and they measure the strength of the crystal field at the active ion site. The U_t are electric-dipole tensorial operators, and they are only weakly dependent on the host lattice and have been tabulated for most of the rare earth ions by Carnall et al. (1968). In the same way, the values S_{MD} for the MD transition strengths do not depend significantly on the host matrix and they can be calculated from the free ion wavefunctions (Carnall et al., 1965) or by using the values obtained with the same ion in another material. We give in Table 6.2 the values of the matrix elements $|\langle \Psi_J \| U^{(t)} \| \Psi_{J'} \rangle|^2$ for several spin – allowed transitions involving the ground state. Of course, because of spin-orbit coupling, the selection rules on the L and S quantum numbers, i.e., $\Delta L = 0$ and $\Delta S = 0$, are relaxed, and many other transitions such as $^4I_{9/2} \leftrightarrow {}^2H_{9/2}$ for Nd^{3+}, $^4I_{15/2} \leftrightarrow {}^2K_{15/2}$ for Er^{3+} and $^3H_6 \leftrightarrow {}^1I_6$ for Tm^{3+} have a magnetic-dipole component.

Table 6.2 Magnetic-dipole matrix elements of some optical transitions

Ion	Transition	$\lvert\langle \Psi_J \| L+2S \| \Psi_{J'} \rangle\rvert^2$
Er^{3+}	$^4I_{15/2} \leftrightarrow {}^4I_{13/2}$	19.2
Tm^{3+}	$^3H_6 \leftrightarrow {}^3H_5$	10.8
Ho^{3+}	$^5I_8 \leftrightarrow {}^5I_7$	25.5
Yb^{3+}	$^2F_{7/2} \leftrightarrow {}^2F_{5/2}$	3.4

We then write

$$S_{ED}^{meas} = A \cdot \Omega, \qquad (6.42)$$

where A is a matrix of $U^{(t)}$ matrix elements with q rows (for the q selected transitions) and three columns (because $t = 2, 4, 6$) and Ω is a matrix with one row and three columns for the three Ω_t values. These Ω_t values are then derived by writing (Krupke, 1971)

$$\Omega_0 = (A^T A)^{-1} A^T S_{ED}^{meas}, \qquad (6.43)$$

where A^T is the transposed matrix of A. The "measured" values S_{ED}^{meas} are then compared with the calculated ones:

$$S_{ED}^{calc} = \boldsymbol{A} \cdot \boldsymbol{\Omega}_0 \tag{6.44}$$

and the quality of the fitting procedure is finally checked by calculating the root mean square error

$$RMS = \sqrt{\frac{\sum_{i=1}^{q} [(S_{ED}^{meas})_i - (S_{ED}^{calc})_i]^2}{3 - q}}. \tag{6.45}$$

Finally, based on the above determined JO parameters Ω_t with $t = 2$, 4 and 6, the radiative lifetime $\tau_r(J')$ for the emitting level J' and the branching ratio $\beta_r(J' \rightarrow J)$ for a particular $J' \rightarrow J$ multiplet-to-multiplet transition can be calculated by using the following expressions

$$\frac{1}{\tau_r(J')} = \sum_J A(J' \rightarrow J) \quad \text{and} \quad \beta_r(J' \rightarrow J) = \frac{A(J' \rightarrow J)}{\sum_J A(J' \rightarrow J)}, \tag{6.46}$$

where

$$A(J' \rightarrow J) = A_{ED}(J' \rightarrow J) + A_{MD}(J' \rightarrow J). \tag{6.47}$$

These ED and MD transition probabilities (spontaneous emission Einstein coefficients) are given by

$$A_{ED}(J' \rightarrow J) = \frac{64\pi^4 e^2}{3h(2J' + 1)} \frac{n(n^2 + 2)^2}{9\bar{\lambda}^3} S_{ED}(J \rightarrow J') \tag{6.48}$$

and

$$A_{MD}(J' \rightarrow J) = \frac{64\pi^4 e^2}{3h(2J' + 1)} \frac{n^3}{\bar{\lambda}^3} S_{MD}(J \rightarrow J'). \tag{6.49}$$

It is worth noting that many authors also use oscillator strengths f instead of transition strengths S. In this case, we can write

$$f^{meas} = f_{ED} + f_{MD} = \frac{mc}{\pi e^2} \int \sigma(\nu) \, d\nu \tag{6.50}$$

with

$$f_{MD} = \frac{8\pi^2 mc}{3h(2J + 1)\bar{\lambda}} n S_{MD}(J \rightarrow J')$$

and

$$f_{ED} = \frac{8\pi^2 mc}{3h(2J + 1)\bar{\lambda}} \frac{(n^2 + 2)^2}{9n} S_{ED}(J \rightarrow J'), \tag{6.51}$$

and

$$A(J' \rightarrow J) = \frac{8\pi n^2}{\bar{\lambda}^2} \frac{g_J}{g_{J'}} \int \sigma(\nu)\, d\nu$$

with

$$g_J = 2J + 1 \quad \text{and} \quad g_{J'} = 2J' + 1. \tag{6.52}$$

Thus, when only the ground-state and first excited multiplets (labeled according to their quantum numbers J and J' or g and e) are considered, Eq. (6.52) leads to the well-know relation:

$$\frac{1}{\tau_r} = \frac{8\pi n^2}{\bar{\lambda}^2} \frac{g_J}{g_{J'}} \int \sigma(\nu)\, d\nu. \tag{6.53}$$

At this point, it must be remembered that such radiative lifetime determination bears upon the approximation of equipopulation of the energy levels. As a matter of fact, when the symmetry of the local field environment is low enough to completely lift the degeneracy of the considered multiplets, it is implicitly assumed that $\frac{g_J}{g_{J'}} = \frac{2J+1}{2J'+1}$. Unfortunately, such approximation may lead to some misinterpretation in systems characterized by large crystal-field splitting. For example, it is well known that in three-level laser systems, such as the one associated with the $^4I_{13/2} \rightarrow {}^4I_{15/2}$ emission transition of the Er^{3+} ion for which $\frac{2J'+1}{2J+1} = \frac{14}{16} = 0.87$, the measured fluorescence lifetime τ_f can be longer than the calculated radiative value τ_r, which is theoretically impossible. This discrepancy is generally ascribed to reabsorption effects. In some cases, however, the same result still can be found, even after having experimentally eliminated all possible sources of reabsorption (large dopant concentration, large crystal size, ...). Such behavior has been observed in the past in the case of Er^{3+} in some glasses characterized by large crystal-field splittings (Auzel, 1969); as a matter of fact, a value of $\frac{g_{J'}}{g_J} = 1.36$ has been calculated. This was a very important point, since with this new ratio, the theoretical value for the radiative lifetime had to be multiplied by a correction factor of 1.57, and it was concluded that the fluorescence quantum yield was much less than expected.

It is sometimes interesting to check the value of the $\frac{\beta_r}{\tau_r}$ ratio thus calculated with the aid of the Judd-Ofelt formalism against the one obtained, when it is

possible, by comparing and adjusting the stimulated emission cross section spectra determined by the reciprocity and Fuchtbauer-Ladenburg methods (Eqs. (6.31) and (6.32)). When the Judd-Ofelt value seems to be reliable, which is the case for example when the considered emission transition is the only multiplet-to-multiplet transition originating from the emitting level, and thus $\beta_r = 1$, and when the calculated radiative lifetime τ_r agrees closely with the measured emission lifetime τ_f, such a comparison gives feedback on the assumed concentration of active ions originally used to derive the absorption cross section spectrum.

6.3 UV-visible Laser Sources

6.3.1 Compact and Tunable UV Lasers Based on Ce^{3+} Doped Crystals: Prospects with Other Ions

In the near UV and VUV spectral domain, trivalent rare earth ions such as Ce^{3+}, Pr^{3+}, Nd^{3+}, and Tm^{3+} are characterized by strong electric-dipole allowed interconfigurational $4f^n \rightarrow 4f^{n-1}5d$ absorption transitions (Dieke, 1968) and, depending on the host materials, by intense $4f^{n-1}5d \rightarrow 4f^n$ emission. As a matter of fact, the absorption and stimulated emission cross sections (and thus gain) are very high, of the order of 10^{-18} cm^2, and as illustrated in Figs. 6.4 and 6.5, the spectra have the form of broad bands, the profiles and positions of which vary strongly from one host lattice to another. In Ce^{3+}, as shown in Fig. 6.6a, the observed emission peaks come from transitions to the two spin – orbit levels $^2F_{5/2}$ and $^2F_{7/2}$, which are splitted and eventually mixed by the local crystal field,

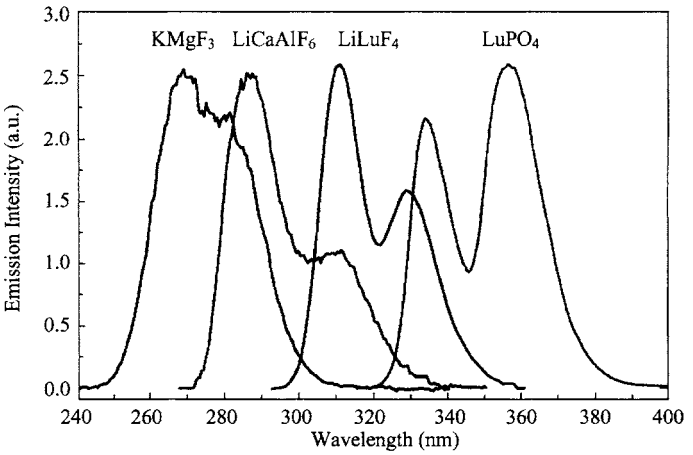


Figure 6.4 Broadband emission of some Ce^{3+} doped crystals

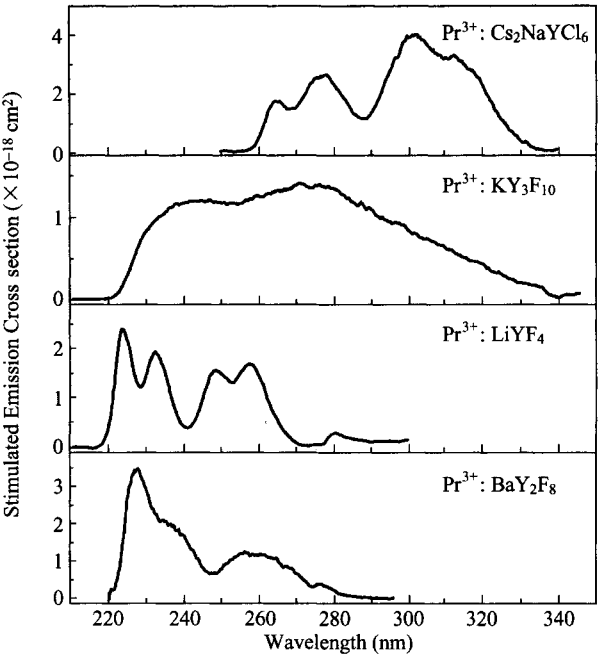


Figure 6.5 Emission spectra of some Pr^{3+} doped crystals

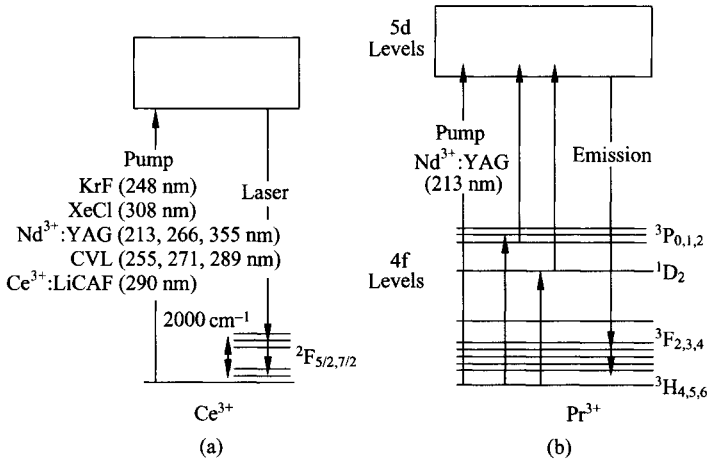


Figure 6.6 Various pumping and emission processes in Ce^{3+} and Pr^{3+} doped systems

depending on the strength and the degree of lattice distortion. In Pr^{3+} (Fig. 6.6b) (but the same observation could be made Nd^{3+} or other rare earth ions), the most important emission peaks correspond to the lowest Stark levels $^3H_{4,5,6}$ and $^3F_{2,3,4}$ of the $4f^2$ ground-state configuration, these levels again being more or less

split by the crystal field and the spin – orbit interaction, with the transitions more or less sensitive to electron-phonon coupling.

In fact, we are dealing with four-levels vibronic laser systems, just as in the case of the transition metal ions (Moncorgé et al., 1994) in Cr^{4+}: $Y_3Al_5O_{12}$ or Ti^{3+}: Al_2O_3, which is the basic material of the now famous Ti: sapphire (Ti: Sa) laser. However, from the point of view of emission cross section σ_e and relative wavelength (or energy) tunability ($\Delta E/E$), rare-earth doped systems are closer to color-center lasers such as KCl: Tl^0. A comparison is shown in Table 6.3 between the values characterizing these various vibronic laser systems and those characterizing the $4f^n \rightarrow 4f^n$ emission transitions involved in the broadband three-levels Er^{3+} (Tm^{3+}) doped glass amplifiers (EDFA and TDFA), and in the four-levels Nd^{3+}: $Y_3Al_5O_{12}$ laser system. The emission cross section of Ce^{3+}: LiCAF ($LiCaAlF_6$), for example, is intermediate between that of KCl: Tl^0 and the recently discovered (Page et al., 1997; Wagner et al., 1999) broad-band infrared laser material Cr^{2+}: ZnSe. Its relative tunability $\Delta E/E$ is of the order of 12%, and thus lower than in Cr: ZnSe and Ti: Sa (the one is exceptionally broad because of a strong Jahn-Teller effect), but much larger than in Er^{3+} or Tm^{3+} doped glass amplifiers, and certainly than in the Nd^{3+}: $Y_3Al_5O_{12}$.

Table 6.3 Typical spectroscopic parameters for broadband solid state vibronic laser systems and comparison with Er^{3+} (or Tm^{3+}) doped glass fibers (EDFA, TDFA) and Nd^{3+}: $Y_3Al_5O_{12}$

Vibronic systems	λ (nm)	σ_{em} (cm^2) τ_f	$\Delta E/E$
Ce^{3+}: $LiCaAlF_6$	280 – 315	6.8×10^{-18}	12%
(Ce: LiCAF)		50 ns	
Ti^{3+}: Al_2O_3	700 – 1000	3×10^{-19}	35%
(Ti: Sa)		3.2 μs	(Jahn-Teller effect)
KCl: Tl^0	1400 – 1600	1.3×10^{-17}	14%
		1.6 μs	
Cr^{2+}: ZnSe	2200 – 2900	8×10^{-19}	27%
		8 μs	
EDFA	1500 – 1600	qqs 10^{-21}	6% – 7%
TDFA	1400 – 1500	qqs ms	
Nd^{3+}: $Y_3Al_5O_{12}$	1064	2.7×10^{-19}	0.06 %
		230 μs	

The only real drawback of systems such as Ce: LiCAF are their short emission lifetime. This implies a high pump saturation intensity $I_p^{sat} \approx$ 3000 kW/cm^2 (compared with $\approx$ 600 kW/cm^2 in Ti: Sa and $\approx$ 10 kW/cm^2 in Nd^{3+}: $Y_3Al_5O_{12}$) and a low energy storage capacity. Thus, it will be difficult, and perhaps impossible, to operate such a Ce doped laser system in CW mode.

However, it works perfectly under short-pulse excitation pumping because of its low pump saturation fluence $F_p^{sat} \approx 150$ mJ/cm^2 (compared with ≈ 1.8 J/cm^2 in Ti: Sa and ≈ 4 J/cm^2 in $Nd^{3+}: Y_3Al_5O_{12}$).

These rare earth based broadband UV laser systems are thus mainly attractive because different types of excitation pumping are possible, and laser emission tunability can be achieved very easily with high efficiency and excellent beam quality in a wavelength domain not covered by any other compact, simple laser sources.

As shown in Fig. 6.6, the energy levels of the $4f^{n-1}5d$ excited electronic configuration are usually excited directly with the aid of UV laser pump sources such as KrF (248 nm), XeCl (308 nm), frequency-tripled, quadrupled or quintupled $Nd^{3+}: Y_3Al_5O_{12}$ (355, 266, and 213 nm, respectively), frequency-doubled or frequency-mixed copper-vapor laser CVL (255, 271, and 289 nm, respectively), or other lasers of the same type, such as a Ce^{3+}: LiCAF laser to pump a Ce^{3+}: LLF ($LiLuF_4$) laser at 290 nm, for example. However, as shown in Fig. 6.6, for ions like Pr^{3+}, for which $4f^n (n=2)$ energy levels extend up into the green and blue spectral region, it is possible to pump by steps using visible pump photons, either via $^3P_{0,1,2}$ or $^1D_2$ levels, the former process being the most efficient because of transition selection rules.

As to the laser emission aspect, it is worth noting here that among all Ce^{3+} or Pr^{3+} doped materials investigated so far, mostly in fact in search for new scintillators, very few give rise to laser action. The first were LaF_3 (Ehrlich et al., 1979) and $LiYF_4$ (YLF) (Ehrlich et al., 1980), then the colquirites $LiCaAlF_6$ (LiCAF) and $LiSrAlF_6$ (LiSAF) (Dubinskii et al., 1993; Marshall et al., 1994; Pinto et al., 1995) and more recently $LiLuF_4$ (LLF) (Sarukura et al., 1995; Rambaldi et al., 1997; McGonigle et al., 1999; Laroche et al., 2000a, 2001a), all being doped with Ce^{3+}. Apart from these systems, UV laser action was only reported in Nd: LaF_3 around 172 nm (Waynant, 1985; Dubinskii, 1992), knowing that, however, pumping was achieved with an F2 molecular laser at 157 nm and that laser action was never reproduced, which still makes the result quite questionable. If we are confident of this result, Ce: LaF_3 is the laser material emitting at the shortest laser wavelength ever obtained with a solid-state laser. No other rare-earth ions in any crystal host ever lased so far, and only one or two new Ce^{3+} doped crystals (see Fig. 6.4), exhibited some positive small-signal gain, i.e., $LuPO_4$ and $KMgF_3$ (Laroche et al., 2001b, c).

This state of the art is rather disappointing, and can be explained first by the fact that not all the materials considered were studied under equivalent conditions. Indeed, probably very few were of the hightest optical quality, which is required for laser action in the UV spectral domain. Consequently, many systems could not lase or exhibit gain under strong UV laser pumping (typically >0.2 J/cm^2) because of the formation of transitory or permanent color centers coming from crystal impurities or defects. These color centers act as traps for optical electrons excited into the conduction band (CB) of the host

material either directly or via ESA in the lower-lying emitting state of the 5d configuration. This is the case, for example, in Ce^{3+} doped $LiCaAlF_6$ when the crystals are not co-doped with monovalent Na^+ for charge compensation.

As discussed extensively in a previous review article (Moncorgé, 2001) in the case of Pr^{3+}, This means that the search for new UV laser crystals must take several parameters into account: (1) crystal growth parameters such as purity of the raw materials, optical, and structural quality of the crystals, and co-doping; (2) spectroscopic parameters such as the fluorescence quantum efficiency (since it strongly depends on the position of the 4f 5d levels (Dorenbos, 2000; Bettinelli and Moncorgé, 2001) above the $4f^2$ levels $^3P_{0,1,2}$), the positions and cross sections of the ESA bands $4f^2 \rightarrow 4f\ 5d$ and $4f\ 5d \rightarrow CB$, and the position of the $4f^2$ energy levels of the rare-earth ion within the bandgap.

Pump-probe experiments, for example, were carried out recently (Laroche, 1999, 2000) to record polarized ESA cross-section spectra corresponding to the transitions $^3P_{0,1,2}$, $^1I_6 \rightarrow 4f\ 5d$ and $^1D_2 \rightarrow 4f\ 5d$. The data were first compared with theoretical *ab initio* calculations to determine the nature of the energy levels of the 4f 5d electronic configuration, more particularly of the lowest emitting ones, since they govern the radiative emission probability of the emission transitions, and thus the value of the stimulated emission cross sections. The data were then used within appropriate models to assess whether two-step excitation pumping could lead to laser operation. The results showed for example in the case of Pr^{3+}: YLF that the splitting of the energy levels of the 4f 5d configuration is dominated, as expected, by the crystal-field coupling of the 5d electron, but also to a noticeable extent by the spin – orbit coupling of the 4f electron and the Coulombic repulsion of the two electrons, the former of these two interactions being somewhat more efficient than the latter in the low-energy part of the 4f 5d configuration.

On the other hand, it has been demonstrated theoretically (Laroche, 1999), for example in the case of Pr^{3+}: KY_3F_{10} (KYF), that 20% gain could be obtained around 260 nm by using excitation laser pulses of the order of 1 mJ around 445 and 355 nm, which correspond to measured wavelengths for the $^3H_6 \rightarrow {}^3P_{0,1,2}$ and $^3P_{0,1,2} \rightarrow 4f\ 5d$ ground state and excited state absorption transitions. This was achieved, however, by neglecting any ESA starting from the 4f 5d emitting level up into the conduction band, and any parasitic absorption due to the formation of transitory or permanent color centers, which was not realistic in the case of Pr^{3+}: KYF. Indeed, this system is very sensitive to UV radiation and solarizes even at moderate pump energies. However, this result is not hopeless, since it was recently discovered (Laroche et al., 2001a) that by co-doping the crystals with an appropriate amount of Yb^{3+} (see Fig. 6.7), the color center absorption bands could be reduced very significantly. Work is still in progress to understand the mechanisms involved and take advantage of them.

In the end, it is worth noting here that up to now the best laser performance was obtained first with Ce^{3+}: LiCAF (and LiSAF), with laser slope efficiencies

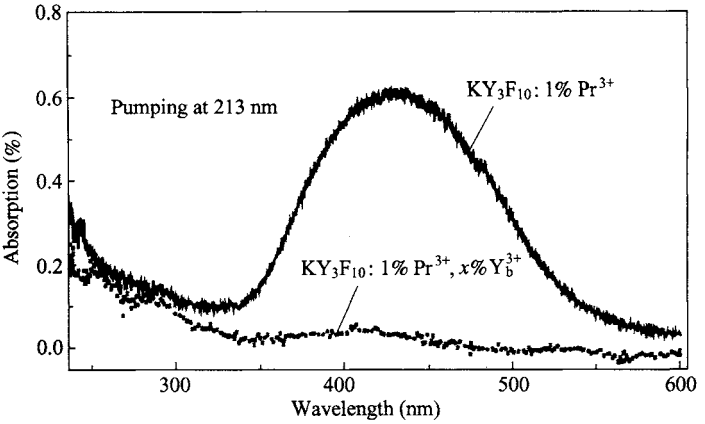


Figure 6.7 Reducing effect of Yb^{3+} codopants on color center formation in Pr^{3+}: KY_3F_{10} crystals (according to Laroche)

of the order of 35% −40% (Marshall et al., 1996) and Ce^{3+}: LLF (Rambaldi et al., 1997; McGonigle et al., 1999, 2001; Laroche et al., 2000a, 2002) with efficiencies of about 45% − 50%. The latter system is certainly the most interesting, since $LiLuF_4$ crystals are easier to grow, can support large laser fluences, and are less prone to color center formation. For example, neither optical damage nor solarisation effects were observed by pumping the crystals with the radiation at 248 nm of a KrF excimer laser with laser pulses up to 4 J/cm^2, which is remarkable (Laroche, 2001c). Thanks to several absorption bands around 210, 245 and 290 nm (Rambaldi et al., 1997), this laser system could be pumped by different laser pump sources: frequency-quintupled Nd^{3+}: YAG at 213 nm (Ohtake et al., 1999), KrF excimer laser at 248 nm (Sarukura et al., 1995), frequency-doubled Copper-Vapor Laser (CVL) at 289 nm (McGonigle et al., 1999) and Ce^{3+}: LiSAF at 290 nm (Rambaldi et al., 1997; Laroche et al., 2000a). Presently, the latter solution is certainly the most compact and efficient one. As shown in Fig. 6. 8, it consists of two laser resonators with intracavity prisms, one Ce: LiSAF laser resonator tuned to 290 nm and pumped by a very compact diode-pumped and frequency-quadrupled Nd^{3+}: $Y_3Al_5O_{12}$ at 266 nm (Thomson-CsF laser), followed by a Ce^{3+}: $LiLuF_4$ resonator (Laroche, 2000a, 2001a and 2001c). With this setup, the wavelength of the Ce: LLF laser could be tuned continuously from 305 to 333 nm with excellent beam quality.

6.3.2 Lasers Based on Nd^{3+} and Yb^{3+} Doped Nonlinear Crystals

Rare-earth doped nonlinear crystals operating more particularly in the visible and the near UV spectral domain offer an interesting alternative to up-conversion lasers and frequency doubling of other solid state lasers. Indeed, when these crystals are doped

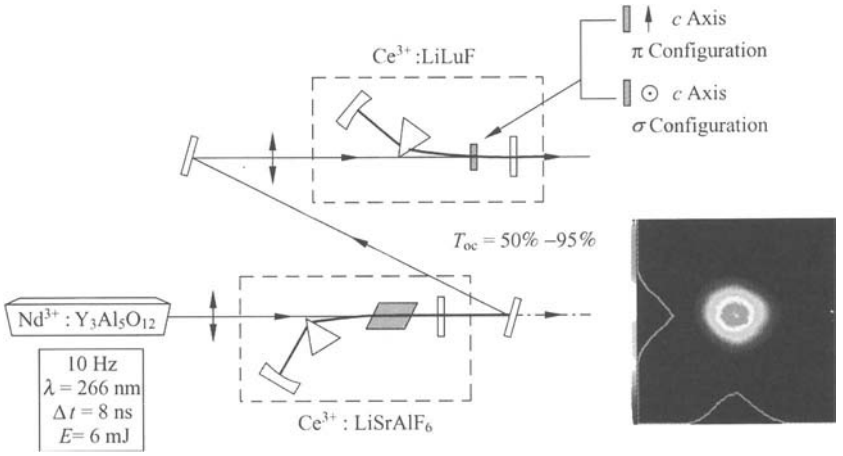


Figure 6.8 Ce^{3+} : $LiLuF_4$ laser pumped by a Ce^{3+} : $LiSrAlF_6$ laser (itself pumped by a diode-pumped frequency-quadrupled Nd^{3+} : $Y_3Al_5O_{12}$) (according to Laroche et al.)

with lasing ions such as Nd^{3+} or Yb^{3+}, when some temperature and angular "phase-matching" conditions are met, and when they are located inside appropriate optical resonators, part of the circulating infrared laser power can be directly converted into another frequency in the visible domain by so-called self-frequency doubling (SFD) and self-frequency summing (SFS) mechanisms (see Fig. 6.9). Compared with laser systems in which the laser medium and the nonlinear crystal are separate elements and the latter is located either inside or outside the laser cavity, laser systems based on rare-earth doped nonlinear crystals, in which both laser action and nonlinear conversion occur simultaneously, lead to more compact and simple, and thus ultimately less expensive devices.

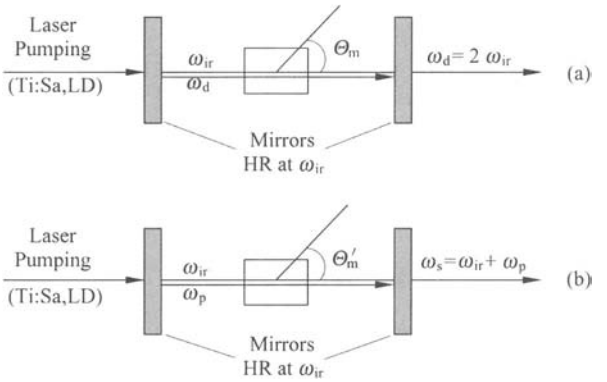


Figure 6.9 Laser setups for the production of green and blue radiation via (a) self-frequency doubling, and (b) self-frequency summing, in Nd^{3+} and Yb^{3+} doped nonlinear crystals

Self-frequency doubling and summing are realized with nonlinear crystals having large second-order nonlinear susceptibility $\chi^{(2)}$. Up to now, most crystals were doped with Nd^{3+} ions and were lased CW around the fundamental laser wavelength of 1.06 μm. The laser materials thus operate as true four-level laser systems with the lowest possible laser thresholds. Some of them, however, were also doped with Yb^{3+} ions and operated around 1.04 μm. In this case, the laser materials operate as quasi three-level laser systems, which is not the best solution in terms of laser threshold, but offers other possibilities because of the broadband emission of the Yb^{3+} ions, such as wavelength tunability and ultrashort-pulse generation.

Concerning first self-frequency doubling and infrared-to-green laser conversion, the best materials are those for which the birefringent phase-matching condition (Dmitriev et al., 1991) $n_e^{\omega} = n_o^{2\omega}$ for "positive" and $n_e^{2\omega} = n_o^{\omega}$ for "negative" uniaxial crystals, also said critical phase-matching condition, can be realized at a reasonable temperature and for a fundamental laser wavelength $\lambda_{ir} = \frac{2\pi c}{\omega_{ir}}$ associated with a reasonably high emission cross section. Moreover, this phase-matching condition corresponds to fundamental and second-harmonic waves with frequencies ω_{ir} and $\omega_d = 2\omega_{ir}$ traveling in the same direction, which is usually specified by the polar angles θ_m (with respect to the axis $z = C$) and φ_r (with respect to x in the plane perpendicular to the z axis). And, for efficient frequency doubling, this direction should be associated with a large effective nonlinear coefficient (d_{eff}). Indeed, the infrared nonlinear loss factor k_{SFD}, which appears in the loss term $-k_{SFD} \cdot q^2$ (q being the infrared photon number in each cavity mode) and accounts for self-frequency doubling, is proportional to d_{eff}^2 according to the expression (Bartschke, 1997)

$$k_{SFD} = a \frac{d_{eff}^2}{\lambda_{ir}^4 n_{\omega}^4}, \tag{6.54}$$

where a is a proportionality constant that only depends on the cavity parameters (length of the resonator, number of oscillating modes, spatial overlap between pump and cavity modes).

As a matter of fact, because of these requirements, the crystals which have led so far to the best laser results are essentially Nd^{3+} doped $LiNbO_3$, eventually co-doped with MgO or Sc_2O_3 to reduce photorefractive damage (Fan et al., 1986; Lallier et al., 1991; Li et al., 1993; Yamamoto et al., 1994; Burlot et al., 1996), $LaBGeO_5$ (Capmany et al., 1998) $YAl_3(BO_3)_4$ (YAB) (Amano and Mochizuki, 1991; Hemmati, 1992; Qiu and Fan, 1993; Bartschke et al., 1997), $CaGd_4(BO_3)_3O$ (GdCOB) (Augé et al., 1999; Zhang, 1999) and $CaY_4(BO_3)_3O$ (YCOB) (Eichenholtz et al., 1999). Some of their nonlinear and spectroscopic properties are reported in Table 6.4.

Table 6. 4 Spectroscopic and nonlinear parameters of the main self-frequency doublers (GdCOB is a biaxial crystal, and θ is specified here with respect to z as defined by Aka et al., 1997)

Material	λ_{ir}(nm) polarization	σ_{ir} (10^{-20} cm^2)	τ_f(μs)	Type and phase-matching angles	d_{eff} (pm/V)
Nd: $LiNbO_3$	1093.5	7	95	Type I negative	6
	σ			$\theta_m \approx 90°$	
Nd: $YAl_3(BO_3)_4$	1064	20	60	Type I negative	1.4
(Nd: YAB)	σ			$\theta_m \approx 33°, \varphi_r = 0°$	
Nd: $CaGd_4(BO_3)_3O$	1061	1.9	80 – 90 for	Type I	0.5
(Nd: GdCOB)	σ		3% – 4% Nd	$\theta = 0°, \varphi = 46°$	

In Nd^{3+}: $LiNbO_3$, for example, it is possible to meet the phase-matching requirement at the fundamental laser wavelength λ_{ir} = 1093 nm for waves propagating, as indicated in the Table 6.4, perpendicular to the main crystallographic axis c ($\theta_m = 90°$ and $\varphi_r = 0°$), provided that the crystal is maintained at a temperature of about 80 ℃ (145 ℃ in the case of MgO: $LiNbO_3$ and 80 ℃ in the case of Sc_2O_3: $LiNbO_3$ (Burlot et al., 1997)). As $LiNbO_3$ is a uniaxial negative crystal, the fundamental ordinary wave is then σ polarized ($E \perp c$), whereas the resulting frequency-doubled green radiation is π polarized. This configuration is associated with what is called noncritical phase-matching which means that it is less sensitive to angular variations. On the other hand, it is not possible to find with Nd^{3+}: $LiTaO_3$ a propagation direction for which the phase-matching condition $n_e^{\omega} = n_o^{2\omega}$ (positive crystal) holds at the fundamental laser wavelength λ_{ir} = 1091 nm around room temperature. In this case, however, it is possible to play with the ferroelectric properties of the material to create alternating ferrroelectric domains (Fejer et al., 1992), allowing one to relax the above phase-matching condition and work in what is called a quasi-phase matching configuration. Many laser devices based on such "periodically poled" doped or undoped $LiTaO_3$ and $LiNbO_3$ crystals called PPLT and PPLN have appeared in recent years (Capmany et al., 1999; Petrov et al., 2000; Capmany et al., 2000).

The best laser performance was obtained with Nd^{3+}: YAB (NYAB) (Bartschke et al., 1997) with a laser emission at about 531 nm, an incident pump power at laser threshold (as given by the extrapolation of the laser curve) of about 225 mW, and a laser slope efficiency of nearly 25%, which is quite remarkable. However, crystal growth of this material (flux grown crystals) remains a problem and there are no negligible ground state and excited state absorption losses. This is why this crystal has largely been snpplanted by the other borates Nd^{3+}: GdCOB and YCOB (Mougel et al., 1999; Augé et al., 1999; Zhang, 1999; Eichenholtz et al., 1999; Hammons et al., 2000), in spite of lower emission cross sections and stronger nonradiative relaxation (Mougel et

al., 1997; Maunier et al., 2000). Indeed, these crystals can be grown via the Czochralski technique, and large and excellent optical quality crystals have already been obtained.

Except for Yb^{3+} doped MgO: $LiNbO_3$ with 60 mW of green laser emission, no other Yb^{3+} doped materials have led so far to substantial laser performance. This is mostly due, as mentioned above, to the three-level laser nature of the lasing ion.

Concerning intracavity self-frequency summing, there are even less data. Blue laser emission was recently obtained in Nd: YAB (Brenier et al., 1999) and Nd: GdCOB (Mougel, 1999) by pumping the crystal around 750 nm. In Nd: YAB for example, this consisted in frequency summing the pump radiation with the 1062 nm laser emission of Nd^{3+} in this material. Laser efficiency was very low, mainly due to the fact that both strong and moderate absorption at the pump wavelength are needed at the same time, both to reach infrared laser threshold and to keep the interaction length of the three interacting waves at ω_p, ω_{ir} and $\omega_s = \omega_p + \omega_{ir}$ as long as possible. Nevertheless, the results remain interesting, since they show the possibility of tuning the laser wavelength over several nm around 440 nm just by tuning the wavelength of the pump laser, which may be of some interest for particular applications.

6.4 Near- and Mid-infrared Laser Sources

6.4.1 High-power and Ultrafast Lasers Based on Yb^{3+} Doped Materials

The usefulness of the Yb^{3+} ion as a laser ion has really become evident only in recent years with the advent and development of high-power InGaAs laser diodes operating around 950 nm (DeLoach et al., 1993). Indeed, Yb^{3+} has only one excited $4f^{13}$ manifold $^2F_{5/2}$ in this wavelength domain, the next higher one being located at much higher energy in the near UV and belonging to the $4f^{12}5d$ excited state configuration. it was therefore difficult to pump this laser system efficiently with broadband light sources such as flash-lamps. Moreover, because of the reduced crystal field splitting of the ground state manifold $^2F_{7/2}$, less than 1000 cm^{-1}, Yb^{3+} is essentially a quasi three-level laser system with a finite population in the lower laser level which strongly depends on the heat generated in the material by the excitation pump light. Thirdly, the infrared emission of the Yb^{3+} doped materials is generally characterized by stimulated emission cross sections around 10 times smaller than they are in Nd^{3+} in the same host. Thus Yb^{3+} solid-state lasers often required cryogenic or thermoelectric cooling and were characterized by relatively high laser thresholds. In the end, since the typical emission wavelength of 1.03 μm of these Yb^{3+} doped materials was very close to the 1.06 μm offered by the low threshold four-level Nd^{3+} laser systems,

the Yb^{3+} ion was not very attractive.

As soon as high-power InGaAs laser diodes became commercially available, everything changed, since several of the former drawbacks turned into advantages.

Firstly, precisely because of the similar emission wavelength domains, Yb^{3+} lasers can directly benefit from the know-how acquired, for example, in the field of reflective and antireflective coatings developed for high-power Nd^{3+} lasers, which is really necessary to compete with a laser system such as Nd^{3+}: $Y_3Al_5O_{12}$.

Moreover, their simplified electronic structure, with no higher-lying excited states other than the emitting one, not only make it possible to avoid losses due to ESA at the pump and laser wavelengths but also losses due to up-conversion as well as cross-relaxation energy transfers at high dopant concentrations and high pump levels (as is the case with Nd^{3+} and many other rare-earth ions). This facilitates working with more heavily doped materials, insofat these materials can be prepared with good enough structural and optical quality, thus limiting the thickness of laser samples while being able to store as much energy. It is important to cool the materials more efficiently and to keep the thermal population of the terminal level of the laser transition, and thus the laser threshold, as low as possible, and this is easier to realize when the laser samples have the form of thin discs (Giesen et al., 1996).

This quasi-three level structure, of course, also yields a much higher quantum conversion factor $\eta_q = \frac{h\nu_l}{h\nu_p} = \frac{\lambda_p}{\lambda_l}$, with a value of the order of 90% ($\lambda_l \approx 1030$ nm, $\lambda_p = 950$ nm) as opposed to 75% ($\lambda_l = 1060$ nm, $\lambda_p = 800$ nm) in the case of Nd^{3+}. According to Eq. (6.2), this yields much higher laser slope efficiencies, typically of the order of 75% instead of 60%. Additionally, most of the pump power is used to excite the active ions, and less is absorbed by the host lattice, so the thermal loading of the sample is limited.

On the other hand, it has long been known that Yb^{3+} ions also give rise to significantly broader optical transitions than most of the other rare-earth ions, it is due to electron – phonon coupling (Hellwege, 1941; Ellens, 1997). Indeed, the strength of the electron – phonon interaction in rare-earth doped materials not only depends on the host matrix but also on the particular ion and optical transition under consideration. As a matter of fact, a simple model can be used (Guyot, 2001) to show that the electron – phonon coupling and the resulting vibronic effects are maximum at both ends of the series (Ce^{3+}, Pr^{3+} and Tm^{3+}, Yb^{3+}) and least at the center (Eu^{3+}, Gd^{3+}, Tb^{3+}), and that three factors can be involved (in order of significance): shielding of 4f electrons, lanthanide contraction and sensitivity of energy levels to crystal field strength. This trend is observed (1) for the average linewidth of the spectral transitions, when they are recorded, for example, at 77 K; (2) for the average relative intensity of the vibrational satellites (which may sometimes lead to confusion in the assignment of zero-phonon and vibronic lines, thus to misinterpretation of the observed

energy levels); and (3) for the average energy distance between contiguous Stark components within a given multiplet.

So, without further pursuing this spectroscopic aspect, three important advantages can be derived from broad optical transitions for laser operation: (1) the possibility of using broadband laser diodes without thermoelectric wavelength control, which saves energy and helps to build more compact and less expensive systems; (2) the possibility of tuning the laser wavelength, which may be of interest for certain applications; and (3) the possibility of generating ultra-short laser pulses, their duration $\Delta\tau$ being linked to the gain bandwidth $\Delta\nu$ of the associated transition by the well-known relation (Lowdernilk, 1979) $\Delta\nu \cdot \Delta\tau \geqslant K$, with $K = 1$ for a rectangular bandshape and $K \approx 0.22 - 0.44$ for a Lorentzian, Gaussian, or hyperbolic secant squared line.

In the end, since the stimulated emission cross sections are usually smaller than in the case of Nd^{3+}, the emission lifetimes are longer, with values of the order of 1 to 2 ms instead of 250 – 500 μs. Therefore, such long lifetimes can be used advantageously to store more energy, and thus to produce higher average or peak output powers.

For example, laser wavelength can be tuned between 1020 and 1090 nm with a CW TiSa-pumped Yb^{3+}: YCOB laser (Shah et al., 1999) and between 1040 and 1090 nm with a CW diode-pumped Yb^{3+}: GdCOB (Augé et al., 1999), and 90-fs pulsescan be generated from a mode-locked laser (Druon et al., 2000). These Yb^{3+} doped borates are indeed broadband emitting systems with properties intermediate between Yb^{3+} doped glasses (Honninger et al., 1998) and crystals (DeLoach et al., 1993) in terms of spectral bandwidth and emission cross section. In fact, with a gain bandwidth of the order of 75 nm, it should be possible to generate short pulses of less than 20 fs duration.

On the other hand, more than 1 kW CW output power could be obtained from a diode-pumped Yb^{3+}: $Y_3Al_5O_{12}$ laser (Hones et al., 2000).

Nevertheless, there still remain some problems to be solved, now mainly related to the laser thresholds and the high average or peak powers involved, in terms of thermal loading and optical quality of the laser samples. Indeed, laser thresholds remain higher than in Nd^{3+} systems and the best crystal hosts remain to be found. This is the reason why the search for new Yb^{3+} doped materials has motivated and still motivates so many groups, first in the USA, particularly at the Lawrence Livermore National Laboratory (DeLoach et al., 1993; Payne et al., 1994) with fluoroapatite crystals $Ca_5(PO_4)F$ and $Sr_5(PO_4)F$ (CFAP and SFAP, respectively), then in the USA and Europe with Yb^{3+}: $Y_3Al_5O_{12}$ and the famous high-power laser disk configuration developed in Germany (Giesen et al., 1997), and more recently in France, the USA, and Belarus with nonlinear borates (Augé et al., 1999; Shah et al., 1999; Druon et al., 2000) $CaGd_4(BO_3)_3O$ and $CaY_4(BO_3)_3O$ (GdCOB and YCOB respectively), silicates (Li, 1992; Haumesser et al., 2001) such as Y_2SiO_5 (YSO) and tunsgstates (Kuleshov et al., 1997) $KGd(WO_4)_2$ and $KY(WO_4)_2$ (KGW and KYW respectively). As

an illustration, we show in Fig. 6.10, the *E//X* polarized absorption and emission spectra of $Yb^{3+}: Y_2SiO_5$.

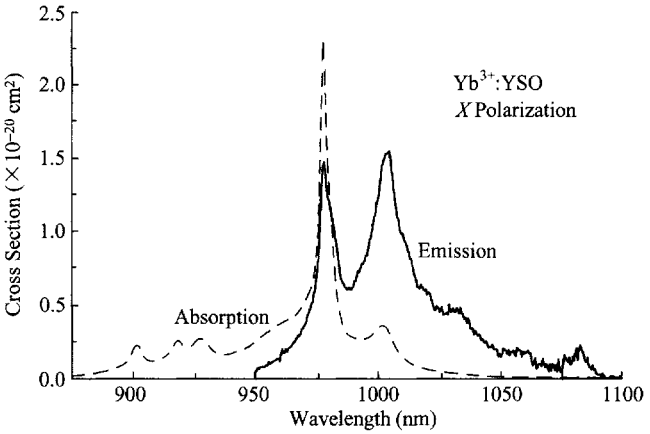


Figure 6.10 Absorption and emission cross section spectra of $Yb^{3+}: Y_2SiO_5$ (according to Haumesser et al.)

Many efforts have been dedicated, for example, to detemining the parameters or a figure of merit which would be most appropriate to choosing the best ytterbium laser. First proposed (DeLoach, 1993) was, Q-switched oscillators and nanosecond pulse amplifiers, a log/log plot of the stimulated emission cross section σ_e versus the minimum pump intensity I_p^{min}, as suggested at the beginning in Section 6.2. Indeed, both a low I_p^{min} and a high σ_e are suited to more easily reaching population inversion and efficiently converting the stored energy into laser power. According to this plot, Yb^{3+}: CFAP and SFAP appear as the most favorable systems with stimulated emission cross sections of the order of 7×10^{-20} cm^2 and minimum pump intensities of less than 0.1 kW/cm^2. In particular, they appear much more favorable than $Yb^{3+}: Y_3Al_5O_{12}$, with σ_e and I_{min}^p values of 2×10^{-20} cm^2 and 1.5 kW/cm^2. However, this does not reflect reality, since $Yb^{3+}: Y_3Al_5O_{12}$ as well as several other materials, Yb^{3+}: KGW and Yb^{3+}: KYW more particularly, already exhibited the same kind of laser performance with laser slope efficiencies exceeding 70% and CW output powers, as mentioned above in the case of $Yb^{3+}: Y_3Al_5O_{12}$, exceeding 1 kW (Hones et al., 2000). We give in Table 6.5 some of the key parameters for these different systems.

Thus, recently, a more complete theoretical analysis (Bernier, 2001), closer to the real experimental CW laser conditions, was developed by taking into account the saturation of the pump because of the unusually long emission lifetimes of these Yb^{3+} doped systems, the stimulated emission at the pump wavelength, the variation of the pump and cavity laser waists along the propagation direction (assuming longitudinal pumping), and the variation of the

Table 6.5 Key parameters for most important Yb^{3+} doped laser materials

Material	τ_f (ms)	β_{min}	I_p^{min} (W/cm^2)	σ_a ($\times 10^{-20}$ cm^2)	σ_e ($\times 10^{-20}$ cm^2)	ΔE (cm^{-1})	κ (W/m · ℃)
KYW	0.6	0.09	234	0.3	3	407	3.8
GdCOB	2.7	0.06	522	0.023	0.36	556	2
SFAP	1.26	0.043	172	0.4	7.3	603	2
YSO	1.04	0.047	620	0.016	0.33	617	4.5
YAG	1.08	0.055	1540	0.15	2	628	10
Y_2O_3	0.85	0.066	660	0.06	0.85	—	13

laser fluence along this direction. Then the calculated laser performance of different systems was evaluated (1) by assuming the same pump power for all systems, (2) by choosing high Yb^{3+} dopant concentrations for crystals having rare-earth crystallographic substitutional sites (like YAG) and low concentrations for those (like CFAP and SFAP) having a low segregation coefficient and (3) by using for each system the optimal crystal length and output mirror transmission. According to this approach, when a linear plot of the laser output yield $\frac{P_{out}}{P_{in}}$ versus the laser slope efficiency η_{slope} is made, Yb^{3+}: KGW and Yb^{3+}: KYW have the highest potential, Yb^{3+}: YAG has the lowest, and Yb^{3+}: SFAP, CFAP, GdCOB and YCOB correspond to an intermediate situation.

This analysis clearly shows that the stimulated emission cross section, at least within the range of values considered ($0.2 \times 10^{-20} - 7 \times 10^{-20}$ cm^2), cannot really be considered a figure of merit, as was done previously (DeLoach et al., 1993). On the other hand, the minimum pump intensity I_p^{min} and the highest fraction of the stored energy that can be extracted, denoted by f_{max}, which is related with the maximum output yield, seem to be meaningful.

Several other parameters, of course, must be considered, the most important probably being the ease of obtaining good optical quality and large crystals, and from this point of view crystals like YAG and YSO are presently the most attractive, at least for high-power applications. In addition, these materials have much better thermal conductivity than other tungstates and borates, which means in particular much-reduced sensitivity of laser performance at high pump power, and thus under high thermal loading. On the other hand, however, for the generation of ultra-short pulses, the tungstates and borates such as KGW and GdCOB have some advantages. Their absorption and emission spectra are broader and their nonlinear properties can be used to produce different types of harmonics via self-frequency doubling and mixing (Brenier, 2001).

The sensitivity of laser performance to thermal loading can be included by considering the temperature variation of β_{min} resulting from the same absorbed pump power per unit volume. Indeed, because of the difference between pump

and laser photon energies (quantum defect) there is nonradiative relaxation, and thus conversion of optical excitation into heat, from the pump band to the upper metastable emitting level, and from the lower laser level to the ground state. According to Fan (1993), the resulting steady-state temperature rise above the ambient temperature ΔT is related to the fraction η_h of absorbed pump power P_{abs} converted into heat:

$$\eta_h = \frac{mc_p \Delta T}{\tau P_{abs}}, \tag{6.55}$$

where τ is the thermal time constant, m the mass of the sample, and c_p its heat capacity per unit mass, related to the thermal conductivity κ by (Cowan, 1965)

$$\kappa = \rho c_p D, \tag{6.56}$$

where $\rho = \frac{m}{V}$ is the density and D the thermal diffusivity.

Thus, ΔT can be expressed as

$$\Delta T = \frac{\eta_h P_{abs} \tau D}{\kappa V}. \tag{6.57}$$

Using Eqs. (6.24) and (6.30), it is easy to demonstrate that

$$\frac{d\beta_{min}}{dT} = \frac{\Delta E}{kT^2} \beta_{min}(1 - \beta_{min}) \tag{6.58}$$

with

$$\Delta E = E_{ZL} - \frac{hc}{\lambda_e}.$$

Thus, starting from about the same nonradiative fractional loss $\eta_h P_{abs}$ for all systems considered, and the same coefficient $\tau D/V$, one obtains

$$\Delta\beta_{min} \approx \chi \frac{\beta_{min}(1 - \beta_{min})}{\kappa}, \tag{6.59}$$

where χ is a proportionality constant. Of course, this expression is not quite rigorous since τD may vary from one system to another, but it surely indicates that the sensitivity of β_{min} to temperature variations should be inversely proportional to the thermal conductivity of the material. To illustrate that particular aspect, Fig. 6.11 shows $\Delta\beta_{min}$ in units of χ and I_p^{min} for the main systems considered above. According to this diagram, considering that Y_2O_3 (because of its high melting temperature of about 2500℃) is very difficult to grow with a good enough optical quality and in large size, and that Yb: SFAP, Yb: KGW, and Yb: GdCOB are more sensitive to temperature variation than

Yb: YSO and Yb: YAG, but that Yb: YAG has a high minimum intensity I_p^{min}, Yb: YSO really appears to be a very attractive system.

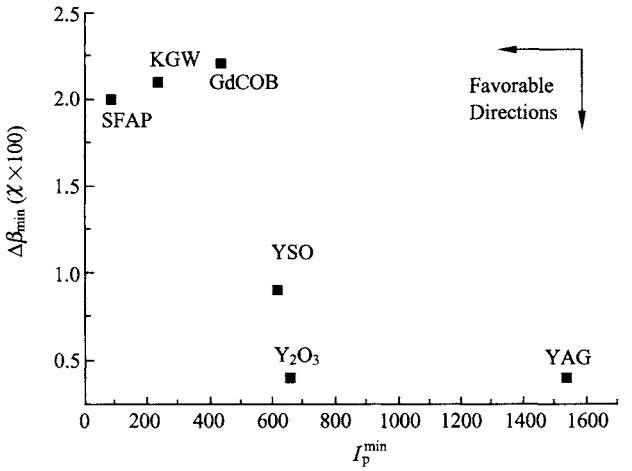


Figure 6.11 Thermal variation $\Delta\beta_{min}$ versus minimum pump intensity I_p^{min} for various Yb^{3+} doped laser materials

6.4.2 Rare-earth Doped Crystals for Telecommunications and Eyesafe Laser Applications

For optical telecommunications and eyesafe laser applications (telemetry, pollutant detection and control in the atmosphere with the LIDAR technique...), the most important wavelength is 1.54 μm. Indeed, this particular wavelength is associated both with the lowest minimum of the attenuation curve of the silica fibers used for long-haul communications, and with strong absorption in the aqueous humor and cornea of the human eye, thereby preventing irreversible damage to the retina, which is essential to vision. Presently, however, because for the increasing need for data transfer at higher volumes and higher rates, extension of this spectral domain (C band) to short (S band) and long (L band) wavelengths is now seriously considered and examined along with the technique of wavelength division multiplexing (WDM) (Bennett, 2000; Bayart, 1999).

Rare-earth doped materials emitting in this wavelength domain, more particularly around 1.54 μm, are already commercially available, and the most widespread are the Er^{3+} doped phosphate glasses (Gapontsev et al., 1982) co-doped with Cr^{3+} or Yb^{3+} (QE – 7 or QE – X series) for flash-lamp or diode-laser pumping from Kigre Inc. Laser emission occurs between the $^4I_{13/2}$ and $^4I_{15/2}$ energy levels of the Er^{3+} ions, after the excitation pump energy has been transferred from Cr^{3+} or Yb^{3+} absorbing (sensitizing) ions (see Fig. 6.12). Cr^{3+} or Yb^{3+} co-doping is necessary to achieve high absorption efficiency without

increasing the Er^{3+} concentration. Indeed, Er^{3+} operates as a three-level laser system, and a high dopant concentration would lead to high reabsorption losses. As a matter of fact, the concentration of the various dopants is a compromise that depends on several parameters, including the absorption coefficient at the pump wavelength and the length of the laser medium (Fan and Byer, 1987). With a relatively high stimulated emission cross section of about 8×10^{-21} cm^2 (at 1.53 μm) and a long fluorescence lifetime of 8 ms, added to excellent optical quality, these materials usually lead to excellent laser performance. CW laser threshold pump powers and laser slope efficiencies of about 10 mW and 40%, respectively, can be obtained, for example, by pumping with InGaAs diode lasers around 970 nm (Thony and Molva, 1996). However, application of these glasses has remained somewhat limited because of their poor thermomechanical properties, which preclude laser applications requiring high energies and high repetition rates. This is why so many studies have been conducted worldwide to find a crystalline host with the same optical properties and laser performance, along with better thermomechanical properties than the phosphate glasses. In particular, much effort dedicated to the search an oxide crystal with high phonon energies in which, as in phosphate glass, radiative emission from the $^4I_{11/2}$ level (1 and 2.8 μm) and up-conversion emission from the $^4S_{3/2}$ level (550 nm and 1.7 μm) of Er^{3+} ions are quenched (see Fig. 6.12), to the advantage of 1550 nm emission from the $^4I_{13/2}$ level.

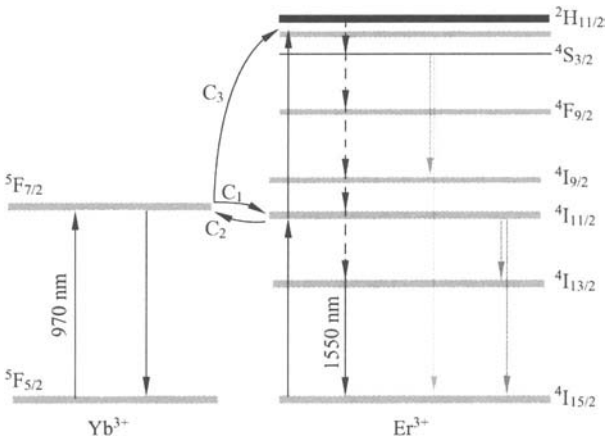


Figure 6.12 Energy transfer and laser schemes in (Yb^{3+}, Er^{3+}) laser systems

Among all possible candidates, those which finally gave rise to laser action and thus led to the greatest hopes and the most active investigations were the silicates Y_2SiO_5 (Li et al., 1992, 1994; Schweitzer et al., 1995) and $Ca_2Al_2SiO_7$ (CAS) (Simondi et al., 1996), the garnet $Y_3Al_5O_{12}$ (YAG) (Schweitzer et al., 1995), the niobate $LiNbO_3$ (Brinkman et al., 1991; Helmfrid et al., 1991;

Suche et al., 1994; Burlot et al., 1999) and the vanadate YVO_4 (Capobianco et al., 1997; Kabro et al., 1997; Doualan et al., 1997; Tsuboi et al., 2000; Kuck et al., 2000). It is to be noted here that Er^{3+}: $LiNbO_3$ only lased as a waveguide and pumped directly into the $^4I_{13/2}$ emitting level with diode lasers operating around 1.48 μm. No results have been reported so far on laser action in Yb^{3+}, Er^{3+}: $LiNbO_3$ after pumping around 970 nm. The main spectroscopic parameters which characterize these laser systems are reported in Table 6.6. In view of these parameters, if one only relies on the emission cross section and lifetime data, several of these systems could have competed efficiently with phosphate glass. Reality was rather disappointing, since the best laser performance was obtained recently (Kuck et al., 2000) with the Er: YVO_4 system at 1.604 μm, which is slighly beyond the eyesafe spectral region, but with a threshold absorbed pump power of the order of 60 mW and with a laser output yield (taking everything into account) of about 17%, which is fairly good but far from the aforementioned performance obtained with the Yb, Er phosphate glass. A lower threshold of a few mW was obtained with the Yb, Er: CAS system by co-doping the crystals with Ce^{3+} ions (Simondi et al., 1996). However, the output yield did not exceed 5%. This situation is mainly due to the inefficient nonradiative relaxation between the $^4I_{11/2}$ and $^4I_{13/2}$ energy levels, and also to strong up-conversion losses, leading in particular to green emission coming from the $^4S_{3/2}$ level. As reported in Table 6.6, for example, the most rapid relaxation between the $^4I_{11/2}$ and $^4I_{13/2}$ energy levels, as given by the fluorescence lifetime $\tau_f(^4I_{11/2})$, was found in Yb, Er: YSO with a value of about 18 μs, but it remained much longer than in phosphate glass, with a time constant of less than 1 μs. The relative efficiency of the Yb → Er energy transfer and of the Er → Yb back transfer also

Table 6.6 Main spectroscopic parameters for (Yb^{3+}, Er^{3+}) laser systems

Material	λ_L(nm)	$\tau_f(^4I_{13/2})$	$\tau_f(^4I_{11/2})$	P_{th}^{abs}(mW)	$C_{Yb\to Er}/C_{Er\to Yb}$
	σ_e($\times 10^{-21}$ cm^2)	(ms)	(μs)	η_{slope}	$C_{Yb\to Er}$($\times 10^{-16}$ $cm^3 \cdot s^{-1}$)
Phosphate	1540	8	<1	10	—
Glass	5			40%	
CAS	1550	6.2	41	20	13
	3.5			5% (with Ce^{3+})	6
YSO	1570 (*E//D*1)	8	18	100	27
	2			5.6%	16
YAG	1646	6.6	800	150	—
	5.5			7%	
$LiNbO_3$	1560 (*E*⊥*c*)	2.8	215		5
	6.5				5.8
YVO_4	1560 (*E//c*)	2.9	27	60	—
	8.5			17%	

plays an important role. From this point of view, as indicated by the microparameters for the Yb→Er and of Er→Yb energy transfers that can be derived spectroscopically from the respective integrals C_1 and C_2 by using equations such as Eqs. (6.15) and (6.16), the Yb, Er: CAS and Yb, Er: YSO laser systems seem to be more favorable than Yb, Er: $LiNbO_3$.

In view of these results, researchers turned their attention towards the $^3H_4 \rightarrow {}^3F_4$ emission of the Tm^{3+} doped systems. These systems do not usually emit in the conventional C and L bands, i. e., above about 1.52 μm, but they emit in the S band, typically between 1420 and 1520 nm, which is perfectly complementary to Er^{3+} doped systems. They operate as four-level laser systems and can be pumped in three ways: (1) directly into the $^3H_4$ emitting level at about 795 nm (Rosenblatt et al., 1990; Braud et al., 1998); (2) indirectly, via Yb^{3+} co-dopant excitation at about 970 nm and energy transfer, with the aid of commercially available high power laser diodes (Diening et al., 1998; Braud et al., 2000a); (3) via two-step excitation, with diode-pumped 1 μm lasers (Percival et al., 1994), in the case of broadband systems such as glasses (see Fig. 6.13).

However, the $^3H_4 \rightarrow {}^3F_4$ laser transition considered takes place between two excited states, which restricts the host materials to those having low phonon energies. Moreover, it is intrinsically self-terminated, in the sense that the lifetime of the terminal level is longer than that of the emitting one [$\tau(^3H_4) \approx$ 10 ms and $\tau(^3F_4) \approx 1$ ms in fluoride crystals, for example], which makes co-doping of the materials with other ions such as Tb^{3+}, Eu^{3+} necessary. Low-energy phonons are necessary to avoid nonradiative quenching of the $^3H_4$ emitting level, whereas Tb^{3+} and Eu^{3+} codopants are used to empty the $^3F_4$ terminal one. It is worth noting here, as illustrated in Fig. 6.13, that indirect excitation at about 970 nm via Yb^{3+} co-dopants, as well as direct pumping via two-step

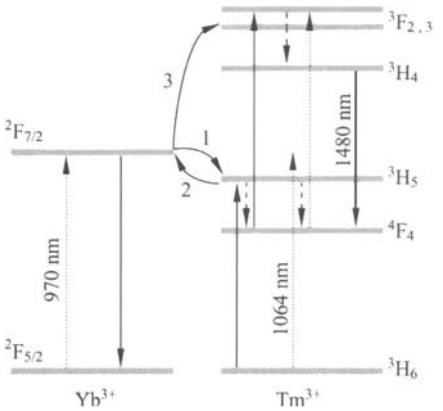


Figure 6.13 Energy transfer and laser schemes in (Yb^{3+}, Tm^{3+}) laser systems

excitation around 1 μm, both efficiently depopulate the $^3F_4$ terminal level of the laser transition. These excitation channels have the additional advantage of avoiding cross relaxation energy transfer processes, which can quench the $^3H_4$ laser level in the Tb^{3+} and Eu^{3+} co-doped systems (Braud et al., 1998).

In view of this situation, much effort has been dedicated in recent years to searching for adequate host materials and dopant combinations, and to understanding, more particularly, to what extent use can be made of ground state and excited-state spectroscopic data to describe and predict laser performance and optimal operating conditions in such complicated laser systems, using models based on classical microscopic energy transfer theories and rate equations, assuming time-independent transfer rates, which are often used without solid justification.

For example, in (Tm, Tb) or (Tm, Eu) systems (see Fig. 6.14), microscopic energy transfer parameters were first derived from ground state absorptions, excited state absorption, and emission spectra, with the aid of overlap integrals as given by Eqs. (6.15) and (6.16). Then, averaged fluorescence lifetimes were calculated from theoretical fluorescence decays obtained by using these microscopic energy transfers, and the results were used to predict laser performance, particularly as a function of dopant concentration. The approach was found to be perfectly valid, at least in describing CW laser operation of the systems. Laser performance could be predicted, for example, by replacing, in the Eq. (6.3), for the laser threshold pump power, the fluorescence lifetime $\tau_f(^3H_4) = \tau_r \eta_r$ of the $^3H_4$ emitting level with some effective time constant τ_f^{eff}, and multiplying Eq. (6.2) for the laser slope efficiency by the factor $\frac{\tau_f^{eff}}{\tau_f}$, τ_f^{eff} being given by (Braud, 1999; Ermeneux, 1999):

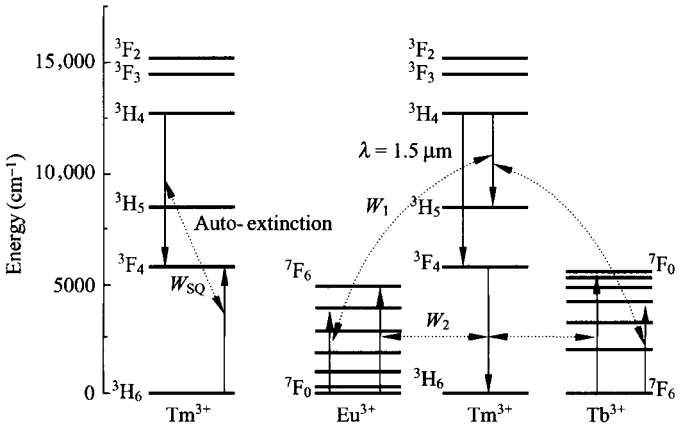


Figure 6.14 Energy transfer and laser schemes in (Tm^{3+}, Tb^{3+}) and (Tm^{3+}, Eu^{3+}) laser systems (according to Braud)

$$\tau_f^{eff} = \tau_f(^3H_4)\left(1 - \frac{N_1}{N_2}\frac{f_1}{f_2}\right) = \frac{\beta' - \beta_{min}}{\beta'(1-\beta_{min})} \approx \tau_f(^3H_4)\left[1 - \frac{\tau_f(^3F_4)}{\tau_f(^3H_4)}\frac{f_1}{f_2}\right], \tag{6.60}$$

i. e., a time constant that does not solely depend on dopant concentrations via the fluorescence lifetimes of the emitting and terminal level $\tau_f(^3H_4)$ and $\tau_f(^3F_4)$, but also on the laser emission wavelength, via the ratio of the respective fractional thermal population factors f_2 and f_1 of the involved Stark sublevels. With $N_1 = N(^3F_4)$ and $N_2 = N(^3H_4)$, the parameter β_{min} has the usual meaning $\beta_{min} = \frac{f_1}{f_1 + f_2}$, whereas $\beta' = \frac{N_2}{N_1 + N_2}$, the inversion ratio relative to the $^3H_4 \rightarrow {}^3F_4$ transition is related to the fluorescence dynamical parameters via the expression

$$\beta' = (1 + A_{21} + 2W_{SQ}N_{Tm} + W_1 N_{Tb/Eu})^{-1} \tag{6.61}$$

where W_{SQ} and W_1 are the self-quenching and $Tm(^3H_4) \rightarrow Tb$ (or Eu) cross-relaxation transfer parameters indicated in Fig. 6.14, and the radiative transition probability A_{21} is given by $A_{21} = \frac{\beta_{32}}{\tau_0(^3H_4)}$, where β_{32} denotes the branching ratio of the $^3H_4 \rightarrow {}^3F_4$ transition and $\tau_0(^3H_4)$ represents the emission lifetime of the $^3H_4$ level in the absence of energy transfer. It is worth noting here that the above expressions also implicitly contain information about the $Tm(^3F_4) \rightarrow Tb$ (or Eu) energy transfer denoted W_2 in the figure, with

$$\frac{1}{\tau_f(^3F_4)} = \frac{1}{\tau_0(^3F_4)} + W_2 N_{Tb/Eu} \tag{6.62}$$

From Eq. (6.60), several remarks follow:

(1) As expected, because of the finite lifetime $\tau_f(^3F_4)$ of the terminal level of the laser transition, the effective lifetime τ_f^{eff} is shorter than the emission lifetime $\tau_f(^3H_4)$ of the emitting level; so according to Eq. (6.3), a higher laser threshold pump power.

(2) When $\beta' \rightarrow \beta_{min}$, it is clear that $\tau_f^{eff} \rightarrow 0$, so $P_{th} \rightarrow \infty$.

(3) The largest is the Tm^{3+} dopant concentration N_{Tm}, the smallest is β', and the largest is the $\frac{N_1}{N_2}$ ratio; this suggests that the Tm^{3+} dopant concentration should be high enough for efficient pumping but low enough to reduce self-quenching as much as possible.

(4) The largest is the Tb^{3+} (or Eu^{3+}) concentration, the smallest is $\tau_f(^3F_4)$, which is favorable; however, this concentration should not be too high, otherwise quenching of the emitting level also occurs and laser thresholds

increase again.

Consequently, there is clearly some compromise to be found both in the Tm^{3+} lasing ion concentration and in that of the codopants depending on the spectroscopic characteristics of the considered system, on the various energy transfer parameters and on the desired emission wavelengths. To illustrate that purpose, it is reported first in Fig. 6. 15, the variation of τ_f^{eff} as a function of Tb^{3+} concentration for a 1% Tm^{3+}: $YLiF_4$ crystal and for the two principal laser wavelengths of 1. 45 and 1. 5 μm. From these data, it was concluded and confirmed experimentally that a Tb^{3+} dopant concentration of about 0. 3 at. % was suitable to operate the system at 1. 5 μm whereas a concentration of about 0. 7 at. % was more adequate for lasing at 1. 45 μm. This was a very interesting result since it proved that it is possible to lase at one particular wavelength without using any intracavity elements or special laser mirrors, just by adjusting the Tb^{3+} dopant concentration.

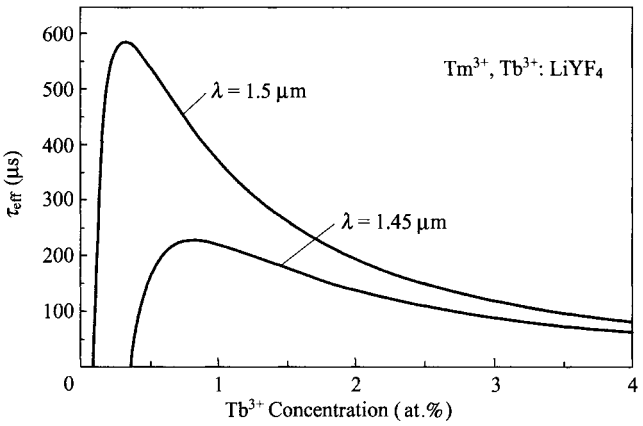


Figure 6. 15 Effective $^3H_4$ emission lifetime versus Tb^{3+} concentration x in (1%) Tm^{3+} (x%) Tb^{3+}: $LiYF_4$

Only two kinds of low-energy phonon materials have really been considered so far: fluorides such as KY_3F_{10}, BaY_2F_8, and $LiYF_4$ (see Fig. 6. 16), and one particular oxide, yttria Y_2O_3. In spite of a very high melting temperature (about 2500℃), which makes it difficult to grow, this particular oxide crystal was very attractive because it is a refractory material with very high thermal conductivity (which is highly desirable for high average power laser applications), and also because it is the only Tm^{3+} doped system giving rise to an intense emission line at the telecommunication and eyesafe wavelength of 1554 nm (Guyot et al., 1996), this being due to a large local crystal field which very strongly splits both the $^3H_4$ and $^3F_4$ energy levels. However, no laser action has been obtained so far, probably due in part to the optical quality of the crystals, but also because of

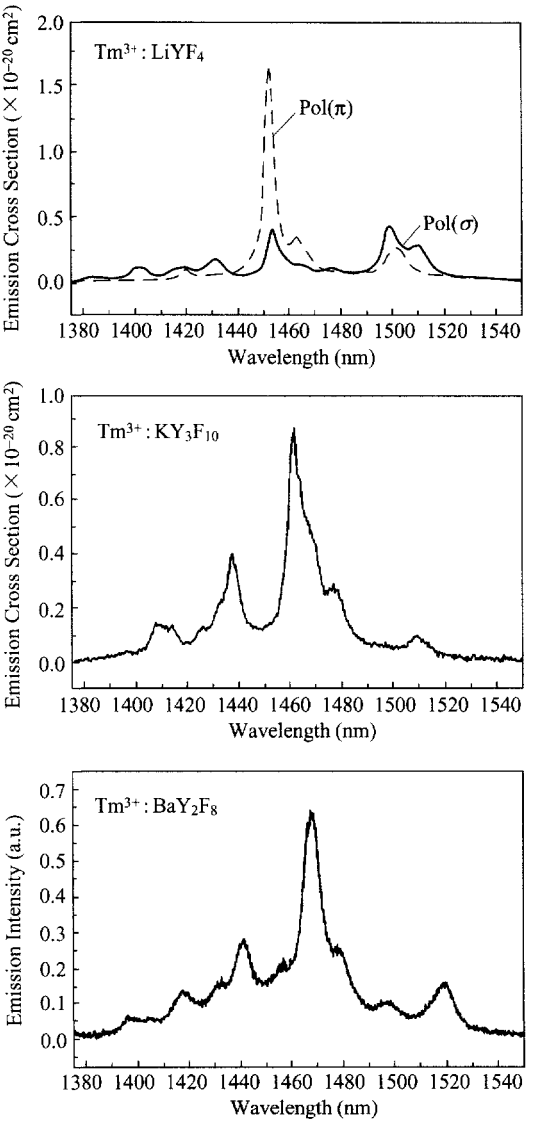


Figure 6.16 Emission spectra of Tm^{3+} doped $LiYF_4$, KY_3F_{10}, and BaY_2F_8

a short emission lifetime $\tau_f(^3H_4) \approx 210$ μs and the difficulty of reducing the lifetime of the terminal level $\tau_f(^3F_4)$ by co-doping with Tb^{3+} ions, without decreasing that of the emitting level significantly. For example (Ermeneux, 1999; Braud, 1999), upon codoping a 0.5% Tm^{3+}: Y_2O_3 crystal with 0.5% Tb, the $\tau_f(^3F_4)$ lifetime decreases from 3.2 ms to 103 μs, but $\tau_f(^3H_4)$ also decreases to the similar value of 102 μs. This finally results in a very low figure

of merit $Q = \sigma_e \cdot \tau_f^{eff}$ of about 1×10^{-24} $cm^{-2} \cdot s^{-1}$, which is something like 10 times smaller than the one found at $\lambda_e = 1.5$ μm in the 1% Tm^{3+}, 0.3% Tb^{3+}: $LiYF_4$ system mentioned above, for which $\tau_f(^3H_4) \approx 660$ μs and $\tau_f^{eff} \approx 430$ μs.

As a matter of fact, although the other fluorides KY_3F_{10} and BaY_2F_8 may exhibit similar performance, only the $LiYF_4$ system has really been studied, and more than 11% laser slope efficiency and a laser threshold pump power of about 65 mW (for an output mirror transmission of 0.5%) were obtained at λ_e = 1.5 μm with a 1% Tm, 0.3% Tb: $LiYF_4$ (Braud, 1999).

Nevertheless, it was quickly found that Tb^{3+} or Eu^{3+} co-doping was not the best way to operate a Tm^{3+}: $LiYF_4$ laser system, since much better laser performance can be obtained by co-doping the materials, as in Er doped systems with Yb^{3+} ions (Diening et al., 1998; Braud, 2000a). In this case, as illustrated in Fig. 6.13, the population mechanism for the $^3H_4$ emitting level, after excitation of the Yb^{3+} ions, includes two consecutive and efficient $Yb^{3+} \rightarrow Tm^{3+}$ energy transfers labeled 1 and 3, and one weak though non-negligible $Tm^{3+} \rightarrow Yb^{3+}$ back-transfer labeled 2. The Yb^{3+} ions thus not only absorb and transfer the excitation energy to the emitting level, but also reduce the effective lifetime of the terminal level of the laser transition, which is absolutely necessary, as discussed above, to avoid bottleneck effects (at least under CW laser conditions), and recycle the energy back into the emitting level. Moreover, as excitation occurs around 970 nm and laser operation, though at a longer wavelength, comes from a higher-lying excited-state, the Yb^{3+}, Tm^{3+}: $LiYF_4$ laser system can be considered a true specimen of up-conversion laser.

As in the case of the Tm^{3+}, Tb^{3+} (or Eu^{3+}) co-doping, a thorough study of the spectroscopic properties and energy transfer processes was also conducted to understand, model and predict the laser performance of this new Yb^{3+}, Tm^{3+}: $YLiF_4$ laser system. Figure 6.17 shows, for example, a simulation of the round-trip gain deduced from the various spectroscopic and dynamic parameters as a function of both the Tm^{3+} and the Yb^{3+} dopant concentrations, a diagram which clearly shows that the Tm^{3+} concentration is rather critical, with an optimal value of about 1at%, while gain remains rather insensitive to Yb^{3+} concentrations ranging between 5at% and 10at%. As a matter of fact, the best laser results were obtained with a 10% Yb^{3+}, 1% Tm^{3+}: $LiYF_4$ crystal, with a laser threshold of about 50 mW and a laser slope efficiency of nearly 27% after pumping around 970 nm with a CW Ti: Sa laser (Braud, 2000a). In the end (Braud, 2000b), the laser wavelength of Yb^{3+}, Tm^{3+}: $LiYF_4$ could be continuously tuned over more than 10 nm from 1493 up to 1505 nm, single-mode operation was obtained by inserting a 150-μm thick etalon inside the laser cavity, and repetitive passive Q-switching using a Co^{2+}: LMA saturable absorber was demonstrated, with the production of 85 ns pulses at a 3 kHz repetition rate, diode under laser pumping.

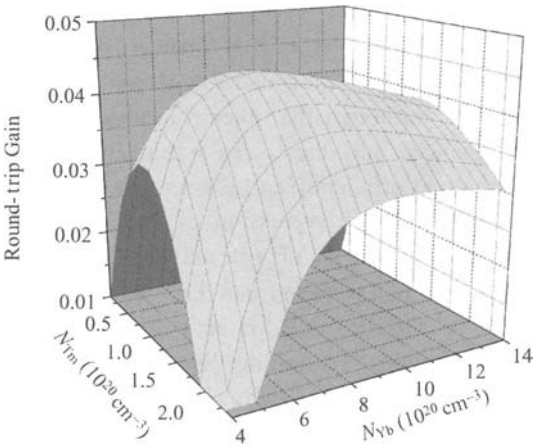


Figure 6.17 Round-trip gain at 1.5 μm in (Yb^{3+}, Tm^{3+}) doped $LiYF_4$ versus Yb^{3+} and Tm^{3+} concentrations (according to Braud et al.)

6.4.3 Low-frequency Phonon Materials for Mid-infrared Lasers

There are numerous laser materials based on rare-earth ions which can be operated in this wavelength domain, i.e., beyond 2 μm. There are those doped with Tm^{3+} or Ho^{3+} ions which emit around 2 μm (Payne et al., 1992), those doped with Er^{3+}, Ho^{3+}, or Dy^{3+} which emit around 2.8 or 3 μm (Wyss et al., 1994; Pollnau et al., 1996; Labbé et al., 1998; Johnson and Guggenheim, 1973), and those doped with Dy^{3+}, Er^{3+}, or Pr^{3+} which emit around 4.3, 4.6, or 7.2 μm (Nostrand et al., 1999; Barnes and Allen, 1991; Djeu et al., 1997; Kirkpatrick et al., 1998; Bowman et al., 1996, 1999; Shaw et al., 1996). However, only those based on Ho^{3+} or Tm^{3+} and those based on Er^{3+} for 2 μm and 2.8 μm lasers, respectively, have so far really exhibited favorable and competitive working conditions and laser performance (compared to other kinds of laser sources). Consequently, only these systems will be considered and discussed below.

Although Ho^{3+} tends to possess more favorable 2-μm emission cross sections for efficient energy extraction (Payne et al., 1992), with values in the range $0.3 \times 10^{-20} - 1.8 \times 10^{-20}$ cm^2, than Tm^{3+}, with values $0.1 \times 10^{-20} - 0.5 \times 10^{-20}$ cm^2, it exhibits several drawbacks, including (1) no adequate absorption bands at the wavelengths of the high power laser diodes, which leads to the necessity of co-doping the materials with other ions such as Cr^{3+} (or Er^{3+}) and/or Tm^{3+} ions acting as sensitizers, and (2) large up-conversion losses. This is why 2-μm laser systems based on Ho^{3+}, which were so extensively studied in the 1980s and the beginning of the 1990s, in particular for medical applications (Moulton, 1992), progressively gave way to laser systems based on materials

(crystals and glass fibers) singly doped with Tm^{3+}. A Ho^{3+}: $Y_3Al_5O_{12}$ laser material, however, could recently be operated very efficiently around 2.1 μm when it is inserted inside the same cavity and pumped with a Tm^{3+}: $Y_3Al_5O_{12}$ laser material emitting around 2.01 μm (Hayward et al., 2001).

Tm^{3+} doped laser materials are very attractive for at least three reasons. As shown in Fig. 6.18, (1) they can be directly pumped into the $^3H_4$ energy level with commercially available high-power laser diodes around 790 nm; (2) at high dopant concentrations, strong cross-relaxation energy transfers occur and lead to very efficient 2-μm laser emission from the $^3F_4$ level; (3) laser emission, because of electron – phonon coupling, is usually broad, which provides the possibility of tuning the laser wavelength over several tens of nm.

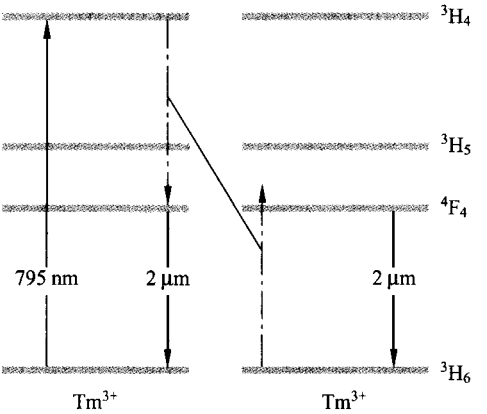


Figure 6.18 Pump and cross relaxation energy transfer processes in 2 μm Tm^{3+} doped laser systems

In principle, in Tm^{3+} doped systems, because of cross relaxation, each pump photon at 790 nm may lead to two laser photons at 2 μm, which means a pump quantum efficiency of two. In fact, this pump efficiency, noted ε_p in the Eqs. (6.2) and (6.3) for the laser slope efficiency and threshold pump power, is given by

$$\varepsilon_p = \frac{W_{nr} + \dfrac{\beta_r}{\tau_r} + 2W_{cr}}{W_{nr} + \dfrac{1}{\tau_r} + 2W_{cr}}, \tag{6.63}$$

where W_{nr}, τ_r^{-1} and β_r respectively denote the nonradiative (multiphonon) and radiative probabilities and the branching ratio for the $^3H_4 \rightarrow {}^3F_4$ transition. W_{cr} is the cross-relaxation energy transfer probability, which can be written

$$W_{cr} \approx \frac{1}{\tau_0}\left[\frac{N_{Tm}}{N_0}\right]^2, \tag{6.64}$$

where τ_0 is the $^3H_4$ emission lifetime at low dopant concentration, N_{Tm} the Tm^{3+} dopant concentration, and N_0 some critical concentration above which cross-relaxation dominates over the other radiative and nonradiative relaxation processes.

In practice ε_p is always less than 2, either because of non-negligible nonradiative relaxation W_{nr}, or because of reduced cross-relaxation energy transfers between neighboring Tm^{3+} ions, the latter being due to a low dopant concentration or a weak interion interaction which manifests itself in poor spectral overlap between the $^3H_4 \rightarrow {}^3F_4$ emission and $^3H_6 \rightarrow {}^3F_4$ absorption bands (overlap integral of the form given by Eqs. (6.15) and (6.16)).

For all these reasons, althought high-energy phonon materials such as $Tm^{3+}: Y_3Al_5O_{12}$ have led to excellent results, great care has been devoted more recently to low energy phonon systems such as $Tm^{3+}: YLiF_4$ and $Tm^{3+}: KY_3F_{10}$ on the one hand, and $Tm^{3+}: Y_2O_3$, an oxide material with a maximum phonon energy of about 450 cm^{-1}, on the other. The main spectroscopic parameters characterizing these four laser systems are reported in Table 6.7. We also display in Fig. 6.19 the absorption and emission cross section spectra for $Tm^{3+}: KY_3F_{10}$.

Table 6.7 $^3F_4$ emission lifetime τ_f, absorption and emission cross sections at the laser wavelength λ_e, and corresponding minimum pump fraction β_{min} and ground-state splitting $\Delta E = E_{ZL} - \frac{hc}{\lambda_e}$ in some Tm^{3+} doped crystals

Materials	$\tau_f(^3F_4)$ (ms)	σ_a (10^{-21} cm^2)	σ_e (10^{-21} cm^2) λ_e(nm)	β_{min}	ΔE (cm^{-1})
YAG	11		2.2 2013	≈0	580
YLF	12	0.3(σ) 0.6(π)	2.5(σ) 4.2(π) 1902(σ) 1880(π)	10%(σ) 12.5%(π)	360
KYF	15.4	1.1	4.2 1850	20%	390
Y_2O_3	3.5	0.8	8 1932	9%	440

As usual, these cross section spectra can be used to determine at which wavelength the laser will likely operate. Indeed, for such a quasi three-level laser system, assuming no ESA, the threshold pump power will be proportional to the relative threshold pump power:

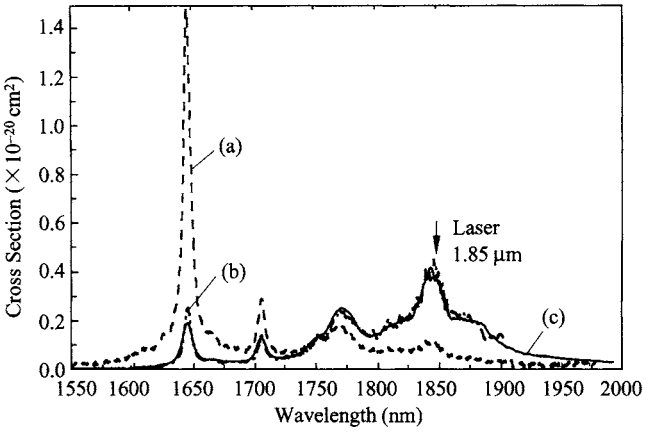


Figure 6.19 (a) Absorption and (b) stimulated emission cross section spectra obtained by using the reciprocity and (c) Fuchtbauer-Ladenburg methods on Tm^{3+}: KY_3F_{10} around 1800 nm ($^3F_4 - {}^3H_6$ transition)

$$P_{rel} = \frac{T+L}{2(\sigma_e + \sigma_a)Nl} + \beta_{min}, \tag{6.65}$$

or $P_{rel} = \frac{T+L}{2\sigma_e Nl} + \frac{\beta_{min}}{1-\beta_{min}}$, if ground-state depletion is neglected, with $\beta_{min} = \frac{\sigma_a}{\sigma_a + \sigma_e}$. Plots of P_{rel} versus $T+L$ for the various emission peaks for which σ_a and σ_e, and thus β_{min}, have been determined, allow to decide at which emission wavelength the laser threshold will be the lowest. This procedure was used for example in the case of Tm^{3+}: Y_2O_3 to demonstrate that lasing will occur at 2050 nm for output mirror transmissions up to 4% – 5%, then at 1950 nm for mirror transmissions ranging between 5% and 11%, then at 1932 nm, in good agreement with the experimental results (Ermeneux, 1999).

All these Tm^{3+} doped laser materials yielded excellent laser performance and the future choice of one rather than another will likely depend on the particular application. What is remarkable about the fluorides is the allowed losses in the cavity, since Tm^{3+}: $YliF_4$ (Budni et al., 2000) as well as Tm^{3+}: KY_3F_{10} (Braud et al., 2001) could be lased CW with laser slope efficiencies up to 50% and output mirror transmissions up to 40%. Moreover, these systems lased preferentially between about 1850 and 1900 nm, in a wavelength domain which is perfectly complementary to the one covered by oxides such as Tm^{3+}: Y_2O_3 and Tm^{3+}: $Y_3Al_5O_{12}$, which lased preferentially at longer wavelengths between about 1900 and 2050 nm. The main drawback with Tm^{3+}: Y_2O_3 is its crystal growth since, as already mentioned above, with melting temperature of nearly 2500℃,

only small crystals can be grown with good enough optical quality. However, this system, with its excellent thermomechanical properties, would be perfectly suitable for high-power applications.

Because of the strong water absorption around 2.9 μm, Er^{3+} doped solid state lasers operating in this wavelength domain also are very attractive and are used very successfully for medical applications such as microsurgery and opthtalmology. Presently, commercial products are based on Er^{3+} doped garnets such $Y_3Al_5O_{12}$ or $Y_3Sc_2Ga_3O_{12}$ (YSGG). However, because of reduced multiphonon relaxation between the emitting and terminal levels $^4I_{11/2}$ and $^4I_{13/2}$ of the laser transition (see Fig. 6.20), and thus higher fluorescence efficiencies, the most promising host materials are more likely fluorides such as $YLiF_4$ (Wyss et al., 1994; Hamilton, 1994; Jensen et al., 1996; Labbe et al., 2000), BaY_2F_8 (Pollnau et al., 1996), CaF_2 (Labbe, 1998, 2000) single crystals or ZBLAN (Sandrock, 1999; Jackson, 1996). Indeed, compared with oxides, these Er^{3+} doped fluorides lead to wider spectra in complementary wavelength domains. Moreover, as shown in Fig. 6.20, they can be efficiently pumped at different wavelengths, in particular with high-power laser diodes around 800 and 980 nm into the $^4I_{9/2}$ and $^4I_{11/2}$ energy levels, respectively. As a result of a complex combination of ESA, up-conversion, and cross-relaxation energy transfers, they can even be lased after pumping around 1480 nm into the $^4I_{13/2}$ emitting level of the laser transition, which is not very common. It is only necessary to work with highly concentrated materials, both to ensure strong enough absorption at the pump frequency and also to depopulate this metastable terminal level and reduce its emission lifetime (to avoid bottleneck effects) via up-conversion energy transfers.

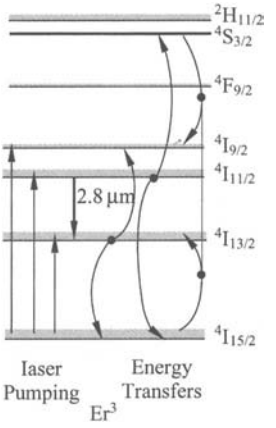


Figure 6. 20 Pump and energy transfer processes involved in the 2.8 μm laser emission of $Er^{3+}:CaF_2$

When they are pumped CW, these laser materials infact give gave rise to much higher laser efficiencies than the oxides, with values ranging between 30% and 50% and threshold absorbed pump powers of the order of 50 mW. It is worth noting here that a 50% efficiency is higher than the quantum conversion limit given by $\eta_q = \frac{h\nu_e}{h\nu_p} \approx 35\%$ for pumping around 980 nm and lasing around 2.8 μm, a result which is precisely interpreted by the strong up-conversion energy transfers taking place in the $^4I_{13/2}$ terminal level of the laser transition followed by the repopulation of the $^4I_{11/2}$ emitting level via mutiphonon and cross-relaxation energy transfers from the $^4S_{3/2}$ upper-lying excited state.

As shown by the gain cross section curves $\sigma_g = \beta\sigma_e - (1-\beta)\sigma_a$ of Er^{3+}: CaF_2 in Fig. 6.21 versus the excitation ratio β, laser emission in this material occurred predominantly around 2.8 μm, with the possibility of tuning the laser wavelength from 2700 to 2900 nm.

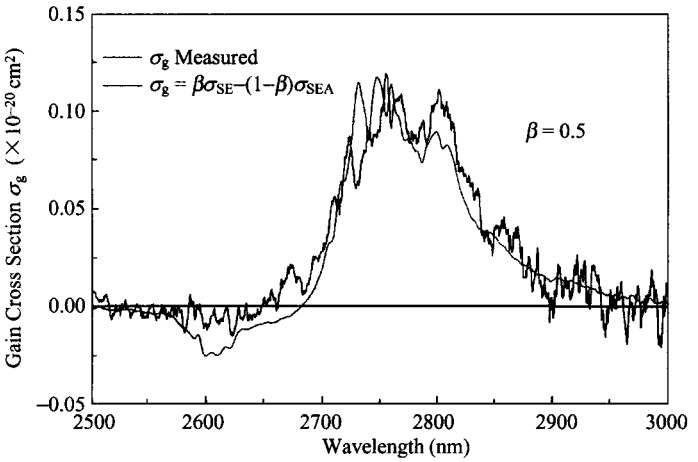


Figure 6.21 Measured and semi-theoretically deduced gain cross section spectra around 2.8 μm in Er^{3+}: CaF_2 (according to Doualan et al.)

6.5 Conclusions

After this short presentation, the reader will certainly realize that many very interesting paths still need to be explored in the field of solid state laser systems based on rare earth ions.

The future development of tunable UV laser sources based on crystals doped with rare-earth ions such as Ce^{3+} will depend both on our ability to grow such single crystals with adequate photochemical stability and on the development of appropriate pump sources. A high average power and high repetition rate solid-state laser pump source such as a frequency-quadrupled diode-pumped Nd^{2+}: $Y_3Al_5O_{12}$ laser operating around 266 nm, for example, would certainly open the door to various kinds of applications for these tunable UV lasers. Moreover, these UV laser crystals may be used in the future to amplify ultra-short UV laser pulses which have been produced, for example, by other compact, diode-pumped and frequency-doubled, tripled, or quadrupled mode-locked infrared laser sources.

Self-frequency doubling of infrared radiation within Nd^{3+} (or Yb^{3+}) doped nonlinear crystals to obtain green radiation is more problematic since very compact laser systems based on the juxtaposition (molecular assembling) of distinct laser and nonlinear elements already exist on the marketplace and already

give fairly good laser performance.

Concerning high-power, tunable, and/or short-pulse lasers based on Yb^{3+} doped laser crystals, big improvements can be expected in coming years and the success of these laser systems will not only depend on the quality of the laser crystals but also on our ability to control temperature, which may not be a simple task, if the energy balance must be kept within a certain limit.

The study and development of laser sources and amplifiers based on Er^{3+} and Tm^{3+} doped materials (crystals and glasses) operating around 1.5 μm will also certainly progress in coming years. On the laser side for example, efforts will be made to find broadband emitting Tm^{3+} doped low phonon energy materials and to develop diode-pumped single-mode, short-pulse, and high repetition rate minilasers which can be tunable within the telecommunication *S* band (1.45 – 1.52 μm), of the telecommunication wavelengths, and thus can be used as testing devices for future DWDM systems.

The development of other infrared laser sources around 2 μm and 2.8 μm will probably grow in the future with the needs of the environmental and medical communities. Diode-pumped 2 μm lasers will also certainly be developed to provide efficient and compact pump sources for other infrared lasers, based on low-energy phonon materials doped with rare-earth or transition metal ions or based on OPOs.

Appendix

6. A Laser Threshold Condition

Using the same approach as that of Kubodera et al. (1979) and Fan and Byer (1987) for four-level and quasi three-level laser systems, respectively, the laser threshold condition (round-trip gain = round-trip losses) can be written as

$$\iiint 2\sigma_g s_0(r, z) N l \mathrm{d}V = L - \ln R, \tag{6. A. 1}$$

where L denotes the round-trip losses, $-\ln R \approx T$ is the output mirror transmission (if it is not too high), N is the total active ion concentration, l is the length of the gain medium, $s_0(r, z)$ is the normalized density of cavity modes, and σ_g is the gain cross section associated with the gain coefficient

$$g = \sigma_g N = \sigma_e N_e - \sigma_a N_g, \tag{6. A. 2}$$

where N_e and N_g are the ion densities in the emitting and terminal level of the laser transition respectively, and σ_a and σ_e the absorption and stimulated emission cross sections at the laser wavelength.

Introducing the emission lifetime τ_f, the normalized pump mode density

$r_p(r, z)$ and the pumping rate $R_p = \frac{P_a}{h\nu_p}$, P_a being the absorbed pump power, and ε_p the pump efficiency, N_e is given by

$$N_e = \varepsilon_p R_p r_p \tau_f \tag{6.A.3}$$

The pumping rate R_p and the density r_p are sometimes approximated by

$$R_p = \varepsilon_p \frac{P_{inc}\sigma_p N l}{h\nu_p} \quad \text{and} \quad r_p \approx \frac{1}{Sl}, \tag{6.A.4}$$

where S is the pumping cross section (which is not really correct since it only applies when $\eta_p \approx \sigma_p N l \ll 1$). Then

$$R_p r_p \approx \frac{\sigma_p I_p}{h\nu_p} N = W_p N \quad \text{with} \quad I_p = \frac{P_{inc}}{S}. \tag{6.A.5}$$

Writing then $N_g = N - N_e$, $S \approx \dfrac{1}{l\iiint s_0(r, z)\, r_p(r, z)\, dV}$ and $P_{inc} \approx P_{th}$ at the laser threshold, it is easy to derive P_{th} as a function of the other parameters.

6.B Minimum Fraction of Excited Population β_{min}

$\beta = \beta_{min}$ the minimum fraction of excited ions necessary to reach transparency is given (assuming $N_e + N_g = N$) when the absorption (gain) coefficient $\alpha(g)$ satisfies

$$-\alpha = g = \sigma_g N = \sigma_e N_e - \sigma_a N_g = 0, \tag{6.B.1}$$

thus when $\sigma_g = \beta\sigma_e - (1-\beta)\sigma_a = 0$ with $\beta = \beta_{min} = \left(\frac{N_e}{N}\right)_{min}$,

$$\beta_{min} = \frac{\sigma_a}{\sigma_e + \sigma_a}. \tag{6.B.2}$$

6.C Energy Transfer Rates

In dipole – dipole inter ion interactions, direct (static) Forster-Dexter and migration-assisted energy transfer rates can be expressed in terms of overlap integrals C_{FD} and C_{mig} according to the relations (Artamonova et al., 1972; Caird

et al., 1991; Payne et al., 1994; Doualan et al., 2000):

$$W_{FD} = \left(\frac{4}{3}\right)^2 \pi^3 N_e C_{FD}$$

and

$$W_{mig} = \pi\left(\frac{2\pi}{3}\right)^{5/2} (N - N_e) \sqrt{C_{FD} C_{mig}}$$

with

$$W \uparrow N_e = W_{FD} + W_{mig}.$$

6. D Einstein Coefficients

For degenerate levels i and j (Weissbluth, 1978) of wavefunctions Ψ_i and Ψ_j,

$$B_{ij} = \frac{1}{g_i} \frac{2\pi q^2}{3h^2 \varepsilon_0} \sum_{k=1}^{g_i} \sum_{l=1}^{g_j} |\langle \Psi_{i(k)} // \boldsymbol{r} // \Psi_{j(l)} \rangle|^2 \qquad (6.D.1)$$

and

$$A_{ji} = \frac{g_i}{g_j} B_{ij} \frac{8\pi h \nu^3}{c^3}, \qquad (6.D.2)$$

$$B_{ij} g_i = B_{ji} g_j. \qquad (6.D.3)$$

6. E List of Acronyms

YAG = $Y_3Al_5O_{12}$
YLF = $LiYF_4$
LLF = $LiLuF_4$
LiC(or S)AF = $LiCa(Sr)AlF_6$
KYF = KY_3F_{10}
Gd(or Y)COB = $CaGd_4(or\ Y_4)(BO_3)_3O$
YAB = $YAl_3(BO_3)_4$
NYAB = Nd: $YAl_3(BO_3)_4$
S(or C)FAP = $Sr_5(or\ Ca_5)PO_4F$
YSO = Y_2SiO_5
KG(or Y)W = $KGd(or\ Y)(WO_4)_2$
CAS = $Ca_2Al_2SiO_7$
LMA = $LaMgAl_{11}O_{19}$
YSGG = $Y_3Sc_2Ga_3O_{12}$
ICP = Induction-coupled plasma
RM = Reciprocity Method

FL = Fuchtbauer-Ladenburg method
SFD = Self-frequency-doubling
CW = Continuous Wave
CVL = Copper vapor Laser
Ti: Sa = Titanium-Sapphire
(D) WDM = (Dense) Wavelength-Division Multiplexing
EDFA = Erbium-doped-fiber-amplifier
TDFA = Thulium-doped fiber amplifier

References

Aka, G., A. Kahn-Harari, D. Vivien, J. M. Benitez, F. Salin, P. Coquelin, P. Colin, D. Pelenc, J. P. Damelet. J. Opt. Soc. Am. B **14**, 2238 (1997).

Amano S., T. Mochizuki, Nonlinear Opt. **1**, 297 (1991).

Artamonova, M. V., Ch. M. Briskina, A. I. Burshtein, L. D. Zusman, A. G. Skleznev, Sov. Phys. JETP **35**, 457 (1972).

Augé, F., F. Mougel, P. Georges, A. Brun, G. Aka, A. Kahn-Harari, D. Vivien. In: *OSA TOPS on Advanced Solid State Lasers*, eds. M. M. Fejer, H. Injeyan, U. Keller, vol. **26** (1999).

Aull, B. F. and H. P. Jenssen. IEEE J. Quant. Electron. QE **18**, 925 (1982).

Auzel, F. Ann. Telecom. **24** (25/26), 199 (1969).

Barnes, N., R. E. Allen. IEEE J. Quant. Electr. QE **27**, 277 (1991).

Bartschke J., R. Knappe, K. J. Boller, R. Wallenstein. IEEE J. Quant. Electr. QE **33**, 2295 (1997).

Bayard, D., Optique et Photonique, vol. **2**, 17 – 23(1999).

Bayramian, A. J., C. D. Marshall, J. H. Wu, J. A. Speth, S. A. Payne, G. J. Quarles, V. Castillo. In: *OSA Trends in Optics and Photonics,* ed. by S. A. Payne and C. Pollock (Optical Society of America, Washington, DC 1996), vol. **1**, 60 (1996).

Bennett, S. C., Laser Focus World 7, 73 – 76 (2000).

Bettinelli, M., R. Moncorgé. J. Lumin. (2001).

Bowman, S. R., S. K. Searles, J. Ganem, P. Schmidt. OSA TOPS vol. **26**, 487 (1999).

Bowman, S. R., L. B. Shaw, B. J. Feldman, J. Ganem. IEEE J. Quant. Electr. QE **32**, 646 (1996).

Braud, A., P. Y. Tigréat, J. L. Doualan, R. Moncorgé. Appl. Phys. B (2001) to be published.

Braud, A., S. Girard, J. L. Doualan, M. Thuau, R. Moncorgé, A. Tkachuk. Phys. Rev. B **61**, 5280 (2000a).

Braud, A., M. Fromager, J. L. Doualan, S. Girard, R. Moncorgé, M. Thuau, B. Ferrand. Ph. Thony. Opt. Comm. **183**, 175 (2000b).

Braud, A. PhD thesis, University of Caen, France (1999).

Braud, A., S. Girard, J. L. Doualan, R. Moncorgé. IEEE J. Quant. Electron. **34**, 2246 (1998).

Brenier, A. J. Lumin. (to be published 2001).

Brenier, A. J. Lumin. **91**, 121 (2000).

Brenier, A., G. Boulon, D. Jaque, J. Garcia Solé. Opt. Mater. **13**, 311 (1999).

Brenier, A. Opt. Comm. **129**, 57 (1996).

Brinkman, R., W. Sohler, H. Suche. Electron. Lett. **27**, 415 (1991).

Budni, P. A., L. A. Pomeranz, M. L. Lemons, C. A. Miller, J. R. Mosto, E. P. Chicklis. J.

Opt. Soc. Am. B **17**, 723 (2000).
Burlot-Loison, R., J. L. Doualan, P. Leboulanger, T. P. J. Han, H. J. Gallagher, R. Moncorgé. J. Appl. Phys. **85**, 4165 (1999).
Burlot-Loison, R., R. Moncorgé, H. Manaa, G. Boulon, Y. Guyot, J. Garcia-Solé, D. Cochet-Muchy. Opt. Mater. **6**, 313 (1996).
Caird, J. A., A. J. Ramponi, P. R. Staver. J. Opt. Soc. Am. B **8**, 1391 (1991).
Capobianco, J. A., P. Kabro, F. S. Ermeneux, R. Moncorgé, M. Bettinelli, E. Cavalli. Chem. Phys. **214**, 239 (1997).
Capmany, J., V. Bermudez, D. Callejo, J. Garcia-Solé, E. Montoya, L. E. Bausa, E. Dieguez. CLEO' urop (Nice, sept 2000) paper CtuF6, p. 71.
Capmany, J., V. Bermudez, E. Dieguez. Appl. Phys. Lett. **74**, 1536 (1999).
Capmany, J., L. E. Bausa, J. Garcia-Solé, R. Moncorgé, A. V. Butashin, B. V. Mill, A. A. Kaminskii. J. Lumin. **60/61**, 78 (1994).
Carnall, W. T., P. R. Fields, Rajnak J. Chem. Phys. **49**, 4412 (1968); **49**, 4424 (1968).
Carnall, W. T., P. R. Fields, B. G. Wybourne. J. Chem. Phys. **42**, 3797 (1965).
Chase, L. L., S. A. Payne, L. K. Smith, W. L. Kway, W. F. Krupke. In: *OSA Proceed. on Advanced Solid State Lasers,* ed. by G. Dubé, L. L. Chase, vol. **10**, 161 (1991).
Cowan, R. D. J. Appl. Phys. **34**, 926 (1965).
DeLoach, L. D., S. A. Payne, L. L. Chase, L. K. Smith, W. L. Kway, W. F. Krupke. IEEE J. Quant. Electron. **29**, 1179 (1993).
Descamps, D. PhD thesis, University of Paris, France (1997).
Dieke, C. *Spectra and energy levels of rare-earth ions in crystals,* Interscience, New York (1968).
Diening, A., P. E. Möbert, G. Huber. J. Appl. Phys. **84**, 5900 (1998).
Djeu, N., V. E. Hartwell, A. A. Kaminskii, A. V. Butashin. Opt. Lett. **22**, 997 (1997).
Dmitriev, V. G., G. G. Gurzadyan. D. N. Nikogosyan. *Springer Series in Optical Sciences* (Springer Verlag, Berlin, 1991).
Dorenbos, P. J. Lumin. **87 – 89**, 970 (2000); **91**, 91 (2000).
Doualan, J. L., C. Maunier, D. Descamps, Landais, R. Moncorgé. Phys. Rev. B **62**, 4459 (2000).
Doualan, J. L., P. Leboulanger, S. Girard, J. Margerie, F. S. Ermeneux, R. Moncorgé. J. Lumin. **72 – 74**, 179 (1997).
Druon, F., F. Balembois, P. Georges, A. Brun, A. Aron, F. Mougel, G. Aka, D. Vivien, A. Courjaud. C. Honninger, F. Salin. Opt. Lett. **25**, 423 (2000).
Dubinskii, M. A., V. V. Semashko, A. K. Naumov, R. Yu. Abdulsabirov, S. L. Korableva. Laser Physics **3**, 216 (1993).
Dubinskii, M. A., A. C. Cefalas, E. Sarantpoulou, S. M. Spyrou, C. A. Nicolaides, R. Yu. Abdulsabirov, S. L. Korableva, V. V. Semashko. J. Opt. Soc. Am. B **9**, 1148 (1992).
Ellens, A., H. Andres, A. Meijerink, G. Blasse. Phys. Rev. B **55**, 173 (1997a).
Ellens, A., H. Andres, M. L. H. ter Heerdt, R. T. Wegh, A. Meijerink, G. Blasse. Phys. Rev. B **55**, 180 (1997b).
Ehrlich, D. J., P. F. Moulton, R. M. Jr. Osgood. Opt. Lett. **5**, 339 (1980).
Ehrlich, D. J., P. F. Moulton, R. M. Jr. Osgood. Opt. Lett. **4**, 184 (1979).
Eichenholtz, J. M., D. A. Hammons, L. Shah Q. Ye, R. E. Peale, M. Richardson, B. Chai. Appl. Phys. Lett. **74**, 1954 (1999).
Ermeneux, F. S., PhD thesis, University of Lyon, France (1999).
Ermeneux, F. S., F. S., Y. Sun, R. L. Cone, R. W. Equall, R. L. Hutcheson. QSA Tops on Advanced Solid State Lasers, vol. 26, 497(1999).
Fan, T. Y.. IEEE J. Quant. Electron. **29**, 1457 (1993).

Fan, T. Y., R. L. Byer. IEEE J. Quant. Electron. **23**, 605 (1987).
Fan, T. Y., A. Cordova-Plaza, M. J. F. Digonnet, R. L. Byer and H. J. Shaw. J. Opt. Soc. Am. B **3**, 140 (1986).
Fejer, M. M., G. A. Magel, D. H. Jundt, R. L. Byer. IEEE J. Quant. Electr. QE **28**, 2631 (1992).
Frantz, L. M., J. S. Nodvik. J. Appl. Phys. **34**, 2346 (1963).
Gapontsev, V. P., S. M. Martitsin, A. A. Isineev, V. B. Kravchenko. Optics and Laser Tech. 189 – 196 (1982).
Giesen, A., U. Brauch, I. Johannsen, M. Karszewski, U. Schiegg, C. Stewen, A. Voss. OSA Tops on Advanced Solid State Lasers, vol. 10, 280 (1997).
Giesen, A., U. Brauch, I. Johannsen, M. Karszewski, U. Schiegg, C. Stewen, A. Voss. OSA Tops on Advanced Solid State Lasers, vol. 1, 11 (1996).
Govorkov, S. V., A. O. Wiessner. OSA Tops on Advanced Solid State Lasers, vol. **19**, 280 (1998).
Gorller-Walrand, C., K. Binnemans. In: *Handbook on the Physics and Chemistry of Rare-Earths*, ed. by K. A. Gschneidner and L. Eyring Chap. **167**, vol. 25, pp. 220 – 229 (1998).
Guyot, Y., J. Margerie, R. Moncorgé, B. Viana. to be published 2001.
Guyot, Y., R. Moncorgé, L. D. Merkle, A. Pinto, B. Mc Intosh, H. Verdun. Opt. Mater. **5**, 127 (1996).
Hamilton, C. E., R. J. Beach, S. B. Sutton, L. H. Furu, W. K. Krupke. Opt. Lett. **19**, 1627 (1994).
Hammons, D. A., M. Richardson, B. H. T. Chai, A. K. Chin, R. Jollay. IEEE J. Quant. Electr. **36**, 991 (2000).
Haumesser, P. H., R. Gaume, B. Viana, E. Antic-Fidancev, D. Vivien. J. Phys. Cond. Matter, to be published 2001.
Hayward, R. A., W. A. Clarkson, D. C. Hanna. Advanced Solid State Lasers 2000, Tech. Digest paper MB8, p. 45.
Hellwege, K. H. Ann. Der Phys. **40**, 529 (1941).
Helmfrid, S., G. Arvidsson, J. Webjorn, M. Linnarsson. T. Pihl. Electron. Lett. **27**, 913 (1991).
Hemmati, H. IEEE J. Quant. Electr. QE **28**, 1169 (1992).
Honea, E. C., R. J. Beach, S. C. Mitchell, P. V. Avizonis, R. S. Monroe, J. A. Skidmore, M. A. Emmanuel, S. B. Sutton, D. G. Harris, S. A. Payne. Advanced Solid State Lasers (Davos Switzerland, 2000) Tech. Digest paper MA6, p. 16.
Honninger, C., F. Morier-Genoud, M. Moser, U. Keuller, L. R. Brovelli, C. Honder. Opt. Lett. **23**, 126 (1998).
Jackson, S. D., T. A. King, M. Pollnau. Opt. Lett. **24**, 1133 (1999).
Jensen, T., A. Diening, G. Huber, B. H. T. Chai. Opt. Lett. **21**, 585 (1996).
Johnson, L. F., H. J. Guggenheim. Appl. Phys. Lett. **23**, 96 (1973).
Judd, B. R., Phys. Rev. **127**, 750 (1962).
Kabro, P., J. A. Capobianco, F. S. Ermeneux, R. Moncorgé, M. Bettinelli, E. Cavalli. J. Appl. Phys. **82**, 3983 (1997).
Kigre, Inc., Tech. Data Sheet, http://www.kigre.com.
Kirkpatrick, S. M., S. R. Bowman, L. B. Shaw, S. Searles. OSA TOPS **19**, 534 (1998).
Koechner, W.*Solid-state laser engineering* (Springer-Verlag, 1988).
Krupke, W. F., M. D. Shinn, J. E. Marion, J. A. Caird, S. E. Stokowski. J. Opt. Soc. Am. B **3**, 102 (1986).
Krupke, W. F. IEEE J. Quant. Electron. QE **7**, 153 (1971).
Kubodera, K., K. Otsuka, S. Miyazawa. Appl. Opt. **18**, 884 (1979).

Kuleshov, N. V., A. A. Lagatski, A. V. Podlipensky, V. P. Mikhailov, G. Huber. Opt. Lett. **22**, 1317 (1997).

Kuo, Y. K., M. F. Huang, M. Birnbaum. IEEE J. Quant. Electron. QE **31**, 657 (1995).

Labbe, C., J. L. Doualan, S. Girard, R. Moncorgé, M. Thuau. J. Phys. Cond. Matter **12**, 6943 (2000).

Labbe, C., J. L. Doualan, S. Girard, R. Moncorgé, M. Thuau. In: *Proceed. Int. Conf. Lasers'98,* ed. by V. J. Corcoran, T. A. Goldman (STS Press, VA, USA, 1999), p. 217.

Lallier, E., J. P. Pocholle, M. Papuchon, M. P. deMicheli, M. J. Li, Q. He, D. B. Ostrowsky, C. Grezes-Besset, E. Pelletier. IEEE J. Quant. Electr. **27**, 618 (1991).

Laroche, M., S. Girard, R. Moncorgé. J. Opt. Soc. Am. B (2002), to be published.

Laroche, M., S. Girard, R. Moncorgé, M. Bettinelli, K. Shimamura, T. Fukuda. CLEO' Europ-EQEC (Munich, Germany, 2001a), Conf. Digest, p. 55.

Laroche, M. PhD thesis, University of Caen, France (2001b).

Laroche, M., S. Girard, R. Moncorgé, G. J. Quarles. J. Y. Gesland, *CLEO' Europ* (Nice, France, 2000a), Conf. Digest, paper CtuF2, p. 69.

Laroche, M., J. L. Doualan, S. Girard, J. Margerie, R. Moncorgé. J. Opt. Soc. Am. B **17**, 1291 (2000b).

Laroche, M., A. Braud, S. Girard, J. L. Doualan, R. Moncorgé, M. Thuau, L. D. Merkle. J. Opt. Soc. Am. B **16**, 2269 (1999).

Lenévé, M. PhD thesis, University of Grenoble University, France (1996).

Li, C., R. Moncorgé, J. C. Souriau, C. Borel, Ch. Wyon. Opt. Comm. **107**, 61 (1994).

Li, C., Ch. Wyon, R. Moncorgé. IEEE J. Quant. Electron. **28**, 1179 (1992).

Li, C. PhD thesis, University of Lyon, France (1992).

Li R., C. Xie, J. Wang, X. Liang, K. Peng, G. Xu. IEEE J. Quant. Electr. QE **29**, 2419 (1993).

Lowenthal, D., J. M. Eggleston. IEEE J. Quant. Electron. QE **22**, 1165 (1986).

Lowdernilk, W. H. *Technology of bandwidth limited ultrashort pulse generation.* In: *Laser Handbook* 3, ed. M. L. Stick (North Holland, Amsterdam, 1979).

Manaa, H., Y. Guyot, R. Moncorgé. Phys. Rev. B **48**, 3633 (1993).

Marshall, C. D., J. E. Speth, S. A. Payne, W. K. Krupke, G. J. Quarles, V. Castillo, B. H. T. Chai. J. Opt. Soc. Am. B **11**, 2054 (1994).

Martin, W. E., D. Milam. IEEE J. Quant. Electron. QE **18**, 1155 (1982).

Maunier, C., J. L. Doualan, R. Moncorgé, A. Speghini, M. Bettinelli, E. Cavalli. *OSA Tops on Advanced Solid State Lasers* (Seattle, WA, USA, 2001).

Maunier, C., J. L. Doualan, G. Aka, J. Landais, E. Antic-Fidancev, R. Moncorgé, D. Vivien. Opt. Comm. **184**, 209 (2000).

McCumber, D. E. Phys. Rev. A **136**, 954 (1964).

McGonigle, A. J., R. Moncorgé, D. W. Coutts. Appl. Optics **40**, 4326 (2001).

McGonigle, A. J., S. Girard, D. W. Coutts, R. Moncorgé. Electron. Lett. **35**, 1640 (1999).

Miloni, P. W., J. H. Eberly. *Lasers* (John Wiley and Sons, New York, 1988).

Moncorgé, R. In: *Ultraviolet Spectroscopy and UV lasers*, ed. P. Misra and M. Dubinskii (Marcel Dekker, Inc., 2001), Part III. 4.

Moncorgé, R. MRS Bull. **24**, 21 (1999).

Moncorgé, R., H. Manaa, B. Boulon. Opt. Mater. **4**, 139 (1994).

Mougel, F., G. Aka, A. Kahn-Harari, D. Vivien. Opt. Mater. **13**, 293 (1999).

Mougel, F., G. Aka, A. Kahn-Harari, H. Hubert, J. M. Benitez, D. Vivien. Opt. Mater. **8**, 161 (1997).

Qui, W., Y. X. Fan. Nonlinear Opt. **4**, 31 (1993).

Moulton, P. F., S. Wright. Laser Focus World **3**, 65 (1992).

Moulton, P. F. J. Opt. Soc. Am. B **3**, 125 (1986).
Nostrand, M. C., R. H. Page, W. F. Krupke, P. G. Schuneman, L. I. Isaenko. OSA TOPS vol. **26**, 441 (1999); Opt. Lett. **24**, 1215 (1999).
Ofelt, G. S. J. Chem. Phys. **37**, 511 (1962).
Ohtake, Z. L. H., N. Sarukura, M. Dubinskii, R. Yu. Abdulsabirov, S. L. Korableva. *Proc. Int. Conf. Lasers' 98* (Tucson, AZ, USA, 1998). Corcoran V. J. and Goldman T. A. (eds). Proc. Int. Conf. Lasers'99 (STS Press, McLean, VA, USA, 1999). p. 421.
Page, R. H., K. I. Shaffers, L. D. DeLoach, G. D. Wilke, F. D. Patel, J. B. Jr. Tassano, S. A. Payne, W. K. Krupke, K. T. Chen, A. Burger. IEEE J. Quant. Electron. **33**, 609 (1997).
Payne, S. A., L. D. DeLoach, L. K. Smith, W. L. Kway, J. B. Tassano, W. K. Krupke, B. H. T. Chai, G. Loutts. J. Appl. Phys. **76**, 497 (1994).
Payne, S. A., G. D. Wilke, L. K. Smith, W. K. Krupke. Opt. Comm. **111**, 263 (1994).
Payne, S. A., L. L. Chase, L. K. Smith, W. L. Kway. IEEE J. Quant. Electron. QE **28**, 2619 (1992).
Payne, S. A., J. A. Caird, L. L. Chase, L. K. Smith, W. K. Krupke. J. Opt. Soc. Am. BXX 726 (1991).
Percival, R. M., D. Szebesta, J. R. Williams. Electron. Lett. **30**, 1057 (1994).
Petrov, K. P., D. J. Bamford, J. L. Patterson. Laser Focus World **3** (2000), p. 159.
Pinto, J. F., L. Esterowitz, G. J. Quarles. Electron. Lett. **31**, 2009 (1995).
Pollnau, M., W. Luthy, H. P. Weber, T. Jensen, G. Huber, A. Cassanho, H. P. Jenssen, R. M. McFarlane. Opt. Lett. **21**, 48 (1996).
Qui, W., Y. X. Fan. Nonlinear Opt. **4**, 31 (1993).
Rambaldi, P., R. Moncorgé, J. P. Wolf, C. Pédrini, J. Y. Gesland. Opt. Comm. **146**, 163 (1998) and Laser Focus World **33**, 26 (1997).
Risk, W. P. J. Opt. Soc. Am. B **5**, 1412 (1988).
Rosenblatt, G. H, R. C. Stoneman, L. Esterowitz. *Advanced Solid-State Lasers,* OSA Proceed. vol. **6**, 26 (1990).
Sandrock, T., A. Diening, G. Huber. Opt. Lett. **24**, 382 (1999).
Sarukura, N., M. A. Dubinskii, Z. Liu, V. Semashko, A. K. Naumov, S. L. Korableva, R. Y. Abdulsabirov, K. Edamatsu, Y. Suzuki, T. Itoh, Y. Segawa. IEEE J. Sel. Top. Quant. Electr. **1**, 792 (1995).
Scherbitsky V., S. Girard, M. Fromager, R. Moncorgé. Appl. Phys. B (2002) to be published.
Schweizer, T., T. Jensen, E. Heumann, G. Huber. Opt. Comm. **118**, 557 (1995).
Shah, L., Q. Ye, J. M. Eichenholtz, D. A. Hammons, M. Richardson. Opt. Comm. **111**, 263 (1994).
Shaw, L. B., S. R. Bowman, B. J. Feldman, J. Ganem. IEEE J. Quant. Electr. QE **32**, 2166 (1996).
Shinn, M. D., F. P. Milanovich, J. N. Roe. *CLEO* (Baltimore, USA) April, 1989.
Siegman, A. E. *Lasers.* University Science Books (1986).
Simondi-Teisseire B., B. Viana, D. Vivien, A. M. Lejus. Phys. Stat. Sol. (a) **155**, 249 (1996) and Opt. Mat. **6**, 267 (1996).
Sokolska, I. E. Heumann, S. Kuck, T. Lubasiewicz. Appl. Phys. B **71**, 1 (2000).
Stoneman, R., L. Esterowitz. IEEE J. Select. Top. Quant. Electron. **1**, 78 (1995).
Suche, H., L. Baumann, D. Hiller, W. Sohler. Electron. Lett. **29**, 1111 (1993).
Svelto, O. *Principles of Lasers 4th* (Plenum Press, 1998).
Thony, Ph., E. Molva E. *Advanced Solid State Lasers*, OSA TOPS 1, 296(1996).
Tsuboi, T. Phys. Rev. B **62**, 4200 (2000).
Wagner, G. J., T. J. Carrig, R. H. Page, K. I. Schaffers, J. O. Ndap, X. Ma, A. Butger. Opt.

Lett. **24**, 19 (1999).
Waynant, R. W., Ph. H. Klein. Appl. Phys. Lett. 46, 14 (1985).
Weissbluth, M. *Atoms and Molecules* (Academic Press, New York, 1978).
Wyss, C., W. Luthy, H. P. Weber, P. Rogin, J. Hulliger. Opt. Comm. **139**, 215 (1997).
Yamamoto, J. K., A. Sugimoto, K. Yamagishi. Opt. Lett. **19**, 1311 (1994).
Zhang, S. J. Cryst. Growth **206**, 197 (1999).

Acknowledgements
Most of the results described in this chapter were obtained with the cooperation of my colleagues at the University of Caen Drs. S. Girard, J. L. Doualan and J. Margerie and within the framework of the thesis of our former PhD students Drs. A. Braud, M. Laroche and C. Maunier. Many thanks are expressed to all of them.

7 Rare Earth Materials in Optical Storage and Data Processing Applications

Y. C. Sun

7.1 Introduction

In this chapter, we give a general overview of the rare-earth materials used in optical storage and data processing. The emphases here are materials and material parameters important to optical data storage and signal processing, rather than a general discussion of the underlying physics.

Since the very beginning of holeburning spectroscopy, it was proposed to use hole burning in optical storage applications, since it is quite natural that different frequency bins could be used as bits in a storage system (Moerner, 1988). Optical storage in the time domain was also proposed, since within the coherence time of the material, the Fourier transform of the pulse sequence can be stored in the system, just as it would be if it were written in the frequency domain (Mossberg, 1982). Rare-earth materials, especially the trivalent rare earth materials, have played an important role in holeburning and coherent transient studies because of the relatively long dephasing times (up to ~ ms) and possible long spectral hole lifetimes due to the weak interaction of the rare-earth ions with the environment.

In recent years, many new techniques have been developed that exploit the holeburning or coherence properties of rare-earth materials to process and store information. These include techniques using the coherence properties of the rare-earth materials (time domain) and those taking advantage of the long spin lattice relaxation times (frequency domain). The time domain technique can be described by two-pulse or three-pulse photon echoes, and the frequency domain technique can be characterized by the holeburning experiment.

Movies have been made with persistent spectral hole burning of a cryogenic Eu^{3+}: Y_2SiO_5 crystal, using a basic holographic configuration by scanning an ultrastable laser continuously within the $^7F_0 - {}^5D_0$ absorption line while the object is in motion, thus permitting the storage, and reconstruction of the moving image (Karaki et al., 1995; Sasaki et al., 1995a, 1995b; Mitsunaga et al., 1994). High-speed storage and retrieval of 500 single-page time-domain holograms have been demonstrated, projecting an achievable frame transfer speed in excess of 13×10^3 frames/s (Shen et al., 1998). Applications of these techniques have resulted in storage densities of 8 Gbits/in^2 in Tm^{3+}: $Y_3Al_5O_{12}$ (YAG) (Lin et al., 1995).

Demonstrations of optical memory have also been carried out in Er^{3+}: Y_2SiO_3, where 1020 bits of data in a 40-MHz wide spectral channel were stored at a single spatial location in the sample, and a raw bit error rate of $\sim 10^{-7}$ was achieved with the use of a simple peak detection scheme(Shen and Kachru, 1998). Optical correlators and true time delay have been demonstrated in Tm^{3+} systems (Wang et al., 1995; Merkel et al., 1996) and Er^{3+} systems (Harris et al., 1998). Electromagnetically induced transparency (EIT) has been observed in Pr^{3+}: Y_2SiO_5(Ham et al., 1998, 1999). It was also proposed that these properties could be used in realizing a quantum logic gate (Lukin et al., 2000).

One parameter important to all these applications has been laser stability, because without it we could not utilize the narrow spectral feature in these materials. Laser stablization has been demonstrated in Tm^{3+} and Er^{3+} materials to both persistent and transient holes, and stabilities of root Allan variance of 20 Hz at 5 ms was achieved in stablizing to Tm^{3+}: $Y_3Al_5O_{12}$(Sellin et al., 1999). Sub-kilohertz stabilities were also achieved by locking to spectral holes in other Tm^{3+} and Er^{3+} systems (Sellin et al., 1999; Strickland et al., 2000; Bötter et al., 2001).

The development of practical coherent transient optical signal processing devices, optically-addressed data storage, and other applications of spatial spectral holography requires design and characterization of new materials with ideal optical properties. One of the properties needed is an ideal wavelength, so that lasers, preferably already available small diode lasers, can be used. Long coherence time T_2 or the related narrow homogeneous linewidth ($\Gamma_h \equiv 1/\pi T_2$), a wide inhomogeneously linewidth (Γ_{inh}), and large oscillator strength are all essential. The ratio Γ_{inh}/Γ_h is important in defining the maximum possible bandwidth. Another important factor, especially in applications such as optical storage, is a long storage time for holes.

The most studied rare-earth systems for these types of applications are Eu^{3+} and Pr^{3+} doped crystals, in no small part due to the early availability of the Rhodamine 6G dye lasers that are resonant with the relevant transitions. In those systems, the hyperfine structure of the Pr^{3+} and Eu^{3+} ions and long spin – lattice relaxation times provide a storage mechanism for spectral hole persisting for hours or even days (Huang et al., 1989; Könz et al., unpublished). Thus, these systems are ideal for long-term storage. In Y_2SiO_5(YO), it has been shown that the optical coherence times T_2 reach the T_1 limit in a modest magnetic field (~ 100 G, 1 G = 10^{-4} T) for both Pr^{3+} and Eu^{3+} ions (Equall et al., 1994, 1995). For Eu^{3+}, $\Gamma_{inh}/\Gamma_h \sim 10^8$. Er^{3+}: Y_2SiO_5 also produced very long dephasing times and demonstrations of a 500-MHz correlator was carried out on this system (Cole et al., 2002).

Tm^{3+} systems are very interesting due to their 1/2 nuclear spin. They thus have no intrinsic hyperfine structure and no quantum beating effect due to the hyperfine splitting (Mitsunaga et al., 1986). They have been a favorite in many demonstrations of coherent transient applications. Er^{3+} systems, due to the

attractive transition wavelength at 1.5 μm, have also attracted considerable attention.

Recent materials developments, especially those that have been used in the demonstration of these applications, will be summarized in this chapter. For example, Pr^{3+}, Eu^{3+}, and Er^{3+} doped Y_2SiO_5 systems have all exhibited very long dephasing times. YSO systems will be the emphasis of the discussion. For Tm^{3+} systems, $Y_3Al_5O_{12}$ will be emphasized.

For earlier developments in coherent and holeburning spectroscopy using rare earth ions, Macfarlane and Shelby's review chapter on the spectroscopy of rare-earth doped solids (Macfarlane and Shelby, 1987) is strongly recommended.

7.1.1 Equivalence of Holeburning and Photon Echoes in Storage and Signal Processing Applications

In an inhomogeneously broadened system, lattice strain and point defects cause the absorption line to be several orders of magnitude larger than the homogeneous linewidth of the individual ion at cryogenic temperatures. Optical pumping using a narrow-band light source can bleach a narrow band in the inhomogeneous line either through saturation (Er^{3+}) or through other storage mechanisms, such as intermediate metastable states (Tm^{3+}), hyperfine storage (Eu^{3+} and Pr^{3+}), Zeeman level storage (Nd^{3+}), and other mechanisms such as photo-ionization and local environment distortion (CaF_2: D^-). This selective bleaching of the absorption line is called spectral holeburning and the bleached section of the line is called a spectral hole. The spectral hole lifetime can vary from the upper state lifetimes or metastable lifetime (ns – ms, saturation holeburning), to the spin lattice relaxation time (up to days, hyperfine level storage) (Könz et al., 2003), and to persistences of weeks or longer with gated holeburning or other mechanisms having high energy barrier for the reversal of the process, such as the deuterated fluoride systems (Macfarlane and Reeves et al., 1987) and the Eu^{2+} systems (Boye et al., 1996).

If we divide the inhomogeneous linewidth Γ_{inh} by the homogeneous linewidth Γ_h, we have the maximum number of frequency bins that can be used as "bits" in an optical storage system. Individual bits can be written in the different frequency bins on the same spatial spot of the material.

If the material has a relatively long T_2, which is related to the homogeneous linewidth by $\Gamma_h = 1/\pi T_2$, then a pulse sequence shorter than T_2 can be used to create a spatial and spectral population grating in the system (hole pattern) that is characterized by the Fourier transform of the pulse sequence. Thus, a brief pulse some time later in the hole's lifetime can be used to read out the stored pattern, since the stimulated echo will be a convolution of the brief pulse and the stored pattern (Mossberg, 1982). This is similar to frequency domain storage, in which

the hole pattern is read out by specific frequency bins. These two processes of time-and frequency-domain storage are equivalent mathematically. Material parameters important to one process will also be important to the other.

Because of the correlation and convolution nature of the stimulated echo process, the pulse sequence designed and the hole patterns modified so that the stimulated echo process can be used for optical signal processing.

7.1.2 Material Parameters for Optical Data Storage

In designing a real storage system there are many parameters to consider. For example, Γ_h (thus T_2), Γ_{inh}, hole lifetime (related to spectral diffusion), temperature dependence, oscillator strength of the transition, and the instantaneous spectral diffusion (ISD, see below) can all be important parameters for specific applications. The importance of Γ_h and Γ_{inh} is quite obvious since the ratio Γ_{inh}/Γ_h determines the ultimate limit of the storage density possible on one spatial spot, the time-bandwidth product noted by some authors. Another important aspect of Γ_{inh} is that it limits the speed of the time domain storage or signal processing applications. A wider Γ_{inh} is sometimes preferred. The storage lifetime of the hole is important since it determines how often the system has to be refreshed. The temperature dependence of all these properties is important because it determines the cryogenic requirement of the system. The oscillator strength again determines the speed of the systems, since the Rabi frequency of the system is determined by the transition dipole moment and the external light field. Instantaneous diffusion behavior of these systems modifies the effective Γ_h of the systems in real applications.

7.1.3 Dephasing and Spectral Diffusion

7.1.3.1 Dephasing Due to One- and Two-Phonon Processes

Several processes involving phonons can affect the optical dephasing rate in different hosts. In crystalline systems, both direct (resonant) and indirect (Raman) processes can play a role in dephasing. If the energy gap between either the ground state or the excited state of the transition and its respective next higher crystal field level is small enough that the available phonons at the operating temperature can span the gap, then the direct process contributes to the total dephasing in the functional form $\Gamma_h \sim (\exp(\Delta_{e,g}/kT) - 1)^{-1}$, where Δ_e and Δ_g are the energy gaps in the excited and the ground states respectively. For systems where the energy levels are widely separated, there will be no phonons energetic enough to span the energy gap, and the Raman process dominates. This process is characterized by a $\Gamma_h \sim T^7$ behavior (for non-Kramers ions) and

relatively constant homogeneous linewidth at low temperature. The onset of $\sim T^7$ behavior depends on the Debye temperature of the host lattice (Orbach, 1961).

7.1.3.2 Dephasing Caused by Spin Flips

Dephasing can also be caused by magnetic dipolar interaction between the active ion and spin – spin flips in the environment, or by spin – lattice relaxations. The spin-spin flip-flops change the local environment of the active ion and causes dephasing. If we call the active rare-earth ion "A" and it has a difference Δg in the g factors of the ground and excited state, and there are another species of spins B with a moment described by a gyromagnetic ratio $\gamma_B = g_B\beta/\hbar$, then the dipolar broadening is described by a half width of $\sim 2.53\Delta_g\beta\gamma_B n_B$, where n_B is the number density of spins B (Meltzer et al., 1992).

Strong magnetic dipoles can also cause the so-called frozen core effect in measurements of the dephasing times. When an active ion is excited, the magnetic moment change due to the excitation causes the ions surrounding the active ion to change their energy and create energy mismatches, generally leading to the slow-down of the spin flip-flops or the frozen core. As the frozen core thaws from the outside, the dephasing behavior of the ion changes with time, and thus the photon echo decays are generally non-exponential. This effect is also observed in spin echo experiments (Mims, 1968). This behavior has been observed in Pr^{3+}: LaF_3 (Rand, 1979), Er^{3+}: $YLiF_4$, ruby (Meltzer, 1992), and recently in Tm^{3+}: LaF_3 and Tm^{3+}: YAG (MacFarlane, 1993b), and Tm^{3+} and Er^{3+} systems in general. This behavior can be fit by the expression

$$I = I_0 e^{-(4\tau/T_M)^x}, \tag{7.1}$$

originally proposed for analogous situations in electron-spin resonance. Here T_M is the phase memory time and x is an exponent that depends on the details of the nuclear spin dynamics, with M in the subscript denoting Mims alth the original expression was written for electric field, not light intensity. We use this expression here to be compatible with the optics literature, since all optical measurements have been using Eq. (7.1). The exponent x depends on the spin flip rate and on the sensitivity of the active ion to the environment. With an external magnetic field, these spin flips can usually be slowed down.

7.1.3.3 Spectral Diffusion

The same mechanism that causes dephasing can also cause spectral diffusion, a process that broadens stored spectral holes. Different models have been proposed, e. g. those of (Hu and Walker, 1978) and (Bai and Fayer, 1989). All these models assume a certain rate of spin flips and describe spectral diffusion as an intial broadening followed by a plateau. The spectral diffusion is usually quite

small in Eu^{3+}, Pr^{3+}, and Tm^{3+} systems on a relevant time scale but can be a very important aspect for Er^{3+} systems.

7.1.3.4 Instantaneous Spectral Diffusion

In the early days of photon echoes for ions in solids, it was found that dephasing times were different when measured at different parts of an inhomogeneous line (Shelby and Macfarlane, 1980). This phenomenon was initially explained as an excitonic effect because of the stoichiometric nature of the material. Later, more materials were found to exhibit this behavior and it was explained by the excess dephasing caused by the electric or magnetic field changes induced by the excitation from the second pulse, so those at the center of the absorption line will have more ions excited and more dephasing. This phenomenon was observed in Tb^{3+}: $LiYF_4$ and Eu^{3+}: Y_2O_3 (Huang et al., 1998; Liu and Cone, 1990). In Tb^{3+} systems, the extra dephasing was attributed to magnetic coupling between the different ions. In the Eu^{3+} systems, it was attributed to the small electric dipole coupling between the small permanent dipoles of the Eu^{3+} ions. This extra dephasing was also studied later in Pr^{3+}: $YAlO_3$, Eu^{3+}: $YAlO_3$, Eu^{3+}: Y_2SiO_5, and many other systems. Thus, in all dephasing time measurements, the laser pulse intensity plays a major role in the numbers obtained.

This extra dephasing is analogous to the instantaneous spectral diffusion (ISD) in spin echo measurements where the second pulse excite some ions and thus change the local environment of those ions prepared by the first pulse. For magnetic dipole coupling between ions, as in Tb^{3+}: $LiYF_4$, this extra broadening can be described by $\sim \Delta_g^2 \beta^2 n'$, where n' is the number of ions that changed state due to excitation of the second pulse. For electric dipole coupling, it can be described by $\sim n' p^2$, where p is the static dipole moment change between the excited and ground state. For a more highly doped material, the same pulse area will excite more ions and thus the measured optical T_2 will be shorter. Even at low doping concentrations, instantaneous spectral diffusion can be important, leading to the measurement of laser power dependent values of T_2. T_2 can usually be obtained by very low excitation power (Huang et al., 1989; Liu and Cone, 1990).

The ISD property of a material is an important aspect for applications because higher concentration allows shorter optical path lengths to be used. Concentration-dependent ISD can be so severe that any advantage gained in the optical path length may be offset by the shortening of T_2. Thus, this simple physical effect can have profound consequences the use of coherent transients in optical storage and signal processing.

7.2 Eu^{3+} Materials

The Eu^{3+} system is unique among rare-earth ions in that it has a $J = 0$ ground state ($^7F_0$), and thus it is a singlet. The $^7F_0 - {}^5D_0$ transition occurs at

approximately 580 nm and the $^7F_0 - {}^5D_1$ transition occurs in the green at ~526 nm. For the 580 nm transition, the transition probability is generally quite weak due to the $J=0$ to $J=0$ nature of the transition. In many systems, this transition is completely forbidden. For systems with lower than C_2 symmetry, this transition may be allowed, and its oscillator strength is very host-dependent, and is approximately 10^{-8} in $Eu^{3+}:Y_2SiO_5$.

The lifetime T_1 for the $^5D_0$ state is generally around 1 – 2 ms, and for $^5D_1$ it is in the tens of microseconds. The lifetime of the lowest $^5D_1$ state is in large part due to nonradiative radiation to the $^5D_0$ states. The $^5D_0$ state, however, has very little nonradiative relaxation thanks to the large energy gap (~10,000 cm^{-1}) between it and the highest $^7F_6$ levels. A relatively long dephasing time is thus expected due to the insensitivity of the $J=0$ states to the environment.

The spectral hole storage mechanism is hyperfine level storage due to the long spin-lattice relaxation time. The nuclear spin for this system is $I=5/2$, and thus in zero magnetic field the hyperfine structure has three levels due to quadrupole interactions with the crystal field gradients. The quadrupole moment of the ^{153}Eu isotope is about 2.54 times that of ^{151}Eu. Two sets of hyperfine splittings exist in the Eu^{3+} materials.

7.2.1 Properties of Y_2SiO_5

Because of the importance of Y_2SiO_5 as a crystal host for Eu^{3+}, Pr^{3+}, and Er^{3+} ions, we summarize the properties of this material before we go on with the properties of Eu^{3+} in this host.

The Y_2SiO_5 host has low nuclear magnetic moments, since Si and O have no nuclear magnetic moment and yttrium only has a small moment of -0.13 μ_N. Y_2SiO_5 crystallizes in a monoclinic cell (C_{2h}^6) described by $a=1.041$ nm, $b=0.6726$ nm, $c=1.249$ nm, and $\beta=102.65°$ (Maksimov et al., 1970). Because this is a monoclinic and thus biaxial crystal, the principal axes of the optical indicatrix do not always coincide with the crystal axes. By symmetry, the C_2 b axis has to be one of the principal axis and the other principal axes lie in the a-c plane. These two axes were labeled as D_1 and D_2 by Li et al. (1992), with D_1 being 79° from the a axis and 24° from the c axis; D_2 is in the a-c plane and perpendicular to D_1 and b. The Y ions occupy two crystallographically inequivalent sites each with a distinct C_1 symmetry. Rare-earth ions substitute yttrium ions at both sites.

The indices of refraction have been measured by Beach et al., who labeled the principal axes of the optical indicatrix x, y, and z (Beach et al.,

1990). The wavelength-dependent refractive indices can be described by the Sellmeier dispersion equation as

$$n^2 = A + \frac{B}{\lambda^2 + C} + D\lambda^2, \tag{7.2}$$

where A, B, C, and D are the Sellmeier coefficients, and λ is the wavelength in μm. The coefficients are listed in Table 7.1.

Table 7.1 Sellmeier coefficients for the principal values of the optical indicatrix in Y_2SiO_5 (Beach et al., 1990)

	A	*B*	*C*	*D*
n_x	3.0895	0.0334	0.0043	0.0199
n_y	3.1173	0.0283	−0.0133	0.00
n_z	3.1871	0.03022	−0.0138	0.00

The X axis here corresponds to the b-axis as defined above, but the correspondence between y, z and D_1, D_2 was not clear. The current author measured the Nd^{3+}: Y_2SiO_5 spectra around 754 nm using an oriented crystal. By comparing these spectra to the Beach et al. spectra, it was concluded that y corresponds to D_1 and z corresponds to D_2.

7.2.2 Eu^{3+}: Y_2SiO_5

The original spectroscopy of Eu^{3+}: Y_2SiO_5 was published by Yano et al. (1991), where they measured the first three manifolds of both the ^7F and ^5D levels. Spectra for two distinct sites were observed, and they were separated by fluorescence excitation. The energy levels are listed in Table 7.2. More complete measurements of the ^7F levels up to $^7F_6$ were given by Könz et al., (2003).

As we can see from the table, the most studied $^7F_0 - {}^5D_0$ transition occurs at 579.879 nm for site 1 and at 580.049 nm for site 2. The inhomogeneous linewidth for these transitions were 8.6 GHz for site 1 and 5.6 GHz for site 2 for their 0.1% sample. Later experiments found that the inhomogeneous linewidth is very concentration- and growth-dependent, and reached about 20 GHz at the 1% doping level (Könz et al., 2003). The two sites are separated by 5 cm^{-1} and have anisotropic absorption coeffcients as listed in Table 7.3. The oscillator strength was estimated to be $\sim 8 \times 10^{-9}$ for site 1.

Table 7.2 Energy levels for the two sites of Eu^{3+}: Y_2SiO_5. Data were taken from Yano et al. (a) All levels were measured at 6 K. The $^5D_1$ levels were also taken from Shen and Kachru, who measured the levels at 3 K (b). The temperature difference is not expected to shift the levels significantly

	Site 1(cm^{-1})	Site 2(cm^{-1})
$^7F_0$	0	0
$^7F_1$	203	224
	418	409
	506	493
$^7F_2$	864	896
	880	1003
	924	1074
	1086	1132
	1283	1183
$^5D_0$	17,240.20	17,235.14
$^5D_1$ [(a)]	18,951	18,955
	18,994	18,997
	19,021	19,016
$^5D_1$ [(b)]	18,952.223	18,955.977
	18,995	18,997
	19,021	19,017
$^5D_1$	21,384	21,409
	21,395	21,424
	21,414	21,445
	21,519	21,494
	21,537	21,519

(a) Yano et al., 1991, 1992a;
(b) Shen et al., 1994.

Table 7.3 Anisotropic absorption coefficients for both sites of a nominally 0.1% Eu^{3+}: Y_2SiO_5 sample. This is a sample grown by Scientific Materials Corp., Bozeman, Montana. The inhomogeneous linewidth was 1.7 GHz for site 1 and 1.4 GHz for site 2 fitted to a Lorentzian lineshape. Total oscillator strengths at other concentrations and growth rates should scale

Polarization	Site 1 (cm^{-1})	Site 2 (cm^{-1})
D_1	3.8	1.7
D_2	1.0	0.3
b	0.0	2.2

Using fluorescence excitation, Pandher et al measured the detailed spectra around the 580 nm region and found 42 different lines in that region, although all

of the extra lines were at least two orders of magnitude smaller than the two main lines described in Tables 7.2 and 7.3. Each of these lines exhibits holeburning and thus should correspond to a distinctive defect site (Pandler et al., 1999).

7.2.2.1 Hyperfine Structure

The hyperfine structures of the $^7F_0$, $^5D_0$, and $^5D_1$ levels were measured by holeburning and ODNMR spectroscopy. The hyperfine parameters are listed in Table 7.4. It can be seen from all these numbers that the quadrupole interaction can be quite different in different states.

Table 7.4 Hyperfine splittings for the different states. The values listed are the gaps between hyperfine levels 1 and 2 and between 2 and 3. Values with three decimal places are from (Könz et al., 2003). The $^5D_1$ values are from Shen and Kachru (Shen and Kachru, 1994). Other values are taken from (Yano et al., 1991). All frequencies in MHz

	Site 1		Site 2	
	^{151}Eu	^{153}Eu	^{151}Eu	^{153}Eu
$^7F_0$	34.544	90.0	29.527	76.4
	46.175	119.2	57.254	148.1
$^5D_0$	75	191[a]	63	160
	102	260	108	274
$^5D_1$	~57	144	43	114
	~57	148	71	183

(a) Yano et al.'s number was 194 MHz.

7.2.2.2 Population and Coherence Lifetimes

The $^5D_0$ population lifetime was 2.0 ms for site 1 and 1.7 ms for site 2, measured by Yano et al. (1991), and 1.9 ms and 1.6 ms measured by Equall et al. (1994). The $^5D_1$ populations lifetime was 25 μs for site 1 and 35 μs for site 2 measured by Yano et al. (1991). Shen and Kachru gave these values as 32 and 42 μs, respectively (Shen and Kachru, 1994).

Photon echo experiments were carried out for the $^7F_0$ to $^5D_0$ transition by Yano et al. (1991) and Equall et al. (1994). In Yano et al. experiment, the temperature was 6 K, so that the temperature dependence of the dephasing time may already play a role. They reported dephasing times of T_2 =477 μs for site 1 and T_2 = 822 μs for site 2. Measurements at different excitation intensities led them to extrapolate the low-intensity limit of T_2 to be 852 μs or Γ_h =374 Hz for site 2.

Equall et al.'s experiment was also run on a 0.1% sample; the temperature was at 1.4 K, so that thermally induced dephasing was minimal. A small magnetic field of 100 G was also applied to the sample to reduce the small contribution of Y – Y spin flips. The echo decay curves are reproduced here in Fig. 7.1 for excitation intensity of 6 W/cm^2 and pulse durations of 1 μs.

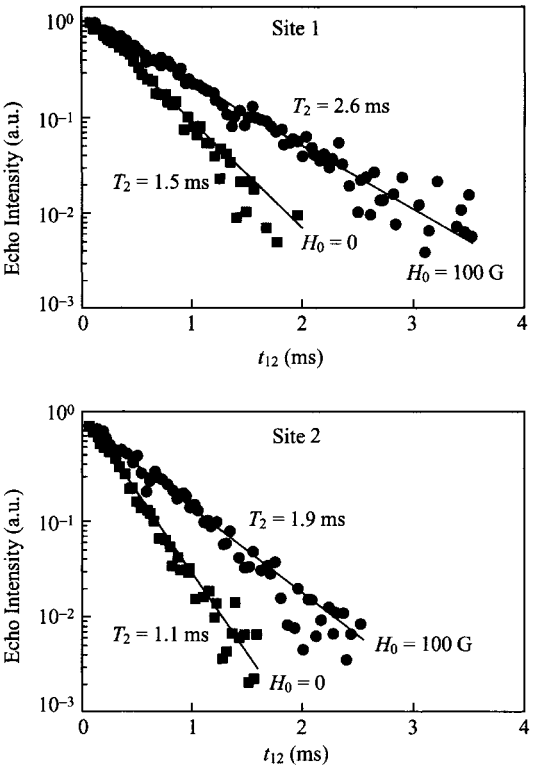


Figure 7.1 Photon echo decay curves for the $^7F_0 - {}^5D_0$ transition of Eu^{3+}: Y_2SiO_5 for both sites at $T = 1.4$ K. Measurements were made both in zero field and at 100 G

Because of the very narrow linewidth of this system, it is generally considered to be very weakly coupled to the host. Since its homogeneous line is so narrow, any such interaction, however small, will be contrasted quite clearly when compared to the linewidth. The instantaneous diffusion effect, discussed earlier, is quite evident when different excitation powers are used in the photon echo experiment. Figure 7.2 shows this effect quite clearly (Equall et al., 1995). Graf et al. also studied this effect with the laser sitting at different parts of the absorption line and proved that the zero-intensity convergence of all the measurements is the same value (Graf et al., 1998).

Figure 7. 2 indicated that the extrapolated linewidths for both sites are 105 Hz at zero power in a 100 G field. Compared to the T_1 limited linewidths of 85 Hz (site 1) and 100 Hz (site 2), this implies that the residual dephasing from all other contributions at 100 G and 1.4 K is 20 Hz (site 1) and 5 Hz (site 2).

Spectral diffusion was also investigated by stimulated photon echoes and it was found that there was no observable spectral diffusion at 5 ms. This again confirms that interaction with the environment is extremely small, and Y – Y spin

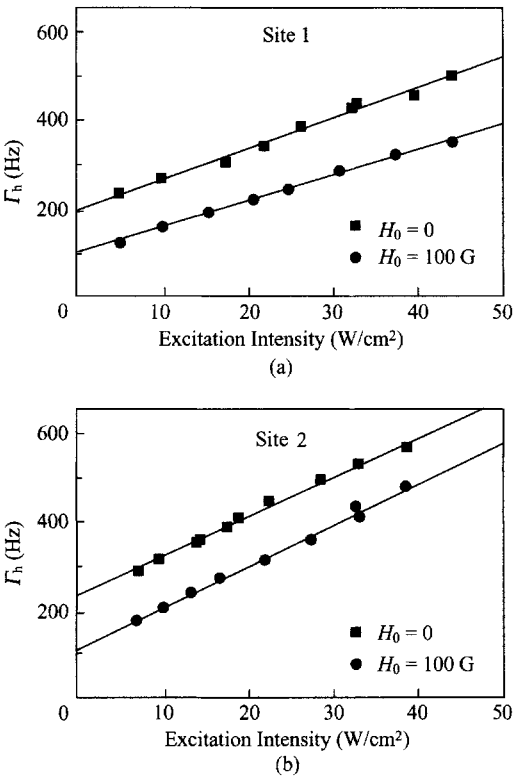


Figure 7. 2 Instantaneous diffusion in the measurement of dephasing times (and thus homogeneous linewidth) for the $^7F_0 - {}^5D_0$ transition of Eu^{3+}: Y_2SiO_5 at 1.4 K. Measurements were made in an unoriented sample using various excitation intensities both in zero field and 100 G

flips do not cause significant spectral diffusion over such time scales.

The dephasing of the $^7F_0 - {}^5D_1$ transition was measured by Shen and Kachru (Shen and Kachru, 1994). The measured dephasing times were 50 μs (site 1) and 56 μs (site 2). Instantaneous spectral diffusion was observed but not tracked, so presumably those numbers will be even longer with lower-intensity excitation and in a magnetic field. The authors used $T_2/2T_1$ as a measure of other dephasing mechanisms and concluded the contribution from the other mechanisms was quite small. If the extra linewidth is considered in this case, it is unlikely that the contributions from other sources will be smaller than in the $^7F_0 - {}^5D_0$ case discussed above.

7.2.2.3 Spectral Hole Lifetimes

One of the most important parameters for both frequency domain and time domain storage is the storage time of the holes or gratings. The hole life times

were measured between 2 K and 18 K and it was found that the site 1 hole lifetime was longer than 20 days at 2 K (Könz et al., 2003). The hole lifetime shortens to ~1 sec at 15 K for site 1 and 18 K for site 2. Since the holes are stored between the hyperfine levels in this system with two isotopes, the relaxation rates between the different levels might be different, so that several different hole decay rates might be present. Because of the very different time-scales involved, the faster component of this relaxation was observed only at 2 K, while the slower components of the decay was observed in the 15 K and short time-scale experiments. At the temperatures in between, more than one component was observed. Because of the two isotopes present, they may also contribute differently on different time scales.

The linewidth was also investigated by Yano et al. (Yano et al., 1991), who found that they last for hours without spectral diffusion, consistent with the above experiment.

7.2.3 Other Experiments in $Eu^{3+}:Y_2SiO_5$

Because of the extremely narrow inhomogeneous linewidth of the material, it has also been used to be investigate fundamental features of instantaneous spectral diffusion, since any increase in linewidth will be easy to quantify.

Aside from the instantaneous spectral diffusion measurements of Equall et al., several other experiments have taken advantage of the long T_2 of Eu^{3+} and studied the dephasing and rephasing behavior of the echo sequence, especially in the presence of a scrambler pulse (Mitsunaga et al., 1992; Altner et al., 1995, 1996a, 1996b; Graf et al., 1997). In some of these experiments, the sample was co-doped with other rare earth ions, so that excitation of other ions influences the active ions in the echo sequence. In the Graf et al. experiment, the measured extra dephasing was explained by dipole – dipole interactions. The predicted extra dephasing from the measured Stark coefficient of 35 kHz/(V · cm^{-1}) for site 1 and 17 kHz/(V · cm^{-1}) for site 2 was within a factor of 2 of the measured excess dephasing value (Graf et al., 1998).

7.2.4 $Eu^{3+}:Y_2O_3$

The $^7F_0 - {}^5D_0$ transition of Eu^{3+}: Y_2O_3 occurs at 580.8 nm at cryogenic temperatures. Holeburning and optical-detection NMR techniques were used to probe the hyperfine structure of both the ground and excited states (Babbitt et al., 1989). The hyperfine splittings for the main line are listed in Table 7.5.

Table 7.5 Hyperfine level structure for $^7F_0$ and $^5D_0$ levels of Eu^{3+}: Y_2O_3 at 4.5 K(Babbitt et al., 1989). The values listed are the gaps between hyperfine levels 1 and 2 and between 2 and 3

	^{151}Eu	^{153}Eu
$^7F_0$	29.35	73.3
	34.0	87.8
$^5D_0$	58	147
	89	225

RF double resonance was later used to study all spectral lines found in the region of the main absorption line. The hyperfine parameters were used to map all these lines, and it was found that the lower hyperfine transition frequency varied smoothly across the absorption profile with a slope of 10 kHz/GHz, with essentially no change in frequency at the upper transition (Yamaguchi et al., 2000). Other more distinct sites were also found when the optical frequency was more than 10 GHz from the main line center.

The upper state lifetime was T_1 = 860 μs, and the dephasing time was measured at the wings of the inhomogeneous line to be 420 μs, corresponding to a homogeneous linewidth of 760 Hz (Macfarlane and Shelby, 1981). The temperature behavior of the homogeneous linewidth was obtained by measuring the echo intensity of the two pulse echo at various temperatures, and was found to be consistent with the two-phonon Raman process. A Debye temperature of 230 K was found, considerably lower than the expected Debye temperature of the material. These were interpreted as the highest phonon modes that can couple to the Eu ion in the lattice. Long ground-state hyperfine thermalization times (>30 h at 4 K) make this an interesting host in the context of spectrally addressable optical memories (Babbitt et al., 1989). Time-resolved holeburning by Sellars et al. revealed a narrow hole 3.5 kHz wide, which was presumably still power-broadened (Sellars et al., 1994). In their samples, they also observed spectral diffusion, which was not seen in the flame fusion sample used by Macfarlane and Shelby and by Babbit et al.'s (Babbitt et al., 1989; Macfarlane and Shelby, 1981).

The spectral diffusion in some samples of Eu^{3+}: Y_2O_3 was also corroborated by interesting dephasing studies in various samples grown in different ways (Flinn et al., 1994a, 1994b, 1994c). Most of these samples were doped in the 1% level, similar to the flame fusion sample. It was found that none of the other growths could match the long dephasing times measured by Macfarlane and Shelby and by Babbitt et al. (Babbitt et al., 1989; Macfarlane and Shelby, 1981). Studies in many different growths of this crystal, especially in those grown by laser-heated pedestal growth, showed very different dephasing behavior ranging from crystalline to glassy.

One of the earliest investigations of instantaneous diffusion was also carried out in this system by Huang et al. (Huang et al., 1989, 1990a, 1990b). Photon

echo experiments conducted in cryogenic Eu^{3+}: Y_2O_3 indicated that resonant excitation of Eu^{3+} ions results in a slight shift of the excited ion's optical transition frequency. This shift was attributed to state-dependent permanent electric dipoles associated with the Eu^{3+} sites. Huang et al.'s ISD experiment concluded that the excess dephasing can be ascribed to a dipolar interaction between Eu^{3+} ions with an electrical dipole change of $\sim 10^{-32}$ cm. This corresponds to a Stark coefficient of $100\ \mathrm{Hz/(V \cdot m^{-1})}$, compared to the measured Stark coefficient of $335 - 455\ \mathrm{Hz/(V \cdot m^{-1})}$ in Eu^{3+}: $YAlO_3$ (Meixner et al., 1992; Graf et al., 1997).

7.2.5 Eu^{3+}: $YAlO_3$

Properties of this system can be found in (Macfarlane and Shelby, 1987). Dephasing was attributed to fluctuating Al^{3+} spins. Optical dephasing times for the $^7F_0$ to $^5D_0$ transition (581.6 nm) were measured to be 58 μs at zero field and 104 μs at 375 G for a 0.25% sample. ISD was not obvious in the early experiments. More recent developments with this material have been the demonstration of optical storage and processing, and studies of the instantaneous diffusion caused by excitation of ions of different species co-doped in the sample. Optical – RF double resonance experiments were also used to map out gradual variations in the hyperfine interactions of the ground state for ions across the inhomogeneously broadened line (Yamaguchi et al., 1998, 1999). It was found that there was a smooth 10 kHz/GHz shift in the lower RF transitions, even for those distinct perturbed sites (some 60 of them over a 400 GHz region).

Simple storage of temporal data was demonstrated in Eu^{3+}: $YAlO_3$ by stimulated echoes. 248 bits of data were stored and retrieved with a storage time of 3.8 h and no loss of echo fidelity (Kim and Kachru, 1989b; Mitsunaga and Uesugi, 1990).

Spectral diffusion measurements using stimulated photon echoes have been carried out on an Eu^{3+}: $YAlO_3$ sample (Yano et al., 1992b). The existence of spectral diffusion was verified by significant broadening (from 1.2 kHz to 7.2 kHz) of the homogeneous linewidth (Γ_h) as the delay between the second and third excitation pulses increased from microseconds to milliseconds. The effect was attributed to the flip of nearby aluminum nuclear spins surrounding the Eu^{3+} ion. A similar broadening effect (from 0.61 kHz to a few kHz) was also observed in the presence of a static magnetic field ($H_0 = 137$ G), but with a much slower diffusion rate. To explain these observations, the authors used three theoretical models: the Bai-Fayer model, the diffusion-equation model, and the Monte-Carlo model. Each agrees reasonably well with the experimental data and indicates flip rates of sub-kHz at $H_0 = 0$ and an order of magnitude lower at 137 G. Using the Bai-Fayer model, the authors used the following equation to fit their observations:

$$\Gamma(T) = \Gamma_0 + \Gamma_1[1 - \exp(-RT)] \tag{7.3}$$

where $\Gamma(T)$ is the homogeneous linewidth at time delay T, Γ_0 is the homogeneous linewidth measured by two photon echoes, Γ_1 is the amplitude of the interaction causing the dephasing, and R is the spin-flip rate. The fit to their experimental results is shown in Fig. 7.3.

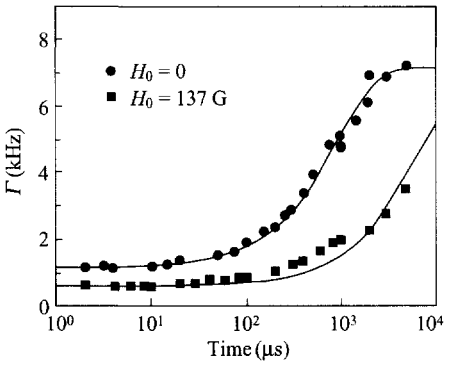


Figure 7.3 Spectral diffusion in Eu^{3+}: $YAlO_3$ in zero field and 137 G. Slowing down of the diffusion process is obvious in a field

Stark-modulated photon echo experiments were used by Meixner et al. (1992) and Graf et al. (1997) to measure the Stark coefficient between two different states. Meixner measured this coefficient to be 45.5 kHz/(V · cm^{-1}), while Graf et al. measured it to be 33.5 kHz/(V · cm^{-1}) directed 13.7 degrees from the a-axis.

7.3 Pr^{3+} Materials

Pr^{3+} doped materials were an early favorite for holeburning studies. The $^3H_4 - {}^1D_2$ transition was the most studied and its coherence properties and hyperfine structure have also been investigated. In (Macfarlane et al., 1987), the detailed spectroscopy of Pr^{3+} doped LaF_3, $YAlO_3$, $LiYF_4$, $LaCl_3$, YPO_4, and $Y_3Al_5O_{12}$ were reviewed. Properties of the Pr^{3+}: Y_2SiO_5 system will be added here. The rather unusual instantaneous diffusion measurements in the Pr^{3+}: $YAlO_3$ system will just also be touched upon.

7.3.1 Pr^{3+}: Y_2SiO_5

The Pr^{3+}: $^3H_4(1) \leftrightarrow {}^1D_2(1)$ transition occurs at 605.977 nm for site 1 and at

607.934 nm for site 2 at $T = 2$ K. Very different absorption coefficients were reported for the two sites (Equall et al., 1994). Recent absorption experiments on an oriented sample determined the very anisotropic absorption coefficients of the two sites, listed in Table 7.6 (Sun et al.). It can be seen from the table that the total absorption strengths of the two sites are very different. These differences were also determined to be caused mostly by the very different occupancies of Pr^{3+} ions at the two crystallographic sites, while the oscillator strengths for the two sites are similar.

Table 7.6 Anisotropic absorption coefficients for the two sites of a nominally 0.05% Pr^{3+}: Y_2SiO_5 crystal. Wavelengths given for the two sites are for the $^3H_4(1) \leftrightarrow {}^1D_2(1)$ transition. Absorption coefficients are given in units of 1/cm. The absorption linewidth for site 1 is 6.2 GHz and that for site 2 is 3.0 GHz, independent of polarization when fitted to a Lorentzian lineshape

Polarization	Site 1(605.977 nm)	Site 2(607.934 nm)
D_1	3.6 ±0.5	6.0 ±0.5
D_2	47 ±5	2.1 ±0.2
b	<0.1	0.6 ±0.1

The lifetime and coherence properties were measured by Equall et al. with $T_1 = 164 \pm 5$ μs for site 1 and T_1 (222 ±5) μs for site 2 (Equall et al., 1994). The $^1D_2$ levels and the lower $^3H_4$ levels are listed in Table 7.7. Hyperfine structure in this crystal was also studied by holeburning and PENDOR experiments, and the parameters are listed in Table 7.8.

Table 7.7 Relevant energy levels for the two different sites of 0.02% Pr: Y_2SiO_5 (Equall et al., 1995). All levels were measured at 2 K. The missing levels in $^3H_4$ for site 1 were not resolved in the spectra but were around 250 cm^{-1}

	Site 1	Site 2
$^3H_4$	0	0
	88	176
	146	257
		416
		632
		653
		842
	758	996
	880	1158
$^1D_2$	16,502	16,449
	16,561	16,703
	16,723	16,754
	17,001	17,396
	17,297	17,518

Table 7.8 Hyperfine splittings for the different states and sites of 0.02% Pr: Y_2SiO_5. The numbers listed are the gaps between levels 1 and 2 and between levels 2 and 3 (Equall et al., 1995; Holliday et al., 1993)

	Site 1		Site 2	
	$^3H_4(1)$	$^1D_2(1)$	$^3H_4(1)$	$^1D_2(1)$
δ_1(MHz)	10.19	4.59	3.78	2.29
δ_2(MHz)	17.3	4.84	4.93	2.29

The coherence properties were reported by Equall et al. and extrapolated to a Γ_h of 2400 Hz for site 1 and 1250 Hz for site 2 at zero intensity excitation in zero field. These linewidths narrowed down to 1800 Hz and 850 Hz respectively in a magnetic field of 77 G. The T_2 for site 1 was also measured by Graf et al. (1998) to be 1650 Hz as the zero intensity limit in zero field. The lifetime-limited linewidth is expected to be 970 Hz and 717 Hz repectively for the two sites. The remaining dephasing, larger than that of Eu: Y_2SiO_5, was attributed to remaining Y – Y spin flips and the higher sensitivity of Pr^{3+} ions due to the larger

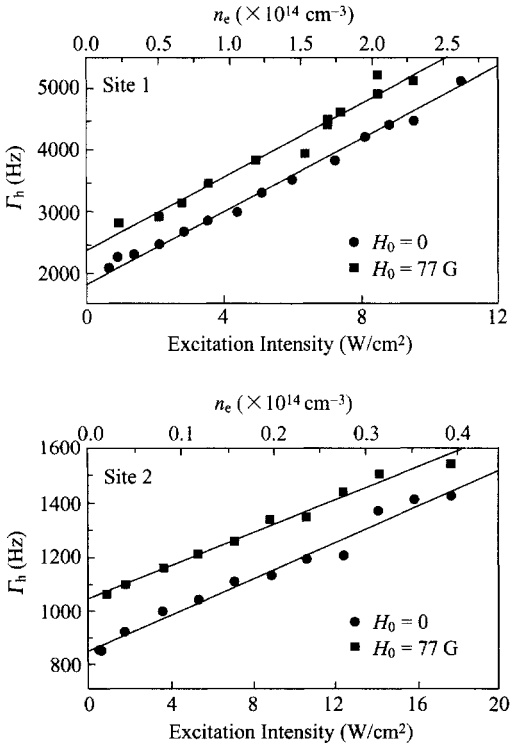


Figure 7.4 Instantaneous diffusion in Pr: Y_2SiO_5 (Equall et al., 1995)

nuclear gyromagnetic ratio of Pr^{3+} relative to Eu^{3+}. For this unoriented sample, the instantaneous diffusion is 1.2×10^{-11} Hz · cm^3 for site 1 and 1.4×10^{-12} Hz · cm^3 for site 2 as shown in Fig. 7.4.

The stark coefficients of both sites in this crystal have been measured by Graf et al. to be 111.6 kHz/(V · cm^{-1}) for site 1 and 92.9 kHz/(V · cm^{-1}) for site 2 (Graf et al., 1998). Graf et al. also investigated a co-doped Eu: Pr: Nd: Y_2SiO_5 system and found that the Pr: Y_2SiO_5 system's extra dephasing involves non-equilibrium phonons generated by nonradiative relaxation of the excitation.

Because of the seemingly larger oscillator strength of this material, it has been used in the study of electromagnetically induced transparency. Combinations of both laser fields and RF fields were used. Optical probe field gain was observed when the RF pulse area was 2 (Ham et al., 1998). Later, the probe laser beam was observed to increase by a factor of exp (1.4) at 12 K when a coupling laser of 1.2 kW/cm^2 was applied to the system (Ham et al., 1999).

7.3.2 Pr^{3+}: $YAlO_3$

$YAlO_3$ is an orthorhombic crystal in which the Y ions occupy a C_s site. The $^3H_4(1) - {}^1D_2(1)$ transition occurs at 610.53 nm. PENDOR, Raman heterodyne spectroscopy, and two-and three-pulse photon echo modulations were all used in elucidating the hyperfine structure, especially in the excited state. The hyperfine splittings in the excited state were 0.92 MHz and 1.567 MHz, and those in the ground-state were 7.07 and 14.13 MHz(Shelby et al., 1982). Site interference of the Raman heterodyne signal was also observed in this system.

The $^1D_2(1)$ state lifetime was 180 μs and the measured dephasing time was 35 μs at zero field and 78 μs with a magnetic field of 80 G along the *c* axis (Macfarlane et al., 1979). Echo measurements with different laser intensities revealed strong instantaneous diffusion, and extrapolation to zero field yielded a zero field T_2 of 70 μs (Kröll et al., 1991a). A holeburning study of this transition also revealed very narrow linewidths of 10.5 kHz, similar to those obtained from photon echo experiments. In the measurement of these narrow holes, a novel feature at the center of the hole was also observed that was a 10 Hz wide ultra-narrow peak due to grating diffraction of the pump beam (Mitsunaga et al., 1993).

The excess dephasing behavior in this system has been investigated by Kröll et al., who found that it cannot be explained simply by excess dephasing caused by the excitation of the second pulse, since there was a significant decrease in measured dephasing times when the first pulse energy was increased (Kröll et al., 1990, 1991a). An excitation area dependence was also reported for the measured dephasing time, which was explained by the 51 cm^{-1} resonant phonons associated with nonradiative relaxation of the excited ions (Bai and Kachru, 1992).

Strong echo modulation was observed by Luo and Kröll in a magnetic field (Luo and Kröll, 1996). The permanent electric dipoles were measured from the

site interference of the Stark modulated echoes, and the Stark coefficient was (57.7 ±2.7) kHz/(V · cm^{-1}), pointing 58.5 degrees from the *a* axis in the *a-b* plane (Graf et al., 1997). This is in contrast to earlier results of (60.8 ± 0.4) kHz/(V · cm^{-1}) and 55 degrees (Macfarlane and Meixner, 1994).

In early demonstrations of information storage, Kröll et al. used a frequency-chirped ring dye laser to store and recall 48 bits of information using the $^3H_4 - {}^1D_2$ transition of Pr^{3+}: $YAlO_3$. The experiments also demonstrated that frequency chirping of the excitation pulses dramatically improves not only pulse shape reproduction by the echo pulse but also the shot-to-shot stability of the amplitude of the recalled data (Kröll et al., 1991b).

7.3.3 Pr^{3+}: $Y_3Al_5O_{12}$

The $^3H_4 - {}^1D_2$ transition in Pr^{3+}: $Y_3Al_5O_{12}$ was studied by ODNMR and other methods. The transition occurs at 609.6 nm. The ground state has the second level at 18 cm^{-1} and the excited state has the second level at 10 cm^{-1}, so T_2 is expected to be quite sensitive to temperature. Seven prominent satellite transitions were also present in the spectrum and they were characterized by absorption and site-selective fluorescence experiments, and their hyperfine structure in the ground state was studied by ODNMR(Wang, 1997). For the main transition, the ground-state splittings were given by Shelby et al. as 33.4 MHz and 41.6 MHz by holeburning (Shelby et al., 1983) and were confirmed by Raman heterodyne detected NMR to be at 33.36 MHz and 41.46 MHz (Wang, 1997). The excited-state hyperfine splittings were given as 6.49 MHz and 8.29 MHz by Shelby et al. (1983) from FID modulation and were confirmed by Wang ' s Raman heterodyne experiments to be 6.41 MHz and 8.32 MHz. Since the Raman heterodyne measurements have cancellations at zero field, the numbers quoted above were measured in a magnetic field and extrapolated to zero field. Angle-dependent studies of the nuclear Zeeman splittings by Wang also confirmed the site to be D_2 (Wang, 1997). Kim and Kachru gave the excited state splittings as 3.42 and 5.96 MHz, inferred from photon echo modulation (Kim and Kachru, 1989c, 1991). This determination was not otherwise confirmed. It is likely that those splittings were due to a defect site present in the system investigated by Wang(1997). For example, the transition at 16,406 cm^{-1} has splittings at 35.11 MHz and 47.76 MHz, very close to the observed strong peaks of 36 and 46 and 82 MHz, which were ascribed to sum and difference frequencies in Kim et al.' s measurements.

The measured T_1 was 230 μs and T_2 = 20 μs in zero field. When short pulses are used, strong modulation occurs, as demonstrated in Kim and Kachru' s experiments (Kim and Kachru, 1991). Photo-gated holeburning was also observed in this system, when a 514.5 nm laser was also present in the hole writing process (Macfarlane et al., 1996). The photon-gating process was attributed to two-step photoionization. Storage and retrieval of optical data pulses

were also demonstrated in this system (Kim and Kachru, 1989a).

7.3.4 $Pr^{3+}:LaF_3$

Because of the importance of $Pr^{3+}:LaF_3$ in early studies of photon echoes, it is a well-studied material. Both the $^3H_4 - {}^3P_0$ transiton at 477.75 nm and the $^3H_4 - {}^1D_2$ transition at 592.5 nm have been used in many demonstrations of optical data storage and signal processing.

Both spatial-image storage and phase conjugation were demonstrated by Kim et al. using a backward-stimulated echo on the $^3H_4 - {}^3P_0$ transition of $Pr^{3+}:LaF_3$. The image storage and the delayed phase conjugation were observed to last for at least 15 s, corresponding to the hyperfine storage time, which had a strong temperature dependence (Kim and Kachru, 1987).

Mitsunaga et al. demonstrated optical storage and retrieval by simultaneous and spatially overlapping multiple photon echoes after application of a single optical pulse followed by multiple pairs of counterpropagating pulses in various directions (Mitsunage et al., 1988).

Two-dimensional image processing on a nanosecond time scale has been demonstrated using the stimulated photon echoes in 0.1 at. % $Pr^{3+}:LaF_3$ (Xu et al., 1990). The stored information is retrieved and processed by a third read pulse, generating the echo that is the spatial convolution or correlation of the input images. These techniques were also used in pattern recognition with a processing speed of 30 ns per processing operation (Shen and Kachru, 1992).

Instantaneous spectral diffusion was also observed in the $^3H_4 - {}^1D_2$ transition by Zhang and Mossberg (Zhang and Mossberg, 1993). The dephasing rates were found to contain a background contribution whose magnitude was dependent upon the specific crystal sample studied, which can be due to the growth method, other preparation details that cause strain, two-level systems, etc., and a second contribution whose magnitude increases with the number of Pr^{3+} ions changing state in the course of the echo excitation sequence. The second contribution to the dephasing rate can be attributed to the presence of optical instantaneous diffusion.

7.4 Tm^{3+} Materials

The Tm^{3+} ion, like all trivalent rare-earth ions with an even number of 4f electrons, has nonmagnetic singlet electronic states when doped into low symmetry crystalline sites, and it is thus relatively insensitive to the homogeneous line broadening induced by fluctuating local magnetic fields arising from mutual nuclear spin flips of host lattice nuclei or electron spin flips of other ions. The Tm^{3+} ion, with a 12-electron configuration, is thus a good candidate for long

optical coherence times at low temperatures. The lowest levels are the $^3H_6$ multiplet.

We are interested in transitions from the $^3H_6$ to the $^3H_4$ levels for which the lowest component to lowest component transitions fall between 790 – 800 nm in most hosts. There are two multiplets between $^3H_6$ and $^3H_4$, the $^3H_5$ and $^3F_4$ multiplets, but the energy gaps are large enough that the multiphonon decay that broadens Γ_h can be minimized. The $^3H_4$ level relaxes to the metastable $^3F_4$ level, which typically has a lifetime of ~10 ms. Although the lifetime of the $^3H_4(1)$ level is usually in the ms range or less, spectral hole lifetimes can be as long as 10 ms due to the presence of this third level $^3F_4$. The metastable level lifetime determines the limit on the storage time of this system in the absence of spectral diffusion.

Tm^{3+} is also interesting because of its lack of zero-field hyperfine structure due to the $I = 1/2$ nuclear spin. It thus does not have the complication of the hyperfine structure in coherent transient applications (Mitsunaga et al., 1986).

Spectral holeburning experiments were carried out by Macfarlane in the $^3H_6(1) \rightarrow {}^3H_4(1)$ transition of Tm: $Y_3Al_5O_{12}$ and Tm: LaF_3 and it was found that the linewidth is close to 2.5 MHz (Macfarlane, 1993a). This linewidth was probably broadened by the experiment. The photon echo decays in Tm : YAG were very nonexponential, with $T_M = 75$ μs, and the exponent was close to 1.5 (Macfarlane, 1993b). Photo-echoes in Tm^{3+}: $Y_2Si_2O_7$ showed that Γ_{inh}/Γ_h is $\sim 10^7$ for that system (Wang et al., 1996).

Sun et al. studied Tm^{3+} doped $Y_3Al_5O_{12}$ (YAG), $Lu_3Al_5O_{12}$ (LuAG), the mixed garnet system $Y_{1.5}Lu_{1.5}Al_5O_{12}$ (YLuAG), $Y_3Ga_5O_{12}$ (YGG), Y_2SiO_5 (YSO), Y_2O_3, and $YAlO_3$ (YAP) to further explore the parameter space involved in Tm doped oxides (Sun et al., b). The Y_2SiO_5 material was a prime candidate because very long T_2 was observed for Pr and Eu in this material due to the very small nuclear moments of the ions in the host, and Y_2O_3 was studied for similar reasons. $YAlO_3$ doped with other ions has been studied widely, and the reported energy level structure in the literature indicated that long T_2 is also possible in this case, though it proved to be otherwise. From Sun et al.'s study, the garnet systems have the best coherence properties and are especially interesting due both to the broad inhomogeneous linewidth Γ_{inh} inherent in the garnet system and to the ability to broaden Γ_{inh} even further in mixed garnets without losing the ideal coherence properties. In the following subsections, we summarize these results from (Sun et al., b) unless otherwise noted.

General spectroscopy for determining the energy level structure is essential to understanding the dephasing behavior, especially that related to phonon-induced dephasing. We present in Table 7.9 some general results and also clear up an ambiguity in the literature. Since only the first levels above the levels involved in the optical transition are important for understanding dephasing, we only included the energy gaps in the ground and excited states $\Delta_g = E[^3H_6(2)] -$

$E[^3H_6(1)]$ and $\Delta_e = E[^3H_4(2)] - E[^3H_4(1)]$. Other spectroscopic information such as transition wavelength, lifetime, and oscillator strengths was also included.

Table 7.9 Spectroscopic properties of Tm^{3+} doped crystals at 2 K

Material	Conc.	λ (nm)	σ (cm^{-1})	T_1 (μs)	Γ_{inh} (GHz)	$\Delta_g(^3H_6)$ (cm^{-1})	$\Delta_e(^3H_4)$ (cm^{-1})	α	f ($\times 10^{-9}$)
$Y_3Al_5O_{12}$	0.10%	793.156	12,604.39	800	20	27	70 or 37	1.9	63
$Lu_3Al_5O_{12}$	2%	793.808	12,594.04		20			12	
$Y_{1.5}Lu_{1.5}Al_5O_{12}$	3%	793.527	12,598.50	325	270	34	33	3.5	49
$Y_3Ga_5O_{12}$	0.1%	795.108	12,573.44	2200	55	70	26	0.06	5.4
$Y_3Ga_5O_{12}$	1%			1600	55	70	26	0.53	
LaF_3	0.1%	796.302	12,554.6	2060	67	19			
Y_2O_3	0.1%	796.286	12,554.85	530	3.6	30	79	4.4	11.4
Y_2SiO_5	0.1%	790.781	12,642.25	55	2.6	13	71	12	
	0.1%	790.769	12,642.44	110	4.5	1.6	66.4	8	
$Y_2Si_2O_7$		790.427	12,651.4	68	100	6		0.4	
$YAlO_3$	0.1%	798.845	12,514.63	760		3	57		
$YAlO_3$	4%	798.845		53		3	57		

7.4.1 $Tm^{3+}:Y_3Al_5O_{12}$

The garnets have the cubic structure with space group O_h^{10}. The Tm^{3+} ions substitute for Y or Lu that occupies local D_2 sites. Both spectroscopy and echo experiments were carried out on crystals with polished $\langle 111 \rangle$ surfaces, with the light propagating along the $\langle 111 \rangle$ direction.

The $^3H_6$ ground state energy gap Δ_g is 27 cm^{-1}. The $^3H_4$ excited state energy gap Δ_e needs further discussion. Gruber et al. (1989) measured this gap to be 72 cm^{-1}. However, Tiseanu et al. (1995) identified the energy gap Δ_e to be 37 cm^{-1}. There are transition lines for both in Sun et al's absorption spectra, although the transition corresponding to a 37 cm^{-1} level is extremely weak. This discrepancy was not resolved, but we note that Δ_e is quite large, so there should be no phonon-induced dephasing at the temperatures of interest.

The $^3H_6(1) \leftrightarrow {}^3H_4(1)$ transition of 0.1% Tm: $Y_3Al_5O_{12}$ occurred at 793.156 nm in air. The linewidth was $\Gamma_{inh} = 20$ GHz (0.7 cm^{-1}) full width half maximum (FWHM), measured by laser absorption, with a peak absorption coefficient of $\alpha = 1.9$ cm^{-1}. More concentrated Tm: $Y_3Al_5O_{12}$ (YAG) samples have similar linewidths, and the absorption coefficients scale with the concentration. The transition dipole for $^3H_6(1) \leftrightarrow {}^3H_4(1)$ was measured by Sun et al. where the optical nutation was measured when the light polarization was

rotated relative to the crystal axis (Sun et al., 2000). Interference due to difference sites in the crystal was observed and simulated. It was determined that the transition dipole is along the $\langle 110 \rangle$ direction of the crystal and has an oscillator strength of 8×10^{-8}, very close to the number obtained directly from absorption and listed in Table 7.9.

The coherence properties of 0.17% Tm: $Y_3Al_5G_{12}$ reported by Macfarlane and he found the echo decays can be fitted by $T_M = 75$ μs and $x = 1.5$ at zero field. In a field of 438 G, the decay becomes exponential and the dephasing time is 105 μs (Macfarlane, 1993b). Additional measurements were made by Sun et al. on 0.1%, 1%, 2%, 3.3% and 4% doped samples and the temperature, field, and power dependences of the two-pulse photon echo were analyzed. Although the most dilute samples allow elucidation of the Tm-host lattice interactions, particularly those arising from the Al^{3+} nuclear magnetic moments, the more concentrated samples are important in applications, because the expected larger absorption coefficients allow thinner samples to be used.

In the 0.1% sample, echo decays taken at intensities varying from 2 W/cm^2 to 180 W/cm^2 showed no indication of instantaneous diffusion. At zero field, the echo decay is very non-exponential. Figure 7.5 shows the echo decay at zero field recorded over seven orders of magnitude in intensity. (Different neutral density filters were placed in front of the detector during different pulse delays and then the data were spliced together to cover seven decades.) Fitting this decay to Eq. (7.1) gave $T_M = 116$ μs and $x = 2.1$. These

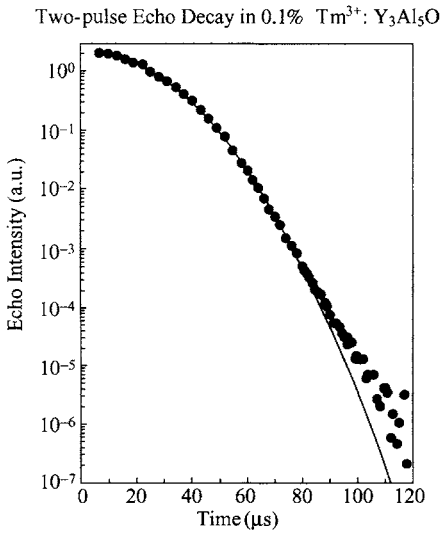


Figure 7.5 Photon echo decay curves in 0.1% Tm^{3+}: $Y_3Al_5O_{12}$. Data were taken with various neutral density filters in front of the detector. The bottom axis is the delay between the two laser pulses

two parameters T_M and x were correlated to a certain extent in the fitting procedure since there was no data with a time delay of zero, and that part is obviously important. The same decay data could also be fit quite well with $T_M = 105$ μs and $x = 1.9$.

Echoes were measured at temperatures varying from 1.4 K to 4.2 K. There was virtually no difference in the echo decay up to 3.5 K. A slight decrease of the dephasing time, from $T_M = 105$ μs to $T_M = 94$ μs at 4.2 K, was observed, with T_M obtained by fixing the exponent at 1.9. Because of this relative insensitivity of the echo decay to temperature, all measurements of the field and intensity dependencies of Tm: $Y_3Al_5O_{12}$ were carried out in superfluid helium ($T < 2.17$ K).

The thermal line broadening of this material was also measured (Macfarlane, 2000) up to 20 K using holeburning and free induction decay, with the result that the direct phonon process dominated the line broadening due to the coupling of the ground state level to the 27 cm^{-1} crystal field level. The homogeneous line broadened to 1 MHz at 6 K and 3.5 MHz at 8 K(Macfarlane, 2000). Using the direct process formalism, this corresponds to a contribution of ~10 kHz at 3 K. This linewidth is slightly wider than that observed by Sun et al., but still consistent with the photon echo measurement, since the hole width was measured by hole burning and probably has a contribution from spectral diffusion.

A small magnetic field dramatically lengthens the echo decay time. In a magnetic field on the order of tens of Gauss, strong modulations arise from the Zeeman splitting of superhyperfine sublevels. In fields above 100 G, the lengthening of the decay essentially saturates, although the echo decay shape continues to change due to the field-dependent modulations. The 100 G decay curve gives approximately T_M = 130 μs and x = 1.3 corresponding to Γ_h = 2.45 kHz. Although the increase of T_M from 103 μs to 130 μs doesn't seem very large, when combined with a much smaller exponent x, the decays in a field are dramatically longer.

No instantaneous diffusion was observed for the 0.1% sample in the power schemes used in these experiments with Rabi frequencies of a few MHz. However, for the more concentrated crystals, instantaneous diffusion became more pronounced since the active ions were closer to each other. To investigate instantaneous diffusion for these crystals, excitation density was varied over two orders of magnitude. It was observed that as the excitation intensity varied from low to high in these samples, not only the decay time but also the echo decay shape (thereby x) changed. As excitation intensity increases, decay times shorten and decay becomes more exponential. There seems to be a correlation between the exponent x and T_M derived from fits to Eq. (7.1). For example, when $T_M = 75$ μs, $x = 1.55$; when $T_M = 45$ μs, $x = 1.2$; and when T_M is shorter than 30 μs, $x = 1.0$. This is because, as the decay becomes shorter, the spin flip rate is slow compared to the dephasing time, and the frozen core thawing effect

is not important before the coherence is dephased. Figure 7. 6 shows the instantaneous diffusion properties of all of these crystals. As can be seen, at extremely low excitation densities, even the more concentrated samples reach the low excitation limit and give the true decay time. Samples with over 2% concentration were not measured to the lowest intensity, but the same behavior was expected. This is quite interesting, since it demonstrates that Tm – Tm interaction does not determine the ultimate limit of the echo decay or dephasing, while that of Tm – Al does, in direct contrast to the Er^{3+} system, where Er – Er dominates the coherent transient behavior.

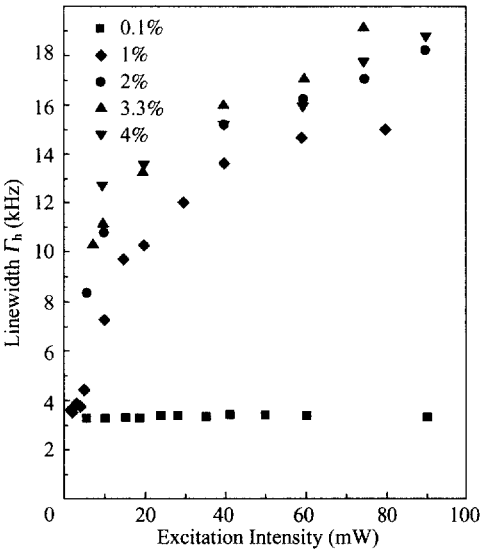


Figure 7. 6 Instantaneous diffusion in Tm^{3+}: $Y_3Al_5O_{12}$ at various concentrations. Instantaneous diffusion was not observed in the 0. 1% sample, but it is more dramatic in the higher concentration samples. The low excitation limits for all samples converge

7.4.2 Tm^{3+}: $Lu_3Al_5O_{12}$

This material has very similar spectroscopic properties to those of $Y_3Al_5O_{12}$ (YAG); the parameters are listed in Table 7. 9. Lutecium has a larger nuclear magnetic moment than yttrium, so there could be some dephasing caused by nuclear spin flips of the lutetium in addition to that caused by aluminum.

Two-pulse photon echo experiments were carried out on a 2% Tm^{3+}: $Lu_3Al_5O_{12}$ crystal. The echo decays were exponential at high excitation densities. At the highest power used, the echo decay time was $T_2 = 27$ μs. As the excitation density was lowered, the echo decay slowed and became non-exponential. At the lowest power used, T_M = 90 μs, and the exponent in

Eq. (7.1) was only $x = 1.3$, much less than for the $Tm^{3+}:Lu_3Al_5O_{12}$ system, where the exponent reached $x = 2.0$ in the low-power limit.

In a magnetic field of 375 G applied perpendicular to the $\langle 111 \rangle$ axis, the echo decay lengthens and is virtually exponential with echo decay time, reaching 120 μs at the low-power limit. Extrapolation of the instantaneous diffusion curve gives about $\Gamma_h = 2.4$ kHz for the homogeneous linewidth at zero power in this field, and $\Gamma_h = 3.2$ kHz for zero-field.

It is interesting to note that the linewidth limit of this material is very similar to that of $Y_3Al_5O_{12}$ in spite of the larger nuclear magnetic moment of Lu. The zero-field linewidth Γ_h for $Y_3Al_5O_{12}$ is about 2.8 – 3.3 kHz, depending on the choice of exponent x. A field of a few hundred Gauss gives a linewidth of 2.3 kHz with exponent $x \sim 1.2$. The much smaller exponent in the decay of $Lu_3Al_5O_{12}$ seems to indicate much different frozen core dynamics, due to the presence of both Lu and Al with different moments and at different distances.

T_M in both $Tm^{3+}:Y_3Al_5O_{12}$ and $Tm^{3+}:Lu_3Al_5O_{12}$ are quite similar. Nuclear spin flips of lutecium were important in the details of the dynamics, but not in the overall decay. This similarity in coherence properties suggest that the mixed garnet system $Y_{1.5}Lu_{1.5}Al_5O_{12}$ would be interesting, since it would inevitably have a broadened inhomogeneous line.

7.4.3 $Tm^{3+}:Y_{1.5}Lu_{1.5}Al_5O_{12}$

In the mixed garnet system $Y_{1.5}Lu_{1.5}Al_5O_{12}$ (YLuAG), where Y and Lu are in 50 – 50 mixture, the $^3H_6(1) \leftrightarrow {}^3H_4(1)$ transition was very broad and the inhomogeneous linewidth was $\Gamma_{inh} = 270$ GHz (9 cm^{-1}), spanning the $Y_3Al_5O_{12}$ and $Lu_3Al_5O_{12}$ difference of 10.4 cm^{-1}. The wavelengths for the same transitions in $Tm^{3+}:Y_3Al_5O_{12}$ and $Tm^{3+}:Lu_3Al_5O_{12}$ fall under the envelope of this broad inhomogeneous line. The center wavelength of this transition was 793.8 nm (12,598.5 cm^{-1}) and the peak absorption coefficient was $\alpha = 3.4$ cm^{-1} for a 3% $Tm^{3+}:Y_{1.5}Lu_{1.5}Al_5O_{12}$ sample. This inhomogeneous linewidth is an order of magnitude greater than that for Tm^{3+} in $Y_3Al_5O_{12}$, providing a significant increase in the potential system bandwidth in memory or processing applications. Emission spectra showed the ground state splitting was $\Delta_g = 34$ cm^{-1}, very similar to that observed in $Y_3Al_5O_{12}$.

Echo decays were slightly non-exponential in zero field. Application of an external magnetic field of 440 G resulted in exponential decays. Zero field data at the center of the absorption line obtained with 3.3 W/cm^2 excitation intensity and fitted to an exponential gave $T_2 = 41$ μs and $\Gamma_h = 7.7$ kHz. Fits of the same zero-field data to Eq. (7.1) gave $x = 1.15$ and $T_M = 44$ μs, indicating that the decays were nearly exponential. Measurements with the same excitation intensity in a field of 440 G gave an exponential decay with $T_2 = 69$ μs, corresponding to a homogeneous linewidth of 4.6 kHz.

Dephasing properties of this material were also investigated across the absorption line since it spans the lines of $Tm^{3+}:Y_3Al_5O_{12}$ and $Tm^{3+}:Lu_3Al_5O_{12}$. It was found that there were no significant variations of the homogeneous linewidth at different parts of the absorption line. There was no observable effect of temperature on the homogeneous linewidth over the range from 1.45 K to 2.17 K for this material.

The dependence of the homogeneous linewidth on laser intensity was also investigated by varying the excitation density from 3.3 to 139 W/cm^2. The homogeneous linewidth exhibited the expected broadening as a function of increased excitation intensity. Decays recorded in an applied magnetic field of 440 G at 1.9 K showed an increase in homogeneous linewidth from 4.6 kHz to 16.4 kHz over this range of excitation intensities.

7.4.4 $Tm^{3+}:Y_3Ga_5O_{12}$

Although it is also a garnet, $Tm^{3+}:Y_3Ga_5O_{12}$ (YGG) is quite different from $Tm^{3+}:Y_3Al_5O_{12}$. The $^3H_6(1)\leftrightarrow{}^3H_4(1)$ transition has a much smaller oscillator strength in $Tm^{3+}:Y_3Ga_5O_{12}$. In the 0.1% $Tm^{3+}:Y_3Ga_5O_{12}$ sample, the peak absorption coefficient α was only 0.06 cm^{-1} with $\Gamma_{inh}=55$ GHz (1.8 cm^{-1}). Even taking into account the wider linewidth, the oscillator strength for this transition is still about 10 times smaller than in $Tm^{3+}:Y_3Al_5O_{12}$. Optical nutation experiments also confirm this result. The difference in energy level structures of these two systems suggests that the transition probability might be very different due to the difference in the crystal field wavefunctions associated with these levels.

Photon echo decays were non-exponential in zero external magnetic field. Application of external magnetic fields up to 440 G resulted in more exponential decays. Fits to Eq. (7.1) resulted in parameters that varied from $T_M=326$ μs and $x=1.65$ ($\Gamma_h=976$ Hz) at zero field to $T_M=460$ μs and $x=1.2$ ($\Gamma_h=692$ Hz) in a field of 440 G. The smaller exponents in the fits quite possibly indicate a different spin flip rate of the gallium nuclei compared to Al in the aluminum garnets.

A "small" temperature dependence was observed for the range from 1.45 K to 2.17 K. Decays recorded in a field of 440 G and excitation density of 8 W/cm^2 appeared to become shorter as temperature was increased, although the total increase was only 300 Hz. This is quite different from the $Tm^{3+}:Y_3Al_5O_{12}$ samples where no T dependence was observed up to 3.5 K. It is unlikely that any direct phonon process is contributing, due to the relatively large crystal field splittings Δ in the ground and excited states. This temperature dependence may be due to two-level system effects introduced by local disorder in the material (Flinn et al., 1994). The $Y_3Ga_5O_{12}$ crystal used was of lesser crystal quality than that of the $Y_3Al_5O_{12}$ sample. Some strains in the crystals were visible between

crossed polarizers.

As in the 0.1% Tm^{3+}: $Y_3Al_5O_{12}$ sample, no instantaneous diffusion was observed in the 0.1% Tm^{3+}: $Y_3Ga_5O_{12}$ sample. No change in the two-pulse photon echo decay (homogeneous linewidth) was observed while varying the of the excitation power density over the range from 8 W/cm^2 to 230 W/cm^2.

For the 1% Tm^{3+}: $Y_3Ga_5O_{12}$ sample, the instantaneous diffusion effect is stronger. The homogeneous linewidth did broaden with increased excitation intensity. However, the effect was very subtle, resulting in only 200 Hz broadening (from 800 Hz to 1 kHz) for two orders of magnitude increase in the excitation intensity in a field of 440 G. The magnitude of the broadening in zero field is similar. This broadening due to instantaneous diffusion is extremely small compared to Tm^{3+} doped aluminum garnets, possibly due to the small excited number density as a result of the small absorption coefficient.

7.4.5 Tm^{3+}: LaF_3

Photon echo measurement gave $T_2 = 7$ μs at zero field and $T_M = 80$ μs and $x = 2$ in a field of 415 G. The dephasing mechanism was attributed to F – F spin flips. The dramatic change in dephasing time was attributed to the slowing down of F – F spin flips (Macfarlane, 1993b).

7.4.6 Tm^{3+}: Y_2SiO_5

Because of the success of the Y_2SiO_5 host for other rare-earth ions, this host was also investigated for the Tm^{3+} ion, since spin flip induced dephasing from the host is expected to be very small. However, photon echo measurements on this system did not produce long dephasing times. The optical dephasing times for transitions to $^3H_4(1)$ of each site were measured using photon echoes in 0.1% Tm^{3+}: Y_2SiO_5. Echo decays were recorded in zero field for the $^3H_6(1) \leftrightarrow {}^3H_4(1)$ transition of site 1 (12,642.25 cm^{-1}) and for the $^3H_6(1,2) \leftrightarrow {}^3H_4(1)$ transitions of site 2 (12,642.44 cm^{-1} and 12,640.8 cm^{-1}). Echo decays for site 1 were taken using pulses of 0.5 μs duration; those for site 2 were taken using pulses of 0.2 μs duration. The measured dephasing times were $T_2 = 4.8$ μs for site 1 and $T_2 = 1.3$ μs for site 2, corresponding to homogeneous linewidths of $\Gamma_h =$ 66 kHz for site 1 and $\Gamma_h = 241$ kHz for site 2 at zero field. Echo decays for the $^3H_6(2) \leftrightarrow {}^3H_4(1)$ transition of site 2 gave a dephasing time $T_2 = 1.1$ μs, corresponding to a homogeneous linewidth of $\Gamma_h = 290$ kHz.

The shorter dephasing times found for both sites in Tm^{3+}: Y_2SiO_5 are attributed to phonon-induced dephasing and Tm – Tm interaction due to the pseudodegenerate ground state of site 2. For site 1, although the energy gap of $\Delta_g = 13$ cm^{-1} should allow a longer T_2 than measured (4 μs) if only phonon-

induced dephasing is present, the site 2 effective spin in the ground state is probably causing the measured short T_2 for site 1. The dominant dephasing mechanism at site 1 should be the Tm (site 1) – Tm(site 2) Tm^{3+} interaction. For site 2, due to the small splitting ($1.6\ cm^{-1}$) in the ground state, phonon-induced dephasing and Tm(site 2) – Tm(site 2) interactions should both be important. This is similar to 0.1% Tm^{3+}: $Y_2Si_2O_7$, where the ground state splitting was $6\ cm^{-1}$ and the dominant dephasing mechnism was the direct phonon process.

Echo decays were also measured in an external magnetic field of 40 kG as moderate fields ~100 G did not split the levels wide enough to affect the measured dephasing time. In the stronger fields, longer dephasing times of 34 – 40 μs (Γ_h ~ 10 kHz) were measured for this material(at both sites). The likely cause of this lengthening of the echo decay is the Zeeman splitting of the pseudo-degenerate ground state of site 2, freezing out the pseudo-spin flips for site 2 and reducing the contributions of the direct phonon process at low temperature. Other reduction factors are likely to be very small compared to this effect.

7.4.7 Tm^{3+}: $Y_2Si_2O_7$

Another form of yttrium silicate, $Y_2Si_2O_7$, was investigated as a host material because of its small host nuclear moment (Wang et al., 1996). The spectrocopic properties are listed in Table 7.9.

The studies were carried out on a 0.1% doped sample. Photon echo decays recorded at temperatures 1.24 K and 2.17 K using a laser excitation intensity of $9.6\ W/cm^2$ yielded dephasing times of $T_2 = (23 \pm 2)$ μs and $T_2 = (1.9 \pm 0.2)$ μs corresponding to homogeneous linewidths of (14 ±2) kHz and (170 ± 20) kHz respectively. Laser excitation intensity-dependent measurements of the homogeneous linewidth at 1.45 K showed that the excess dephasing is proportional to the number of ions changing state during the echo pulse sequences, consistent with the instantaneous diffusion picture. Since $T_1 \gg T_2$, the number of ions changing state due to population decay during the echo measurement process is small, and thus the effects due to the first pulse are negligible. The extrapolated linewidth $\Gamma_0 = 25.6$ kHz comes mostly from the direct phonon process.

Measurements of Γ_h temperature dependence between 1.24 K and 2.17 K was ascribed to resonant phonon interactions between the $^3H_6(1)$ ground state and the next higher crystal field level $^3H_6(2)$. Fitting the data gave an energy gap $\Delta = 6.7\ cm^{-1}$, in good agreement with the $(6 \pm 1)\ cm^{-1}$ value measured in fluorescence experiments. The $T = 0$ K homogeneous linewidth of (6 ±2) kHz obtained from the fit contains a contribution of (2.3 ±0.1) kHz from the phonon process. The residual 3.7 kHz was attributed to other interactions, including dipole coupling between the relatively sensitive Tm^{3+} ions and the lattice.

7.4.8 $Tm^{3+}:Y_2O_3$

Two-pulse photon echo measurements on a 0.1% $Tm^{3+}:Y_2O_3$ sample characterized the homogeneous linewidth and dephasing mechanisms as a function of temperature, applied external magnetic field, and laser excitation intensity. Photon echo decays were slightly non-exponential with and without an applied external magnetic field. At 1.3 K and zero magnetic field, the measured linewidth is $\Gamma_h = 12.5$ kHz.

Application of an external magnetic field of 440 G narrowed the homogeneous linewidth by about 15%. This is expected due to the small magnetic moment of the yttrium ion. A clearly measurable temperature dependence of Γ_h between 1.45 and 2.17 K was observed. Over this temperature range the homogeneous linewidth increased by a factor of 2 from 17 to 34 kHz measured at 14.6 W/cm^2. Since the ground state energy gap was about Δ_g = 30 cm^{-1} and the excited state energy gap was $\Delta_e = 79$ cm^{-1}, contributions from the direct phonon process were not expected to be significant. The temperature-dependent mechanism was probably local phonon modes, as was observed by Flinn et al. in many $Eu^{3+}:Y_2O_3$ samples (Flinn et al., 1994a).

In $Tm^{3+}:Y_3Al_5O_{12}$ and Tm^{3+}: YGG, with similar splittings, T_2 were hundreds of microseconds long compared to ~20 μs in this system. In the garnets, due to the larger aluminum nuclear magnetic moment, Al^{3+} play a more significant role in the dephasing mechanism than yttrium does in Y_2O_3, due to the much smaller yttrium nuclear magnetic moment. So the host nuclear moment should not be the dominant dephasing mechanism. It was also postulated that the dephasing might be caused by Tm^{3+} ions at the C_{3i} site. If the Tm^{3+} ions at the C_{3i} sites have a degenerate or pseudo-degenerate ground state, then it can be very sensitive to temperature and field, spin flips from those sites could cause the dephasing of the C_2 site Tm^{3+}. It is not conclusive as to what causes the dephasing but the two-level system and Tm^{3+} at the C_{3i} site seem to be the most logical.

Dependence of the homogeneous linewidth on laser intensity was measured at 1.56 K by varying the power from 2 to 73 W/cm^2. This resulted in a change in Γ_h from 19 to 22 kHz (~16%). Compared to the measurements in 0.1% $Tm^{3+}:Y_3Al_5O_{12}$, the higher instantaneous diffusion in this sample can also be caused by the higher absorption coefficient, since more ions are involved in the transitions than in the garnet experiments.

7.4.9 $Tm^{3+}:YAlO_3$

This system is the antithesis of long T_2 systems. Attempts on both a 0.1% doped sample and a 4% doped sample failed to produce a photon echo. Such a short T_2 is due to the small 3.1 cm^{-1} energy gap between the two lowest levels of $^3H_6$. This small gap was not reported in earlier literature. Compared to Tm^{3+}:

Y_2SiO_5, which produced an echo even though it had a even smaller energy gap ($1.67\ cm^{-1}$), it is probably caused by the stronger nuclear spin of Al^{3+} compared to Y^{3+}, and also the phonon density difference in these two crystals.

7.4.10 Tm^{3+} Materials Summary

The coherence parameters are summarized in Table 7.10. We note that the ratio Γ_{inh}/Γ_h can be as large as 10^8 ($Y_{1.5}Lu_{1.5}Al_5O_{12}$). Among all Tm^{3+} materials studied, the best choice for coherent transient applications seems still to be the garnet systems. The $Tm^{3+}:LaF_3$ system has reasonably long dephasing times in a small field, but the higher F nuclear magnetic moments probably will cause more spectral diffusion than in the garnet systems for storage in the metastable level.

Table 7.10 Coherence properties and bandwidth data in the weak excitation limit for the Tm^{3+} materials studied

Material	Γ_{inh}(GHz)	T_M(μs)	x	$\Gamma_{inh}/\Gamma_h(10^6)$	T_M(μs)	x	$\Gamma_{inh}/\Gamma_h(10^6)$
			($B=0$)			($B>100$ G)	
$Y_3Al_5O_{12}$	20	116	2.1	7.3	130	1.3	8.2
$Lu_3Al_5O_{12}$	20	90	1.3	6	120	1.0	7.5
$Y_{1.5}Lu_{1.5}Al_5O_{12}$	270	55	1.1	46	75	1.0	64
$Y_3Ga_5O_{12}$	55	326	1.65	55	460	1.2	78
LaF_3		7			80	2	
Y_2SiO_5(1)	2.6	4.8	1.0	0.04	same[a]		
Y_2SiO_5(2)	4.5	1.3	1.0	0.018	same[a]		
Y_2O_3	3.6	19	1.15	0.21	21.4	1.0	0.248
$YAlO_3$	unfavorable levels, no echo						

(a) The linewidths do not change in a weak field under 1 kG. A stronger field in a superconducting magnet lengthens the echo decay and narrows the linewidth.

For the aluminum garnet systems, the oscillator strength of the transition is close to 10^{-7}, with T_M close to 100 μs in zero field for the lower concentrations. Instantaneous diffusion is more dramatic for more heavily doped materials. The gallium garnet has even longer T_M, approaching those of Eu^{3+} systems, but the oscillator strength is smaller at $\sim 10^{-8}$, also similar to the Eu^{3+} systems. Because of the narrower linewidth, it could be used as a probe of small dynamical interactions in the lattice just as Eu^{3+} and Pr^{3+} have been. The experimental realization would be simpler with Tm because of the lack of long-term storage.

Because of the near degeneracy of the ground state, $Tm^{3+}:YAlO_3$ failed to produce an echo, and the T_M was estimated to be less than 1 μs at zero field.

The low nuclear magnetic hosts Y_2O_3, Y_2SiO_5, and Y_2SiO_7 did not

produce more advantageous results. In the silicates, near degeneracy in the ground state causes very fast dephasing due to phonon coupling and magnetic interactions. The Tm^{3+}: Y_2O_3 system was more puzzling. The dephasing mechanisms were postulated to be either two-level systems of the crystal or the influence of the C_{3i} sites of the crystal, with the first possibility much more likely. It was also postulated that the T_2 for that system could be very growth-dependent, just as in Eu^{3+}: Y_2O_3.

7.5 Er^{3+} Materials

Er^{3+} is one of the first paramagnetic ions studied for optical coherent transients with the possible exception of ruby. The 1.5 μm transition falls within the important telecommunications band and has thus attracted a lot of attention. The same transition is utilized in erbium doped amplifiers in telecommunications.

The $^4I_{15/2}$ to $^4S_{3/2}$ transition at 18,557 cm^{-1} in Er^{3+}: LaF_3 was studied by Macfarlane and Shelby (Macfarlane and Shelby, 1982) and the $^4I_{15/2}$ to $^4F_{9/2}$ for Er^{3+}: $YAlO_3$, Er^{3+}: $LiYF_4$, and Er^{3+}: LaF_3 around 649 nm was studied by Ganem et al. (Ganem et al., 1991) In the latter work, the photon echo decays were non-exponential and the dephasing times reached the superhyperfine limit at high magnetic field (~30 kG); the exponent reached 2.4 in that limit. Similar behavior was also found in ruby. Photon echo decays can be described by Eq. (7.1).

Optical dephasing of the 1.5 μm Er^{3+}: $^4I_{15/2} - {}^4I_{13/2}$ transition was first studied by Silberberg et al. (Silberberg et al., 1992) in Er^{3+} doped fibers at 1.5 K by accumulated echoes, and the dephasing time there was ~1 ns. Two pulse echoes on this transition in Y_2SiO_5 have proven that the dephasing time is much longer in crystals (Macfarlane et al., 1997). In this section, we only review the coherence properties of the 1.5 μm Er^{3+}: $^4I_{15/2} - {}^4I_{13/2}$ transition in different oxide crystals. These experiments were generally carried out using systems with very dilute Er doping to minimize Er – Er interaction.

The basic spectroscopic parameters for these Er materials are listed in Table 7.11. In these materials, Er^{3+}: $YAlO_3$ has a transition at much shorter wavelength than others. All others have similar wavelength in the 1535 nm region. The upper state lifetime of this transition is generally about 10 ms, and thus contribute very little at the homogeneous linewidth. In the following discussions, the results are all from (Sun et al., c) unless otherwise noted.

Table 7. 11 Spectroscopic Parameters for Er^{3+} systems. The oscillator strength of Er^{3+}: $^4I_{15/2} - {}^4I_{13/2}$ for all systems is $\sim 10^{-7}$ with the exception of Er^{3+}: $SrWO_4$, which is ten times smaller

Material	λ (nm)	σ (cm^{-1})	Γ_{inh} (GHz)	$\Delta_g(^3H_6)$ (cm^{-1})	$\Delta_e(^3H_4)$ (cm^{-1})
Y_2SiO_5(site 1)	1536.14	6508.04	0.2 - 3	64	40.5
Y_2SiO_5(site 2)	1538.57	6497.76	0.2 - 3	47	38.5
Y_2O_3	1535.57	6511.69	1 - 2	38.9	32
$YAlO_3$	1514.38	6601.56	1 - 2	50.7	38.6
$LiNbO_3$	1531.52	6527.68	250	63	62
$Y_3Al_5O_{12}$	1526.97	6547.13	~30	22	50
$CaWO_4$	1532.30	6524.35	1 - 2	20	8.3
$SrWO_4$	1533.55	6519.04	1 - 2	12.3	4.9

7.5.1 Properties of Er^{3+}: Y_2SiO_5

The $^4I_{15/2}(1) \leftrightarrow {}^4I_{13/2}(1)$ transitions occur at 1536.14 nm (site 1) and 1538.57 nm (site 2) for Er^{3+}: Y_2SiO_5. The $^4I_{13/2}$ level has a lifetime of 8 ms for a 1% doped sample at room temperature (Li et al., 1992) so the lifetime should be a little longer for the more dilute sample at low temperature. Böttger measured these to be 11.4 ms for site 1 and 9.2 ms for site 2 at 2 K. The orientation-dependent absorption coefficients and the linewidths for both sites are listed in Table 7. 12. The absorption strength ($\sim \alpha\Gamma_{inh}$) of the crystals should scale with dopant concentration. The absorption was not very polarized for site 1, with the absorption similar along all three major optical axes. The absorption for site 2 was more anisotropic; the maximum absorption was along D_1, and absorption along the other two axes was quite weak.

Table 7. 12 Peak absorption coefficients and inhomogeneous linewidth for both sites in a 0.005% Er^{3+}: Y_2SiO_5 crystal. The linewidths are FWHM from Lorentzian fits

	D_1	D_2	b	Γ_{inh}(MHz)
Site 1	4.8	9.0	8.0	500
Site 2	9.6	1.2	0.75	380

EPR on Er^{3+}: Y_2SiO_5 (Kurkin and Chernov, 1980) shows that Er^{3+} ions has maximum g-factors of 15.465 and 14.804 in the ground state; the maximum g directions are different for the two sites, and are not along any of the major optical axes. EPR in the $D_1 - D_2$ plane indicates that the g factors are 6 and 15.3 in the D_1 direction, and 1.5 and 10 in the D_2 direction (Sun et al.). It is clear

that the field should be applied along D_1 to freeze out Er – Er interactions more effectively. Optical Zeeman experiments found the correlation of these g factors with the optical transitions and determined the g factors for the excited states. The g factors for both the ground and excited states are listed in Table 7.13. More recent measurements by Böttger mapped out the ground and excited state g factors in the $D_1 - D_2$, $b - D_1$, and $b - D_2$ planes. His measurements confirmed the results listed in the above Table 7.13(Böttger, 2002).

Table 7.13 g factors in the ground and excited states as measured by EPR and optical Zeeman experiments

	D_1		D_2	
	$I_{15/2}(1)$	$I_{13/2}(1)$	$I_{15/2}(1)$	$I_{13/2}(1)$
Site 1	6	5	10	7
Site 2	15.3	12.8	1.5	1.5

Photon echoes were carried out in crystals with doping levels from 0.001% to 0.1%. The photon echoes were very weak in zero and low field, with the echo intensity increasing dramatically with applied magnetic field as T_2 lengthens. Very strong modulation occurs at fields below 2 kG, making it diffcult to determine true value of T_2 or T_M. At higher fields, this modulation was not observed, since the level splittings were wider than the spectral width of the excitation pulses. As expected from the g factors listed in Table 7.13, lengthening of the dephasing time is much weaker for fields along the D_2 direction than along the D_1 direction.

In Fig.7.7, the decay curves for site 1 of a 0.0032% sample are presented with the magnetic field applied along the D_1 direction. The zero field dephasing times were $T_2 = 3.7$ μs for site 1 and $T_2 = 3.3$ μs for site 2. There are several interesting features. (1) echo decays lengthened with the field; (2) the echoes became non-exponential in a field but became exponential again in a high field; (3) the decay at 16 kG was actually shorter than at 8 kG; (4) the decay curve at long delay time becomes noisier. This noise was caused by the laser frequency jitter of the external cavity diode laser between the two excitation pulses. At time scales longer than 200 μs, the frequency difference between the two pulses could be comparable to or larger than the Fourier transform-limited linewidth of the pulses, causing instability in the echoes. This is a very interesting problem in the measurement of narrow linewidths using time-domain techniques. An echo decay curve produced by signal averaging will be more indicative of laser performance than the material property at long times. To mitigate this problem in the measurements of the longer dephasing times, the envelope of the largest echoes on the oscilloscope was used as the measurement of the true echo intensity, since the largest echo was expected when the two pulses have perfect overlap in

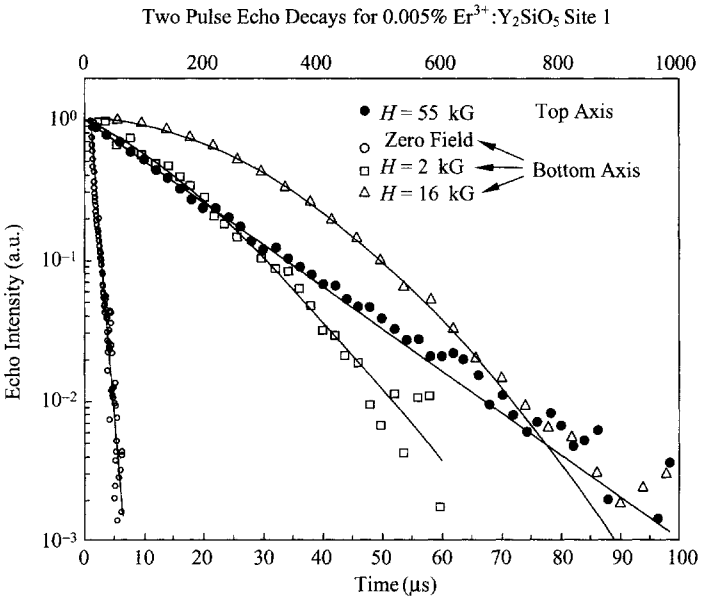


Figure 7.7 Two pulse photon echo decays for Er^{3+} in site 1 of Y_2SiO_5 for several values of the magnetic field. Notice the data use different horizontal axes because of the different times scales involved

frequency. It should be noted that in these experiments, the echo intensity fluctuation from shot to shot was less than 5% at short delays when the laser is stable enough for good overlap between the spectra of the two excitation pulses. Figure 7. 8 shows the difference between the measurement using envelope detection and signal averaging at long time scales. These data are taken on a 0. 001% sample in a field of 70 kG along D_1. The decay curve obtained via envelope detection is very close to exponential and smooth, while that obtained by signal averaging is noisy. Measuring echo decay by many-shot averaging is a convolution of the echo decay and laser characteristics. The T_2 measured using the envelope at this field was 4. 08 ms, corresponding to a homogeneous linewidth $\Gamma_h = 1/\pi T_2$ of 78 Hz.

The field dependence of the homogeneous linewidth is shown in Fig. 7. 9 for the 0. 0032% sample. Other samples gave similar field behavior, although the more concentrated samples tend to have shorter T_2 at lower field. It can be seen from the graph that the lengthening of the dephasing is still not saturated at the highest field used. One interesting feature is that the decays were exponential at low and high field, but very non-exponential and short at 20 kG, with the exponent reaching 2. The dephasing time at 10 kG was greater than at 20 kG. The narrower linewidth at 10 kG was explained as the motion narrowing as observed in the spin echoes (Mims, 1968). The initial lengthening was caused by the freezing out of Er – Er spin interactions.

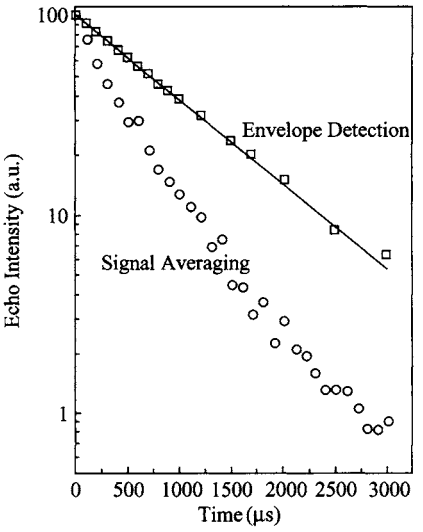


Figure 7.8 Echo decay curve for a 0.001% Er: Y_2SiO_5 sample at 7. Data in the top curve were obtained from the envelope function of the scope, while data in the bottom trace was obtained via signal averaging

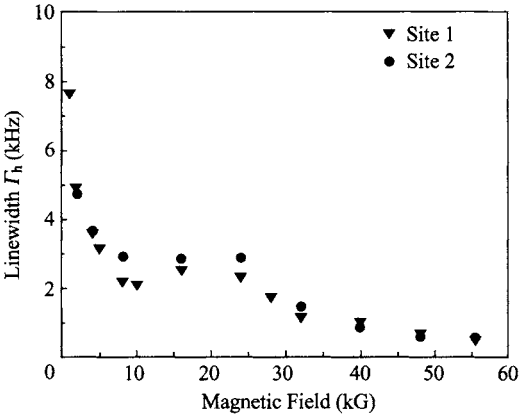


Figure 7.9 Magnetic field dependence of the homogeneous linewidth at the two sites of Y_2SiO_5. Notice the wider linewidths at 2 T compared to those at 1 T

No ISD was observed with the maximum power available, probably due to the large distance between ions at low doping levels.

7.5.2 Properties of $Er^{3+}:Y_2O_3$

Y_2O_3 is an interesting material because it is similar to Y_2SiO_5, being a low nuclear magnetic moment host. Long dephasing times are expected in these hosts. The Y_2O_3 crystal has T_h^7 symmetry. Two crystallographic sites exist for the Y (or Er) ions with C_2 and C_{3i} local symmetry. Spectroscopy and photon echoes experiments were carried out on a 0.005% $Er^{3+}:Y_2O_3$ crystal. The C_2 site transition occurs at 1535.277 nm in air (6512.13 cm^{-1}) and the C_{3i} site transition occurs at 6470.2 cm^{-1} (Reinemer, 2003). The photon echo studies were carried out for the C_2 site by Sun et al. and the C_{3i} site was measured by Reinemer (Reinemer, 2003).

In zero field, this sample has very weak echoes, much like the case for $Er^{3+}:Y_2SiO_5$. The echo intensity increases by an order of magnitude in a very small field (~100 G). Beyond a few hundred gauss, no enhancement of the echo intensity was observed in a stronger magnetic field. Because of the inequivalent splittings of the different magnetic sites, the echo became weaker in a strong field when the magnetic field split the different sites so that the absorption of a certain line is less than the total value. No instantaneous diffusion was observed as expected from the extremely low concentration of the active ion. In a strong field, the lower component of the transitions for all sites have very similar dephasing properties, even though some of them have larger or smaller Zeeman splittings. These are indications that the dephasing is an effect of the whole lattice rather than a local effect.

The measured low field (~100 G) echo decay is non-exponential; a fit to Eq. (7.1) gave $T_M = 18$ μs, and $x = 1.86$. With applied external magnetic field, T_M lengthened but the lengthening saturated at about 45 kG. In a weak magnetic field below 1 kG, there were strong modulations in the echo decay, making it impossible to obtain a good fit to any expression normally used for echo decays. At the higher field limit, the echo decay saturates to about $T_M = 100$ μs and $x = 1.4$. There was an interesting feature in the field dependence of Γ_h between 10 and 30 kG that is reminiscent of $Er^{3+}:Y_2SiO_5$. The decay became, much like the case in $Er^{3+}:Y_2SiO_5$ at 20 kG. The exponent x became shorter large again for both systems and peaks around 15 kG. In even stronger fields, the decay became exponential again in Y_2SiO_5, but the exponent x is 1.4 in this crystal even in the strongest field. Another difference between these systems is that the echo decay still lengthens in the maximum field achievable (8 T) in Y_2SiO_5, while the lengthening of T_M saturates in a much smaller field of about 45 kG in 0.005% $Er^{3+}:Y_2O_3$.

7.5.3 Properties of $Er^{3+}:LiNbO_3$

$LiNbO_3$ has been used widely in nonlinear optical applications. It has also been

used in photorefractive holographic storage demonstrations. Because of the presence of the Li^+ anti-site, it has been thought to be glassy (Macfarlane et al., 2000). The inhomogeneous linewidth for the 1.5 μm transition in Er^{3+}: $LiNbO_3$ is much broader than in all other materials, but the coherent transient properties were found to be similar across the 270-GHz line width and the homogeneous line was much narrower than would be expected in a glassy system.

The spectroscopy of Er^{3+} doped $LiNbO_3$ has been published (Gabrielyan et al., 1970); relevant information is listed in Table 7. 11. The absorption coefficient is 4 cm^{-1} the absorption peak (Sun et al.) ESR on this system was reported by Milori et al. (Milori et al., 1995); the g factors are $g_{//} = 15.13$ and $g_{\perp} = 2.14$ for the ground state. Optical Zeeman experiments indicate that though there could be many sites contributing to the absorption lineshape, all these sites behave similarly in a magnetic field. That transition has a differential g factor $\Delta_g \approx 2$, so the excited state should also have its maximum g factor along the c direction, with a value of 13. Because of the small difference in the g factor in the two states, even in a field of 5 Tesla, the transition shifts only about 2.5 cm^{-1}. The echo experiments for the field dependence measurements were carried out with the laser at a fixed frequency.

Echo experiments were carried out on two 0.06% doped crystals from different preparations; no difference was found in the transient behavior. The magnetic field was applied along the c axis. No echo was observed at zero field, but the echo was observable in a weak magnetic field of 1 kG. The echo decay was non-exponential and the exponent in Mims' expression becomes larger with increasing magnetic field. The echo became very strong above 10 kG, a few percent of the excitation. The dependence of the homogeneous linewidth on the applied magnetic field is shown in Fig. 7.10. The echo decay time was about 9 μs, x = 1 at 1 kG, and the lengthening of the decay saturates at a field of 25 kG to $T_M = 170$ μs and $x = 2.05$. This field dependence is in direct contrast to Er^{3+}: Y_2SiO_5 where a "bump" occurs at about 2 T.

No instantaneous diffusion was observed in this crystal. Echo decay measurement across the line every 10 GHz found no observable variation in the decay constants. All decays give the same T_M and x.

Spectral diffusion experiments were carried out on this crystal in a field of 10 kG. Data fit to Yano's expression (Eq. (7.3)) yield Γ_0 = 1.55 kHz, Γ_1 = 63 kHz, and $R = 1.42$ kHz, the rate of spin flips that are causing the dephasing.

7.5.4 Properties of Er^{3+}: $YAlO_3$

$Y_3Al_5O_{12}$ (YAG) and $YAlO_3$ are the two most successful solid state laser materials. The dephasing properties of Er^{3+} in these crystals are determined by Er – Er interaction and the Al^{3+} nuclear spin flips. The spectroscopy of Er^{3+}: $YAlO_3$ has been reported (Donlan and Santiago, 1972). The $^4I_{15/2}(1) \leftrightarrow {}^4I_{13/2}$

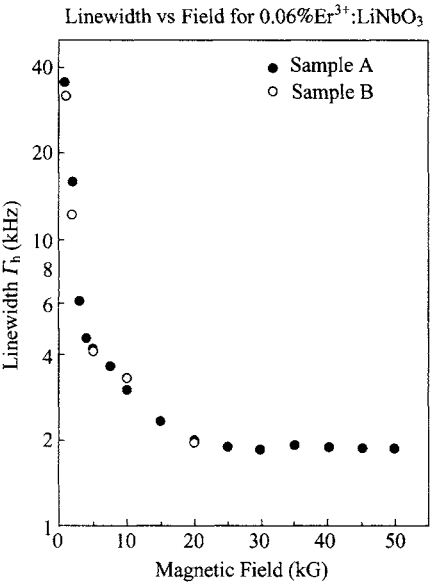


Figure 7. 10 Magnetic field dependence of the homogeneous linewidth in 0. 06% Er: $LiNbO_3$. Both samples gave the same results

(1) transition occurs at 1514. 38 nm, with an excited state lifetime of T_1 = 7. 2 ms (Payne et al., 1992).

Of all the materials studied, Er^{3+}: $YAlO_3$ has the highest energy or the shortest wavelength for this transition. All echo experiments were carried out using only a diode laser. Two-pulse echoes were carried out with the light propagating along the *b*-axis and the magnetic field along the *a*-axis. The sample used was optically thick, and total absorption occurs at the center of the line. The echo was stronger in the wings of the line.

Photon echo studies were carried out by Sun et al. on a 0. 005% sample. No zero-field echoes were observed in this crystal, much as in $Y_3Al_5O_{12}$ and $LiNbO_3$, and a small echo is observed starting at 3 kG. The echo appeared to be close to exponential in the weak field; the decay time was about 5 μs at 4 kG. With applied magnetic field, the echo decay lengthens and the exponent in Mims' expression slowly grows. The lengthening of the echo decays saturated at a field of 40 kG with T_M = 260 μs and x = 2. 2. The general dependence of Γ_h on the magnetic field is very similar to 0. 06% Er^{3+}: $LiNbO_3$.

Spectral diffusion measurements, as described earlier, were carried out at 15 kG. Fitting to Yano's expression (Eq. (7. 3)) gives the spin flip rate that is influencing spectral diffusion at 31 kHz, and the spin flip rate causing diffusion was 3. 4 kHz. This is similar to what we expect for the Al nuclear spin flip at this field.

Similar to the 0.1% Er^{3+}: $Y_3Al_5O_{12}$ described below, Al spin flips dominate the dephasing, and the spectral diffusion of the Er is due both to Er – Er interaction and Er – Al interaction. In a strong field, the Er – Al interaction probably dominates the dephasing and the spectral diffusion in both cases, although in a weak field the Er – Er interaction in 0.1% Er^{3+}: $Y_3Al_5O_{12}$ is much stronger due to the higher concentration of Er. The echo intensity increases very dramatically at low field and saturates at higher field. This saturation field is expected to have a faster onset when the field is applied in the *b* direction for the larger *g* factors, and a slightly narrower linewidth is expected.

7.5.5 Properties of Er^{3+}: $Y_3Al_5O_{12}$

The $^4I_{15/2}(1) \leftrightarrow {}^4I_{13/2}(1)$ transition occurs at 1526.973 nm or 6547.46 cm^{-1} (Koningstein and Geusic, 1964; Zhang et al., 1997). The excited state lifetime was reported by Payne et al. to be T_1 = 6.9 ms (Payne et al., 1992), and by Zhang et al. (1997) to be 10 ms. This transition is broad (~30 GHz) compared to other materials except Er: $LiNbO_3$, so a more concentrated sample was required for the desired absorption in an echo experiment. EPR of this material has been reported by Ball et al. (1961), who measured $g_x = 7.75$, $g_y = 3.71$, and $g_z = 7.35$, where the *x* and *y* directions were along ⟨110⟩ and ⟨110⟩ and the *z* direction was along ⟨001⟩. From the anisotropy of the *g* factor we can see that there is no direction that maximizes the splittings for all the inequivalent sites. However, for the major axes, ⟨111⟩ and ⟨100⟩ are better choices than ⟨110⟩ for applying the magnetic field.

Earlier photon echo experiments were carried out from 1 – 7 K using pulsed tunable dye lasers on a 0.1% sample. The dephasing time was about 50 ns in a magnetic field of 100 G, and varied little with temperature (Zhang et al., 1997). The echo experiments carried out by Sun et al. used a CW laser on a 0.1% Er^{3+}: $Y_3Al_5O_{12}$ crystal. Because of the longer pulses, no echo was observed at zero field due to the strong Er – Er interaction at such high concentration. The echo was first observed in a field of 7.5 kG; the decay constant was slightly non-exponential and very short (3.8 μs), corresponding to a linewidth of 83 kHz. Echo intensity became much stronger and the decay constant lengthened but the decay was still very non-exponential. In a field of 40 kG, the decay constant can be described by T_M = 80 μs and $x = 1.85$.

The spectral diffusion of this system was measured in a field of 30 kG. There was definitely spectral diffusion happening in this crystal even in such a high field. The variation of the stimulated echo intensity with the delay of the reading pulse was also measured in such a field; the echo intensity drops by one order of magnitude at delays of 500 μs.

7.5.6 Properties of Er^{3+} Doped Tungstates

$CaWO_4$ and $SrWO_4$ have the space group C_{4h}^6(I41/a) with 4 formula units per tetragonal cell, with $a=5.2437$ Å and c = 11.3754 Å([111]) for $CaWO_4$, and $a=5.40$ Å and $c=11.90$ Å for $SrWO_4$. The trivalent rare-earth ions substitute for the Ca or Sr ion in S_4 symmetry, and are charge-compensated by Na^+ ions at interstitial sites. No evidence of local distortion was seen in the EPR spectrum, indicating that the charge compensation may not be local to the Er^{3+} ions. The tungstate lattices are generally considered softer than the silicates or aluminates, so the availability of higher-frequency phonons may influence the dephasing time of the dopant ion differently. The tungstates also have relatively small lattice nuclear magnetic moments compared to the aluminates. In both $CaWO_4$ and $SrWO_4$, the Er^{3+} g factor is smaller along the c-axis (1.247 and 0.86, respectively), and considerably larger along the a-axis (8.38 and 8.47, respectively) (Tarasov and Shakurov, 1993; Kurkin and Tsvetkov, 1970).

The photon echo measurements were all made with the magnetic field in the a direction and light propagating in the a' direction. Measurement in the residual field of a superconducting magnet (~100 G) gave T_2 of 15 μs for the 0.005% Er^{3+}: $CaWO_4$ crystal, and much shorter T_2(< 4 μs) for the 0.05% Er: $SrWO_4$ crystal. In a magnetic field, the decay times increase substantially and the decays become non-exponential at higher fields around 25 kG; they are still nonexponential at the highest field of 55 kG. The longest T_M measured for the 0.005% Er^{3+}: $CaWO_4$ sample was 160 μs, corresponding to a homogeneous linewidth of $\Gamma_h = 2$ kHz in a field of about 50 kG. For the 0.05% Er: $SrWO_4$ sample, the longest T_M measured in a field of 50 kG was 80 μs, corresponding to a homogeneous linewidth $\Gamma_h = 4$ kHz.

The shorter T_2 in the $SrWO_4$ sample is most probably due to the higher concentration of Er in the crystal, and Er – Er interaction is the dominant dephasing machanism in the crystal. Another important dephasing mechanism in these systems is the direct phonon process due to the very small energy gap. Because of these small gaps, the temperature dependence of T_2 in these materials is quite strong, and the experiments must be carried out at the lowest temperatures.

7.5.7 Er^{3+} Materials Summary

All of these Er^{3+} systems have long echo decays at low temperature in a strong external magnetic field. For some systems, the dephasing time reached the superhyperfine limit in these materials (Ganem et al., 1991). For example, the saturated value of the dephasing time was T_M = 170 μs, $x=2.05$ for the 0.06% Er^{3+}: $LiNbO_3$ sample, and T_M = 263 μs, $x=2.2$ for the 0.005% Er^{3+}: $YAlO_3$ sample. The 0.1% Er^{3+}: $Y_3Al_5O_{12}$ sample, although not saturated, gave T_M =

80 μs, $x = 1.85$ in a field of 40 kG. The limit of the saturated linewidth can be understood as having the superhyperfine interaction-limited linewidths, since in a strong field and at low temperature, the Er-Er interactions are frozen out. The superhyperfine interaction-limited linewidths, defined by the strength of the magnetic dipole – dipole interaction between the nuclear and electronic spins, sets the limit of the achievable. The coherence properties of these materials are summarized in Table 7.14.

Table 7.14 Coherence properties and bandwidth data for the Er^{3+} materials studied

Material	Γ_{inh}	T_M(μs)	x	Γ_{inh}/Γ_h($\times 10^6$)	T_M(μs)	x	Γ_{inh}/Γ_h($\times 10^6$)
	(GHz)	(Low-field limit)			(High-field saturation)		
YSO(1,2)	0.5	3.3	1	7.3	4.1	1	3
Y_2O_3	1	18	1.85	6	105	1.4	0.3
$LiNbO_3$	200				170	2.0	100
$YAlO_3$	1				265	2.2	0.8
$CaWO_4$	1				140	1.5	0.44
$SrWO_4$	1				72	1.0	0.22
YAG	30				75	1.5	7

One of the most interesting phenomena we observed is that of the echo decay shape and field dependence in low nuclear magnetic moment hosts. In Y_2SiO_5 and Y_2O_3, the decays are exponential in stronger fields, although both have a characteristic increase in homogeneous linewidth at around 20 kG. On the other hand, for $YAlO_3$, $LiNbO_3$, and $Y_3Al_5O_{12}$, the decay gets more non-exponential in stronger fields and saturates at a certain level. The measured linewidth of 78 Hz in 0.001% Er^{3+}: Y_2SiO_5 at 7 T is the narrowest linewidth known in a solid.

There is also a strong difference between the Er^{3+} doped Y_2O_3 and $LiNbO_3$ since it seemed that the coupling of the ion to the two-level systems in the crystals is much weaker for Er compared to Eu^{3+} or Pr^{3+}.

These materials have also been used in demonstrations of laser frequency locking (Bottger et al., 2001; Sellin et al., 2001), data packet header decoding (Harris et al., 1998), and other signal processing applications (Cole et al., 2002).

7.6 Other Materials

Aside from the materials reviewed above, namely the Eu^{3+}, Pr^{3+}, Tm^{3+}, and Er^{3+} doped crystalline systems, other rare-earth doped systems have also been studied for fundamental science and for applications. We briefly review a few

developments.

7.6.1 Eu^{2+} Materials

In many applications, materials with higher oscillator strength are needed. Eu^{2+} has been studied for this purpose. Eu^{2+} materials were studied both by coherent transient techniques and by holeburning. Both population and persistent holeburning were observed in Eu^{2+} doped fluorides. Persistent holeburning was also observed in the CaS and MgS hosts.

The ground state of the Eu^{2+} materials is very similar to Gd^{3+}. Due to the sensitivity of the 5d levels to the crystal field, the $4f^7 - 4f^6 5d$ transition can be the lowest optical transition in some hosts. The wavelength of the lowest transition in the Eu^{2+} materials varies more from host to host than in trivalent materials because of the stronger interaction of the 5d electron with the host crystal field. In CaF_2, the lowest transition occurs at 413 nm and the upper state lifetime is 700 ns, giving an oscillator strength of $\sim 3.65 \times 10^{-3}$.

Spectral hole burning in the zero-phonon line of the $4f^7(S_8(7/2) \rightarrow 4f^6 5d)$ transition of Eu^{2+} occurs by two mechanisms in CaF_2: Eu^{2+}. At zero magnetic field, persistent spectral hole burning occurs by two-step photoionization where the hole burning survives cycling to room temperature. The observed hole spectrum is consistent with a calculated pattern that considers the small Eu^{2+} ground-state splitting and both the ground- and excited-state hyperfine interactions. In a magnetic field above 1 T, transient spectral hole burning occurs by population redistribution among the ground-state hyperfine levels. Long-lived (minute) holes are observed for this half integral spin system. The resulting hole spectrum consists of holes, antiholes, and a nuclear spin-flip sideband, and can be explained in terms of the hyperfine interactions in the ground and excited states. The dominant hole decay occurs by phonon-induced transitions among hyperfine levels of the $M(s) = -7/2$ and $M(s) = -5/2$ electron-spin sublevels. Central hole linewidths of 200 MHz are observed at zero magnetic field. Hole linewidths at high magnetic fields are as narrow as 40 MHz, but these are inhomogenously broadened by superhyperfine interactions with the F nuclear spins. The gated hole-burning quantum efficiency were estimated at 2×10^{-3} (Boye et al., 1996).

Photon echoes in the $4f^7$ to $4f^6 5d$ transition of Eu^{2+} ions in CaF_2 showed that for $T = 1.5$ K and $H = 30$ kG, $T_2 = 40$ ns for both 0.01% and 0.001% Eu^{2+} concentrations, indicating that Eu – Eu interactions are not the dominant dephasing mechanism. T_2 is determined by a combination involving the electron-phonon direct process coupling the excited state spin levels, and the Eu – F super-hyperfine interaction (Boye et al., 1998).

Transient spectral holes due to the redistribution of population among the ground-state hyperfine levels have also been observed in the 401-nm zero-phonon

transition of Eu^{2+} in an SrF_2 crystal. Similar to Eu^{2+}: SrF_2, the hole profile consists of a narrow central hole (~80 MHz) and a pattern of side holes and antiholes determined by the hyperfine splittings in both the ground and excited states. The hole spectrum is accompanied by strong and narrow (~33 MHz at 1.5 K) nuclear spin-flip side holes associated with an F nuclear spin flip. Magnetic (up to 6.5 T) and temperature (1. 5 – 3.8 K) studies reveal rapid relaxation among strongly coupled and closely spaced vibronic Jahn-Teller levels. The observed broadening of the hole line width as the burning frequency is tuned to the high-energy side of the inhomogeneously broadened line is consistent with rapid relaxation among these states (Boye and Meltzer, 1999).

Persistent spectral hole burning has also been observed in the zero-phonon lines of the main and several perturbed sites of Eu^{2+} in CaS: Eu single crystals. Hole burning occurs by two-step photoionization and can be strongly gated with IR irradiation. This takes place by excited-state absorption from the metastable $4f^6 5d$ excited state to the conduction band followed by electron transport to Eu^{3+} centers, which are the dominant traps. Unusually broad 100-GHz wings were observed in the hole spectrum for perturbed Eu^{2+} sites. This is explained by a new off-resonant hole-burning mechanism due to the linear Stark effect of inversionless Eu^{2+} sites in time-varying internal Coulomb fields produced by dynamical recharging of Eu ions in the course of the hole-burning process (Kaplyanskii et al., 1998; Hasan et al., 1998).

Photoionization-induced holeburning has also been observed in the MgS: Eu^{2+} system. These systems have very wide inhomogeneous lines; holes harrower than 5 GHz were burnt using pulsed lasers. This hole width is presumably limited by the laser linewidth. Thousands of holes were burned in the inhomogeneous line as probed by fluoresence excitation. The holes survived thermal cycling to about 150 K with no loss of information (Hasan et al., 1998).

7.6.2 Deuterated Fluorides

Another class of persistent holeburning materials are the rare-earth doped fluorides with deuteration. Some of the rare-earth centers formed due to deuteration exhibit persistent holeburning behavior due to the motion of neighbor hydrogenic ions such as D^- following resonant excitation of ions. This holeburning have been observed in Pr^{3+}, Tm^{3+}, and Er^{3+} ions, and should be has extendable to other ions as well, since the holeburning mechanism is not ion specific (Macfarlane et al., 1987). These spectral holes persist for days and can survive thermal cycling up to 77 K (Strickland et al., 1999). The holewidth at 2 K ranges from 18 – 40 MHz. They have been used as the frequency reference in laser locking experiments with excellent results (Strickland et al., 2000; Sellin et al., 2001).

7.6.3 Eu^{3+} Persistence

Persistent holeburning was also observed by Liu et al. and Li et al. in Eu^{3+}: BaFCl, where laser excitation of the $^7F_0$ to $^5D_0$ transition induces structural distortions so that some Eu^{3+} sites transform to other sites. The activation energy was high enough that the resulted holes last up to 150 K. The persistent hole width was 500 MHz at 3 K, with an erasure temperature of 150 K (Liu et al., 1999; Li et al., 1999).

7.6.4 Nd^{3+} Systems

7.6.4.1 $Nd^{3+}:LaF_3$

Macfarlane et al. studied holeburning in the Nd^{3+}: LaF_3 system, where the storage mechanism is the population storage in the electronic Zeeman sublevels. This was shown by optical pumping of the ground-state Kramers doublet of the $^4I_{9/2} \leftrightarrow {}^2H_{11/2}$ (6248.9 Å) and $^4I_{9/2} \leftrightarrow {}^4G_{5/2}$ (5777.1 Å) transitions with a narrow-band CW dye laser. Experiments were carried out at 1.6 K in external fields of 100 G. Hole recovery times of hundreds of milliseconds are shorter than expected at these low temperatures and fields, and it was postulated that the shorter lifetime was caused by optical spectral diffusion due to mutual spin flips in the ground state (Macfarlane and Vial, 1987).

7.6.4.2 $Nd^{3+}:YVO_4$

Sun et al. reported photon echo studies of the $^4I_{9/2} - {}^4F_{3/2}$ transition in Nd^{3+}: YVO_4, where the high oscillator strength yields an advantage over other trivalent rare earth ions (Sun et al., 2002). Excellent coherence properties are achieved at modest magnetic fields.

The $Nd^{3+}:YVO_4$ $^4I_{9/2} - {}^4F_{3/2}$ transition occurs at 879.705 nm (11,364.4 cm^{-1}). The upper $^4F_{3/2}(1)$ level is the lasing level for the renowned 1.06 μm Nd^{3+} lasers. This transition was very strongly π-polarized and overabsorbing at the center of the absorption line for a 0.68 mm sample of 0.001% doping. The weakly absorbing σ polarization has a linewidth of 0.9 GHz. For this sample, the total absorption strength is 3.4 cm^{-1}/cm, corresponding to a calculated oscillator strength of $f = 8 \times 10^{-6}$. This value can be compared with the oscillator strength of the $^3H_6(1) - {}^3H_4(1)$ transition of Tm^{3+}: YAG, where a 0.1% doped sample exhibits a total absorption of 1.6 cm^{-1}/cm (Sun et al., 2000).

In this material, the electronic magnetic moment of the ground state can be characterized by g-factors of $g_{//} = 0.91$ and $g_{\perp} = 2.36$, and the excited state

has $g_\perp \approx 0.5$. In a magnetic field along the a-axis, the transition probabilities between all Kramers components are essentially identical; thus, the oscillator strength for transitions between levels split by a magnetic field is estimated to be 4×10^{-6}.

Photon echo experiments carried out on a 0.68 mm thick sample of 0.001% Nd^{3+}: YVO_4 showed that no echo was observable in fields below 1 kG. Starting at 1.5 kG, an echo can be observed with a decay curve that modulates strongly due to the quantum interference between transitions involving different components of the superhyperfine structure. This modulation is reduced at higher magnetic fields as the hyperfine splittings become larger than the Fourier linewidth of the pulses. This modulation effect makes it difficult to determine the exact dephasing time at lower fields.

The dephasing time T_2 lengthens (with a corresponding narrowing of Γ_h) as the applied field is increased, as shown in Fig. 7.11. This lengthening of T_2 is similar to what is expected from Nd – Nd spin-flip induced dephasing estimated from the ground state g-factor of Eq. (2.36). In a field stronger than 15 kG, the dephasing is in the"superhyperfine limit", where the dephasing is defined by the interaction between the Nd^{3+} and surrounding vanadium nuclei.

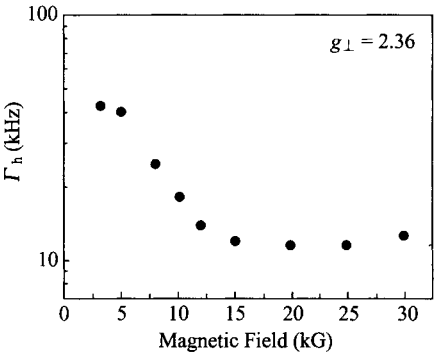


Figure 7.11 Magnetic field dependence of the homogeneous linewidth in 0.001% Nd^{3+}: YVO_4

Three pulse echo experiments were also carried out in this system at 15 kG. It was found that relatively weak spectral diffusion was observed over a 5-ms time scale, and stimulated echo decays have been found to have two different decay constants, a 37.5 μs component due to the upper state lifetime and a 3.3 ms component corresponding to the ground state Zeeman sub-level storage time. This time scale was faster than even that observed in the Nd^{3+}: LaF_3 system, perhaps indicative of the higher magnetic fields used in this measurement. The initial intensity of the slower second component was about 3% of the fast component.

7.7 Conclusions

Of the rare-earth materials studied for and used in coherent transient applications, all have merits and shortcomings that depend on the specific application. Thus, it becomes important to choose the right material for each application according to its specific needs. It is not just a materials problem, although it might seem that all problems would solved if there were one magic material for all applications. Many of the unique properties of the trivalent rare-earth ions, such as their sharp spectral lines and long coherence times at low temperature, stem from their weak interaction with the environment. It is also this weak interaction that limits the oscillator strength of the transitions, since all of these transitions are inducedelectric dipole in nature, and depend on the symmetry breaking of the environment to exist.

More materials, either the current ions in new materials, or other ions that have not been studied much, should be investigated. These new parameter spaces should be probed more thoroughly given the current state of affairs.

References

Altner, S. B., G. Zumofen, U. P. Wild, and M. Mitsunaga. Phys. Rev. B **54**, 17, 493 (1996a).

Altner, S. B., M. Mitsunaga, G. Zumofen, and U. P. Wild. Phys. Rev. Lett. **76**, 1747 (1996b).

Altner, S. B., U. P. Wild, M. Mitsunaga. Chem. Phys. Lett. **237**, 406 (1995).

Babbitt, W. R., A. Lezama, and T. W. Mossberg. Phys. Rev. B **39**, 1987(1989).

Bai, Y. S., R. Kachru. Phys. Rev. B **46**, 13, 735 (1992).

Bai, Y. S. and M. D. Fayer. Phys. Rev. B **39**, 11, 066 (1989).

Ball, M., G. Garton, M. J. M. Leask, D. Ryan, and W. P. Wolf. J. Appl. Phys. **32**, 267S (1961).

Beach, R., M. D. Shinn, L. Davis, R. W. Solarz, and W. F. Krupke. IEEE J. Quant. Elect. **26**, 1405 (1990).

Böttger, T. Ph. D. Thesis, Montana State University-Bozeman, 2002.

Böttger T., Y. Sun, G. J. Pryde, G. Reinemer, and R. L. Cone. J. Lumin. **94 – 95**, 565 (2001).

Boye, D. M., R. S. Meltzer. J. Lumin. **83 – 84**, 385 (1999).

Boye, D. M., S. P. Feofilov, and R. S. Meltzer. J. Lumin. **76 – 77**, 60 (1998).

Boye, D. M, R. M. Macfarlane, Y. Sun, and R. S. Meltzer. Phys. Rev. B **54**, 6263 (1996).

Cole, Z., T. Bottger, R. K. Mohan, R. Reibel, W. R. Babbit, R. L. Cone, and K. D. Merkel. Appl. Phys. Lett. **81**, 3525 (2002).

Deshpande V. T., S. V. Suryanarayana. J. Mater. Sci. 7, 255 (1972).

Donlan V. L., A. A. Santiago. J. Chem. Phys. **57**, 4717 (1972).

Equall R. W., R. L. Cone, and R. M. Macfarlane. Phys. Rev. B **52**, 3963(1995).

Equall R. W., Y. Sun, R. L. Cone, and R. M. Macfarlane. Phys. Rev. Lett. **72**, 2179 (1994).

Flinn G. P., K. W. Jang, J. Ganem, M. L. Jones, R. S. Meltzer, and R. M. Macfarlane. Phys. Rev. B **49**, 5821 (1994a).

Flinn, G. P., K. W. Jang, J. Ganem, M. L. Jones, R. S. Meltzer, and R. M. Macfarlane. J. Lumin. **58**, 374 (1994b).
Flinn, G. P., K. W. Jang, J. Ganem, M. L. Jones, and R. S. Meltzer. Phys. Rev. B **49**, 5821 (1994c).
Gabrielyan, V. T., A. A. Kaminskii, and L. Li. Phys. Stat. Sol. (a) **3**, K37(1970).
Ganem, J., K. W. Jang, D. Boye, M. L. Jones, R. S. Meltzer, and W. M. Yen. Phys. Rev. Lett. **66**, 695 (1991).
Graf, F. R., A. Renn, G. Zumofen, and U. P. Wild. Phys. Rev. B **58**, 5462(1998).
Graf, F. R., B. H. Plagemann, A. Renn, U. P. Wild, and M. Mitsunaga. Opt. Lett. **22**, 181 (1997).
Graf, F. R., A. Renn, U. P. Wild, and M. Mitsunaga. Phys. Rev. B **55**, 11,225(1997).
Gruber, J. B., M. E. Hills, R. M. Macfarlane, C. A. Morrison, G. A. Turner, G. J. Quarless, G. J. Kintz, and L. Esterowits. Phys. Rev. B **40**, 9464 (1989).
Ham, B. S., S. M. Shahriar, and P. R. Hemmer. JOSA B **16**, 801 (1999).
Ham, B. S., S. M. Shahriar, and P. R. Hemmer. JOSA B **15**, 1541 (1998).
Harris, T. L., Y. Sun, R. L. Cone, R. M. MacFarlane, and R. W. Equall. Opt. Lett. 23, 636 (1998).
Hasan, Z., L. Biyikli, P. I. Macfarlane, and Y. Pei. Appl. Phys. Lett. **72**, 3399(1998).
Hasan, Z., M. Solonenko, P. I. Macfarlane, and Y. Pei. Appl. Phys. Lett. **72**, 2373 (1998).
Holliday, K., M. Croci, E. Vauthey, and U. P. Wild. Phys. Rev. B **47**, 14,741(1993).
Hu, P., L. R. Walker. Phys. Rev. B **18**, 1300 (1978).
Huang, J., J. M. Zhang, A. Lezama, and T. W. Mossberg. J. Lumin. **45**, 392(1990a).
Huang, J., J. M. Zhang, and T. W. Mossberg. Opt. Comm. **75**, 29 (1990b).
Huang, J., J. M. Zhang, A. Lezama, and T. W. Mossbery. Phys. Rev. Lett. **63**, 78(1989).
Huang, J., J. M. Zhang, A. Lezama, and T. W. Mossberg. Phys. Rev. Lett. **63**, 78 (1989).
Kaplyanskii, A. A., S. A. Basun, M. Raukas, U. Happek, J. Rennie, J. C. Vial, W. M. Yen, and R. S. Meltzer. J. Lumin. **76 – 77**, 292 (1998).
Karaki, K., H. Sasaki, and M. Mitsunaga. Proc. SPIE **2577**, 182 (1995).
Kim, M. K., R. Kachru. Phys. Rev. B **44**, 9826 (1991).
Kim, M. K., R. Kachru. Appl. Opt. **28**, 2186 (1989a).
Kim, M. K., R. Kachru. Opt. Lett. **14**, 423 (1989b).
Kim, M. K., R. Kachru. Phys. Rev. B **40**, 2082(1989c).
Kim, M. K., R. Kachru. J. Opt. Soc. Am. B **4**, 305 (1987).
Koningstein J. A., G. E. Geusic. Phys. Rev. **136**, A726 (1964).
Könz, F., Y. Sun, C. W. Thiel, R. L. Cone, R. W. Equall, R. L. Hutcheson, and R. M. Macfarlane. Phys. Rev. B **68**, 085, 109(2003).
Kröll, S., E. Y. Xu, M. K. Kim, M. Mitsunaga, and R. Kachru. Phys. Rev. B **41**, 11, 568 (1990).
Kröll, S., E. Y. Xu, and R. Kachru. Phys. Rev. B **44**, 30 (1991a).
Kröll, S., L. E. Jusinski, and R. Kachru. Opt. Lett. **16**, 517 (1991b).
Kurkin I. N., K. P. Chernov. Physica B **101**, 233 (1980).
Kurkin I. N., E. A. Tsvetkov. Sov. Phys. Solid State **11**, 3027 (1970).
Li, S. T., G. K. Liu, and W. Zhao. Opt. Lett. **24**, 838 (1999).
Li, C., C. Wyon, and R. Moncorgé. IEEE J. Quant. Elect. **28**, 1209 (1992).
Lin, H., T. Wang, and T. W. Mossberg. Opt. Lett. **20**, 1658 (1995).
Liu, G. K., S. T. Li, and J. V. Beitz. J. Lumin. **83 – 84**, 343 (1999).
Liu G. K., R. L. Cone. Phys. Rev. B **4**, 6193 (1990).
Lukin, M. D., P. R. Hemmer. Phys. Rev. Lett. **84**, 2818 (2000).

Luo, B., and S. Kröll. Phys. Rev. B **54**, 9834 (1996).
Macfarlane, R. M. J. Lumin. 85, 181 (2000).
Macfarlane, R. M., F. Könz, Y. Sun, and R. L. Cone. J. Lumin. **86**, 311(2000).
Macfarlane, R. M., T. L. Harris, Y. Sun, R. L. Cone, and R. W. Equall. Optics Letters 22, 871 (1997).
Macfarlane, R. M., and G. Wittmann. Opt. Lett. **21**, 1289 (1996).
Macfarlane R. M., A. J. Meixner. Opt. Lett. **19**, 987 (1994).
Macfarlane, R. M. Opt. Lett. **18**, 829 (1993a).
Macfarlane, R. M. Opt. Letters **18**, 1958 (1993b).
Macfarlane, R. M., and R. M. Shelby. In: *Spectroscopy of Solids Containing Rare Earth Ions.* eds. Kaplyanskii and Macfarlane (North-Holland, Amsterdam, 1987).
Macfarlane, R. M., J. C. Vial. Phys. Rev. B **36**, 3511 (1987).
MacFarlane, R. M., R. J. Reeves, and G. D. Jones. Opt. Lett. **12**, 660 (1987).
Macfarlane R. M., R. M. Shelby. Opt. Commun. **42**, 346 (1982).
Macfarlane, R. M., R. M. Shelby. Opt. Commun. **39**, 169 (1981).
Macfarlane, R. M., R. M. Shelby, and R. L. Shoemaker. Phys. Rev. Lett **43**, 1726 (1979).
Maksimov, B. A., V. V. Ilyukhin, Yu. A. Kharitonov, and N. V. Belov. Krystallografiya **15**, 926 (1970).
Meixner, A. J., C. M. Jefferson, and R. M. Macfarlane. Phys. Rev. B **46**, 5912 (1992).
Merkel, K. D., W. R. Babbitt. Opt. Lett. **21**, 71 (1996).
Meltzer, R. S., J. Ganem, Y. P. Wang, D. Boye, W. M. Yen, D. P. Landau, R. Wannemacher, and R. M. Macfarlane. J. Lumin. **53**, 1 (1992).
Mims, W. B. Phys. Rev. **168**, 370 (1968).
Milori, D. M. B. P., I. J. Moraes, A. C. Hernandes, R. R. de Souza, M. Siu Li, M. C. Terrile, and G. E. Barberis. Phys. Rev. B **51**, 3206 (1995).
Mitsunaga, M., N. Uesugi, H. Sasaki, and K. Karaki. Opt. Lett. **19**, 752(1994).
Mitsunaga, M., N. Uesugi, K. Sugiyama. Opt. Lett. **18**, 1256 (1993).
Mitsunaga, M., T. Takagahara, R. Yano, and N. Uesugi. Phys. Rev. Lett. **68**, 3216 (1992).
Mitsunaga, M., N. Uesugi. Opt. Lett. **15**, 195 (1990).
Mitsunaga, M., M. K. Kim, R. Kachru. Opt. Lett. **13**, 536 (1988).
Mitsunaga, M., K. Kubodera, H. Kanbe. Opt. Lett. **11**, 339 (1986).
Moerner, W. E. Persistent Spectral Hole-Burning: Science and Applications, In: *Topics in Current Physics Vol.* 44. ed. W. E. Moerner (Springer, Berlin, Heidelberg, 1988).
Mossberg, T. W., Opt. Lett. 7, 77 (1982).
Orbach, R. Proc. R. Soc. London, Ser. A **264**, 458 (1961).
Pandher, R. S., A. Jackson, A. Davis, and B. R. Reddy. Appl. Opt. **38**, 5662(1999).
Payne, S. A., L. L. Chase, L. K. Smith, W. L. Kway, and W. F. Krupke. IEEE J. Quant Elect. **28**, 2619 (1992).
Rand, S. C., A. Wokaun, R. G. DeVoe, and R. G. Brewer. Phys. Rev. Lett. **43**, 1868 (1979).
Reinemer, G. Ph. D. Thesis, Montana State University, 2003.
Sasaki, H., K. Karaki, and M. Mitsunaga. Opt. Soc. America (Washington, DC, USA). **455**, 308 (1995a).
Sasaki, H., K. Karaki, M. Mitsunaga, and N. Uesugi. J. Lumin. **64**, 273(1995b).
Sellars, M. J., R. S. Meltzer, P. T. H. Fisk, and N. B. Manson. J. Opt. Soc. AM. B **11**, 1468 (1994).
Sellin, P. B., N. M. Strickland, T. Bottger, J. L. Carlsten, and R. L. Cone. Phys. Rev. B **63**, 155, 111 (2001).
Sellin, P. B., N. M. Strickland, J. L. Carlsten, and R. L. Cone. Opt. Lett. **24**, 1038

(1999).
Shelby, R. M., A. C. Tropper, R. T. Harley, and R. M. Macfarlane. Opt. Lett. **8**, 304 (1983).
Shelby, R. M., R. M. Macfarlane, and R. L. Shoemaker. Phys. Rev. B **25**, 6578 (1982).
Shelby, R. M., R. M. Macfarlane. Phys. Rev. Lett. **45**, 1098 (1980).
Shen, X. A. and R. Kachru. Proc. SPIE. **3531**, 11 (1998).
Shen, X. A., R. Kachru. J. All. Comp. **250**, 435 (1997).
Shen, X. A., and R. Kachru. JOSA B, 591 (1994).
Shen, X. A. and R. Kachru. Opt. Lett. **17**, 520 (1992).
Silberberg, Y., V. L. da Silva, J. P. Heritage, E. W. Chase, and M. J. Andreco. IEEE J. Quant. Elect. **28**, 2369 (1992).
Strickland, N. M., P. B. Sellin, Y. Sun, J. L. Carlsten, and R. L. Cone. Phys. Rev. B **62**, 1473 (2000).
Strickland, N. M., R. L. Cone, and R. M. Macfarlane. Phys. Rev. B **59**, 14, 328 (1999).
Sun, Y., G. M. Wang, R. L. Cone, R. W. Equall, and M. J. M. Leask. Phys. Rev. B **62**, 15, 443 (2000).
Sun, Y., F. Könz, and R. L. Cone. Phys. Rev. B, to be published(a).
Sun, Y., G. Wang, R. L. Cone, and R. W. Equall. Phys. Rev. B, to be published(b).
Sun, Y., T. L. Harris, R. L. Cone, R. M. Macfarlane, and R. W. Equall. Phys. Rev. B, to be published(c).
Tarasov V. F., and G. S. Shakurov. Phys. Solid State **35**, 121 (1993).
Tiseanu, C., A. Lupei, and V. Lupei. J. Phys.: Condens. Matter **7**, 8477(1995).
Wang, T., H. Lin, and T. W. Mossberg. Opt. Lett. **20**, 2541 (1995).
Wang, G. Ph. D. Thesis, Montana State Uiversity, Bozeman, 1997.
Wang, G. M., R. W. Equall, R. L. Cone, M. J. M. Leask, K. W. Godfrey, and F. R. Wondre. Opt. Lett. **21**, 818 (1996).
Xu, E. Y., S. Kröll, D. L. Huestis, R. Kachru, and M. K. Kim. Opt. Lett. **15**, 562 (1990).
Yamaguchi, M., K. Koyama, and T. Suemoto. J. Lumin. **87 – 89**, 1099 (2000).
Yamaguchi M., K. Koyama, Suemoto-T; M. Mitsunaga. Phys. Rev. B **59**, 9126 (1999).
Yamaguchi M., K. Koyama, Suemoto-T; M. Mitsunaga. J. Lumin. **76 – 77**, 681 (1998).
Yano R., M. Mitsunaga, and N. Uesugi. JOSA B **9**, 992 (1992a).
Yano R., M. Mitsunaga, and N. Uesugi. Phys. Rev. B **45**, 12, 752 (1992b).
Yano R., M. Mitsunaga, and N. Uesugi. Opt. Lett. **16**, 1884 (1991).
Zhang, Y., X. A. Shen, and R. Kachru. Opt. Lett. **22**, 1068 (1997).
Zhang J., T. W. Mossberg. Phys Rev B **48**, 7668 (1993).

Acknowledgements
The author wishes to thank R. L. Cone, R. S. Meltzer, and R. M. Macfarlane. From them he has learned much of rare-earth spectroscopy.

8 Rare Earth Doped Confined Structures for Lasers and Amplifiers

B. Jacquier, L. Bigot, S. Guy, A. M. Jurdyc

Abstract

Rare-earth (RE) doped insulating materials exhibit varieties of luminescent behavior with applications in solid-state physics, high energy physics, biophysics, photochemistry, medical sciences, and telecommunications, as well as in fundamental research. Recently the incorporation of trivalent rare-earth ions into waveguides has created a considerable upsurge of interest in the field of signal processing for telecommunications, based on the success of the very efficient erbium doped fiber amplifier (EDFA) for long haul transmissions together with the explosion of Internet. Wavelengths division multiplexing (WDM) is nowadays increasing the amount of channel information over a wide energy range in the low-loss region of silica fibers. However, to cover the 25 THz available window, new materials are required, implying the use of new doping and amplifier structures. In the course of this research, new laser sources were obtained at various wavelengths, using up-conversion pumping schemes, for instance. Furthermore, the development of RE-doped integrated optics is now considered for compactness and low-cost devices, offering a new challenge for RE-doped materials and luminescence processes. Finally, in a promising development, extremely miniaturized devices make possible subwavelength optics that capitalize on the dynamics of a very small number of photons, which can be analyzed for example in the new RE-doped optical microcavities and nanostructures.

8.1 Introduction

Erbium doped fiber amplifiers (EDFA) represen a key step in the development of all-optical telecommunications and, of course, the explosion of the internet traffic. The advent of highly transparent silica fiber in the 1970s was promptly followed during the 1980s by rare-earth (RE) doped silica fiber in several laboratories around the world. This was not a complete surprise because RE doped glass material to produce laser emission was produced many years before (Snitzer, 1961). However, the major improvement of this idea arrived only many years later, when the transparency performance of silica fiber allowd for

efficient pump beam propagation in the core of the fiber. The subsequent realization of single-mode optical fibers and their association with new infrared solid state laser sources led to optimal pumping of the excited states of erbium ions incorporated into the glass material (Miniscalco, 1991).

At that time, the major goal was to achieve high gains and the best power conversion, as well as a good noise figure with respect to the opto-geometrical parameters of the fiber, together with the spectroscopic characteristics of the erbium-doped glass. Further developments took advantage of the wide line broadening of the 1.54 μm emission of erbium in a glass which could then support several tens of wavelength channels to improve the capacity of the optical transmissions. In that respect, flatness and wide broadening of the amplifiers are required which in turn raises many fundamental questions about the glass composition, doping and co-doping level, etc. The other trend considers other RE-doped ions such as thulium, praseodymium, neodymium, or dysprosium, which can increase the wavelength domain of transmission towards higher energy, up to 1.3 μm. This later development involved glass hosts other than silica, such as fluoride, tellurite, chalcogenide, or even chloride, for which phonon energies are much lower than in silica. It follows that there is a need for spectroscopic investigations of new glass materials for which emission probabilities must be fully studied and understood.

In near future, it is expected that advantage will be taken of WDM transmission in metropolitan networks to fully exploit the huge capacity and high bit rate of long-haul transmission. Then routing without losing speed and capacity will be a challenge, together with the miniaturization or integration of passive, and active waveguides (planar waveguides from meter to μm), and reduced costs, of course. It is a domain where any original and efficient solution should be considered, including RE-doped crystalline microchips or waveguides. If we push further, optics is also a future trend to increase the performance of our computers. more precisely beyond the optical diffraction limit (<1 μm), this will be possible with new materials designed to have a periodicity of their refractive index (photonic band gap materials), including the possibility of controlling the emission probability of any luminescent center, RE-doped materials for instance.

In this chapter, we take advantage of the overall knowledge of the spectroscopy of RE-doped solids developed in this book and apply it to refractive waveguides and one-dimesional photonic band gap material. The first part will define all the opto-geometrical and spectroscopic parameters necessary to understand propagation and amplification in RE-doped active waveguides, and some other specific properties such as photosensitivity or photorefractivity. The second part will describe the state of art of fiber laser and amplifiers, as well as RE-doped integrated devices. Within this part, we shall address the fundamental question of line broadening, already discussed in other chapters of this book, but in the context of WDM applications. The last part will concern the new developments relating to strongly confined structures such as optical microcavities.

8.2 Propagation and Amplification: the Key Parameters

There are two types of parameters which govern the performance of optical active waveguides: the opto-geometrical parameters of the waveguides and the spectroscopic parameters of the RE-doped materials. Full theoretical development of these two types of parameters has been well established in many text books (see for example, Saleh, 1991), and in this volume for spectroscopy. However, we recall the major results needed for the reader to understand the following results and discussions.

8.2.1 Opto-geometrical Parameters

A waveguide is a structure consisting of by a dielectric core (a is the core radius of an optical fiber or thickness of a planar structure) with a refractive index n_1 slightly higher than the refractive index n_2 of a surrounding cladding. Using the Snell-Descartes law, one can easily calculate the numerical aperture (NA), which characterizes the divergence of the emerging light(defined by angle θ) : $NA = \sin\theta = \sqrt{n_1^2 - n_2^2}$. Typical values of 0.2 or 0.3 are used for both fibers and planar waveguides, together with a of a few microns. This is why solid state laser beams have characteristics so useful to couple light into waveguides. In order to clearly understand the advantages of waveguides, a wave approach is necessary to accurately describe the propagation of light using Maxwell's Maxwell equations. There are many types of index profiles of waveguides: the most common step index with an abrupt change at the interface core/cladding (used for amplification), gradient index with a smooth variation in the index of refraction, or more complicated structures with several steps of high and low index for dispersion management, for instance. Depending upon the opto-geometrical parameters a, n_1, and n_2, a waveguide can propagate several modes, which are observed at its output as a result of interference effects. The important parameter is the so-called "normalized waveguide parameter" $V = \frac{2\pi}{\lambda} a \sqrt{n_1^2 - n_2^2}$. For a given structure, a, n_1 and n_2 tells the number of propagating modes can be deduced from the diagram of the normalized propagation constant b versus V; $b = \frac{\left(\frac{\beta^2}{k_0^2}\right) - n_2^2}{n_1^2 - n_2^2}$ with $k_0 = 2\pi/\lambda$ and β/k is the effective refractive index of the mode.

For instance, any arrangement of a, $\Delta n = n_1 - n_2$ and λ which fulfills the condition $V < 2.45$ corresponds to single-mode propagation. Thus one can define a cut off wavelength λ_c above which only single mode is propagating for a waveguide of given dimension and refractive index. As an example, the standard

single-mode optical fibers for telecommunications have a cutoff wavelength around 1 μm for propagation modes higher than the fundamental mode (TEM_{00}, i. e., totally symmetric mode). It is important to note that in the single-mode regime of propagation, the electric field distribution of the propagating electromagnetic wave is more strongly confined near cut off than at longer wavelengths, for which the wave spreads into the cladding. This property should be considered in the optimization of amplification or laser action for the best overlap between pump and signal beams.

8.2.2 Spectroscopic Parameters

Interaction of light with an RE-doped solid as well as laser conditions have been developed in several of the previous chapters. Their authors have already defined the main parameters such as absorption and emission cross sections, radiative and nonradiative probabilities, and so on and the major mechanisms: energy transfer, migration, up-conversion by energy transfer or by excited state absorption, etc. We will cite relevant equations and develop specific approaches here as necessary.

8.2.2.1 Absorption and Radiative Processes

As a simple approach, let us consider a two-level system (Fig. 8. 1) for which the transition rates are respectively $W_{ij} = \sigma_{ij} \frac{I(\nu)}{h\nu}$ and $A_{21} = \frac{1}{\tau_{rad}}$ (the cross sections σ_{ij} have the dimensions of area).

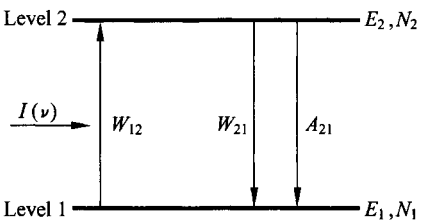


Figure 8. 1 Fundamental mechanisms: absorption (W_{12}), spontaneous emission (A_{21}), and stimulated emission (W_{21})

In general, for RE ions there are several downward transitions, so it is necessary to introduce their branching ratio $\beta = \frac{A_{jj'}^{rad}}{\sum_{j'} A_{jj'}^{rad}}$. All these parameters can be extracted from experiments: absorption, emission, and lifetime measurements when all the data are available. An alternative approach to

determining radiative probabilities and branching ratio uses the well known Judd-Ofelt theory (Judd, 1962; Ofelt, 1962) (developed in the first chapter of this book) based on absorption spectra. This approach, first developed for disordered systems (liquids), establishes a direct link between the absorption coefficient $\alpha(\lambda)$ and the electric dipole strength S_{ed} of $J \rightarrow J'$ transitions using three phenomenological parameters Ω_t through the expressions

$$S_{ed}^{mes}(J \rightarrow J') = \frac{9n}{(n^2+2)^2} \cdot \frac{3hc(2J+1)}{8\pi_3 N\lambda} \frac{4\pi\varepsilon_0}{e^2} \int_{J \rightarrow J'} \alpha(\lambda) d\lambda$$

and

$$S_{ed}^{cal}(J \leftrightarrow J') = \sum_{t=2,4,6} \Omega_t \mid \langle 4f_n[S, L]J \parallel U_t \parallel 4f_n[S', L']J' \rangle \mid^2,$$

where n is the refractive index, N the RE concentration, $\bar{\lambda}$ the mean wavelength of the transition, and U_t the reduced matrix elements tabulated in the literature.

Then the Ω_t obtained by fitting the absorption spectrum make it possible to recalculate the radiative transition probabilities, branching ratios, and lifetimes. As noticed in other chapters of this book, this approach gives quite good results for the near infrared range of Nd^{3+}, Er^{3+}, Tm^{3+}, and others. On the other hard, some transitions called "hypersensitive", as for Pr^{3+} or Eu^{3+}, are poorly described. Modified theories have been proposed to better reproduce these transition probabilities, but with limited success (Quimby, 1994; Goldner, 1996; Gorller-Walrand, 1998).

8.2.2.2 Nonradiative Relaxation and Energy Transfer Mechanisms

Other fundamental mechanisms can greatly influence the performance of these lasers and amplifiers, since they affect the dynamics of the excited state populations. One can list a number of effects such as nonradiative relaxation via the vibrations of the host. It has to be noticed that the weak coupling of the electrons and nuclei explains the strong overlap between absorption and emission spectra, the sharpness of the zero-phonon line, and the richness of the fluorescence of RE ions in solids. However, if two metastable levels are close to each other (ΔE separation greater than two phonons energy), the probability that the higher energy level relaxes nonradiatively to the lower one is governed by the so-called "energy gap law": $W_{nrad}(T = 0, \Delta E) = C\ e^{\alpha \Delta E}$, where C and α are positive constants characteristic of the host. These values have been reported for various types of inorganic glasses in the literature (Miniscalco, 1994; Jacquier, 1997). It is clear that silica hosts with phonon energy spreading up to 1100 cm^{-1} will exhibit fewer radiative transitions than heavy metal fluoride glasses (HMFG), for which the cutoff phonon energy is around 590 cm^{-1} (Lucas, 1984). Table 8.1 reports all maximum phonon energies characterizing the major

glass compositions used to fabricate waveguides.

Table 8.1 Maximum phonon energy for various glass compositions

Glass	Borate	Phosphate	Silicate	Tellurite	Fluoride	Chalcogenide
Phonon energy(cm^{-1})	1400	1200	1000	700	590	350

This phonon interaction will be discussed in more detail in the next part because it contributes to the bandwidth of the amplifier.

An important class of mechanisms has been already discussed in this book: energy transfer processes involving more than one excited ion, cross-relaxation with two or more ions, up-conversion energy transfer by addition of photons (APTE), and further cooperative phenomena (Fig. 8.2). They may involve either identical or different ions, and they can be resonant or not.

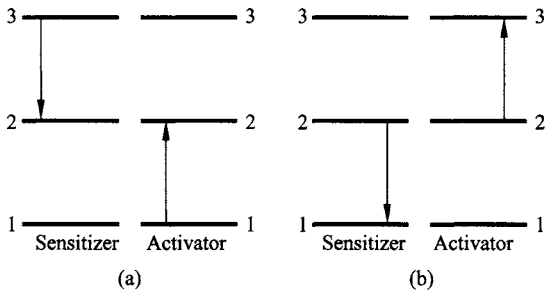


Figure 8.2 Example of energy transfer mechanisms: (a) Cross-relaxation; (b) APTE

The two major parameters which affect their probabilities are the distance between the two ions involved and the overlap between absorption and emission spectra of these absorbing and emitting ions. Concentration of ions is therefore a critical parameter which should be precisely adjusted (in the range of mol%) to improve the desired fluorescence quantum efficiency. In turn, high doping levels can strongly reduce the transparency of the waveguide or lead to inhomogeneous ion distribution and then quenching effects.

8.2.2.3 Excited State Absorption and Photon Avalanche

Because of the richness of the RE energy diagram and the metastability of their excited states, successive absorptions of photons are possible in many cases when light is injected into the waveguide. Within this structure it is easy to achieve high excitation density along the whole length of the waveguide. So it is quite easy to achieve high population. storage in the excited states, which may produce fluorescence at shorter wavelengths than the pump. This is for instance the case in RE-doped HMFG up-conversion lasers (Scheps, 1996). These two- or three-photon processes are also used to efficiently amplify light emission in

thulium doped fiber amplifier (TDFA) (Allen et al., 1993; Percival and Williams, 1994; Komukai et al., 1995).

The strong spatial and spectral overlap between the pump beam and the emitted fluorescence propagating into the waveguide can also develop a reabsorption process. At low pump power, this reabsorption modifies the output spectral dependence of the fluorescence, and in the stimulated regime amplified spontaneous emission is generated, which affects the noise figure of the amplifier or is used to develop super-fluorescent sources with broadband emission (Wysocki, 1994).

A particularly interesting pumping scheme is the selective grouping of weak ground-state absorption, high excited-sate absorption and cross relaxation, so-called "photon avalanche" because it behaves nonlinearly beyond a threshold (Joubert et al., 1993). Considering a three-level scheme (Fig. 8.3), the laser excitation wavelength is resonant between the excited states 2 and 3 but out of resonance for the transition 1↔2.

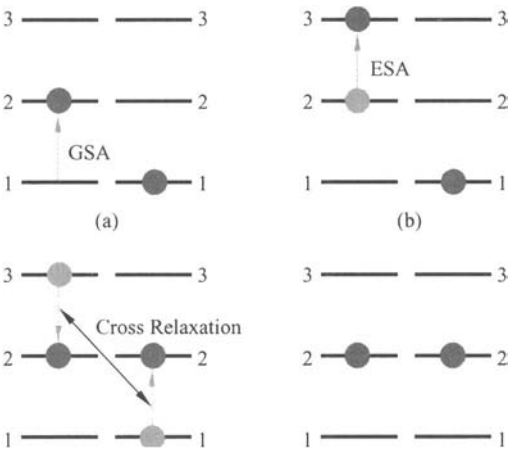


Figure 8.3 Photon-avalanche process

After a weak first-step absorption (a), a second photon of the same beam populates level 3 (b); efficient cross-relaxation (3, 1→2, 2) (c), although non-resonant, feeds the intermediate metastable state 2. Then two more photons of the pump beam can again promote the two excited ions in level 3 and so on. Qualitatively, this process can occur under the following conditions: the first absorption step is weak, level 2 has a long lifetime compared to level 3, and the cross-relaxation energy transfer is fast enough with respect to other relaxation mechanisms. This process has been used several times for up-converted laser emission (Scheps, 1996; Joubert, 1999) but never yet used for amplification in waveguide, even though high cross-relaxation rate (Tm^{3+} concentration was high but not consistent with the photon avalanche regime) has been achieved with quite good gain performance in TDFA (Aozasa et al., 2000, 2001).

8.2.2.4 Evaluation of the Spectroscopic Parameters

Three parameters are important in understanding amplification and laser operation: absorption cross section, lifetime, and stimulated emission cross section. The first two are easily determined.

(1) The absorption cross section is given by the relation $\sigma_a(\lambda) = \frac{\alpha(\lambda)}{N}$; notice that $\alpha(\lambda) = \frac{2.3}{L}\log T$ for length L of waveguide with transmission $T(\%)$.

(2) The inverse lifetime is defined as: $\frac{1}{\tau_j^{mes}} = \sum_i (P_{ji}^{rad} + P_{ji}^{nrad}) = \frac{1}{\tau_j^{rad}} + \frac{1}{\tau_j^{nrad}}$ where P_{ji}^{rad} and P_{ji}^{nrad} are the radiative and nonradiative probabilities, and the τ's are the respective lifetimes. In addition the quantum efficiency (QE) is $QE = \eta_j^{rad} = \frac{\tau_j^{mes}}{\tau_j^{rad}}$. Lifetime measurements are difficult because it is necessary to populate the excited state just enough for detection, with a pulse width much smaller than any relaxation time constant. Precision is therefore about 10%.

(3) The stimulated emission cross section is the most difficult parameter to measure. Several methods of measurement or calculation have been proposed.

The Futchbauer-Ladenburg method consists in converting the fluorescence spectrum $I_e(\lambda)$, knowing the radiative lifetime τ_j^{rad} and the branching ratio β, as necessary, using the relation (Barnes, 1991)

$$\sigma_e(\lambda) = \frac{1}{8\pi c n_2}\beta\frac{1}{\tau_j^{rad}}\lambda^4\frac{I_e(\lambda)}{\int I_e(\lambda)}\,d\lambda.$$

The branching ratio β can be determined either experimentally or theoretically using the Judd-Ofelt method. Even though this method is not very accurate because of the poor precision of τ_j^{rad}, it is very useful in a system involving laser transitions between excited states, as the 1.48 μm emission, of thulium-doped materials.

The MacCumber method is the most popular and uses the reciprocal relationship between absorption and emission but weighted by the statistical occupancy of the excited and ground multiplets given by the Boltzmann law:

$$\sigma_e(\nu) = \sigma_a(\nu)e\left[\frac{\varepsilon(T) - h\nu}{kT}\right],$$

where $\varepsilon(T)$ is the chemical potential,

$$e\left(\frac{\varepsilon(T)}{kT}\right) = \frac{1 + \sum_{k=2}^{g_1} e^{\left(-\frac{E_{1k}}{kT}\right)}}{1 + \sum_{k=2}^{g_2} e^{\left(-\frac{E_{2k}}{kT}\right)}} e^{\left(\frac{E_0}{kT}\right)},$$

where E_0 (cm^{-1}) is the energy gap of the transition taken between the lowest Stark component of each manifold. E_{jk} is the position of the Stark component k within one manifold j and g the degeneracy of each manifold.

One major difficulty of this method is to determine the Stark splitting of the two manifolds. That is the reason why Miniscalco Quimby has proposed for the 1.54 μm emission of erbium in a glass to replace E_0 by the average energy of each manifold and to assure equidistant adjacent Stark components in each manifold (Miniscalco, 1991). This method gives better results than the Futchbauer-Ladenburg approach.

8.2.3 Amplification into a Waveguide

There are few very good textbooks which develop the full theory of RE-doped waveguide lasers and amplifiers (Desurvire, 1994; Becker et al., 1999; Digonnet, 1993). Here we sketch out a schematic description of a quasi three-level system to illustrate the main spectroscopic features governing the performances of the amplifiers. Assuming an energy level diagram similar to that of EDFA's represented in Fig. 8.4, the amplification regime can be derived from the propagation equations of the pump and the signal beams. As a first approach, taking into account only absorption and emission processes of the pump (index p) and the signal (index s), the power variations (dP) along the direction of propagation and at a z position are

$$\frac{dP_s(z,\lambda)}{dz} = \left[\sigma_{es}(\lambda)N_2(z) - \sigma_{as}(\lambda)N_1(z)\right]P_s(z),$$

and

$$\frac{dP_p(z,\lambda)}{dz} = \left[\sigma_{ep}(\lambda)N_2(z) - \sigma_{ap}(\lambda)N_1(z)\right]P_p(z).$$

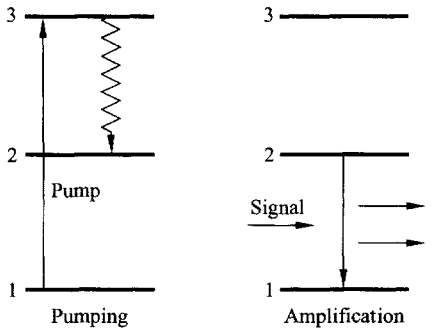


Figure 8.4 Schematic principle of amplification for a three-level system

The local gain for the signal can be simply expressed as

$$g_{\text{loc}}(z,\lambda) = \sigma_{\text{es}}(\lambda)N_2(z) - \sigma_{\text{as}}(\lambda)N_1(z).$$

This expression will be used extensively in coming sections to compare the optical gain bandwidth of various erbium doped materials. The second term of the above expression is very important in the case of EDFA, but not in the typical four-levels system such as Nd^{3+} and Pr^{3+}, for which dosorption at the signal wavelength λ is reduced.

The absolute gain G of a fiber amplifier of l length is then

$$G = \frac{P(l)}{P(0)} = e^{\int_0^l g_{\text{loc}}(z)\,dz},$$

and in decibel (dB)

$$g_{\text{dB}} = 4.34\int_0^l [\sigma_{\text{es}}N_2(z) - \sigma_{\text{as}}N_1(z)]\,dz.$$

Since σ's are wavelength dependent, one can vary the population inversion $\frac{N_2 - N_1}{N_2 + N_1}$ % to probe the range of spectral gain in the case of EDFA. This shows that around 60% population inversion gives rise to a rather flat gain in the range 1530 – 1560 nm (the so-called C-band conventional band), and around 40% is required for the L-band (1570 – 1610 nm (Long band)).

The length of the waveguide is crucial mainly for EDFA, for which the gain increases linearly and reaches a maximum before decreasing at longer length. The maximum length depends upon the power as shown in Fig. 8.5 (in the

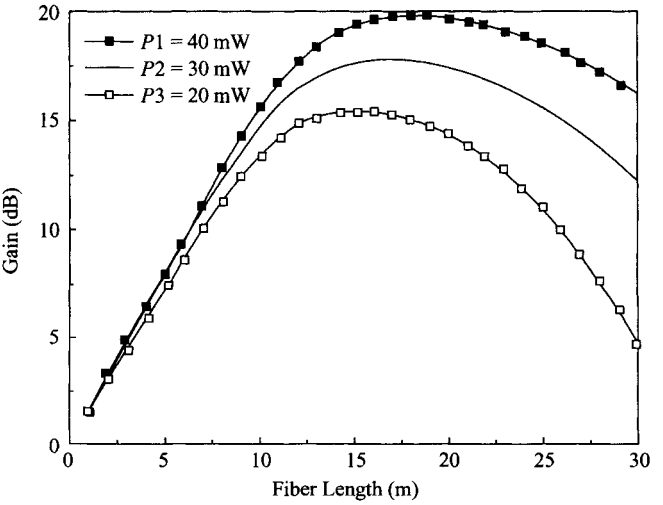


Figure 8.5 Gain as a function of fiber length for three different pump powers

small-signal approximation).

Another parameter of interest that we will use later quantifies the flatness of the spectral gain and determines the spectral range: $\frac{\Delta G}{G} = \frac{G_{max} - G_{min}}{G_{min}}$, where G_{max} and G_{min} are the maximum and minimum values of G over a given wavelength range. It is generally reasonable to assure that a flatness of 0.1% is necessary for amplifiers used in long-haul systems.

Gain generally increases with pump power, but when the local population inversion saturates at high pump power the gain reaches an asymptotic limit (see Fig. 8.6b). Similar behavior occurs for the signal power (see Fig. 8.6a). A very important consequence of signal saturation is its wavelength dependence, which can contribute to the flatness of the gain curve (Fig. 8.7).

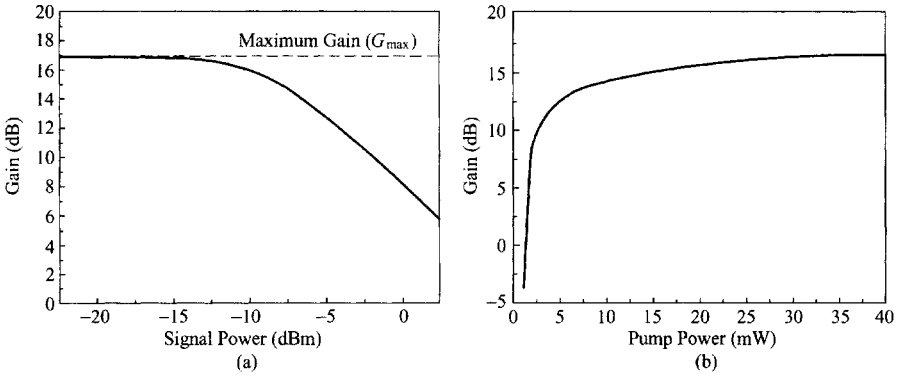


Figure 8.6 Gain saturation as a function of (a) signal power and (b) pump power

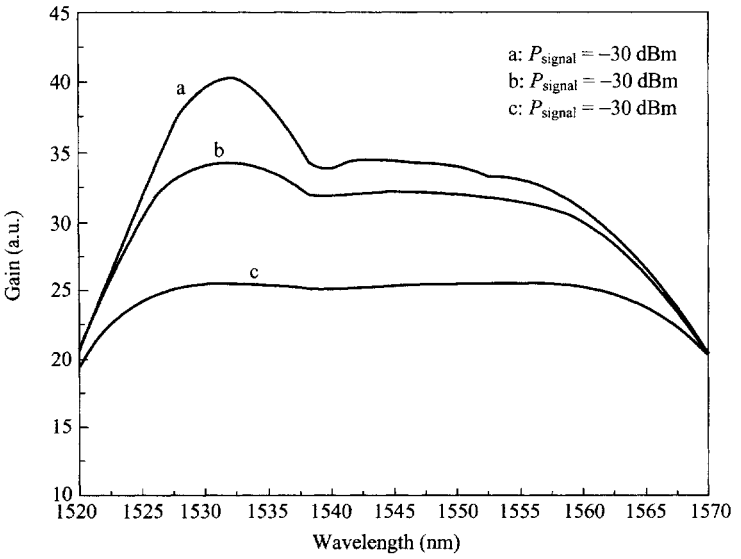


Figure 8.7 Spectral dependence of the gain with signal power

However, in WDM applications, signal wavelength can locally saturate the gain, leading to a hole in the gain shape. This effect will mainly affect long-haul transmission with cascaded of fiber amplifiers.

Another important source of signal degradation is noise introduced by amplification, due mainly to amplified spontaneous emission (ASE). This corresponds to spontaneous emission amplified by stimulated emission, and it can be shown that at frequency ν_s, the ASE power at the output of the amplifier in spectral width $\Delta\nu$ can be written as

$$P_{\mathrm{ASE}} = 2n_{\mathrm{sp}}h\nu_s(G-1)\Delta\nu,$$

where $n_{\mathrm{sp}} = \dfrac{\sigma_{\mathrm{es}}\bar{N}_2}{\sigma_{\mathrm{es}}\bar{N}_2 - \sigma_{\mathrm{es}}\bar{N}_1}$, where $\bar{N}_i$ is the average population of level i over fiber length, and G is the gain of the amplifier.

It is clear from the expression for n_{sp} that ASE power is large when population inversion is low. This can be explained by the fact that when population inversion is high, signal photons can only be amplified, whereas when population inversion is low, they can be amplified or absorbed. In the latter case, absorbed photons can lead to stimulated and spontaneous emission, leading to a degradation of the noise figure, defined as

$$F = \frac{SNR_{\mathrm{In}}}{SNR_{\mathrm{Out}}},$$

where SNR_{In} and SNR_{Out} are the signal-to-noise ratio at the amplifier input and output, respectively.

8.2.4 Material Requirements for Fabrication of Waveguide

Fabrication methods for optical fibers are well developed, and produce the best fiber for many kinds of applications. Among the many RE-doped glass compositions only few have thermodynamic properties that allow fiber to be drawn for lasers and amplifiers. The main parameters are the temperature of glass formation $T_g$during the cooling process and the temperature of crystallization T_X. The larger the difference $T_g - T_X$, the better the stability and homogeneity of the glass. An important parameter is the viscosity, which must be high enough, and compatible between core and cladding. This is not a problem for silica-based optical fiber, but it is more difficult to achieve for exotic glasses (HMFG, chalchogenides, etc.).

Only a few generic techniques have been used to fabricate high-quality optical fiber, and can be classified into two types: the chemical vapor deposition (CVD) techniques and classical methods starting from bulk materials (rod and

tube, rotational casting, etc.). There is an abundant literature devoted to the fabrication of optical fibers see Nagel, 1982, for instance.

The last point to mention is the capacity of the glass lattice to incorporate the optimal concentrations of RE ions. In some cases such as silica based glasses it is a real challenge to incorporate erbium with concentrations more than hundred ppm wt (ppm by weight) because of the formation of clusters or aggregates that will affect the fluorescence quantum efficiency. Alumina-doped silica has considerably improved the incorporation of erbium ions (up to few thousand ppmwt), but contributes significantly to substantial line broadening, as discussed in the next section. On the other hand, multicomponent glasses (HMFG, phosphate, etc.) can be easily doped with 10^4 ppmwt without any quenching or saturation of the fluorescence intensity. Ultimatiely, that only a few glass compositions have been pulled, mostly because of poor quality of propagation due to high losses.

Active planar devices are becoming more popular because of the development of optical communications in the metropolitan range and fiber-to-the-home (FTTH) in the near future. Moreover, a larger variety of materials and techniques than for optical fibers can be potentially used to fabricate passive or active waveguides. The realization of channel guides and their performance are less impressive than in optical fiber amplifiers, but they aim to support a strong research effort. Fabrication may be divided into two categories: deposition techniques (molecular beam epitaxy, sputtering, flame hydrolysis deposition, physical vapor deposition, liquid phase epitaxy, sol/gel, etc.), and modification (ion exchange processes, ion implantation) of bulk materials (either glass or crystal). Both require lithography techniques (dry etching, reactive ion etching, etc.) to realize stripes on the surface or inside the bulk material. This lithography procedure requires advanced technology, and it is generally a limiting step because of the chemical nature of materials to etch. Losses less than 10 dB/m can be reached, which should be compared to less than 0.001 dB/m in RE-doped silica fibers, and tenths of a dB/m in RE-doped fluoride fibers. To ensure compactness and miniaturization of such devices, high RE concentrations (generally more than one order of magnitude greater than in fibers) should be incorporated into the waveguides. That is why multicomponent glasses lead to greater gain per unit length. Finally, it should be noted that crystal waveguides may be fabricated by epitaxy techniques: liquid phase epitaxy (Douysset-Bloch et al., 1997) or molecular beam epitaxy (Daran et al., 1993) and more recently by H^+ or He^+ ion implantation techniques that make it possible to exploit the laser performances of bulk solid sate materials in confined structures (Moretti et al., 2003).

8.2.5 Other Specific Properties: Photosensitivity and Photorefractivity

There are several other electronic properties of RE-doped glass or crystalline materials which are responsible for some interesting functionality in the

waveguides. Two properties deserve to be discussed in this chapter because they contribute to the huge development of information technologies through optical devices for filtering or modulation, for instance.

Since 1978, photosensitivity of glass waveguides has been extensively studied in germanium-doped silica fiber and H_2 loaded silica-based fiber. The amplitude of change of refractive index under adequate UV light illumination (wavelength and dose) make it possible to write gratings with index contrast up to 10^{-2}. In silica-based optical fiber, the triggering mechanisms of the photosensitivity effect mainly involve photon absorption and changes of polarizability (via the Lorenz-Lorentz relation) of ions and bonds (Ge – O in germanium-doped silica glass). Several types of photosensitivity have been identified depending upon the sign of the refractive index change and the dynamics of the processes. similarly, cerium doped silica (Broer, 1991) or fluoride fibers (Poignant et al., 1994) and other highly polarizable materials (HMFG with lead or bismuth, etc., Boulard et al., 1998) exhibit strong photosensitivity, which may be used to achieve new functionality in RE-doped waveguides. At the microscopic scale, it has been shown that part of the refractive index change is due to densification of various glass compositions occurring under 248 nm laser radiation, and to variation of the absorption coefficient via the Kramers-Kronig relation (Niay et al., 1999).

The nonlinear properties of the host lattice, mostly in crystalline environments can be exploited for RE-doped materials to generate visible laser light by means of self frequency doubling or self-sum-frequency mixing of laser and pump radiations. Not too many nonlinear materials can accept RE-doping leading to laser action in the near infrared (strontium baryum niobate family (Romero et al., 2001) or lanthanide calcium oxoborate crystals (Mougel et al., 1999; Vincent, 2003) are the best examples). The difficult problem to solve lies with optimal geometries (including polarization requirements) for both interactions: nonlinear properties and laser action. In that sense RE-doped crystalline waveguides may represent an innovative trend to improve conversion efficiency compared to that of already commercialized potassium niobate.

8.3 Waveguide Amplifiers and Lasers

The first RE-doped fiber laser was reported by Snitzer (Snitzer, 1961), almost as early as the first solid state laser demonstration, but it did not totally take advantage of the confinement provided by the fiber geometry. Indeed pumping mode was ensured by a flash lamp with doped fiber rolled around, stimulated emission was guided along the fiber improving gain because of the length mainly. However, multimode propagation as well as propagation losses limited the efficiency of the laser. The 1980s showed great improvement of both quality of the fibers and the use of pump and signal copropagation (Mears et al., 1987, in the case of EDFA). It is also trivial to note that the weak absorption cross

sections of the f – f transitions of RE ions in glass are well compensated by the length of waveguide if losses are not too significant. In a fundamental approach, low doped-waveguide combined with long interacting media may attenuate negative concentration quenching effects. On the other hand, for integrated optics reduced dimension devices may face serious problems of efficiency, as will be shown later. After a survey of the properties of the main fiber amplifiers and lasers, integrated optical active devices are examined.

8.3.1 Erbium-doped Fiber Amplifier

The most popular and best studied system is the erbium-doped fiber amplifier (EDFA), because erbium infrared emission occurs at 1.54 μm, in the third window of silica fiber transmission for telecommunications. Stimulated emission involves the two first manifolds $^4I_{13/2}$ and $^4I_{15/2}$ when the erbium ions are pumped in one of the higher excited states in the silica-based optical fibers (see Fig. 8.8).

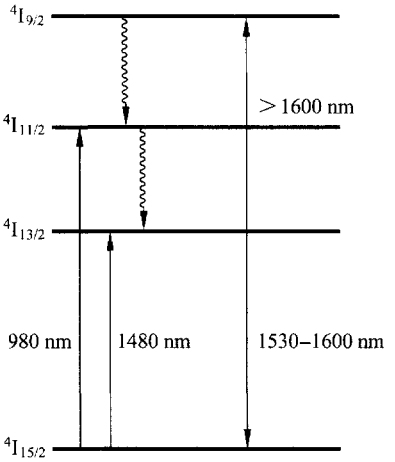


Figure 8.8 First energy levels and pumping scheme of the EDFA

8.3.1.1 Pumping Scheme and Gain

From a technological point of view, only pump wavelengths at 0.98 μm and 1.48 μm are used because of the strength of the absorption cross sections, limited effects of nonradiative relaxation, up-conversion losses, and availability of compact low-cost pump sources. For instance, 0.8 μm pump wavelength could be used because of cheap laser diode modules, but the gain efficiency suffers from an efficient two-step excitated state absorption (ESA) process of the pump due to resonances with higher excited states. Both 0.98 μm and 1.48 μm pump wavelengths enter in devices for preamplifiers or boosters respectively. Indeed, a 0.98 μm pump source permits a very high population inversion rate

due to the three-level system together with a low-noise figure, while the 1.48 μm wavelength avoids losses due to nonradiative relaxation, enabling high output power, but with non-negligible noise due to the absorption of the signal. For these two pump wavelengths, there is still controversy surrounding the fact that almost half of the absorbed pump power does not contribute to the gain efficiency. This may be related to the lifetime of the metastable $^4I_{13/2}$ state of the erbium ion in conjunction with up-conversion mechanisms. The radiative lifetime of the $^4I_{13/2}$ state itself is an unsolved question at the moment (Polman, 1997).

To improve pump efficiency, double-clad erbium/ytterbium-doped fibers are now commercially available, based on the well-known efficient energy transfer from Yb^{3+} to Er^{3+} ions (Snitzer, 1965). From a complementary point of view, a simple way to increase gain performance is to incorporate more erbium active ions in the glass fiber. However, this faces at least two major correlated problems: solubility of erbium ions in the glass composition and concentration quenching effects. For instance, it is well known that the close-packed silica lattice which exhibits the best transparency at 1.54 μm does not easily accept the incorporation of large trivalent RE ions. Many dopant ions (Ge, P, Al, ...) have been tested to facilitate RE doping of the core of the fiber. Aluminium is the most popular because a few percent gains one order of magnitude in erbium concentration without excessive RE clustering effects (Arai, 1986), and produces a flat gain over more than 30 nm in the C-band. Physically, aluminium doping introduces not only tetrahedral groups, but also octahedral entities acting as a modifier of the silica lattice. As a result it contributes to create a specific environment around each RE ion with a coordination number higher than in the silica tetrahedral arrangement that is generally required. Furthermore, this reduces the steric effect due to the large ionic radius of Ln^{3+} ions (compared to silicon or germanium) together with a total energy of the structure much less than in the case of pure silica or germanosilicate compositions. Experimentally, it is found that beyond a low critical aluminium concentration, erbium emission exhibits a typical broad profile which does not evolve with aluminium concentration to a certain extent. Further studies by EXAFS have given structural evidence of this behavior (Peters and Houde-Walter, 1998) but a full description of the local environment of the erbium is still an unsolved problem. One important problem raised by the increase in RE concentration is the formation of pairs or clusters. As commonly accepted, concentration quenching of EDFA is attributed to an up-conversion process in which two excited erbium ions in the $^4I_{13/2}$ manifold interact to produce one ion in a higher excited state and the other in the ground state (see Fig. 8.2). Then, the higher excited state relaxes radiatively or nonradiatively towards a lower level (either the "laser" level or the ground state), losing at most two absorbed photons or one absorbed photon respectively. Two questions are debated in the literature and are presently unsolved: does this up-conversion process explains the limitation of the total power conversion efficiency (PCE) and does it implies for the physical description of glass structure. For the first question two main approaches have

been developed, based on spectroscopic measurements consisting of an experimental determination of the up-conversion transfer rate (W_{up}) or theoretical statistical determination (Sergeyev et al., 2000) on the one hand, and on saturated absorption measurements of EDFA showing a non-saturable regime on the other (Delevaque et al., 1993). Descriptions have been supported by simulation and theoretical models (Delevaque et al., 1993; Digonnet et al., 1994). In both cases, the difference between a random distribution of single excited ions which may interact because of the long lifetime of the excited state and an inhomogeneous distribution of excited ions introducing pairs or more complex aggregates (Myslinski et al., 1997) has been considered. No direct observation of pairs in RE-doped glasses has been reported other than by modeling the absorption saturation measurements by considering collection of single excited ions and a variable percentage of coupled ion pairs. Some authors have reported more than 10% −20% of pairs depending upon erbium concentration and chemical nature of the hosts. An accurate study of spectral line broadening could perhaps help to better discriminate between coupled and uncoupled ions.

8.3.1.2 Homogeneous and Inhomogeneous Spectral Broadening

Several erbium-doped glass compositions have been studied and tested as EDFA s including aluminosilicate, tellurite, multicomponent glasses, phosphate, fluoride, fluorosilicate, chalcogenide, and others They differ according to position and profile of the IR emission, as can be seen on Fig. 8.9.

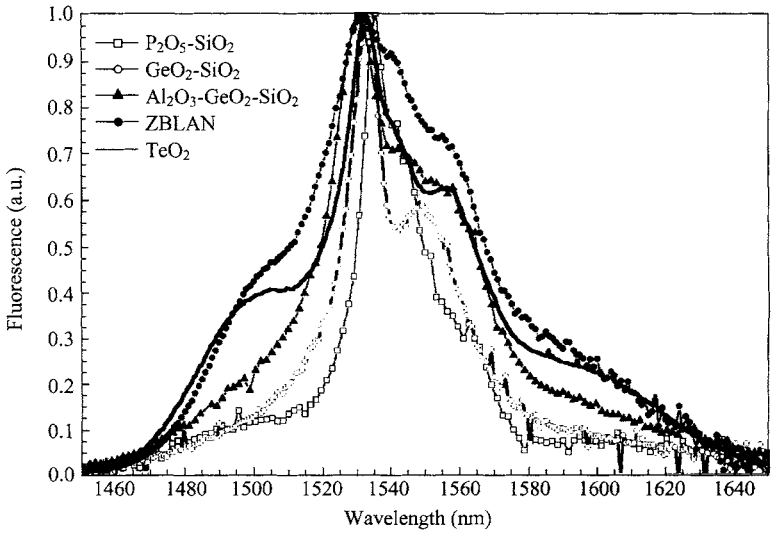


Figure 8.9 Room temperature IR emission of erbium for different glass compositions

A red shift of the emission is generally observed with increasing covalent nature of the erbium-ligand bounding. This is quite well explained by the so-

called nephelauxetic effect reported some years ago in several electronic transitions of various RE ions (Caro and Beaury, 1976). However, it is not possible to derive a general approach based on electronegativity or basicity of anions and cations of the different chemical compositions to fully explain and predict the behavior of the erbium emission in all glass compositions. Too many parameters are included in one single parameter variation, for instance the ionic field may well explain the trend between different classes of glass (fluoride, oxide, etc.) but not with in a specific class (oxide). It has been proposed that the ionicity of the RE-ligand bond might be related to the Judd and Ofelt Ω_6 parameter as a sensitive function of the overlap of the 4f and 5d wavefunctions with ligand (Tanabe and Ohyagi, 1992, 1993).

Broadband emission of erbium-doped glasses is well-used to implement whiteband optical amplifiers in the transmission links. As known for many years, the broadening of RE ion emission depends on the chemical composition of the glass. A direct consequence of this behavior on the spectral dependence of the gain (equation for g_{dB} in Section 8.2.3) is illustrated in Fig. 8.10 for four very different types of erbium-doped inorganic glasses. Not only is the broadening important, but so is the flatness of the gain curve.

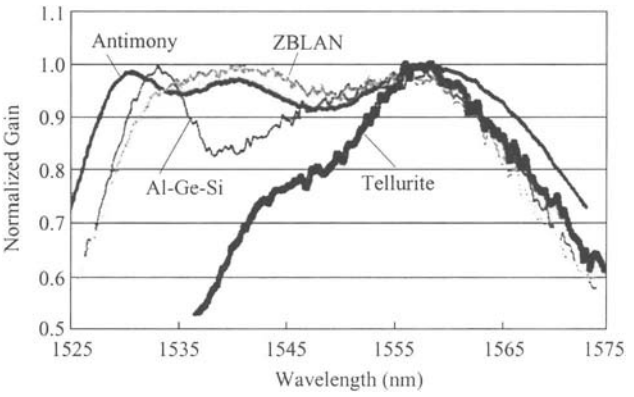


Figure 8.10 Examples of normalized gain bandwidth for very different glass compositions (from Ellison et al., 1999)

It has recently been demonstrated that the emission profile depends on three main parameters: (1) the crystal field splitting of both ground and first excited manifolds; (2) the inhomogeneous broadening; and (3) the homogeneous profile of transitions between individual Stark components (Bigot, 2002a). The first two parameters can be deduced from low-temperature selective emission spectra (nonresonant fluorescence line narrowing (FLN) measurements), while the latter requires knowledge of the temperature dependence of resonant fluorescence (resonant FLN). Determination of the $^4I_{15/2}$ Stark splitting in various hosts shows

that for overall splitting below 350 cm^{-1}, a quasi equidistance between individual Stark components is observed, while this equidistance no longer exists beyond. This observation underlines significant differences between the "symmetry" of the erbium sites (Huang et al., 2001a, 2001b) especially considering alkalisilicate glasses. One can suggest that during the formation of the glass a quasi-crystalline arrangement remains effective. This is also supported by the intensity differences observed for individual transitions between Stark components reported in various glass compositions.

A $T^{1.5}$ temperature dependence of the homogeneous profiles in individual transitions has recently been reported for series of glasses, emphasizing the significant contribution of the direct one-phonon process at low temperature (30 – 150 K), while a two-phonon Raman process (T^2 temperature law) is more likely at higher temperature. Subsequently, it was possible to reproduce the erbium IR emission profile at low temperature without any parameters (Bigot, 2002b). Above approximately 100 K (depending on the glass composition), the emission profile strongly depends on the Stark splitting of the $^4I_{13/2}$ manifold, which is hardly available in high phonon energy glass compositions. Within this approach, the overall full width at half maximum (FWHM) of the homogeneous line width of the erbium IR transition can be extrapolated at room temperature, and its value compares well with that deduced from gain spectral holeburning measurements (Sulhoff, 1997; Joindot, 1997; Bigot, 2002a).

As shown in Fig. 8. 10, extension of the gain curve towards long wavelength chall enges chemists to develop new chemical compositions. Solutions based on antimony or other multicomponent glasses have recently been proposed, giving rise to a large improvement in gain bandwidth (Ellison et al., 1999; Mori et al., 1997a; Baniel et al., 2001). However, beyond 1. 6 μm, the gain efficiency is reduced by ESA towards higher excited states (see Fig. 8. 8), and this is strongly glass composition dependent (Mori et al., 1997b).

Finally, wavelength division multiplexing across the C and L amplification bands of erbium gain emission have considerably advanced the actual capacity of the optical fiber network, but a limit is still predictable. There are not so many ways to increase this capacity again except by reducing the spacing between channels (or wavelengths), increasing the broadening of the erbium emission as shown above, or opening up new amplification bands. The two former solutions are already limited by wavelength selectivity of filter devices and glass composition, respectively. The latter proposal offers better prospects with two main complementary directions: the Raman optical fiber amplifier (Dianov, 2002; Bayart, 2003), and rare-earth optical fiber amplifier doped with ions other than erbium. Several groups have proposed using dysprosium (Samson et al., 1997), and, as presented below, praseodymium and thulium doped glasses and fibers for the different wavelength ranges 1. 3 μm and 1. 48 μm respectively, including new hosts.

8.3.2 Praseodymium-doped Fiber Amplifier

This amplifier was proposed and studied in the early 1990s because one of its infrared emissions at around 1.3 μm due to the electronic transition $^1G_4 \rightarrow {}^3H_5$ (see Fig. 8.11) falls into the second window of telecommunications (O-band original).

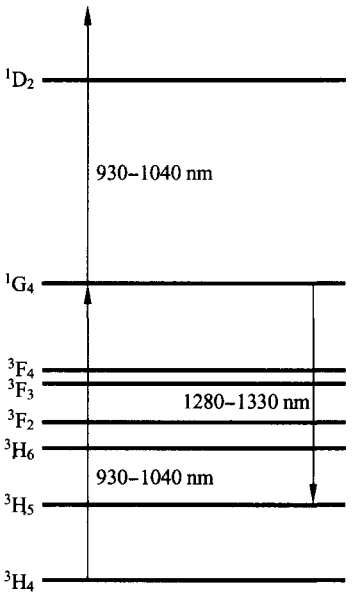


Figure 8.11 Energy level scheme of the PDFA: pumping and relaxation

The praseodymium doped fiber amplifier (PDFA) works as a three-level system with two major disadvantages: a $^1G_4 \rightarrow {}^3H_5$ relaxation at 1.3 μm mostly nonradiative requireing low phonon energy glass and very weak absorption cross section in the $^1G_4$ manifold that requires a long fiber or a high concentration. Consequently, this amplifier has been exploited with fluoride and chalcogenide glasses which, in turn, suffer from fiber losses, >1 dB/m, much higher than in silica fibers. The higher efficiency has been obtained by Hoya Corporation (Itoh et al., 1999) in InF_3/GaF_3 based fluoride glass fibers (0.29 dB/mW) and GaLaS glass fibers (0.81 dB/mW). Recent theoretical analysis by Quimby shows that dual-wavelength pumping should reduce $^3H_5 - {}^1G_4$ excited state absorption and increase the efficiency of the amplifier (Quimby et al., 2001). Because of the large broadening of the absorption transition, pump wavelengths extending from 0.95 μm to 1.07 μm have been tested with limited success. It is then necessary to use twice the pump power of a regular EDFA. To reinforce absorption efficiency, increasing of the Pr^{3+} concentration as a simple solution is not possible because it favors cross-relaxation energy transfer and/or up-

conversion energy transfer, depending on the pump wavelength (Remillieux et al., 1996a, 1996b). Co-doping with ytterbium was also tested, but the gain was lower due to back transfer and intense blue emission.

8.3.3 Thulium-doped Fiber Amplifier

This amplifier was first proposed in 1993 (Komukai, 1993; Percival and Williams, 1994; Komukai et al., 1995), but outstanding performance was only recently obtained with an overall power efficiency of 52% (Roy et al., 2001) in single pass configuration and 57% (Aozasa et al., 2002) in double-pass configuration. The thulium-doped fluoride fiber amplifier (TDFFA) works in the so-called S-band (short band) between 1450 nm and 1480 nm or in the shifted band S + (1470 − 1510 nm) in a range where absorption of the silica fiber is still low (~0.25 dB/km). Spectroscopy of this amplifier is not yet well understood because of the complexity and richness of Tm^{3+} electronic structure (see Fig. 8.12), shown by laser demonstrations in wavelength ranges as different as blue, red, deep red and infrared (Allain et al., 1989; Grubb et al., 1992; Allen et al., 1993). In low-lying states involved in infrared emission, the laser transition takes place between the two excited states $^3H_4$ and $^3F_4$ and the final level ($^3F_4$) has a lifetime (~11 ms) longer than the $^3H_4$ excited level subsequently (~1.5 ms). several pumping schemes using either two-step excitation or two pump lasers have been reported to circumvent this bottleneck

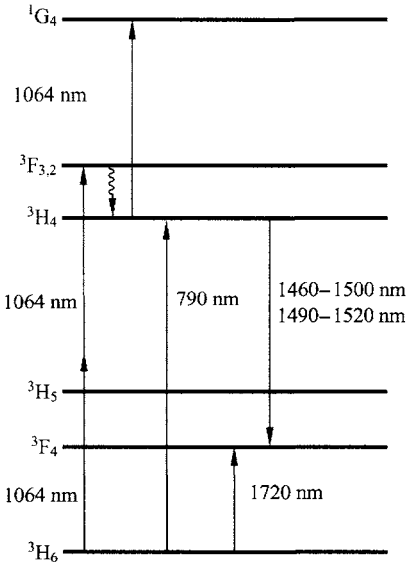


Figure 8.12 Energy levels involved in amplification process in TDFA

effect by depleting the $^3F_4$ population. An alternative to deplete the $^3F_4$ state is to co-dope the host with europium or terbium ions, thanks to efficient cross-relaxation energy transfer between the low-lying states of these ions and the $^3F_4 \leftrightarrow {}^3H_6$ transition of thulium (Percival, 1993; Vega-Durán et al., 2001). Another necessary condition requires good radiative relaxation of the $^3H_4$ state, which is only satisfied in low phonon energy material such as heavy metal fluoride glass (Adam, 2000), but not in a silica-based host (Cole and Dennis, 2001).

Considering the different pumping schemes, two types of up-conversion pumping have been proposed. The first uses a single laser excitation involving an resonant excited state (at 1064 nm or 1047 nm) and nonresonant ground state absorption (Sakamoto et al., 2000). The second uses direct dual-wavelength pumping at 800 nm in the $^3H_4$, together with a secondary laser at around 1500 nm to deplete the $^3F_4$ state (Roy et al., 2001) or an alternative proposal to use pumps at 980 nm and 1500 nm (Zhang et al., 2001). All these mechanisms require fundamental knowledge of the quantitative spectroscopic parameters, mainly the energy level scheme and absorption cross sections. In Fig. 8. 13, direct measurements of the excited state absorption (ESA), including low-temperature excited state excitation (ESE) measurements, allow a clear identification of all excited states involved (Guy et al., 2001). Although ESA experiments are generally difficult, has been taken advantage of confinement of light over the length of the fiber to make accurate measurements of excited state absorption cross sections. The complexity of the energy level scheme and dynamics of the excited states of thulium require first a selective two-photon

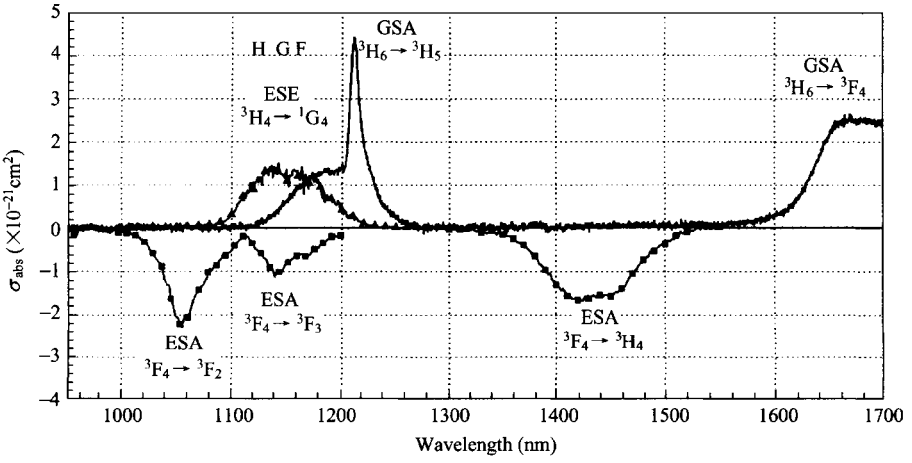


Figure 8. 13 Ground and excited state absorption (GSA and ESA) together with excited state excitation spectra for a thulium-doped fluoride fiber, showing strong overlaps between excited state transitions

excitation to identify each absorption band, and then temporal discrimination of the population of the excited states using delayed excitation pulses.

8.3.4 Fiber Lasers

In all optical telecommunications or sensor applications, rare-earth doped fiber lasers and super-fluorescent sources possess significant advantages over bulk solid state lasers because of the long interaction length of the laser media. For the super-fluorescent source it provides for broad-band behavior that can be exploited for intracavity ring-down spectroscopy of gas impurities in the atmosphere; for instance, among others, the 2 μm range of thulium ($^3F_4 \rightarrow {}^3H_6$) is particularly interesting (Yamamoto et al., 1994). RE glass fibers have the advantage of generating broad-band emission that is very useful for the realization of ultrashort light pulses (Galvanauskas et al., 2001). However, due to high peak pulse intensities non-linear behavior is often encountered, making applications more delicate because of the spectral distribution of the output. In contrast, providing low-power single or multiple channel sources for DWDM applications, with very short pulses, of selected wavelengths for the amplification spectral gain is a real challenge for a laser operating in the stretched-pulse mode-locking regime. Although a lot of work has been addressed to such topics, it seems quite far-fetched to expect an all-optical fiber device to fulfill conditions of high bit-rate transmissions. A New generation of optical fibers with large mode area (photonic glass fibers) may help in that regard (Knight et al., 1998).

Because of the strong confinement of the light due to the fiber or channel configuration, up-conversion processes can be nicely optimized. However a low phonon energy material is generally required to give access to most of the metastable and radiative excited states. That is why, together with the possibility of drawing fiber, only RE-doped heavy metal fluoride materials have been successfully used. They have taken advantage of the ESA process, in which a very low threshold of saturation of the first excitation step is generally observed, and a linear dependence is measured for the output power of the up-converted laser emission. More complex scenarios have been tested, involving up-conversion energy transfer with ytterbium and praseodymium for blue emission, for instance (Scheps, 1996). Finally, substantial broadening of the absorption and emission bands has proven detrimental to the relative absorbed pump power efficiency, and it outweighs the positive effect of the long interaction length of the fiber.

8.3.5 Optical Integrated Amplifiers and Lasers

8.3.5.1 Optical Integrated Amplifiers

An alternative to all-optical fiber links for the realization of metropolitan networks and further FTTH connetions is the development of integrated optical devices allowing different complementary functions such as amplification, multiplexing, and, moreover, reduction in price due to mass production. Again, rare-earth doped materials show capacity to provide compact optical amplifiers compatible with long-distance transmission signals. Most of the known chemical compositions used for optical fiber amplifiers have been proposed to implement integrated amplifiers with the two requirement of low-loss propagation and high concentration. Furthemore, erbium-doped silica, phosphates, aluminosilicates, and more recently heavy metal fluoride materials have been tested (Shmulovich, 1992; Barbier et al., 1999; Snoeks, 1996; Delavaux et al., 1999; Lebrasseur, 1998, 1999). The best results so far, for gain, noise figure and pump efficiency have been obtained in ytterbium – erbium co-doped channel waveguides fabricated by the ionic exchange process (Barbier et al., 1998). This rather good efficiency was mostly due to the ability to dope phosphate composition with high rare-earth concentrations without fluorescence quenching effects, as generally observed for other oxide compositions. However, this amplifier is constrained to work within a limited spectral bandwidth which does not satisfy the WDM conditions unless equalizer filters are used, at the expense of maximum gain (as for other oxides). These are important to note that phosphate compositions have been used to realize the best gain performance so far within a few centimeter long fiber (Hu et al., 2001). Fluoride materials exploited with anionic exchange process or physical vapor deposition techniques have been successfully used to achieve gain in erbium-doped channel waveguides (Lebrasseur et al., 1999). These are then expected to accommodate multiwavelength transmission because of the known flatness of the spectral gain curve of erbium-doped fluoride fiber amplifies. As noted earlier, other transmission windows may be available with other doping such as thulium (1.48 μm) or praseodymium (1.3 μm). It is also interesting to note that such fluoride integrated fabrication methods may renew interest in RE-doped frequency upconversion systems for the development of powerful and compact new visible sources.

8.3.5.2 Planar Lasers

Besides telecom applications, waveguide lasers can be used in the area of high average power diode-pumped solid state lasers. Diode lasers are very cheap, compact, and powerful sources but they deliver highly non-diffraction-limited beams. The idea is to use the beam of a diode laser, to pump another laser, which produces a diffraction-limited beam. Indeed, a wide variety of applications in the industrial, military, medical, and research sectors are interested in efficient, compact, robust and high beam-quality lasers. One of the major issues of

diode-pumped lasers is to couple the highly divergent, asymmetric and non-diffraction-limited light from the high-power diode laser into the lasing medium.

One immediate advantage of waveguide structure is to work at higher pump intensity than in the bulk counterpart. Thus laser action in waveguides occurs at threshold well below the bulk threshold. Diffraction-limited beam in the confined direction is automatic, providing single-mode structure. While traditional rod geometry suffers from thermal lensing and fracture limitation (Koechner, 1988), the slab geometry of a planar waveguide is very well suited to evacuating extra heat from the lasing region (Eggleston et al., 1984). A planar guide has the added advantage that the guiding dominates the one-dimensional thermal lensing (Shepherd et al., 2001). Moreover, the asymmetric slab-like geometry of waveguides directly matches the line type beam of a strip diode, which facilitates the coupling of pump light.

Some difficulties are inherent in the waveguide structure: fabricating waveguide with low propagation losses, efficiently launching the pump light, getting a single-mode spatial output in the non-guided direction. A review of high-power planar dielectric waveguide lasers (Shepherd et al., 2001).

Edge, cladding, and face pumping have all been developed as techniques for pump delivery for active planar waveguide. In edge and cladding pumping, the diode beam is launched into the waveguide with simple focusing optics, the laser cavity being made up of two plane mirrors butted on each face (Shepherd et al., 1999; Bonner et al., 1998). Cladding pumping into a second, high-*NA* waveguide to an inner planar waveguide improves compatibility with diode bar radiation. In that case, pumping radiation is guided into the outer waveguide and absorbed into the inner core. If the *NA* is sufficiently high, there is no need of focusing optics; the coupling being done by positioning the diode bar close to the waveguide (Mackenzie et al., 2003). Best results are obtained in Nd^{3+}: $Y_3Al_3O_{12}$ waveguides are impressive: optimized diffraction-limited output powers of 4.3 W, 3.5 W, and 2.7 W are obtained with absorbed pump powers of 7 W for the transitions at the lasing wavelengths of 1.064 m, 946 nm, and 1.3 μm, respectively (Mackenzie et al., 2003). Face pumping within a reflective, slotted mirror pump chamber make it possible to pump active media with a few hundreds watts, producing >100 W in the high brightness regime (Lee et al., 2002).

8.4 Optical Microcavities and Nanoconfinement

Much interest has concerned optical processes in microcavities over the past decade, on optical processes in microcavities. For example, Fabry-Perot cavities (De Martini et al., 1987), micrometer-sized semiconductor lasers (Deppe and Lei, 1991), optical fibers (Knight, 1992) (microscopic in two dimensions, extended in the third), and micrometer-sized dielectric spheres (Hill and Benner,

1988) have been proposed. While the quantization of electromagnetic modes in a microwave cavity has been known for a long time (Purcell, 1946), it is only recently that its effect on the control of photon – matter interaction has been experimentally investigated in optical wavelength-scale structures. One obtains naturally the two limiting cases of interaction when a single-photon mode interacts with the atomic system: the strong coupling case leading to the Rabi oscillation when the damping of either the photon mode or the atomic system is weak, the weak-coupling case leading to the exponential decay of the atom from its excited state when the damping of either the photon mode or atomic system is strong. Among other atomic systems, rare-earth ions in solids provide a unique physical situation for which excitation is strongly localized, make it possible to examine the two limiting cases of interaction.

8.4.1 Optical Confinement

Optical microcavities are resonators that have at least one dimension on the order of the transition wavelength. In these structured materials light emission properties are greatly altered compared to those in those in large size cavities used for conventional laser oscillators. Optical confinement of a microcavity results in a rearrangement of the mode density in two ways simultaneously: one is nonuniform spatial redistribution, and the other is spectral redistribution. In general, a change of spatial pattern of spontaneous emission would be accompanied by a change in the spontaneous emission rate. Such effects have been reported in different cavities and for different visible and infrared rare-earth emissions (Schubert et al., 1992, 1993; Rigneault et al., 1997a, 1997b; Robert et al., 1998; Belarouci et al., 1999). The dielectric resonators are generally fabricated by conventional deposition techniques, and they are composed of alternating thin layers of high and low refractive index (with a difference as high as possible, Si/SiO_2 and Ta_2O_5/SiO_2 for IR and visible respectively, for instance) and a central spacer of optical path length $k\lambda/2$ n optical length (with k integer > 1) introducing either the reflective or transmissive narrow-band filtering. Cavities are optimized for resonant wavelength emission of the rare-earth ion considered. In most microcavities studies, doping of the central layer is realized by rare-earth ion implantation of typically 150 – 300 keV ion beams and an average fluence of 10^{15} ions/cm^3 (giving rise to typical concentration of 10^{20} ions/cm^2 near the surface of the spacer) before deposition of the top mirror of the cavity. After implantation, thermal annealing is generally carried out on the samples at around 400℃ for 1 h to 10 h in order to restore the fluorescence properties of the rare earth ions. Alternatively, a sol/gel technique, including the doping process, has been used to fabricate RE-doped microcavities (Bellessa, 2001).

8.4.2 Experimental Evidences

As said before, two coupling limits between the electronic states and the electromagnetic modes have been explored.

In the weak coupling limit (in such case quality factor Q is at most few hundreds), spectral and spatial changes have been reported together with some evidence of modification of radiative properties (see Fig. 8.14). Erbium and praseodymium ions have been used to identify such effect in the infrared and in the visible ranges at 1.5 μm, 0.54 μm and 0.63 μm, 0.48 μm, respectively. A specific experimental setup has been implemented to collect both radiative and

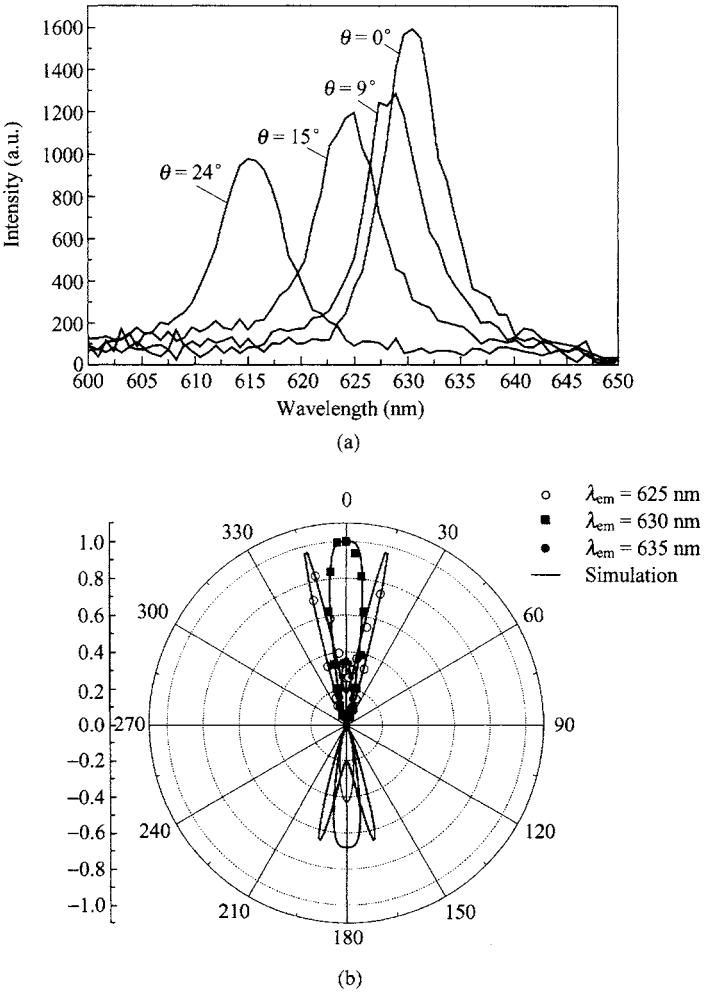


Figure 8.14 Pr^{3+} doped microcavity: spectral (a) and spatial (b) changes of resonance with the angle of detection with respect to the normal axis of the cavity

guided modes of the structure by using a fiber optics bundle and decoupling prism. It allows an experimental determination of the total emitted power of the structure, which can be compared to a theoretical approach (Rigneault, 1999). Furthermore time domain measurements give access to radiative properties of the rare-earth ion excited states involved (Belarouci et al., 2001). It is important to note that one maximum of the fundamental electromagnetic mode of the microcavity may overlap the implanted zone near the surface, resulting in efficient pumping of the rare-earth ion. Narrowing of the line shape of the emission in agreement with the spectral response of the Fabry-Perot filter and strong enhancement of the main peak fit well with either a classical dipole theory or quantum theory. Moreover, a strong reduction in lifetime increase of the radiative probability with respect to the Fermi Golden rule is a direct consequence of both interference effects and redistribution of the electromagnetic modes (Fermi golden rule). The variation in time constant across the emission bandwidth is observed and explained by the fact that at long wavelengths, the resonance conditions are still satisfied in contrast to the short-wavelength side (Belarouci et al., 2001). Similar behavior was demonstrated by varying the angle of detection.

Although the micro-cavity Q factor is small, light confinement can be notably increased by a higher rare earth concentration the spacer, leading to strong photon – Er coupling as suggested by Lipson (Lipson and Kimerling, 2001) in the case of erbium. This physical situation can be described by two coupled oscillators inducing splitting in the frequency spectrum. Indeed, splitting measured in the low temperature reflectivity spectrum of a microcavity with a spacer containing stoichiometric erbium sesquioxide layers has been interpreted as vacuum Rabi splitting (VRS). The anticrossing behavior of the VRS splitting seems to probe the strong photon – Er coupling regime as its first observation in condensate matter.

8.4.3 Various Devices

Among other confined systems, microspheres represent an interesting physical situation because of the high Q values (up to 10^9) taht have been reached due to the spherical geometry, quality, and nature of the materials used to fabricate them. Very good surface roughness allows light to propagate with in the gallery modes in the equatorial plane with low loss. Then laser action with very low threshold involving 10^5excited ions has been reported for rare-earth doped silica (Treussart et al., 1996) and more recently in fluoride glass spheres (von Klitzing et al., 1999). However, from a technological point of view it seems difficult to combine such devices in integrated optical systems. More realishcally, a RE-doped planar microcavity including ring and straight waveguides compatible with optical fiber geometry seems to open a new area in the field of microphotonics and optoelectronics for optical intercomects for instance (Hrynievicz, 2000).

8.5 Conclusions

In this chapter, we have presented a simple picture and shown some advantages of the fiber or channel configuration of rare-earth doped materials with respect to photon emission. It is clear that the most spectacular event was the EDFA as an example of breakthrough in the field of all-optical telecommunications. A lot of physics underlies the success of the EDFA, and can be directly transposed to other rare-earth doped waveguides, as shown with the TDFA or integrated amplifiers. The question of the extent to which extreme light confinement can be reached and be helpful with rare-earth doped materials, to take advantage of the richness of their excited states, is interesting not only from a technological standpoint but also from fundamentals, the illustration of our knowledge at a microscopic scale for which waveguides have the greatest impact. For optical structures having dimensions below the wavelength, the coupling of the electromagnetic waves with the dipole atomic transition wavefunctions demonstrates the possibility of controlling optical properties of the emitting centers. Then the next step, which has already been investigated (see Meltzer's chapter in this book), concerns the behavior of the rare-earth ion emitters imbedded in a nanoscale object. In that size range, it is clear that thermodynamic behavior of the materials must play an important role in close connection with the environnement of the nanostructure, underscoring the impact of surface effects with respect to the volume of the particle.

References

Adam, J. L. In: *Adavanced Inorganic Fluorides: synthesis characterization and applications,* eds. T. Nakajima, B. Zemva, A. Tressaud (Elsevier Amsterdam, 2000).

Allain, J. Y., M. Monerie, H. Poignant. Electron. Lett. **25**, 1660 – 1661 (1989).

Allen, R., L. Esterowitz, I. Aggarwal. J. of Quantum Electronics, **29**(2), 303 (1993).

Aozasa, S., H. Masuda, T. Sakamoto, K. Shikano, M. Shimuzu. Electron. Lett. **38**, 361 (2002).

Aozasa, S., H. Masuda, H. Ono, T. Sakamoto, T. Kanamori, Y. Ohishi, M. Shimizu. IEE Electr. Lett. **37**(19), 1157 (2001).

Aozasa, S., T. Sakamoto, T. Kanamori, K. Hoshino, M. Shimizu. IEE Electr. Lett. **36** (5), 418 (2000).

Arai, K. Namikawa, H & al J. Appl. Phys. **59**(10), 3430 – 3436 (1986).

Barbier, D., P. Bruno, Cassagnettes, Trouillon, M. Hyde, R. L. Kervokian. A. Delavaux J-M. P. OFC'98, paper 45 (1998).

Barbier, D., P. Gastaldo, B. Hyde, J. M. Jouanno, A. Kervokian. ECIO, paper TuC4 (1995).

Barnes, W. L., R. Laming, E. J. Tarbox, P. R. Morkel. IEE J. of Quantum Electronics **27**, 1004 (1991).

Baniel P., S. Blanchandin, F. Roy, L. Bigot. European patent, EP 1 270 526 A1.

Bayart, D. CR Physique **4**, 65 – 74 (2003).

Beach R. J., S. C. Mitchell, H. E. Meissner, O. R. Meissner, W. F. Krupke, J. M. McMahon, P. C. Becker, N. A. Olsson, J. R. Simpson (Academic Press, N. Y., 1999).

Belarouci, A., B. Jacquier, P. Moretti, S. Robert, H. Rigneault. J. Opt. Soc. Am. B **18** (7), 1 – 7 (2001).

Belarouci, A., F. Menchini, B. Jacquier, P. Moretti. H. Rigneault, S. Robert. J. Lumin. **83 – 84**, 275 – 282 (1999).

Bellessa, J., S. Rabaste, J. C. Plenet, J. Dumas, J. Mugnier, O. Marty. Appl. Phys. Lett. **79**, 2142 (2001).

Bennet, W. J., D. P. Shepherd, Opt. Lett. **26**(12), 881 – 883 (2001).

Bigot, L., A. M. Jurdyc, B. Jacquier, L. Gasca, D. Bayart. Phys. Rev. B **66**, 214, 204 (2002a).

Bigot, L. Thèse Lyon (2002b).

Bonner, C. L., C. T. A. Brown, D. P. Shepherd, A. C. Tropper, W. A. Clarkson, D. C. Hanna, B. Ferrand, Opt. Lett. **23**, 942 – 944(1998).

Boulard, B., L. Brilland, H. Poignant. Electron. Lett. **34**, 267 – 268 (1998).

Broer, M. M., R. L. Cone, J. R. Simpson. Opt. Lett. **16**, 1391 – 1393 (1991).

Caro, P., O. Beaury. J. Phys. **37**(6), 671 – 676 (1976).

Cole, B., M. L. Dennis. OFC'01 paper TuQ3 (2001).

Daran, E., L. E. Bausà, A. Muñoz-Yagüe, C. Fontaine. Appl. Phys. Lett. **62**, 2616 – 2618 (1993).

Delevaque E., T. Georges, M. Monerie, P. Lamouler , and J-F. Bayon. IEEE Photon. Tech. Lett. **5**, 73 (1993).

Delavaux, J-M. P., C. Mcintosh, J. Shmulovich, A. J. Bruce, R. K. Pattnaik, B. R. Wirstiuk. OFC'2000, paper WA2-1/3 (2000).

De Martini, F., G. Innocenti, G. R. Jacobovitz, P. Mataloni. Phys. Rev. Lett. **59**, 2955 – 2958 (1987).

Deppe, D. G., C. Lei. J. Appl. Phys. **70**, 3443 – 3448 (1991).

Desurvire, E. *Erbium-doped fiber amplifiers* (John Wiley & Sons, N. Y., 1994).

Dianov, E. M. J. Light. Tech. **20**, 1457 (2002).

Digonnet M. J. F., M. K. Davis, P. H. Pantell. Opt. Fiber. Tech. **1**, 48 (1994).

Douysset-Bloch, L., B. Ferrand, M. Couchaud, L. Fulbert, M. F. Joubert, G. Ghadeyron, B. Jacquier, J. Alloys and Comp. **275 – 277**, 67 – 71 (1998).

Eggleston, J. M., K. Kane, T. J. Kuhn, J. Unternahrer, R. L. Byer. IEEE J. Quantum Electronics **20**, 289 – 301 (1984).

Ellison A. J. G., J. E. Dickinson, D. E. Goforth, D. L. Harris, J. T. Kohli, J. D. Minelly, B. N. Samson. Proc. Topical Meeting on Optical Amplifiers and Applications, 107 (2000).

Galvanauskas, A., Z. Sartania, M. Bischoff. CLEO'01 paper CMA1 Baltimore (2001).

Goldner P., F. Auzel. J. of Appl. Phys. **79**, 7972 (1996).

Gorller-Walrand, C., K. Binnemans. Spectral intensities of f – f transitions, *Handbook on the Physics and Chemistry of Rare Earths* (1998).

Guy, S., W. Meffre, A. M. Jurdyc, B. Jacquier, F. Roy, P. Baniel, D. Bayart, A. Le Sauze, C. Collet, J. J. Girard. OAA'01 paper OWB5 (2001).

Grubb, S. G., K. W. Bennett, R. S. Cannon, W. F. Humer. *CLEO, CPD18* (Anaheim, CA, USA, 1992).

Hill, S. C., R. E. Benner. *Morphology-dependent resonances in optical effects associated with small particles* (World Scientific, Singapore, 1988).

Hrynievicz, J. V., P. P. Absil, B. E. Little, R. A. Wilson, P. -T. Ho. IEEE Phot. Tech. Lett. **12** (3), 1041 – 1043 (2000).

Hu, Y., S. Jiang, T. Luo, K. Seneschal, M. Morrell, F. Smektala, S. Honkanen, J. Lucas, N. Peyghambarian. IEEE Photon. Tech. Lett. **13**, 657 – 659 (2001).

Huang, Y. D., M. Mortier, F. Auzel. Opt. Mat. **15**, 243 – 260 (2001a).

Huang, Y. D., M. Mortier, F. Auzel. Opt. Mat. **17**, 501 – 511 (2001b).
Itoh, K., H. Yanagita, H. Tawarayama, K. Yamanaka, E. Ishikawa, K. Okada, H. Aoki, Y. Matsumoto, A. Shirakawa, Y. Matsuoka, H. Toratani. JNCS **256**, 1 (1999).
Jacquier, B. *Rare earth-doped fiber lasers and amplifiers* (Kluwer Academic Publishers, Boston, 1997).
Joubert, M. F. Opt. Mat. **11**, 181 (1999).
Joubert, M. F., S. Guy, B. Jacquier. Phys. Rev. B **48**, 10, 031 (1993).
Judd, B. R. Phys. Rev. **127**, 750 (1962).
Knight, J. C., T. A. Birks, R. F. Cregan, P. St Russel, J. P. de Sandro. Lett. **34**, 1347 – 1348 (1998).
Knight, J. C., H. S. T. Driver, G. N. Robertson. J. Sc. **88**, 162 (1992).
Koechner, W. *Solid-State Laser Engineering*, 2nd (Springer Verlag, New York 1988).
Komukai, T., T. Yamamoto, T. Sugawa, Y. Miyajama. J. Of Quantum Electronics **31** (11), 1880 (1995).
Komukai, T., Y. Yamamoto, T. Sugawa, Y. Miyajima. Electron. Lett. **29**, 110 (1993).
Lebrasseur, E., Y. Gao, B. Boulard, B. Jacquier. ECOC'99 paper I – 54 (1999).
Lebrasseur, E., B. Jacquier, M. C. M. Marco de Lucas, E. Josse, J. L. Adam, G. Fonteneau, J. Lucas, Y. Gao, B. Boulard, C. Jacoboni, J. E. Broquin, R. Rimet. J. Alloys and Comp. **277**, 716 – 720 (1998).
Lee, J. R., H. J. Baker, G. J. Friel, G. J. Hilton, D. R. Hall. Opt. Lett. **27**, 7 (2002).
Lipson, M., L. C. Kimerling. Opt. Mat. **16**, 47 – 52 (2001).
Lucas, J., C. A. Angell. Mat. Res. Bull. **19**, 945 (1984).
Mackenzie, J. I., C. Li, D. P. Shepherd. IEEE Journal of Quantum Electronics **39**(3), 493 – 500 (2003).
Mears, R. J., L. Reekie, I. M. Jauncey, and D. N. Payne. Electron. Lett. **23**, 1026 (1987).
Miniscalco W. J., J. Lightwave. Tech. **9**, 234 (1991).
Moretti, P., M. F. Joubert, S. Tascu, B. Jacquier, M. Kaczkan, M. Malinowskii, J. Samecki. Opt. Mat. In press (2003).
Mori A., Y. Ohishi, and S. Sudo, Electron. Lett. **33**, 863 (1997a).
Mori A., Y. Ohishi, M. Yamada, H. Ono, and S. Sudo, European Conference on Optical Communications, 135 (1997b).
Mougel, F., K. Dardenne, G. Aka, A. Khan-Harari, D. Vivien. J. Opt. Soc. Am. B **16**, 164 (1999).
Myslinski P., D. Nguyen, and J. Chrostowski, J. Lightwave Tech. **15**, 112 (1997).
Niay, P., M. Douay, P. Bernage, W. X. Xie, B. Leconte, D. Ramecourt, E. Delevaque, J. F. Bayon, H. Poignant, B. Poumellec. Opt. Mat. **11**, 115 – 129 (1999).
Ofelt, G. S. J. Chem. Phys. **37**, 511 (1962).
Percival, R. M., J. R. Williams, Electron. Lett. **30**(20), 1684 (1994).
Percival R. M., D. Szebesta, and S. T. Davey. Electron. Lett. **29**, 1054 (1993).
Peters, P. M., S. N. Houde-Walter, J. Non-Cryst. Solids **239**, 162 – 169 (1998).
Poignant, H., S. Boj, E. Delevaque, M. Monerie, T. Taunay, P. Niay, P. Bernarge, W. X. Xie. Electron. Lett. **30** (16), 1339 – 1340 (1994).
Polman, A. J. Appl. Phys. **82**(1), 1 – 39 (1997).
Purcell, E. M. Phys. Rev. **69**, 681 (1946).
Quimby, R. S., B. N. Samson, B. G. Aitken. Amplifiers and their Applications OSA Trends in Optics and Photonics series. **44**, 143 – 149 (2001).
Quimby, R. J. of Appl. Phys. **75**, 613 (1994).
Remillieux, A., B. Jacquier. Proc. SPIE **2841**, 134 – 143 (1996a).
Remillieux, A., B. Jacquier, C. Linarès, C. Le Sergent, S. Artigaud, D. Bayard, L. Hamon, J. L. Beylat. J. Phys. D: Applied Physics **29**, 963 (1996b).

Rigneault, H., B. Jacquier, P. Moretti, A. M. Jurdyc, A. Belarouci, S. Robert. Mat. Sci. Forum **239 – 241**, 717 – 720 (1997a).

Rigneault, H., S. Robert, S. Begon, B. Jacquier, P. Moretti. Phys. Rev A **55**, 1497 (1997b).

Robert. S., H. Rigneault, F. Lamarque. J. Opt. Soc. B **15**, 1773 – 1779 (1998).

Romero, J. J., D. Jaque, J. Garcia Solé, A. A. Kaminskii, Appl. Phys. Lett. **78**(14), 1961 – 1963 (2001).

Roy, F., A. Le Sauze, P. Baniel, D. Bayart. OAA'01 post-deadline paper PD4 (2001).

Sakamoto, T., S. Aozasa, T. Kanamori, K. Hoshino, M. Shimizu. OFC'00 post-deadline paper PD4 (2000).

Saleh, B. E. A., M. C. Teich. *Fundamentals of Photonics* (John Wiley, New York, 1991), p. 238.

Samson, B. N., T. Schweizer, D. W. Hewak, R. I. Laming, Opt. Lett. **22**(10), 703 – 705 (1997).

Scheps, R. Prog. Quant. Electr. **20**(4), 271 (1996).

Schubert, E. F., N. E. J. Hunt, A. M. Vredenber, T. D. Harris, J. M. Poate, D. C. Jacobson, Y. H. Wong, G. J. Zydsik. Appl. Phys. Lett. **63**, 2603 – 2605 (1993).

Schubert, E. F., A. M. Vredenber, N. E. J. Hunt, V. H. Wong, P. C. T. D. Becker, J. M. Poate, D. C. Jacobson, L. C. Feldman, G. J. Zydsik. Giant. Appl. Phys. Lett. **61**, 1381 – 1383 (1992).

Sergeyev, S. V., B. Jaskorzynska. Phys. Rev. B **62**, 15, 628 – 15, 633 (2000).

Shepherd, D. P., S. J. Hettrick, C. Li, J. I. Mackenzie, R. J. Beach, S. C. SMitchell, H. E. Meissner. J. of Phys. D: Appl. Phys. **34**, 2420 – 2432 (2001).

Shepherd, D. P., C. L. Bonner, C. T. A. Brown, W. A. Clarkson, A. C. Tropper, D. C. Hanna, H. E. Meissner, Opt. Comm. 1999.

Shmulovich, J., et al. Electron. Lett. **28** (23), 1181 – 1182 (1992).

Snitzer, E. Appl. Phys. Lett. **6**, 45 (1965).

Snitzer, E. J. Appl. Phys. **32**, 36 (1961).

Snoeks, E., et al. IEEE J. of Quantum Elec. **32**(9), 1680 – 1684 (1996).

Tanabe, S., T. Ohyagi. J. Appl. Phys. **73** (12), 8451 – 8454 (1993).

Tanabe, S., T. Ohyagi. Phys. Rev. B **46** (6), 3305 – 3310 (1992).

Treussart, F., V. Sandoghdar, J. Hare, V. Lefevre, J. M. Raimond, S. Haroche. Phys. Rev. A **54**, 1777 (1996).

Vega-Durán, J. T., L. A. Díaz-Torres, M. A. Meneses-Nava, M. A. Maldonado-Rivera, O. Barbosa-García. J. Phys. D **34**, 3203 – 3208 (2001).

Vincent, B., A. Boudrioua, J. C. Loulergue, P. Moretti, S. Tascu, B. Jacquier, G. Aka, D. Vivien. Opt. Lett. **28**(12), 1 – 3 (2003).

W. von Klitzing, E. Jahier, R. Long, F. Lissilour, V. Lefèvre, J. Hare, J. M. Raimond, S. Haroche. Electronic Letters **35**, 1745 (1999).

Yamamoto, T., Y. Miyajima, T. Komukai. Elec. Lett. **30**, 220 (1994).

Zhang, E., S. Wilson, D. Crippa, R. Di Muro, A. Maroney. OAA'01 paper OWB2 (2001).

9 Rare Earth Luminescent Centers in Organic and Biochemical Compounds

J. -C. G. Bünzli

9.1 Introduction

Luminescence has played an essential role in the discovery of the rare earth elements (Crookes, 1885). Since the finding of a powerful red-emitting luminescent material, yttrium oxide doped with a few percents of trivalent europium $Y_2O_3:Eu^{3+}$, by the French chemist Georges Urbain at the start of the 20^{th} century (Gschneidner, 1981), a lot of attention has been focused on the design of lanthanide-containing inorganic phosphors. These materials possess light emitting and/or light conversion properties and are in daily use in color displays, fluorescent lamps, amplifiers for fiber-optic communications, materials for optical storage, electroluminescent devices and X-ray intensifying screens (see Chapters 5 – 9).

The first report on the luminescence of a coordination compound (in which a central metal ion is surrounded by one or several organic molecules, having electron donor properties and termed "ligands") was published in the early 1940's (Weissman, 1942). Using the sun as a source of light, Weissman noted that absorption of radiation with wavelength in the range 320 to 440 nm by the organic part of several Eu^{3+} complexes resulted in the characteristic line luminescence from the f – f transitions of trivalent europium. Studying several anionic chelating agents such as β-diketonates, benzoates, salicylates or picrates, he observed that the efficiency of excitation varies greatly with the nature of the compounds, as well as with the temperature and the solvent, and speculated that in some cases a quantum yield of unity was obtained at low temperature. The intermolecular energy transfer process between an organic ligand and a luminescent metal ion is presently designated as the "antenna effect" (Sabbatini et al., 1987). The discovery stirred interest but no immediate application was found and, moreover, coordination chemistry of the Ln^{3+} ions did not develop much until the 1960's when it was finally recognized that these ions usually display a large coordination number (Bünzli et al., 2000a), which inevitably influences the design of adequate receptors. It was also during the same decade that a concrete proof of the role of the ligand triplet state in the intramolecular

energy transfer process was brought forward (Crosby et al., 1961), at least for β-diketonates. A summary of the early work in the field can be found in a review (Crosby, 1966) which outlines the major conclusions reached at that time:

(1) The excited state of luminescent Ln^{3+} ions can be populated by a fast intramolecular energy transfer process from a triplet state of the ligand (itself populated from a singlet state by intersystem crossing). Estimates for the transfer rate range between 10^6 to 10^9 s^{-1};

(2) Adduct formation between the luminescent chelate and a neutral molecule (such as phenanthroline for instance) usually increases the quantum yield, as does deuteration of either the ligand or the solvent.

Nevertheless, the field was not quite ready for the highlights, despite that laser action was demonstrated for the $^5D_0 \rightarrow {}^7F_2$ transition of Eu^{3+} in some β-diketonates, and for a while authors turned to the use of luminescent lanthanide ions (mainly europium and terbium) as structural reporters for biomolecules such as proteins and enzymes. These investigations take advantage of the chemical similarities between Ln^{3+} ions and Ca^{2+}, Zn^{2+}, the rare earth ions acting as replacement probes, and of the special spectroscopic properties of Ln^{3+} ions: narrow bands and positions of the main transitions not changing significantly from one compound to the other, except for the crystal-field induced fine structure. The reader is referred to a review covering the literature published in this field up to the early 1980's (Horrocks, 1982).

A big stimulus came in the mid 1980's when a small Finnish company, Wallac Oy from Turku marketed bioassays based on time-resolved luminescence of Eu^{3+} (Hemmilä et al., 1995b). These fluoroimmunoassays (FIA) rely on antibodies labeled with a lanthanide chelate which specifically react with the targeted antigens. Since then, many research groups, including several ones traditionally working in the field of organic chemistry, have been developing carefully engineered organic molecules able to encapsulate the Ln^{3+} ions and to enhance their luminescent properties. This growing interest for molecular devices build from organic molecules is also motivated by the development of other recent biomedical applications such as DNA and RNA labelling (Elbanowski and Makowska, 1996) or cancer phototherapy (Guo and Sadler, 1999) and by the design of luminescent responsive systems for in vitro trace analysis (Parker, 2000). Furthermore, organic ligands for the selective complexation of lanthanide ions have also come under the scrutiny of developers of high-performance optical materials and systems (tunable lasers, light-emitting diodes, electro-optical switches).

In this chapter, we discuss the energy conversion mechanisms occurring in lanthanide-containing luminescent probes based on organic receptors, and we selectively review some applications of these systems.

9.2 Sensitizing the Luminescence of Trivalent Lanthanide Ions

9.2.1 Establishing the Importance of the Triplet State

Which ions are of interest in the reviewed field? In fact, most Ln^{3+} ions are luminescent, but the applications of interest to this review require the use of organic complexes in aqueous solution and, for in vivo bioanalyses, at physiological pH of 7.4, which severely limits the choice of potentially interesting ions. Indeed, the emission intensity is qualitatively inversely proportional to the energy gap between the lowest lying excited (emissive) state of the metal ion and its ground manifold. Emission from higher excited states is rarely seen in solution. When the gap is small, it can be easily bridged by nonradiative processes involving vibrational levels, which are numerous in organic complexes. Taking this requirement into account, the best ions are therefore Eu^{3+}, Gd^{3+}, and Tb^{3+}, with energy gaps around 12,150, 32,000, and 14,800 cm^{-1}, respectively (Fig. 9.1). However, Gd^{3+} emits in the UV and is not much useful since its luminescence will interfere with either luminescence or absorption processes in the organic part of the complex molecule. Developments of dual FIA has stirred interest for the luminescence of Sm^{3+} (gap 7400 cm^{-1}) and, more recently, the advent of multiple FIA and chiral luminescent probes emitting in the far infrared has turned attention to Dy^{3+} (7850 cm^{-1}), Nd^{3+} (5500 cm^{-1}) and Yb^{3+} (10,400 cm^{-1}), despite their low quantum yield (usually a few percents at most).

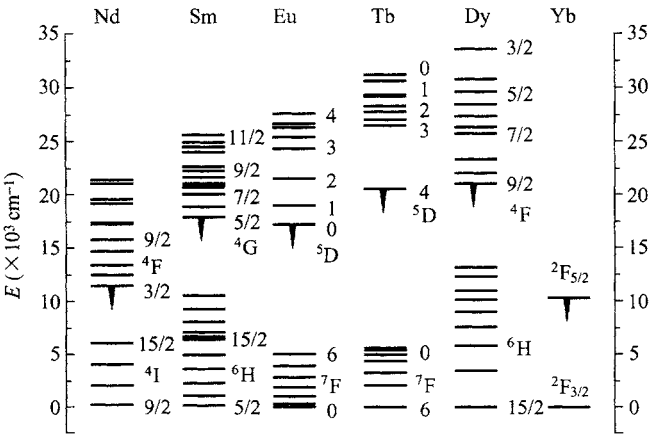


Figure 9.1 Partial energy diagrams for the luminescent Ln^{3+} ions discussed in this chapter

Most of the electronic transitions of the trivalent Ln^{3+} ions involve a redistribution of electrons within the 4f sub-shell. Electric dipole selection rules forbid such transitions, but these rules may be relaxed by several mechanisms. An important one is the coupling with vibrational states, where a molecular vibration temporarily changes the geometric arrangement around the metal ion and, therefore, its symmetry. The strength of the coupling between vibrational and electronic parts of the total wave-function depends on the intensity of the interaction between the 4f orbitals and the surrounding ligands. Since Ln^{3+} ions have [Xe] $4f^n$ electronic configurations, in which the 4f electrons are shielded from external interactions by the $5s^2 5p^6$ filled sub-shells, the vibronic interaction remains weak for these ions. The immediate consequence is that the f – f transitions are extremely narrow (atom-like) and faint, the molar absorption coefficients being usually smaller than 1 $M^{-1} \cdot cm^{-1}$. Other mechanisms which cause a breakdown of the selection rules are the *J*-mixing and the mixing with charge transfer states, but, again, the degree of mixing remains small. Therefore even if many lanthanide-containing compounds display a good quantum yield, direct excitation of the Ln^{3+} ions rarely yields highly luminescent materials. Indirect excitation (called sensitization or antenna effect) has to be used and proceeds in three steps. First, light is absorbed by the immediate environment of the Ln^{3+} ion through the attached organic ligands (chromophores); energy is then transferred to the metal ion mainly through the ligand triplet state; and, finally, the metal ion emits light (Fig. 9.2). This process results in light-converting devices, since usually UV or blue light is absorbed, while green (Tb), yellow (Dy), orange (Sm), red (Eu) or near IR (Nd, Yb) light is given off.



Figure 9.2 Sensitization of the metal-centred luminescence through the attached ligands

After the initial work of Weissman, it was soon understood that the lowest triplet state of the ligand plays a major role in the energy transfer process (Fig. 9.3), although other energy migration paths cannot be excluded (see below). This main pathway has essentially be inferred from steady-state photophysical measurements. More recently, a detailed investigation has been

performed in real time on Tb^{3+} encapsulated in the (2.2.1) cryptand (1)① and on the 1:1 adduct of this cryptate with acetylacetonate (Yu et al., 1991). The luminescence of $[Tb\subset(2.2.1)]^{3+}$ (the sign $\subset$ indicates that the metal ion is encapsulated into the cavity of the cryptand) is enhanced by three orders of magnitude upon complexation with acac (see Appendix 9. B Line 3), which brings compelling evidence that energy migrates from electronically excited acac onto the Tb^{3+} ion. The enhanced emission arises essentially from the fact that the absorption cross section of the cryptate is around 1 $M^{-1}\cdot cm^{-1}$ at 298 nm while that of the ternary complex amounts to about 10,000 $M^{-1}\cdot cm^{-1}$. Insight into the kinetics of the energy transfer process could be revealed by time-resolved picosecond laser spectroscopy. The luminescence decay of the acac triplet state alone is characterized by a lifetime of (1.7 ± 0.4) ns. In the presence of $[Tb\subset(2.2.1)]^{3+}$, the decay becomes bi-exponential and two lifetimes are extracted, 1.7 ns and (103 ± 23) ps; the fraction of the short component increases with increasing cryptate concentration, so that this component is assigned to acac bound to the cryptate. It is noteworthy that in $[Tb(acac)_3]$, a single lifetime is observed with a value of 160 ps, while the decay time amounts to 1.4 ns for $[Gd(acac)_3]$ in which no energy transfer occurs onto the metal ion. Finally, the authors estimated the rise time of the Tb^{3+} luminescence in $[Tb\subset(2.2.1)(acac)]^{2+}$ and found it close to the fast component decay of bound acac. Although these data do not exclude other mechanisms, for instance involving the $^5D_3$ state, they firmly establish that a main energy migration path is the one described in Fig. 9.4 and that the $^3\pi\pi^*$ (acac)-to-Tb^{3+} ($^5D_4$) transfer rate is very fast, amounting to $k_{et} = 9.7\times10^9\ s^{-1}$.

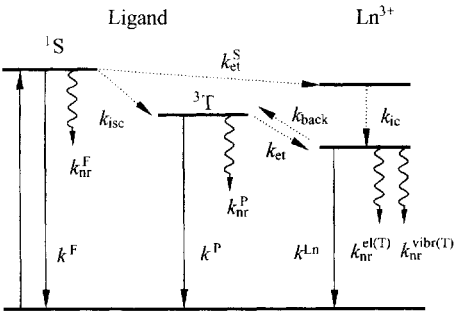


Figure 9.3 Simplified diagram showing the energy migration paths in a Ln^{3+} complex (^1S = singlet state, ^3T = triplet state, F = fluorescence, P = phosphorescence, isc = intersystem crossing, nr = nonradiative, ic = internal conversion, et = energy transfer, back = back transfer, T = temperature-dependent, el = electronic, vibr = vibrational)

① Similarity to **1**, all the boldfaced number express different molecule structures, see Appendix 9. A.

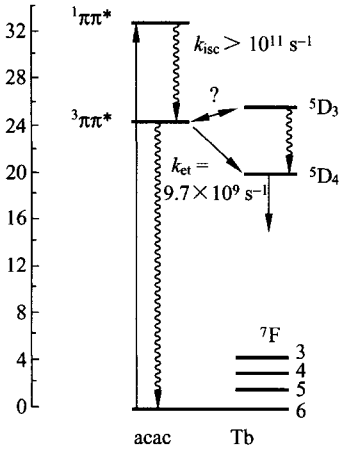


Figure 9.4 Schematic representation of the $^3\pi\pi^*$-to-Tb^{3+} energy transfer path in the ternary complex $[Tb\subset(2.2.1)(acac)]^{2+}$. Redrawn from the work of (Yu et al., 1991)

9.2.2 Mechanisms of Energy Transfer

Looking into the energy transfer processes in more details reveals that essentially two situations may develop. In the first one, depicted on the configuration coordinate diagram of Fig. 9.5 (left part), which is commonly encountered in the literature, and in which excitation of the triplet states leads to a relatively large expansion of the Ln-X distance, energy transfer occurs only as long as the higher vibrational levels of the triplet state are populated. Once internal conversion to the zeroth vibrational level of the $^3\pi\pi^*$ is achieved, transfer to the metal ion can no more happen, and the triplet state deactivates either through phosphorescence or through a nonradiative path. The luminescence spectrum of the complex therefore usually displays a residual emission from the triplet state.

In the second case (Fig. 9.5, right part), where the Ln-X expansion is smaller, transfer is feasible as long as the triplet state is populated; therefore, if k_{et} is large enough (with respect to k^p and k^p_{nr}), most of the energy stored in the triplet state is transferred onto the lanthanide ion. This is of course the sought for situation.

Other energy transfer paths not involving the triplet state, such as direct transfer from the excited ligand singlet state either onto the metal ion emitting level or onto a higher energy level (k^S_{et}, Fig. 9.3), have also been proposed but seem to play a less prominent role, although sometimes metal-centred luminescence is seen upon ligand excitation despite the fact that the luminescent excited state of the metal ion lies under the ligand $^3\pi\pi^*$ state. Some transfer processes are also assisted by vibrations.

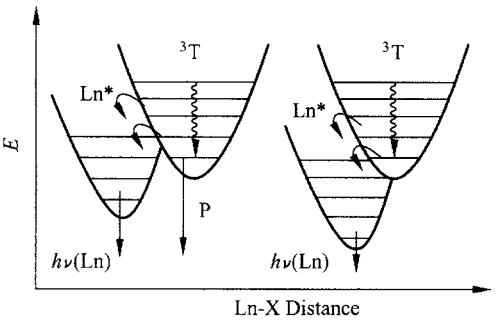


Figure 9. 5 Schematic representation of two potential situations in the $^3\pi\pi^*$-to-Ln^{3+} energy transfer process

In principle, two mechanisms may be invoked to explain the transfer of energy from the ligand triplet state to the metal ion (Fig. 9. 6). Note that for the sake of simplicity, two paired electrons only are shown for both the ligand and

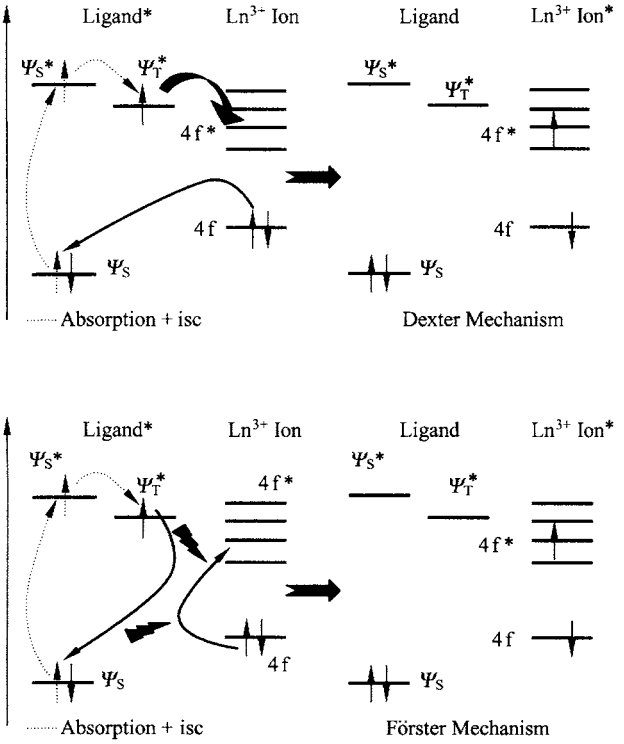


Figure 9. 6 Possible mechanisms of energy transfer

the metal ion. The first mechanism, known as the Dexter or exchange mechanism, involves a double electron transfer. After excitation into the ligand singlet state and suitable intersystem crossing to the ligand triplet state, one electron is transferred from that state onto one of the excited levels of the Ln^{3+} ion while an electron from the highest occupied energy level of the latter is transferred onto the ligand, filling the gap created by the initial photo-excitation of the ligand (Dexter, 1953). This type of transfer with a $e^{-\alpha r}$ distance dependence, requires a good overlap between the ligand and metal orbitals (as well as the conservation of the total spin of the system), which renders it less probable in the case of Ln^{3+} ions in view of the shielding of the 4f orbitals.

The second mechanism has been worked out by Förster. After excitation into the ligand singlet state and suitable intersystem crossing to the ligand triplet state the dipole moment associated with deexcitation of the $^3\pi\pi^*$ state couples with the dipole moment of the 4f orbitals and energy flows from the donor to the acceptor. Known also as the dipole-dipole mechanism, this process has been often documented for Ln^{3+}-containing edifices. The yield of transfer is proportional to the overlap integral J between the emission spectrum of the donor and the absorption spectrum of the acceptor, and depends on the inverse sixth power of the ligand-metal distance, $1/r_{da}^6$ (Förster, 1948).

9.3 Preventing Nonradiative Deactivation of the Metal Ion Luminescent States

To keep the lanthanide-containing edifices as luminescent as possible, one has to design them in such a way that nonradiative deactivation pathways are minimized. Schematically, these processes may be divided into two classes: vibration activated processes and electronic processes.

9.3.1 Vibrational Deactivation Processes

When the luminescent lanthanide ion is coupled to a chemical environment, nonradiative deexcitation takes place through its vibrations. Transitions within a ligand-field multiplet are mediated by acoustical phonons and are quite fast phenomena, as exemplified by rate constants larger than 10^{10} s^{-1}. This explains why emission of light usually originates from the lowest energy sub-level of the ligand-field multiplet. Multi-phonon processes may then bring the excited metal ion further down to its fundamental state. These processes are of course temperature dependent, providing a way to identify them. An equation has been worked out to explain the temperature dependence of the vibrational quenching, characterized by the emission of n phonons and by the rate constant k_{nr}^{nT} at a given temperature T (Hüfner, 1978):

$$k_{nr}^{nT} = k_{nr}^{n0}(1 - e^{-\hbar\omega/k_B T})^{-n},$$

where k_{nr}^{n0} is the rate of spontaneous emission of n phonons at 0 K, and $\hbar\omega$ is the energy of the phonon under consideration.

Another important factor in the deactivation process is the distance between the quenching oscillator and the metal ion. A multipole-multipole Coulombic interaction is usually invoked for the quenching mechanism, where in the dipole-dipole component is predominant, so that the energy transfer rate between the excited metal ion state and the vibrating oscillator is inversely proportional to the 6^{th} power of their distance r:

$$k_{nr} = K \cdot r^{-6},$$

where K is a complicated expression containing the energy of the resonant transition, the line shapes of the emission and absorption (vibrational) spectra, the oscillator strengths and an orientation factor. ① Therefosre, the relationships presented below have to be taken with some care since distances are not always identical in different complexes.

9.3.1.1 Quenching by OH Vibrations

The theory for mutiphonon deactivation by OH vibrations has been proposed first by J. Heber for hydrated salts of trivalent europium and terbium ions. The larger the energy gap between the emitting level, the more energetic component of the ground state level, and the lower the nonradiative deactivation rate constant will be since the number of phonons required to bridge the gap increases. That the latter number is crucial is demonstrated by the data collected in Table 9.1: for instance when OH oscillators (with typical energy of 3600 cm^{-1}) are replaced by OD moieties (2200 cm^{-1}), the observed lifetime (and quantum yield) increases substantially (Heber, 1967).

Table 9.1 Multiphonon deactivation of Ln^{3+} ions

Ln	ΔE(cm^{-1})	Nr of phonons, n		τ($ms^{(a)}$)	
		OH	OD	H_2O	D_2O
Gd	32,100	9	15	2.3	n. a.
Tb	14,800	4	7	0.47	3.8
Eu	12,300	3 - 4	5 - 6	0.11	4.1
Dy	7850	2 - 3	3 - 4	0.002	0.06
Sm	7400	2	3	0.002	0.08

(a) in dilute solutions of perchlorate salts, at room temperature.

① Note that this expression is identical to that described for the dipole-dipole energy transfer mechanism(§9.2.2).

Phonon-assisted deactivation has been taken advantage of first by Haas and Stein (Haas and Stein, 1971), and then by Horrocks (Horrocks and Sudnick, 1979; Supkowski and Horrocks, 2002) to determine the number of water molecules coordinated onto Eu^{3+} and Tb^{3+} ions by measuring the lifetime τ of the excited ^5D_J level both in water and deuterated water. Assuming that nonradiative processes other than the quenching by high energy vibrations are the same in both cases, and that water exchange is fast, the difference in the measured rate constants will be proportional to the number of coordinated OH oscillators, that is to the number q of coordinated water molecules:

$$\Delta k_{obs} = k_{obs}(H_2O) - k_{obs}(D_2O) = \tau^{-1}(H_2O) - \tau^{-1}(D_2O) \propto q.$$

Calibrating the relationship with compounds for which the number of coordinated water molecules is known (for instance by X-ray crystallography) allows one to determine the proportionality constant. The main hypothesis made is that each bound OH oscillator contributes equally to the quenching process, which in turn implies that the Ln-OH distance is the same in compounds in which both only a few or many water molecules are bound into the first coordination sphere of the metal ion. The assumption seems to hold fairly well and accuracy of about ± 0.3 to ± 0.5 water molecule can be reached.

Similar relationships have been established for other Ln^{3+} ions (Sm, Dy) and also for Cm^{3+} (Kimura and Kato, 1995) (Kimura and Choppin, 1994), while a correction for closely diffusing water molecules (i. e. water molecules in the outer coordination sphere) has been recently proposed in the specific case of Eu^{3+}, Tb^{3+} and Dy^{3+} complexes with cyclen derivatives (Beeby et al., 1999). Relevant equations are given in Table 9.2.

9.3.1.2 Quenching by NH Oscillators

The quenching by NH oscillators (ν(NH) $\approx 3300\ cm^{-1}$) from amine groups located in the first coordination sphere of the metal ion is also effective, but far less documented. For terbium, each NH oscillator contributes 0.09 ms^{-1} to the overall deexcitation rate, while the process is much more efficient for europium, with a value of 1.2 ms^{-1} per NH oscillator. These values are again given for the specific case of complexes with cyclen derivatives. On the other hand, NH oscillators outside the inner coordination sphere also contribute to the deactivation process, but to a lesser extent. For instance, many of the complexes derived from the cyclen framework have amide groups coordinated to the metal ion and the attached NH groups have been shown to contribute to the quenching process of Eu^{3+} with an associated rate constant of 0.075 ms^{-1} per NH group (Beeby et al., 1999). Relevant equations are given in Table 9.2.

Table 9.2 Relationships allowing the determination of the number of bonded water (q_w) or alcohol (q_a) molecules in the inner coordination sphere[a]

Ion	Equation	Reference
Sm	$q_w = 0.026k_{obs} - 1.6$	(Kimura and Kato, 1995)
Eu	$q_w = 1.05\Delta k'_{obs}$ $q_a = 2.1\Delta k'_{obs}$	(Horrocks and Sudnick, 1979)
	$q_w = 1.11(\Delta k_{obs} - 0.31)$	(Supkowski and Horrocks, 2002)
	$q_w = 1.1k_{obs} - 0.7$	(Choppin and Peterman, 1998)
	$q_w = 1.2(\Delta k_{obs} - 0.25 - 0.075q^N)$[b]	(Beeby et al., 1999)
Tb	$q_w = 4.2\Delta k_{obs}$ $q_a = 8.4\Delta k'_{obs}$	(Horrocks and Sudnick, 1979)
	$q_w = 4.0k_{obs} - 1.0$	(Choppin and Peterman, 1998)
	$q_w = 5(\Delta k_{obs} - 0.06)$	(Beeby et al., 1999)
Dy	$q_w = 0.024k_{obs} - 1.3$	(Kimura and Kato, 1995)
Yb	$q_w = 1.0(\Delta k_{obs} - 0.20)$[c]	(Beeby et al., 1999)
Cm	$q_w = 0.65k_{obs} - 0.9$	(Kimura and Choppin, 1994)

(a) $k_{obs} = 1/\tau_{obs}$; $\Delta k_{obs} = k_{obs}(D_2O) - k_{obs}(H_2O)$, $\Delta k'_{obs} = k_{obs}(ROD) - k_{obs}(ROH)$; units of k_{obs} and k'_{obs} are ms^{-1};

(b) The correction of -0.25 ms is applied when closely diffusing OH oscillators are present; q^N is the number of NH oscillators when amide groups are coordinated to the metal ion;

(c) k_{obs} in μs^{-1}.

9.3.1.3 Quenching by Proximate CH Oscillators

Early reports on this quenching [$\nu(CH) \approx 2900\ cm^{-1}$] were made following a study of lanthanide salts in various non deuterated and deuterated organic solvents (Kropp and Windsor, 1965). For instance, in water, the lifetime of europium acetate is 0.17 ms while it increases to 0.21 ms for [$Eu(CD_3CO_2)_3$] in the same solvent, which corresponds approximately to a quenching rate of 0.1 ms^{-1} per CH oscillator. For complexes with cyclen derivatives, a value four times smaller (0.028 ms^{-1}) has been estimated for the axial CH of the cyclen framework while one CH oscillator of each CH_2CO groups, the one which is close enough to the Eu^{3+} ion, contributes 0.045 ms^{-1}. These effects are much larger in the case of Yb^{3+} (11 and 13 ms^{-1}, respectively) in view of the far smaller energy gap in the latter ion (see Fig. 9.1) (Beeby et al., 1999).

9.3.2 Electronic Deactivation Processes

9.3.2.1 Photo-induced Electron Transfers

When a molecule is excited by absorption of light, its electron donor or electron acceptor properties are modified. For instance, it may become a more powerful electron donor. Consequently, an electron transfer, not feasible in the ground state, may occur upon photo-excitation. This phenomenon is known as photo-induced electron transfer (PET), the theory of which has been worked out by Weller (Weller, 1968). Although these processes often prevent the design of

highly luminescent complexes, they may prove useful in the planning of analytical methods or in the development of signaling processes and molecular logic gates (De Silva et al., 1997a). For instance, the receptor shown on Fig. 9. 7 has been designed to be comprised of three different functional units: (1) a central lanthanide coordinating core based on a terpyridine (terpy) derivative, (2) two potassium ion complexing moieties comprised of a monoaza-18-crown-6 ether (N-18C6, **5**), and (3) two electronic relays featuring phenyl groups. In methanol, the receptor complexes Eu^{3+} with $K = 4.8$; in absence of potassium ions, irradiation in the UV results in the electronic density of the nitrogen atom lone pairs from the N-18C6 units to be transferred through the electronic relays onto the Eu^{3+} ion, which is formally reduced to Eu^{2+} (see right part of Fig. 9. 7). As a consequence, the Eu^{3+} luminescence is quenched and the quantum yield amounts to only 2. 6%. When potassium ions are present, they are harvested by the N-18C6 units ($\lg K = 4.3$). Complexation of these ions polarizes the *N*-atom lone pairs, so that the electronic transfer does not occur and the PET process becomes inactive. As a result, the Eu^{3+} luminescence is restored and the quantum yield reaches 47%, an 18-fold increase. The receptor also works for sodium ions, but to a lesser extent, the N-18C6 coronand being better suited for potassium complexation (De Silva et al., 1997b).

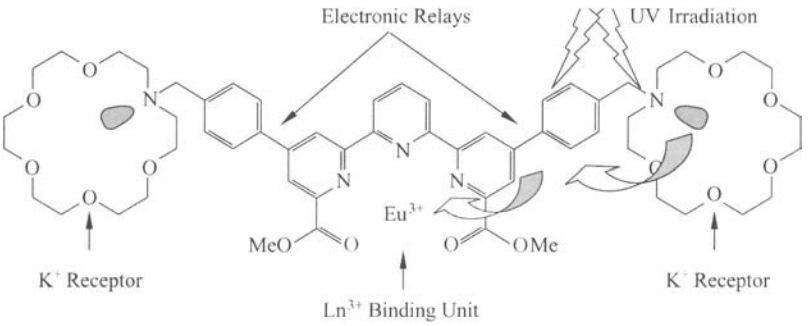


Figure 9. 7 Potassium ion sensor based on the quenching of Eu^{3+} luminescence by PET processes (De silva et al., 1997b)

When such PET processes involve the direct reduction (or oxidation) of a metal ion, one often speaks of ligand-to-metal charge transfer (LMCT), or of metal-to-ligand charge transfer (MLCT). In view of the redox potentials of the Ln^{3+} ions, only Sm^{3+}, Eu^{3+}, and Yb^{3+} are amenable to reductive LMCT processes, while MLCTs can essentially occur with Ce^{3+} and Tb^{3+}. In any case, these processes, which are usually very fast, efficiently compete with the Ln^{3+*} deactivation and quench the luminescence. We shall discuss one example involving dimetallic complexes with para-substituted calix [8] arenses (Bünzli et al., 2000b). The X-ray crystal structure of the homodimetallic 2:1 Eu^{3+} complex with b-LH_8, $[Eu_2(b\text{-}LH_2)(DMF)_5] \cdot 4DMF$, where b-$LH_8$ stands for

p-tert-butylcalix arene(see Appendix 9. B), shows both Eu^{3+} ions encompassed by the ligand in essentially identical environments with pseudo C_4 symmetry (Furphy et al., 1987), as confirmed by luminescence measurements. The ligand adopts a double-bladed propeller shape and the metal ions are 8-coordinate with a Eu-Eu distance of 3. 69 Å. The absorption spectrum of the 2∶1 Eu^{3+} complex displays a band centered at 400 nm and assigned to a LMCT transition (ε = 720 $M^{-1}\cdot cm^{-1}$), in addition to the weak f-f transitions. However, the 4f-LMCT mixing is substantial and results in an unusually intense $^5D_0 \leftarrow ^7F_0$ transition, with ε = 5. 1 $M^{-1}\cdot cm^{-1}$ and, more generally, in enhanced $^5D_J \leftarrow ^7F_0$ transitions (Bünzli et al., 1993). Another effect of the low lying LMCT state is a quenching of the Eu^{3+}-centered luminescence. On the other hand, the Tb^{3+} ion is conveniently sensitized, and the detection limit of the Tb^{3+} dimetallic complex in DMF is as low as 10^{-10} M. The replacement of p-tert-butyl groups by electron-attracting nitro groups to give *n*-LH_8 produces complexes with the same structure as those with b-LH_8 (Bünzli et al., 1998), but having substantially different photophysical properties. The $^1\pi\pi^*$ and $^3\pi\pi^*$ states of the ligand undergo a bathochromic shift so that the ligand-to-metal energy transfer is suppressed for Tb^{3+}, since the $^3\pi\pi^*$ state lies under the $^5D_4$(Tb) excited state. In addition, the LMCT state of the Eu^{3+} complex is shifted to higher energy compared with the situation for b-LH_8, decreasing the 4f-LMCT mixing as shown by the smaller molar absorption coefficient of the $^5D_0 \leftarrow ^7F_0$ transition (0. 84 vs 5 × 10 $M^{-1}\cdot cm^{-1}$). The ensuing effect is a much better sensitization of Eu^{3+}. Therefore, the simple change from a tert-butyl to a nitro substituent switches the sensitizing properties of the calix [8]arene: b-LH_8 is a good Tb^{3+} sensitizer, but quenches Eu^{3+}, while *n*-LH_8 insures a good energy transfer to Eu^{3+} but is unable to excite Tb^{3+} (Figs. 9. 8 and 9. 9).

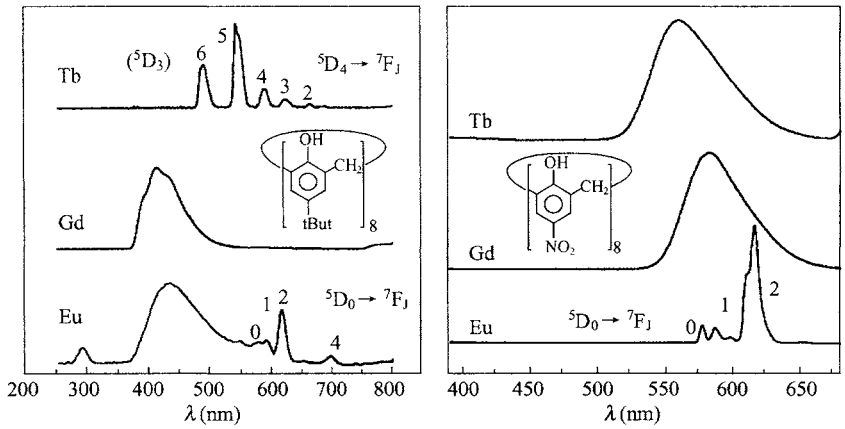


Figure 9. 8 Luminescence spectra of [Ln_2(b-LH_2)(DMF)$_5$] (left) and [Ln_2(*n*-LH_2)(DMF)$_5$] (right) at 77 K in frozen dmf solutions(λ_{exc} = 290 nm and 360 nm, respectively) (Bünzli et al., 1993; Bünzli and Ihringer, 1996)

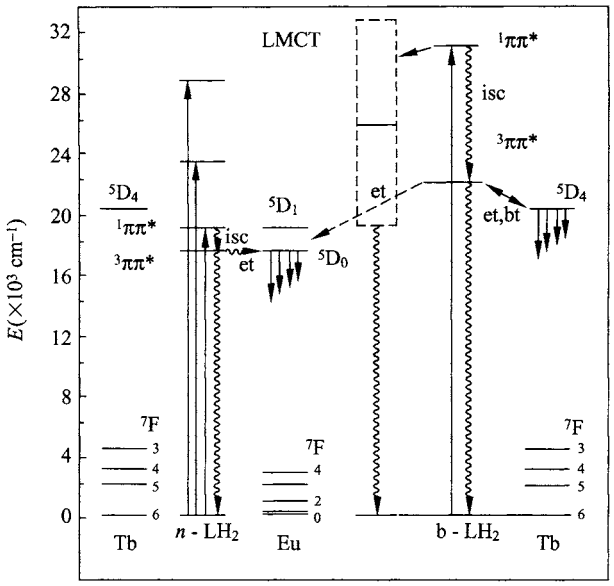


Figure 9.9 Energy transfer processes in europium and terbium bimetallic complexes with carlix [8] arenes; isc = intersystem crossing, et = energy transfer, bt = energy back transfer (Bünzli et al., 1993; Bünzli and Ihringer, 1996)

9.3.2.2 Energy Back Transfer

Another quenching process is the back transfer of energy from the excited metal ion state to the triplet state of the ligand, which occurs when both levels lie close in energy. This process is often assisted by vibrations and the temperature dependence of the lifetime can be described by an Arrhenius-type equation (Kleinerman and Choi Sang-Il, 1968):

$$\ln(\tau^{-1} - \tau_0^{-1}) = A - E_A/RT,$$

where τ is the actual lifetime, τ_0 the lifetime in absence of back transfer (frequently taken as the lifetime at very low temperature), while E_A is the activation energy of the process which often matches a vibration of the molecule under study, for instance a Ln-O or Ln-N mode. It is noteworthy that the excitation energy is then degraded by a phonon-assisted process, since no concomitant enhancement of the $^3\pi\pi^*$ state phosphorescence is usually observed. For instance, such a back transfer has been evidenced in the 2:2 complex between Tb^{3+} and p-tert-butylcalix[5]arene, $[Tb_2(b-L'H_2)_2(DMSO)_4]$. In this edifice, the metal ion is 8-coordinate being bonded to eight oxygen atoms, five from a calix[5]arene tri-anion, one of them bridging to the second Ln^{3+} ion, two from DMSO molecules and one from the second, bridging, anionic ligand, as inferred from the X-ray structure of the Eu^{3+} compound (which also

presents a low lying LMCT state). The conveniently located $^3\pi\pi^*$ state ($24,000\ cm^{-1}$) transfers energy on Tb^{3+} leading to sizable luminescence from the $^5D_4$ (Tb) state. However, the absolute quantum yield, 5.1% in THF, remains modest because of a back transfer process identified through the $^5D_4$ lifetime dependence on temperature: (1.12 ± 0.04) ms at 10 K, and(0.2 ± 0.01) ms at 295 K. Analysis of this dependence yields an "activation barrier" of $180\ cm^{-1}$ pointing to a Tb-O phonon assisted back transfer (Charbonnière et al., 1998).

9.4 Designing a Luminescent Probe

9.4.1 Qualitative Rules

From the above discussion it is obvious that many intramolecular energy transfer processes have to be mastered if one wishes to design an efficient lanthanide-containing luminescent probe. Fig. 9.3 describes 11 different processes, each characterized by a rate constant. And the picture is not exhaustive, since we have not taken into account intermolecular processes which may gain in importance either in solids where Ln^{3+} ions lie at relatively short distances so that energy can migrate from one metallic site to the other (Blasse and Grabmaier, 1994) or in solution where collisions with other molecules may result either in beneficial energy transfers (Schrott et al., 1996) or in the deactivation of the metal ion excited state. Polymeric structures containing both luminescent and non-luminescent Ln^{3+} ions may also lead to enhanced luminescent properties through energy transfer from the non-luminescent centers onto the luminescent ones (Latva et al., 1995).

In absence of a good predictive theoretical model, experimentalists have to rely on rules of thumb, and several of them have been established for given series of Eu^{3+} and Tb^{3+} compounds. Two main processes have to be optimized (Fig. 9.3): the intersystem crossing (k_{isc}) and the $^3\pi\pi^*$-to-metal energy transfer (k_{et}). On the other hand, deactivation processes have to be avoided at all stages (k^i_{nr}), as well as light emission from the ligand ($k^F$and k^P). From organic photochemistry data, it is known that efficient isc takes place when ΔE ($^1\pi\pi^* - {}^3\pi\pi^*$) is at least $5000\ cm^{-1}$. Regarding the triplet-to-metal ion transfer, two series of compounds have been studied in details and are often referred to:

(1) Latva et al. have investigated more than 40 Eu^{3+} and Tb^{3+} polyaminocarboxylates and have demonstrated that their quantum yield increases considerably when the energy of the triplet state becomes close to resonance with one of the excited ^5D_J levels ($J = 0$, 1 or 2 for Eu^{3+}). When $\Delta E(^3\pi\pi^* - {}^5D_J)$ is smaller than about $1800\ cm^{-1}$, however, back transfer becomes important, especially for Tb^{3+} (Latva et al., 1997).

(2) In another study, Steemers et al. have shown that the targeted ΔE is around $3500\ cm^{-1}$ for triphenylene-substituted calix[4]arene receptors. It is to be

stressed here that the triplet state energy has to be taken as the energy of its 0 – 0 transition (Steemers et al., 1995).

Energy differences are of course only one aspect of the problem, since the overlap integral J between the emission spectrum of the donor ($^3\pi\pi^*$ state) and the absorption spectrum of the acceptor (^5D_J state) has also to be taken into consideration. This quantity may vary considerably depending upon the width of the $^3\pi\pi^*$ emission spectrum and, also, upon the orientation of the chromophore with respect to the Ln^{3+} ion. Moreover, the distance between the chromophore and the Ln^{3+} ion is crucial since the dipole-dipole transfer fades off as $(r_{DA})^{-6}$.

Trying to summarize the experimental data so far reported, the ideal receptor should include the following features:

(1) Strong donor groups in order to coordinate efficiently the Ln^{3+} ions, to meet its coordination number requirements (Bünzli, 1998) and to lead to highly thermodynamically stable edifices while providing a rigid metal ion environment;

(2) Large molar absorption coefficients;

(3) Absence of OH, NH or other groups with high energy vibrations (even in the second coordination sphere);

(4) $\Delta E(^1\pi\pi^* - ^3\pi\pi^*) > 5000\ cm^{-1}$;

(5) For Eu^{3+}, $2500 < \Delta E(^3\pi\pi^* - ^5D_0) < 3500\ cm^{-1}$ and $E(LMCT) > 25,000\ cm^{-1}$;

(6) For Tb^{3+}, $2500 < \Delta E(^3\pi\pi^* - ^5D_4) < 4000\ cm^{-1}$.

As said before, the distance and orientation of the chromophore to and with respect to the Ln^{3+} ion have also to be optimized.

9.4.2 Quantitative Estimates

Modeling of luminescent probes is still difficult to achieve in view of the many parameters to account for. During the last years, however, a descriptive theory has been developed which uses direct and exchange Coulomb interaction models to determine the energy transfer rates between the ligand and Ln^{3+} levels (de Sá et al., 2000). Good matches between calculated and experimental data have been so far obtained, and there is no doubt that refinement of the model will lead to a more profound understanding of the energy transfer processes (Malta et al., 1999). This model has been recently applied in the author's group in order to explain a dramatic decrease in the quantum yield of the Eu^{3+}-centered luminescence observed in going from [Eu(NO_3)(mbzimpy)] (2.8% in acetonitrile) to [Eu(mbzimpy)$_3$] (ClO_4)$_3$ ($\approx 8 \times 10^{-5}$%). A first photophysical and electrochemical study pointed to the LMCT state, located at much lower energy in the 1:3 complex with respect to the 1:1 compound, as the main cause of this decrease (Petoud et al., 1999). In order to understand more precisely which energy transfers are affected by the presence of the LMCT, a theoretical calculation of the quantum yield in both compounds has been undertaken (Gonçalvès e Silva et al., 2000). Such an estimate requires the knowledge of the molecular structures, which fortunately were at hand. In a first step, the ligand

electronic levels, transition energies and oscillator strengths were determined by the INDO/S-CI method. The overall ligand-to-Eu^{3+} energy transfer rate W_{ET} was then taken as the sum of three contributions:

$$W_{ET}^{mp} = \frac{2\pi}{\hbar}\frac{e^2 S_L}{(2J+1)G}F\sum_{\lambda}\gamma_\lambda\langle\alpha' J'\|U^{(\lambda)}\|\alpha J\rangle^2, \qquad (9.1)$$

which corresponds to the dipole-multipole mechanism($\lambda = 2$, 4 and 6),

$$W_{ET}^{dd} = \frac{2\pi}{\hbar}\frac{e^2 S_L}{(2J+1)GR_L^6}F\sum_{\lambda}\Omega_\lambda^{ed}\langle\alpha' J'\|U^{(\lambda)}\|\alpha J\rangle^2 \qquad (9.2)$$

the dipole-dipole mechanism($\lambda = 2$, 4 and 6), and

$$W_{ET}^{ex} = \frac{8\pi e^2(1-\sigma_0)^2}{3\hbar(2J+1)R_L^4}F\langle\alpha' J'\|S\|\alpha J\rangle^2\sum_m|\langle\phi|\sum_k\mu_z(k)s_m(k)|\phi'\rangle|^2 \qquad (9.3)$$

the exchange mechanism. In the above equations J represents the total angular momentum quantum number of the rare-earth ion, α specifies a given 4f spectroscopic term, G is the degeneracy of the ligand initial state, S_L is the electric dipole strength associated with the ligand transition $\phi\rightarrow\phi'$, The quantities $\langle\|\|\rangle$ are reduced matrix elements of the unit tensor operators $U^{(\lambda)}$, and R_L is the distance from the rare-earth ion nucleus to the region of the ligand molecule where the ligand donor (or acceptor) state is localized. In Eq. (9.3), S is the total spin operator of the rare-earth ion, μ_z is the z component of the electric dipole operator and s_m ($m=0$, ±1) is a spherical component of the spin operator, and σ_0 is a distance-dependent screening factor. The matrix elements $\langle\phi|\sum_k\mu_z(k)s_m(k)|\phi'\rangle$ were calculated from the molecular orbital wave functions given by the INDO/S-CI method; Ω_λ^{ed} are the contributions of forced electric dipole to the intensity parameters. The quantities γ_λ and F are given by

$$\gamma_\lambda = (\lambda+1)\frac{\langle r^\lambda\rangle^2}{(R_L^{\lambda+2})^2}\langle 3\|C^{(\lambda)}\|3\rangle^2(1-\sigma_\lambda)^2, \qquad (9.4)$$

$$F = \frac{1}{\hbar\gamma_L}\sqrt{\frac{\ln 2}{\pi}}\exp\left[-\left(\frac{\Delta}{\hbar\gamma_L}\right)^2\ln 2\right], \qquad (9.5)$$

where $\langle r^\lambda\rangle$ is the radial expectation value of r^λ for 4f electrons, $C^{(\lambda)}$ is a Racah tensor operator, the σ_λ's are screening factors, γ_L is the ligand state bandwidth at half-height, and Δ is the difference between the donor and acceptor transition energies involved in the transfer process.

The next step involves the determination of the selection rules to assess which energy levels of the Eu^{3+} ion and of the ligand can be involved in the

transfer process and, finally, a numerical solution of the rate equations is worked out. The normalised level populations, η_i, are described by a set of rate equations which have the general form:

$$\frac{d\eta_i}{dt} = -\sum_{\substack{j=1 \\ j\neq i}}^{N} k_{ij}\eta_i + \sum_{\substack{j=1 \\ j\neq i}}^{N} k_{ji}\eta_j, \qquad (9.6)$$

where the indices i and j indicate the energy levels of the compound involved in the energy transfer process; k_{ij} or k_{ji} correspond to the transition rates between levels i and j, or between states j and i, respectively, and N is the total number of states involved in the energy transfer mechanism. In the steady state regime all the $d\eta_i/dt$ are equal to zero and the set of algebraic equations can be solved analytically in terms of the transition and transfer rates. In the present case, the rate equations were solved numerically by using the 4th order Runge-Kutta method with an adaptive integration step. This set of coupled differential equations belongs to the initial value category, where the populations (η_i) at t = 0 were set equal to 1 for the ground state population and to zero for the other states. The total time of propagation was around 0.01 s and the initial step size was equal to the inverse of the largest transfer rate ($\sim 10^{-9}$ s). The numerical solutions of the rate equations yield the time dependence of the energy level populations, which reach the steady-state regime after $10^{-6} - 10^{-5}$ s. These steady-state populations were then used to calculate the emission quantum yield given by

$$Q = \frac{A_T \eta_2}{\theta \eta_1}, \qquad (9.7)$$

where the sub-indices 1 and 2 indicate the ground state and the emitting level ($^5D_0$), respectively, in the complex, A_T is the sum of the coefficients of spontaneous emission for the $^5D_0 \rightarrow {}^7F_{0,1,2,4}$ transitions, and θ is the pumping rate.

The kinetic scheme used is depicted on Fig. 9.10. It is noteworthy that the energy of the $^1\pi\pi^*$ and $^3\pi\pi^*$ states is about the same in the two compounds (as measured on the La^{3+} complexes at 77 K). The calculated energy transfer rates from the triplet state are larger for the $^5D_0$ and $^5D_1$ levels but a substantial amount of energy is also flowing from the singlet state to the higher excited states of Eu^{3+} (Table 9.3). Once these rates calculated, the quantum yield of [$Eu(NO_3)_3$ (mbzimpy)] was estimated by varying the values of k_{21}, k_{31} and k_{32}. The best calculated value without taking into account the LMCT state (which is known to lie at relatively high energy) is 2.7% when these constants are equal to 10^9, 10^8, and 10^8 s^{-1}, respectively. This is in excellent agreement with the experimental data and the k_{21} rate, although quite high, is in agreement with those found for other Eu^{3+} chelates. The same rate constants lead to a calculated quantum yield of about 1% for the 1:3 compound, again without taking the LMCT into account, and no combination of rate constants could be found which

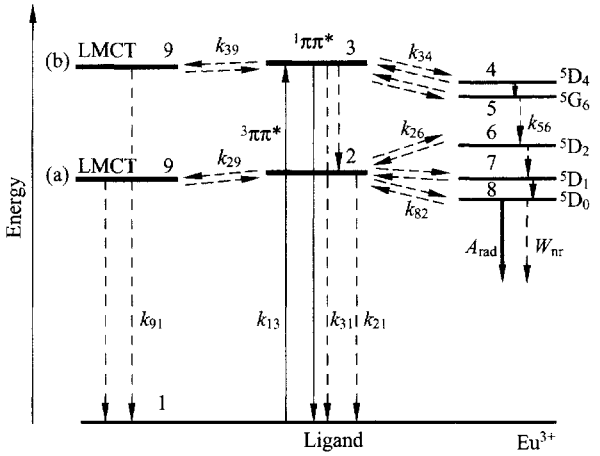


Figure 9. 10 Diagram of the states involved in the energy transfer processes in 1:1 and 1:3 complexes with mbzimpy. The solid and dashed arrrows represent radiative and nonradiative processes, respectively. Two energy positions for the LMCT are taken into consideration. Reprinted, with permission from(Gonçalvès e Silva et al., 2000)

fit the experimental quantum yield under these conditions. Calculations were therefore done allowing for the LMCT state and two situations were considered, with the LMCT state close to the triplet and to the singlet states, respectively. Interestingly, a good agreement with the experimental value could only be achieved in the second situation with the following final rates: $k_{21} = 10^9\ s^{-1}$, $k_{31} = 10^9\ s^{-1}$, $k_{32} = 10^7\ s^{-1}$, and $k_{39} = 5 \times 10^{11}\ s^{-1}$. The calculated quantum yield, $6.7 \times 10^{-5}\%$ compares well with the experimental one ($8.2 \times 10^{-5}\%$).

Table 9.3 Calculated energy transfer rates (s^{-1}) in [Eu(NO_3)$_3$(mbzimpy)(MeOH)] and [Eu(mbzimpy)$_3$](ClO_4)$_3$ (see Fig. 9.10 for definitions). Arrows indicate the direction of the energy transfer. From (Gonçalvès e Silva et al., 2000)

Ligand state (cm^{-1})		4f state (cm^{-1})	Transfer rate	Back-transfer rate
[Eu(NO_3)$_3$(mbzimpy)(MeOH)]				
Triplet (19,622)	→	$^5D_0$(17,300)	$k_{28} = 1.47 \times 10^8$	$k_{82} = 5.51 \times 10^2$
Triplet (19,622)	→	$^5D_1$(19,070)	$k_{27} = 7.29 \times 10^8$	$k_{72} = 5.25 \times 10^7$
Triplet (19,622)	←	$^5D_2$(21,500)	$k_{26} = 4.91 \times 10^2$	$k_{62} = 3.78 \times 10^6$
Singlet (28,785)	→	$^5G_6$(26,750)	$k_{35} = 1.80 \times 10^7$	$k_{53} = 1.11 \times 10^3$
Singlet (28,785)	→	$^5D_4$(27,600)	$k_{34} = 6.61 \times 10^6$	$k_{43} = 2.33 \times 10^4$
[Eu(mbzimpy)$_3$]$^{3+}$				
Triplet (19,662)	→	$^5D_0$(17,300)	$k_{28} = 9.04 \times 10^7$	$k_{82} = 2.80 \times 10^2$
Triplet (19,662)	→	$^5D_1$(19,070)	$k_{27} = 2.67 \times 10^9$	$k_{72} = 1.59 \times 10^8$
Triplet (19,662)	←	$^5D_2$(21,500)	$k_{26} = 0.89 \times 10^2$	$k_{62} = 5.63 \times 10^5$
Singlet (27,700)	→	$^5G_6$(26,750)	$k_{35} = 8.37 \times 10^6$	$k_{53} = 9.06 \times 10^4$
Singlet (27,700)	→	$^5D_4$(27,600)	$k_{34} = 2.67 \times 10^6$	$k_{43} = 1.65 \times 10^6$

Such a procedure is relatively lengthy and requires the knowledge of many experimental parameters, from structural to photophysical data, and moreover several parameters have to be estimated. Nevertheless, it certainly can be used to optimize the one or the other parameter of a complex system and future improvements in the procedure should render it more predictive.

9.5 Luminescent Lanthanide Complexes with Organic Ligands

Many systems have been developed during the last two decades with the aim of exploiting the luminescent properties of the lanthanide ions in either structural or analytical probes. Several ligand families are encountered in these studies, such as polyaminocarboxylates, β-diketonates, Schiff bases, macrocyclic molecules bearing various substituents and/or functionalized pendant arms. A systematic review would exceed the scope of the present chapter so that we shall present only selected examples in this section, some of them illustrating the principles underlined in the previous section.

Figure 9. 11 depicts the behavior of two series of Eu^{3+} complexes with respect to the energy difference $E(^3\pi\pi^* - {}^5D_0)$ between the ligand triplet state (taken as the 0 − 0 transition) and the metal ion excited state. In the first example, the ligand L is a Schiff base, and there is a strict correlation between the energy difference $E(^3\pi\pi^* - {}^5D_0)$ and the quantum yield of the metal-centered luminescence (Archer et al., 1998). This work also exemplifies that the triplet state energy does not determine alone the overall quantum yield. Indeed, compounds with a 1: 2 stoichiometry, such as $Na[EuL_2]$, exhibit a quantum yield 60% −70% larger compared to the one measured for $[Eu_2L_3]$, despite that $E(^3\pi\pi^*)$ is the same for pairs of compounds with the same ligand (as measured on the Y^{3+} analogues at 77 K) and despite that the coordination number, 8, is the same. In fact, half of the Eu^{3+} ions in the 2: 3 compounds attain this coordination number by completing their coordination sphere with water molecules, which explains the lower quantum yield.

The β-diketonate complexes display a more common behaviour (right part of Fig. 9. 11), in that the maximum quantum yield is obtained when the ligand triplet state lies about 2700 cm^{-1} above the $Eu(^5D_0)$ level and 2500 cm^{-1} above the $Tb(^5D_4)$ level (Sato and Wada, 1970). In this detailed study, the authors have demonstrated that the triplet state energy predominantly flow through the Eu ($^5D_1$) level. The energy difference between the $^5D_1$ and $^5D_0$ levels amounts to about 1700 cm^{-1}, so that rapid nonradiative deexcitation to the lowest sub-level of the excited term occurs, especially if the chemical environment of the metal ion provides vibrations with energy in this range (cf. Bünzli and Yersin, 1982). Consequently, luminescence from the $^5D_1$ level is sometimes observed, but its intensity is typically one or two orders of magnitude lower than that originating

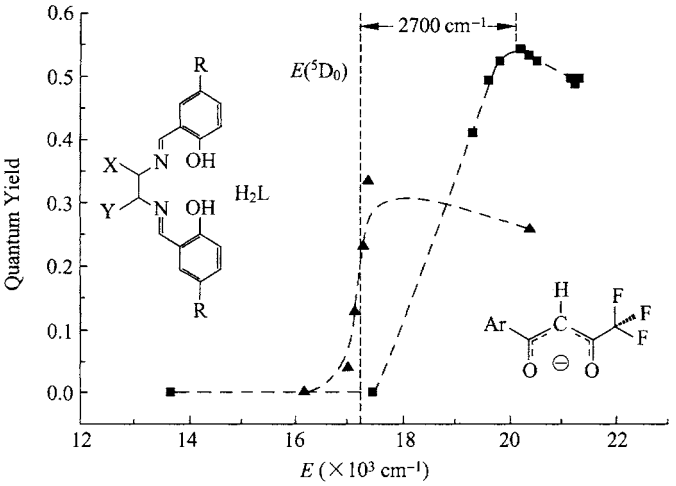


Figure 9. 11 Quantum yield of the Eu^{3+}-centred luminescence upon ligand excitation in $[Eu_2L_3]$ Schiff base complexes $10^{-3} - 10^{-4}$ M in frozen dmf at 77 K (▲) and in β-diketonates in acetonitrile at room temperature(■), as a function of the ligand triplet state (Archer et al., 1998; Sato and Wada, 1970)

from the $^5D_0$ level. The authors have modeled the situation and have reached a good agreement with experimental values, using the following rate constants (see Fig. 9. 3 for the definitions): $k^F + k_{nr}^F = 0$, $k^P + k_{nr}^P = 2 \times 10^7\ s^{-1}$, $k(^5D_1 \rightarrow {}^5D_0) = 10^6\ s^{-1}$, $k^{Ln} = 10^3\ s^{-1}$, and $k_{et} = 10^7 - 10^8\ s^{-1}$.

Adequate tuning of the triplet state energy may result in edifices with specific properties, e. g. suitable for the selective excitation of given Ln^{3+} ions. For instance, attachment of adequate chromophoric groups on the wider rim of a calix[4]arene framework leads to selective sensitization of Eu^{3+} and Tb^{3+} ions (Sato and Shinkai, 1993), as sketched on Fig. 9. 12. The triplet state of the ligand with four identical arms (**8a,** see Fig. 9. 12), located on the phenol groups, lies above both $^5D_J (J = 1, 4)$ levels and its energy can in principle be transferred on both Eu^{3+} and Tb^{3+} ions; however, the presence of a C = O-to-Eu^{3+} LMCT state for the former at approximately the same energy as the $^3\pi\pi^*$ state prevents transfer onto Eu^{3+} and only Tb^{3+} is sensitized: the quantum yields in acetonitrile amount to 0. 2% and 16%, respectively. When a phenyl group is introduced into one of the arms to give ligand **8b,** the lowest triplet state, now mainly located on the phenacyl group, $^3n\pi^*$, is shifted to lower energy, and both ions are sensitized, the quantum yields in acetonitrile being 6% and 27% for Eu^{3+} and Tb^{3+}, respectively. Replacing the phenyl group by a biphenyl unit to give ligand **8c** further lowers the energy of the $^3n\pi^*$ state which is now almost in resonance with the $Tb(^5D_4)$ level. As a result, extensive back transfer occurs and the luminescence of the Tb^{3+} ion is no more sensitized (the quantum yield in

acetonitrile amounts to 0.01%), while the luminescence of Eu^{3+} is maintained (quantum yield in acetonitrile: 6.1%).

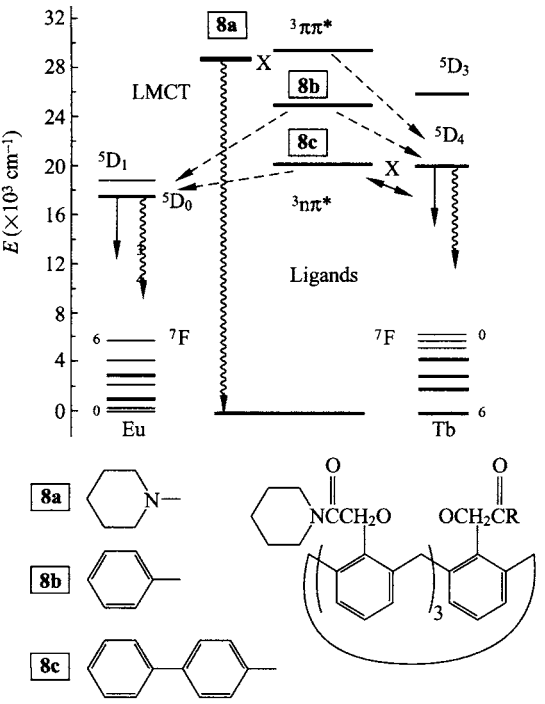


Figure 9.12 Partial energy diagram scheme showing the sensitization of Eu^{3+} and Tb^{3+} luminescence by triplet states located on substituted calix[4] arenes (Sato and Shinkai, 1993)

Interesting systems have been investigated which take advantage of the encapsulation of Ln^{3+} ions either by cryptands or by macrocycles fitted with pendant arms. In the first category, the Eu^{3+} cryptate with (bpy. bpy. bpy), a cryptand based on three bipyridine units (**9**) is well known because it is used in commercial fluoroimmunoassays. This compound is written [Eu ⊂ (bpy. bpy. bpy)]$^{3+}$ to point to the inclusion of the metal ion into the macrocycle. It has, however, a deceptively low quantum yield in water (0.02), mainly because the complexed species contain 2 – 3 water molecules directly bonded onto the metal ion (one water molecule contributes about 1 ms^{-1} to k_{nr}). The [Tb ⊂ bpy. bpy. bpy]$^{3+}$ cryptate also displays a low quantum yield (0.03) because, in addition to quenching by OH oscillators (here one water molecule contributes about 0.25 ms^{-1} to k_{nr}), the energy of the ligand triplet state is only 1200 cm^{-1} above $E(^5D_4)$ and an efficient thermally-activated back transfer process takes place. Modification of the cryptand design by introducing N-oxide groups improved

considerably the photophysical properties of the corresponding supramolecular assemblies: the quantum yields of $[Eu \subset (\mathbf{10a})]^{3+}$ and $[Eu \subset (\mathbf{10b})]^{3+}$ amount to 0.15 and 0.20, respectively. However, the Tb^{3+} luminescence cannot be sensitized because the ligand triplet state lies at too low energy, a reason why the branched macrocycle **11** was developed : $[Tb(\mathbf{11})]^{3+}$ is now highly luminescent with $Q^{Tb} = 0.38$ (Sabbatini et al., 1996).

Another interesting system has been developed which encompasses a calix[4]arene bearing a fluorescein substituent attached to the calixarene framework by an amide function (**12**). The aim of the authors is the application of organic lanthanide complexes in polymer-based optical amplifiers operating at 1.3 and 1.5 μm (Wolbers et al., 1998). That is, the use of ions emitting in the far infrared portion of the electromagnetic spectrum is required. Both Nd^{3+} and Er^{3+} ions would be suitable for this purpose. Er^{3+} has not been included in Fig. 9.1 despite its extreme importance in solid state inorganic materials, for instance as amplifier for optical fibers used in overseas telecommunication cables or in up-conversion processes (Jacquier, 1995), because its luminescence is rarely seen in solution or in organic complexes in the solid state. The transition of interest here is between the $^4I_{13/2}$ and $^4I_{15/2}$ (ground level) states. The Er^{3+} ion has another luminescent state, $^4S_{3/2}$, located at about 18,350 cm^{-1} and which gives off green light, but the energy gap between this luminescent level and the highest sub-level of the ground multiplet ($^4I_{9/2}$) is only 3000 cm^{-1}, leading to easy nonradiative deactivation. In the system of interest here, both ions are sensitized in DMSO and d_4 – methanol, although luminescence from the fluorescein moiety is still seen. The energy transfer is fast for both spacers (3 and 6 methylene groups, respectively, see scheme), but the sensitization, which exclusively goes through the fluorescein substituent, is better with the ligand bearing the shorter spacer. It is noteworthy that lifetimes are reasonably long : 1.2 – 1.3 μs for Nd^{3+} and 1.6 – 1.7 μs for Er^{3+}. The same research group has designed another, simpler ligand, fluorexon (**13**), also derived from fluorescein, with four aminocarboxylate functions as Ln^{3+} binding site (Werts et al., 2000). Excitation into fluorexon results in the sensitized near-infrared emission of Nd^{3+}, Er^{3+} and Yb^{3+} with a high photosensitization efficiency (0.5 – 1.0). However, nonradiative deactivation processes are very fast, so that the overall quantum yield remains low (2×10^{-4} to 5×10^{-3}).

The field of luminescent lanthanide containing organic complexes is sustaining a hefty development and many new systems are being investigated. Among them are ligands derived from salicylamide and 2-hydroxyisophatalamide (**14** – **16**). The latter moieties are known as being good complexing groups for trivalent lanthanides ions, as well as good chromophores. They can be inserted either into podands (**14**, **15**) or cryptands (**16**). The resulting ligands yield highly stable complexes, especially at physiological pH since the hydroxy proton has a pk_a value around 6 – 6.5. In addition, these groups provide an excellent

sensitization of several Ln^{3+} ions, particularly Tb^{3+}. For instance, the quantum yield of $[Eu(\mathbf{16}-H)_2]^+$ amounts to 0.10 in water and it reaches 0.45 for the Tb^{3+} analogue. On the other hand, the encapsulating ligand **14** produces an entity $[Tb(\mathbf{14}-2H)]^+$ with a quantum yield as large as 0.60 in water (Raymond et al., 2000a, 2000b). It is foreseen that derivatives of these podands and cryptands will have application in homogeneous multiple fluoroimmunoassays.

In view of the relative difficulty in inserting the Ln^{3+} ions in protective pre-organized cavities, another strategy is also being tested, which uses self-assembly processes. These take advantage of the induced fit concept and are appealing since they use flexible molecules in order to optimize the interactions with the metal ions. The latter act as template agents and the increased entropic cost of the complexation process compared with pre-organized systems is overcome by the programming of stabilizing intramolecular non-covalent interactions which can be modulated by a judicious design of the receptor (Piguet and Bünzli, 1999). During the last decade, we have developed several series of ligands suitable for such processes and enabling the formation of monometallic or dimetallic (f – f and f – d) assemblies. Dimetallic edifices are appealing since they may contain two luminescent centers in one stain, although it is not obvious to design receptors specifically able to complex two different 4f metal ions and therefore to lead to true heterodimetallic architectures. Several ditopic ligands coded for the complexation of two 4f metal ions have been synthesized, which self-assemble with these ions to give triple-stranded dimetallic helicates $[Ln_2(L)_3]^{6+}$ (L = **17a, 17b, 17d**) and $[Ln(\mathbf{17c}-2H)_3]$. The crystal structures of $[Eu_2(\mathbf{17a})_3]^{6+}$ (Piguet et al., 1993), $[Tb_2(\mathbf{17b})_3]^{6+}$ (Martin et al., 1998) and $[Ln(\mathbf{17c}-2H)_3]$ (Ln = Eu, Tb, Yb) (Elhabiri et al., 1999) show the wrapping of the three ligands around a pseudo – C_3 or pseudo – D_3 axis and the



Figure 9.13 Triple stranded helicate $[Eu(\mathbf{16c}-2H)_3]^{3+}$. The white arrows point to the Ln^{3+} ions (Elhabiri et al., 1999)

lanthanide ions have a saturated pseudo-tricapped trigonal prismatic coordination sphere which protects them well from external interactions (Fig. 9. 13). The luminescence of the Eu-helicate with **17a** is poor due to the presence of a quenching LMCT state while that of $[Eu_2(\mathbf{17b})_3]^{6+}$ is 40 times as large; however, both edifices are not stable in water, so that they are not suitable as luminescent probes. On the other hand, the neutral $[Ln(\mathbf{17c}-2H)_3]$ helicates are highly stable in water ($\log \beta_{23} \approx 50$) and the Eu^{3+} and Tb^{3+} members display a reasonable luminescence intensity. Improvement of the photophysical properties are within reach by attaching a chromophoric group on the 4-position of the pyridine moieties. A first step toward this goal is the synthesis of ligand **17d** which will be used as a synthon for further substitution deemed to allow coupling with biological materials (Platas et al., 2000).

9.6 Applications in Biomedical Analyses

The need for efficient analytical and diagnostic tools in medicine is growing and transition metal complexes with organic ligands which present a variety of specific structural, photochemical and electrochemical properties are well suited for such purpose. Lanthanide ion complexes are presently used in several of these applications and we describe a few of them below.

9.6.1 Fluoroimmunoassays

Classical fluoroimmunoassays and DNA hybridization assays using organic fluorescent molecules (such as for instance fluorescein isothiocyanate) have a lower sensitivity than radiochemical diagnostic techniques, because of high background emission and, also, of the very short lifetime of the $^1\pi\pi^*$ emitting state. Since the social pressure for avoiding the cumbersome disposal of radioactive wastes is strong, scientists have been turning to metal ions with long-lived excited states as luminescent labels and in this respect Ln^{3+} ions represent ideal candidates. In the mid 1980's, Hemmilä and co-workers developed what is now known as the Delfia technology (Hemmilä et al., 1995b). They first described an immunoassay for hepatitis B surface antigen (Siitari et al., 1983) in which immunoglobin is coated onto the surface of polystyrene strip wells. The analyte is then incubated into these wells in the presence of a specific antibody labeled with an europium chelate. After reaction, the tubes are washed and the Eu^{3+} ions bound to the antibody conjugated with hepatitis B are released by lowering the pH. The europium chelate is a polyaminocarboxylate so that protons easily compete with the coordination of the metal ion. Then, a buffered enhancement solution is added to produce micelles. This solution contains a β-diketonate, 2-naphtoyltrifluoroacetone, which forms a 1:3 complex with Eu^{3+}, trioctylphosphine oxide to complete the inner coordination sphere of the metal ion

and to avoid water coordination, and Triton X-100 to encapsulate the chelates into protective micelles. The role of the latter is to eliminate second-sphere water interactions, so that nonradiative deexcitation processes are minimized. The quantum yield of the europium micellar system amounts to about 70%. The Sm^{3+} ion may also be used, but its quantum yield is far lower, at about only 2%. The key to the very high sensitivity of these assays, besides the large quantum yield, lies in measurements conducted in time-resolved mode. A UV pulse (about 1 μs) is shined onto the sample, triggering both the fast background emission and the luminescence from the Eu^{3+} ion (after sensitization through its bonded ligand molecules). Measurement is started only after the background emission has vanished. The lifetime of the Eu($^5D_0$) level is around 0.7 ms, so that cycles of a few milliseconds can be used, which means that within a minute, tens of thousands of data can be acquired, henceforth leading to a considerable enhancement of the signal-to-noise ratio (Fig. 9.14).

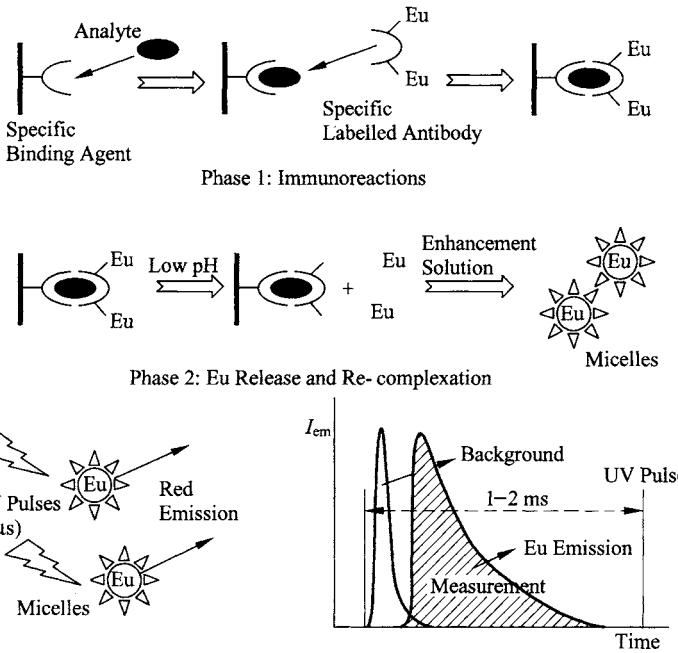


Figure 9.14 Principle of heterogeneous time-resolved fluoroimmunoassays based on Eu^{3+} (Delfia technology) (Hemmilä et al., 1995b)

Numerous analyses have been developed based on time-resolved FIA, for instance competitive assays of testosterone and cortisone (Lövgren et al., 1984) where testosterone is immobilized in the solid state phase as an ovalbumin conjugate; cortisone is added together with the Eu-labeled antibody and the two steroids compete for its binding sites. The luminescence of the enhanced solution

is then inversely proportional to the concentration of cortisone. Dual-label assays using Sm^{3+} and Eu^{3+} ions have also been proposed in which two different hormones can be determined simultaneously, for instance the luteinizing hormone (LH) and the follicle stimulating hormone (FSH) (Xu et al., 1991). In this assay, the monoclonal antibodies anti-β-LH and anti-β-FSH are fixed on the walls of the strip wells by monoclonal antibodies conjugating with their α subunits before being reacted with the labeled antibodies. After addition of the enhancement solution, the luminescence of the Eu^{3+} and Sm^{3+} ions is read sequentially.

To avoid the somewhat time-consuming phase 2 of these heterogeneous fluoroimmunoassays (Fig. 9. 14), two solutions have been proposed. The first one relies on highly luminescent chelates as the labeled antibody, which puts more stringent requirements on the coordinating ligand. One example is 4, 7-bis(chlorosulfophenyl) -1, 10-phenanthroline-2, 9-dicarboxylate (19): its two sulfonyl chloride groups react under mild conditions with the amino groups of the protein to be labeled and the ligand sensitizes sufficiently the Eu^{3+} luminescence so that direct measurements become possible (Evangelista et al., 1988). The other way out has been proposed by Mathis and co-workers who developed homogeneous fluoroimmunoassays based on two differently labeled antibodies, one with an Eu^{3+} cryptate and the other with an organic acceptor, the phycobilliprotein allophycocyanine (APC) (Mathis, 1998). Both antibodies are fixed onto the analyte by the immunoreaction so that the lanthanide ion and APC lie at a close enough distance for an efficient Förster-type energy transfer process to take place (Fig. 9. 15). The lifetime of the APC fluorescence (at 680 nm) depends on the population of its $^1\pi\pi^*$ state by the energy transfer process, which is determined by the Eu($^5D_0$) lifetime; the decay of the red emission takes therefore place with the lifetime of the europium ion.

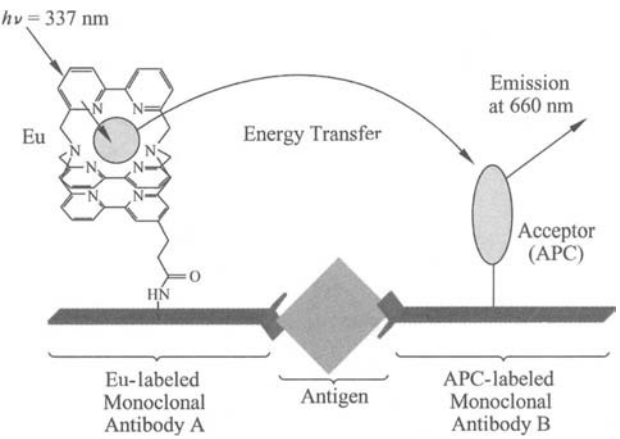


Figure 9. 15 Principle of homogeneous time-resolved fluoroimmunoassays (Mathis, 1998)

In fact several commercial systems are presently available (Table 9.4) and the trend is to develop multiple labeling with Sm^{3+}, Eu^{3+}, Tb^{3+}, and Dy^{3+} for use in simultaneous detection of several biomolecules (Hemmilä, 1995a). Dual-label essays have been developed quite early and are usually based on Sm^{3+} and Eu^{3+} chelates. However, the quantum yield of the Sm^{3+} chelate is much lower than that of the Eu^{3+} label so that the component targeted by the Sm^{3+} stain must be in much higher concentration, unless multiple Sm-labeling is used. To avoid this problem, Eu^{3+}-Tb^{3+} pairs are now being advocated, as demonstrated by a recently published dual assay for α-fetoprotein (AFP) and carcinoembryonic antigen (CEA) (Yuan et al., 2001). A new nonadentate ligand, *N, N, N′, N′*-[2, 6-bis(3′-aminomethyl-1′-pyrazolyl)-4-phenylpyridine]-tetrakis(acetic acid) (**20**), allows a very efficient sensitization of Tb^{3+}, the quantum yield in borate buffer (pH = 9.1) being unity, and a good sensitization of Eu^{3+} (quantum yield = 13%). The detection limits reached were 42 pg/ml for AFP and 70 pg/ml for CEA.

Table 9.4 Some commercially used luminescent systems in time-resolved fluoroimmunoassays

Trade or given name	Ln^{3+}	Chelating agent	Formula	Reference
DELFIA	Eu	2-naphtolytrifluoroacetonate/TOPO/ Triton X-100	**18**	(Hemmilä et al., 1995b)
FIAgen	Eu	4, 7-bis-(chlorosulfodiphenyl)-1, 10-phenanthroline-2, 9 carboxylic acid	**19**	(Diamandis and Christopoulos, 1990)
CyberFluor	Eu	4, 7-bis-(chlorosulfodiphenyl)-1, 10-phenanthroline-2, 9 carboxylic acid	**19**	(Evangelista et al., 1988)
TRACE[a]	Eu	(bpy. bpy. bpy)	**9**	(Mathis, 1998)
EA-FIA[b]	Tb	5-fluorosalicylate/edta		(Christopoulos and Diamandis, 1992)

(a) time-resolved amplified cryptate emission;
(b) enzyme-amplified time-resolved fluoroimmunoassay.

9.6.2 Responsive Systems

Responsive systems are chemical (often supramolecular) devices having properties which can be modulated upon binding to a specific substrate or reactant. In our case, we are especially interested in modulating luminescent properties. One example of a responsive supramolecular device was demonstrated for the analysis of polyaromatic hydrocarbons (Pikramenou and Nocera, 1992). The basic process is the complexation of the latter by cyclodextrins, and this process is monitored by changes in the luminescence of an attached lanthanide probe (Fig. 9.16). For this purpose, a cyclodextrin (cyclic oligosaccharide, **21**) molecule has been functionalized with the macrocycle 1, 4, 10, 13-tetraoxa-7, 16-diaza-cyclooctadecane (2.2, **22**) known to strongly complex lanthanide ions

(Bünzli, 1987). The result is a bifunctional architecture: the catenation of the (2.2) moiety provides a receptor for the lanthanide ions while the conical cavity of the β-CD used provides an ordered medium capable of forming inclusion complexes with a variety of molecules, particularly aromatic hydrocarbons. When Eu^{3+} is used, the metal ion may be excited either through the f – f transitions or through a LMCT band at 313 nm (involving the nitrogen atoms of the ligand) and the bright red luminescence is observed in acetonitrile or D_2O solutions. When benzene is added to the solution, the total luminescence intensity increases markedly (+ 80% for 4.3×10^{-3} M). It is assumed that energy absorbed by the aromatic moiety is transferred onto the metal ion. The drawback of the system lies in a relatively large exposure of the lanthanide ion to solvent interactions, so that another derivatized CD has been synthesized to ensure a cradle geometry to the lanthanide receptor by attaching both nitrogen atoms of the (2.2) ligand to the CD through amide bridges. The resulting Tb^{3+}-containing system displays indeed a good response in water to the insertion of naphtalene and tetramethylbenzene into the CD cavity (Mortellaro and Nocera, 1996). The mechanism of the energy transfer from the inserted aromatic hydrocarbons has been studied by time-resolved spectroscopy in the case of biphenyl and Tb^{3+} and the following rate constants could be determined (cf. Fig. 9.3): $k_{isc} = 5.2 \times 10^8\ s^{-1}$, $k_{et} = 8.3 \times 10^4\ s^{-1}$, $k^{Tb} = 1.7 \times 10^4\ s^{-1}$ (Rudzinski et al., 1998).

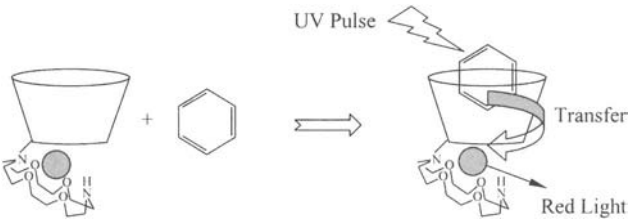


Figure 9.16 Photoresponsive supramolecular device for the analysis of aromatic hydrocarbons. Redrawn from (Mortellaro and Nocera, 1996)

Responsive luminescent probes have also been largely used to monitor the ionic composition of aqueous samples in environmental chemistry or of physiological samples. Parker and co-workers have designed substituted cyclen receptors able to strongly complex lanthanide ions and featuring a phenanthridine group which is a good sensitizer of the Ln^{3+} luminescence (Parker, 2000). Moreover, protonation of the nitrogen atom of the latter leads to pH sensitive luminescence. For instance, the neutral Eu(**23**) complex gives rise to very weak sensitized emission from Eu^{3+} at pH > 6 while lowering the pH to 2 induces an intense red luminescence (estimated enhancement factor : 500) from the protonated species [Eu(H**23**)]$^+$. Therefore, this system represents a pH switch wherein protonation triggers the Eu^{3+} luminescence. The ligand fluorescence

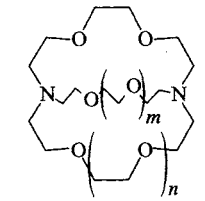
follows the same trend, both in the Eu^{3+} and Tb^{3+} complexes but in the latter, the pH dependence of the metal-centred luminescence is opposite that of Eu^{3+}, with no sensitization at low pH and a substantial one at basic pH. The reason lies in the energy of the phenanthridine $^3\pi\pi^*$ state which is lowered from $22,000\ cm^{-1}$ in the unprotonated form to $21,300\ cm^{-1}$ in the protonated one, allowing a more efficient back-transfer process to take place. The Eu^{3+} and Tb^{3+} complexes of **24** display a behaviour which parallels that of Eu(**23**). In addition, the luminescence of the Tb^{3+} complexes is sensitive to the presence of oxygen in the solution. Finally, the complexes of **23** and **24** are also sensitive to the presence of hydroxide and halide ions (Parker et al., 1998).

9.7 Conclusions

Sensitization of lanthanide ion luminescence by energy transfer from organic ligands attached to these ions allows one to design very sensitive and dedicated luminescent probes. In this chapter, we have tried to show the main challenges with regard to the engineering of such functional edifices and to illustrate some examples. The development of non radioactive fluoroimmunoassays based on lanthanide ions has prompted a large interest in these compounds and new applications are emerging. For instance in the field of site-selective lanthanide chelates for enhanced imaging of cancer (Bornhop et al., 1999), of lanthanide luminescent tags for time-resolved microscopy (Charbonnière et al., 2001), of self-assembled dimeric heterodimetallic lanthanide electro-excited luminescent probes (Ala-Kleme et al., 2000) and of organic light emitting diodes (Zhao et al., 1999). There is therefore no doubt that this field will continue to attract interest both from scientists, engineers and medical doctors.

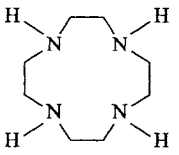
Appendix

9.A Chemical Formulae of Compounds Cited in the Text



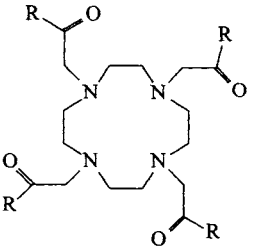
(2(*m*+1)·(*n*+1)) cryptand

1



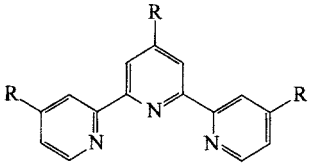
cyclen

2



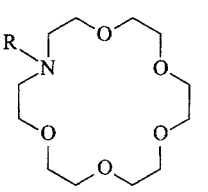
substituted cyclen

3



2′,2″; 6′,6″ -terpyridine, terpy

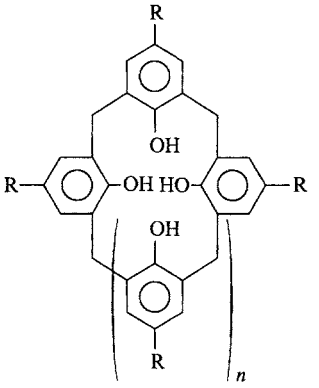
4



R = OH dota

monoaza -18- crown- 6

5



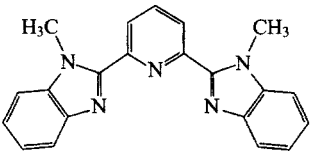
R = H
n = 2: calix[5]arene
n = 5: calix[8]arene

R = $C(CH_3)_3$
n = 2: b-$L'H_5$
n = 5: b-LH_8

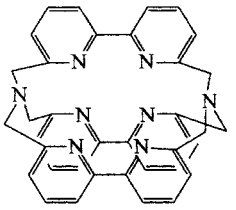
R = NO_2
n = 5: *n*-LH_8

6

mbzimpy

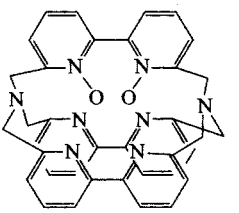


7

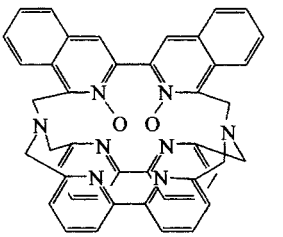


(bpy·bpy·bpy)

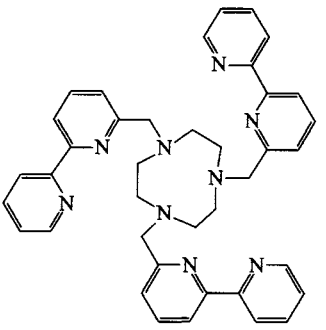
9



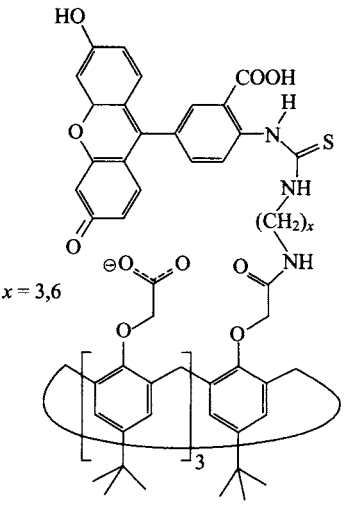
10a



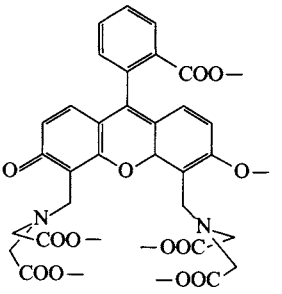
10b



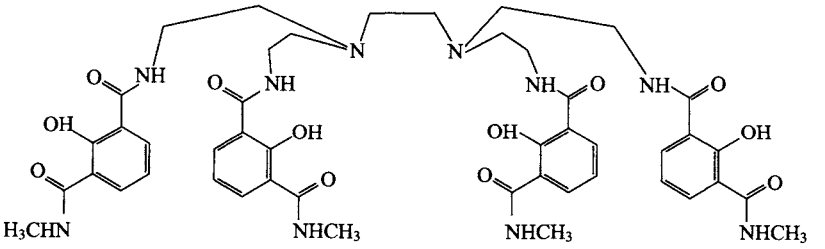
11


HO
COOH
H
O
N
S
NH
$(CH_2)_x$
O
NH
$x = 3,6$
$\ominus O$
O
O
O
O
3

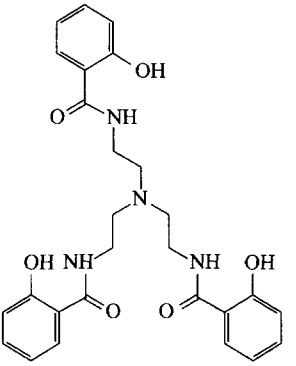
12


COO−
O
O
O−
N
COO−
COO−
N
−OOC
−OOC

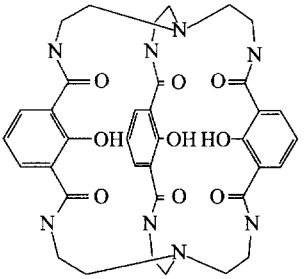
13


N
N
O
NH
OH
O
H_3CHN
O
NH
OH
O
$NHCH_3$
NH
O
OH
O
$NHCH_3$
NH
O
OH
O
$NHCH_3$

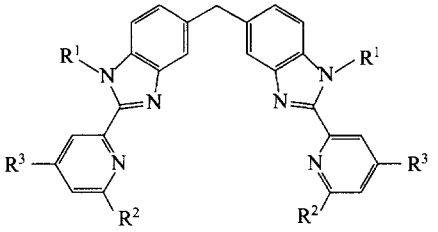
14



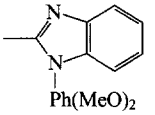
15

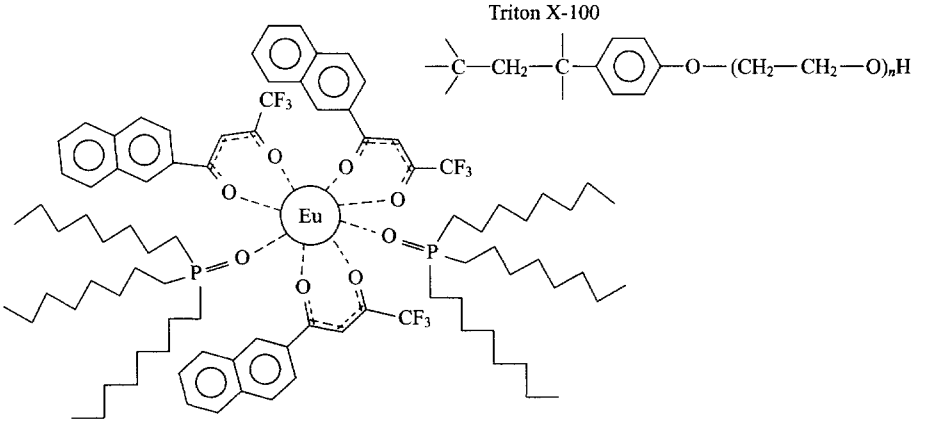


16

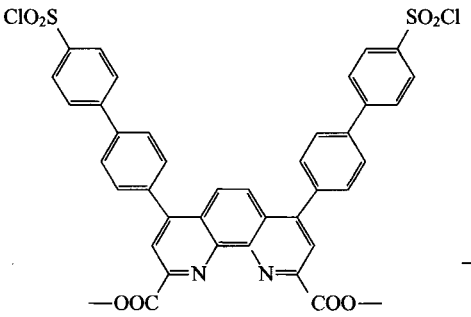


17

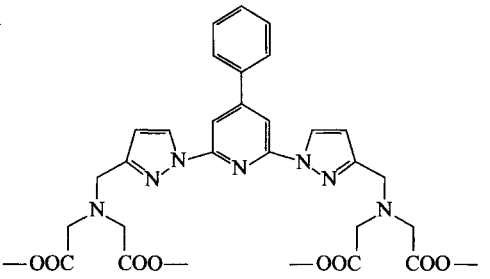
	R^1	R^2	R^3
17a	Me		H
17b	Et	— $CO(NEt_2)$	H
17c	Et	— COOH	H
17d	Et	— $CO(NEt_2)$	Cl



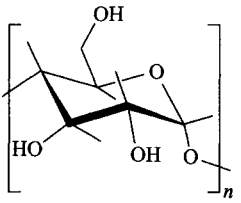
18



19

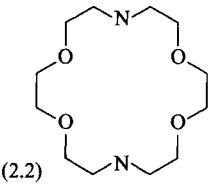


20



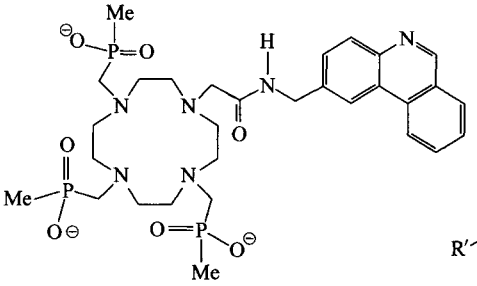
$n = 6$
β-CD

21

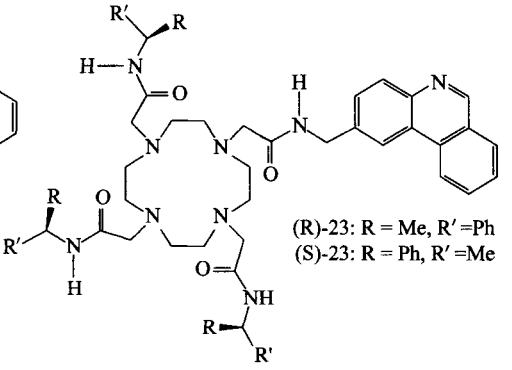


(2.2)

22



23



(R)-23: R = Me, R′ =Ph
(S)-23: R = Ph, R′ =Me

24

9. B Glossary and Chemical Formulae

(Bold numbers in parentheses refer to the structures presented on the preceding schemes)

acac	acetylacetonate
bpta	*N, N, N′, N′*-[2, 6-bis(3′-aminomethyl-1′-pyrazolyl)-4-phenylpyridine]-tetrakis(acetic acid)
AFP	α-fetoprotein
APC	allophycocyanine
b-L′H_5	*p-tert*-butylcalix[5]arene(**6**)
b-LH_8	*p-tert*-butylcalix [8] arene (**6**)
bpy	bipyridine
(bpy. bpy. bpy)	cryptand based on bipyridine (**9**)
CD	cyclodextrin
cyclen	1, 4, 7, 10-tetraazacyclododecane (**2**)
DNA	desoxyribonucleic acid
dota	1, 4, 7, 10-tetraazacyclododecane-1, 4, 7, 10-tetraacetic acid (**3**)
dmf	*N, N′*-dimethylformamide
edta	ethylenediamine tetraacetic acid
FIA	fluoroimmunoassay
FSH	follicle stimulating hormone
INDO/S-CI	intermediate neglect of differential overlap/spectroscopic configuration interaction
isc	intersystem crossing
LH	luteinizing hormone
MLCT	ligand-to-metal charge transfer state
LMCT	metal-to-ligand charge transfer state
mbzimpy	2, 6-bis(1-methyl-benzimidazol-2-yl) pyridine (**7**)
N-18C6	monoaza-18-crown-6: 1-aza-4, 7, 10, 13-pentaoxacyclooctadecane (**5**)
n-LH_8	*p*-nitrocalix[8]arene (**6**)
PET	photoinduced electron transfer
RNA	ribonucleic acid
terpy	2, 2′; 6, 2″-terpyridine (**4**)
thf	tetrahydrofuran
TOPO	trioctylphosphine oxide

References

Ala-Kleme, T., M. Latva, and K. Haapakka. Anal. Chim. Acta **403**, 161(2000).

Archer, R. D., H. Y. Chen, and L. C. Thompson. Inorg. Chem. **37**, 2089(1998).

Beeby, A., I. M. Clarkson, R. S. Dickins, S. Faulkner, D. Parker, L. Royle, A. S. de Sousa, J. A. G. Williams, and M. Woods. J. Chem. Soc., Perkin Trans. **2**, 493 (1999).

Blasse, G., and B. C. Grabmaier. *Luminescent Materials* (Springer-Verlag, Berlin-Heidelberg, 1994).

Bornhop, D. J., D. S. Hubbard, M. P. Houlne, C. Adair, G. E. Kiefer, B. C. Pence, and D. L. Morgan. Anal. Chem. **71**, 2607(1999).

Bünzli, J. -C. G., N. André, M. Elhabiri, G. Muller, and C. Piguet. J. Alloys & Compnds. **303/304**, 66(2000a).

Bünzli, J. -C. G., F. Besançon, and F. Ihringer In: *Calixarenes for Separations,* eds. G. J. Lumetta, R. D. Rogers, and A. Gopalan (American Chemical Society, Washington D. C., 2000b), Ch. 14.

Bünzli, J. -C. G. In: *Rare Earths,* eds. R. Saez Puche, P. Caro (Editorial Complutense, Madrid, 1998), p. 223.

Bünzli, J. -C. G., F. Ihringer, P. Dumy, C. Sager, and R. D. Rogers. J. Chem. Soc., Dalton Trans. 497(1998).

Bünzli, J. -C. G. In: *Handbook on the Physics and Chemistry of Rare Earths,* eds. K. A. Gschneidner Jr., and L. Eyring (Elsevier Science Publ., Amsterdam, 1987), Vol. 9, Ch. 60.

Bünzli, J. -C. G., P. Froidevaux, and J. M. Harrowfield. Inorg. Chem. **32**, 3306(1993).

Bünzli, J. -C. G., F. Ihringer. Inorg. Chim. Acta **246**, 195(1996).

Bünzli, J. -C. G and J. -R. Yersin. Helv. Chim. Acta **65**, 2498(1982).

Charbonnière, L. J., R. Ziessel, M. Guardigli, A. Roda, N. Sabbatini, and M. Cesario. J. Am. Chem. Soc. **123**, 2436(2001).

Charbonnière, L. J., C. Balsiger, K. J. Schenk, and J. -C. G. Bünzli. J. Chem. Soc., Dalton Trans. 505(1998).

Choppin, G. R., D. R. Peterman. Coord. Chem. Rev. **174**, 283(1998).

Christopoulos, T. K., E. P. Diamandis. Anal. Chem. **64**, 342(1992).

Crookes, W. Phil. Trans. Roy. Soc. London A **176**, 691(1885).

Crosby, G. A. Mol. Cryst. **1**, 37(1966).

Crosby, G. A., R. E. Whan, and R. M. Alire. J. Chem. Phys. **34**, 743(1961).

de Sá, G. F., O. L. Malta, C. D. Donega, A. M. Simas, R. L. Longo, P. A. Santa-Cruz, and da Silva E. F. Coord. Chem. Rev. **196**, 165(2000).

De Silva, A. P., H. Q. N. Gunaratne, T. Gunnlaugsson, A. J. M. Huxley, C. P. McCoy, J. T. Rademacher, and T. E. Rice. Chem. Rev. **97**, 1515(1997a).

De Silva, A. P., H. Q. N. Gunaratne, T. E. Rice, and S. Stewart. Chem. Commun. 1891 (1997b).

Dexter, D. L. J. Chem. Phys. **21**, 836(1953).

Diamandis, E. P., T. K. Christopoulos. Anal. Chem. **62**, 1149A(1990).

Elbanowski, M., B. Makowska. J. Photochem. Photobiol. A: Chem. **99**, 85(1996).

Elhabiri, M., R. Scopelliti, J. -C. G. Bünzli, C. Piguet. J. Am. Chem. Soc. **121**, 10, 747 (1999).

Evangelista, R. A., A. Pollak, B. D. Allore, A. F. Templeton, R. C. Morton, E. P. Diamandis. Clin. Biochem. **21**, 173(1988).

Förster, Th. Ann. Phys. **2**, 55(1948).

Furphy, B. M., J. M. Harrowfield, D. L. Kepert, B. W. Skelton, A. H. White, and F. R. Wilner. Inorg. Chem. **26**, 4231(1987).
Gonçalvès e Silva, F. R., R. Longo, O. L. Malta, C. Piguet, and J. -C. G. Bünzli. Phys. Chem. Chem. Phys **2**, 5400(2000).
Gschneidner, K. A., Jr. *Industrial Applications of Rare Earth Elements, A. C. S. Symposium Series 164* (American Chemical Society, Washington D. C., 1981).
Guo, Z. J., P. J. Sadler. Angew. Chem. Intl. Ed. Engl. **38**, 1513(1999).
Haas, Y., G. Stein. J. Phys. Chem. **75**, 3677(1971).
Heber, J. Phys. kondens. Mat. **6**, 381(1967).
Hemmilä, I. J. Alloys & Compnds. **225**, 480(1995a).
Hemmilä, I., T. Ståhlberg, and P. Mottram *Bioanalytical Applications of Labelling Technologies* (Wallac Oy, Turku, 1995b).
Horrocks, W. deW. Jr. Adv. Inorg. Biochem. **4**, 201(1982).
Horrocks, W. deW. Jr., D. R. Sudnick. J. Am. Chem. Soc. **101**, 334(1979).
Hüfner, S. *Optical Spectra of Transparent Rare Earth Compounds* (Academic Press, New York, 1978).
Jacquier, B. J. Alloys & Compnds. **225**, 15(1995).
Kimura, T., Y. Kato. J. Alloys & Compnds. **225**, 284(1995).
Kimura, T., G. R. Choppin. J. Alloys & Compnds. **213/214**, 313(1994).
Kleinerman, M., Choi Sang-Il. J. Chem. Phys. **49**, 3901(1968).
Kropp, J. L., M. W. Windsor. J. Chem. Phys. **42**, 1599(1965).
Latva, M., H. Takalo, V. M. Mukkala, C. Matachescu, J. -C. Rodriguez-Ubis, J. Kankare. J. Luminesc. **75**, 149(1997).
Latva, M., H. Takalo, K. Simberg, J. Kankare. J. Chem. Soc., Perkin Trans. 2995(1995).
Lövgren, T., I. Hemmilä, K. Pettersson, J. U. Eskola, E. Bertoft. Talanta **31**, 909 (1984).
Malta, O. L., F. R. Gonçalvès e Silva, R. Longo. Chem. Phys. Lett. **307**, 518(1999).
Martin, N., J. -C. G. Bünzli, V. McKee, C. Piguet, G. Hopfgartner. Inorg. Chem. **37**, 577(1998).
Mathis, G. In: *Rare Earths,* ed. by R. Saez Puche, and P. Caro. (Editorial Complutense, Madrid, 1998), p. 285.
Mortellaro, M. A., D. G. Nocera. J. Am. Chem. Soc. **118**, 7414(1996).
Parker, D. Coord. Chem. Rev. **205**, 109(2000).
Parker, D., P. K. Senanayake, and J. A. G. Williams. J. Chem. Soc., Perkin Trans. **2**, 2129(1998).
Petoud, S., J. -C. G. Bünzli, T. Glanzman, C. Piguet, Q. Xiang, and R. P. Thummel. J. Luminesc. **82**, 69(1999).
Piguet, C., J. -C. G. Bünzli. Chem. Soc. Rev. **28**, 347(1999).
Piguet, C., J. -C. G. Bünzli, G. Bernardinelli, G. Hopfgartner, and A. F. Williams. J. Am. Chem. Soc. **115**, 8197(1993).
Pikramenou, Z., D. G. Nocera. Inorg. Chem. **31**, 532(1992).
Platas, C., M. Elhabiri, M. Hollenstein, J. -C. G. Bünzli, and C. Piguet. J. Chem. Soc., Dalton Trans. 2031(2000).
Raymond, K. N., S. Petoud, S. M. Cohen, and J. D. Xu. Patent WO 00/48,990 (8.24. 2000a).
Raymond, K. N., S. Petoud, S. M. Cohen, and J. D. Xu. Patent WO 00/48,991 (8.24. 2000b).
Rudzinski, C. M., W. K. Hartmann, and D. G. Nocera. Coord. Chem. Rev. **171**, 115 (1998).

Sabbatini, N., M. Guardigli, and I. Manet. In: *Handbook on the Physics and Chemistry of Rare Earths,* eds. by K. A. Gschneidner Jr., and L. Eyring (Elsevier Science Publ., Amsterdam, 1996), Vol. 23, Ch. 154.

Sabbatini, N., S. Perathoner, V. Balzani, B. Alpha, and J.-M. Lehn. In: *Supramolecular Chemistry,* ed. by V. Balzani (D. Reidel Publishing Co., Dordrecht, 1987), p. 187.

Sato, N., S. Shinkai. J. Chem. Soc., Perkin Trans. **2**, 621(1993).

Sato, S. M. Wada. Bull. Chem. Soc. Jpn. **43**, 1955(1970).

Schrott, W., H. Büchner, and U. Steiner. J. Inf. Recording **23**, 79(1996).

Siitari, H., I. Hemmilä, K. Pettersson, and T. Lövgren. Nature **301**, 258(1983).

Steemers, F. J., W. Verboom, D. N. Reinhoudt, E. B. Vandertol, and J. W. Verhoeven. J. Am. Chem. Soc. **117**, 9408(1995).

Supkowski, R. M., W. dew.. Horrocks Jr. Inorg. Chim. Acta. **340**, 44(2002).

Weissman, S. I. J. Chem. Phys. **10**, 214(1942).

Weller, A. Pure Appl. Chem. **16**, 115(1968).

Werts, M. H. V., J. W. Verhoeven, and J. W. Hofstraat. J. Chem. Soc., Perkin Trans. **2**, 433(2000).

Wolbers, M. P. O., F. C. J. M. Vanveggel, F. G. A. Peters, E. S. E. Vanbeelen, J. W. Hofstraat, F. J. Geurts, and D. N. Reinhoudt. Chem. Eur. J. **4**, 772(1998).

Xu, Y. Y., I. Hemmilä, V. M. Mukkala, S. Holttinen, and T. Lövgren. Analyst **116**, 1155(1991).

Yu, J. A., R. B. Lessard, L. E. Bowman, and D. G. Nocera. Chem. Phys. Lett. **187**, 263(1991).

Yuan, J. G., G. L. Wang, K. Majima, and K. Matsumoto. Anal. Chem. **73**, 1869 (2001).

Zhao, D. X., W. L. Li, Z. R. Hong, X. Y. Liu, C. J. Liang, and D. Zhao. J. Luminesc. **82**, 105(1999).

10 Rare Earth Ions in Advanced X-ray Imaging Materials

M. Z. Su, W. Zhao

10.1 X-ray Phosphors

Almost immediately after W. C. Roentgen discovered X-rays in 1895, he realized that as this particular radiation struck human hands, some radiation was absorbed, while other portions passed through undeviated. The intensity varied from area to area and formed an image on a photographic film. Since the wavelength of the X-rays did not correspond with the spectral sensitivity of the film, the X-rays were not very efficient in exposing the film. As a consequence, long irradiation time was required for taking an image on the film. Roentgen initiated a search for phosphors that would absorb the X-rays and emit light more efficiently. The emitted light would correspond with the spectral sensitivity of the film and would, therefore, blacken the film more efficiently, thus shortening the irradiation time.

Today we know that long time irradiation is harmful to patients, which is a practical objection against long irradiation time. In addition, because a patient is a moving object and his or her heart blood vessels and breath organs are constantly in motion, sharp images can only be obtained when the irradiation time is very short.

The first phosphor found by Pupin was calcium tungstate $CaWO_4$, which was quite good in enhancing the light output of X-rays (pupin, 1975). With a density of 6.06 g/cm^3, reasonable X-ray absorption in the range of 20 keV to 100 keV, and a blue emission centered around 430 nm, $CaWO_4$ appeared to be quite adequate, despite of its low X-ray-to-light conversion efficiency of 5 percent. $CaWO_4$ is a rather enduring phosphor and has served all needs for X-ray intensifying screens for a century. Only with the advent of rare earth phosphors and their applications in lasers, lamps, and color television (TV), has $CaWO_4$ lost its predominate position. With the availability of individual elements of rare earths of high purity and reasonable cost, many new X-ray phosphors have been studied and developed. Examples are Gd_2O_2S: Tb, LaOBr: Tb, BaFCl: Eu, $YTaO_4$: Tb, and $GdTaO_4$: Tb, etc. (Brixner, 1987). These rare earth X-ray phosphors have greater densities, improved X-ray absorption, and higher X-ray-to-light conversion efficiency.

X-ray phosphors are luminescence materials that can absorb X-rays and

convert the absorbed energy efficiently into luminescence. According to their luminescence processes and their application fields, X-ray phosphors can be further subdivided into two categories: X-ray phosphors and scintillators. X-ray phosphors are used in applications where integrating techniques are used to measure light intensity under continuous X-ray excitation. The light intensity is position sensitive, which yields an image. A well-known example is the case of X-ray imaging in medical diagnostics or safeguards. Scintillators are used in applications where counting techniques are used to digest the radiation excited by a single pulse. The radiation yields the information about existing events. A well-known example is the use of scintillators in electromagnetic calorimeters to count photons, electrons and other high energy particles.

When a phosphor is irradiated by X-rays, a series of dynamic processes occurs, which include X-ray absorption, energy migration from the matrix to activator ions, excitation of activator ions, and radiative transition of activator ions from their excited states to ground states accompanied by the characteristic light emission of the activator ions. The mechanism of X-ray luminescence is ambiguous and could be considered as an analog to that of cathodoluminescence.

The X-ray absorption of a phosphor can be obtained using a computer program based on the mass absorption coefficient μ of the phosphor (Hubbel, 1969) and the fundamental absorption equation for X-rays (Clark, 1963; Sonda, 1983):

$$I/I_0 = e^{-\mu\rho x}, \tag{10.1}$$

where I_0 is the incident X-ray beam intensity, I is the transmitted beam intensity, ρ is the phosphor density, and x is the thickness of the phosphor film.

When X-rays interact with an atom or an ion, they may remove an electron from the K shell of that atom or ion if the energy of an X-ray photon is higher than the binding energyE_K of the K shell electrons. X-ray absorption increases strongly with the atomic number of the heavy ions contained in a phosphor. The absorbed X-ray energy may excite certain groups of matrices, such as WO_4^{2-} in $CaWO_4$, or it may excite activator ions, such as Eu^{2+} in BaFCl. When these groups or activator ions return from their excited states to their ground states, they give rise to their characteristic luminescence.

Recently it has been found that some rare earth phosphors can temporarily store X-ray energy for several hours or even days. These phosphors are called as X-ray storage phosphors or photostimulable phosphors. The stored X-ray energy can be released as luminescence by stimulation with a longer wavelength light. The luminescence is known as X-ray induced photostimulated luminescence (PSL).

X-ray storage phosphors have been used to make image plates (IPs) as new X-ray area detectors. Computed diagnostic radiography systems and automated single crystal X-ray diffraction systems have been constructed utilizing the IPs (Sonda, et al., 1983; Amemiya and Miyahara, 1988). In these systems, the phosphors receive and store the X-ray photons that penetrate through a human

body or are diffracted by a crystal. A two-dimensional latent image is formed as a distribution of color centers on the IPs. The stored latent image is then read out and recovered as optical luminescence through high-speed *X-Y* scanning the IPs with a focused laser beam of red or infrared wavelength within microseconds. The resulting integrated luminescence intensity given off at a stimulated point on the IPs is proportional to the density of the color centers, which is, in turn, proportional to the number of X-ray photons absorbed at that point during X-ray irradiation. With the aid of a photomultiplier tube and an analog-to-digital converter in a computer, the luminescence is detected and a digital image is created. At the time of recording, spatial frequency and gradational enhancement are performed by a high-speed image processing computer. The readout, processing, recording, and display are carried out simultaneously. The IPs have high sensitivity, a wide dynamic range, and a large effective area. They can reduce the X-ray exposure time on one to two orders of magnitude. They facilitate the crystal structure determination of samples such as proteins, genes and other biological materials that might be damaged by long duration X-ray irradiation.

10.2 X-ray Phosphors Used for Intensifying Screens

In this section, we discuss some characteristics associated with phosphors that are used to manufacture X-ray intensifying screens for conventional radiological imaging purposes.

X-ray used in medical radiography are most commonly generated by an X-ray tube with a tungsten target working at a tube voltage of 50 kV to 120 kV and a tube current of 50 mA to 1000 mA. The X-ray energy ranges from 30 keV to 100 keV. The structure of conventional intensifying screens used in medical radiography systems is represented in Fig. 10.1.

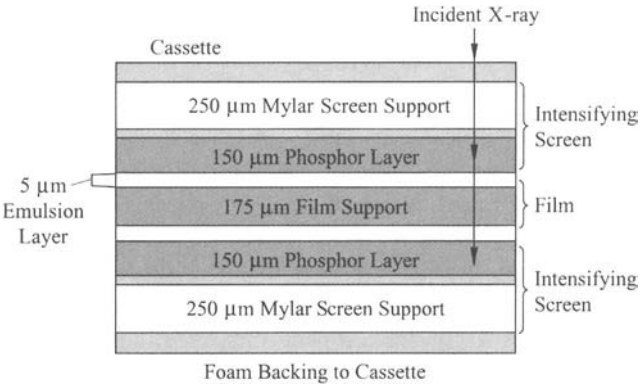


Figure 10.1 Cross section of X-ray cassette showing two screens and double emulsion film (Brixner, 1987). Reproduced with permission from Elsevier Science

The X-ray transmitted through a patient's body are detected by a phosphor coated on a plastic substrate. The phosphor absorbs X-ray energy and gives rise to luminescence at specific wavelengths. The emitted luminescence is recorded on a photographic film. The spectral energy distribution of the emitted luminescence should coincide optimally with the spectral sensitivity of the film. Two types of screen films are popularly used in hospitals: a blue-emitting screen with a blue-sensitive film and a green-emitting screen with a green-sensitive film. A combination of the two screen-films is also used in nondestructive detection of materials and structures such as high-pressure vessels and tubes, etc.

There are several requirements for X-ray phosphors for intensifying screens: (1) high X-ray absorption, (2) high efficiency for X-ray-to-light conversion, (3) coincidence of the phosphor's emission spectrum with the spectral sensitivity of a film, (4) luminescence stability, (5) suitable crystal morphology and sizes of the phosphors, and (6) an acceptable cost.

Crucial to the application of X-ray phosphors for intensifying screens is the efficiency with which the incident X-ray energy is converted to useful light energy as given by the expression:

$$\eta = \eta_a \eta_c \eta_t, \qquad (10.2)$$

where η_a and η_c are the efficiency of X-ray absorption and the efficiency of X ray to light conversion, respectively, and η_t is the efficiency with which the light energy is transmitted through the screen to the film. The processes concerning η_a and η_c are easy to understand. However, the process related to η_t, which involves sub-processes of the transmission, scattering and absorption of the emitted light, is extremely complex. The process contains such parameters as phosphor particle size, size distribution, particle shape, the refractive indexes of the phosphor particles and binding polymers, and the particle packing density of the screen, etc. All these parameters determine the structural mottle of the intensifying screen. No measurements can be made to account for these sub-processes individually. Comparisons using modulation transfer function measurements involve all image degrading processes. The sharpness of definition of images formed on the film depends upon X-ray quantum fluctuation (quantum noise) and the screen structural mottle (structural noise). To reduce the structural mottle and improve the phosphor packing density, spherical and polyhedral shaped phosphor particles are the most desirable. An average particle size between 5 μm and 10 μm and a narrow size distribution would facilitate the closest packing of the phosphor particles in a screen. The closer the refractive indexes between the phosphor and the binding high polymers are, the less refractive light loss occurs. All these factors would result in an even density on the film after exposure to the screen, so as to give an image with high definition.

10.2.1 Calcium Tungstate

Although $CaWO_4$ does not contain any rare earth elements in its composition, we

discuss it here because it was the first X-ray phosphor and is still used today. Additionally, the experience of preparing $CaWO_4$ intensifying screens is still useful and beneficial.

$CaWO_4$ was discovered as early as 1896 and has been used for a century. It has some favorable as well as some rather unfavorable properties. For its favor, the X-ray excited emission of $CaWO_4$ is centered at 430 nm in the blue region, which matches the blue-sensitive film very well, and its crystal form is polyhedral, which can result in closer particle packing in the screen. Therefore, the screen gives rise to a detailed image with high sharpness on the film. In addition, $CaWO_4$ is a low cost, very stable material. It is easy to synthesize by reacting Na_2WO_4 with $CaCl_2$ in a hot solution and then firing the precipitate at 800℃ for one hour. Its unfavorable properties include its poor X-ray absorption. At 50 keV, a 200 μm thick $CaWO_4$ screen absorbs only 35 percent of the X-rays. More detrimental, however, is its extremely poor X-ray-to-light conversion efficiency of only 5%.

It is known that complexes of transition metal ions with empty d-shells often show intense broad band emissions with large Stokes shifts. $CaWO_4$ is an example with one of these complexes. As it is X-rayed, its excited state is a charge-transfer state. Electrons move from the oxygen ligands to the central tungsten ion and then transit to their ground states, which are accompanied with a broad band emission in the blue spectral region.

10.2.2 Rare Earth Tantalate Based Phosphors

Rare earth tantalate based phosphors constitute the most recent entry into the list of new X-ray phosphors. They are the first oxide-based compositions after $CaWO_4$ phosphors and are physically similar to $CaWO_4$. Although there are at least five different rare earth tantalates ($LnTa_7O_{19}$, $LnTa_5O_{14}$, $LnTaO_4$, $LnTa_3O_9$ and Ln_3TaO_7), only one composition, $LnTaO_4$, shows X-ray luminescence. In particular, for fergusonite $YTaO_4$ (Ferguson, 1957), its M′ modification is the only matrix structure exhibiting superior X-ray luminescent properties. When it is doped with different rare earth ions or niobium ions, it emits photo- and X-ray luminescence with wavelengths from the UV region to near infrared.

Wolten (1967), and Brixner and Chen (1983) have investigated the crystal structure of $YTaO_4$. It has two types of structure: (1) $I2/a$ (or M type, known as fergusonite structure) and (2) $P2/a$ (or M′ type). The M′ $YTaO_4$ modification has twice as efficient luminescence as the M type $YTaO_4$ under X-ray excitatiotn. The M′ type structure is a very stable one at room temperature. M′ $YTaO_4$ consists essentially of cube like 8-coordinated Y polyhedrons that can be best described as a distorted square anti-prism(Fig. 10.2). The average Y – O distance is 2.355 Å. The tantalum atoms are in a distorted

coordination with four shorter Ta – O bonds at 1.86 Å and 1.95 Å and two longer Ta – O bonds at 2.23 Å. The octahedral Ta coordination in the M′ type $YTaO_4$ is the major difference from the M type $YTaO_4$. M′ $YTaO_4$ can be converted into the $I4_1/a$ symmetry of scheelite via a reconstructive transformation at $T > 1450$ ℃. It will not be formed again upon cooling. Therefore we should pay attention to the firing temperature which should not exceed 1450 ℃ during the synthesis of M′ $YTaO_4$.

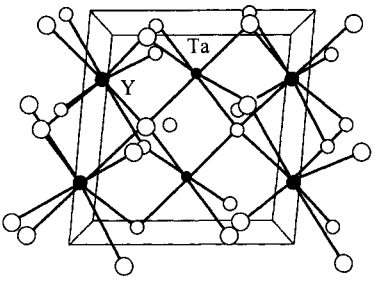


Figure 10.2 M′ $YTaO_4$ unit cell, showing 6-coordinated Ta and 8-coordinated Y (Brixner, 1987). Reproduced with permission from Elsevier Science

In the other two important M′ type hosts $GdTaO_4$ and $LuTaO_4$, the rare earth ions are also in an eight coordination (a distorted square antiprism with a C_2 site symmetry). The cell dimensions and densities of M′ $LnTaO_4$ (Ln = Y, Gd, and Lu) are summarized in Table 10.1.

Table 10.1 Cell dimensions and densities of M′ type $YTaO_4$, $GdTaO_4$ and $LuTaO_4$

Compounds	a (Å)	b (Å)	c (Å)	β (°)	$d_{X\text{-ray}}$ (g/cm^3)
$YTaO_4$	5.298	5.451	3.11	96.45	7.55
$GdTaO_4$	5.356	5.509	5.168	96.7	8.81
$LuTaO_4$	5.239	5.425	5.060	96.1	9.75

M′ $YTaO_4$ is prepared by the reaction of Y_2O_3 and Ta_2O_5. Due to the outstanding stability and refractory nature of these starting materials and the product, the reaction must take place at a high temperature for a long time with an appropriate flux. We have found a rather good procedure for preparing M′$YTaO_4$: Preheat the reactants Y_2O_3 and Ta_2O_5 at 1000 ℃ for 12 h in order to remove any possibly contained moisture and oxalates as well as to activate both oxides by forming more defects in the samples. Then mix the reactants in stoichiometric amounts with 20 wt. % Li_2SO_4 flux. Grind the mixture thoroughly in a ball mill. Heat this blend at 1000 ℃ for 12 h. When the blend is cooled

down to room temperature, wash it with deionized water to free the product from the flux. Dry the final product at 120 ℃. The obtained $YTaO_4$-based phosphor is a pure single M′ phase without any other possible impurities, such as Y_3TaO_7, $LiTaO_3$, Li_3TaO_4 and M $YTaO_4$ that appear in the product when it is prepared at 1200 ℃ or higher.

The photoluminescence spectrum of M′ $YTaO_4$ is shown in Fig. 10. 3. The broad emission band peaks at 328 nm and is quite similar to its X-ray excited emission spectrum (Fig. 10. 4). Its excitation band monitored at 328 nm is centered at 225 nm with a half-height width 24 nm and is assigned to the charge transfer excitation of the TaO_4 group. This excitation involves charge transfer from the fully-occupied valence band formed by the oxygen anions to the empty conduction band formed by the d shells of Ta ions.

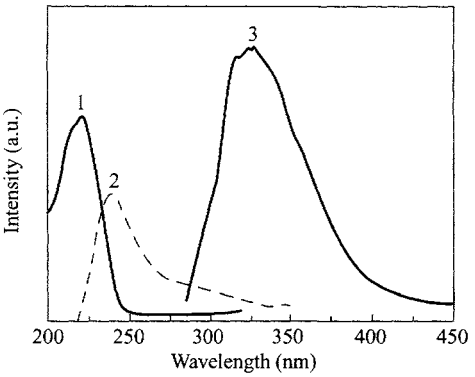


Figure 10. 3 Photoluminescence spectra of M′ $YTaO_4$. 1: Excitation spectrum, 2: Difussive reflectance, and 3: Emission spectrum

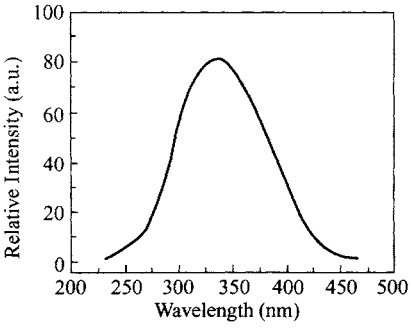


Figure 10. 4 X-ray luminescence of M′ $YTaO_4$

As shown in Fig. 10. 4, the host M′ type $YTaO_4$ gives a broad emission band at 337 nm under X-ray excitation. The absorption of X-ray is due to both the K_α absorption edge of the Y atom at 17. 04 keV and the TaO_4 group. The

emission originates from the charge-transfer radiation of the TaO_4 group, just like that of the WO_4 group in $CaWO_4$. When M′ $YTaO_4$ is doped with a few percent of Nb_2O_5, the NbO_4 group gives rise to quite efficient X-ray luminescence, as shown in Fig. 10.5, because the NbO_4 group is an efficient luminescent center in the $YTaO_4$ matrix (Blasse et al., 1994). The most efficient phosphors are those with Nb doping concentrations between 0.02 mol and 0.05 mol per mole $YTaO_4$. Their X-ray-to-light conversion efficiency is 8 to 9 percent.

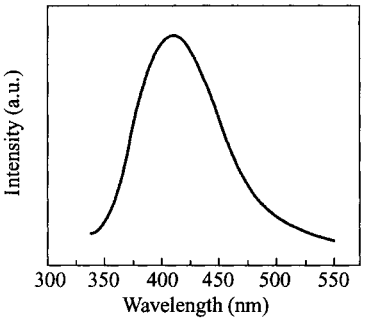


Figure 10.5 X-ray luminescence of M′ $YTaO_4$: Nb

The predominant feature of M′ $LnTaO_4$(Ln = Y, Gd, and Lu) is that they can be doped with other rare earths to give emissions from UV to red light. For example, when M′ $YTaO_4$ is doped with Eu^{3+}, it shows strong line emissions of Eu^{3+} in the range of 400 nm to 720 nm and a weak emission band of TaO_4 at 335 nm under the excitation of 220 nm UV light (Fig. 10.6). The most intense emission line of 612.7 nm originates from $^5D_0 \rightarrow {}^7F_2$ transition of Eu^{3+} ions, which are situated at the Y^{3+} sites of a C_2 symmetry. The less intense emission lines at 598 and 706 nm originate from $^5D_0 \rightarrow {}^7F_1$ and $^5D_0 \rightarrow {}^7F_4$ transitions of Eu^{3+} ions, respectively. The weak emission band is attributed to the charge-transfer of the TaO_4 group. When more Eu^{3+} ions are doped in M′ $YTaO_4$, the emission of TaO_4 is gradually diminished, as shown in Fig. 10.6. This is due to the energy transfer from the TaO_4 groups to the Eu^{3+} ions since the emission band of TaO_4 and the charge transfer excitation band of Eu^{3+} are partially overlapping each other.

Similar to that of Eu^{3+}-doped M′ $YTaO_4$, the photoluminescence of Tb^{3+}-doped M′$YTaO_4$ consists of a weak emission band of TaO_4 and a set of strong emission lines of Tb^{3+}. There is energy transfer from the TaO_4 groups to the activators Tb^{3+} ions. When Tb^{3+} concentration increases, the emission intensities of Tb^{3+} ions increase. Meanwhile the TaO_4 group emission is gradually diminished.

The X-ray luminescence of rare earth doped M′ $YTaO_4$ phosphors shows the same features as their photoluminescence (Li, 1999). A composition of M′ $Y_{0.998}$

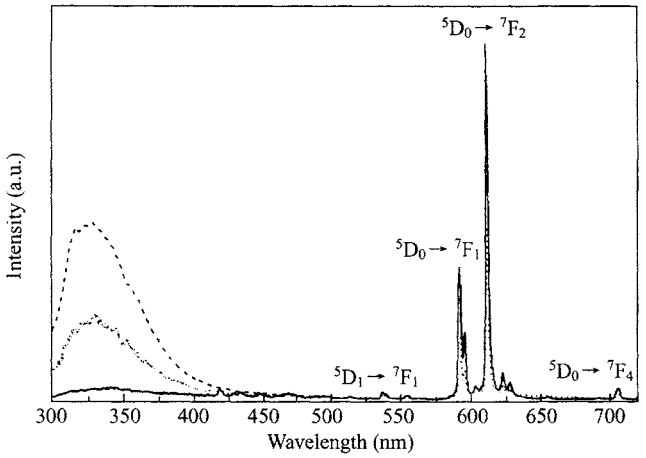


Figure 10.6 Emission spectra of M′ Y_{1-x} Eu_xTaO_4 excited by 220 nm UV light (dash line: $x=0$, dot line: $x=0.004$, and solid line: $x=0.02$)

$Tm_{0.002}TaO_4$ is promising to be a good X-ray phosphor for intensifying screens. The X-ray excited emission spectrum of this phosphor is shown in Fig. 10. 7, which is composed of a TaO_4 group emission band at 349 nm and a Tm emission band at 450 nm. Fig. 10. 8 shows the X-ray excited emission spectra of M′ $Y_{1-x}Dy_xTaO_4$ under different Dy concentrations. It is clear that energy transfer from TaO_4 to Dy^{3+} also occurs. The X-ray luminescence of other rare earth-doped M′ $YTaO_4$ has also been studied in our group (Li, 1999). These phosphors all show the characteristic emissions of doped rare earth ions and the intrinsic emission of the tantalate group.

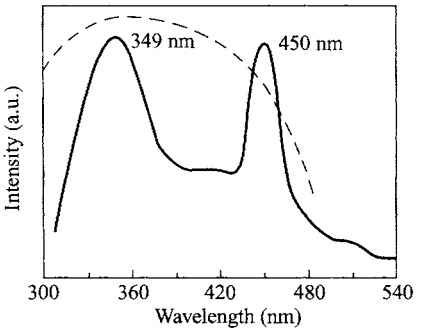


Figure 10.7 30 kV Mo radiation X-ray excited emission spectrum of M′ $Y_{0.998}Tm_{0.002}TaO_4$ (Brixner, 1987). Reproduced with permission from Elsevier Science

In addition to M′ $YTaO_4$ and M′ $GdTaO_4$, M′ $LuTaO_4$ can also be used as a host for rare earth-doped X-ray phosphors because of its high density of

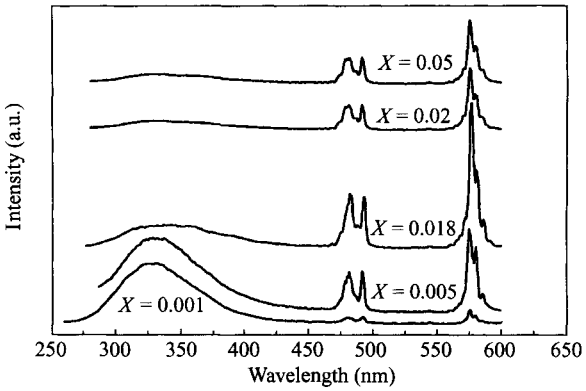


Figure 10.8 X-ray excited emission spectra of M′ $Y_{1-x}Dy_xTaO_4$

9.75 g/cm^3 (Table 10.1). With a completely filled f^{14} shell, the outer electron configuration of Lu^{3+} is very similar to that of Y^{3+}. The luminescence of $LuTaO_4$ should behave similarly to that of $YTaO_4$. M′ $LuTaO_4$: Nb has been evaluated to be a good X-ray phosphor, but has not been practically used because of its high cost. Although the price of Lu_2O_3 is too high today, $LuTaO_4$-based phosphors are worth studying in further detail.

10.2.3 Europium Activated Barium Fluoro-chloride Phosphors

BaFCl crystallizes in a tetragonal P4/nnm Mattlokite structure of PbFCl. The Ba ion is located in a C_{4v} symmetric site with five Cl ions on its topside and four F ions beneath it at an equal distance. Four of the Cl ions are at an equal distance from the Ba ion, and the fifth one locates on the symmetrical axis at a distance a little farther away. The whole crystal consists of alternate layers of ions arranged as F-Ba-Cl′-Cl″ -Ba-F-... A general unit cell of MFX (M = Sr, Ba; X = Cl, Br, and I) is depicted in Fig. 10.9.

BaFCl, BaFBr, and their solid solutions with other MFX crystals are good matrices for X-ray phosphors, scintillators, and X-ray storage phosphors where rare earth ions can be doped as activators that occupy Ba or Sr sites.

BaFCl is synthesized from stoichiometric amounts of BaF_2, $BaCl_2 \cdot 2H_2O$, and one mo % $EuCl_3 \cdot 6H_2O$ by solid state reaction at 750 ℃ under a mild reducing atmosphere of H_2-N_2 or even in air. In air, $EuCl_3$ could undergo a disproportion reaction and give rise to divalent Eu ions (Su et al., 1983). The overall reaction could be

$$EuCl_3 \rightarrow EuCl_2 + \frac{1}{2}Cl_2 \qquad (10.3)$$

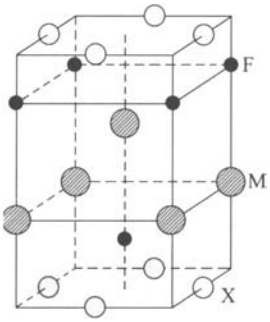


Figure 10.9 The crystal structure of MFX($M = Ca^{2+}$, Sr^{2+}, Ba^{2+}; $X = Cl^-$, Br^-, I^-) (Blasse and Grabmaier, 1994). Reproduced by permission

$$BaFCl + xEuCl_3 \rightarrow Ba_{1-x}Eu_xFCl + xBaCl_2 + \frac{x}{2}Cl_2 \qquad (10.4)$$

Since the c axis is much longer than the axes a and b in the crystal structure, the BaFCl: Eu crystal is plate like with a layered structure and is highly anisotropic along the c axis. This morphology is a problem since irregular plates will pack randomly in an intensifying screen and, thus, increase light scattering, which would cause image blur. Preparation by spry drying of a suspension of BaFCl in solution with excess $BaCl_2$ followed by firing of the dried droplets would improve the phosphor morphology to be more or less polyhedral.

Despite its relatively low density, BaFCl: Eu shows improved X-ray absorption because of the location of the K_α absorption edge of Ba at 37.4 keV. A comparison of its absorption properties with $CaWO_4$ and other X-ray phosphors is shown in Fig. 10.10.

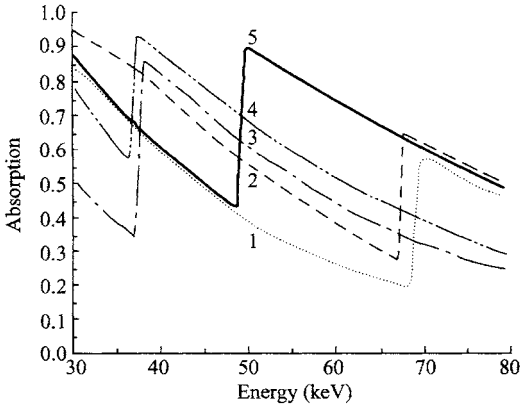


Figure 10.10 X-ray absorption of 200 μm thick screens of (1) $CaWO_4$, (2) $YTaO_4$, (3) BaFCl, (4) LaOBr, and (5) Gd_2O_2S. Reproduced with permission from Elsevier Science (Brixner, 1987)

BaFCl: Eu is a blue-emitting X-ray phosphor. The emission under UV light excitation is shown in Fig. 10. 11a, which is similar to the X-ray excited emission. The emission band at around 390 nm is attributed to the $4f^6 5d \rightarrow 4f^7 ({}^8S_{7/2})$ transition of Eu^{2+}. The sharp line at 362.2 nm overlapping on the emission band is ascribed to the $4f^7({}^6P_{7/2}) \rightarrow 4f^7({}^8S_{7/2})$ transition of Eu^{2+}. In Fig. 10. 11, some alkaline earth fluoro-halides do exhibit this f – f transition, but some do not show it. The appearance of this f-f transition depends on whether the lowest excited level of the 5d state is lower or higher than the $4f({}^6P_{7/2})$ state, which is, in turn, determined by the crystal field strength acting on the splitting of the 5d state (Su and Lin, 1986).

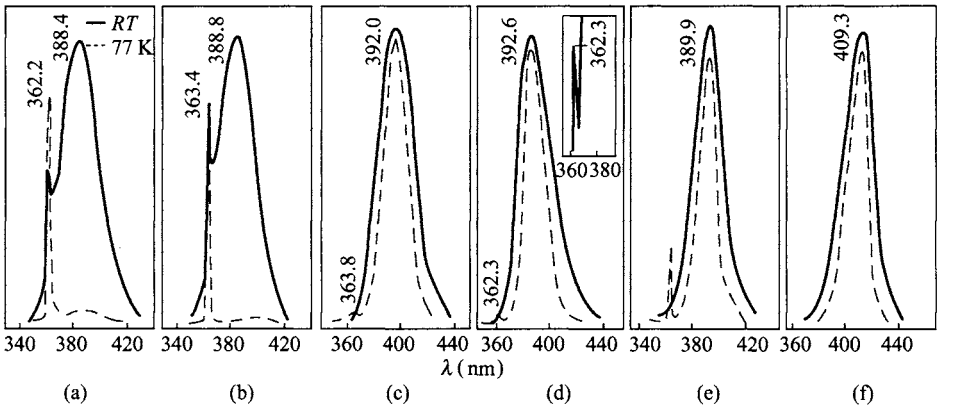


Figure 10. 11 Emission spectra of MFX: Eu^{2+} ($M = Ca^{2+}$, Sr^{2+}, Ba^{2+}; $X = F^-$, Cl^-, I^-) under excitation of UV light at room temperature (solid line) and liquid N_2 temperature (dash line). (a) BaFCl: Eu; (b) SrFCl: Eu; (c) CaFCl: Eu; (d) BaFBr: Eu; (e) SrFBr: Eu; (f) BaFI: Eu

Pure BaFCl: Eu shows an extensive lag, i. e. a delayed emission after X ray excitation. This lag is caused by thermally detrapped electrons from some shallow color centers. It can be eliminated by adding a very small amount of KCl to the phosphor blend before firing.

10.2.4 Tb- and Tm-activated Lanthanum Oxybromides

Tb^{3+}- and Tm^{3+}- activated LaOBr phosphors have been used to manufacture good intensifying screens commercially. The host LaOBr is isostructural with BaFCl, where O^{2-} replaces F^- and La^{3+} replaces Ba^{2+} in the lattice. Its cell parameters are: $a = 4.145$ Å, $c = 7.359$ Å, $V = 126.4$ Å^3, and $d_{X\text{-ray}} = 6.13$ g/cm^3.

Phosphor-quality host LaOBr is prepared by firing a blend of La_2O_3 and NH_4Br with some KBr as a flux. It crystallizes in a plate-like morphology with a layered structure similar to BaFCl.

LaOBr is slightly hydroscopic, which could cause phosphors made of it to lose their luminescence gradually. The mechanism of deterioration of LaOBr has been studied by electroconductivity and thermal gravimetry measurements in combination with X-ray power diffraction analysis (Su and Wang, 1982; Schwarz et al., 1993). It was found that LaOBr deterioration undergoes the steps of moisture adsorption, hydration by forming $LaOBr \cdot H_2O$, and hydrolysis by forming $La(OH)_2Br$ and, finally, $La(OH)_3$. Once the intermediate hydrolysis product $La(OH)_2Br$ is formed, the degeneration is accelerated. We have found that the phase purity of the phosphor LaOBr: Tb plays an important role in its stability. A treatment of the LaOBr-based phosphor, such as washing it with dilute acetic acid to remove any hydrolysis intermediates that might exist, would improve its stability. Prevention of hydrolysis can also be achieved by coating the phosphor particle layer surface with a film of a water-insoluble transparent compound formed by a surface reaction. Some water-soluble inorganic salts, Na_2MoO_4, Na_2WO_4, and KF etc., are used as reactants to treat the phosphor.

When excited by X-rays, Tb^{3+}-activated LaOBr emits blue light, which comes mainly from $Tb^{3+}\ ^5D_3 \rightarrow\ ^7F_j$ transitions at Tb^{3+} concentrations smaller than 0.03 mol per mol LaOBr, and green light of mainly $Tb^{3+}\ ^5D_4 \rightarrow\ ^7F_j$ transitions at Tb^{3+} concentrations higher than 0.03 mol per mol LaOBr. This color change is due to the cross-relaxation between Tb^{3+} ions at high concentrations. Tm^{3+}-activated LaOBr is an even better X-ray phosphor than LaOBr: Tb, particularly in combination with a blue-sensitive film (Schwarz et al., 1993). It emits in the UV and blue region, as shown in Fig. 10.12.

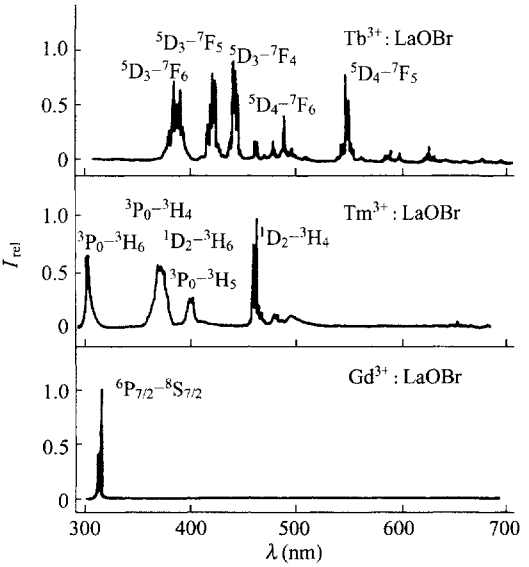


Figure 10.12 X-ray excited emission spectra of Tb^{3+}: LaOBr, Tm^{3+}: LaOBr and Gd^{3+}: LaOBr (Schwarz et al., 1993). Reproduced with permission from Elsevier Science

In the case of LaOBr: Tm^{3+}, Gd^{3+} (Schwarz et al., 1993), the overall efficiency of the phosphor increases markedly due to the additional Gd^{3+} emission at 315 nm, the intensity of which accounts for nearly 35 percent of that of a phosphor doped only by Tm^{3+}.

10.2.5 Tb^{3+}-activated Gadolinium Oxysulfide

Gd_2O_2S: Tb^{3+} was developed in the search for advanced phosphors for color TV and lamps in the late sixties. It was soon recognized as an excellent X-ray phosphor. Its fundamental properties were described by Tekotzky (Tekotzy, 1968) and Wichersheim (Wichersheim et al., 1970).

The crystal structure of the matrix Gd_2O_2S has been reported by Zachriasen (Zachariasen, 1949) and Eick (Eick, 1958). All Ln_2O_2S rare earth oxysulfides (Ln = La – Lu) crystallize in P3m1 hexagonal symmetry. The structure of Gd_2O_2S is shown in Fig. 10.13, where Gd is 7-coordinated by 3 sulfur atoms and 4 oxygen atoms. The cell constants are a = 3.8514(5) Å and b = 6.667(2) Å. The density of Gd_2O_2S is summarized in the Table 10.2 together with those of two other rare earth oxysulfides, Y_2O_2S and La_2O_2S.

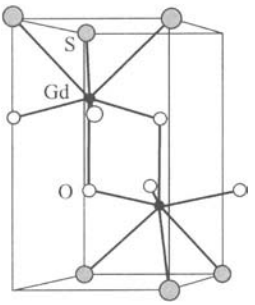


Figure 10.13 The structure of Gd_2O_2S showing 7-coordinated Gd(Brixner, 1987). Reproduced with permission from Elsevier Science

Table 10.2 Densities of Tb-doped Ln_2O_2S

Composition	Density (g/cm^3)
Y_2O_2S: Tb	4.90
La_2O_2S: Tb	5.73
Gd_2O_2S: Tb	7.34

Under X-ray and UV light excitation, all of the Tb-doped Y_2O_2S, La_2O_2S, and Gd_2O_2S show blue emissions of Tb^{3+} $^5D_3 \rightarrow {}^7F_j$ manifold transitions at lower Tb concentrations and show mainly yellowish green emissions of Tb $^5D_4 \rightarrow {}^7F_j$

transitions at higher Tb concentrations.

The Gd_2O_2S: Tb phosphor is prepared by a solid state reaction of a blend of Gd_2O_3, Tb_4O_7, sulfur, and Na_2CO_3 at 1100 ℃ in the presence of K_3PO_4 as a flux. During this process, rare earth oxides are partially sulfurized to oxysulfides by sodium polysulfide, which is formed from S and Na_2CO_3. After the flux is cooled and excess sodium polysulfide is washed out with water by decantation, the phosphor is recovered by filtration, washing with alkaline water (pH = 11), and drying. Gd_2O_2S: Tb crystallizes in near perfect polyhedra. It exhibits superior absorption of X-rays and high efficiency for X-ray-to-light conversion of about 18%.

An intensifying screen of Gd_2O_2S: Tb requires a combination with a green sensitive X-ray film that needs a stricter safe-light procedure in a hospital darkroom for developing. The exposure on the combination of a Gd_2O_2S: Tb screen with a green-sensitive film corresponds to a panchromatic exposure, therefore the image quality can be greatly improved.

10.3 X-ray Storage Phosphors and Their Applications

As we discussed in section 10.1, X-ray storage phosphors can store X-ray energy temporarily. Under optical or thermal stimulation, the stored energy could be released as luminescence.

Thermally stimulable phosphors, such as CaS: Dy, Mg_2SiO_4: Tb, and LiF: Mg, Ti, have been used in personal radiation dosimeters. As they are irradiated by ionizing radiation, color centers are created and accumulated in the matrices with concentrations proportional to the absorbed radiation dosage. By heating them to certain temperatures, the irradiated phosphors will give rise to luminescence with corresponding intensity.

As for the photostimulable X-ray storage phosphors, the stored X-ray energy can be released as luminescence by the stimulation of light of longer wavelength than the emission wavelength. About seventeen years ago, Fuji Film Corporation in Japan introduced a new technique for X-ray imaging. This technique uses the photostimulable X-ray storage phosphor BaFBr: Eu to make the image plate(IP) as a new area detector for X-rays. Computed diagnostic radiography and automated X-ray diffraction systems for crystallography have been constructed utilizing the IP (Takahashi et al., 1985; Sonada et al., 1983; Amemiya et al., 1987). The IP receives and stores X-ray photons that penetrate through a human body or are diffracted by a crystal. A two-dimensional latent image is formed as a distribution of trapped electrons and holes. The traps are localized energy states in the band gap due to lattice defects and impurities. If the trap depth E is much larger than the value of kT, the probability for electron thermal escape from the trap will be negligibly small and a metastable state is created at room temperature (von Seggern, 1992).

The stored latent image is read out and recovered as luminescence by X-Y scanning the IP with a focused He-Ne laser beam of 632.8 nm within microseconds. The integrated luminescent intensity given off at a stimulated point

on the IP is proportional to the concentration of trapped electrons and holes, which is, in turn, proportional to the number of X-ray photons absorbed at that point during X-ray irradiation. With the aid of a photomultiplier tube and an analog-to-digital converter, the luminescence is detected, and a digital image is formed. The digital image can be processed for spatial frequency and gradational enhancement by a computer so a high quality image can be obtained. It can be displayed on a screen, printed on a film by a laser camera, or stored on a CD. The digital image can also be stored in the PACS (Picture Archiving and Communication System), which would facilitate remote diagnosing of illness.

The IP-based computed radiography system offers several advantages over the conventional screen film radiography. The IP has high sensitivity, a wide dynamic range, a large effective area, and a reduced exposure time by one to two orders of magnitude shorter than that required by the conventional screen-film combination radiography. The response of the IP to the X-ray irradiation is linear over at least five orders of magnitude in X-ray dosage ($10^{-3} - 10^{2}$ mR). This wide dynamic range prevents overexposure and underexposure and results in a good image. The high sensitivity is also because the system adopts a photomultiplier tube that has high efficiency of light-to-electricity conversion. Therefore, the IP-based computed radiology system benefits the medical diagnostics tremendously.

In addition to the above-mentioned advantages in medical diagnostics, the IP-based computed radiology system can also be used in crystallography, especially for determining the structure of organic, genetic, and biological specimens, such as proteins and viruses that might be damaged by long duration X-ray irradiation (Bilderback, 1988). Many other applications of the IP-based computed radiology system have also been foreseen (Amemiya et al., 1987).

A good X-ray storage phosphor has to meet a number of requirements:

(1) A high yield of photostimulated luminescence (PSL), which minimizes the noise contribution due to photon intensity fluctuations.

(2) A high X-ray absorption coefficient, which reduces the contribution of quantum noise and minimizes the doses required for a high quality image.

(3) The existence of certain kinds of defects in its band gap, which serve as the electron and hole traps for a long term storage.

(4) A good separation between the PSL emission wavelength and the wavelength of the stimulating light.

(5) A short PSL emission decay time (< 1 μs), which provides fast readout of the stored information by fast laser beam scans and minimizes the overlap of signals from neighboring areas of the image.

(6) A wide dynamic range of the PSL intensity with the irradiation dose (Gurvuch et al., 1996).

10.3.1 Physical Mechanism of Photostimulated Luminescence

As an excellent X-ray storage phosphor currently used for commercial computed clinical radiography and X-ray crystallography, the PSL mechanism of BaFBr:

Eu^{2+} has drawn a lot of attention.

The inventors of the phosphor, Takahashi et al., have proposed a simple model for the process of X-ray irradiation and photostimulation of the phosphor (Takahashi et al., 1984; Iwabuchi et al., 1994). They proposed that upon X-ray irradiation, some holes are trapped by Eu^{2+} ions, forming Eu^{3+} ions, and some electrons are trapped by halide vacancies by forming F centers. Thus X-ray energy is stored temporally. Upon photostimulation by a He-Ne laser beam of 632.8 nm, the phosphor would liberate the trapped electrons, which in turn recombine with the Eu^{3+} ions, resulting in the radiation transition of Eu^{2+} from the $4f^6 5d$ excited state to the $4f^7$ ground state. This transition gives rise to a characteristic blue emission of 390 nm.

Our group has also proposed a quite similar simplified model for the PSL processes of Ce-, Pr-, Sm-, and Tb-doped BaFX phosphors (X = Cl, Br). There are some common features of the PSL of these phosphors (Lin and Su, 1988). A proposed mechanism for the X-ray excitation and optical stimulation process of BaFCl: Ce^{3+} is depicted in Fig. 10.14.

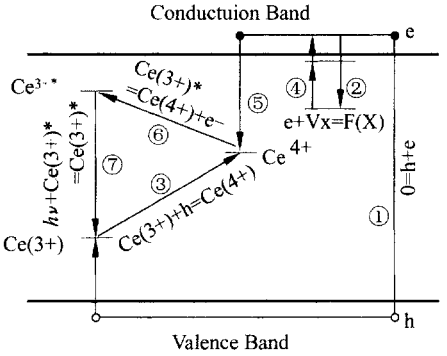


Figure 10.14 A proposed mechanism of photostimulated luminescence of BaFCl: Ce^{3+} crystal (Lin and Su, 1988). Reproduced with permission from Elsevier Science

Lately many detailed investigations have revealed that the above-suggested model for the PSL process of BaFBr: Eu^{2+} is too simplified. This model has some contradiction with experimental results (Su et al., 1995): (1) The concentration ratio of Eu^{2+}/Eu^{3+} in BaFBr: Eu crystals remains unchanged, i.e., no more Eu^{3+} is formed during X-ray irradiation. This indicates that Eu^{2+} ions are not ionized by X-ray irradiation to Eu^{3+}. (2) The linear response of BaFBr: Eu to a dose of X-rays extends over a wide range of 5 orders of magnitude from 10^{-3} to 10^2 mR. That is to say that the response is not limited by the minute amount, i.e. 10^{-3} mol, of Eu^{2+} doped in the crystal. (3) The PSL intensity of X-ray irradiated BaFBr: Eu decays from the radiative transition of activator Eu^{2+} ions exponentially. It is observed that the PSL lifetime of BaFBr: Eu^{2+} is identical to its photoluminescence (PL) lifetime, 0.75 μs, while the discrete PL of BaFBr: Eu^{2+} originates from the transition $4f^6 5d \rightarrow 4f^7$ of Eu^{2+}. It

is reasonable to assume that in a PSL process there is an electron-hole recombination step prior to the radiative transition of the Eu^{2+} ions. Because the lifetimes of PSL and PL are equal, the electron-hole recombination step should be a very fast process with negligible duration. That means that the electrons stimulated from the traps perhaps recombine with trapped holes directly through tunneling, not via the conduction band. (4) The recombination through tunneling can be further confirmed by temperature-dependence studies of PL, PSL, and photostimulated electroconductance (PSC) of BaFBr: Eu. Our experiments show that the temperature-dependent luminescence of PL and PSL is the same and both are practically temperature independent (Dong and Su , 1995; Zhao and Su, 1993). But the PSC of BaFBr: Eu is definitely thermally activated and temperature dependent, i. e., it increases as the temperature is raised. (5) The PSL decay curves of BaFBr: Eu under continuous photostimulation with a He-Ne laser at different temperatures indicate that the PSL intensity I decays linearly as the photostimulation time t increases by following $I \propto 1/(t+\eta^{-1})$, where η is an experimental parameter that depends upon the temperature, the duration of X-ray irradiation, and the wavelength and intensity of the stimulating light. The result indicates that the PSL decay obeys the time reciprocal t^{-1} law, which suggests that the PSL of BaFBr: Eu^{2+} proceeds mainly according to a monomolecular recombination mechanism via tunneling (Zhao and Su, 1993).

Seggern et al. at Siemens Research Lab (von Seggern et al., 1988; Thomas et al., 1991) and Spaeth et al. at the University of Paderborn (Hangleiter et al., 1990; Spaeth et al., 1993) have conducted more detailed investigations on the mechanism of the PSL process of BaFBr: Eu^{2+}. Seggern et al. proposed a model in which the F center after X irradiation has to be in close proximity to the recombination center of a Eu^{2+}-hole complex. The electron transport was assumed to be photostimulated tunneling from the relaxed excited state of the F center into the recombination center thus forming an excited Eu^{2+} ion that gives rise to the Eu^{2+} emission. Speath presented direct experimental evidence that the X-ray created electron centers, hole centers, and the Eu^{2+} activators are correlated spatially and not statistically distributed by measuring cross-relaxation effects among them using optically detected electron paramagnetic resonance. They also found that BaFBr still retained 50 ppm or more O^{2-} even after treated with special procedures for removing oxygen (Koschnick et al., 1992). The inevitably existing O^{2-} impurities in ordinarily prepared BaFBr form point defects of O_{F-}, which are charge compensated by halide vacancies V_x^+ (F^+ centers). During X ray irradiation, holes are trapped by O_{F-}, to form O_{F+}, and electrons are trapped by F^+ centers to form F centers. Therefore, a PSL center in BaFBr: Eu^{2+} consists of a spatially correlated F center, an O_{F-}, center and a Eu_{Ba}^+ center.

These results illustrate how complex and difficult it is to explain the mechanism of X-ray excited and photostumulated luminescence in a simple compound like BaFBr.

Today the PSL physical mechanism of BaFBr: Eu is still incompletely understood, though it has presented important practical applications. The

understanding of the mechanism may ultimately reveal new features of this phosphors and help us to design new PSL phosphors for potential applications. The mechanisms of other storage phosphors may be different, but no systematical studies have been conducted yet. We expect that more investigations and new results will appear in the coming years (Schweizer, 2002).

10.4 X-ray Phosphors for Computed Tomography

By means of X-ray computed tomography (CT), it is possible to construct a cross-sectional image of a human body. The prototype of the CT was introduced by Hounsfield in 1972 (Hounsfield and Brit, 1972). In this system, the X-ray tube and the detector are rigidly coupled and rotated around a patient in the scan. During the rotation, a planar, fan-shaped beam of X-rays passes through a cross-sectional slice of the patient's body and strikes the detector. The fan-shaped X-ray beam is coupled with as many as 1000 single detector elements. The principle is shown in Fig. 10.15.

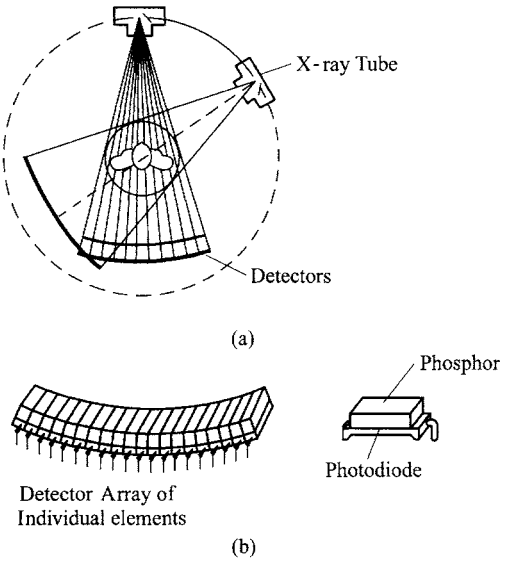


Figure 10.15 (a) Scanning system of X-ray CT with fan-beam design and rotation principle. (b) Solid state detector scanner for CT (Blasse and Grabmaier, 1994). Reproduced by permission

During a scan, the X-ray tube-detector system executes a 360° rotation around a body within one to two seconds. After one rotation scan at one part of the body, the body is moved horizontally at an equal distance and irradiated rotationally again. Each part of the body is scanned and irradiated from several different viewing directions. Thus, it is able to get the X-ray attenuation profiles of each part in three dimensions. The 1000 detector channels generate sequential

electronic signals corresponding to the beam attenuation. The electronic signals are digitized and processed by a computer, which results in a computed tomography image of the patient.

Each detector element of 1 mm width is made by a single crystal of a X-ray phosphor that is coupled with a photodiode. The array of 1000 individual detectors is arranged along the rotation circle in opposition to the X-ray tube. The geometric arrangement of the X-ray source and the collimation of the X-rays to the detector array determine the spatial resolution of the CT system.

The key feature of the CT is not the spatial resolution but the contrast resolution, which should have an accuracy of a few parts per thousand within a dynamic range of 10^6. X-ray attenuation of a few percent in soft tissue parts has to be detected and differentiated precisely from the highest attenuation, in the case of bones, simultaneously. Therefore the properties of a good CT phosphor have to satisfy the following requirements:

(1) The X-ray absorption coefficient should be high, i. e., the phosphor compound should contain elements of high atomic number and have a high density.

(2) The X ray conversion efficiency and optical quality should be high, which would result in high light output.

(3) The emission spectrum should match the spectral sensitivity of the photodiode.

(4) A fast decay (<0.1 ms) with low afterglow is necessary because it can prevent image degeneration from memory effects.

(5) Phosphors have to meet some technical requirements, such as chemical stability, non-toxicity, stability under irradiation, and machining processibility.

Through the two decades of X-ray CT history, image quality has been improved considerably. Today CT images show high contrast and fine spatial resolution of bone structures as well as soft tissue parts. Advanced image quality comes from the improvement in computer techniques, image reconstruction, and X-ray detection. The detection system itself plays an essential role in delivering the database for image reconstruction.

For advances in X-ray detection, scintillator-based solid state detectors have been used successfully, based on their high conversion efficiency, high light output, and low afterglow behavior. The characteristic data of such single crystal scintillators are listed in Table 10.3 together with some new ceramic phosphors.

Among these phosphors, NaI: Tl is not suitable for CT detectors because of the serious afterglow, hydroscopic behavior, and mismatched emission maximum in the blue region. The light outputs of $ZnWO_4$ and $Bi_4Ge_3O_{12}$ are too low for X-ray CT applications. Thallium-doped cesium iodide CsI: Tl, one of the most efficient scintillators, is widely used in the X-ray CT, but it shows an excessive afterglow, which cannot be improved by co-doping. In addition, its light output depends on the irradiation history. One promising single crystal is cadmium tungstate $CdWO_4$. It shows an intrinsic luminescence of the WO_4 group with a low afterglow, a short decay time, and a sufficiently high light output. In

Table 10.3 Characteristic data of various phosphors for CT detectors

Phosphors	NaI:Tl	CsI:Tl	$CaWO_4$	$ZnWO_4$	$Bi_4Ge_3O_{12}$	$(Y,Gd)_2O_3:Eu,Pr$	$Gd_2O_2S:Pr,Ce,F$	$Gd_3Ga_5O_{12}:Cr,Ce$
Type	Single crystal	Single crystal	Single crystal	Single crystal	Single crystal	Ceramic	Ceramic	Ceramic
Structure	Cubic	Cubic	Monoclinic	Monoclinic	Cubic	Cubic	Hexagonal	Cubic
Density(g/cm^3)	3.67	4.52	7.99	7.87	7.13	(5.9)	7.34	7.09
Attenuation coeff. 150 keV(cm^{-1})	2.20	3.21	7.93	7.80	9.93	(3.40)	6.86	4.36
Emission maximum (nm)	415	550	480	480	480	610	510	730
Light output 80 keV (rel.)	118	100	30	20	10	~60	~60	~60
Decay time (μs)	0.23	0.98	5	5	0.3	~1000	~3	140
Afterglow	90‰ (150 ms)	7‰–15‰ (20 ms)	<1‰ (3 ms)	<1‰ (30 ms)	<1‰ (20 ms)	~30‰ (3 ms)	≤1‰ (3 ms)	0.01‰
Optical property	Clear	Clear	Clear	Clear	Clear	Transparent	Translucent	Transparent
Chemical stability (attacked by)	Water vapor	Water Vapor	HCl	HCl	Conc. HCl	Conc. HCl	HCl	Conc. HCl
Mechanical behavior	Brittle Cleavable	Plastic Deformable	Brittle Cleavable	Brittle Cleavable	Brittle	Brittle High strength	Brittle High strength	Brittle Low strength

addition, $CdWO_4$ is nearly insensitive to pre-irradiation. However, it is toxic, very brittle and has the tendency to crack during machining.

There are technical problems with using single crystal phosphors for X-ray CT applications, which arise from crystal growth techniques since single crystals can be grown reproducibly and economically only if some distinct and sufficient conditions are fulfilled. These conditions include the congruent melting behavior, melting points below 2000 ℃ for oxide materials, and distribution coefficients of about 1 for dopants that act as activators or sensitizers.

As a consequence, luminescent ceramics are introduced as a new class of scintillators with a wide range of suitable chemical compounds and dopants that include the most important rare earth ions with well-known $4f-4f$ transitions.

10.4.1 Scintillators for X-ray Computed Tomography

As nuclear particles or ionizing electromagnetic radiations strike on the so-called scintillators, pulsed light occurs with a decay time less than 1 μs. This phenomenon is known as scintillation. Today scintillators are widely used in detection of radiation and nuclear particles to give information on quantities, such as the kind of radiations, their intensity and energy, the time of emission, the direction of emission, and the position of emission. Scintillation detection is used in chemistry, high-energy physics, nuclear physics, space physics, materials science, and industry, as well as in medical diagnostics, as mentioned here.

Some existing polycrystalline phosphors have been considered as candidates for use in the X-ray CT with appropriate modifications. These phosphors include lamp and projection-TV phosphor Y_2O_3: Eu, cathode-ray phosphor Y_2O_2S: Eu, X-ray phosphor Gd_2O_2S: Tb, and deluxe lamp and projection-TV garnet phosphors $Y_3Al_5O_{12}$: Ce^{3+} and $(Y, Gd)_3(Al, Ga)_5O_{12}$.

From the point of view of solid state chemistry of phosphors, the first choice of a phosphor for scintillator application is the one with composition $(Y_{1-x}Gd_x)_2O_3$: Eu^{3+}. The matrix is prepared from Y_2O_3 and Gd_2O_3. Both oxides have the same crystalline structure of isotropic cubic type and can form complete solid solutions with Gd_2O_3 content up to 50 mol %. The Gd in the matrix has a high X-ray absorption coefficient. Europium and other rare earth ions can be doped into the matrix to tune its luminescent properties.

The sintered scintillators are prepared under high temperatures and static pressures. Ceramic solid solutions of $(YGd)_2O_3$ can be prepared by several techniques, such as sintering the mixture in different starting forms, including the mechanically mixed oxides, the coprecipitated mixed oxides, and the sol-gel processed mixed oxides, as well as by single crystal growth. In the order of

preparation techniques from the mixture of mixed oxides to single crystal growth, the transparency of resulted ceramics increases, and consequently, their light outputs also increase. The composition dependence of the light output and of the X-ray stopping length of sintered Y_2O_3-Gd_2O_3 (3 mol % Eu_2O_3) is shown in Figs. 10.16 and 10.17, respectively.

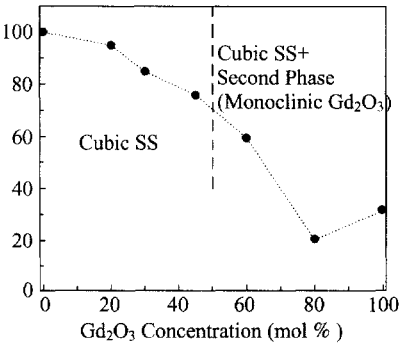


Figure 10.16 The composition dependence of the light output of a sintered scintillator Y_2O_3-Gd_2O_3-Eu_2O_3 (3 mol %) (X-ray: 120 kV, 2 mA, pulse width 1 s)

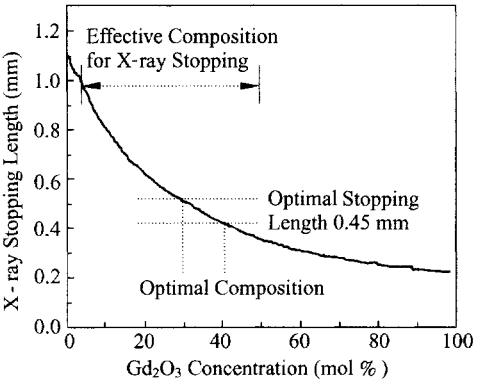


Figure 10.17 Gd_2O_3 concentration dependence of 73 kV X-ray stopping length of a sintered Y_2O_3-Gd_2O_3 solid solution

(Y Gd)$_2O_3$: Eu^{3+} shows the characteristic emissions of Eu^{3+} $^5D_0 \rightarrow {}^7F_j$ transitions, but the decay time is too long for the X-ray CT application. Although the decay time can be shortened by co-doping other rare earth ions, such as Yb^{3+}, Sm^{3+}, Dy^{3+} and Pr^{3+}, the emission intensity is also decreased. In Gd_2O_2S matrix, the Pr^{3+} ion is used as an activator with mainly $^3P_0 \rightarrow {}^3H_j$, ^3F_j emissions and a decay time of 3 μs.

A new scintillator for the X-ray CT is Gd_2O_2S: Pr, Ce, F, the growth of its transparent single crystal under high sulfur pressure is unsuccessful. Therefore its sintered ceramics are sought, which can be prepared at 1500℃ and under high static pressure of 1000 atm (1 atm = 101.325 Pa) of ar gon. The obtained ceramics have a density corresponding to 99.9% theoretical density and are optically translucent (transmittance $T_{1mm} = 45\%$). This phosphor emits green light of Pr^{3+} $^3P_0 \rightarrow {}^3H_j$, ^3F_j transitions and has a decay time of 3 μs. It can be coupled with a silicon photodiode to construct a detector element (Fig. 10.18), of which the detecting sensitivity is 1.3 to 1.5 times larger than that of a Xe-ionization detector and 1.8 times larger than that of a $CdWO_4$ detector.

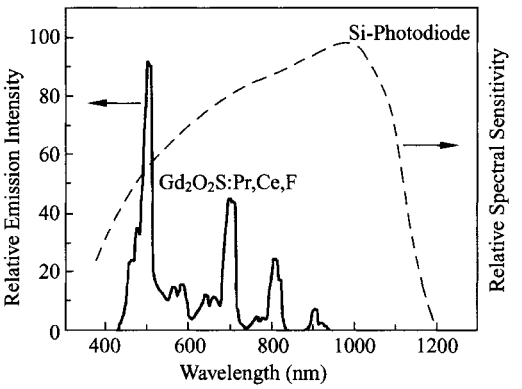


Figure 10.18 Emission spectrum of ceramic scintillator Gd_2O_2S: Pr, Ce, F(λ_{ex} = 254 nm) and spectral sensitivity of Si-photodiode

$Gd_3Ga_5O_{12}$: Cr, Ce phosphor is also promising for the X-ray CT scintillator application. It yields a broad infrared emission band ranging from 750 nm to 1100 nm due to the $^4T_2 - {}^4A_2$ transition of Cr^{3+} ions in a d^3 configuration. The decay time is relatively long at 140 μs due to the parity selection rule.

In medical diagnostics, scintillators are also used to construct γ ray cameras for measuring the radiation emitted from the radioisotope-labeled compound that is introduced into the body. The γ ray cameras can give a two-dimensional image of the radioactive distribution. This technique is called single-photon emission computed tomography.

The development of very sensitive three-dimensional imaging positron emission tomography (PET) systems is very interesting. PET is also an in-vivo tracer technique, but uses the annihilation of positrons. One is confined to positron emitters for in-vivo studies of the distribution of elements in biologically active compounds, namely, carbon, nitrogen and oxygen. Metabolism of brain, tumor, heart blood flow and oxygen consumption can be studied by PET. The emitted positrons cannot penetrate far into tissues. The distance is only a few millimeters. An emitted positron, after slowing down in tissues, is annihilated

with an electron of the tissues to be studied. Two γ ray photons, with energy of 511 keV, are emitted colinearly with a positron. PET exploits the collinear emission by putting a coincidence arrangement on two detectors opposed to each other. The event detected simultaneously in the two detectors implies that the annihilation takes place somewhere along the line between the two points of the detectors. From the coincidence data, an image is constructed, which presents the three-dimensional distribution of the radioactivity.

10.5 Scintillators for Electromagnetic Calorimetric Detection

There are several ways in which nuclear particles and high energy electromagnetic radiation interact with matter: (1) Charged particles, α- and γ-rays can ionize atoms or excite them to their excited states and result in the radiative transitions; (2) The interaction of neutrons with matter can induce nuclear reactions and then give rise to charged particles or electromagnetic radiation; (3) When γ or X-rays act on matter, there occur the photoelectric effect, Compton effect, and/or pair production dependent on the energy of photons. Nearly all of these effects produce secondary electrons.

One spectacular application of scintillators is in electromagnetic calorimeters. At present, the large high luminosity accelerators with colliding beams for high energy physics produce hundreds of particles at the points of interaction every 20 ns. In the detection systems set up at these points, energies and positions are determined by means of electromagnetic calorimeters. The largest colorimeter was built at CERN, the European Organization for Nuclear Research in Geneva, in late 1980s. It contains 12,000 $Bi_4 Ge_3 O_{12}$ single crystals of 3 cm × 3 cm × 24 cm, grown by the Shanghai Institute of Ceramics, Chinese Academy of Sciences. It can determine the kind of radiations and particles, their intensity, energy, direction, and positions. The energy collected in the calorimeter yields a light of 200 photons per MeV. In order to detect these photons, the scintillators are coupled with photomultiplier tubes, in which the photons are converted into photoelectrons that are multiplied and give a pulse with an amplitude proportional to the number of photons.

Scintillators used for electromagnetic calorimetric detection have some characteristics, i. e., they are ionic crystals with high atomic number atoms and high densities and have high light yields, short decay times, no afterglow, and appropriate emission wavelengths matching the sensitivity of the light sensor.

The existing inorganic scintillators are NaI: Tl, CsI: Tl, $ZnWO_4$, $CdWO_4$, and $Bi_4Ge_3O_{12}$ et al.. In these, CeF_3 and several other trivalent cerium-activated compounds are good scintillators. The luminescence of Ce^{3+} has a short decay time of a few ns because of its fully parity-allowed emission transition 5d→4f. Their properties are listed in Table 10.4.

Table 10.4 Properties of Ce^{3+}-activited scintillators

Host Lattice	Ce^{3+} conc. (mol %)	Emission max. (nm)	Light yield (photons/MeV)	Decay time (ns)	Density (g/cm^3)
BaF_2	0.2	310, 325	7000	60	4.89
LaF_3	10	290, 350	900	27	5.8
CeF_3	100	310, 340	4000	30	6.169
$YAlO_3$	0.1	350, 380	17,000	30	5.55
Gd_2SiO_5	0.5	440	9000	60	6.71
Lu_2SiO_5		420	25,000	40	7.4
Glass	4	390	1500	70	2.5
$Y_2Al_5O_{12}$	0.4	550	14,000	65	5

10.5.1 Cerium Fluoride

CeF_3 is one of the candidates for a new generation of high-precision electromagnetic calorimeters to be used for the new large proton collider to be built in CERN (Geneva). For that purpose, one needs a total crystal volume as large as 60 m^3 (Leoq, 1994), which is nearly two orders of magnitude more than present 1.2 m^3 $Bi_4Ge_3O_{12}$ crystal volume. Therefore, a lot of research has already been performed on CeF_3 (Moses et al., 1994).

Although CeF_3 is a material with 100% activator concentration, the emission of Ce^{3+} in CeF_3 is not quenched at room temperature. Because of the large Stokes shift of Ce^{3+} emission, the emission band is apart from the excitation band, i. e., the spectral overlap between the absorption and the emission is small. As a consequence, $Ce^{3+} - Ce^{3+}$ energy transfer does not occur.

CeF_3 has been investigated by a number of experimental techniques including time-resolved luminescence spectroscopy, ultraviolet photoelectron spectroscopy, and transmission spectroscopy. The excitation region has been extended up to tens of eV by using synchrotron radiation. The emission depends strongly on the excitation energy as shown in Fig. 10.19. Under X-ray excitation, the intrinsic Ce^{3+} emission consists of a narrow band with maxima at about 284 and 300 nm. These are ascribed to transitions from the lowest excited state of the 5d configuration to the two 4f ground state levels, $^2F_{5/2}$ and $^2F_{7/2}$. Under γ ray excitation, an additional emission band appears at longer wavelength centered at 340 nm. This band is ascribed to Ce^{3+} ions close to defects. Extrinsic Ce^{3+} ions are Ce^{3+} ions near to imperfections in the crystal lattice. Actually, the 340 nm emission shows a build-up, which is equal to the decrease of the 290 nm emission. The decay times of these emissions are about 30 and 20 ns, respectively.

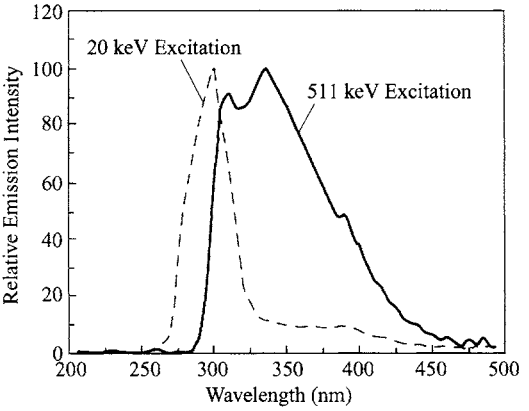


Figure 10. 19 Emission spectra of powdered CeF_3 (20 keV X-ray excitation) and crystalline CeF_3 (511 keV γ ray excitation) (Moses et al., 1994). Reproduced with permission from Elsevier Science

The light yield of the CeF_3 is low, about 4000 photons/MeV, which shows that large part of the emission is quenched. This is because fluoride crystals always contain a small amount of oxide ions, which occupy the fluoride site to form O_F^- defects. The Ce^{3+} ions neighboring those O_F^- defects have to become Ce^{4+} for charge compensation. Thus, a bulky quenching center is created, of which intervalence charge-transfer transitions are at low energy and yield no emission.

10.5.2 Ce^{3+}-activated Gd_2SiO_5 and Lu_2SiO_5

The compound Gd_2SiO_5 has a complicated crystal structure with two crystallographic sites for rare earth ions. The crystal structure of Gd_2SiO_5 shows one Gd^{3+} ion [Gd (Ⅰ)] coordinated by eight oxygen ions belonging to silicate tetrahedron and one oxygen that is not bounded to silicon. The latter oxygen is coordinated tetrahedrally by four rare earth ions. The other Gd^{3+} ion [Gd (Ⅱ)] is coordinated by four oxygen ions belonging to silicate tetrahedron and three oxygen ions that are not. Gd (Ⅱ) ion is more strongly covalently bonded because oxygen ions without silicon neighbors do not have enough positive charge in their immediate surroundings to compensate their two-fold negative charge. Consequently, for Ce^{3+}-activated Gd_2SiO_5, the Ce^{3+} ion replacing the Gd(Ⅱ) ion is at a lower energy level than the Ce^{3+} ion replacing the Gd(Ⅰ) ion (Lammers, 1987).

The compound Gd_2SiO_5 has become popular as a scintillator. Suzuki et al. have investigated the UV- and γ ray excited luminescence of Gd_2SiO_5: Ce^{3+} (Suzuki et al., 1992). They were able to find luminescence at 11 K from two

different Ce^{3+} ions, one with an emission maximum at 425 nm, the other with an emission maximum at 500 nm. The corresponding excitation bands have their maxima at 345 and 380 nm, respectively, and their corresponding decay times are 27 and 43 ns, respectively. Under γ ray excitation at room temperature, the luminescence is dominated by the 425 nm emission. Time decay measurements show that there is an unusual long decay component with τ = 600 ns in Gd_2SiO_5: Ce^{3+}, which is not observed for Y_2SiO_5: Ce^{3+} and Lu_2SiO_5: Ce^{3+}. The long decay component of Gd_2SiO_5: Ce^{3+} can be ascribed to the fact that some electron-hole pairs formed by γ ray irradiation are captured by Gd^{3+} ions. Thus, the excitation energy migrates over the Gd^{3+} ions. In this way the Ce^{3+} ions are populated in a delayed way, so that a long decay component is observed.

The host lattices Lu_2SiO_5: Ce^{3+} and Y_2SiO_5: Ce^{3+} have different crystal structures. Luminescence of Ce^{3+}-activated Lu_2SiO_5 does not show obvious quenching of Ce^{3+} emission at room temperature and, therefore, should give rise to a much higher light yield than Gd_2SiO_5: Ce^{3+}. The scintillator formed by Lu_2SiO_5: Ce^{3+} seems to have more advantages. Unfortunately, the cost of Lu_2O_3 is extremely high, which makes Lu_2SiO_5: Ce^{3+} not be used commercially.

For many years there has been such an opinion that new scintillators should be found through trial and error because the physical mechanism is unknown and theoretical prediction could not be made. But now, this opinion is no longer justified. It is believed that the knowledge from other fields of luminescence, modern experimental instrumentation in studying fundamental processes, and a wide cooperation between materials sciences and physical and chemical sciences such as using novel combinatorial synthesis and screening technology (Sun and Jabbour, 2002), will definitely facilitate the finding of new efficient scintillators.

10.6 Conclusions

Rare earth doped advanced X-ray imaging phosphors have presented numerous applications including medical diagnostics, X-ray crystallography and high energy physics (Dusseau et al., 2001). The understanding of the fundamental aspects of these materials is crucial for these applications. More research is needed to address the physical mechanism of the luminescence of the phosphors by using various advanced techniques, which may provide useful information for the design of new phosphors with unique optical properties for the applications.

References

Amemiya, Y., J. Miyahara. Nature **336**, 89(1988).
Amemiya, Y., K. Wakabayashi, K. Tanaka et al. Science **237**, 164(1987).
Bilderback, D., K. Moffat, J. Owen et al. Nucl. Instrum. Methods A **266**, 636(1988).
Blasse, G., G. J. Cirksen, L. H. Brixner, and M. K. Crawford. J. Alloys Compds. **209**, 1(1994).
Blasse, G., A. Bril. J. Lumin. **3**, 109(1970).

Brixner, L. H. Mater. Chem. Phys. **16**, 253(1987).
Brixner, L. H., H. Y. Chen. J. Electrochem. Soc. **130**, 2435(1983).
Clark, G. *The Encyclopedia of X rays and Gamma Rays* (Reinhold Publishing Corp., New York, 1963).
Dusseau, L., G. Polge, S. Mathias, J. R. Vaille, R. Germanicus, R. Broadhead, B. Camanzi, M. Glase, F. Saigne, F. Fesquet, and J. Gasiot. IEEE Trans. Nucl. Sci. **48**, 2056(2001).
Dong, Y., M. Z. Su. J. Lumin. **65**, 263(1995).
Eick, H. A. J. Am. Chem. Soc. **80**, 63(1958).
Ferguson, R. B. Can. Mineral. **6**, 72(1957).
Gurvuch, A. M., C. Hall, I. A. Kaminskikh, I. H. Munro, V. V. Mikhailin, J. S. Worgan. J. X ray Sci. Technol. **6**, 48 (1996).
Hangleiter, T., F. K. K oschnick, and J. -M. Spaeth et al. J. Phys, Conden. Mat. **2**, 6837 (1990).
Hounsfield, G. N. Brit. J. Radiology **46**, 1016(1972).
Hubbel, J. H. NSRS-NBS, **29**, 7(1969).
Iwabuchi, Y., N. Mori, K. Takahashi, T. Matsuda, and S. Shionoya. J. Appl. Phys. **33**, 178(1994).
Koschnick, F. K., J. -M. Spaith, and R. S. Eachus. J. Phys. Conden. Mat. **4**, 3015 (1992).
Lammers, M. J. J., G. Blasse. J. Electrochem. Soc. **134**, 2068(1987).
Leoq, P. J. Lumin. **60/61**, 948(1994).
Li, B. Ph. D. Thesis, Peking University, 1999.
Lin, J. -H., M. -Z. Su. J. Lumin. **40/41**, 155(1988).
Moses, W. W., S. E. Derenzo, M. J. Weber, F. Cerrina, and A. Ray-Chandhuri. J. Lumin. **59**, 89(1994).
Pupin, M., Radiological Sciences for Technologists, eds. C. V. Mosby, St. Louis, 1975, p. 8.
Schwarz, L., A. M. Gurvich, D. Starick, and G. Herzog. Nucl. Tracks Radiat. Measur. **21**(1), 35(1993).
Schweizer, S. Phys. Status Solidi A-Appl. Res. **187**, 335(2002).
Sonda, M., M. Takano, J. Miyahara, and H. Kato. Radiology **148**, 833(1983).
Sonada, M., M. Takano, J. Miyahara, and H. kato. Radiology **48**, 833(1983).
Spaeth, J. -M., F. K. Koschnick, R. S. Eachus et al., Nucl. Tracks Radiat. Measur. **21**, 73(1993).
Storm, E., H. I. Isreal. Photon cross section from 0.001 to 100 MeV for elements 1 through 100, Report LA 3753 Los Alamos Scientific Lab. University of California, 1967.
Su, M. -Z., W. Zhao, W. Chen, Y. Dong, and J. -H. Lin. J. Alloys Compds. **225**, 539 (1995).
Su, M. -Z., and J. -H. Lin. Chem. J. Chinese Universities **7**(6), 479(1986).
Su, M. -Z., X. -L. Xu, S. -K. Ruan, and M. -L. Gong. J. Less-Common Met. **93**, 36 (1983).
Su, M. -Z., Y. -J. Wang. Chem. J. Chin. Universities **3**, 7(1982).
Sun, T. X., G. E. Jabbour. MRS Bull. **27**, 309(2002).
Suzuki, H., Y. A. Tombrello, C. L. Melcher, and J. S. Schweitzer. Nucl. Instrum. Methods A **320**, 263(1992).
Takahashi, K., J. Miyahara, and Y. Shibahara. J. Electrochem. Soc. **132**, 1492(1985).
Takahashi, K., K. Kohda, J. Miyahara, Y. Kanemitsu, K. Amitani, and S. Shionoya, J. Lumin. **31/32**, 266(1984).
Tekotzy, M. Electrochem. Soc. Meeting Boston, 5(1968).
Thomas, M., H. von Seggern, and A. Winnacker. Phys. Rev. B **44**(17), 9240 (1991).
von Seggern, H. Nucl. Instrum. Methods A **322**, 467 (1992).

von Seggern, H. T. Voigt, and K. Schwarzichel. Siemens Forsch. Entwickl. Ber. **17**(3), 125(1988).
Wichersheim, K. A., R. A. Alves, R. A. Buchanan. IEEE Trans. Nucl. Sci. **17**(1/2), 57 (1970).
Wolten, G. M. Acta Cryst. **23**, 939(1967).
Zachariasen, W. H. Acta Cryst. **2**, 60(1949).
Zhao, W., M. -Z. Su. Mater. Res. Bull. **28**(2), 123(1993).

Appendix A Effective Operator Calculations

M. F. Reid

Effective operators are used in many types of calculations. They have found wide use in calculations relevant to the spectra of rare-earth systems, where calculations are carried out (as in Chapters 1 and 2) using matrix elements of operators between pure $4f^N$ states or between $4f^N$ and $4f^{N-1}$ 5d states.

The purpose of this appendix is to provide a brief introduction to the concept of effective operators and some of the issues that surround their use. A large literature exists and the interested reader is urged to refer to that literature for clarification of the many subtleties in this area (Brandow, 1967; Hurtubise and Freed, 1993, 1994; Bryson and Reid, 1998; Newman and Ng, 2000; Duan and Reid, 2001; Naguleswaran et al., 2003). In this Appendix we concentrate on explaining the concepts, rather than rigorous derivations.

A.1 Effective Hamiltonians and Effective Operators

Effective Hamiltonians and effective operators are defined within a model space M. In most cases of interest in this book the model space is the $4f^N$ configuration.

Consider eigenstates of the full Hamiltonian H,

$$\mathscr{H}|a\rangle = E_a|a\rangle. \tag{A.1}$$

The aim is to define an effective Hamiltonian H_{eff} that gives identical eigenvalues for model-space eigenstates $|a_0\rangle$, i.e.

$$\mathscr{H}_{\text{eff}}|a_0\rangle = E_a|a_0\rangle. \tag{A.2}$$

Transformations may be defined that connect the full states and the model-space states:

$$|a\rangle = k|a_0\rangle \tag{A.3}$$

and

$$|a_0\rangle = l|a\rangle. \tag{A.4}$$

There is some flexibility (and many subtleties) in the choice of k and l. In the simplest case l is simply the projection operator for the model space (commonly written as P) and k is the wave operator (commonly written Ω). However, this choice can lead to non-intuitive behavior such as non-orthogonal model-space eigenstates and non-Hermitian effective operators. This is not a significant issue for most energy-level calculations, but is problematical for intensity calculations. Fortunately, it is possible to choose a canonical operator $\hat{k}$ so that

$$|a\rangle = \hat{k}\,|a_0\rangle \tag{A.5}$$

and

$$|a_0\rangle = \hat{k}^\dagger\,|a\rangle. \tag{A.6}$$

Note that $\hat{k}$ transforms between two spaces of different dimension, and while, $\hat{k}^\dagger\hat{k}=1$, $\hat{k}\hat{k}^\dagger\neq 1$ (but is, instead, the model-space projection operator).

In our development we will use the $\hat{k}$ operator. This has little effect at low order, but it should be noted that for higher orders of perturbation the requirement of Hermiticity and normalization leads to expressions that are more complex than those commonly found in quantum-mechanics texts.

In analogy to an effective Hamiltonian an effective operator (such as the operator for a dipole moment) has the same matrix elements between the model eigenstates as the full operator has between the full eigenstates, i.e.

$$\langle b_0\,|\,A_{\text{eff}}\,|\,a_0\rangle = \langle b\,|\,A\,|\,a\rangle. \tag{A.7}$$

This implies that the effective operator may be calculated from

$$A_{\text{eff}} = \hat{k}^\dagger A \hat{k}. \tag{A.8}$$

A.2 Perturbation Expansions

The transformations discussed in the previous section are seldom used directly. In a realistic calculation it is impossible to use the "full" space and the usual approach is to construct H_{eff}, $\hat{k}$, and A_{eff} using a time-independent Rayleigh-Schrödinger perturbation expansion. The Rayleigh-Schrödinger (rather than the Brillioun-Wigner) form is used so that the effective Hamiltonian and effective operators do not depend on the exact energies of the states. This has many important consequences, such as the symmetry arguments presented below. It is also essential to the development of a "linked-diagram" perturbation expansion (Hurtubise and Freed, 1994), the details of which we will not go into here. Perhaps the most obvious practical reason for using the Rayleigh-Schrödinger

expansion is that the energy-level and transition-intensity calculations discussed in Chapters 1 and 2 make use of matrices that need to be generated only once, then combined together, multiplied by phenomenological or *ab initio* values of the appropriate parameters. Dealing with matrices whose elements changed as the Hamiltonian parameters were varied would be completely impractical.

The first step in a perturbation-theory calculation is to partition the Hamiltonian into a zero-order part $\mathscr{H}_0$ and a perturbation V. The total Hamiltonian is

$$\mathscr{H} = \mathscr{H}_0 + V. \tag{A.9}$$

Eigenstates of $\mathscr{H}_0$ are labeled with Greek letters,

$$\mathscr{H}_0 \mid \alpha\rangle = E_\alpha^{(0)} \mid \alpha\rangle, \tag{A.10}$$

and the eigenstates of H with Roman letters,

$$\mathscr{H} \mid a\rangle = E_a \mid a\rangle. \tag{A.11}$$

An effective (e. g. crystal field) Hamiltonian H_{eff} may now be constructed to act within the model space M. The equations are simpler if all members of M are eigenstates of $\mathscr{H}_0$ with identical eigenvalues, E_0, i. e. the model space is *degenerate*. This simplification will be used in what follows.

In the case of particular interest here the model space is the $4f^N$ configuration and a typical choice for H_0 is the Hartree-Fock Hamiltonian (see Chapter 1). The perturbation V is then a sum of several terms:

$$V = V_{\text{Coulomb}} + V_{\text{spin-orbit}} + V_{\text{CF}} + \cdots, \tag{A.12}$$

This expression includes the non-spherical part of the potential arising from the Coulomb repulsion between the 4f electrons, the spin-orbit interaction, and the crystal field potential V_{CF} arising from the interaction of the ion with its ligands. The model-space eigenstates $\mid a_0\rangle$ will be linear combinations of the $\mid 4f^N \alpha SLJM\rangle$ states

We require an effective Hamiltonian that gives identical eigenvalues for model-space states as the full Hamiltonian does for the complete states (Eqs. (A. 1) and (A. 2)). This leads to a Rayleigh-Schrödinger perturbation expansion for $\mathscr{H}_{\text{eff}}$ (Hurtubise and Freed, 1994):

$$\mathscr{H}_{\text{eff}} = \mathscr{H}_0 + V + \sum_{\beta \notin M} \frac{V \mid \beta\rangle\langle\beta \mid V}{E_0 - E_\beta^{(0)}} + \sum_{\gamma \notin M} \sum_{\beta \notin M} \frac{V \mid \gamma\rangle\langle\gamma \mid V \mid \beta\rangle\langle\beta \mid V}{(E_0 - E_\gamma^{(0)})(E_0 - E_\beta^{(0)})}$$

$$-\frac{1}{2}\sum_{\beta\notin M}\sum_{\alpha\in M}\frac{V|\beta\rangle\langle\beta|V|\alpha\rangle\langle\alpha|V}{(E_0-E_\beta^{(0)})^2}$$
$$-\frac{1}{2}\sum_{\alpha\in M}\sum_{\beta\notin M}\frac{V|\alpha\rangle\langle\alpha|V|\beta\rangle\langle\beta|V}{(E_0-E_\beta^{(0)})^2}$$
$$+\cdots \qquad (A.13)$$

where M refers to the model space. This expression is more symmetrical than expressions that the reader may encounter in quantum-mechanics textbooks. This symmetry is necessary to ensure that $\mathscr{H}_{\text{eff}}$ is Hermitian.

The eigenstates of $\mathscr{H}_{\text{eff}}$ (i. e. the phenomenological crystal-field eigenstates) are $|a_0\rangle$ and the exact states may be generated by

$$\begin{aligned}|a\rangle &= |a_0\rangle + \sum_{\beta\notin M}\frac{|\beta\rangle\langle\beta|V|a_0\rangle}{E_0-E_\beta^{(0)}}\\ &+\sum_{\gamma\notin M}\sum_{\beta\notin M}\frac{|\gamma\rangle\langle\gamma|V|\beta\rangle\langle\,|V|a_0\rangle}{(E_0-E_\gamma^{(0)})(E_0-E_\beta^{(0)})}\\ &-\sum_{\beta\notin M}\sum_{\alpha\in M}\frac{|\beta\rangle\langle\beta|V|\alpha\rangle\langle\alpha|V|a_0\rangle}{(E_0-E_\beta^{(0)})^2}\\ &-\frac{1}{2}\sum_{\alpha\in M}\sum_{\beta\notin M}\frac{|\alpha\rangle\langle\alpha|V|\beta\rangle\langle\beta|V|a_0\rangle}{(E_0-E_\beta^{(0)})^2}\\ &+\cdots \qquad (A.14)\end{aligned}$$

The last term is a normalization factor. In eqs. (A. 13) and (A. 14) we have carried the expansion to second order in V. Though in Chapters 1 and 2 we only make explicit use of the expressions up to first order in V it is important to realize that taking the calculations to higher order is a rather complex matter.

We can now use equation (A. 14) to write the matrix elements of an effective operator (such as the dipole-moment operator), recalling that $E_i^{(0)} = E_f^{(0)} \equiv E_0$. To first order in V as the effective operator is

$$\begin{aligned}\langle b|A|a\rangle &= \langle b_0|A|a_0\rangle + \langle b_0|A\sum_{\beta\notin M}\frac{|\beta\rangle\langle\beta|V}{E_0-E_\beta^{(0)}}|a_0\rangle\\ &+\langle b_0|\sum_{\beta\notin M}\frac{V|\beta\rangle\langle\beta|}{E_0-E_\beta^{(0)}}A|a_0\rangle\\ &+\cdots \qquad (A.15)\end{aligned}$$

Higher-order expressions are easily derived from Eq. (A. 14) (Hurtubise and Freed, 1994; Bryson and Reid, 1998).

We require an effective operator A_{eff} such that the matrix elements of A_{eff}

between eigenstates of H_{eff} are identical to the matrix elements of A between the exact eigenstates (if the expansion is carried to infinite order), i. e.

$$\langle b_0 \mid A_{\text{eff},q} \mid a_0 \rangle = \langle b \mid A \mid a \rangle. \tag{A.16}$$

The required operator may be read from Eq. (A. 15) as follows

$$A_{\text{eff}} = A + A \sum_{\beta \notin M} \frac{|\beta\rangle\langle\beta| V}{E_0 - E_\beta^{(0)}} + \sum_{\beta \notin M} \frac{V|\beta\rangle\langle\beta|}{E_0 - E_\beta^{(0)}} A + \cdots \tag{A.17}$$

The denominators in the two summations in Eq. (A. 17) are equal term by term and if A is Hermitian then the effective operator is also Hermitian. We refer the reader to Hurtubise and Freed (1993, 1994) for a careful discussion showing that for Hermitian operators (such as the dipole moment operator) it is always possible to construct effective operators that are Hermitian Hurtubise and Freed (1993) and perturbation expansions that are Hermitian order by order in V Hurtubise and Freed (1994). Note that the right hand side of Eq. (A. 17) is only defined for the model space. We have omitted model-space projection operators from our equations for the sake of clarity.

A. 3 Symmetries and Selection Rules

An important feature of effective-Hamiltonian and effective-operator calculations is that if the canonical transformation $\hat{k}$ is used then symmetries and selection rules for the full Hamiltonian also apply to the effective Hamiltonian (Hurtubise and Freed, 1993). If the Hamiltonian commutes with a symmetry operator S

$$[H,S] = 0 \tag{A.18}$$

then the model-space projections of H and S also commute:

$$[H_{\text{eff}}, S_{\text{eff}}] \equiv [\hat{k}^\dagger H \hat{k}, \hat{k}^\dagger S \hat{k}] = 0 \tag{A.19}$$

The existence of these commutation relations within the model space is essential for any application of symmetry arguments and is implicit in most treatments of crystal field calculations. Eq. (A. 19) implies that if the full Hamiltonian is symmetric under certain operations (rotations, reflections, Hermitian conjugation, time reversal, etc.), then so is the effective Hamiltonian.

It is important to realize that not all commutation relations apply in the model space. In general, commutators between operators that do not commute with H are not preserved under projection into the model space. An important example of this is the commutator of the position and momentum operators.

A.4 Implications

We have given a very brief introduction to the basic concepts of model spaces, effective Hamiltonians, and effective operators. If the canonical $\hat{k}$ operator is used then in most cases model-space calculations work as expected. In particular, effective Hamiltonians are Hermitian and obey the symmetries of the full Hamiltonian. Hermitian operators give rise to Hermitian effective operators. Also, in a perturbation expansion using the Rayleigh-Schrödinger formalism, these properties are preserved order by order. The ability to construct effective Hamiltonians and effective operators that are Hermitian, and obey symmetries order by order in perturbation theory, is essential to applying symmetry arguments to determine the necessary effective operators. For example, in Chapter 1 we see that the crystal-field parameters B_q^k for $4f^N$ are only non-zero if k is even.

Many misconceptions permeate the literature surrounding the use of effective-operator (i. e. crystal-field) calculations in rare earth and actinide systems. We are now in a position to discuss some of these.

It is sometimes claimed that the crystal field model works for 4f-electron systems because the 4f orbitals do not mix strongly with the ligand states. This is not the case. An effective-Hamiltonian treatment will work even in the situation of large mixing with ligands (as in the case of the 5d orbitals of the $4f^{N-1}5d$ configuration). Consider, for example, an ion with one p electron and a single ligand on the Z axis. The p_z orbital may be strongly mixed with the ligand orbitals, whereas the p_x and p_y orbitals may be essentially pure p. From a molecular-orbital point of view this mixing will change the energy of the p_z-plus-ligand orbital relative to the other atomic orbitals. From a crystal-field point of view there would be a single parameter (B_0^2) governing this splitting. Both molecular-orbital and crystal-field pictures predict a splitting of the states. The magnitude of the mixing between the p_z and ligand orbitals can not be determined by merely measuring the energy-level splittings, but only from some other type of measurement, sensitive to the mixing, or from first-principles calculations.

Conversely, the fact that crystal-field fitting provides a satisfactory phenomenological model for rare earths and actinides is sometimes taken as evidence that the mixing with ligands is small, or that a simple point-charge calculation is adequate to explain the crystal field. This is also a flawed argument since the crystal-field model makes use only of symmetry to determine which parameters are non-zero. The sizes of the parameters must be compared to first-principles calculations if we want to know the size of various contributions point-charge, overlap, covalency, etc. (Ng and Newman, 1987; Newman and Ng, 2000) to the splittings.

For intensity calculations (Chapter 2) Eq. (A. 17) is used to calculate the dipole moment operator. Zero-order denominators, constant for each configuration, such as $4f^N$ or $4f^{N-1}5d$ appear in the calculation. This is often referred to as "closure". It is seen here to arise naturally from the perturbation expansion, rather than something that has to be imposed. Higher-order terms

will, of course, modify the effective operators. These modifications could be interpreted as " correcting " the " closure assumption " of degenerate configurations. However, we prefer to think of them as simply higher-order terms in the perturbation expansion.

References

Brandow, B. H. Rev. Mod. Phys. **39**, 771 (1967).
Bryson, A. R., M. F. Reid. J. Alloys Comp. **275/277**, 284 (1998).
Duan, C. K., M. F. Reid. J. Alloys Comp. **323/324**, 726 (2001).
Hurtubise, V., K. F. Freed. Adv. Chem. Phys. **83**, 465 (1993).
Hurtubise, V., K. F. Freed. J. Chem. Phys. **100**, 4955 (1994).
Naguleswaran, S., M. F. Reid, G. E. Stedman. Mol. Phys. **101**, 917(2003).
Newman, D. J., B. K. C. Ng. *Crystal Field Handbook* (Cambridge University Press, Cambridge, 2000).
Ng, B., D. J. Newman. J. Chem. Phys. **87**, 7110 (1987).

Appendix B Matrix Elements of Tensor Operators

M. F. Reid

Many of the calculations described in this book rely on the use of angular-momentum theory and group theory. There are a number of books available that give a complete introduction to angular-momentum calculations (Judd, 1963; Wybourne, 1965; Weissbluth, 1978; Lindgren and Morrison, 1986). The aim of this appendix is to give a brief introduction to allow the reader to make sense of the calculations described in Chapters 1 and 2.

B. 1 Angular Momentum States and Operators

The essential concepts of angular momentum in quantum mechanics may be derived from considering basic angular momentum operators their eigenstates and their commutators. We begin with the general angular-momentum operators J_x, J_y and J_z, with well-known commutation relations

$$[J_x, J_y] = iJ_z, \tag{B.1}$$

and cyclic permutations (we have set $\hbar = 1$). The operator $J^2 = J_x^2 + J_y^2 + J_z^2$ commutes with each of the, J_x, J_y, and J_z operators and it is traditional to use the simultaneous eigenstates of J^2 and J_z^2 as basis functions in atomic calculations. These basis states are labeled $|jm\rangle$ and have the following properties:

$$J_z|jm\rangle = m|jm\rangle, \tag{B.2}$$

$$J^2|jm\rangle = j(j+1)|jm\rangle, \tag{B.3}$$

$$D(R)|jm\rangle = \sum_{m'} D^{(j)}_{m'm}|jm'\rangle \tag{B.4}$$

where the last equation describes the behavior of the states under the rotation R, with $D(R)$ being the operator and $D^{(j)}_{m'm}$ the rotation matrix for a particular j.

B. 2 Clebsh-Gordan Coefficients and 3-j Symbols

The coupling of angular momenta is a key concept that we require for any serious calculation. We may be coupling spin and orbital angular momentum, or the

angular momenta of two electrons. In either case, the idea is to create a linear combination of angular-momentum states that behave as an angular-momentum state, as defined by Eqs. (B. 2) – (B. 4). This is accomplished by the Clebsh-Gordan coefficients (sometimes called coupling coefficients) defined by

$$|jm\rangle = \sum_{m_1,m_2} |j_1 m_1\rangle |j_2 m_2\rangle \langle j_1 m_1, j_2 m_2 | jm\rangle. \qquad (B.5)$$

It is often convenient to use the more symmetrical 3-j symbol, defined by

$$\begin{pmatrix} j_1 & j_2 & j_3 \\ m_1 & m_2 & m_3 \end{pmatrix} = (-1)^{j_1 - j_2 - m_3} \frac{1}{\sqrt{2j_3 + 1}} \langle j_1 m_1, j_2 m_2 | j_3 - m_3 \rangle. \quad (B.6)$$

In the derivation of selection rules (Chapters 1 and 2) the properties of the 3-j symbols play a key role. The 3-j symbol is zero unless $m_1 + m_2 + m_3 = 0$, $|m_1| < j_1$, $|m_2| < j_2$, $|m_3| < j_3$, and j_1, j_2 and j_3 form a triangle ($|j_1 - j_2| \leqslant j_3 \leqslant j_1 + j_2$).

B. 3 Tensor Operators and the Wigner-Eckart Theorem

Tensor operators have angular-momentum quantum numbers, just like angular-momentum states. A tensor operator $T_q^{(k)}$ may be defined by its commutation relations, such as

$$[J_z, T_q^{(k)}] = qT_q^{(k)}, \qquad (B.7)$$

or by its behavior under rotations

$$D(R) T_q^{(k)} D(R)^\dagger = \sum_{q'} D_{q'q}^{(k)} T_{q'}^{(k)}. \qquad (B.8)$$

The latter equation emphasizes that the transformation properties of tensor operators and state kets are intimately related.

The matrix elements of tensor operators may be written in terms of the 3-j symbols as

$$\begin{aligned} &\langle \alpha JM | T_q^{(k)} | \alpha' J' M' \rangle T_q^{(k)} | \alpha' J' M' \rangle \\ &\quad = (-1)^{J-M} \begin{pmatrix} J & k & J' \\ -M & q & M' \end{pmatrix} \langle \alpha J \| T_q^{(k)} \| \alpha' J' \rangle. \end{aligned} \qquad (B.9)$$

The final braket on the right hand side is known as a reduced matrix element. The key concept of the Wigner-Eckart theorem is that the "angular dependence" on the M quantum numbers is decoupled from the "physical" dependence of the

reduced matrix element.

The properties of the 3-j symbols discussed in the previous section give important selection rules on these matrix elements. For example, one-electron operators within the $4f^N$ configuration must have $k \leqslant 6$.

B.4 More Complex Situations

The calculations in Chapters 1 and 2 involve complicated angular momentum couplings of the $4f^N$ configuration, based on techniques pioneered by Racah over 50 years ago and discussed in detail in various books (Judd, 1963; Wybourne, 1965; Weissbluth, 1978; Lindgren and Morrison, 1986). We do not reproduce here all the equations involving the 3-j, 6-j and 9-j symbols, but emphasize that in principle the tools (and computer programs) exist to carry out such calculations. Thus we are free to concentrate on the physical meaning of the results.

As an example, we consider the one-electron $4f^N$ operators required for the crystalfield calculations of Chapter 1 and the intensity calculations of Chapter 2. The commonly-used states are labeled by the $\alpha SLJM$ quantum numbers, where α are extra labels required in complex configurations which may have several states with the same S and L. Reduced matrix elements of the unit tensor operators $\boldsymbol{U}^{(k)}$ may be found in the tables of Nielson and Koster (1963) or in computer data files (see Appendix 3). These reduced matrix elements are at the SL level $\langle \alpha Sl \| \boldsymbol{U}^{(k)} \| \alpha' S' L' \rangle$. To obtain reduced matrix elements at the J level we must apply the Wigner-Eckart theorem in the following form (Judd, 1963; Weissbluth, 1978)

$$\langle \alpha SLJ \| \boldsymbol{U}^{(k)} \| \alpha' S' L' J' \rangle = \delta(S,S')(-1)^{S'+L'+J+k} \sqrt{(2J+1)(2J'+1)} \times \begin{Bmatrix} J & k & J' \\ L' & S & L \end{Bmatrix} \langle \alpha SL \| \boldsymbol{U}^{(k)} \| \alpha' S' L' \rangle. \quad \text{(B.10)}$$

Eqs. (B.9) and (B.10) may be combined to obtain an expression for $\langle \alpha SLJM \| \boldsymbol{U}_q^{(k)} \| \alpha' S' L' J' M' \rangle$.

The crystal-field parametrization used in Chapter 1 uses the spherical tensor operators $C_q^{(k)}$, rather than the unit tensor operators. However, the matrix elements are simply related and to the matrix elements of the $C_q^{(k)}$ within the $4f^N$ configuration are obtained from matrix elements of the $\boldsymbol{U}_q^{(k)}$ by multiplying by

$$(-1)^l (2l+1) \begin{pmatrix} l & k & l \\ 0 & 0 & 0 \end{pmatrix}, \quad \text{(B.11)}$$

with $l = 3$ for 4f electrons.

The spherical tensor operators differ from spherical harmonics by only a factor of $\sqrt{4\pi/(2k+1)}$. The lowest-rank spherical tensor operators may be

written in cartesian form as

$$
\begin{aligned}
C_0^{(0)} &= 1 \\
C_0^{(1)} &= z \\
C_{\pm 1}^{(1)} &= \mp \sqrt{\frac{1}{2}}(x \pm \mathrm{i}y) \\
C_0^{(2)} &= \sqrt{\frac{1}{4}}(3z^2 - r^2) \\
C_{\pm 1}^{(2)} &= \mp \sqrt{\frac{3}{2}} z(x \pm \mathrm{i}y) \\
C_{\pm 2}^{(2)} &= \sqrt{\frac{3}{8}}(x \pm \mathrm{i}y)^2 .
\end{aligned}
\qquad \text{(B.12)}
$$

These expressions are often useful for working out selection rules and symmetry operations.

References

Judd, B. R., *Operator techniques in optical spectroscopy*(McGraw-Hill, 1963).

Lindgren, I., J. Morrison. *Atomic Many-Body Theory*(Springer-Verlag, Berlin, 1986).

Nielson, C. W., G. F. Koster, *Spectroscopic coefficients for the p^n, d^n and f^n configurations* (M. I. T. Press, 1963).

Weissbluth, M., *Atoms and Molecules* (Academic Press, New York, 1978).

Wybourne, B. G., *Spectroscopic properties of rare earths* (Wiley-Interscience, New York, 1965).

Keywords Index

absorption cross section 96, 97, 269, 302, 322, 323, 325, 328, 332, 336, 340, 437,443,444,449,451,466
adiabatic representation 131
Afterglow 519,524
angular momentum 4,7,11,13,16,29, 32,66,67,72,74,478,537,539
antenna effect 462,465
anti-shielding 68,71,77
bioassays 463
branching ratio 96,299,332,336,338, 360,365,433,434,437
calixarene 484,497
charge compensation 195,196,213,222, 242,344,420,526
charge-transfer radiation 507
charge-transfer state 58,101,122,504
chelate 463,479,486–489,491
configuration interaction 15, 16, 24, 48–50,60,496
constants 130
cooperative effect 279,281
cooperative luminescence 277,278,281, 284,285,312,313,315
cooperative states 211,212
coordination compound 462
coronand 473
Coulomb interaction 3,4,7,11,16,47, 50,59,60,103,119,120,121,123,140, 268,269,477
coupling constant 5,87,130,139–144, 151, 158, 161, 164, 168, 169, 171, 175, 177,181,184,185,272
cross-relaxation 185,266,268,275,296, 298, 299, 307, 309, 310, 327, 350, 360, 365,366,368,435,436,449,451,512,517
cross section 96, 269, 302, 303, 306, 322,323,325,326,328–336,340,342, 344,347–349,351–353,356,357,364, 366,369–371,433,437,443,444,449, 451,466,528
cryptate 466,483,488,489
crystal-field analysis 40,50,51
crystal-field Hamiltonian 28–30, 38, 39,41,42,44,46,47,50,56,60,104,106
crystal-field interaction 1, 4, 26, 28, 30–32,38,41,46,48–50,52–54,60,71
crystal-field parameters 23, 24, 27, 28, 30,34,36–42,44–46,48,50,54–56, 61,62,69,87,107,111,112,118,139,535
crystal-field spectrum 54
crystal-field splitting 3,24,27,29–31, 37–39,47,50,51,62,66,68,102,222, 339
crystal-field theory 2–4,27,37,47,48
data processing 379
Debye-Waller factor 149,151
density matrix 130,145–147,149
dephasing 175, 176, 204–211, 214, 227, 228, 232, 233, 236, 240, 242, 243, 245,255,256,313,379–385,388–394, 396,397,399–404,406–411,413,414, 416,417,419,420,422,425
descent-of-symmetry 34,36
diketonate 462,463,481,486
dipole-dipole mechanism 469,478
ditopic ligand 485
down-conversion 266,268,275,315
dual-label 489
dynamical crystal field 130,166,168
effective operator 3,4,6,11,12,15–17,23,27,28,30,37,47,54,83,102–106,110,111,124,125,530,531,533–536
effective-operator Hamiltonian 3,4,11, 16,17,24,41,43,48,50,57,59,87

eigenstate 7, 83, 106, 122, 123, 126, 530 – 534, 537
eigenvector 11, 106, 111
electric dipole 51, 52, 54, 60, 69, 96 – 100, 105, 106, 109, 110, 113, 124, 126, 150, 166 – 168, 270, 284, 333, 384, 393, 397, 426, 434, 465, 478
electric quadrupole 68 – 70, 72 – 76, 78, 80, 85, 96, 110
electron correlation 46, 47, 125
electronic interactions 2 – 6, 27, 41
electronic structure 1, 26, 41, 350, 450
electronic transition 1, 2, 37, 50, 61, 64, 72, 74, 88, 102, 122, 132, 150, 158, 170, 192, 197, 204, 208, 216, 226, 447, 449, 465
electron nuclear interaction 64, 67
electron-phonon coupling 133, 137, 149, 154, 156 – 158, 160, 169, 185, 273, 342
electron-phonon interaction 130, 131, 133, 137 – 141, 145, 147, 148, 150 – 155, 159, 160, 163, 166, 167, 169 – 171, 174, 180, 182, 185, 186, 205, 251, 254, 255, 257
electron transfer 469, 472, 496
electrostatic interaction 7, 11, 12, 30, 38, 41 – 44, 46, 271, 272
energy back transfer 475
energy diffusion 267 – 269, 278, 280
energy-gap law 159
energy transfer 54, 159, 185, 200, 208, 210, 211, 217, 266 – 280, 288, 309, 312, 314, 325, 327, 328, 333, 350, 356 – 361, 363, 365, 366, 368, 371, 433 – 436, 445, 449, 451, 452, 462, 463, 465 – 468, 470, 474 – 480, 484, 488, 490, 491, 507, 508, 525
erbium doped fiber amplifier 430
exchange charge model 27, 41, 42, 45, 130, 140, 141, 145, 157, 168 – 170, 175, 184, 185
exchange interaction 38, 211, 270 – 272
exchange mechanism 469, 478
excitation-induced frequency shift 208, 209, 235, 238
excited-state absorption 326, 423
fiber laser 295, 296, 431, 443, 452, 460
fluorescence line-narrowing 202, 205, 215, 273
fluoroimmunoassay 463, 483, 485 – 489, 491, 496
Franck-Condon integral 149
free-ion Hamiltonian 13, 15, 17, 30, 37, 47, 50, 59, 108
free-ion interaction 3, 4, 11, 13, 16 – 18, 21, 23, 27, 31, 41, 48, 54, 56, 59
free-ion splitting 3, 60
gated holeburning 381, 398
grating 215, 236, 238, 329, 381, 390, 397, 443, 501
harmonic approximation 133, 134, 177
holeburning spectroscopy 379, 381
homogeneous broadening 192, 193, 202, 204, 212 – 214, 239, 273
homogeneous line width 64, 88, 89, 448
Huang-Rhys parameter 150, 160, 166
hydroscopic behavior 519
hyperfine interaction 4, 64, 65, 67, 68, 70, 72, 73, 77, 81, 85 – 89, 201, 202, 214, 221, 230, 234, 249, 393, 421, 422
hyperfine splitting 3, 64, 67, 68, 74, 76, 77, 86 – 89, 184, 192, 199, 202, 214, 216, 220, 235, 236, 249, 380, 385, 388, 391, 396 – 398, 423, 425
hyperfine structure 3, 72, 74, 89, 176, 184, 202, 203, 219, 236, 380, 385, 388, 391, 394, 395, 397, 398, 400, 425
inhomogeneous broadening 64, 122, 192 – 194, 196, 201, 205, 214, 216, 225, 251, 252, 257, 273, 321, 447
instantaneous spectral diffusion 382, 384, 390, 391, 399
intermediate coupling 7, 11, 17, 18, 55, 56, 71, 78
intersystem crossing 463, 466, 469, 475, 476, 496
ion displacement 134, 135, 147, 149, 151, 152, 154, 167, 182
ion-lattice interaction 2, 130, 131, 151, 152, 165, 166, 185
ion-ligand hyperfine interaction 3, 72
ion-ligand interaction 4, 27, 41, 89
ion-phonon interaction 46, 130, 131, 145, 170, 205
IR imaging 312
irreducible representation 8, 43, 98, 167, 174, 182
isotope shifts 89, 201, 202
J-mixing 30, 56, 65, 82, 465
Judd-Ofelt formalism 336, 337, 340
Judd-Ofelt model 120
Judd-Ofelt theory 434

laser amplifiers 320
laser efficiency 321,322,349
laser threshold 294,311,323,330,334, 335,347 – 351,356,359,360,363,367, 370,371
lattice deformation 138,143,160,168
lattice vibration 1, 130, 133, 134, 136, 139,141,148,152,157,166,168,172,185
least-squares fitting 18,23,38,54,55,84
ligand 1,2,27,32,35,36,38 – 45,47, 58,64,70,72,74,87 – 89,91,95,102, 103,105,107,112,114 – 120,123,124, 140,141,151,154,155,160,162 – 164, 167,168,170 – 173,183,446,447,462, 463,465,467 – 469,473 – 478,480 – 491, 496,504,532,535
ligand-to-metal charge transfer 473,496
ligand-to-metal energy transfer 474
light emitting diode 288,491
line shift 130,148,167
line strength 96,97,99,106,111
localized electronic state 64
LS coupling scheme 7 – 10,17,65
luminescent probe 463, 464, 476, 477, 486,490,491
macrocycle 483,484,489
magnetic dipole 5, 87, 89, 96 – 99, 108 – 114,150,166 – 169,209,220,333, 383,384,421
magnetic relaxation 145
metal complexes 486
multiphonon relaxation 131,158 – 160, 163,164,177,333,368
nanocrystals 186,251,252,255 – 257
nanostructure 238,430,458
nephelauxetic effect 47,139,446
nonradiative deactivation 469,470,484
nonradiative transition 130, 149, 155, 160,162,170,173,177,180,181
Nuclear electric quadruple interactions 76
nuclear quadrupole splitting 77,80,82
ODNMR 74,78,80,83 – 85,87 – 89, 388,398
one-electron operator 5,41,47,56,103, 121,539
one-photon transition 95,102,124,280
optical confinement 295,311,455
optical data storage 379,382,399
optical free induction decay 227,229
optical storage 191,224,243,248,251, 379 – 381,384,393,399,462
optical transition 64, 89, 95, 98, 100, 145,151,155,166,182,192 – 195,200 – 204,213,215,220,224 – 226,228,230, 244, 252, 333, 337, 350, 351, 393, 400, 413,422
opto-geometrical parameters 431,432
oscillator strength 97, 246, 271, 304, 338,380,382,385 – 387,395,397,401, 402,406,410,412,422,424 – 426,470, 478
parameterization 18, 24, 27, 37, 38, 46 – 48,50,56,57
persistent spectral hole burning 220, 379,422,423
phase-matching condition 334,347,348
photo-induced electron transfers 472
photoionization 123, 205, 220, 222 – 224,249,398,422,423
photon avalanche 266, 267, 296, 297, 302,306,308,310,435,436
photon echo 85,88,89,205,208 – 210, 215,230,232 – 238,256,257,383,388, 389,392,394,397,398,400,402 – 404, 406 – 409,411,413,416,418 – 420,424, 425
photorefractivity 431,442
photosensitivity 431,442,443
photostimulated luminescence 501,515, 516
pseudoquadrupole interaction 71
Q-switching 324,352,363
quantum counter 267
quantum efficiency 322,323,344,365, 422,435,437,442
quantum yield 333,339,462 – 465,470, 473,476,477,479 – 485,487,489
quenching 82,200,276,292,315,333, 358,360,435,442,444,445,453,469 – 475,483,486,526,527
radiative lifetime 96,98,209,257,322, 323,334 – 336,338 – 340,437,445
Raman process 206,207,382,392,448
Raman scattering 95,124,125,154,182, 192,208,229,243,245,253,254
RE-doped optical microcavities 430
relativistic effect 15,16,22
relaxation broadening 173,182,184
selection rule 37, 51, 52, 54, 98, 100, 109, 112, 114, 123, 169, 205, 213, 336,

337,343,465,478,523,534,538 – 540
self-assembly 485
self-frequency doubling 346, 347, 353, 369
self-quenching 268,275,276,360
sensitization 277, 279, 281, 286, 465, 474,482 – 484,487,489,491
signal processing 379 – 382, 384, 399, 421,430
site-selective spectroscopy 197,199,216
slater parameter 60,140,151
solid-state lasers 1,349,377
spectral density 135, 136, 148, 162 – 164,166,173
spectral diffusion 89,211,214,217,220, 225, 230, 233, 236, 238, 249, 256, 382, 383,389 – 394,400,417 – 419,424,425
spectral function 158
spectral hole burning 74, 77, 78, 80, 85 – 89,156,194,199,202,205,214,215, 218, 220, 223, 224, 236, 244, 249, 253, 255,379,422
spin flip-flops 233,383
spin-lattice relaxation 144, 145, 155, 186,385
spin-orbit coupling 3, 4, 6, 10, 11, 14, 52,68,109,337
spin-orbit interaction 3,5,7,9,14 – 16, 18,59, 60, 103, 121, 123, 125, 139, 140, 532
spin-spin interaction 208,209,213
spontaneous emission 98,153,166,298, 311,321,334,338,433,441,455,470,479
Stark shift 225
stimulated emission 322,323,325,329, 332,334, 340, 344, 349, 351 – 353, 356, 366,370,433,437,443,444
stimulated photon echoes 389,393,399
superposition model 27, 41, 45, 105, 107,108,112,116,119,120,140
thermally stimulable phosphors 514
time-domain spectroscopy 227
time-resolved microscopy 491
transition probability 102,147,148,150, 154,160 – 164, 167, 168, 180, 181, 270, 360,385
triplet state 462 – 469, 475 – 477, 479, 481 – 484
two-dimensional image 399,523
two-phonon Transition Rate 153
two-photon transition 51, 54, 95, 122, 126
two-step excitation 53,91,344,358,450
up-conversion 1, 266, 267, 276 – 283, 286 – 296,304,306 – 308,310 – 316,318, 325 – 328, 345, 350, 356, 357, 363, 364, 368,430, 433, 435, 444 – 446, 449, 451, 452,484
UV laser 312,340,343,344,369,376
UV tunable lasers 311
vibration 101, 102, 109, 116, 123, 159, 465,469,475
vibronic band 61,102,123,169
vibronic sidebands 152,166 – 169,203, 204
vibronic transition 95, 100, 101, 109, 116,166,168
wave function 2,3,5 – 7,10,11,17,39, 40, 43, 44, 52, 55, 65, 67, 72, 87, 102, 132 – 134, 137, 138, 142, 148, 149, 151, 280,284,478
waveguide 239, 246, 308, 357, 430 – 432,435 – 439,441 – 444,453,454,457, 458
Wigner-Eckart theorem 11,17,28,114, 538,539
X-ray imaging material 500
X-ray phosphor 500 – 504, 508 – 513, 518,519,521
Zeeman effect 4,51,52,64 – 68,73,82, 85 – 87,216,224
zero-phonon line 61,102,109,116,123, 148,151,168,192,195,196,203 – 205, 224,247 – 249,422,434
zero-phonon transition 158, 222, 248, 249

Materials Index

Ce^{3+} 58, 61, 170, 195, 321, 340, 343, 350, 357, 369, 473, 516, 524 – 527
-in BaFCl 170, 516
-in BaFX phosphors (X = Cl, Br) 516
-in CaF_2 60
-in Gd_2SiO_5 526, 527
-in $LiLuF_4$ (LLF) 343, 345
-in $LiCaAlF_6$ (LiCAF) 342 – 344
-in $LiLuF_4$ 312, 345
-in LiSAF 342 – 344
-in $LiYF_4$ 60, 156
-in Lu_2SiO_5 527
-in silica 443
-in $Y_3Al_5O_{12}$ 521
-in Y_2O_3 252
-in YPO_4 60
-in Y_2SiO_5 527
CeF_3 524 – 526
Ce_2O_2S 140, 513
Ce^{4+} 194, 526

Dy^{2+} 194
Dy^{3+} 157, 197, 288, 364, 464, 471, 489, 508, 522
-in CaS 514
Dy_2O_2S 140, 513
Dy^{3+}-Er^{3+} 288

La^{3+} 84, 479, 511
$Ba_{1-x}La_xF_{2+x}$ 243
$KLaF_4$ 221
$LaBGeO_5$ 347
$La(OH)_3$ 512
$La(OH)_2Br$ 512
$LaPO_4$ 252
La_2O_2S 513
$La_{1-x}Nd_xP_5O_{14}$ 276
$LaMgAl_{11}O_{19}$ (LMA) 372
$Na_5La(WO_4)_4$ 168, 169
$MALaF_6$ (M = Ca, Sr; A = Na, K, Rb) 245

Lu^{3+} 509
$LuPO_4$ 343
$LuVO_4$ 333
Lu_2O_3 509, 527
Lu_2O_2S 513

Er^{3+} 1, 89, 150, 173, 180, 196, 201, 220, 233, 276, 288, 307, 339, 355, 385, 417, 420
-in $BaCl_2$ 288
-in $Ba(Y,Yb)_2F_8$ 293
-in CaF_2 60, 293, 368, 369
-in $CaWO_4$ 420
-in cesium-cadmium bromide 170
-in $Cs_2Na_2YCl_6$ 116
-in ErX_3 (X = Br, I) polycrystalline phosphors 516
-in fluoride glass 302, 306, 368
-in KYF_4 294
-in LaF_3 233, 411
-in $LiNbO_3$ 357, 358, 416 – 418, 421
-in $LiYF_4$ 89, 175, 176, 196, 220, 225, 226, 228, 229, 233, 292, 302, 383, 411
-in phosphate glasses 320, 355
-in $SrWO_4$ 412
-in Tungstates 420
-in vitroceramics 282
-in $WO_4Na_{0.5}Yb_{0.5}$ 314
-in $YAlO_3$ 234, 411, 417, 418, 420
-in $Y_3Al_5O_{12}$ 368, 419, 420
-in YF_3 282, 421
-in Y_2O_3 196, 252, 416
-in $Y_3Sc_2Ga_3O_{12}$ (YSGG) 368
-in $YScO_3$ 196
-in Y_2SiO_3 380
-in Y_2SiO_5 233, 380, 381, 412, 416, 417,

421
-in ZBLAN 307,308,311
Er-Er 229
Er-Yb 279,286 – 288,291,293,315
PbF_2-GeO_2-YbF_3-ErF_3 288
$Y_{0.85}Er_{0.15}O_2S$ 281

Eu^{2+} 31,125,158,169,170,194,220 – 222,249,250,422,423,473,511,516,517
-in BaF_2 205
-in BaFBr 511,514 – 517
-in BaFCl 500,501,510,511
-in BaFI 511
-in CaF_2 222,248,250,422,428
-in CaS 222,224,423
-in CdF_2 250
-in $KMgF_3$ 204
-in MgS 423
-in SrF_2 169,423
-in SrFBr 511
-in SrFCl 511
-in ZnS 251

Eu^{3+} 56,64,70,76 – 83,85,109,112, 169, 192, 195, 222, 235, 249, 253, 254, 380,384,393,423,464,473,481,490,516
-in BaFBr 511,514 – 517
-in BaFCl 424,500,510,511
-in BaFI 511
-in CaF_2 60,77,200
-in Gd_2O_2S 140
-in fluorophosphate glass 217,241
-in Gd_2O_2S 140
-in KY_3F_{10} 112,113,115
-in LaF_3 76 – 79,82,83,85,255
-in LaOCl 139
-in $LiYF_4$ 77 – 79,80,156,169
-in $M'YTaO_4$ 507
-in $YAlO_3$ 77,198,199,207,233,238, 384,393,394
-in Y_2O_3 241,252,253,255,384,391 – 393,409,411,462
-in Y_2O_2S 521
-in $(Y_{1-x}Gd_x)_2O_3$ 521,522
-in YPO_4 60
-in $Y_{2-2x}Sc_{2x}O_3$ 241
-in Y_2SiO_5 201,205,207,218,232,252, 305,381,384,386 – 389,391,396,397
$[Eu\subset(\mathbf{10a})]^{3+}$ 484
$[Eu\subset(\mathbf{10b})]^{3+}$ 484
$[Eu(\mathbf{16}-H)_2]^+$ 485
$[Eu(\mathbf{16c}-2H)_2]^+$ 485
$[Eu(\mathbf{17a})_3]^{6+}$ 485
$[Eu(\mathbf{17b})_3]^{6+}$ 486
$[Eu(\mathbf{17c}-2H)_3]$ 485
$[Eu_2(b-LH_2)(DMF)_5]\cdot 4DMF$ 473
$[Eu\subset(bpy.\,bpy.\,bpy)]^3$ 483
$Eu(CD_3CO_2)_3$ 472
$EuCl_3$ 509
$EuCl_3:6H_2O$ 201
Eu-Eu 422,474
$[Eu(\mathbf{H23})]^+$ 490
$[Eu(mbzimpy)_3](ClO_4)_3$ 480
$Eu(NO_3)(mbzimpy)$ 479,480
Eu_2O_3 252,253,522
Eu_2O_2S 513
EuP_5O_{14} 77,78
Eu^{3+}-Tb^{3+} 489
Eu_xTaO_4 507
$EuVO_4$ 77,78,83,199
$Na[EuL_2]$ 481
Y_2O_3-Gd_2O_3-Eu_2O_3 522

Gd^{3+} 30,31,122,125,158,169,350, 422,464,505,513,521,526,527
-in $LiYF_4$ 156
-in LaOBr 512
$CaGd_4(BO_3)_3O$(GdCOB) 347,351
$CaY_4(BO_3)_3O$ 351
$[Gd(acac)_3]$ 466
GdCOB 348,353
Gd_2O_3 514,521,522
Gd_2O_2S 510,513,522
$Gd(OH)_3$ 212
Gd_2SiO_5 525,526
$GdVO_4$ 333
$KGd(WO_4)_2$ 351
$(YGd)_2O_3$ 521
Y_2O_3-Gd_2O_3 522
$(Y,Gd)_3(Al,Ga)_5O_{12}$ 521
[Gd(Ⅰ)] 526
[Gd(Ⅱ)] 526

Ho^{3+} 47,48,88,89,142,157,173,175, 196,202,295,309,364
-in CaF_2 89,202

-in cesium-cadmium bromide 170
-in $Gd_2Ga_5O_{12}$ 301

-in $LiYF_4$ 89
-in $Y_3Al_5O_{12}$ 365
Ho_2O_2S 140,513
Ho^{3+}-Tm^{3+} 301,309
Ho-Yb 293
$LiHoF_4$ 145

Nd^{2+} 58
-in $Y_3Al_5O_{12}$ 369
Nd^{3+} 2,13,47,58,117,150,173,180,201,213,249,297,321,332,341,369,381,424,434,484
-in CaF_2 213,243
-in $CaGd_4(BO_3)_3O$-YF_3 243,348
-in cesium-cadmium bromide 170
-in GdCOB 349
-in $LaCl_3$ 46,139
-in LaF_3 117,249,293,312,343,424,425
-in $LiNbO_3$ 347,348
-in $LiTaO_{34}$ 348
-in $LiYF_4$ 156,191,301
-in $Sr_5(VO_4)_3F$ 152,156
-in YAB 348,349
-in $Y_3Al_5O_{12}$ 1,48,49,115,117,231,291,320,332,333,342,343,345,454
-in Y_2SiO_5 386,397
-in YLF 333
-in Y_2O_3 117
-in Y_2SiO_5 386,397
-in YVO_4 320,333,424,425
NdF_3 241,246
NdP_5O_{14} 291
Nd_2O_2S 140,513
Nd-Nd 425

Pr^{2+} 23,58
Pr^{3+} 23,30,48,58,64,73,89,121,157,168,183,197,202,213,222,241,256,281,295,296,340,344,350,364,380,394,396,397,410,421,456,522
-in CaF_2 243
-in BaFX phosphors (X = Cl,Br) 516
-in cesium-cadmium bromide 170
-in $CsCdCl_3$ 152
-in $CsCdBr_3$ 176,184
-in Gd_2O_2S 523
-in KY_3F_{10} 344
-in $LaAlO_3$ 115
-in $LaCl_3$ 73,74,139,296,297,310
-in LaF_3 73,74,83,200,202,214,216,220,234,235,256,281,283,394,399
-in $LiYF_4$ 115,156
-in PrF_3 281
-in silica glass 243,301
-in SrF_2 74
-in YAG 224,234,242,398
-in $YAlO_3$ 235-238,394-398
-in YLF 344
-in Y_2O_3 241
-in YPO_4 40
-in Y_2SiO_5 380,394,395,397
-in YSZ 242
-in ZBLAN 311
Pr_2O_2S 140,513
Pr^{3+}-Yb^{3+} 311
Pr^{4+} 8

Sm^{2+} 58,89,144,154,158,169,192,224,247,249
-in BaClF 223,224,243
-in $BaFCl_{0.5}Br_{0.5}$ 224
-in BaFX phosphors (X = Cl,Br) 516
-in CaF_2 224,249,320
-in $Ca_{0.5}Sr_{0.5}FCl$ 245
-in CaClF 224,245
-in MFCl 139
-in $Sr_{0.65}Ba_{0.35}FCl_{0.5}Br_{0.5}$ 245
-in $Sr_xCa_{1-x}FCl$ 251
-in $SrFCl_xBr_{1-x}$ 199,245,251
-in SrF_2 224,320
-in SrFCl 140,224
-in ZnS 224
-in Y_2O_3 252
Sm^{3+} 58,157,244,251,464,473,488,489,522
Sm_2O_2S 140,513

Tb^{3+} 30,50,56,61,87,89,157,211,243,358-361,384,464-466,474,482-486,507,512
-in BaFX phosphors (X = Cl,Br) 500,516
-in Gd_2O_2S 500,513,514,521
-in $GdTaO_4$ 500,505
-in LaF_3 54,55
-in LaOBr 500,512,513
-in $LiTbF_4$ 56

-in $LiYF_4$ 51 – 57, 61, 66, 85, 86, 88, 156, 361, 363, 384
-in Mg_2SiO_4 514
-in $Y_3Al_5O_{12}$ 292
-in YPO_4 60
-in $YTaO_4$ 507
-in Y_2O_3 252
-in Y_2O_2S 513
$LiTbF_4$ 51, 54, 145, 211
$M'YTaO_4$ 507
$[Tb\subset(2.2.1)]^{3+}$ 466
$[Tb\subset(2.2.1)(acac)]^{2+}$ 466, 467
$[Tb(acac)_3]$ 466
$[Tb_2(b\text{-}L'H_2)_2(DMSO)_4]$ 475
$[Tb\subset bpy.\ bpy.\ bpy]^{3+}$ 483
$[Tb(\mathbf{14}-2H)]^{+}$ 485
$[Tb(\mathbf{17b})_3]^{6+}$ 485
$[Tb(\mathbf{17c}-2H)_3]$ 485
TbGG 26
Tb_4O_7 514
$Tb(OH)_3$ 211
Yb-Tb 280, 281

Tm^{2+} 144, 152, 169
-in CaF_2 60
Tm^{3+} 44, 88, 144, 157, 168, 173, 177, 222, 233, 256, 277, 279, 286, 296, 309, 317, 337, 342, 358 – 360, 380, 384, 399, 407, 421, 434, 450, 513
-in aluminum garnets 407
-in BIGaZYTZr glass 302
-in $Gd_2Ga_5O_{12}$ 301
-in KY_3F_{10} 366, 367
-in LaF_3 383, 400, 407, 410
-in LaOBr 511, 512
-in $LiYF_4$ 156, 361, 363, 364, 366, 367
-in $LuAl_5O_{12}$ 404, 405
-in $Y_{1.5}Lu_{1.5}Al_5O_{12}$ 405
-in $Y_3Al_5O_{12}$ 156, 365 – 367, 379, 380, 400 – 407
-in $YAlO_3$ 301, 409, 410
-in $Y_3Ga_5O_{12}$ (YGG) 406, 407, 409
-in Y_2O_3 362, 366, 367, 409, 411
-in YOCl 168
-in Y_2SiO_5 407, 409
-in $Y_2Si_2O_7$ 400, 408
-in ZBLAN 295
Tm_2O_2S 140, 513
Tm-Tm 404, 407

Yb^{3+}-Tm^{3+} 277, 286, 287, 290, 315, 363

Y^{3+} 36, 112, 144, 171 – 173, 175, 196, 410, 481, 507
-in $LiYF_4$ 170
-in $MAYF_6$ (M = Ca, Sr; A = Na, K, Rb) 245
-in Y_2O_3 196, 240 – 242, 255, 354, 361, 400, 502, 521, 522
BaY_2F_8 361, 363, 368
$CaY_4(BO_3)_3O$ (YCOB) 347, 351
Cs_2NaYCl_6 98, 116
$KY(WO_4)_2$ 197, 351
$M'Y_{1-x}Eu_xTaO_4$ 507, 508
$NaYF_4$ 286
$Na_2Y_3F_{11}$ 286
$Y_3Ga_5O_{12}$ (YGG) 400
$Y_{1.5}Lu_{1.5}Al_5O_{12}$ (YLuAG) 400, 401, 405, 411
YOCl 140, 168, 169
$Y_{2-2x}Sc_{2x}O_3$ or $Y_{2(1-x)}Sc_{2x}O_3$ 242
YSGG 272, 368
Y_2SiO_5 (YSO) 205, 207, 209, 210, 236, 252, 351, 356, 372
YSZ 241
Y_3TaO_7 506
YVO_4 213, 252, 333, 357

Yb^{2+} 170, 194
Yb^{3+} 20, 40, 157, 269, 276, 279, 281, 290, 310, 349, 352, 363, 364, 369, 445, 464, 472, 484, 522
-in CFAP 352
-in $CsCdBr_3$ 184
-in $Cs_3Y_2Br_9$ 313, 314
-in GdCOB 351, 354
-in fluoroindate glasses 217
-in phosphate glasses 285
-in $LiYF_4$ 156
-in KGW 352 – 354
-in MgO: $LiNbO_3$ 349
-in SFAP 353, 354
-in $Y_3Al_5O_{12}$ 351 – 353, 355
-in YCOB 351
-in Y_2SiO_5 352, 354, 355
-in ZBLAN 311
YbGG 26
Yb_2O_2S 140, 513
Yb-Yb 281, 285, 286

Springer Series in

MATERIALS SCIENCE

Editors: R. Hull R. M. Osgood, Jr. J. Parisi H. Warlimont

10 **Computer Simulation of Ion-Solid Interactions**
By W. Eckstein

11 **Mechanisms of High Temperature Superconductivity**
Editors: H. Kamimura and A. Oshiyama

12 **Dislocation Dynamics and Plasticity**
By T. Suzuki, S. Takeuchi, and H. Yoshinaga

13 **Semiconductor Silicon**
Materials Science and Technology
Editors: G. Harbeke and M. J. Schulz

14 **Graphite Intercalation Compounds I**
Structure and Dynamics
Editors: H. Zabel and S. A. Solin

15 **Crystal Chemistry of High-T_c Superconducting Copper Oxides**
By B. Raveau, C. Michel, M. Hervieu, and D. Groult

16 **Hydrogen in Semiconductors**
By S. J. Pearton, M. Stavola, and J. W. Corbett

17 **Ordering at Surfaces and Interfaces**
Editors: A. Yoshimori, T. Shinjo, and H. Watanabe

18 **Graphite Intercalation Compounds II**
Editors: S. A. Solin and H. Zabel

19 **Laser-Assisted Microtechnology**
By S. M. Metev and V. P. Veiko
2nd Edition

20 **Microcluster Physics**
By S. Sugano and H. Koizumi
2nd Edition

21 **The Metal-Hydrogen System**
By Y. Fukai

22 **Ion Implantation in Diamond, Graphite and Related Materials**
By M. S. Dresselhaus and R. Kalish

23 **The Real Structure of High-T_c Superconductors**
Editor: V. Sh. Shekhtman

24 **Metal Impurities in Silicon-Device Fabrication**
By K. Graff 2nd Edition

25 **Optical Properties of Metal Clusters**
By U. Kreibig and M. Vollmer

26 **Gas Source Molecular Beam Epitaxy**
Growth and Properties of Phosphorus Containing III–V Heterostructures
By M. B. Panish and H. Temkin

27 **Physics of New Materials**
Editor: F. E. Fujita 2nd Edition

28 **Laser Ablation**
Principles and Applications
Editor: J. C. Miller

29 **Elements of Rapid Solidification**
Fundamentals and Applications
Editor: M. A. Otooni

30 **Process Technology for Semiconductor Lasers**
Crystal Growth and Microprocesses
By K. Iga and S. Kinoshita

31 **Nanostructures and Quantum Effects**
By H. Sakaki and H. Noge

32 **Nitride Semiconductors and Devices**
By H. Morkoç

33 **Supercarbon**
Synthesis, Properties and Applications
Editors: S. Yoshimura and R. P. H. Chang

34 **Computational Materials Design**
Editor: T. Saito

35 **Macromolecular Science and Engineering**
New Aspects
Editor: Y. Tanabe

36 **Ceramics**
Mechanical Properties, Failure Behaviour, Materials Selection
By D. Munz and T. Fett

37 **Technology and Applications of Amorphous Silicon**
Editor: R. A. Street

38 **Fullerene Polymers and Fullerene Polymer Composites**
Editors: P. C. Eklund and A. M. Rao

Springer Series in

MATERIALS SCIENCE

Editors: R. Hull R. M. Osgood, Jr. J. Parisi H. Warlimont

39 **Semiconducting Silicides**
Editor: V. E. Borisenko

40 **Reference Materials in Analytical Chemistry**
A Guide for Selection and Use
Editor: A. Zschunke

41 **Organic Electronic Materials**
Conjugated Polymers and Low Molecular Weight Organic Solids
Editors: R. Farchioni and G. Grosso

42 **Raman Scattering in Materials Science**
Editors: W. H. Weber and R. Merlin

43 **The Atomistic Nature of Crystal Growth**
By B. Mutaftschiev

44 **Thermodynamic Basis of Crystal Growth**
P–T–X Phase Equilibrium and Non-Stoichiometry
By J. Greenberg

45 **Thermoelectrics**
Basic Principles and New Materials Developments
By G. S. Nolas, J. Sharp, and H. J. Goldsmid

46 **Fundamental Aspects of Silicon Oxidation**
Editor: Y. J. Chabal

47 **Disorder and Order in Strongly Nonstoichiometric Compounds**
Transition Metal Carbides, Nitrides and Oxides
By A. I. Gusev, A. A. Rempel, and A. J. Magerl

48 **The Glass Transition**
Relaxation Dynamics in Liquids and Disordered Materials
By E. Donth

49 **Alkali Halides**
A Handbook of Physical Properties
By D. B. Sirdeshmukh, L. Sirdeshmukh, and K. G. Subhadra

50 **High-Resolution Imaging and Spectrometry of Materials**
Editors: F. Ernst and M. Rühle

51 **Point Defects in Semiconductors and Insulators**
Determination of Atomic and Electronic Structure from Paramagnetic Hyperfine Interactions
By J.-M. Spaeth and H. Overhof

52 **Polymer Films with Embedded Metal Nanoparticles**
By A. Heilmann

53 **Nanocrystalline Ceramics**
Synthesis and Structure
By M. Winterer

54 **Electronic Structure and Magnetism of Complex Materials**
Editors: D.J. Singh and D. A. Papaconstantopoulos

55 **Quasicrystals**
An Introduction to Structure, Physical Properties and Applications
Editors: J.-B. Suck, M. Schreiber, and P. Häussler

56 **SiO_2 in Si Microdevices**
By M. Itsumi

57 **Radiation Effects in Advanced Semiconductor Materials and Devices**
By C. Claeys and E. Simoen

58 **Functional Thin Films and Functional Materials**
New Concepts and Technologies
Editor: D. Shi

59 **Dielectric Properties of Porous Media**
By S.O. Gladkov

60 **Organic Photovoltaics**
Concepts and Realization
Editors: C. Brabec, V. Dyakonov, J. Parisi and N. Sariciftci

61 **Fatigue in Ferroelectric Ceramics and Related Issues**
By D.C. Lupascu